

FIRE **SPALLING** **2019**

Proceedings of the 6th International Workshop on Concrete Spalling due to Fire Exposure

**Sheffield, United Kingdom,
19–20 September 2019**

Scientific Editors:
Dr Shan-Shan Huang
Prof Ian Burgess



**The
University
Of
Sheffield.**

**Department
Of
Civil & Structural
Engineering.**



Proceedings of the 6th International Workshop on Concrete Spalling due to Fire Exposure

The University of Sheffield
Sheffield, UK
19-20 September, 2019

Dr. Shan-Shan Huang (Chair)

The University of Sheffield

Prof. Ian Burgess

The University of Sheffield

Organizer



Published by

The University of Sheffield

ISBN: 978-1-5272-4135-0

Copyright © The University of Sheffield

All rights reserved

Organized by:



Supported by:



Preface

Controlling the susceptibility of concrete to spalling during fire exposure is one of the major issues in the design and construction of concrete structures and infrastructure today.

Real fire scenarios indicate that the fire-induced spalling of concrete is capable of producing serious consequences, and is a phenomenon that should be considered when designing buildings for fire resistance. Recent achievements in concrete mix design have led to new types of concrete which, apart from an increased performance at ambient temperature, have also shown an enhanced sensitivity towards fire spalling. However, the fire spalling of concrete is far from being fully understood, and more research is needed to control its likelihood.

The 6th International Workshop on Concrete Spalling due to Fire Exposure concentrates on real-world experiences and observations, practical applications, experimental and numerical advances, as well as structural design. The aim of the workshop is to obtain an overview of the current level of knowledge, and to stimulate discussion between researchers and structural designers, authorities and code-making bodies, in order to promote a more universal level of understanding. The workshop covers topics such as codes and standardisation, the effect of spalling on fire resistance, modelling, high-temperature testing of concrete, spalling tests and protective measures.

The workshop has been arranged in collaboration with the RILEM TC 256-SPF – Spalling of Concrete due to Fire: Testing and Modelling.

We welcome all participants in the 6th International Workshop on Concrete Spalling due to Fire Exposure.

Scientific Committee

Chair: Dr. Shan-Shan Huang

The Scientific Committee includes the members of RILEM TC 256-SPF – Spalling of Concrete due to Fire: Testing and Modelling

Australia

Dr. Cristian Maluk

Austria

Dr. Johannes Kirnbauer Dr. Matthias Zeiml

Bangladesh

Dr. MD Jihad Miah

Belarus

Prof. Sergei Leonovich

China

Prof. Jianzhuang Xiao

Czech Republic

Dr. Lenka Bodnarova Prof. Ing. Rudolf Hela

Finland

Mrs. Ulla-Maija Jumppanen

France

Dr H�el�ene Carr�e	Dr. Stefano Dal Pont	Dr. Maxime Lion
Prof. Fekri Meftah	Dr. Alain Millard	Dr. Jean-Christophe Mindeguia
Ms. Ing. Berenice Moreau	Dr. Pierre Pimienta	Dr. Ing. Fabienne Robert

Germany

Prof. Dr. Steffen Anders	Dr. Ing. Josipa Bosnjak	Prof. Dr. Ing. Frank Dehn
Prof. Dr. Ing. Ulrich Diederichs	Mr. Michael Juknat	Dr. Manfred Korzen
Mr. Hitesh Lakhani	Dr. Klaus Pistol	Mr. Ludwig Stelzner
Dr. Ing. Frank Weise		

Greece

Associate Prof Kosmas K.Sideris

India

Dr. Umesh Kumar Sharma

Italy

Prof. Roberto Felicetti Dr. Francesco Lo Monte Dr. Ing. Francesco Pesavento

Japan

Dr Associate Prof Mitsuo Ozawa

Poland

Dr. Izabela Hager Ms. MSc. Katarzyna Mróz

Portugal

Prof. Joao Paulo Correia Rodrigues

Slovenia

Dr. Tomaž Hozjan Dr. Jerneja Kolsek

Spain

Dr. Maria Cruz Alonso

Sweden

Dr. Lars Boström Dr. Robert Jansson McNamee

Switzerland

Dr. Benedikt Weber

United Kingdom

Dr. Harris Angelakopoulos	Prof. Luke Bisby	Prof. Ian Burgess
Ms. Jenny Burrige	Dr. Colin T. Davie	Dr. Susan Deeny
Dr. Danny Hopkin	Dr. Shan–Shan Huang	Mr. Tom Lennon
Mr. MSc. Ieuan Rickard	Dr. Bernice Wong	

Organising Committee

Dr. Shan-Shan Huang (Chair), The University of Sheffield

Prof. Ian Burgess, The University of Sheffield

Ms. Tracey McNeilly, The University of Sheffield

Ms. Natalie J Eyre, The University of Sheffield

Table of Contents

Keynotes

Fire spalling theories – Realistic and more exotic ones

*Robert Jansson McNamee
Brandskyddslaget, Sweden*

Experimental investigations into the spalling of high strength concrete and the fire performance of tunnel linings

*Tom Lennon
BRE Group, UK*

Codes and Standardisation

Application of concrete spalling mitigation: a north American perspective

*Kevin Mueller¹, Stephen Stacey², Anthony Bentivegna²
¹ Thornton Tomasetti, USA
² Jensen Hughes, USA*

Spalling Tests

Mitigation of fire-induced spalling of concrete using recycled tyre polymer fibre

*Yifan Li¹, Shan-Shan Huang¹, Kypros Pilakoutas¹, Harris Angelakopoulos², Ian Burgess¹
¹ The University of Sheffield, UK
² Twincon Ltd, UK*

Experimental study of the spalling behaviour of ultra-high performance fibre reinforced concrete during fire

*Martin Schneider¹, Aljoša Šajna²
¹ Carinthia University of Applied Sciences, Austria
² Slovenian National Building and Civil Engineering Institute, Slovenia*

Investigation of size effects in concrete spalling

*André Klimek, Sascha Hothan, Andreas Rogge
Bundesanstalt für Materialforschung und -prüfung, Germany*

Effect of geometry in concrete spalling risk subjected to high temperatures for thermal inertia studies

*Tamara Lucio-Martin, Javier Puentes, Maria Cruz Alonso
Eduardo Torroja Institute for Construction Sciences (IETcc-CSIC), Spain*

In situ concrete spalling risk assessment in tunnel by means of a mobile oil-fired furnace

Dominique Pardon¹, Pierre Pimienta¹, Benoît-Louis Marie-Jeanne¹, Stéphane

Hameury¹, Nicolas Pinoteau¹, Bérénice Moreau², Laetitia D'aloia Schwartzentruber², Catherine Larive², Pierre Peyrac³, Xavier Thollard⁴

¹ CSTB, France

² CETU, France

³ DRIEA-IF, France

⁴ SETEC Bâtiment, France

Investigation of the preventive effect on fire spalling of natural jute fibre in high performance concrete through ring-restrained specimen tests

Mitsuo Ozawa, Makiho Sukekawa, Haruka Akasaka
Gunma University, Japan

Fire-related spalling evaluation of ring-restrained polymer cement mortar and normal cement mortar

Yusuke Sugino¹, Mitsuo Ozawa², Toru Tanibe¹

¹ Taiheiyo Materials, Japan

² Gunma University, Japan

Spalling behaviour of UHPC with modified microstructure due to fire load

Johannes Kirnbauer
Vienna University of Technology, Austria

Australian large scale structural fire test facility for concrete tunnel linings

Maurice Guerrieri¹, Sam Fragomeni¹, Carlos Sanabria², Wei Ming Lee², Esteban Pazmino³

¹ Victoria University, Australia

² Lendlease Engineering Pty Ltd, Australia

³ John Holland Group, Australia

Prevent high strength concrete from spalling subject to ISO 834 fire

Yong Du¹, Honghui Qi²

¹ Nanjing Tech University, China

² National University of Singapore, Singapore

Experimental Study on Mechanical Behaviors of Cementitious Grouts after Elevated Temperatures

Lianglin Liu, Jianzhuang Xiao, Jiangtao Yu, Xian Liu
Tongji University, China

High Temperature Testing of Concrete

Influence of the chemical and physical properties of hardened cement paste on the fire-induced spalling of concrete

Jochen Reiners, Christoph Müller
Research Institute of the Cement Industry, Germany

Heat-induced concrete spalling of new and aged concrete encased steel columns in hydrocarbon pool and jet fires

Holly Warren, David Wickham
AkzoNobel, UK

Evolution of thermal conductivity on CAC concrete at high temperatures and during thermal fatigue tests

Tamara Lucio-Martin¹, Maria Cruz Alonso¹, Marta Roig-Flores^{1,2}, Luís Guerreiro³

¹ Eduardo Torroja Institute for Construction Sciences (IETcc-CSIC), Spain

² Universitat Politècnica de València, Spain

³ University of Evora, Portugal

Transport and reconfiguration of moisture in HPC due to unilateral heating

Ludwig Stelzner¹, Frank Weise¹, Tyler Oesch¹, Raphael Dlugosch², Bartosz Powierza¹

¹ Bundesanstalt für Materialforschung und -prüfung, Germany

² Leibniz Institute for Applied Geophysics, Germany

Effect of Spalling on Fire Resistance

Effect of loss of concrete cover on the fire resistance of reinforced concrete (RC) beams: Numerical study using fiber beam-column element

Hitesh Lakhani, Jan Hofmann
University of Stuttgart, Germany

Modelling

Concrete spalling failure: a coupled buckling instability and crack failure analytical model

Matteo De Poli¹, Kees Blom^{2,3}, Bas Lottman⁴

¹ Fluor Infrastructure, Netherlands

² Delft University of Technology, Netherlands

³ Municipality of Rotterdam, Netherlands

⁴ Witteveen+Bos, Netherlands

Open issues in modelling concrete at high temperature

Benedikt Weber
Empa, Switzerland

The effect of micro-structural mechanisms on the macro-level behaviour of cementitious materials at elevated temperatures

Jiayi Wang, Colin T Davie, Enrico Masoero
Newcastle University, UK

Flash vaporization next to an opening crack: a possible explanation of the explosive nature of concrete spalling

Roberto Felicetti¹, Ramin Yarmohammadian¹, Stefano Dal Pont², Alessandro

Tengattini³

¹ Politecnico di Milano, Italy

² Université Grenoble Alpes, France

³ Institut Laue-Langevin, France

Other Research Topics

Correlation between concrete tensile strength and intrinsic permeability towards the evaluation of spalling susceptibility

Johann van der Merwe¹, Fangxia Lu², Mario Fontana¹

¹ ETH Zürich, Switzerland

² Baertschi Partner AG, Switzerland

Assessing spalling risk in buildings: Considering spalling in probabilistic fire safety design

Ieuan Rickard¹, Ian Fu¹, Danny Hopkin¹, Luke Bisby²

¹ OFR Consultants, UK

² The University of Edinburgh, UK

Thermal and mechanical response of reinforced concrete slabs under natural and standard fires

Siyimane Mohaine¹, Nataša Kalabd, Jean-Marc Franssen², Luke Bisby³, Alastair Bartlett³, Jean-Christophe Mindeguia⁴, Robert McNamee⁵, Jochen Zehfuss⁶, Fabienne Robert¹

¹ CERIB, Epernon, France

² Liège University, Belgium

³ The University of Edinburgh, UK

⁴ University of Bordeaux, France

⁵ Brandskyddslaget, Sweden

⁶ IBMB, Germany

Atomic structural evolution of calcium-containing alkali-activated metakaolin exposed to fire conditions

Karina Alventosa, Claire E. White

Princeton University, USA

Protective Measures

Application of laminated ferrocement, high tensile laminated ferrocement and cellular concrete to fire prevention and fire restoration of concrete structures

Michael Pemberton¹, Alasdair Beal², Anthony Tucker¹, Paul Nedwell³, Martin Pullan¹

¹ Trafalgar Marine Technology Ltd, UK

² Thomasons Ltd, UK

³ Manchester University (Retired), UK

Experimental and numerical study of the influence of the PP fiber diameter on spalling behaviour of concrete

Fariza Sultangaliyeva¹, Chhainan Leang², H  l  ne Carr  ¹, Christian La Borderie¹, Nicolas Roussel³

¹ *Universit   de Pau et des Pays de l'Adour, France*

² *INSA Rennes, France*

³ *IFSTTAR, France*

Experimental contribution to the optimization of the choice of polypropylene fibers in concrete for its thermal stability

Fariza Sultangaliyeva¹, Bruno Fernandes¹, H  l  ne Carr  ¹, Pierre Pimienta², Christian La Borderie¹, Nicolas Roussel³

¹ *Universit   de Pau et des Pays de l'Adour, France*

² *CSTB, France*

³ *IFSTTAR, France*

FIRE SPALLING THEORIES – REALISTIC AND MORE EXOTIC ONES

Robert McNamee*

Brandskyddslaget, Stockholm, Sweden

* Corresponding author

(robert.mcnamee@brandskyddslaget.se)

ABSTRACT

We do not know in detail what is causing the spalling phenomena, but a variety of realistic and more exotic explanations have been postulated through the years. Thermal stresses from expansion of the heated layers and stresses from trapped water are the two main stresses put forward as an explanation for the phenomena. This article gives an overview of different ideas with some critical discussion added. The purpose of the article is to make an overview of the ideas to inspire researchers to continue to deepen our knowledge in this area.

KEYWORD: Fire, Spalling theories, Concrete

INTRODUCTION

Concrete is widely used as a construction material, chosen because it is easy to use and gives durable structures. While concrete is not flammable it has still been known for more than 150 years that it presents some very specific challenges when exposed to fire [1]. It has been well-documented that the fire spalling of concrete can be very severe when structures are exposed to fire [2]. At the same time, there are cases where severe fire exposure does not lead to fire spalling. Further, even in cases where severe fire spalling has occurred, the fire spalling in itself has not necessarily led to collapse or fatalities. Despite this, significant effort has been made to understand the fire spalling phenomenon and endeavour to minimise its occurrence. In particular, in the case of tunnel constructions there are often requirements on fire performance that aim to minimise or even eliminate fire spalling. The reason for these requirements is not only life-safety, but also to minimise societal costs in the shape of direct costs for refurbishing as well as indirect costs due to loss of tunnel access which can translate into increased transport cost to businesses, loss of travellers and tourism.

Numerous studies have been conducted in modern history to investigate the phenomenon of fire spalling, and many and varied theories to explain the occurrence and mechanism of fire spalling have emerged. A historical overview of fire spalling research was presented at the 3rd Fire Spalling Workshop in Paris 2013 [3]. The previous paper presented both recorded behaviour from a selection of real fires, a compilation of experimental results and theories. This paper will explore a number of fire spalling theories in greater detail and discuss their respective pros and cons.

TYPICAL OBSERVATIONS OF FIRE SPALLING OF CONCRETE

Fire spalling of concrete is an event leading to the loss of cross-section of the exposed concrete structure, during fire exposure. It does not occur during every fire, but in its mildest form, that is slight flaking from the surface, it is very common during real fires. The British Concrete Society Committee on Fire Resistance made a survey of near 100 reported fire accidents and found that in over 80% fire spalling was mentioned, but that none of the spalling events led to the collapse of a structure [4].

Two examples of fire spalling without collapse are shown in Figure 1. The left picture shows surface flaking of the ceiling slab that did not result in the exposure of any reinforcement, and the right picture shows spalling that penetrated the concrete slab to reach the reinforcement layer of the wall element. Note that despite significant spalling of the wall element, there was no spalling of the ceiling element. There might be two reasons for this difference, i) differences in the concrete quality between the wall and ceiling and/or (ii) differences in the load situation for these two construction elements. Indeed, these are two of the main factors influencing fire spalling. The examples shown in Figure 1 are both from car park fires where relatively few, three and five, cars burned. In a more recent car park fire in Kings Dock, London, in 2017 more than 1000 vehicles were involved, and extensive damage was caused by fire spalling [5].



Figure 1 Fire spalling of concrete in parking garages. The heat source in the left picture was five burning cars and in the right picture three burning cars. (Photo Robert McNamee)

THERMAL STRESSES THEORIES

Concrete is a composite material with the two major components, cement paste and aggregates. These two materials expand and contracts to a different degree during heating, giving rise to stresses and microcracks. As concrete has a relatively low thermal diffusivity and high density, high thermal gradients are created close to the fire exposed surface. This leads to the creation of an area close to the surface that wants to expand, while at the same time an inner colder volume restricts this expansion. As a result, during heating of concrete, thermal stresses are created on different scales.

When conducting fire resistance tests on post-stressed slabs of thickness 200-250 mm, bending of the slabs in two directions caused by the expansion of the surface layers can be detected directly when the test starts [6]. During these experiments bending in the direction of the pre-stress was less than in the opposite direction, see Figure 2. After the experiment, cores were drilled and extracted. Measurement on these cores showed that the speed of sound in the load direction was higher than in the unloaded direction close to the surface, illustrated in Figure 3. How much of this difference that was caused by the difference in load during heating and how much was caused by the difference in bending is difficult to know, but the results illustrate that the stress situation, when heating concrete, changes both the behaviour and the properties in a rather complex way.

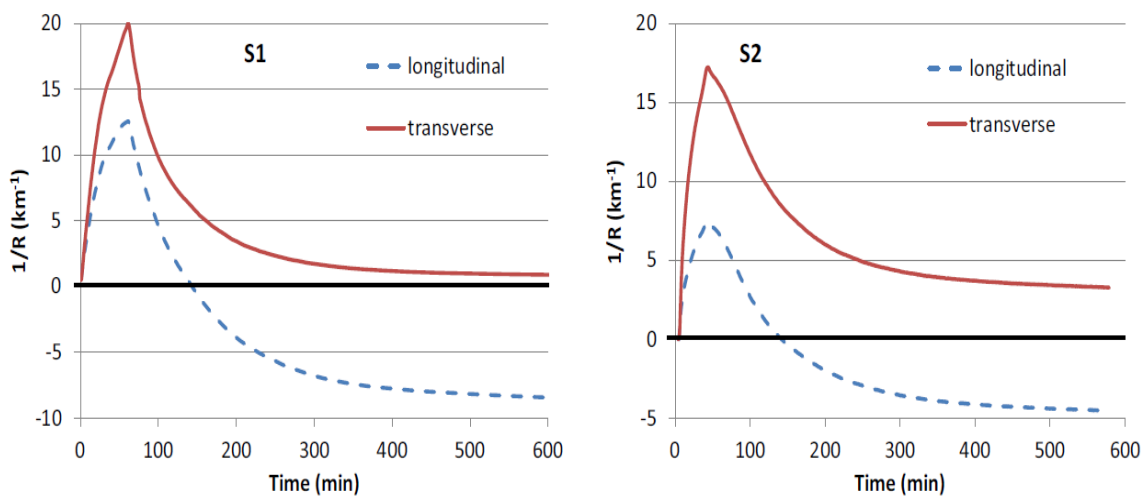


Figure 2. Inverse radii of gyration in transverse and longitudinal direction (load direction) during heating. S1 is a $1700 \times 1200 \times 200 \text{ mm}^3$ slab and S2 a $1700 \times 1200 \times 250 \text{ mm}^3$ slab. A positive value indicates a concave upper surface, i.e. bowing towards the hot surface [6].

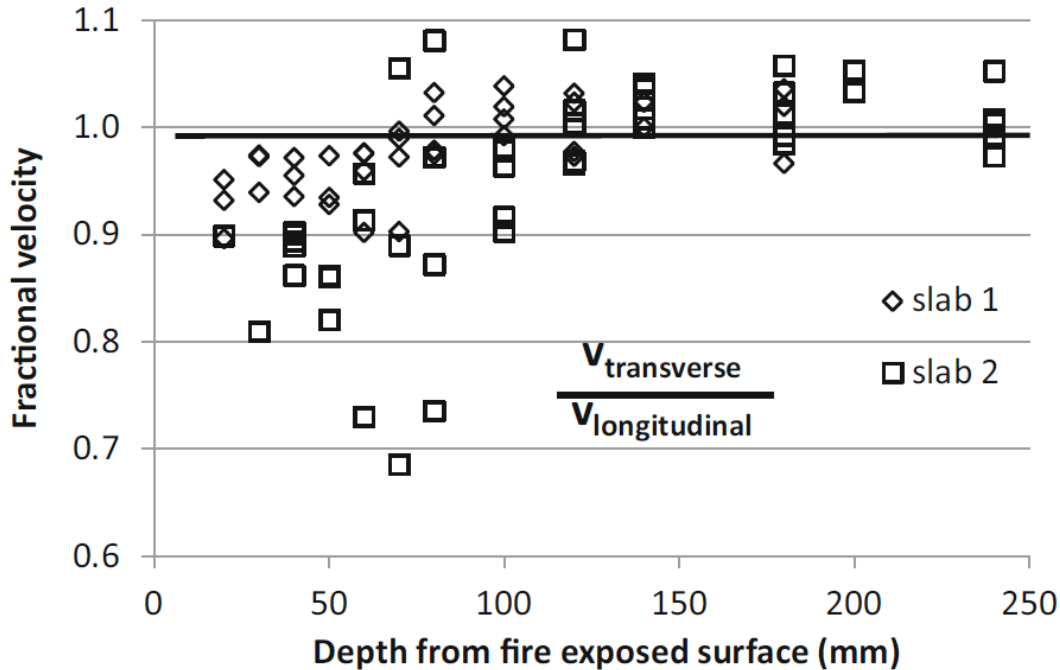


Figure 3. Fraction of pulse velocities in transverse and longitudinal (load) direction measured after fire testing on drilled cores [6]. More damage is indicated close to the surface in the non-loaded direction.

According to Bažant [7], the thermal stresses evolving from the non-uniform temperature distribution can lead to a spalling phenomenon caused by a “brittle fracture and delamination buckling caused by compressive biaxial thermal stresses parallel to the heated surface”. This is similar to the theory for fire spalling that Preston and White postulated for heated clay in 1934 [8]. Bažant also concluded that pore pressure can be a trigger of the fire spalling phenomenon, but then have a secondary role as the pore pressure in practice will be zero directly when the crack is opened and the available space for the trapped steam is orders of magnitude larger. This is clearly a simplification which might be valid for the case when only steam is present and the steam acts like a compressible spring. If liquid water is present in the pore system, however, the expansion due to phase transition is 1600 times greater (valid for atmospheric pressure, smaller at higher pressures), which creates significantly greater potential expansion.

Further, high strength concrete exhibits a greater brittleness than ordinary strength concrete. This higher strength is not complemented by a concurrent rise in fracture energy, which can explain why high strength concrete is more prone to spalling than ordinary strength concrete [7]. There are, however, indications that this explanation is a simplification of the mechanism, as high strength concrete with steel fibres also spalls, although in some cases later and in a more violent manner [9].

Another aspect on the thermal stresses theory is that the strength [10] and fracture properties [11] change in zones with high moisture [2][12]. In a study on small mortar specimens, the effect of boiling in water for 3, 10 or 20 minutes exhibited a dramatic reduction in strength [13], as illustrated in Figure 4. In experimental studies, when splitting concrete under heating, it has been shown that a zone of liquid moisture can develop already after 15 minutes of standard fire exposure [14] and that this zone can be rather wide [1], as seen in Figure 5.

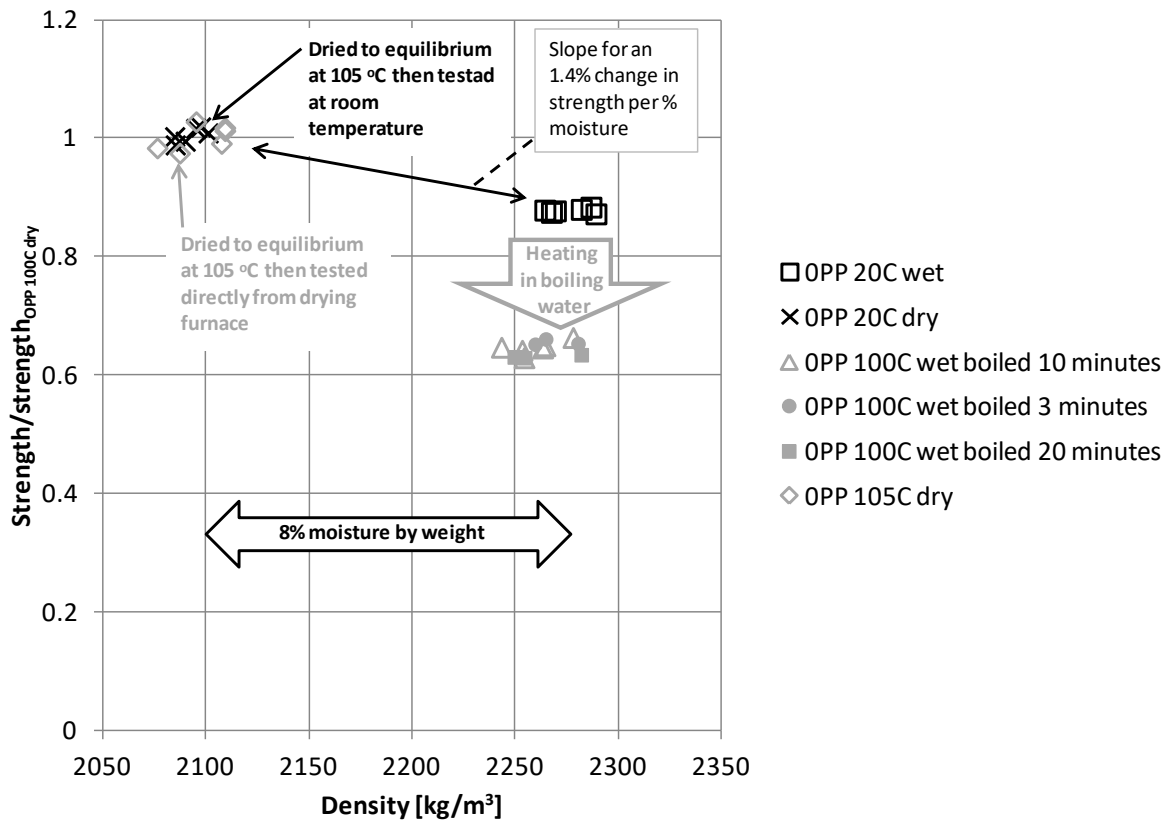


Figure 4. Differences in strength versus density for different pre-conditioning, chosen reference is the average of the dry strength at room temperature. Test on mortar specimens 20 x 20 x 40 mm³ [13].

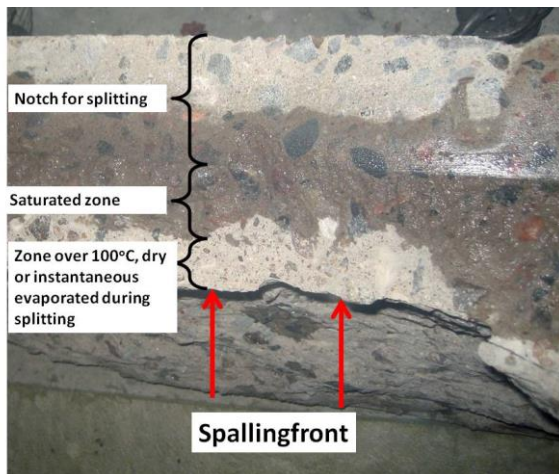


Figure 5. The moisture zone in front of the spalling front. Visualised by splitting a 600 x 500 x 200 mm³ concrete slab during a fire test [1]. Photo Robert McNamee

THE VAPOR PRESSURE AND MOISTURE CLOG THEORY

Clearly moisture can influence the mechanical properties of the heated zone as described in the previous section, but can it also give a direct effect by adding stresses from trapped steam to the stresses arising from thermal expansion described above?

As shown in Figure 5 and described already in 1905 [15], liquid moisture can be formed during the heating of concrete. The theory behind this process was described in more detail for the first time by Shorter and Harmathy in 1961 [16]. A more refined explanation was attempted subsequently by Harmathy in 1965 [17]. According to this “moisture clog” theory, the steam pressure in the pores is rising close to the surface when a concrete cross section is exposed to a fire. This rise in pore pressure will not only drive steam out on the fire exposed side but also push steam further inwards, towards the cold cross section. When the steam pushed inwards meets colder concrete it will condense and when the process has continued for a sufficient period of time a fully saturated region of a “considerable thickness” will be created (see figure 5). When this moisture clog is created, it slows down further moisture transport inwards to the colder region which leads to the development of a rapid rise in pore pressure. When this pressure exceeds the tensile strength of concrete, a piece is spalled off. A more refined explanation, including the influence for development of an impermeable carbonisation layer on the surface, has also been developed, but this theory has been developed in an attempt to explain the “fact” that old concrete spalls more than young concrete [18]. However, this is not a plausible twist on the moisture clog theory.

The question remains as to whether there exists any direct experimental proof of the moisture clog theory, including the spalling caused by vapour pressure, as Harmathy suggested? Unfortunately, no clear experimental support has been presented to date. A saturated region, moisture clog, seems to be created in many situations and it is common during fire testing that liquid moisture is pushed out through cracks on the non-fire exposed side during fire testing [15][19], but the direct connection between measured pore pressure and fire spalling is weak during fire exposure [12][20-23]. Indeed, when testing large externally loaded specimens, concrete with the addition of polypropylene fibres that does not spall has been seen to exhibit higher pore pressure than a concrete without polypropylene fibres that spalls [23].

THE FULLY SATURATED PORE PRESSURE THEORY

The thermal pressurisation coefficient in fully saturated cement paste is 0.6 MPa/°C at room temperature [24] and between 0.2-1.6 MPa/°C from 10°C to the critical point of water at 373°C [25]. When heating concrete during fire exposure this stress is enormous and will break and weaken the pore structure if no drainage is present. Further, if more than 32% of a closed pore is initially filled with water, the water will expand during heating and force the trapped air into solution, resulting in fully saturated pores at elevated temperatures. This phenomenon is actually used as the activation mechanism for sprinklers with bulb activation, where a glass container is filled with water and a bubble. When the temperature rises sufficiently the water expands and the air is forced into solution in the water until the whole bulb is filled and breaks due to the build-up of hydraulic pressure. Some researchers see this as a probable explanation of the fire spalling phenomenon [26-27], but it is very difficult to prove in practice.

THE BLEVE THEORY

When liquid water is heated under pressure over 100 degrees and the pressure is suddenly released, liquid water will convert into steam very rapidly as all energy accumulated during heating over 100°C will be released in an instantaneous boiling process that is classified as an explosion. The Boiling Liquid Expanding Vapour Explosion (BLEVE) theory can be a component in the spalling process of high strength concrete [28]. A similar theory includes the rapid expansion of super-heated water [29]. According to this theory the walls between closed pores with super-heated water and adjacent open pores with lower pressure can be destroyed by the pressure difference, and this can lead to the progressive breakdown of the

microstructure. It seems that this phenomenon can be a part of the process leading to the unstable crack growth that results in spalling, but once again it is very difficult to prove it in practice.

THE FRICTIONAL FORCES FROM VAPOUR FLOW THEORY

When water is transported from the zone with highest pore pressure outwards to the heated surface, frictional forces will arise in the flow path. At the same time as the strength of the material is lower closer to the surface, this force caused by wall friction may result in tensile stresses in the capillary system making spalling probable [31][32]. This was assessed by doing a theoretical calculation assuming all moisture must be expelled during heating and comparing influences from different parameters on this process [31]. However, no compelling experimental evidence has been presented for this theory either.

DISCUSSION AND CONCLUSIONS

We do not know in detail what causes the spalling phenomena, but we have a variety of realistic and exotic explanations that have been presented in the previous sections. The confusion regarding the origin of the phenomena has been present since the phenomenon itself was recognised and is a result of the fact that the underlying mechanism is complex. In Table 1 and Table 2 a survey made by Malhotra summarizes what different researches believed to be the main factors leading to spalling in the 1960's and 1970's.

Table 1 Main spalling theories with subgroups according to Malhotra [4].

1) Moisture	1a) Vapour pressure
	1b) Moisture clogging
	1c) Vapour pressure enhanced by frictional resistance
2) Stress	2a) Initial compression
	2b) Initial compression + thermal stress
	2c) Initial compression + thermal stress + stress caused by frictional resistance
3) Cracking	3a) Aggregate expansion
	3b) Internal cracks
	3c) Reinforcement expansion

Table 2. Highlighted theories by different researchers, compilation by Malhotra [4].

Researcher	Main factors	Secondary factors
Saito (1965)	2a, 2b, 2c	1a
Harmathy (1965)	1b	-
Meyer-Ottens (1972)	1c, 2b	2c, 3c
Dougill and Sertmehmetoglu (Sertmehmetoglu,1977)	1b, 3b	2a
Akhtaruzzaman and Sullivan (1970)	1a	Dense surface layer
Gustaferrero (Kordina, 1970)	1a	3a
Copier (1979)	2a, 1a	--

When looking at all theories summarized in this paper and highlighted by Malhotra's survey above, it is clear that there is no consensus regarding the details of the origin of fire spalling of concrete. If we are to proceed and truly understand the physics involved, more innovative experimental techniques need to be developed. This is best done in parallel with the development of more detailed theoretical models. In a previous article presented at the 4th spalling workshop in Leipzig 2015, three experiments to validate basic functions in fire

spalling models was presented [19]. It is the authors humble opinion that this is a good starting point to further development of our understanding of the origin of fire spalling of concrete.

REFERENCES

- [1] Barret "On the French and other methods of constructing iron floors", Civil Engineering and Architect's Journal, Vol XVII, pp 94, 1854
- [2] Jansson R, "Fire spalling of concrete- Theoretical and Experimental studies" PhD Thesis, KTH, Stockholm Sweden, 2013
- [3] Jansson R. "Fire spalling of concrete - A historical overview" Key note at the 3rd International RILEM Workshop on Concrete Spalling due to Fire Exposure, Paris, France, Sept. 2013
- [4] Malhotra H. L. (1984) "Spalling of concrete in fires", Technical note 118, CIRA, London, UK.
- [5] Merseyside Fire & Rescue Service "Kings Dock Car Park Fire", Protection report, April 2018
- [6] Sjöström J, Lange D, Jansson McNamee R. and Boström L. "Anisotropic Curvature and Damage of Unbonded Post-tensioned Concrete Slabs During Fire Testing" Fire Technology, May 2017, Volume 53, Issue 3, pp 1333–1351
- [7] Bažant , Z. P. (2005) "Concrete Creep at High Temperature and its Interaction with Fracture: Recent Progress", Concreep-7 Conference: Creep, Shrinkage and Durability of Concrete and Concrete Structures, Nantes, France, pp 449–460
- [8] Preston F. W., White H. E. (1934) "Observations on spalling" Journal of the American Ceramic Society, Volume 17, Issue 1-12, pp 137-144.
- [9] Hertz K. "Danish Investigations on Silica Fume Concretes at Elevated Temperatures" ACI Materials Journal, July-August, 1992
- [10] Lankard DR, Birkimer DL, Fondriest FF, Snyder MJ (1971) Effects of moisture content on the structural properties of portland cement concrete exposed to 500 F. ACI Special Publication SP 25, Detroit
- [11] Bazant, Z.P., and Prat, P. C., Effect of temperature and humidity on fracture energy of concrete, ACI Materials Jour. 84 (July), 262–271
- [12] Jansson R. "Material properties related to fire spalling of concrete" Licentiate Thesis. Report TVBM-3143, Lund University of Technology, Lund Sweden, 2008
- [13] Jansson R. and Boström L. "Fire spalling in concrete - The moisture effect part II" 3rd International RILEM Workshop on Concrete Spalling due to Fire Exposure, Paris, France, Sept. 2013.
- [14] Jansson R., Boström L. (2009) "Fire spalling – The moisture effect" 1st International Workshop on Concrete Spalling due to Fire Exposure - From Real Life Experiences and Practical Applications to Lab-scale Investigations and Numerical Modelling, MFPA Institute Leipzig, Germany 3 - 5 September 2009
- [15] Miller R. P. (1905) Contribution to the discussion at the end of the report "Investigation of the Effect of Heat Upon the Crushing Strength and Elastic Properties of Concrete" by Ira Woolson, Proceedings of the American Society for Testing Materials, Philadelphia, USA.
- [16] Shorter G. W. & Harmathy T. Z. Discussion on the article "The fire resistance of concrete beams" by Ashton and Bate, Proceedings, Institute of Civil Engineers, Vol. 20, p. 313.
- [17] Harmathy, T. Z.(1965) "Effect of moisture on the fire endurance of building materials", Moisture in Materials in Relation to Fire Tests, ASTM Special Technical Publication No. 385, pp 74-95, 1965.
- [18] Kalos G. M. "Influence of the "carbonatization" of the concrete on the explosive spalling under fire conditions" Technical Chamber of Greece, CIB Commission, Athens , 1973
- [19] Jansson McNamee R., Boström L. "Three experiments to validate basic functions in fire

spalling models" The 4th International RILEM Workshop on Concrete Spalling due to Fire Exposure, Leipzig, Germany, October 8-9, 2015

[20] Phan L. T. "Pore pressure and explosive spalling in concrete" *Materials and Structures* Vol 41, pp 1623–1632, 2008

[21] Mindeguia J-C. (2009) "Contribution Experimentale a la Comprehension des Risques D'instabilite Thermique de Betons", PhD thesis, Université de Pau et des pays de l'Adour, France

[22] Mindeguia J-C., Pimienta P., Carre H., La Borderie C. (2009) "Experimental study on the Contribution of Pore Vapour Pressure to the Thermal Instability Risk of Concrete", *Proceedings of the 1st International Workshop of Concrete Spalling due to Fire Exposure*, Leipzig, 2009

[23] Jansson R. and Boström L. (2010) "The influence of pressure in the pore system on fire spalling of concrete" *Fire Technology*, Vol 43, No 1, pp 217-230.

[24] Ghabezloo S, Sulem, J and Saint-Marc J (2009) "The effect of undrained heating on a fluid-saturated hardened cement paste" *Cement and Concrete Research* No 39, pp. 54–64

[25] Fellingner J. H. H. and Breunese A. J. (2005) "Evaluation of the fire test procedure for the spalling behaviour of concrete mixes" TNO Report of NewCon project, Project number 006-47110, Delft, The Netherlands

[26] Khoylou N. 'Modelling of moisture migration and spalling behaviour in non-uniformly heated concrete', PhD thesis, University of London, London, United Kingdom, 1997.

[27] Breunese A.J., Fellingner J. H. H. 'Spalling of Concrete - An Overview of Ongoing Research in the Netherlands', Workshop - Structures in Fire, Ottawa, Canada, 2004.

[28] Ichikawa Y. (2000) "Predictions of pressures, heat and moisture transfer leading to spalling of concrete in fire", PhD Thesis, Imperial Collage, London, Great Britain, 2000.

[29] Petrov-Denisov V.G., Maslennikov L.A. and Pitckob A.M. (1972) "Heat- and moisture transport during drying and first heating of heat resistant concrete. *Concrete and Reinforced Concrete* 1972;2: 17–8 (In Russian). as cited by [28]

[30] Hertz K. (2003) "Limits of Spalling of Fire-Exposed Concrete" *Fire Safety Journal* 38 (2003), pp.103-116.

[31] Waubke N. V. and Schneider U. (1973) "Tensile stress in concrete due to fast vapour flow", *Proceedings of the international RILEM symposium "Pore Structure and Properties of Materials"*, Prauge, September, 1973.

[32] Meyer-Ottens C. (1972), "Zur Frage der Abplathigh-performanceauteilen aus Normalbeton bei Brandbeanspruchung", PhD-thesis, Braunschweig, Germany.

Experimental Investigations into the Spalling of High Strength Concrete and the Fire Performance of Tunnel Linings

Octavian Lalu¹, Tom Lennon^{1,*}
¹ BRE Global, Watford, UK

* Corresponding author (lennont@bre.co.uk Bucknalls Lane, Watford WD25 9XX)

ABSTRACT

The paper reviews a number of experimental programmes undertaken at BRE in the UK on the performance in fire of high strength concrete with a particular focus on mix design to alleviate the effects of spalling. The experimental programmes include tests on concrete columns (both with and without reinforcement) and tunnel linings.

The paper will provide information on the parameters that lead to explosive spalling of tunnel linings in a fire situation and on the measures available to mitigate this hazard. Information will be provided on the types of fire exposure normally used to evaluate the performance of tunnel linings subject to fire and discusses the possibilities for providing some form of harmonized procedure for the future.

KEYWORD: Spalling, High Strength Concrete, Tunnel Linings

INTRODUCTION

Concrete structures generally perform extremely well during and after a fire and the majority of fire-damaged concrete structures have been repaired and re-used¹. Although spalling of concrete structures following real fires has been observed, it does not necessarily have implications for the stability of the structure. There is a need to establish the circumstances under which spalling would have serious consequences. The use of high strength concrete in buildings is an important innovation that can reduce the size of structural elements compared to those made from normal strength concrete. This can provide for more efficient construction such as maintaining a constant column size throughout the building by using high grade concrete for the lower storey columns carrying the highest loads. One restriction to its widespread use however is concern over its performance in fire, in particular its increased susceptibility to spalling. A consideration of the literature and experience gained over the course of many years suggest that spalling is more likely in the event of high moisture content, high concrete strength, rapid increase in temperature or high levels of restraint (or applied load) or any combination of these factors.

The purpose of this paper is to bring together information derived from a number of experimental programmes, to identify the significant parameters that influence spalling and to highlight areas where further research is required. The information and expertise derived from experimental programmes into the behaviour of high strength concrete in fire has been used to undertake a number of high-profile commercial testing programmes to assess and evaluate the performance of tunnel lining segments in the event of a fire.

PARAMETERS THAT INFLUENCE SPALLING OF CONCRETE STRUCTURES

Given certain conditions virtually all types of concrete will spall in a fire situation. The most significant parameters contributing to the spalling of concrete structures are heating rate, moisture content, permeability, strength, restraint to thermal expansion, aggregate type, curing regime, geometry and nature and extent of reinforcement.

It is generally recognised that there are three main categories of spalling; aggregate, corner and explosive. Of these explosive spalling is the most significant in terms of its impact on structural performance. For normal strength concrete and for high strength concrete covered by European Class 1 and 2 with silica fume contents less than 6% by weight of cement explosive spalling is assumed to be principally a function of the moisture content and the environmental conditions. EN 1992-1-2² states that where the moisture content is less than 3% by weight and where members are designed to exposure class X0 (concrete inside buildings with very low air humidity) and XC1 (concrete inside buildings with low air humidity) then explosive spalling does not need to be considered explicitly. The current revision of the fire part of the Eurocode for the design of concrete structures will revisit these assumptions and update the rules based on the current state of knowledge in relation to spalling and the material behaviour of high strength concrete.

The difference between high strength concrete and normal concrete lies principally in the water to cement ratio used in the mix. For high strength concrete, lower water to cement ratios are used, the required workability of the fresh concrete being provided by superplasticisers. The effect of lowering the water to cement ratio is a reduction in the permeability of the hardened concrete, which, in most structural contexts, increases both strength and durability. Unfortunately, the reduction in permeability has been found to be detrimental to performance in fire. This is because pore pressure is produced in concrete at high temperatures. Unless there is an escape route for the steam, internal pressures are generated that, in conjunction with other stresses can exceed the tensile strength of the concrete. The overall result of all the factors relating to the increase in concrete grade is an increased susceptibility to spalling. The danger of spalling of concrete in fire is not only the loss of section but also the possibility of early yield of the steel reinforcement as it becomes directly exposed to high temperatures.

RESEARCH AT BRE

The performance in fire of high strength concrete columns³

Initial research on the performance of high strength concrete columns in fire aimed to investigate the effect of the use of monofilament polypropylene (p/p) fibres to improve performance. At this time (1997-1998) the use of p/p fibres for fire performance was an innovative application of an existing technology generally used to prevent early age cracking of floor slabs. Two different experimental programmes were undertaken on both unreinforced and reinforced columns.

The fire test facility is shown in Figure 1. The columns were placed inside a gas fired furnace with the fuel input controlled to follow the standard fire curve⁴ for a period of 45 minutes. The columns were subject to an axial compressive load kept constant for the duration of the fire exposure. The initial programme of tests was undertaken on unreinforced columns to provide a worst-case scenario in terms of spalling. The columns measured 1500mm high x 200mm x 200mm. The concrete mixes were C85 and C105 (with micro silica). The coarse aggregate was crushed limestone and the moisture content at the time of test was 3.5%. Half the columns included 3 kg/m³ of p/p fibres (12mm long x < 0.1mm thick). Half the columns were tested whilst under 40% of the calculated ultimate load and the other half tested under 60% of the calculated ultimate load.

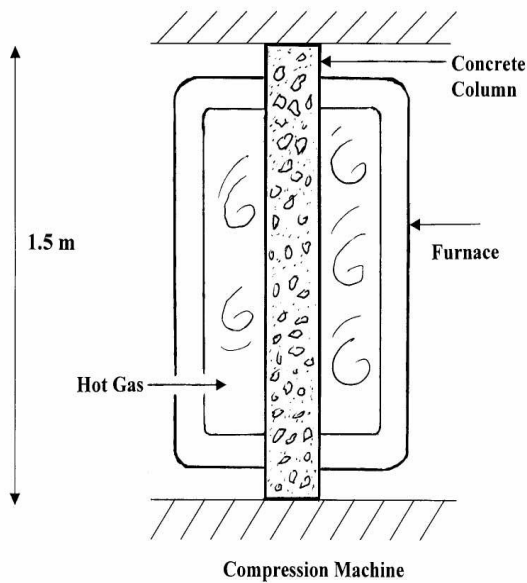


Figure 1 Experimental set-up for fire testing of high strength concrete columns.

The results are illustrated in Figure 2. Only four specimens (of 30) remained intact at the end of the test and of these three included p/p fibres. None of the specimens under 60% load survived the test regardless of the inclusion of p/p fibres. Figure 3 is a comparison of the one specimen without fibres that survived the test and the corresponding sample including fibres. The results show two things very clearly. Firstly p/p fibres can reduce, delay or eliminate spalling in high strength concrete and secondly the predominate factor in terms of fire performance is the load ratio or degree of utilization of the columns.

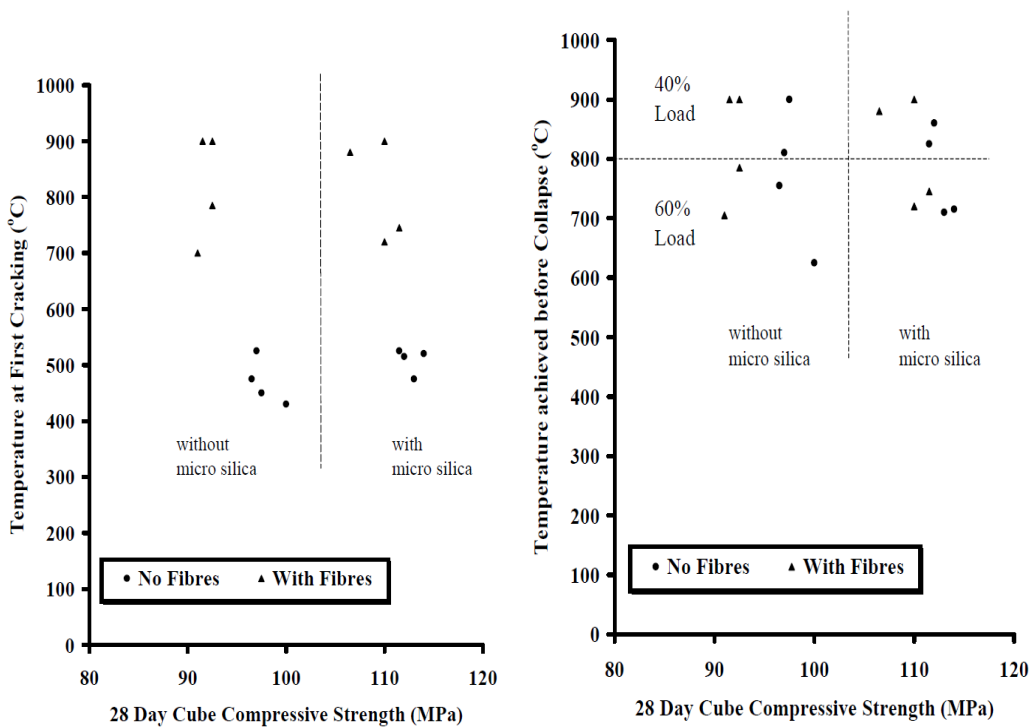


Figure 2 Temperature at first cracking and collapse temperature (unreinforced columns).



Figure 3 Comparison between high strength unreinforced columns with (right) and without (left) fibres.

The second programme of tests were on reinforced columns of the same overall size as the unreinforced specimens. The reinforcement details are illustrated in Figure 4. The range of concrete grades was extended to cover C45 and C65 grades as well as the C85 and C105 grades used previously. Two different fibre dosages were used, 3kg/m^3 and 6kg/m^3 , the moisture content was 3% and the test procedure was the same as that used previously. In all cases the applied axial load was one third of the calculated ultimate capacity.

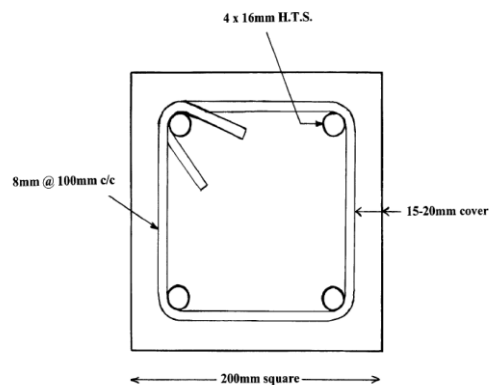


Figure 4 Section through reinforced concrete columns.

No collapses occurred for any of the reinforced columns although the degree of spalling varied according to the mix design. Figure 5 is a comparison of three of the C85 columns containing from left to right no fibres, 3kg/m^3 p/p fibres and 6kg/m^3 fibres.

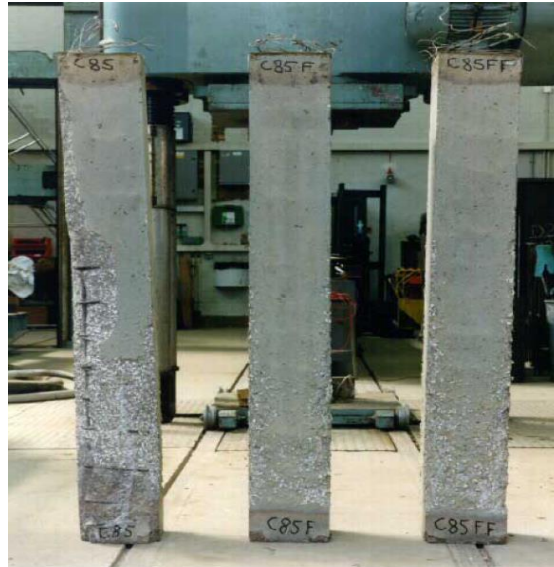


Figure 5 Comparison of C85 test specimens after test (no fibres on left, 3kg/m³ p/p fibres in middle and 6kg/m³ p/p fibres on right).

The residual strength of all specimens was determined by compression testing following exposure to fire. The measured residual strengths are shown in Table 1, expressed as a proportion of the calculated ultimate load capacity at ambient temperature. The results show that for those members not containing p/p fibres there is a larger loss of residual strength and that this loss increases with increasing grade. This is in line with the observations of relative damage following the fire tests.

Table 1 Residual compressive strengths of the fire tested columns.

Concrete Type (F = 3kg/m ³ p/p fibres, FF = 6kg/m ³ p/p fibres)	Residual Strength (percentage of calculated ultimate failure load prior to testing)
C45	70%
C45F	75%
C45FF	75%
C65	60%
C65F	65%
C65FF	65%
C85	55%
C85F	70%
C85FF	70%
C105	55%
C105F	60%
C105FF	65%

Cardington large-scale fire test⁵

A large-scale fire test was undertaken on the ground floor of the European Concrete Building Project (ECBP) at BRE's large scale test facility at Cardington in 2001. The flat slab was supported by a number of high strength (C85) concrete columns containing 2.7kg/m³ monofilament p/p fibres to reduce the tendency for explosive spalling. The test area included one completely exposed internal column and eight partially exposed columns at the boundaries of the compartment.

All of the columns survived the fire test without any significant spalling suggesting that the p/p fibres had a significant impact particularly in the light of spalling to the soffit of the flat

slab (Figure 6).

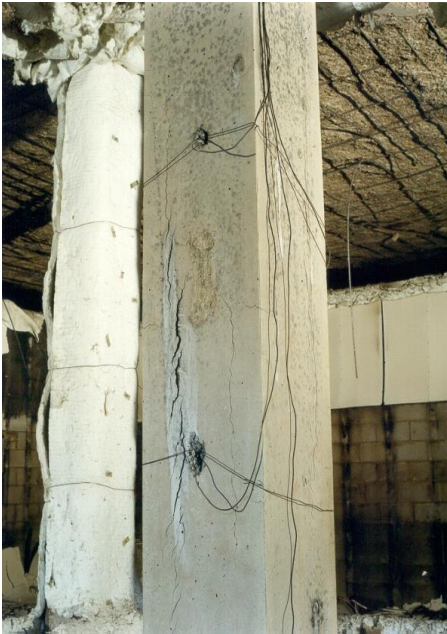


Figure 6 Longitudinal cracks in internal column from Cardington concrete building fire test.

EXPLOSIVE SPALLING AND TUNNELS

As mentioned above explosive spalling is a function of a number of inter-related parameters. The most significant in relation to explosive spalling (as opposed to spalling in general) is the rate of temperature rise, the presence of restraint against thermal expansion and the permeability (related to porosity, density and strength) of the concrete. Tunnels often involve the use of high strength concrete. The nature of the construction involves significant restraint to thermal expansion and the nature of the potential fire load (petro-chemical fuel tankers) leads to a rapid rise in temperature in the event of a fire.

Given the potential consequences of failure to a tunnel lining, the nature of tunnel fires and the form of construction used in tunnels it is essential to ensure that the proposed design solution is capable of resisting a hydrocarbon fire exposure while under load.

There is currently no standardised approach for the testing and approval of tunnel lining segments in terms of fire performance. Some attempts have been made to produce standardised procedures while still allowing some flexibility in the fire exposure curve to be adopted⁵. However, the specification does not require the specimens to be tested under load. For major infrastructure projects the requirements are often tailored to the specific circumstances of the project.

Tunnel fire testing at BRE

BRE have been involved in fire tests in a number of high-profile infrastructure projects to demonstrate compliance with client requirements for both road and rail tunnels. Figure 7 is a comparison of specimens with and without p/p fibres tested under load and subject to a hydrocarbon fire exposure for a high-speed rail tunnel. Figure 8 is a comparison between (from left to right) panels subject to a hydrocarbon fire exposure while under load and containing 1kg Polyvinyl alcohol (PVA) fibres, no fibres and 1kg p/p fibres. The expertise derived from projects such as this provided input to the specification for fire testing for sprayed concrete linings for the Crossrail project.



Figure 7 Comparison of test specimens with (right) and without (left) p/p fibres.



Figure 8 Comparison of specimens following hydrocarbon fire test (1kg/m³ PVA fibres on left, no fibres in middle and 1kg/m³ p/p fibres on right)

Two different specifications were provided for fire testing of specimens for the Crossrail project. One for precast linings and one for sprayed concrete linings (SCL). Both test methods specify exposure to the Eureka time-temperature curve illustrated in Figure 9. The specification for SCL defined the parameters for both large panel tests for compliance and smaller scale tests on unloaded cylinders to establish the potential suitability of trial mixes. The specification for testing of large panels for SCL consists of loading panels with nominal dimensions of 1.5m high by 0.75m wide by 0.3m thick to the prescribed load level and subjecting one face of the panel to a hydrocarbon fire exposure corresponding to the Eureka fire curve. The performance criteria were based on depth of spalling, temperature rise within the slab and an evaluation of the impact of temperature rise on the integrity of the waterproof membrane and the residual strength of the heated concrete.

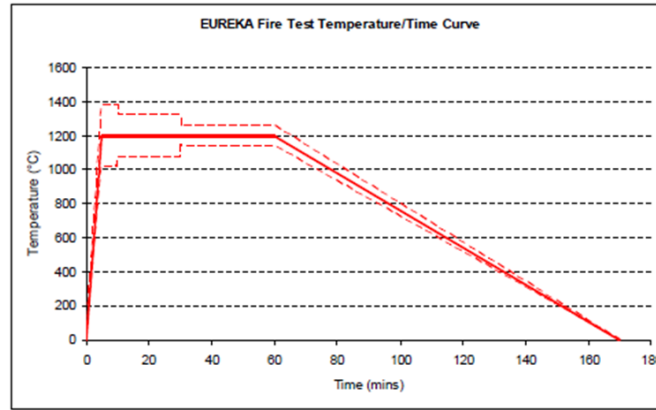


Figure 9 Eureka time-temperature curve.

Thermocouples are installed in the specified locations on site (Figure 10) at the time the panels are cast. Prior to testing the samples are stored and cured under controlled conditions (40°C and 60% RH) (Figure 11) until the test date (nominally 28 days). The specification for precast linings used for Crossrail was completely different and required facilities not currently available within the UK.



Figure 10 Thermocouple installation on site.



Figure 11 Curing samples under controlled conditions (40°C and 60% RH).

The next major infrastructure project is the HS2 high speed rail link. A specification for fire testing of concrete used for underground tunnels has been prepared based largely on the specification used for Crossrail.

CONCLUSIONS

This paper has reviewed a number of experimental programmes undertaken at BRE to investigate the spalling of concrete structures with a particular focus on high strength concrete. The expertise derived was used to provide a means of test and assessment for a number of high-profile infrastructure projects where evidence was required of concrete performance when subject to a hydrocarbon fire exposure.

There is a need for a standardised approach to the assessment of the performance of tunnel linings in fire to be developed. However, any standardised test and assessment procedure should allow for the flexibility required for specific projects in terms of fire exposure and load level to be applied.

The Crossrail SCL specification and the current HS2 specification could provide a useful starting point to develop a standardised procedure that considers the most significant aspects of structural behaviour in fire without imposing an unreasonable financial burden on contractors.

REFERENCES

- [1] Tovey A K and Crook R N, Experience of fires in concrete structures, in ACI Symposium on Evaluation and repair of fire damage to concrete, San Francisco, 16-21 March, 1986, American Concrete Institute, Detroit, Ref SP-92
- [2] British Standards Institution, BS EN 1992-1-2: 2004, Eurocode 2: Design of concrete structures – Part 1-2: General rules – Structural fire design, BSI, London, February 2005
- [3] Clayton N and Lennon T, Effect of polypropylene fibres on performance in fire of high grade concrete, BR 395, Published by Construction Research Communications (CRC), 2000
- [4] British Standards Institution, BS EN 1363-1: 1999, Fire resistance tests - Part 1: General requirements, BSI, London, November 1999
- [5] Lennon T, Bailey C and Clayton N, The Performance of High Grade Concrete Columns in Fire, in Proceedings of the 6th International Symposium on Utilization of High Strength/High performance Concrete, Volume 1, Leipzig, 2002, 341-354

Application of Concrete Spalling Mitigation: A North American Perspective

Kevin Mueller, PhD, PE^{1,*}; Stephen Stacey, PE²; Anthony Bentivegna, PhD, PE²

¹Thornton Tomasetti, Chicago, Illinois, USA

²Jensen Hughes, Chicago, Illinois, USA

* Corresponding author

(kmueller@thorntontomasetti.com, 330 N Wabash Ave, Chicago, IL 60611, USA)

ABSTRACT

The American Society of Civil Engineers (ASCE) Standard 7-16 “Minimum Design Loads and Associated Criteria for Buildings and Other Structures” was recently published. It includes a new Appendix E, “Performance-Based Design Procedures for Fire Effects on Structures,” which provides an optional performance-based design procedure addressing structural integrity, fire load development, heat transfer, and structural response. As engineers in North America start to apply these procedures, the mitigation of concrete spalling will become a critical design consideration. The heat transfer and structural analysis of reinforced concrete elements is highly dependent on the thickness of concrete cover during the fire exposure, which can be significantly damaged or even completely removed under a fire event if spalling mitigation is not considered during design and construction.

This paper addresses the current state of practice to mitigate concrete spalling under fire in North America. First, it provides an exhaustive code review for North American structural concrete design under fire, including ACI, ASCE, NBC, NFPA, ASTM, and SFPE, with emphasis on how each document addresses spalling. Second, it explores the structural, materials, and experimental testing applications towards evaluating and mitigating concrete spalling through mixture proportion optimization and materials consulting. Third, it provides a proposed design procedure and approach that engineers can follow when designing new structures as well as retrofitting existing structures. Project examples are provided highlighting application of the design procedure and approach.

KEYWORD: concrete spalling, structural fire, mitigation, material testing, forensics

INTRODUCTION

Prescriptive fire resistance ratings have been used in North America for decades. These ratings attempt to relate the capability of structural members or construction assemblies to resist a standard fire for a specified duration. The member is tested by itself in a furnace under service level load. The fire resistance rating is related to the duration of fire the member survives with respect to temperature propagation limits. While the member cannot fail structurally during the fire exposure, there are no serviceability, deflection, or spalling depth limits.

As fire protection and structural engineers move to performance-based design methods (in lieu of prescriptive fire resistance ratings) the structural capacity, deflection, thermal expansion, and spalling potential of concrete members will be of paramount importance. Finite element models and simplified structural analysis procedures can determine the structural response of the members during and after the fire exposure. However, the implementation of spalling into these analysis procedures is not trivial.

Spalling of concrete at high temperatures during a fire is a complex and highly variable phenomenon. It can occur over a range of exposure temperatures and conditions resulting in a wide spectrum of damage, from small localized surface scabs and cracking to several inches of depth loss over multiple square feet of the concrete surface area. Bazant and Kaplan [1] classifies types of spalling into three groups.

- 1) General or destructive (progressive) spalling: the violent removal of material early in the heat process that may result in extensive damage to the concrete element.
- 2) Local spalling: similar to general or destructive spalling but is limited to corners and aggregate splitting.
- 3) Sloughing off: progressive form of breakdown (ablation) that involves partial separation of material that continues through the latter stages of heating.

The more extreme cases of explosive spalling have been correlated with very fast rising fire temperatures that peak at 1,000°C or higher within a few minutes. Occurrences of extensive spalling have been documented in several major fires throughout the last few decades. Experience in the field has been further companioned through laboratory fire testing that simulates severe heating exposures, such as the UL1709 [2] or RWS time-temperature curve [3]. The most common hypothesized cause for explosive spalling of concrete is the combination of extremely high temperatures and thermal gradients induced during the early stages of extreme fires, which abruptly drives the movement of water originally spread throughout the concrete matrix towards the surface exposed to the elevated heat. The gradient between the near surface (where all the free water has been evaporated) and the free moisture turning into steam just below the surface induces elevated pore pressure build-up. If this pressure build-up is greater than the tensile strength of the concrete, the pressure is forced to be relieved through explosive spalling. Spalling will result in loss of concrete section to varying depths and surface area, including the critical protective cover to internal steel reinforcing. The more severe spalling incidents can substantially and prematurely weaken structural concrete elements and reinforcing steel during a fire event.

The implementation of concrete spalling in design analyses is complicated. First, concrete spalling typically occurs over time in seemingly random locations across the fire-exposed surface. Second, the depth of spalling is not uniform and is highly dependent on the location of the rebar cage. Finally, the concrete constituent properties and environmental exposure heavily influence the spalling potential and severity.

The development of structural fire engineering as an interface between fire protection and structural engineers requires the careful consideration of concrete spalling as it affects both heat transfer and structural capacity. The use of structural fire engineering (SFE) herein refers to both the fire protection and structural requirements when fire is considered as an extreme load in a performance-based structural design process. The use of structural fire engineers herein, refers to either the fire protection or structural engineer who is engaged in the design or analysis of a structural system under extreme fire loading. It is expected that engineers of both disciplines are aware of the entire SFE process and not just their respective field.

NORTH AMERICAN CODE REVIEW

Structural fire engineers have several codes and standards available in North America. They are highly dependent on the local jurisdiction and type of structure under design. In general, the International Building Code (IBC) [4] is widely adopted throughout the United States. The IBC further adopts various structural and material specific codes or standards, as shown in Table 1.

Table 1 Summary of North American Codes and Standards for Concrete Design

Ref.	Scope	Document	Latest Version	Code/Standard
[4]	General	IBC	2018	International Building Code
[5]		NBC	2015	National Building Code of Canada
[6]	Structural Loads	ASCE 7	2016	Minimum Design Loads for Buildings and Other Structures
[7]	Fire Loads	SFPE S.01	2011	Standard on Calculating Fire Exposures to Structures
[8]		ASTM E119	2018	Standard Test Methods for Fire Tests of Building Construction and Materials
[9]		ULC S101	2014	Standard Methods of Fire Endurance Tests of Building Construction and Materials
[10]		SFPE/Springer	5 th ed.	Handbook of Fire Protection Engineering
[11]	Structural Properties	ACI/TMS 216.1	2014	Code Requirements for Determining Fire Resistance of Concrete and Masonry Construction Assemblies
[12]		NFPA 502	2017	Standard for Road Tunnels, Bridges, and Other Limited Access Highways
IBC NBC ASCE SFPE ASTM UL(C) ACI TMS NFPA	International Building Code National Building Code of Canada American Society of Civil Engineers Society of Fire Protection Engineers American Society for Testing and Materials Engineers Underwriters Laboratory (Canada) American Concrete Institute The Masonry Society National Fire Protection Association			

General

The IBC and NBC are the major governing codes throughout North America. They address almost all aspects of building design, including fire and smoke protection. Fire is addressed through prescriptive requirements, where the structural member or construction assembly is tested in a furnace. Thermal propagation is the primary failure mode, as the unheated surface is not allowed to increase in temperature past a certain set point. In addition, reinforced concrete members have minimum cover thicknesses to the reinforcement which must be followed. There is no mention of concrete spalling in the NBC. The only mention of concrete spalling in the IBC is in a footnote in Table 721.1(1), "Minimum Protection of Structural Parts based on Time Periods for Various Noncombustible Insulating Materials" which states that "Adequate provisions against spalling shall be provided by U-shaped or hooped stirrups spaced not to exceed the depth of the member with a clear cover of 1 inch." This provision does not stop spalling from occurring and only prevents it from extending beyond the clear cover of 1 inch.

Structural Loads

Service level loads on buildings is determined from ASCE 7. This covers all dead, live, wind, rain, snow, seismic, and tsunami loading conditions. Up until the 2016 edition, there was no mention of fire loading. Recently, Appendix E and its associated commentary was added to address "Performance-based Design Procedures for Fire Effects on Structures." These sections are primarily intended to guide the structural fire engineer through the entire design process. Specific design considerations that are unique to structural elements when subjected to fire are highlighted. Concrete spalling is repeatedly discussed; however, no explicit mitigation suggestions are provided. For example, ASCE 7-16 states in CE.3 that "Section loss resulting from fire exposure (e.g., because of spalling or charring) may also contribute...". Essentially, ASCE 7-16 only states that concrete spalling is a structural concern and should be considered in design. Specific methods to mitigate spalling are not covered.

Fire Loads

Traditional fire loading is achieved by applying either the ASTM E119 (United States) or ULC S101 (Canada) standard time-temperature curve. This relationship was developed to certify fire protection products and assemblies based on discrete fire ratings (i.e., 1hr, 2hr, 3hr). Fire protection engineers have moved into performance-based design methods using the SFPE/Spring Handbook of Fire Protection Engineering as the primary source for empirical relationships and fire dynamics input parameters. In addition, SFPE S.01 was developed specifically to guide fire protection engineers when designing custom fire exposure for buildings.

The SFPE S.01 standard has little mention of concrete spalling, except for a short definition of what parameters are necessary when analysing the structural response. The omission of concrete spalling from heat transfer discussions is important, as section loss can accelerate the rise of unheated surface temperatures.

The SFPE/Springer Handbook of Fire Protection Engineering has a much more detailed discussion on concrete spalling in Chapter 9. A full background on concrete spalling initiation is provided, along with recommendations on polyurethane fibre mitigation strategies. In addition, the document discusses concrete spalling in the following chapters: 34-finite element modelling, 52-building assemblies and frames, 54-concrete members, 86-building envelope, and 88-vehicle tunnels.

Structural Response

The NFPA 502 standard contains special provisions for passive fire protection which are intended to prevent collapse of the tunnel structure during a worst-case fire event on the roadway. The bounding exposure specified for such conditions and the requisite fire protection is the 2-hr Rijkswaterstaat (RWS) fire curve. This type of severe exposure represents actual tunnel fires for various combustibles, but not necessarily all hazardous materials or flammable liquids that may be transported throughout North America.

The standard building fire prescribed in ASTM E119, and its acceptance criteria, is traditionally used for fire resistance ratings of US building construction. These are markedly different from those in NFPA 502 for tunnel fire protection during a RWS fire. The standard RWS fire exposure subjects the construction to fast rising and much higher temperatures than the standard ASTM E119 building fire. These substantial heating differences have been demonstrated to have an adverse effect on exposed concrete, relative to its progressive (explosive) spalling risks during an RWS fire. In contrast to the conventional ASTM E119 ratings and practices that do not impose any temperature limits or require any

external fire protection on exposed (unprotected) concrete, the NFPA 502 criteria specifically require concrete designs and/or fire protection to prevent explosive spalling. Hence, the passive fire protection used for these potentially significantly more severe fire conditions must be qualified through full-scale tests subject to the 2-hr RWS exposure and based on the NFPA 502 acceptance criteria.

Even though the RWS fire is intended for tunnel exposures, the spalling discussion and performance requirements in NFPA 502 are still applicable to other structures and fire environments. During a 120-minute period of fire exposure, NFPA 502 Section 7.3.3 specifies that concrete structural elements shall be designed or protected to prevent progressive spalling.

SPALLING MITIGATION

There are two primary methods to prevent or mitigate concrete spalling damage attributed to extreme fire exposure.

1) Supplemental fire protection:

Vendors have developed passive fire protection products tested against standard fire curves to provide the necessary prescriptive fire rating. These products tend to be expensive and may require costly maintenance throughout the life of the structure. The use of these materials may also limit the utilization of performance-based design methods as the products are tested using standard fire curves. Their behavior and under fire curves developed specifically for the design basis threat at a particular project site are typically unknown and will require fire testing to provide certification.

2) Concrete mixture composition:

The development of spalling resistant concrete can be improved in the selection of concrete constituents and the development of the concrete mixture proportions. Certain constituents and mixture proportions have been shown to be generally successful but not absolute in limiting damage due to explosive spalling.

Although designing for a concrete structure that is resilient towards fire induced concrete spalling does not offer a steadfast approach, the authors propose the following guidance towards the selection of concrete constituents and the development of the concrete mixture proportions. The following mixture controls have been shown to minimize the potential for explosive spalling damage during severe fire exposures.

Concrete Constituents

Aggregates: Aggregate mineralogy, which includes the chemistry, crystal structure, and physical properties, significantly affects a concrete's potential for explosive spalling. Concrete constructed with calcareous aggregates (limestone) have substantially higher heat capacity than concrete constructed with siliceous aggregates [13]. In the same manner, basaltic sand as a fine aggregate replacement offers more stability at high temperature levels [14]. It is recommended that only calcareous aggregates (limestone) be used when spalling mitigation is required.

Aggregate gradation and nominal maximum size properties have varying impact on concrete's performance in fire and the potential for explosive spalling. Generally, the recommended nominal maximum coarse aggregate size should be limited to ≤ 19 mm and graded such that smaller coarse aggregates are incorporated into the concrete mixture [15].

Historically, lightweight aggregates have been specified to minimize the potential for explosive spalling, but due to the porous nature of the lightweight aggregate requires the

material to be fully saturated prior to batching. The excess free water contained in the porous lightweight aggregates as well as the lack of control with respect to excess water maintained on the surface of the aggregates at the batch plant facility; all contribute to higher vapor pressure under fire exposure and explosive spalling [16].

Cementitious Materials and Quantity: The quantity and type of cementitious materials selected for concrete mixture proportions impacts a concrete's potential for explosive spalling. Fundamentally, concrete mixtures with higher cementitious contents have been shown to have an increased potential for explosive spalling. This behavior is due to the increase in water demand and total water content.

Supplementary cementing materials (SCMs) (i.e. fly ash, slag cement, silica fume, etc.) can impact the potential for explosive spalling. SCMs are added to concrete to densify the cement matrix and thereby decrease the permeability of the concrete. The densification and bond strength of the cement matrix is further demonstrated at the interfacial transition zones (paste to aggregate interface) that would otherwise offer outlets for moisture migration, thereby effectively lowering permeability and increasing the possibility of explosive spalling. Therefore, it is not recommended to use fillers or certain SCMs, such as silica fume or limestone cements [15]. However, not all SCMs have been shown to have a negative impact on the spalling potential. Slag cement has been found to offer stability at high temperature as well as mitigate risks associated with post cooling spalling [14].

Fibers: Polypropylene (PP) fibers have been found to be the most effective in mitigating explosive spalling due to their relatively low melting point (170°C) which allows for the creation of cavities and thereby increasing the interconnectivity between the concrete pores prior to the concrete reaching spalling temperatures between 190°C and 250°C [17]. The prescribed length of the fibers is dependent on the size of the coarse aggregate; the larger the size of the coarse aggregate, the longer is the optimum length of fibers for spalling protection of concrete [18]. Although thinner fibers decrease concrete workability they have proven to be more effective in developing micro-channels for pressure relief [15].

Concrete Properties

Permeability: A governing factor influencing resistance to spalling under elevated temperatures is the concrete permeability and/or ability to readily transport pore water through the cement matrix. Less dense concrete is desirable when designing concrete resistance towards fire induced explosive spalling. This can be accomplished by reducing the overall concrete unit weight; lowering the cementitious content while maintaining a low total water content and restricting the use of select SCMs containing particles sizes smaller than the cement grains (i.e., silica fume) [19].

Concrete Strength: High strength concrete has an increased potential for explosive spalling due to the low permeability and high cementitious content. High strength concrete with a compressive strength 70 to 95 MPa will have a permeability 1000x less compared to normal strength concrete of 28 to 42 MPa compressive strength [20]. Targeting a lower compressive strength concrete effectively lowers the concrete permeability, and thus, decrease explosive spalling associated with high strength concrete.

Free Moisture: Higher moisture content significantly increases the risk of explosive spalling since more vapor pressure must be released depending on the permeability of the concrete. High cement content increases the total amount of water added to the concrete, even when the concrete has a low water–cementitious ratio. Concrete mixture proportions with less than 3 wt% moisture will have a lower risk of spalling [19].

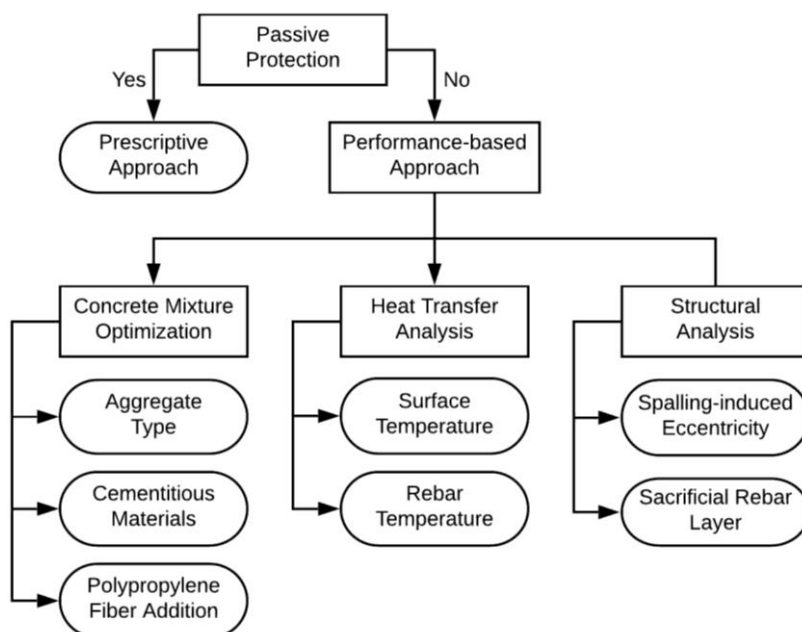
Structural Analysis

Spalling-induced Eccentricity: An eccentricity can develop during unsymmetrical heating of reinforced concrete [21]. As the concrete heated face spalls, the cross section is reduced from one side only. The applied gravity load, while concentric prior to fire exposure, is now eccentric with respect to the reduced cross section. This unintended eccentricity can cause out-of-plane movement and substantial tension forces to develop which may not have been captured in the initial structural design. The structural engineer of record (SEOR) should assume that the cover concrete has spalled and analyze the structural element's capacity to carry this newly developed eccentric load.

Sacrificial Rebar Layer: Spalling typically stops at the first layer of reinforcement in the structural member [21]. In addition, one of the failure criteria in NFPA 502 is the rebar temperature, knowing that it is likely spalling could occur to this point, but not further. One possible mitigation strategy, if there is sufficient room, is to install a sacrificial (outer) layer of reinforcement. The SEOR ignores this sacrificial rebar and cover during the ambient design to carry service level loads. However, the concrete cover between the sacrificial rebar and structural (inner) rebar is assumed to be present during the entire fire exposure, regardless if any concrete constituent mitigation was done. The resulting temperature of the structural rebar will be much lower and help provide adequate strength to the structural member during the fire exposure.

PROPOSED DESIGN PROCEDURE

As shown in Figure 1, the first step of any design procedure to mitigate spalling is to discuss long-term serviceability requirements with the owner. Several insulation products have been developed to protect concrete members from fire exposure in accordance with the standards and codes discussed herein. However, routine inspection and maintenance costs may make these products significantly more expensive when considering total life-cycle costs of the structure. If the owner proceeds with a properly designed prescriptive protection system, then concrete spalling mitigation may not be required.



Once a performance-based approach is selected by the owner, a series of design modifications and analyses must be performed by the design team. This involves several disciplines including the architect, contractor, batch plant, concrete material consultant, fire protection engineer, and structural engineer. There are three main items that need to be considered: 1) concrete mixture optimization; 2) heat transfer analysis; 3) structural analysis.

Figure 1 Spalling Mitigation Flowchart.

Concrete Mixture Proportions

The concrete constituents and mixture proportions are developed by the concrete materials consultant in coordination with the contractor, batch plant, and structural engineer. A concrete mixture will be developed that properly addresses spalling mitigation considering locally available materials, costs and the parameters reported previously; while also meeting the structural demand and requirements. The contractor and batch plant should schedule a trial batch early in the construction process to cast cylinders. A petrographer, following ASTM C856 [22] and ASTM C1723 [23], will analyse the test cylinders and verify that all spalling mitigation measures are properly incorporated. Once the final mixture proportions are selected, the contractor and batch plant will need to use this concrete throughout the structure where spalling mitigation is required.

Recently, the authors developed concrete mixture proportions for a twin-tube highway tunnel in Louisville, KY. The authors were able to implement the above described approach to develop a concrete mixture that contained calcareous coarse aggregates, moderate w/cm, PP fibres, and no SCMs. After a few iterations, the concrete mixtures were evaluated and approved using optical and scanning electron microscopy and materials consulting.

Later, the concrete mixture proportions were validated with representative-scale fire testing. Specimens were cast, cured at >90% relative humidity (RH) for three months, conditioned to one of two internal RH (75% and 90%), applied service-level load, and evaluated with simulated 50 MW fire curves. During and after the testing, no explosive spalling was visually observed or recorded. Optimization of the concrete mixture proportions reduced construction cost, by eliminating the need for passive fire protection.

Heat Transfer Analysis

To perform a SFE analysis, the cross-section temperatures of the concrete must be determined using the principles of heat transfer. Under steady-state conditions, this can be done using a simple hand calculation. Under transient conditions, which is most likely for natural structural fire environments, a finite-element or finite-difference analysis program can be readily used. Since spalling is random across the heated surface of the concrete, several analyses should be completed investigating various cover loss depths. The cover loss should be bounded between zero (no spalling) and full cover (to first rebar layer). It is conservatively assumed that the entire heated surface spalls at the same time and at the same depth.

One recent project that the authors completed is in Boston, MA. A high-rise building was designed to span over a highway and commuter rail tracks, creating a new tunnel directly below the structure. This triggered the requirement that the structural system at the roadway/track level be designed to satisfy NFPA 502. The primary load-bearing capacity of the structure was provided using 915 mm thick concrete walls on both sides of the highway and tracks. The heat transfer was analysed using Abaqus [24].

As shown in Figure 2a, due to the size of these bearing walls, a sacrificial layer (i.e., outer layer) of reinforcement was installed within the cover of the main reinforcing. This outer layer of reinforcement was not accounted for in the structural analysis, so its failure during an extreme fire event would have no impact on the load-carrying capacity of the structure.

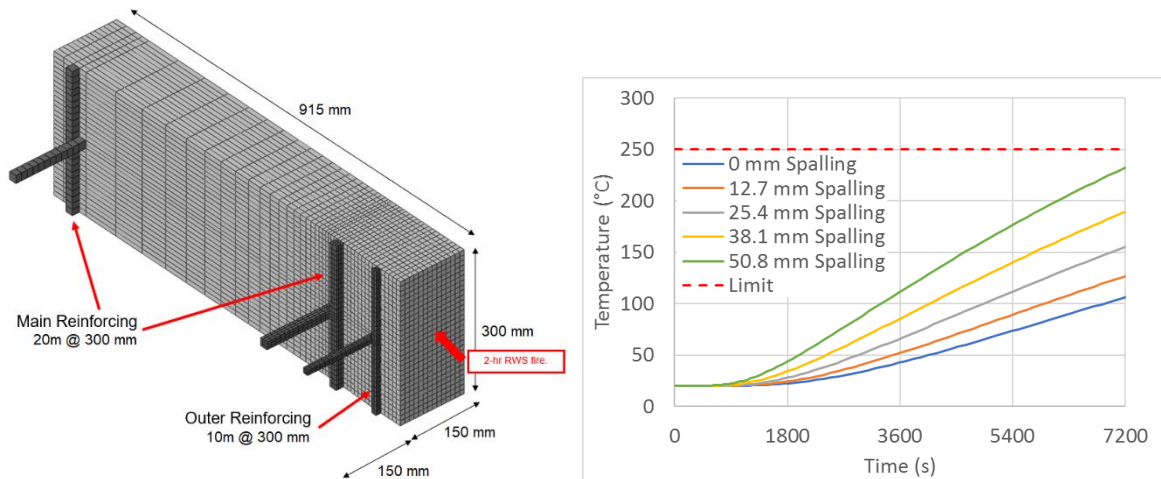


Figure 2 Concrete Wall Results: (a) Finite Element Mesh; (b) Main Reinforcing Temp.

The heat transfer model was analysed under five (5) cover-loss depths; 0mm (representing no spalling), 12.7mm, 25.4mm, 38.1mm, and 50.8mm (representing the full cover). As shown in Figure 2b, these analyses give insight on how spalling accelerates the heat transfer through the concrete thickness by plotting the temperature of the main structural (inner) reinforcement with time (fire duration). The dashed line represents the maximum allowable temperature according to NFPA 502. For this project, the sacrificial layer of reinforcement allowed the entire cover to spall and still result in an acceptable temperature for the main structural reinforcement.

Structural Analysis

To finish the SFE analysis, the through-thickness temperatures calculated during the heat transfer study must be mapped over to the structural model. For NFPA 502 projects, there are discrete temperature limits that must be met. While this does not necessarily require a structural analysis, the design team must make the final determination if those temperature limits are sufficient to fully protect the structure from extreme fire exposure.

If the temperature limits are not sufficient the structure must be analysed under the fire exposure. This process should follow the procedures as outlined in ASCE Manual of Practice 138 [25]. This includes obtaining temperature-dependent material properties for the concrete and reinforcing steel, properly modelling the boundary conditions, and investigating the cooling phase of the fire exposure (if necessary).

SUMMARY AND CONCLUSIONS

Reinforced concrete is a common construction material used in North America. Most standards and codes do not discuss concrete spalling or offer mitigation options. As structural and fire engineers move towards a performance-based design process the mitigation of concrete spalling must be considered. This paper provides a proposed methodology to address concrete spalling throughout the design process, from the concrete constituents to the heat transfer and structural analysis.

REFERENCES

1. Bazant, Z., Kaplan, M. (1996), *Concrete at High Temperatures: Material Properties and Mathematical Models*, Longman Group Ltd, Essex England.
2. UL 1709, "Rapid Rise Fire Tests of Protection Materials for Structural Steel," Underwriters Laboratory, Northbrook, IL, 2017
3. Breunese, A.J., Both, C., Wolsink, G.M., "Fire testing procedure for concrete tunnel linings," Efectis Netherlands Report no. 2008-Efectis-R0695, September 2008.
4. International Building Code (IBC), International Code Council, 2018.
5. National Building Code (NBC) of Canada, 2015.
6. ASCE/SEI 7, "Minimum Design Loads and Associated Criteria for Buildings and Other Structures," American Society of Civil Engineers, 2016.
7. SFPE S.01, "SFPE Engineering Standard on Calculating Fire Exposures to Structures," Society of Fire Protection Engineers, 2011.
8. ASTM E119, "Standard Test Methods for Fire Tests of Building Construction Materials," American Society of Testing and Materials, 2018.
9. CAN/ULC S101, "Standard Methods of Fire Endurance Tests of Building Construction and Materials," Underwriters' Laboratories of Canada, 2014.
10. Hurley, M., "SFPE Handbook of Fire Protection Engineering," Society of Fire Protection Engineers, Fifth Edition, 2016.
11. ACI 216, "Code Requirements for Determining Fire Resistance of Concrete and Masonry Construction Assemblies," American Concrete Institute, 2014.
12. NFPA 502, "Standard for Road Tunnels, Bridges, and Other Limited Access Highways – 2017 Edition," National Fire Protection Association, Quincy, MA, 2017.
13. Kodur, V.K.R., Sultan, M.A., "Thermal Properties of High Strength Concrete at Elevated Temperatures," NRCC-42052, SP 179-29, 1998.
14. Iravani, A., Anders, S. "Effects of cement type, aggregate type and concrete age on the mass loss of concrete exposed to elevated temperature." 5th International Workshop on Concrete Spalling due to Fire Exposure, 2017.
15. Connolly, R. (1997). "Spalling of concrete." *Fire Eng. J.*, 57(186).
16. Bilodeau, A., Malhotra, V.M., and Hoff, G.C. (1998). "Hydrocarbon Fire Resistance of High Strength Normal Weight and Light Weight Concrete Incorporating Polypropylene Fibres", International Symposium on High Performance and Reactive Powder Concrete, Sherbrooke, QC.
17. Kalifa, P., Menneteau, F.D., Quenard, D., Spalling and pore pressure in HPC at high temperatures," *Cement and Concrete Research Journal*, V.30, 2000.
18. Heo, Y., et al., "Relationship between inter-aggregate spacing and the optimum fiber length for spalling protection of concrete in fire." *Cement and Concrete Research* 42.3, 2012.
19. Hertz, K. "Limits of spalling of fire-exposed concrete." *Fire Safety Journal* 38.2, 2003.
20. Kodur, V.K.R. "Spalling in high strength concrete exposed to fire: concerns, causes, critical parameters and cures." *Advanced Technology in Structural Engineering*. 2000.
21. Mueller, K.A., Kurama, Y.C., "Out-of-Plane Behavior and Stability of Five Planar Reinforced Concrete Bearing Wall Specimens under Fire," *ACI Structural Journal*, V. 112, No. 6, Nov-Dec 2015.
22. ASTM C856, "Standard Practice for Petrographic Examination of Hardened Concrete," ASTM International, 2017.
23. ASTM C1723, "Standard Guide for Examination of Hardened Concrete Using Scanning Electron Microscopy," ASTM International, 2016
24. Abaqus/CAE, Dassault Systemes Simulia Corporation, Providence, RI, 2017.
25. ASCE Manuals and Reports on Engineering Practice No. 138, "Structural Fire Engineering," American Society of Civil Engineers, 2018.

Mitigation of Fire-Induced Spalling of Concrete using Recycled Tyre Polymer Fibre

Yifan Li^{1,*}, Shan-Shan Huang¹, Kypros Pilakoutas¹, Harris Angelakopoulos² & Ian Burgess¹

¹ Department of Civil & Structural Engineering, The University of Sheffield, Sheffield, UK

² Twincon Ltd, Sheffield, UK

* Corresponding author (yli101@sheffield.ac.uk)

ABSTRACT

Under extreme circumstances, such as rapid heating or high temperatures, concrete can spall explosively. The propensity of fire spalling is higher for High Performance Concrete (HPC) than normal concrete, mainly due to its low permeability. Effective spalling mitigation measures include the use of small quantities of micro-polymer fibres, such as polypropylene (PP) fibres. To improve the sustainability of this mitigation method, this paper presents a study on a novel substitution of manufactured PP fibres with Recycled Tyre Polymer Fibres (RTPF) that require only a fraction of the energy needed to make equivalent manufactured fibres. To examine the effects of RTPF on fire spalling propensity, experiments were conducted on self-compacting HPC specimens. A new radiant panel heating system was developed to replicate realistic fire conditions. The test results demonstrate the effectiveness of RTPF in the mitigation of fire-induced spalling. The severity of fire spalling is shown to be related to the surface moisture content rather than overall moisture content.

KEYWORD: fire, spalling, concrete, recycled fibre

1. INTRODUCTION

Fire-induced spalling is one of the most complex and poorly understood phenomena affecting concrete structures. It is defined in CIRIA Technical Note [1] as: “*the breaking-off of layers of pieces of concrete from the surface of a structural element when it is exposed to the high and rapidly rising temperatures experienced in building fires*”. It is generally accepted that the fire spalling of concrete is caused by a combination of mechanisms, which includes thermal expansion, chemical degradation, hydraulic phase change and moisture transportation [2-5]. Concrete contains free capillary water and chemically bonded water due to hydration. In fire conditions, the heating causes dehydration and the evaporation of water. As water is confined inside the pore system, pore pressure is built-up. Once the pore pressure generates stresses which exceed the critical tensile stress of concrete, cracking and spalling occur. The pore pressure may act as a trigger of explosive spalling [2]. The actual occurrence of explosive spalling may also depend on the thermal-mechanical behaviour of concrete. Due to the low thermal conductivity of concrete, rapid heating, in particular, will generate a highly non-uniform temperature distribution within a cross-section. This can induce high compressive stresses close to the heated surface due to restrained thermal-expansion. The differential stresses between the hotter outer layer and the cooler concrete core lead to local fractures, which may cause the spalling-off of the whole section [4].

The damage caused by fire spalling has detrimental effects on structures, as it reduces the effective cross-sectional area of structural elements, causing reduced load capacity. The loss of concrete also leads to the direct fire exposure of steel reinforcement, which can significantly decrease its mechanical properties. Based on the damage level observed on structural

elements, the severity of fire-induced spalling was classified by Jansson & Odeen [6], from Level 1 of slight spalling of the concrete surface to Level 5 of bottom reinforcement falling off.

Conventionally, the characteristics of non-combustibility and low thermal conductivity make concrete an inherently good fire-resistant material. However, the development of modern HPC with a much denser pore system amplifies the risk of fire spalling [7, 8]. Spalling of concrete has been observed in tunnel fires, such as the Channel Tunnel fire 2008 [9], the Mont Blanc Tunnel fire 2001 [10], and building fires such as the HengZhou Building fire 2003 [11] and the Kings Dock Car Park Fire 2017 [12].

Four mandatory measures are provided to mitigate spalling of concrete in Clause 6.2 of Eurocode 2-1-2 [13]. One of these measures is to include more than 2kg/m^3 of monofilament PP fibres in the concrete mix. The addition of PP fibres into high strength concrete has been demonstrated experimentally to increase its fire resistance [14-18]. Common PP fibres have a typical melting point of around 160°C , while at around 200°C their complete melting and diffusion creates pathways through the concrete pore system, which increase permeability. This enables the release of pore pressure build-up, facilitating the migration of the moisture clog, and hence mitigating the propensity to spalling [19] [20].

Sustainability is one of the global grand challenges [21, 22] with existential consequences if it is not addressed effectively. More than 3.5 million tonnes of waste tyres are dumped in Europe every year, but the disposal of the tyres is challenging, because they are non-biodegradable and highly durable. Recycling end-of life tyres, which comprise 80% rubber 15% steel and 5% polymers, is of interest to both the construction and waste management industries [23].

In contrast to manufactured PP fibres, RTPF is more environment-friendly, as it requires only a small amount of energy for its production. Since RTPF has a melting point similar to PP fibres, it also has the potential to mitigate fire spalling. However, unlike manufactured fibres which are of certain length and diameter, recycled fibres have distributions of lengths and diameters, are agglomerated and contaminated with rubber [24]. To utilise RTPF in concrete, they need to be cleaned, separated and then effectively integrated into the concrete. Therefore, a prototype of RTPF cleaning and integration system has been adopted which allows the cleaned and separated fibres to be uniformly dispersed into concrete during the mixing stage.

This paper presents the results of fire spalling tests on HPC specimens with and without RTPF, in order to investigate the effect of RTPF on fire spalling mitigation. A new radiant panel heating system was used for fire spalling tests. As moisture content significantly affects the occurrence of fire spalling, the moisture content distribution through the specimen's depth, as well as its evolution over time, were measured and are presented in this paper.

2. EXPERIMENTAL DETAILS & METHODOLOGY

The fire spalling tests were carried out using the radiant panel heating system built at the University of Sheffield. The system comprises a 36KVA three-phase transformer, a Eurotherm temperature controller, a heating element radiant panel, a loading frame and a NI data acquisition system, as shown in Figure 1. This setup can develop 2500KW of power, 1500kN of compression and can simulate the first 30min of the ISO834 standard fire.

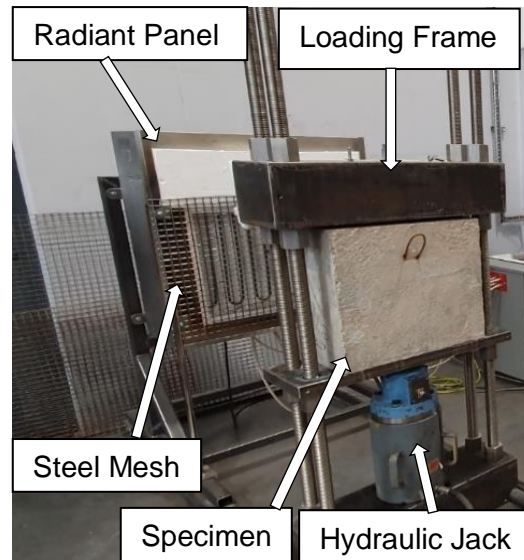


Figure 1 Experimental set-up of the fire spalling testing system.

2.1 Fibre processing

Contaminated RTPF (Figure 2a) are firstly cleaned to remove rubber particles and dirt, and a sample of clean fibres is shown in Figure 2b. The fibre length of clean RTPF ranges from 2mm to 6mm and the fibre diameter ranges from 11 μ m to 23 μ m. The clean fibres are separated using a vibrating wire arrangement before being blown into the mixer. This enables a homogeneous dispersion, and once mixed in the concrete the fibres can barely be seen.



Figure 2 (a) Raw RTPF; (b) Dispersed clean RTPF.

2.2 Concrete mix design

Details of the mix design for a self-compacting high strength concrete, C50/60, are shown in Table 1.

Table 1 Concrete mix design.

Materials		Dry Weights
Type	Source	
CEM I	Cemex - South Ferriby	440 (kg/m ³)
0/2 mm	HumberSide Aggs-North Cave	250 (kg/m ³)
4/10 mm	Cemex - Doveholes	970 (kg/m ³)
Fine Limestone	Cemex - Doveholes	620 (kg/m ³)
Admix 1	Cemex WRA-CP105	2930 (ml/m ³)
Admix 2	Cemex Superplasticiser - CSP313	5280 (ml/m ³)
W/C	Free water/Cement Ratio	0.35
RTPF Mix	Recycled Tyre Polymer Fibre	2 (kg/m ³)

Ready-mix concrete was used. Six concrete specimens were cast in 500mm × 500mm × 250mm moulds, three specimens were plain concrete and the other three contained 2kg/m³ of RTPF. Thermocouples were placed in one specimen at depths 1mm, 5mm, 10mm, 20mm, 50mm from the heated surface, to measure the temperature distribution through the depth of the specimen. Cubes and cylinders were also cast for measurement of compressive strength and moisture content.

2.3 Moisture content monitoring

As fire spalling occurs near the surface of concrete, its spalling propensity is expected to be more dependent on the heated surface moisture content than the average moisture content overall. A convenient method to determine moisture content is to extract a core from a specimen, dry it, and determine the relative weight loss. However, the coring process requires cooling water to protect the cutting saw, and this may affect the moisture content of the sampled core. To solve this problem, cylinders of 200mm height and 100mm diameter were cast from the same batch and cured under the same conditions as the test specimen. Before curing, all cylinders were cut at 5mm, 10mm, 15mm from the top surface, and reassembled to maintain the length of the moisture path, as shown in Figure 3a. The circumferential surface of each slice was sealed individually using aluminium tape, and the joints between adjacent layers were sealed using water-proof plastic tape, as shown in Figure 3b. This arrangement allowed for a unidirectional moisture transport condition, as for the main test specimens.

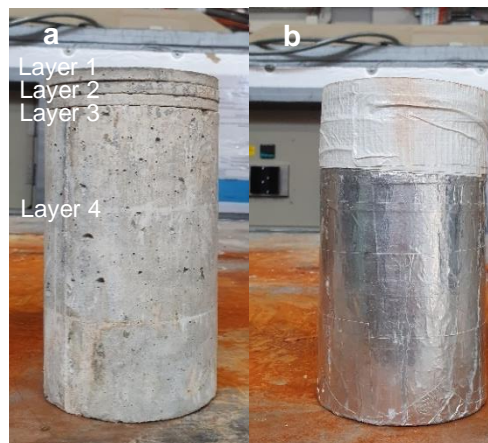


Figure 3 (a) Cylinder cut into slices at heights 5mm, 10mm and 15mm; (b) Sliced cylinder wrapped with aluminium foil and plastic tapes.

After the curing stage, one cylinder from each mix was oven dried at 105°C and until its weight was stabilised. The initial concrete moisture content (by mass) can be calculated by subtracting the dried weight from the total weight of wet cylinders. The moisture content of all slices gives the moisture distribution across the depth of the concrete specimen.

To investigate the effect of surface moisture content on the severity of fire spalling, the specimens and control cylinders are divided into three groups, as shown in Table 2.

Table 2 Drying condition of two groups.

Groups	Specimen	Time of drying
Series 1	P1 F1	1 Day
Series 2	P2 F2	15 Days
Series 3	P3 F3	35 Days

Note: P = plain concrete; F = specimens with 2kg/m³ of RTPF

2.4 Test Calibration

The concrete specimens were heated by the radiant panel following the ISO 834 standard fire curve [25]. A plate thermometer was placed close to the centre of the heated surface of a specimen to calibrate the radiant panel system. Through the calibration process, the heating outputs of the radiant panel over the testing period were tuned for the plate thermometer measurements (approximately representing the adiabatic surface temperature of the concrete specimen [26]) to match the ISO 834 standard fire curve. The temperature calibration data is shown in Figure 4. The “Concrete surface” curve is the temperature-time relationship measured by the plate thermometer.

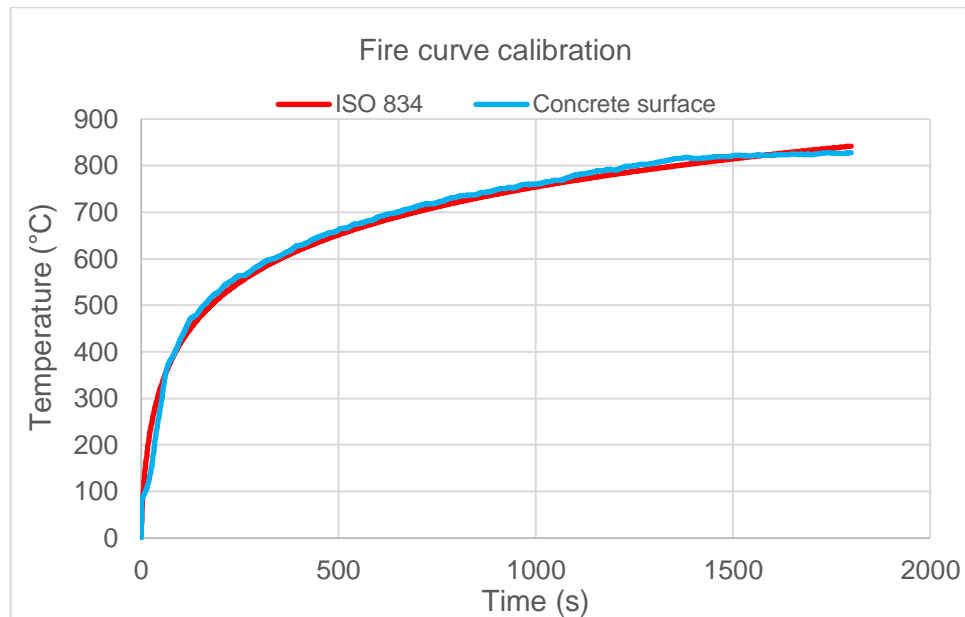


Figure 4 Temperature calibration curve of the radiant panel.

2.5 Test procedure

Before testing, all specimens were aged for 18 months. The average compressive strength of concrete cubes was around 49 MPa. The distance between the concrete specimen and the radiation panel was fixed at 100mm. Two steel meshes were used, as shown in Figure 5, to protect the heating elements from being damaged by concrete debris generated during the explosive spalling. Two cameras were used to record the test. One camera faced the heated concrete surface to monitor spalling and the other faced the back of the concrete specimen to monitor the appearance of surface water. Fire blankets were used for isolating the loading frame from the heat. A uniformly distributed load was imposed on the bottom of the specimen to provide a uniaxial compression of 10MPa, 20% of the compressive strength of the concrete (C50/60).

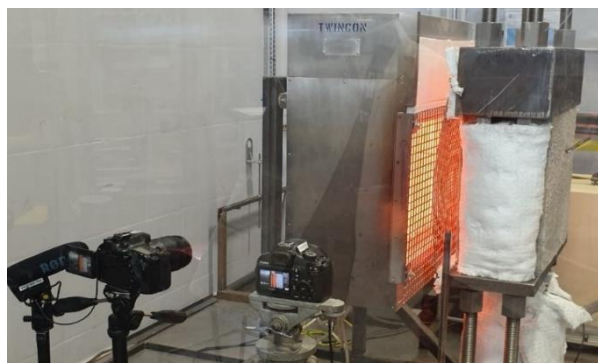


Figure 5 Fire spalling test in procedure.

After each spalling test, the profile of spalled specimens was examined using a laser scanning system. This comprises a laser head, a supporting frame and a two-dimensional stepper motor. The laser scanner determines the spalling depth across the concrete surface. The point data were collected and processed using a MATLAB code to output the maximum spalling depth, spalling volume and the 3-D spalling profile.

3. RESULTS AND DISCUSSIONS

3.1 Moisture Content

The specimens were moisturised to increase the surface moisture content, and thus test the effectiveness of the RTPF in fire spalling mitigation in a relatively severe situation. The measured moisture content distributions in the specimens on the testing dates are shown in Figure 6.

The moisture content of the top layer of the cylinder is the largest (7.3%) on Day 1, decreasing from the surface towards the inner part of the cylinder. From Day 1, the specimens were exposed to the lab environment, and the surface moisture content decreased over time since then. After Day 20, the Layer 4 (from depth 15mm to 200mm) had the highest moisture content and stabilised at about 5.9% until Day 35.

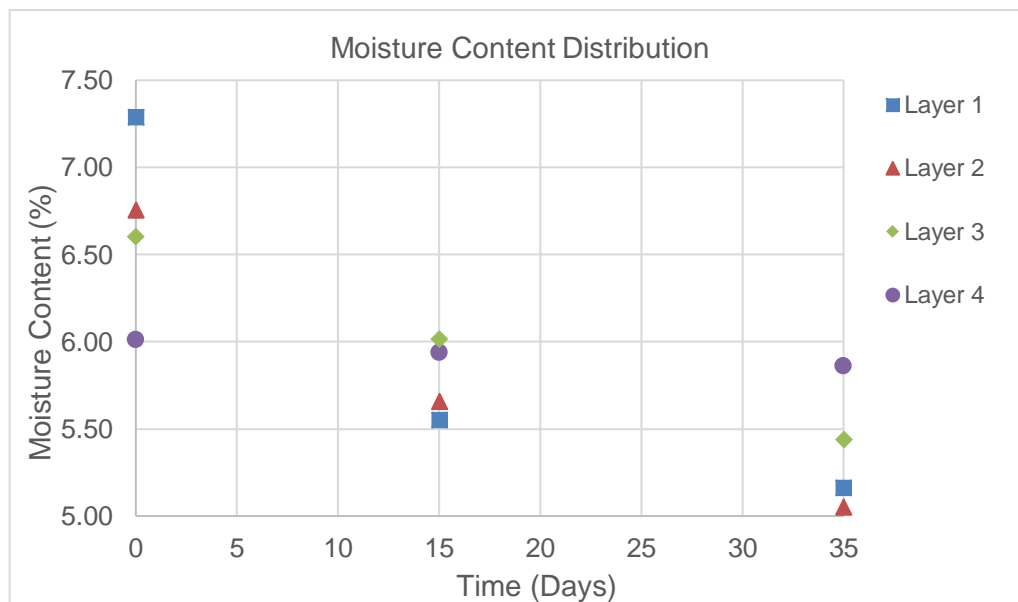


Figure 6 Moisture content distribution.

3.2 Temperature

Specimen F1 was instrumented with five thermocouples at different depths, as described in section 2.2. The temperature distribution of one specimen during the fire spalling test is shown in Figure 7, where “F1” is the specimen name and “x mm” indicates the location of the thermocouple, as its distance from the heated surface.

In the temperature range between 100°C and 200°C, several plateaux can be seen in curves “F1 1mm”, “F1 10mm”, and “F1 50mm”. The plateau is believed to be caused by the latent heat needed for vaporization of water. After 270°C, the water saturation pressure is expected to exceed 5MPa [27], which is higher than the tensile strength of HPC with compressive strength of 50Mpa to 80Mpa [28, 29]. Beyond this temperature, cracks are expected to develop in the pore system, which release the moisture, and hence no temperature plateau is expected beyond this point.

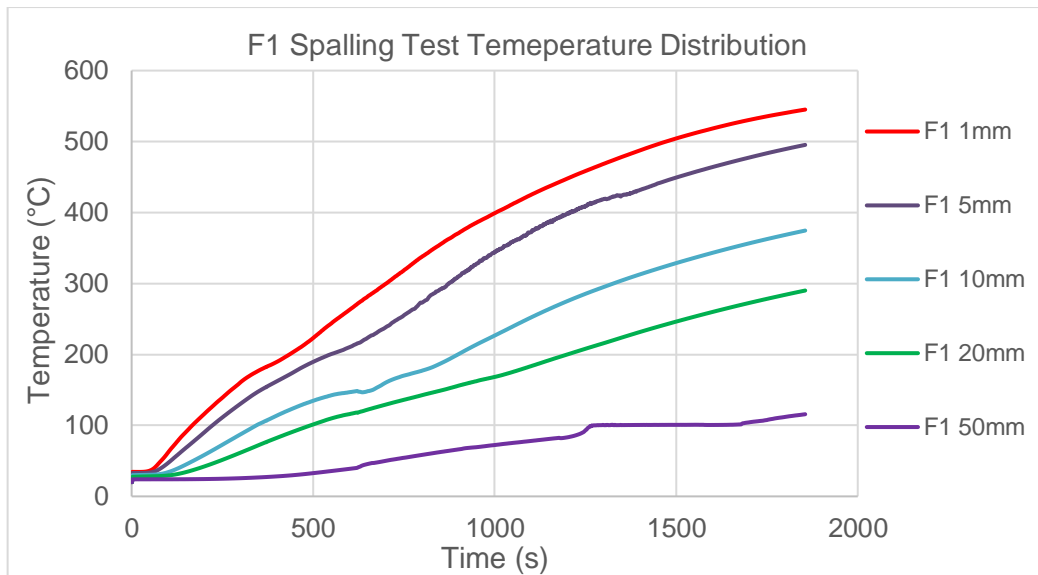


Figure 7 The temperature distribution of RTPF specimens at depths of 1, 5, 10, 20,50mm from the heated surface.

3.3 Spalling

The spalling events for all test series were recorded using in-situ cameras. Several phenomena were observed during the fire spalling tests:

- (1) Series 2 & 3 specimens tended to spall into smaller pieces of concrete, with a crisp sound like a bullet shot. Series 1 specimens spalled much more violently, with large concrete pieces exploding with a loud blast sound. The spalling sound was loudest for specimen P1.
- (2) Water leaking, a common phenomenon in fire spalling tests, was observed from some of the unheated surfaces of the specimens.
- (3) For specimens with RTPF, a significant amount of vapour release was seen from the heated surface and the sides of the specimen, due to the increased permeability caused by the melting of the RTPF.

The spalling profile is shown in Figure 8:

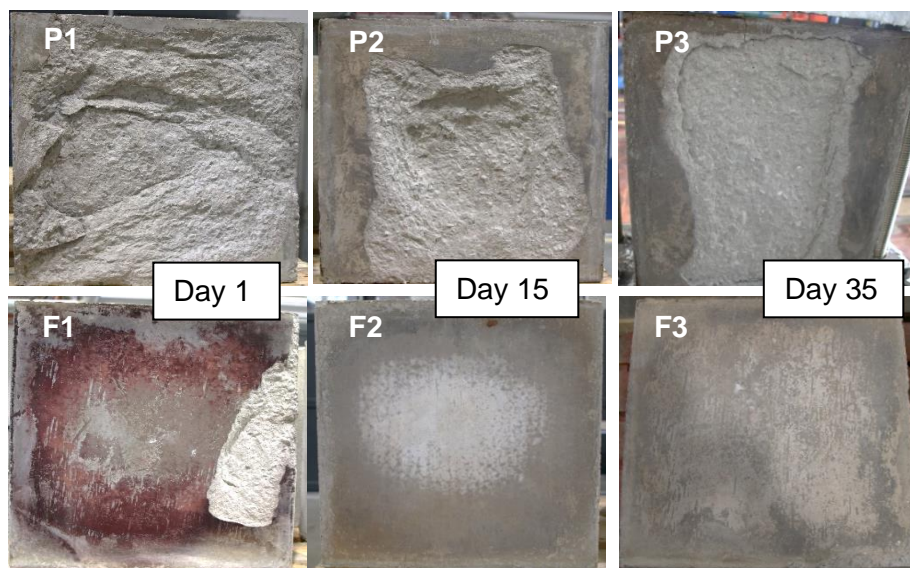


Figure 8 Specimens at 1, 15 and 35 days of drying.

Figure 8 illustrates the conditions of all the specimens from Test Series 1, 2 and 3. All plain concrete specimens experienced fire-induced spalling. The spalling damage was generally more severe for Test Series 1, as shown in Table 3. Maximum spalling occurred in P1 with volume loss of 3.65 L, followed by P2 (2.04 L) and P3 (1.43L).

For RTPF concrete, only the specimen tested at 1 day after drying spalled. “F1” lost a layer of concrete at its edge rather than the heated centre, which appeared to be due to surface delamination, possibly due to weakness caused during concrete casting.

Since both “F2” and “F3” exhibited no spalling, it can be concluded that the RTPF fibres were effective in the mitigating fire-induced spalling at $2\text{kg}/\text{m}^3$ when the average moisture content was below 6%.

The average moisture content, which is widely believed to be a dominating factor influencing the spalling behaviour of concrete, did not appear to be the decisive factor in this experiment. In fact, the average moisture content of all specimens was around 6%, but Series 1 specimens had much higher surface moisture after 1 day of drying. This implies that the volume of fire spalling is more closely related to the moisture content of the surface layer of concrete, rather than the average moisture content of the whole specimen.

Due to the limited number of tests, there are no clear indications of the factors affecting maximum spalling depth. Moreover, the complexity of concrete’s properties and spalling mechanisms appears to be the main reason for the variation in spalling time and the extent of spalling in each experiment. The details of spalling events and other parameters are shown in Table 3 below.

Table 3 List of all specimens and corresponding spalling details.

Specimens	RTPF dosage ($2\text{kg}/\text{m}^3$)	1st Spalling Time	Number of Spalling	Volume of Concrete Loss (Litre)	Maximum Spalling Depth (mm)	Average moisture content (%)
P1	0	10:08	5	3.65	36	6.08
P2	0	09:20	6	2.04	45	5.96
P3	0	07:07	5	1.43	24	5.81
F1	2	--	0	--	--	6.08
F2	2	--	0	--	--	5.96
F3	2	--	0	--	--	5.81

4. CONCLUSIONS

This paper presents results from experiments that were carried out to demonstrate the effectiveness of RTPF in mitigating fire-induced spalling, as an environmentally friendly alternative to PP fibres.

The following initial conclusions can be made based on the behaviour of the tested specimens subject to the testing condition:

- The addition of RTPF at a dosage of $2\text{kg}/\text{m}^3$ could be sufficient to mitigate fire-induced spalling in concrete.
- The severity (volume) of spalling is more influenced by the surface moisture content than by the average moisture content.

Future research will focus on the determination of the optimum dosage of RTPF and will examine parametrically different fire and loading conditions. Numerical analysis will be undertaken in the development of a better understanding of the spalling mechanism.

REFERENCES

- [1] H. L. Malhotra, "CIRIA Technical Note 118," *Spalling of Concrete in Fires*, 1984.
- [2] Z. P. Baiant, "B. IO Analysis of Pore Pressure, Thermal Stress and Fracture in Rapidly Heated Concrete," 1997.
- [3] D. Gawin, C. Alonso, C. Andrade, C. E. Majorana, and F. Pesavento, "Effect of damage on permeability and hygro-thermal behaviour of HPCs at elevated temperatures: Part 1. Experimental results," *Computers and Concrete*, vol. 2, no. 3, pp. 189-202, 2005.
- [4] Y. Fu and L. Li, "Study on mechanism of thermal spalling in concrete exposed to elevated temperatures," *Materials and structures*, vol. 44, no. 1, pp. 361-376, 2011.
- [5] G. Choe, G. Kim, M. Yoon, E. Hwang, J. Nam, and N. Guncunski, "Effect of moisture migration and water vapor pressure build-up with the heating rate on concrete spalling type," *Cement and Concrete Research*, vol. 116, pp. 1-10, 2019.
- [6] R. Jansson and K. Ödeen, "Fire in storehouse 6 in the free port of stockholm," 2011: RILEM Publications SARL, pp. 205-210.
- [7] V. K. R. Kodur, "Spalling in high strength concrete exposed to fire: concerns, causes, critical parameters and cures," in *Advanced Technology in Structural Engineering*, 2000, pp. 1-9.
- [8] H. Mostafaei, "State-of-the-Art on Fire Resistance of Concrete Structure Structure-Fire Model Validation," 2014.
- [9] I. Rickard, C. Maluk, F. Robert, L. Bisby, S. Deeny, and C. Tessier, "Development of a Novel Small-Scale Test method to Investigate Heat-Induced Spalling of Concrete Tunnel Linings," 2015 2015, pp. 195-205.
- [10] R. M. Faure and M. Karray, "Investigation of the concrete lining after the mont blanc tunnel fire," *Structural engineering international*, vol. 17, no. 2, pp. 123-132, 2007.
- [11] Y. Li, X. Lu, H. Guan, M. Ying, and W. Yan, "A case study on a fire-induced collapse accident of a reinforced concrete frame-supported masonry structure," *Fire technology*, vol. 52, no. 3, pp. 707-729, 2016.
- [12] M. F. R. Service, "Kings Dock Car Park Fire Protection Report," April 2018.
- [13] *Eurocode 2: Design of concrete structures - Part 1-2: General rules - Structural fire design*, B. Standard, 2004.
- [14] P. Kalifa, G. Chene, and C. Galle, "High-temperature behaviour of HPC with polypropylene fibres: From spalling to microstructure," *Cement and concrete research*, vol. 31, no. 10, pp. 1487-1499, 2001.
- [15] M. R. Bangi and T. Horiguchi, "Effect of fibre type and geometry on maximum pore pressures in fibre-reinforced high strength concrete at elevated temperatures," *Cement and Concrete Research*, vol. 42, no. 2, pp. 459-466, 2012.
- [16] Y. Ding, C. Zhang, M. Cao, Y. Zhang, and C. Azevedo, "Influence of different fibers on the change of pore pressure of self-consolidating concrete exposed to fire," *Construction and Building Materials*, vol. 113, pp. 456-469, 2016.
- [17] A. Bilodeau, V. K. R. Kodur, and G. C. Hoff, "Optimization of the type and amount of polypropylene fibres for preventing the spalling of lightweight concrete subjected to hydrocarbon fire," *Cement and Concrete Composites*, vol. 26, no. 2, pp. 163-174, 2004.
- [18] Y. Li, K. H. Tan, and E.-H. Yang, "Influence of aggregate size and inclusion of polypropylene and steel fibers on the hot permeability of ultra-high performance concrete (UHPC) at elevated temperature," *Construction and Building Materials*, vol. 169, pp. 629-637, 2018.
- [19] G. A. Khoury, "Polypropylene fibres in heated concrete. Part 2: Pressure relief mechanisms and modelling criteria," *Magazine of concrete research*, vol. 60, no. 3, pp. 189-204, 2008.

- [20] P. Kalifa, F.-D. Menneteau, and D. Quenard, "Spalling and pore pressure in HPC at high temperatures," *Cement and concrete research*, vol. 30, no. 12, pp. 1915-1927, 2000.
- [21] (2013). *Construction 2025, Industrial Strategy: government and industry in partnership*.
- [22] E. J. Yan and B. Liu. "Construction and projects in China: overview." (accessed 01/August, 2019).
- [23] M. Serdar, A. Baričević, M. Jelčić Rukavina, M. Pezer, D. Bjegović, and N. Štirmer, "Shrinkage behaviour of fibre reinforced concrete with recycled tyre polymer fibres," *International Journal of Polymer Science*, vol. 2015, 2015.
- [24] S.-S. Huang, H. Angelakopoulos, K. Pilakoutas, and I. Burgess, "Reused tyre polymer fibre for fire-spalling mitigation," *Applications of Structural Fire Engineering*, 2016.
- [25] *Fire Resistance Test, Part 1: General Requirements*, B. S. Publication, 2012.
- [26] U. Wickström, R. Jansson, and H. Tuovinen, "Validation fire tests on using the adiabatic surface temperature for predicting heat transfer," ed, 2009.
- [27] E. T. Box. "Water - Saturation Pressure [online]." https://www.engineeringtoolbox.com/water-vapor-saturation-pressure-d_599.html (accessed 29/July, 2019).
- [28] M. B. Dwaikat and V. K. R. Kodur, "Hydrothermal model for predicting fire-induced spalling in concrete structural systems," *Fire safety journal*, vol. 44, no. 3, pp. 425-434, 2009.
- [29] M. F. M. Zain, H. B. Mahmud, A. Ilham, and M. Faizal, "Prediction of splitting tensile strength of high-performance concrete," *Cement and Concrete Research*, vol. 32, no. 8, pp. 1251-1258, 2002.

Experimental Study of the Spalling Behaviour of Ultra-High Performance Fibre Reinforced Concrete during fire

Martin Schneider¹, Aljoša Šajna²

¹ Laboratory of Building Materials, Carinthia University of Applied Sciences, Austria (m.schneider@fh-kaertnen.at)

² Laboratory for Concrete, Stone and Recycled Materials, ZAG - Slovenian National Building and Civil Engineering Institute, Slovenia (aljosa.sajna@zag.si)

ABSTRACT

UHPFRC is one of the most powerful hydraulic bounded material, which has the prospect for using in sustainable concrete technology. In the last years, the number of realized projects has increased, and the experience in concrete technology has improved. This development opens the question of the behaviour of UHPFRC at high temperatures. The exposure of high strength concrete to fire needs special focus, as it seems to be different compared to ordinary concrete due to hard stone aggregates and dense cement matrix. Recently the united research group of ZAG and CUAS has started a research project on "Behaviour of Ultra-High Performance Fibre Reinforced Concrete during Meso-Scale Fire Tests". The goal is to evaluate the behaviour of UHPFRCs, different in content of PP-fibres and aggregate at high temperatures. The performance of concrete plates during the fire test, made of five different UHPFRCs, was monitored by measuring the temperatures in different depths and by using acoustic emission (AE) techniques. The acoustic emission recordings enable the concrete performance monitoring during the whole period of temperature increase. Surprisingly large differences in the performance of five UHPFRC mixes during the temperature increase were observed. The conclusions drawn from AE tests compare well with the damage observed on the plates at the end of the test; the resistance to fire of the tested UHPFRCs depends not only on the quantity of PP-fibres but also on the aggregate size.

KEYWORD: ultra-high performance concrete, spalling, UHPFRC

1 INTRODUCTION

When talking about UHPFRC, we usually talk about an Ultra High Performance Fibre Reinforced Concrete which means a finest compound system with the finest components smaller than 0.5 mm including silica fume, extreme dosage of admixture and steel fibres. Because of the very fine ingredients, the concrete has a very high packing density, which leads to a compressive strength of 150 – 250 MPa. This is in fact 5 times higher than the strength of NSC (normal strength concrete) and because of that it is possible to save concrete volumes (e.g. in cases of columns under compression up to 40% of the cross section can be reduced). The high packing density also leads to some other positive aspects like hardly any capillary porosity, low permeability, almost negligible carbonation depths and lower chloride penetration. All these advantages also lead to a much higher durability (this can be up to 5 times higher than that of NSC) and sustainability [1, 2]. Under fire treatment, the properties of UHPFRC are changing, like those of NSC. The

compressive strength decreases from the origin room temperature at 20°C to 80% at 800°C. At 750°C the tensile strength decreases to 55% of the origin and the modulus of elasticity decreases by about 50% to 80% at 600°C [3, 4].

The negative fact of the high packing density in case of fire is that there are no pores for water to expand and so it comes to spalling. Some former single tests show that the influence of PP fibres leads to a reduction of spalling during fire [3, 5] and that the spalling intensity is much higher than NSC. Fire load without PP fibres leads to a complete collapse and because of that the study does not check mixtures without fibres. Furthermore the test of spalling is current discussed in the RILEM TC SPF. A recommendation of test specimen and test conditions is under construction.

The study, which is presented in this paper, deals with massive plates without restraint during the tests. Two possibilities of mixtures for decreasing spalling of UHPFRC were examined. One solution could be the addition of PP (Polypropylene) fibres and the second one could be the usage of coarse aggregates. The idea behind these two possibilities is that in case of fire the PP fibres melt and so new pores for expanding of water will occur or, if coarse aggregates are used, such pores will occur already during the mixing process.

2 UHPFRC MIXTURES AND SPECIMENS

2.1 Mix design

Determining the fire resistance of structures starts with the definition of materials and their properties during fire. According to Eurocode 2 concrete mixtures shall include PP-fibres if the targeted compressive strength class is more than C50/60 and if pronounced fire-induced concrete spalling has to be avoided. Because of that different dosages of PP-fibres were used in UHPFRC mixes in the testing programme. Another possibility which could contribute to a reduction of spalling intensity is the usage of coarse aggregates. That is why a variation of coarse aggregates was chosen, containing basalt stone with a very high compressive strength of more than 180 MPa. The bulk density of the basalt stones is 2970 kg/m³. To test the influence of different contents of PP fibres and coarse aggregates, the following mixtures were prepared for the lab-batch:

Table 1 UHPFRC mixtures.

	M1 no basalt	M2 no basalt	M3 no basalt	M4 with basalt	M5 with basalt
CEM I 42,5 R	127.5	127.5	127.5	127.5	127.5
Silica fume	21.45	21.45	21.45	21.45	21.45
Quartz flour	36.75	36.75	36.75	36.75	36.75
Quartz sand 0.1 – 0.4 mm	129.75	129.75	129.75	89.96	89.96
Super-plasticizer	3.0	3.0	3.0	3.0	3.0
PP fibers Ø 0.018 mm / length 6 mm	0.15	0.30	0.60	0.30	0.60

The constant amount of 23.55 kg steel fibers Ø 0.2 mm / length 15 mm and w/c ratio of 0.2 was

used.

2.2 Preparation of meso-scale plates and accompanying cube specimens

Five plates were prepared from the designed 5 UHPFRC mixtures to be tested in a meso-scale fire experiment (Fig. 1). First, suitable moulds were designed in the way that each plate would fit exactly into a corresponding opening of the front cover of the fire-testing furnace (Fig.2). The frame was designed in a very high stiffness so that the sensors could remain in place during concreting despite high pressures of the low viscosity fresh concrete. K type Ni-Cr-Ni (2×0.5 mm) thermocouples with ceramic braided insulation were attached to U-bars. In addition to the 5 meso-scale plates, several cubes were also prepared from the same UHPFRC mixtures for the determination of two of the most important material parameters as nowadays known for influencing spalling-related phenomena [6, 7], i.e. compressive strength (the latter was tested at regular time intervals during curing and conditioning of the plates) and moisture content (measured on the day of fire testing). For measurements of compressive strength, 100 mm × 100 mm × 100 mm cubes were used. For measurements of moisture, one 200 mm × 200 mm × 200 mm cube was used per UHPFRC mixture. Four sides of the 200 mm cubes were coated with paraffin to simulate the unidirectional drying of the plates.

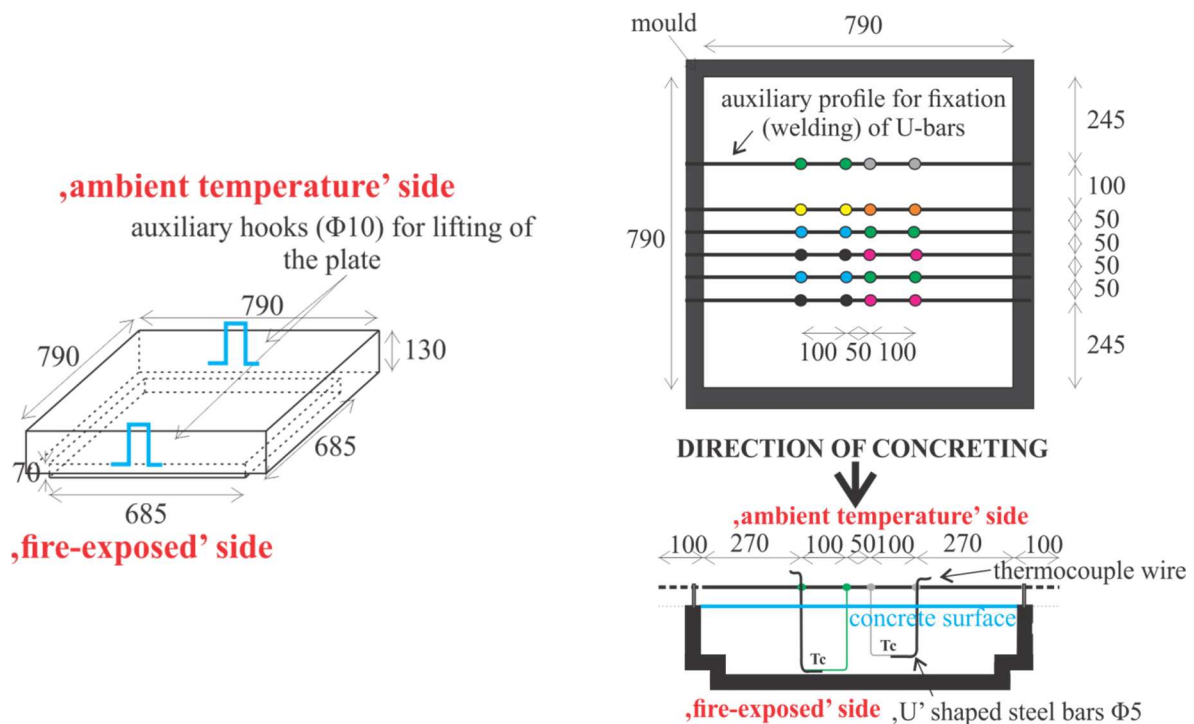


Figure 1: (a) Sketch of one plate (in mm). (b) Sketch of preparation of the plates.

Coloured circles represent stiff fixations of the U-bars onto auxiliary profiles. The U-bars are represented by different colours which denote different depths of the bars, i.e. different positions of the hot junctions of the thermocouples with respect to the fire-exposed concrete surface: 25 mm (green), 40 mm (black), 55 mm (yellow), 60 mm (grey), 70 mm (blue), 85 mm (pink), 100 mm (orange). Moreover, after 163 days of curing, the prepared specimens were put into a climate chamber 23°C/50% RH and conditioned for 95 days. According to EN 1363-1:2012, such conditioning is necessary to ensure that the equilibrium moisture content is established in the concrete specimens at the time of fire loading. This should correspond to the value expected under normal service. Just before the fire test the moisture content of the concrete was measured using the cubes by the oven drying

technique described in EN 1363-1.

2.3 Acoustic emission based monitoring

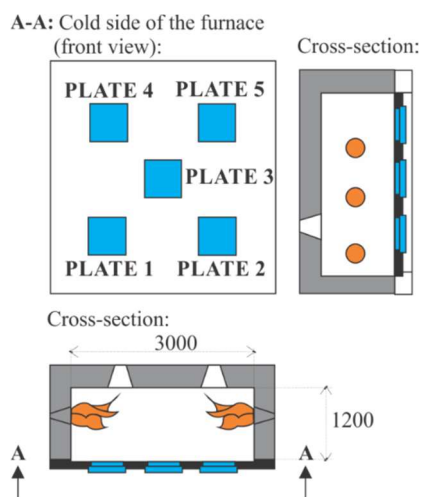
The acoustic technique is one of the most promising non-destructive techniques that can be used to monitor development of defects in the structural elements. Acoustic emission (AE) is a phenomenon of registering transient elastic waves resulting from local internal micro-material movements. The main principle of this method consists in detecting fast discharge of elastic energy caused by micro-scale deformations or defects inside the loaded material. These waves can be detected by piezoelectric sensors. AE method can be applied to different materials, processes and structures. An active crack can be detected much earlier by AE methods than with the unaided eye of an inspector. AE methods can be used for detecting active cracks, corrosion, leaking, etc. The location of the event can also be identified when an array of sensors is used.

The AE technique has been used for studying the explosive spalling in high-strength concrete [9]. He showed that AE can be successfully used for monitoring explosive spalling of high-strength concrete due to fire.

In this study the AE measurements were performed following the RILEM TC 212-ACD Recommendations [10].

3 SET-UP OF THE FIRE TEST

While the 200 mm cubes were measured for moisture content, the installation of the plates onto the furnace began. The plates were placed in a frame which forms one side (i.e. the front wall) of an oil-burned vertical furnace of dimensions 3000 × 3000 × 1200 mm (Fig. 3a) and mounted in the way that during the test only one of the larger sides of the plate would be exposed to fire while the other one would face normal ambient conditions. After being mounted firmly, air-permeability of concrete was measured according to SIA 262/1:2003 on each of the plates. In addition, each plate was equipped with one Physical Acoustic PK6I acoustic emission (AE) sensor [8].



(a)

(b)

Figure 3: (a) Scheme of the furnace with two cross-sections and a front view. (b)

As the plates tested were isolated from the furnace frame by isolating material no

environmental noise was detected by the AE system before starting of the fire test. Prior testing the AE system was tested both by using pencil-lead break and Automatic Sensor Test application of AEWin Physical Acoustic software. Unexposed side of one of the plates with visible AE sensor and thermocouple wires extended out from the UHPFRC plate. The fire test commenced right after installation and testing of AE sensors and followed standard ISO 834 testing conditions.

4 RESULTS OF THE TESTING

4.1 Basic material data measured prior to fire testing

This section presents results of measurements of basic material characteristics of the prepared UHPFRC specimens, i.e. compressive strength measured during different storage conditions and ages of the concrete (Table 2), concrete moisture content measured on the day of fire testing (Table 3), and air-permeability (Table 4).

Table 2: Results of compressive strength of the UHPFRC mixtures.

Testing age	M1	M2	M3	M4	M5
	[MPa]				
7 days	132.3*	117.0*	114.3*	119.9*	111.2*
28 days	176.0*	155.6*	153.6*	167.8*	153.6*
	163.9**	148.2**	144.1**	154.3**	128.8**
163 days***	201.1*	161.9**	-	180.4**	151.9**
	174.3**				

* water stored / ** component support / *** day of testing

The influence of storage condition leads to a higher difference of the results of compressive strength. It seems that the influence of surface (cracks, shrinking, drying, pore structure etc.) during component support leads to a decrease of compressive strength. It was not a target of the project to explain this influence but it is important that the compressive strength of the plates at the age of testing is more than 150 MPa, this is shown in table 2.

Table 3: Moisture content on the day of fire testing.

	M1	M2	M3	M4	M5
mass as delivered [kg]	19.290	19.039	18.584	20.114	19.783
dry mass [kg]	19.070	18.812	18.169	19.845	19.510
moisture content [% by mass]	1.2%	1.2%	2.3%	1.4%	1.4%
density of dry UHPFRC [kg/m ³]	2,384	2,352	2,271	2,481	2,439

Table 4: Measured air-permeability.

Mix	M1	M2	M3	M4	M5
Air-Permeability [10 ⁻¹⁶ m ²]	0.52	0.01	0.46	0.06	0.01

4.2 Results of fire testing

Figure 3 shows the exposed side of the front cover of the furnace with 5 tested plates mounted. The photograph was taken after the termination of the test and 24-hours cool-down (note that no additional spalling was obtained during cool-down; the front cover of the furnace with the plates still embedded was cooled-down naturally, in the air). The extent of the spalled areas is clearly visible in Fig. 4a (see the grey areas visible on each plate except on the plate 5). In addition, there is some information regarding spalling depth in Table 5.



Figure 3: Exposed side of the front cover of the furnace after the fire test with visible spalling damage of the 5 plates.

Table 5: Maximal spalling depth.

Plate (Mix)	M1	M2	M3	M4	M5
Max spalling depth [mm]	51	99	42	56	7

In table 6 the damage is estimated by grades from 1 to 5 with respect to detected spalling intensity (the intensity of spalling was evaluated considering the time of the start and the end of the detected AE signal and its time-averaged strength).

Table 6: Spalling intensity of the plates.

Plate (Mix)	M1	M2	M3	M4	M5
Spalling intensity	4	5	1	2	0*

*no spalling observed

4.3 Acoustic emission test results

The acoustic emission test results in the form of number of hits vs. time are presented in Figure 6. The Chanel 1 was used to measure the AE activity of the mix 1 plate, the Chanel 2 for the mix 2 plate, the Chanel 6 for the mix 3 plate, the Chanel 7 for the mix 4 plate and the Chanel 8 for the mix 5 plate.

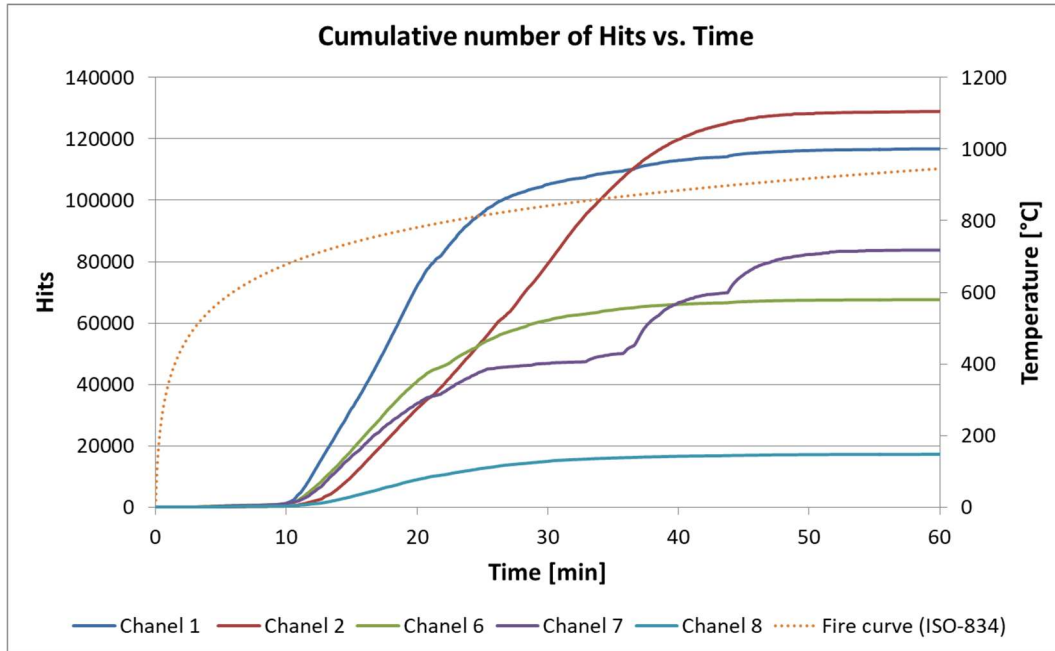


Figure 6: Acoustic emission activity; cumulative number of hits vs. time

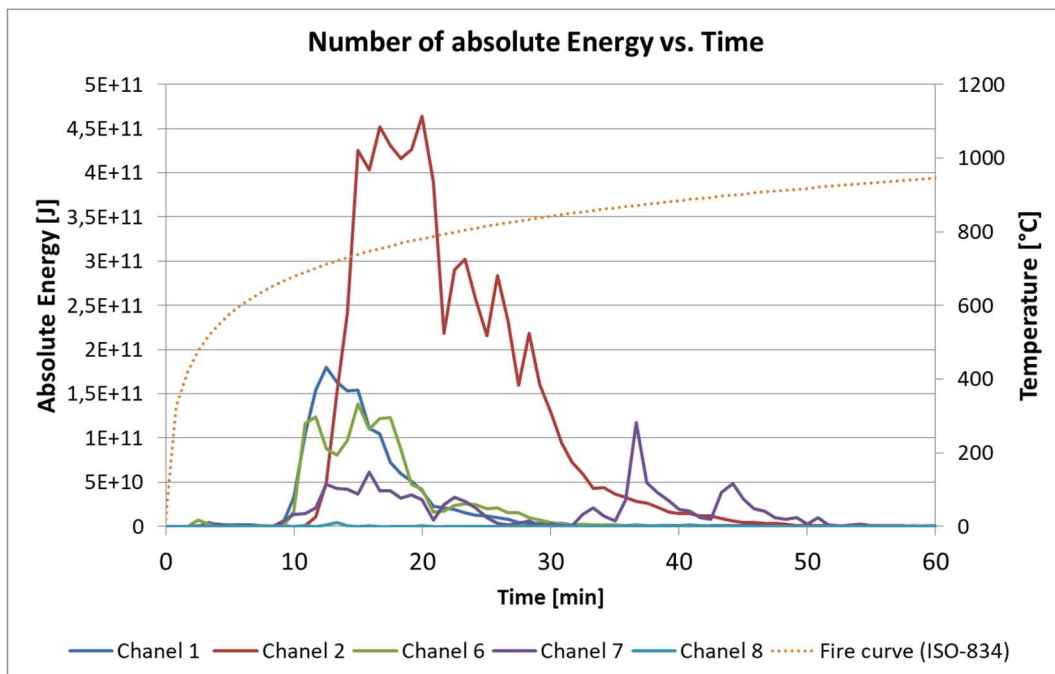


Figure 7: Acoustic emission activity; absolute energy vs. time

From Figure 6 clear differences in AE activity of different concrete mixes can be observed. If the cumulative number of hits can be considered as a measure for damage, mix 2 is the

most damaged and the mix 5 the least. Plates made of Mixes 3 and 4 exceed similar number of AE hits. The AE results are in good correlation with visual observations of plates' damage after the test. From the graph also the rate of spalling can be seen; the fastest spalling rate was recorded on Mix 1, the slowest on Mix 5. Some irregularity in the graph of Mix 4 can be explained by inhomogeneity of the concrete in the plate, probably having more or fewer fibres in some areas. For all mixes the spalling starts at app. 10 min and dies out at 50 min. Similar conclusions can be made based on the absolute energy test results presented in Figure 7.

6. CONCLUSION

The influence of the test conditions is important. This study was made with plates without restraint; that means the storage in the oven did not lead to restraint in the plate due to thermal elongation. The amount of 2 kg PP fibres was not enough to prevent the spalling effect. Other publications have shown that a PP fibre ratio of 2 to 3 kg was sufficient to avoid spalling [11]. The importance of tests is shown in the project because the behaviour of the material is different according to the information in literature. Mixtures of UHPFRC are very specific and the behaviour during tests is very sensitive. Another aspect is the validation of spalling. In this study the authors confine the spalling value on maximum spalling depth and spalling intensity, measured by acoustic emission activity. From the 5 fire-tested UHPFRC plates only the one with basalt aggregates and 4 kg/m³ of PP fibres survived the test with only some surface cracks. The mixes 1 to 3 increase the amount of PP fibres from 1 kg to 4 kg without adding some coarse aggregates of basalt stones. The spalling was not completely avoided with adding PP-fibres during the chosen test condition. The mixtures 4 and 5 contain coarse aggregates and PP-fibres. It is observed that the amount of 2 kg PP fibres leads to spalling during the chosen test condition. The results of this study clearly imply that adding PP-fibres to the examined UHPFRC mixes was not enough to substantially reduce the spalling intensity. However, a big improvement can be expected if in addition appropriate aggregate size is selected.

7. OUTLOOK

This work is an ongoing research on the field of fire resistance of UHPFRC. Important influences of the spalling behaviour of UHPFRC were detected. In the next step the influence of the test procedure is more in focus according to RILEM TC SPF. In the study basalt stones were used as coarse aggregate. The mineral composition of the stone has an influence certainly. This variation is also included in the ongoing research.

8 ACKNOWLEDGMENT

This work was founded by INTERREG SI-AT. The work was done by the FIREEXPERT group. Very special thanks to the supported institutions for bringing their knowledge into the program.

9 REFERENCES

- 1 Randl, N. et al, "Development of UHPC mixtures from an ecological point of view", *Construction and Building Materials*, 67, 373-378, 2014.
- 2 Schneider, M. et al, "Economical Effect on Ultra-High Performance Concrete by Using of Coarse Aggregates", *Proceedings of the International Conference on Concrete Sustainability (ICCS16)*, Madrid, 2016.
- 3 AFGC Recommendations, "Ultra High Performance Fibre-Reinforced Concretes", Paris, 2013.
- 4 Sanchayan, S.; Foster, S.J., "Load Induced Thermal Strains in Ultra High Performance Concrete at elevated temperature", *Proceedings of the RILEM-fib-AFGC International*

- Symposium on Ultra-High Performance Fibre-Reinforced Concrete, Marseille, 2013.
- 5 Siemaon, M.; Hosser, D., "Assessment of coupled Thermo-Mechanical Behaviour of Ultra High Performance Concrete columns in Case of Fire", Proceedings of the International Symposium on Ultra-High Performance Fibre-Reinforced Concrete, Marseille, 2013.
- 6 Gawin D, Pesavento F, Schrefler B. A., "Towards prediction of the thermal spalling risk through a multi-phase porous media model of concrete", Computer Methods in Applied Mechanics and Engineering, 195, 5707–5729, 2006.
- 7 J. Kolšek, I. Planinc, M. Saje, T. Hozjan, "The fire analysis of a steel–concrete side-plated beam", Finite Elements in Analysis and Design, 74, 93–110, 2013.
- 8 http://www.physicalacoustics.com/search.php?search_query=PK6I
- 9 Ozawa, M. et al, "Study of mechanisms of explosive spalling in high-strength concrete at high temperatures using acoustic emission", Construction and Building Materials, 37, 621–628, 2012.
- 10 Recommendation of RILEM TC 212-ACD, "Acoustic emission and related NDE techniques for crack detection and damage evaluation in concrete, Measurement method for acoustic emission signals in concrete", Materials and Structures, 43, 1177–1181, 2010.
- 11 Piementa, P. et al, "Literature Review on the Behaviour of UHPFRC at High Temperature", Proceedings of Hipermat 2012 - 3rd International Symposium on UHPC and Nanotechnology for Construction Materials, Kassel, 2012.

Investigation of Size Effects in Concrete Spalling

André Klimek¹, Sascha Hothan¹ und Andreas Rogge^{1,*}

¹Bundesanstalt für Materialforschung und -prüfung, Berlin, Germany

* andreas.rogge@bam.de

ABSTRACT

Spalling of concrete due to fire exposure can lead to severe damage of building components. It is a much-discussed subject in structural engineering and not yet completely understood. Generally, it is assumed that thermohydraulic and thermomechanical processes induce tensile stresses in the concrete. Furthermore, the tensile strength of concrete is reduced due to increasing temperatures. The combination of an increasing tensile stress and a decreasing tensile strength result in the occurrence of explosive spalling. The spalling behaviour of concrete is influenced by many parameters, for instance the water-cement ratio, porosity, permeability of concrete as well, the presence of steel reinforcement and polypropylene fibres, also the size and geometry of the fire exposed area. Within the current research project at Bundesanstalt für Materialforschung und -prüfung (BAM), the susceptibility to spalling of six different concrete mixtures is analysed to quantify the size effect using small-scale, intermediate-scale and full-scale tests. A special fire test setup was built to test specimens simultaneously to enable a better comparability. All specimens are tested without additional mechanical load and unrestraint to prevent external induced cracking at the fire exposed site. Thermocouples are used to measure in-situ the temperature distribution as an indication on the thermal degradation of the concrete during the fire tests. Afterwards the maximum spalling depth and the damaged area of the specimen are illustrated by a photogrammetric measurement system. The contribution to the spalling workshop presents the results of four concrete mixtures tested in intermediate-scale and full-scale fire tests. The comparisons are based on the concrete temperature as well as the obtained photogrammetric data. The results show that the spalling depth and the spalling area are significantly affected by the size of the fire exposed area.

KEYWORDS: Spalling, Concrete, Size Effect, Photogrammetry, Fire Test

INTRODUCTION

Fire induced explosive spalling processes on concrete are related to various microscopic and macroscopic structural changes. Due to the low thermal diffusivity [1] a large temperature gradient is formed during unilateral heating of concrete. This imbalance of the concrete temperature leads to two processes that are commonly considered as main causes for concrete spalling. One process is the thermohydraulic spalling mechanism which goes along with a built up of thermohydraulic pore pressure due to the expansion of vaporized water near the surface [2]. The thermal expansion of the vaporised water increases the pore pressure. A system of microcracks in the concrete establishes. The vaporized water streams

to the surface and leaks towards the flame. Furthermore, the steam flows into deeper regions of the concrete [3]. Based on the large temperature gradient, the vaporized water condensates in larger depths due to lower temperatures. With a prolonged period of fire, the condensation inside a certain depth goes on and a zone of saturated capillary pores forms [4]. This zone is called the “moisture-clog”. Its first theoretical existence was discussed by Harmathy [5] and the experimental evidence of the “moisture clog” was published by Dorjan et al. [6] using neutron tomography. It is an impermeable volume for the vaporized water in a low permeable region of the concrete. Therefore, the vaporized water accumulates in front of the “moisture-clog” and the pore pressure increases. At a certain point during the fire, the pore pressure exceeds the tensile strength of the concrete. At this point a series of cracks are developed in a very short time in a small volume of the concrete and explosive spalling occurs.

Another large impact on spalling is caused by thermomechanical processes. The large temperature gradient effects a different thermal expansion of the concrete ingredients [7]. For an unrestraint and unilateral heated specimen, the thermal expansion at the fire exposed surface differs from the rest of the specimen. Near the surface the aggregates expand while the deeper parts remain unchanged. The stiffness of the concrete hinders the free, thermal expansion. Thus, radial tensile stress occurs and forms cracks. If the tensile stress exceeds the tensile strength, explosive spalling occurs.

These two processes depend on several factors, for instance 1) concrete mixture, 2) temperature and 3) size of the specimen. The ingredients of the concrete and the conditioning time have a large impact on strength, moisture content, porosity and permeability of the specimen and hence the susceptibility of concrete spalling.

In fracture mechanics the size effect is a widely discussed phenomenon, but on concrete spalling it is still a small partial subject in research. Previous investigations modelled, tested and described the fracture building mechanics of different sized and shaped specimens [8-10]. The reduction of the specimen volume leads to a reduction of the spalling depth, while a reduction of the aggregate size increases the spalling depth and leads to more explosive spalling events [11].

Further investigations consider the crack form energy as an important factor that is highly dependent on the specimen size [12]. This study investigates the impact of the size for diverse concrete mixtures, different fire curves and various fire exposed areas.

EXPERIMENTS

Experimental set-up

The experimental set-up for this study is designed to ensure equal heat conditions for every specimen size. A ceiling testing facility is reduced by closing walls into a tunnel furnace with dimensions of 4045 x 1220 mm² as shown in Figure 1. Two oil burners are installed on both endings of the furnace to provide the heat conditions and simulate real fire scenarios. High temperature wool (HTW) is set between the closing walls and the specimen for unrestraint testing without a heat loss in the furnace.

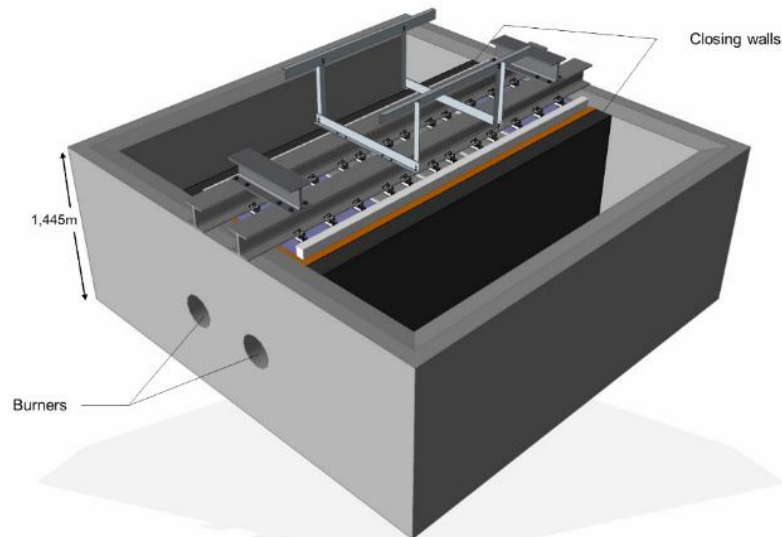


Figure 1 Test set-up for all experiments [after 13]

Using this unique test facility, it is possible to test one full-scale (1840 x 1220 x 300 x mm³), six intermediate-scale (600 x 600 x 300 mm³) or twelve small-scale cylindrical (\varnothing 200 mm x 300 mm) specimens simultaneously. Figure 2 shows the arrangement of the intermediate-scale specimen with six samples. Each specimen is attached to a H-beam with embedded assembly rails. On both longitudinal sites are two enclosing concrete specimens with HTW-insulation on the bottom. These concrete specimens close the furnace site to ensure equal the heat distribution during the fire tests.

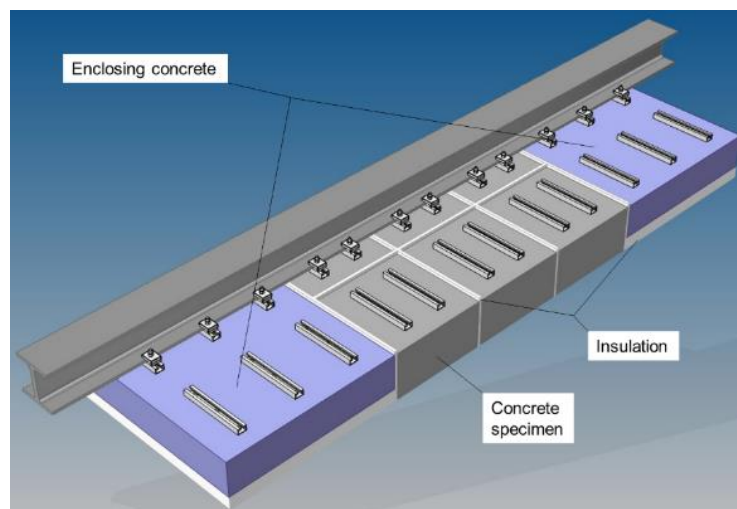


Figure 2 Experimental set-up of the 600x600x300 mm³ test specimens

Concrete mixtures and fire tests

During the still ongoing study six different concrete mixtures will be tested and the size effect is analysed. Two concrete mixtures, which are developed for tunnel segments, with (A1) and without (A2) polypropylene fibres (PP-fibres), one high performance concrete (B1) and one self-compacting concrete (B2) are already tested for the full-scale and intermediate-scale size. The mix design is shown in Table 1. Mixture A1 and A2 are typical concrete mixtures that are used in tunnel formwork constructions. Therefore, both concrete mixtures are tested with the RABT-ZTV curve that represents a fire inside a tunnel. The main difference of the mixtures is the addition of PP-fibres in mixture A2. Several studies have already shown the decreasing effect of concrete spalling due to the application of PP-fibres [14-16]. It is expected that mixture A2 is less prone to spalling than mixture A1. Concrete B1 is a pure

research concrete and is very prone to spalling in case of fire due to its very low porosity and permeability. This mixture is used to show an extremum of spalling. Concrete B2 is an exposed concrete that is placed as an inside wall of a building. B1 and B2 are usually considered to be used in buildings, thus the testing curve for both mixtures in this study is the standardized temperature time curve (ISO 834) [17]. During the fire tests with the RABT-ZTV all oil burners are used to reach the target temperatures. In contrast to the test with the RABT-ZTV during the fire test with the ISO 834 only two oil burners diagonally opposed on each side of the furnace are active. All specimens are tested unilateral and unrestrained for 60 minutes.

Table 1 Concrete mix designs

Type of Material	Tunnel Segment Concrete without PP-Fibres	Tunnel Segment Concrete with PP-Fibres	High Performance Concrete	Self-Compacting Concrete	
	A1	A2	B1	B2	
	Content [kg/m ³]	Content [kg/m ³]	Content [kg/m ³]	Content [kg/m ³]	
Cement (CEM I 42,5 R)	320	320	580	300	
Water	160	160	170	180	
Additive (fly ash)	80	80	0	0	
Additive (silica fume)	0	0	63,8	0	
Additive (limestone meal)	0	0	0	301	
Superplasticizer	3,52	11,2	14,5	8,55	
PP-Fibres	0	2	0	0	
Aggregates	-	-	-	-	
0 / 2,0	[mm]	675	666	764	668
2,0 / 4,0		160	158	229	116
4,0 / 8,0		231	228	535	116
8,0 / 16,0		711	702	0	652
Strength Class	C30/37	C30/37	C80/95	C45/55	
Fire Curve	RABT-ZTV (train)	RABT-ZTV (train)	ISO 834	ISO 834	

Furthermore, thermocouples measure the temperature in depths of 5 mm, 50 mm and 100 mm at several points of the concrete (Figure 3). The furnace temperature is measured on the northern and southern site of the full-scale specimens, whereas the furnace temperature for the intermediate-scale specimens is quantified on the northern and southern site and in between the specimens. With these measurements the system automatically regulates the furnace temperature for the implemented fire test curve.

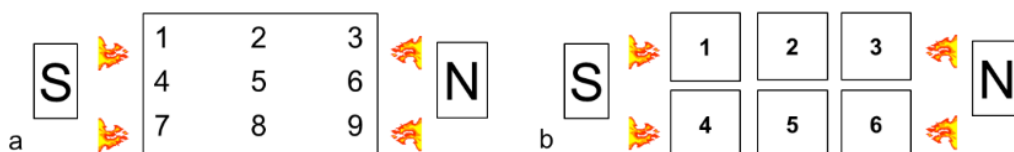


Figure 3 Configuration of the thermocouples in the full-scale specimens (a) and intermediate-scale specimens (b)

In addition to the temperature measurements, photogrammetry is used to analyse the spalling depth of the concrete specimens. The measurements take place before and after

every fire test with the GOM ATOS III System. A frame with reference points is turned down (Figure 1, on top of the H-beams) to provide a scan in the same vector matrix of the photogrammetric system. Before the fire test several pictures from different angles are taken and saved in a point cloud and the system calculates a 3D-model of the specimen. After the fire test pictures are taken in the same reference system with the specimen at the exact same position. The system is now able to calculate the vertical distance of every cloud point. The result is a differential image of the specimen before and after the fire test.

RESULTS

Results of the full-scale fire tests

The images of the full-scale concrete specimens in combination with the associated photogrammetric measurements after the fire tests are presented in Figure 4. The pictures show a large destruction of the fire exposed surface. The first layer of the reinforcement corpus of every specimen is uncovered. In this case the spalling depth in this area exceeds 50 mm. Furthermore, the images b) and e) in Figure 4 display concrete spalling deeper than the reinforcement bars. The photogrammetric results provide a more detailed information about the exact spalling depth. Comparing all full-scale specimens, the concrete mixture B1 spalled the most with a maximum depth of 250 mm. The other two concrete specimen have a maximum spalling depth of 150 mm. At this point, the interesting fact is the centred maximum spalling depths of mixture B1 and B2, whereas the maximum depth of mixture A1 is located at the edge of the concrete specimen. The macroscopic damage caused by the unilateral heating of the specimens induces two main spalling mechanisms: "corner"-spalling and explosive spalling.

At the edge of the specimen the concrete stiffness is different to the stiffness in the centre of the specimen. Here, the specimens are mainly damaged by "corner"-spalling [18]. "Corner"-spalling occurs due to the fact of the altered stress environment. At the edge the specimen expands without horizontal stress in at least one direction and the thermal induced stress reduces. Further, the vaporized water leaks through the occurring microcracks, which reduces the pore pressure. In this case it is possible that spalling not always occurs at the edge while explosive spalling occurs at the centred surface. In some case the concrete fragments at the front side of the specimen are held by the friction of the HTW and fall of after the enclosing concrete specimens and the HTW are removed from the fire tested specimen.

In the central part of the specimen surface the concrete expansion is hindered by the stiffness of the concrete. With an increase of the surface temperature, the horizontal compressive stress increases also and leads to radial tensile stress. If the tensile stress exceeds the tensile strength, cracks form radial to the surface. Further, thermohydraulic stress of the "moisture-clog" leads also to crack growth parallel to the surface. The combination of both crack systems exceeds the tensile strength of the concrete and small concrete fragments begin to spall off explosively.

Furthermore, the reinforcement bars have also a large influence on the spalling behaviour of the concrete (Figure 5). The reinforcement bars increase the stiffness and the radial tensile forces of the concrete. Therefore, more spalling occurs due to the hindered thermal expansion until the five-centimetre concrete cover are spalled off. If the reinforcement bars are directly exposed to the fire, constraint forces lead to spalling that forms a crater structure (Figure 5 c). If the gradient of the crater increases, the adhesive bond between concrete and reinforcement bar is reduced and the concrete spalls of the steel (Figure 5 b). From this point on, the concrete continuously spalls of the reinforcement bars until the concrete is completely disconnected from the steel (Figure 5 a).

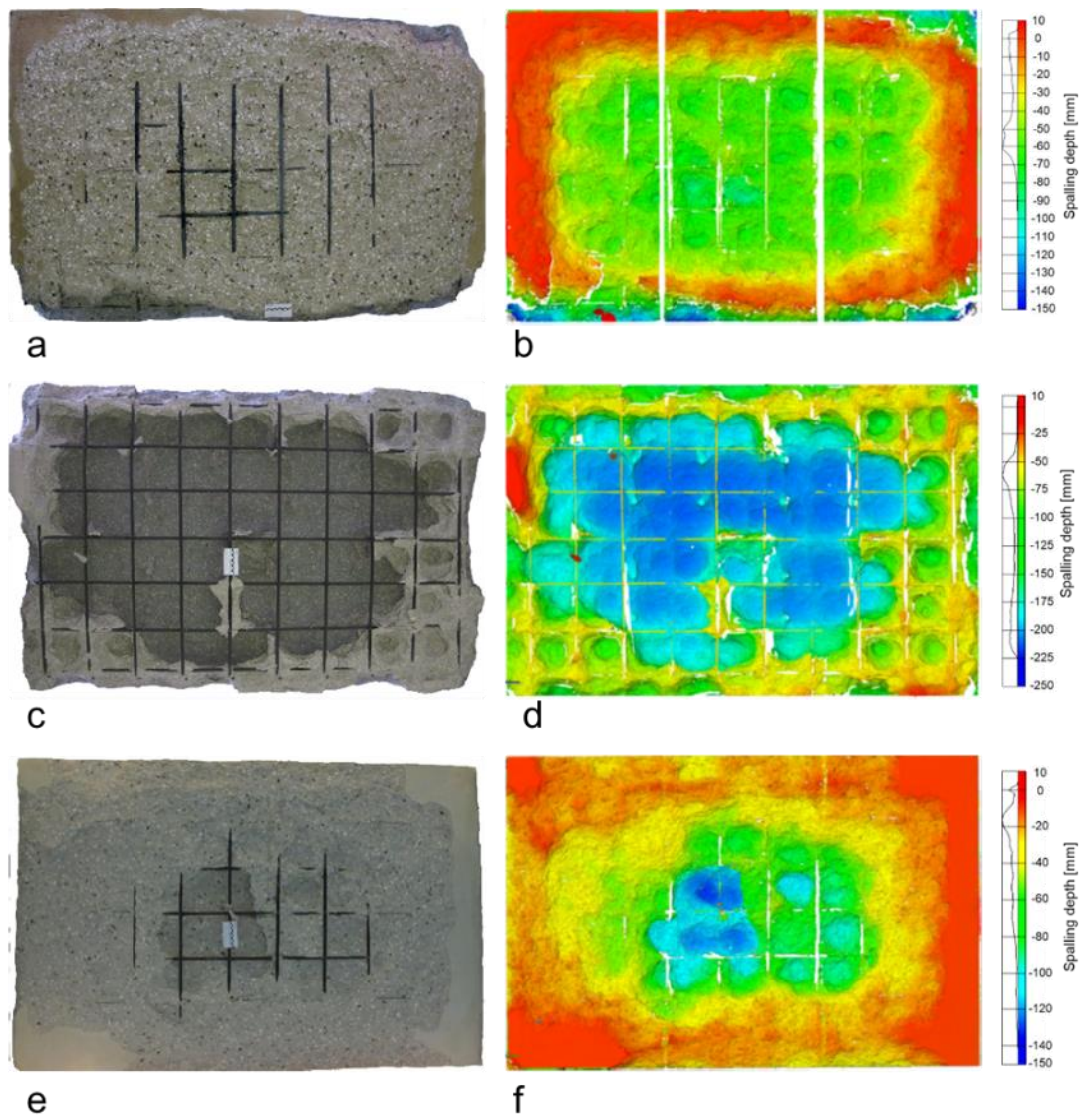


Figure 4 Photographs and photogrammetric result of the full-scale fire tests of mixture A1 (a-b), B1 (c-d) and B2 (e-f)

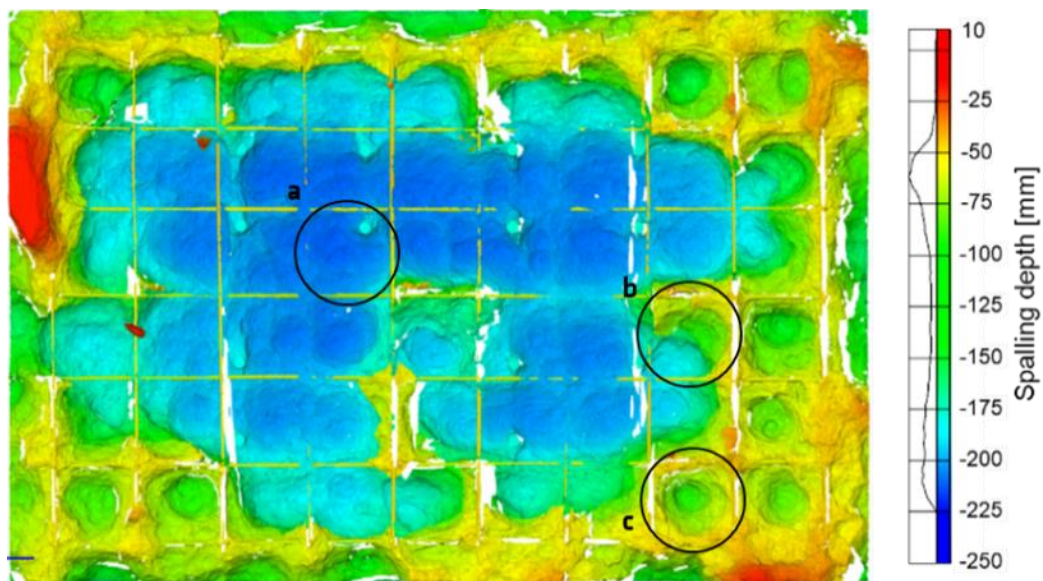


Figure 5 Photogrammetric result of the full-scale fire test of mixture B1

Results of the intermediate-scale fire tests

The results for the intermediate-scale fire tests are presented in Figure 6. The images a) - d) in Figure 6 represent the mixtures A1 and A2 and the images e) – h) show the results of mixture B1 and B2. All four specimens are placed in the middle of the three-row line in the set-up (Figure 2). The spalling depth of every specimen is reduced in comparison to the full-scale specimens of the same mixture. The maximum spalling depth in the centre of mixture A1 is reduced by about 50 mm, the spalling depth of mixture B1 is reduced by 150 mm and the spalling depth of mixture B2 is reduced by 130 mm (compare Figure 5 and Figure 6). This means that a size effect for the same mixtures under equal heating conditions can be noticed.

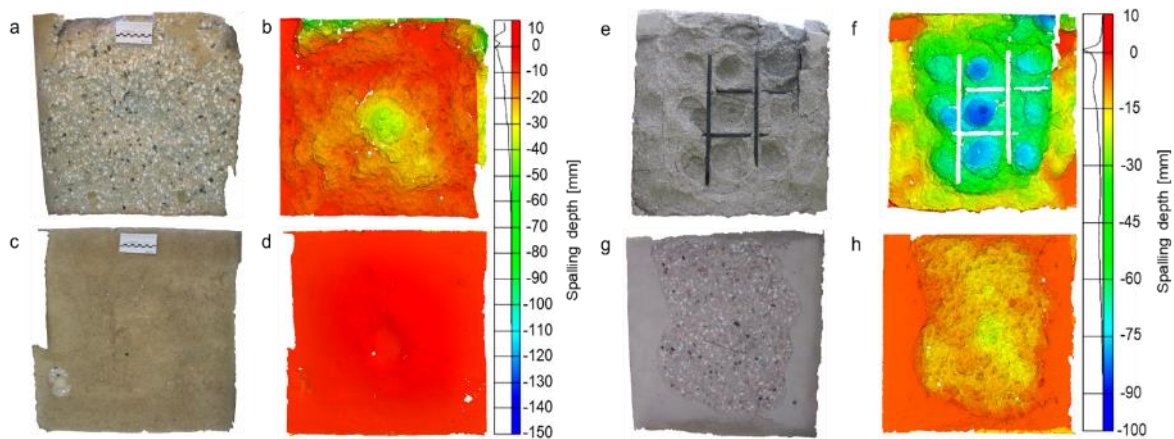


Figure 6 Photographs of the intermediate-scale concrete specimen after the fire tests and the associated photogrammetric results (a and b: Mixture A1; c and d: Mixture A2; e and f: Mixture B1; g and h: Mixture B2).

Three different possible causes for a size effect must be discussed. A first reason is the conditioning time of the concrete, which is different for every specimen (Table 2). All conditioning times for the full-scale specimens are shorter than the conditioning time for the intermediate-scale specimens. The least conditioning time difference occurs for mixture B2 with 41 d and the largest time span is 84 d for mixture A1 (Table 3). A longer conditioning time leads to denser structure of the concrete, while the concrete loses more unbound water with the ongoing curing time. The denser structure increases the risk of spalling. Fewer water inside the concrete results in less spalled concrete fragments. Both conversed mechanisms influence the results.

Table 2 Conditioning times

Specimen	Conditioning Time [d]	Maximum Spalling Depth [mm]
Full-scale A1	98	100
Full-scale A2	97	-
Full-scale B1	140	250
Full-scale B2	127	150
Intermediate-Scale A1	182	50
Intermediate-Scale A2	168	-
Intermediate-Scale B1	203	100
Intermediate-Scale B2	168	20

Table 3 Relation of the conditioning time difference to the maximum spalling depth

Mixture	Conditioning Time Difference Full-Scale/Intermediate-Scale	Spalling Depth Difference Full-Scale/Intermediate-Scale
A1	84	50
A2	71	-
B1	63	150
B2	41	130

The results show that mixture A1 has the fewest spalling depth reduction but the largest conditioning time difference. Additionally, the results display that the absolute curing time is independent to the specimen size (Table 2).

The second important indication of differing spalling behaviour is the temperature distribution over time. Thermocouples that are placed in the centre of the specimen which measured the temperature during the full-scale and intermediate-scale fire tests are shown in Figure 7 and Figure 8. Within the first 100 mm the temperature distribution is similar for each mixture in the first 10 minutes. Only the temperature of mixture A1 for the full-scale specimen is significantly raised compared to the intermediate-scale specimen. A possible explanation is that the increased temperature of the RABT-ZTV curve forces a faster concrete spalling for a larger surface area. In this case a fast increase of the furnace temperature induces a size effect.

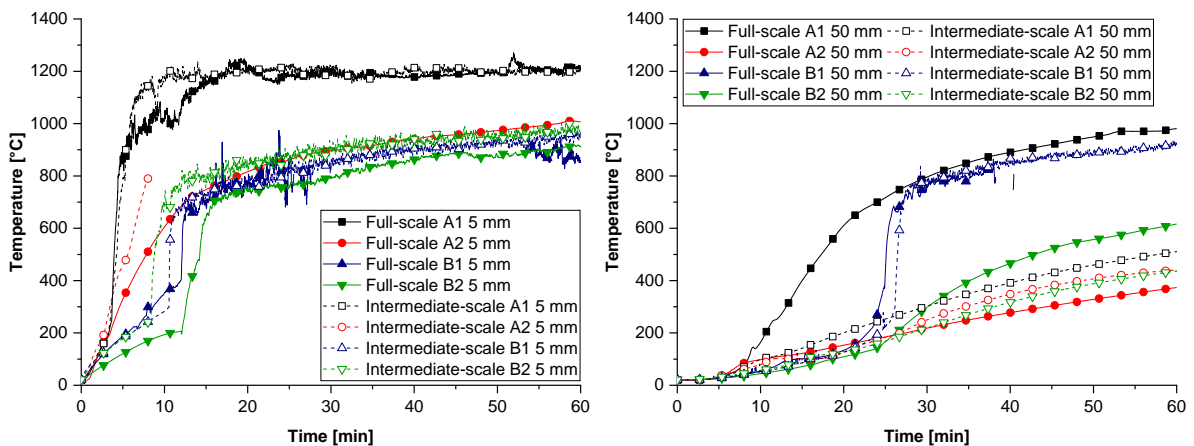


Figure 7 Temperature distribution of the centrally placed thermocouples in 5 mm (left) and 50 mm (right) depth

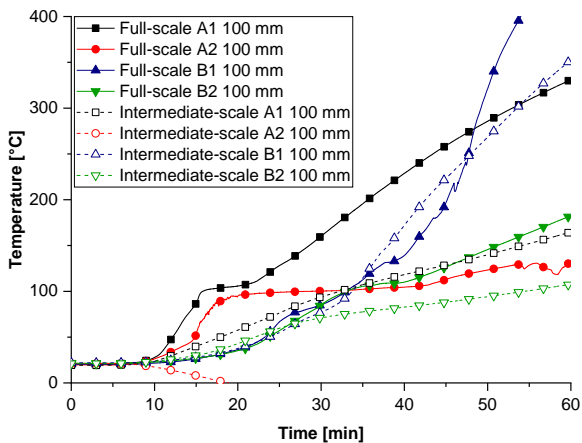


Figure 8 Temperature distribution of the centrally placed thermocouples in 100 mm depth

The third cause for a possible size effect is the size of the tested surface area. In comparison to the full-scale specimen the size of the intermediate-scale specimen surface area is reduced by 84 %. At the same time the spalling depth is reduced by 50 % for the mixture A1, 60 % for the mixture B1 and 87 % for the mixture B2 (compare Figure 4 and Figure 6). Due to the large temperature gradient of the concrete the surface area is the most significant part of the specimen that is affected by the temperature. By reducing the fire exposed area, the internal stresses, due to thermohydraulic and thermomechanical processes, are decreased in comparison to the full-scale specimen. In this case the spalled fragments are smaller and in the same testing time overall the spalled depth is lower.

CONCLUSIONS

The following points can be concluded from this ongoing study:

- The reduction of the fire exposed surface has a major impact on the spalling behaviour of the concrete. Due to the large temperature gradient the surface area is the most damaged part of the specimen during unilateral heating. Therefore, a smaller surface area decreases the internal stresses of the specimen and thereby the spalling is reduced. In this case a size effect occurs.
- The thermocouple measurements show a similar distribution of the temperature within the first 50 mm from the fire exposed surface regarding the full-scale and intermediate-scale specimen of the same mixture. Only the temperature of the full-scale specimen of mixture A1 is increased compared to the temperature of the intermediate-scale specimen. This phenomenon only occurs during tests with the RABT-ZTV curve. Hence, the temperature curve influences the spalling behaviour of different sized concrete specimens.
- In this study the absolute conditioning time of the tested specimen sizes is independent to spalling behaviour. It is more likely that the concrete mix design affects the reaction of a specimen to fire.
- Further investigations are still in progress. Two other concrete mix designs will complement the studies of the concrete mixtures impact on the size effect. Additionally, fire test on cylindrical specimens with a length of 300 mm and a diameter of 150 mm are planned.

ACKNOWLEDGEMENTS

The authors would like to acknowledge the German Research Foundation (DFG) for their funding of this project. Further, we gratefully acknowledge every employee of the Fire Science Department, the Building Materials Department and Building Technology Department at BAM for their support.

REFERENCES

- [1] Herwig, H, Wärmeübertragung A-Z, Springer, 2000
- [2] Wittmann, F.H., Grundlagen eines Modells zur Beschreibung charakteristischer Eigenschaften des Betons, Deutscher Ausschuss für Stahlbeton, 290, Ernst & Sohn, 45-101, 1977
- [3] Stelzner, L., Bartosz, P., Weise, F., Oesch, T., Dlugosch, R. and Meng, B., Analysis of moisture transport in unilateral-heated dense high-strength concrete, 5th International Workshop on Concrete Spalling due to Fire Exposure, Borås, Sweden, 2017

- [4] Jansson, R., Fire Spalling of concrete – Theoretical and Experimental studies, PhD Thesis, KTH, Stockholm Sweden, 2013
- [5] Hamarthy, T.Z., Experimental study on moisture and fire endurance of Building Elements, Fire Technology, 2, 74-95, 1965
- [6] Dorjan, D., Tengattini, A., Dal Pont, S., Toropovs, N., Briffaut, M., Weber, B., Analysis of moisture migration in concrete at high temperature through in-situ neutron tomography, Cement and Concrete Research, 111, 41-55, 2018
- [7] Schneider, U, Behaviour of Concrete at High Temperatures, Deutscher Ausschuss für Stahlbeton, Ernst & Sohn, 1982
- [8] Bažant, Z. P., Size Effect in Blunt Fracture: Concrete, Rock, Metal, Journal of Engineering Mechanics, 110, 518-535, 1984
- [9] Hillerborg, A., Modéer, M., Petersson, P-E., Analysis of Crack Formation and Crack Growth in Concrete by means of Fracture Mechanics and Finite Elements, Cement and Concrete Research, 6, 773-782, 1976
- [10] Reinhardt, H.W., Maßstabseinfluss in Schubversuchen im Licht der Bruchmechanik, Beton u. Stahlbetonbau, Berlin, 76(1), 19-21, 1981
- [11] Mohd Ali, A. Z., Sanjayan, J., Guerrieri, M., Specimens size, aggregate size, and aggregate type effect on spalling of concrete in fire, Fire and Materials, 42, 59-68, 2018
- [12] Ožbolt, J., Maßstabseffekt und Duktilität von Beton- und Stahlbetonkonstruktionen, Habilitation, Institution für Werkstoffe im Bauwesen, Stuttgart, 1995
- [13] Brecht, K., Pistol, K., Klemmstein, F. and Rogge, A., Novel Test Setup for the Quantification of the Size Effect in Spalling Tests, 5th International Workshop on Concrete Spalling due to Fire Exposure, Borås, Sweden, 2017
- [14] Huisman, S., Materialverhalten von hochfestem Beton unter thermomechanischer Beanspruchung, PhD Thesis, Technische Universität Wien, 2010
- [15] Khoury, G.A., Polypropylene fibres in heated concrete. Part 2: Pressure relief mechanisms and modelling criteria, Magazine of Concrete Research, Vol. 60, 189-204, 2008
- [16] Kalifa, P. Chéné, G., Galle, C., High-temperature behaviour of HPC with polypropylene fibres – From Spalling to microstructure, Cement and Concrete Research, Vol 31, 1487-1499, 2001
- [17] Maraveas, C., Vrakas, A., Design of Concrete Tunnel Linings for Fire Safety, Structural Engineering International, 2014
- [18] Lo Monte, F., Gambarova, P. G., Corner spalling and tension stiffening in heat-damaged R/C members: a preliminary investigation, Materials and Structures, 48, 3657-3673, 2015

Effect of geometry in concrete spalling risk subjected to high temperatures for thermal inertia studies

T. Lucio-Martin¹, J. Puentes¹ & M.C. Alonso^{1,*}

¹ Eduardo Torroja Institute for Construction Sciences (IETcc-CSIC), Madrid, Spain

* Corresponding author (mcalonso@ietcc.csic.es, Serrano Galvache 4, CP: 28033, Madrid, Spain)

ABSTRACT

Several studies have demonstrated the feasibility of using concrete as a thermal energy storage material. An experimental procedure must be established during the concrete mix design to validate its performance when subjected to high temperature (up to 600°C) in order to extend the service life. The initial cement paste dehydration is considered to be the most critical part of the start-up of the concrete, due to the high probability of spalling. In addition, the material after this stage starts to be following heating and cooling cycles between 290 and 550°C.

The aim is to evaluate the thermal inertia of the concrete in order to minimise the risk of spalling in the dehydration stage of the concrete, as well as the damage evolution in the successive thermal fatigue cycles. A small-scale experimental study has been carried out using a Self-compacting concrete (SCC) thermally designed for energy storage in concrete. Specimens of different geometries were made to assess the behaviour against several factors: heating rate, thermal gradient, sample geometry and crack formation.

For this purpose, three different sizes and geometries of SCC samples have been manufactured. The temperature gradient has been monitored during the test at different depths. Results indicate that the geometry determines the heating rates within the material and hence, the risk of spalling. Not only thermal gradients affected the spalling, but it also was influenced by the time of exposure. On the other hand, the long-term performance of the concrete mix was proved to be used as suitable for thermal storage because of its low degradation propagation after exposure of concrete to thermal fatigue cycles.

KEYWORDS: High temperature, thermal gradient, self-compacting concrete, spalling

INTRODUCTION

The behaviour of concrete exposed to high temperatures has been studied for a long time from the point of view of the material in the presence of fire. However, in recent years, new applications in energy infrastructures have consolidated their own line of research. The use of concrete as thermal energy storage in concentrated solar power plants (CSP) has been verified recently [1-3]. The highest concern in relation to this type of use of concrete is the thermal stability of the concrete when exposed to heat charge and discharge.

From the point of view of the development of high temperature concrete design, several alternatives have allowed a better performance. The use of polypropylene fibres (PPF) [2, 4], thermal stable and low expansion aggregates and its size distribution in the mix [2] has been proved useful to have a better performance. Concrete spalling risk is one of a major case of

failure of concrete when exposed to high temperature and fire. Different authors have related the concrete spalling with the specimen dimensions [5-6] but the geometry effect is not clear yet and needs to go for deeper study.

One of the riskiest factors, when concrete is exposed to high temperature in a CSP, is the spalling. The first heating, when the concrete undergoes dehydration, is fundamental in the operation of the elements used for energy storage in CSP. The maximum temperature of use is limited up to 600°C [2] and it is considered the most critical stage. Besides the further thermal stability of the concrete element under heat cycles is critical and no much experience exist [1, 3].

In order to go deeper, this study investigates both the first heating and the thermal fatigue cycles for concrete designed to resist high temperature, to be suitable for thermal storage up to 550°C. The present paper studies the effect of geometry in the risk of spalling during the dehydration of concrete and the thermal gradients owing to the heating process. Moreover, the thermal stability of concrete exposed to fatigue thermal cycles has been studied through the crack evolution.

EXPERIMENTAL PROCEDURE

Material and production of samples

Concrete was fabricated using CEM II containing 30% of micro blast furnace slag. This binder was blended with fly ash class F up to 20%. Calcareous and basalt aggregates (0-6 and 6-12 mm) were selected as considered to have good thermal stability up to the maximum temperature (550°C). Also, clinker as aggregate (0-5.6 mm size) was added. Finally, limestone filler was included to achieve the self-compacting ability to produce the concrete. Table 1 shows the concrete composition and Table 2 summarizes mechanical properties at fresh and hardened conditions.

Table 1 Concrete composition

Component	C-1 mix
CEM II/B-S 52.5 R (kg/m ³)	319
Fly Ash (kg/m ³) / %bcm	130/20
Limestone Filler (kg/m ³)	157
Calcareous (0-6mm) (kg/m ³)	465
Basalt (0-6mm) (kg/m ³)	212
Clinker (0-5.6mm) (kg/m ³)	191
Calcareous (6-12 mm) (kg/m ³)	531
Basalt (6-12 mm) (kg/m ³)	315
Superplasticizer additive 1	1
Superplasticizer additive 2	1.2
Viscosity modifier additive	0.9
w/b	0.39

Table 2 Mechanical properties of fresh and hardened concrete

Fresh properties		Hardened properties	
J-ring SFJ (mm)	SF1-520	Density (kg/m ³)	2400
J-ring t500J (s)	21	Open porosity (%)	4.51
J-ring Final PJ (mm)	20	f _{ck} ^a 7 days (MPa)	66.1
Air content %	2.5	f _{ck} ^a 28 days (MPa)	84.5
		MIP porosity (%)	6.61

^aThe compressive strength was measured on cubic specimens (150 x 150 x 150 mm³).

The influence of heat on spalling has been analysed in one concrete mix varying the type of

geometry and size of the element: cylindrical (\varnothing 75 mm x H 150 mm), cubic ($150 \times 150 \times 150 \text{ mm}^3$), and prismatic ($150 \times 150 \times 400 \text{ mm}^3$). The samples had K-type thermocouples embedded. Figure 1 shows the samples and thermocouples embedded in each specimen, and Table 3 specifies the location of thermocouples with respect to the reference system shown in Figure 1.

Figure 1 Geometries and thermocouples located inside the concrete samples

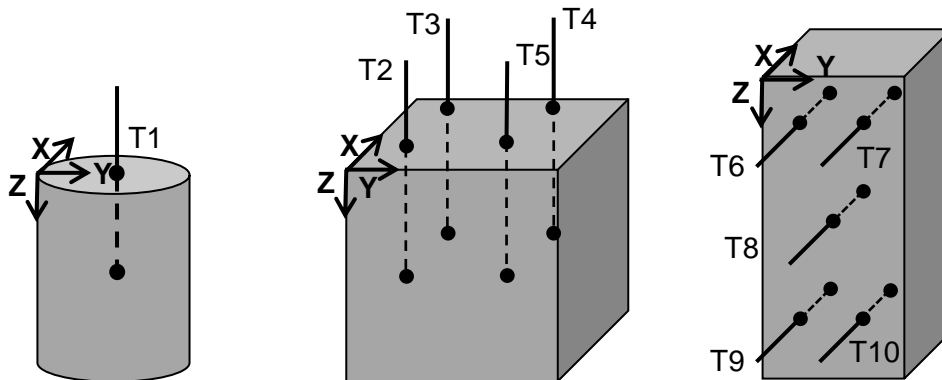


Table 3 Location of thermocouples.

Geometry	ID	Coordinates (mm)			Geometry	ID	Coordinates (mm)		
		X	Y	Z			X	Y	Z
Cylindrical	T1	0	37.5	75	Prismatic	T6	75	50	50
Cubic	T2	30	30	75		T7	75	115	50
	T3	120	30	75		T8	75	75	200
	T4	120	120	75		T9	75	50	350
	T5	30	120	75		T10	75	115	350

Before starting the thermal test, samples were stored in a humidity chamber at 20°C and 98% of relative humidity (RH). At the time of testing, the samples had an age varying between 28 and 90 days, as it is shown in Table 4. The variables under study were: the effect of geometry in spalling risk, the thermal fatigue and thermal cracking. The sample geometry, dimensions, and the surface (S), the volume (V) and the S/V ratio are included in Table 4.

Table 4 Specimen characteristics and the relationship between shape, size and volume

Test	Curing Conditions	Ageing (days)	Shape	Dimensions (mm)	S/V (m^{-1})
Effect of geometry in spalling risk	$20^\circ\text{C}/98\%\text{RH}$	$\cong 28$	Cylindrical	75x150	66.67
		$\cong 90$	Cubic	150x150x150	40
$\cong 28$		Prismatic	150x150x400	31.67	
Thermal fatigue effect		$\cong 28$	Cylindrical	75x150	-
		$\cong 90$	Cubic	150x150x150	-
Thermal cracking		$\cong 28$	Cylindrical	75x25	-

Thermal test

Before starting the thermal tests, samples were dried inside the furnace at 105°C for 3 days to reduce the free water from the pores. After that, the thermal test was launched. Two stages are under consideration in the study:

- **Dehydration stage (25-550°C):** During the first heating, the dehydration of cement paste takes place liberating vapour. During this stage, the risk of spalling is higher

mainly because of two aspects: i) The thermal gradients generated between the heated surfaces and the core of the samples, which induce high thermal stresses. ii) The accumulation of vapour in the bulk of the concrete limiting the vapour to be released and generating high pressures in the bulk [5, 7-9].

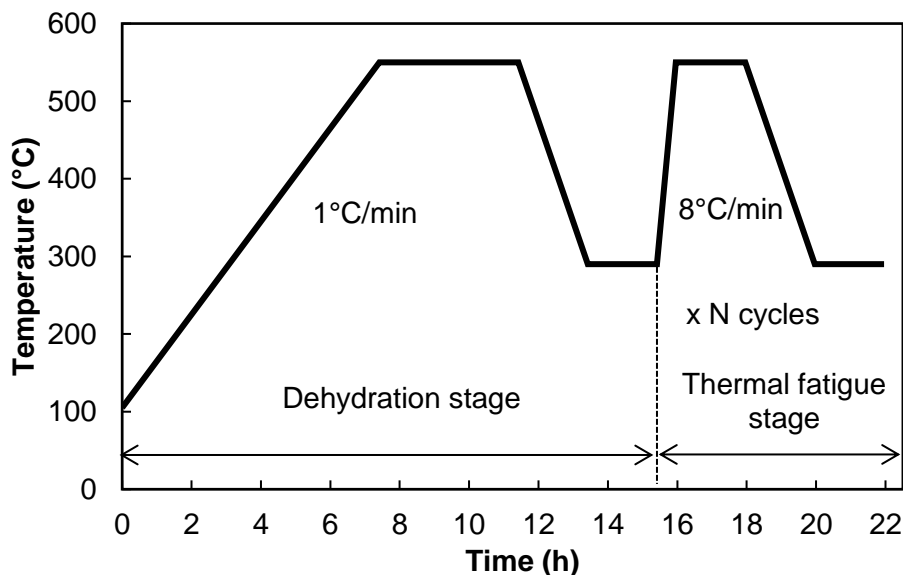
For these reasons, the first heating stage must be slow ($1^{\circ}\text{C}/\text{min}$) in order to decrease the risk of spalling.

Once the concrete has been dehydrated, the risk of spalling decreases and the following thermal cycles are performed at higher heating rates simulating daily charge and discharge heat processes of a real case.

- **Thermal fatigue stage (290°C to 550°C):** The second stage began after dehydration and consists of performing cycles between 290 - 550°C since it will be the operating regime of the concrete in the application studied. In this stage, the heating rate was $8^{\circ}\text{C}/\text{min}$. The plateaus at constant temperature (290 and 550°C) have been considered to last 2 hours to guarantee stabilisation of the bulk of the concrete sample at each heat cycle level. It was repeated a number of thermal cycles to evaluate the thermal fatigue effect.

The different heating regimes is summarised in Figure 2.

Figure 2 Thermal fatigue test



Thermal cracking

The microcracking generation due to heating was studied in cylinders of $\varnothing 75$ mm x H 25 mm, to quantify the effect of thermal fatigue on durability performance. Cracking development and propagation was studied after 1, 25 and 75 thermal fatigue cycles. Pictures were taken in several regions of the sample by using an optical microscope Nikon SMZ-2T. The crack-mappings were obtained through analysis of digital images by using open software GIMP. With these mappings, it was possible to establish the percentage of cracks per area. Moreover, the maximum crack width was determined by measuring ten times and the result is the mean value for every thermal cycle.

RESULTS AND DISCUSSION

The risk of spalling during dehydration stage

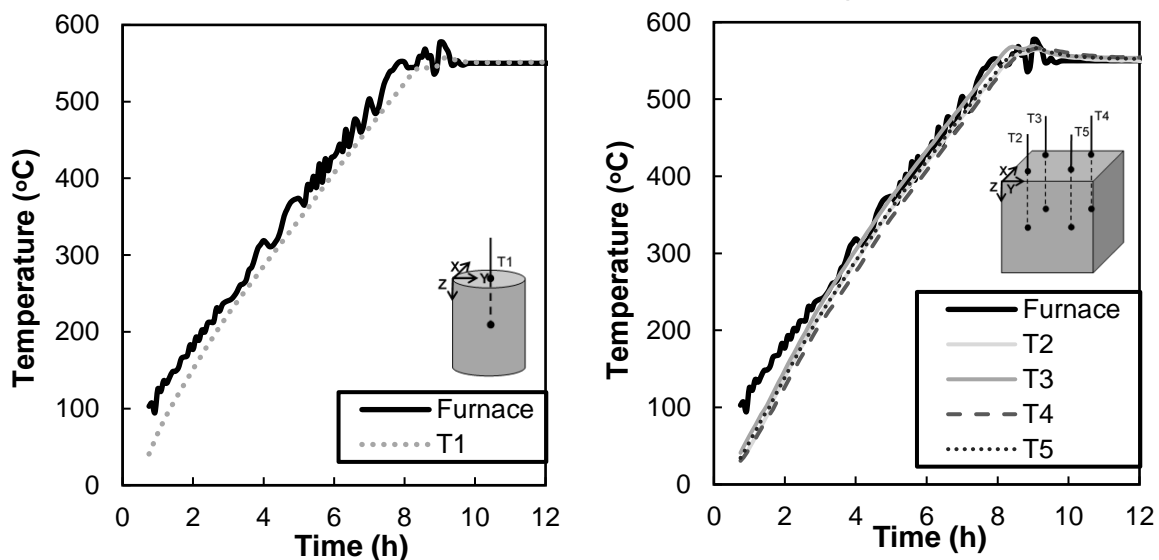
- **Thermal gradients**

The first to be analysed regarding the spalling risk at high temperature is the dehydration stage. Figure 3 shows the evolution of temperature recorded by thermocouples located inside the specimens and in the furnace during the first heating from room temperature up to

550°C. According to geometry, cylindrical and cubic specimens adapted fast to temperature changes following almost the same heating rate of the furnace as shown in Figure 3. This is mainly due to the smaller specimen size, which means that heat reaches the geometrical centre of the specimen earlier and vapour evacuate also easily. Moreover, smaller specimen sizes mean a higher amount of air inside the furnace, which improves the convection heat transfer mechanism between the furnace and the samples.

Regarding thermal gradients, the difference in temperature inside the concrete sample was higher in the cubic and lower in the cylindrical. Thermocouples T2, T3, T4 and T5 distanced 30 mm from the heated surface recorded almost the same temperature than T1 located 37.5 mm from the heated surface. This is explained because of the “corner effect” that makes the heat cross more slowly through the sample before arriving at the geometrical centre of the specimen. Taking into account that the temperature in the centre of the cubic sample was not recorded, this critical point would have experienced higher thermal gradients because of the distance from the heat source and the corner effect. The furnace heating rate was fixed in 1°C/min but the real heating rate inside the samples was 0.9°C/min for both specimens.

Figure 3 First dehydration stage: *CYLINDRICAL* and *CUBIC* samples



- **Spalling risk**

The risk of spalling in relation to the sample geometry is appreciated in Figure 4. The evolution of temperature is recorded with the thermocouples in the prismatic sample. During the first 5 hours of testing, the thermal gradients between the furnace and the internal part of the sample increased achieving more than 100°C of difference. Thermocouple T8 recorded the highest difference because it distanced 75 mm to the heated surfaces, and this location was the critical point of the specimen. When the furnace was at 400°C the sample underwent spalling. At this time, T8 was at 250°C and the difference of temperature was 150°C in 75 mm. This generated high thermal stresses within the concrete and the material underwent spalling, as it is shown in Figure 5. In spite of having the same cross-section than the cubic sample, the thermal gradients were bigger in the prismatic one. Therefore, thermal gradients are not only influenced by the distance from the heat source but also for the geometry.

Figure 4 First dehydration stage: PRISMATIC sample

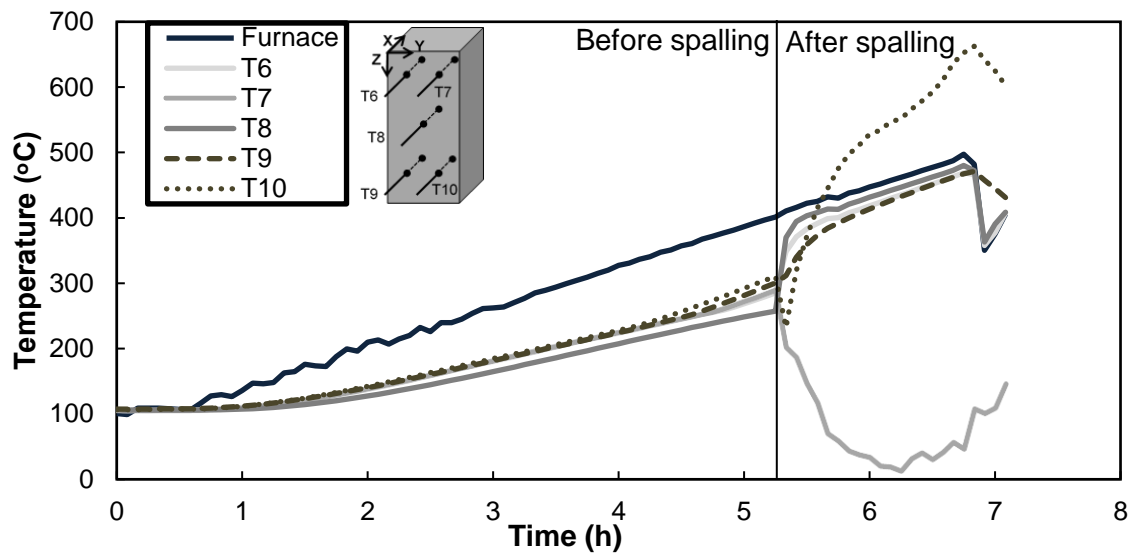


Figure 5 Prismatic sample after spalling



- **Effect of geometry in spalling risk**

Analysing the three geometries of samples with the same concrete, Figure 6 shows the evolution of temperature inside the three geometries during the dehydration stage up to 550°C. Moreover, Table 5 quantifies the difference of temperature between the furnace and the thermocouple T1 (cylindrical), T4 (cubic) and T8 for the prismatic. The heating rate of the heat source (furnace) was fixed in 1°C/min but the real heating rate inside the samples was 0.9°C/min for the cylindrical and cubic and 0.6 for the prismatic geometry, determined from the temperature evolution over time in the core of the specimens. This is owing to internal stresses, which increase the risk of spalling when the sample size is increased. For that reason, the geometry and dimensions of the specimens should be considered when carrying out the dehydration process before starting the high temperature test.

Several authors have evaluated the section size effect on concrete spalling. For the same concrete mix and heating rate (1°C/min), a reduction of size by 50-75% eliminated the risk of spalling [10]. Kanéma et al. [5] also analysed the effect of size and observed that spalling happened only in large samples despite undergoing the same thermal gradients than the small

ones. Liu et al. [6] give the explanation that smaller samples facilitate the escape of moisture out of the concrete and this induces lower pore pressure. In the present study, the thermal gradients were higher in the prismatic specimen (Table 5) and the spalling happened after being exposed to high thermal gradients for a long time (6 hours).

On the other hand, thermal gradients were bigger in the first heating instants because of thermal inertia, Table 5. At those moments, the furnace was being heated but the core of the material needed time to receive the heat. After that, thermal gradients decreased in both the cylindrical and cubic specimens whereas the prismatic sample continued increasing with the time of exposure, Figure 6.

In order to reduce the spalling risk during the first heating in case of concrete for CSP heat storage, the geometry must be taken into account. The spalling risk might be avoided by doing the first heating by steps and remain at plateaus of constant temperature until the core reaches a homogeneous temperature. Doing that, the thermal gradients would be reduced and, hence, the risk of spalling too. An additional contingency is the incorporation of PPF.

Figure 6 First dehydration stage for all geometries

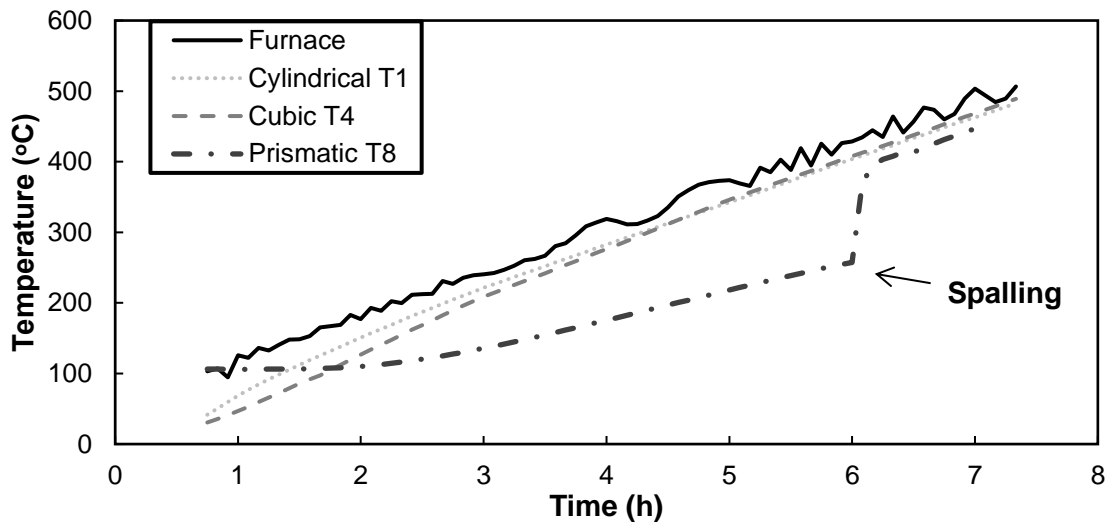


Table 5 Thermal gradients between the furnace and the core of the specimens

	Thermal gradient, ΔT (°C)			
	Furnace	Cylindrical T1	Cubic T4	Prismatic T8
Time (h)	T_{Furn}	ΔT_{cyl}	ΔT_{cub}	$\Delta T_{prism.2}$
1.5	150	37	63	57
3	240	19	32	87
4.5	335	22.5	24	115.5
6	428.5	24	24	Spalling
7.5	531	35	32	
Heating rate (°C/min)	1	0.9	0.9	0.6

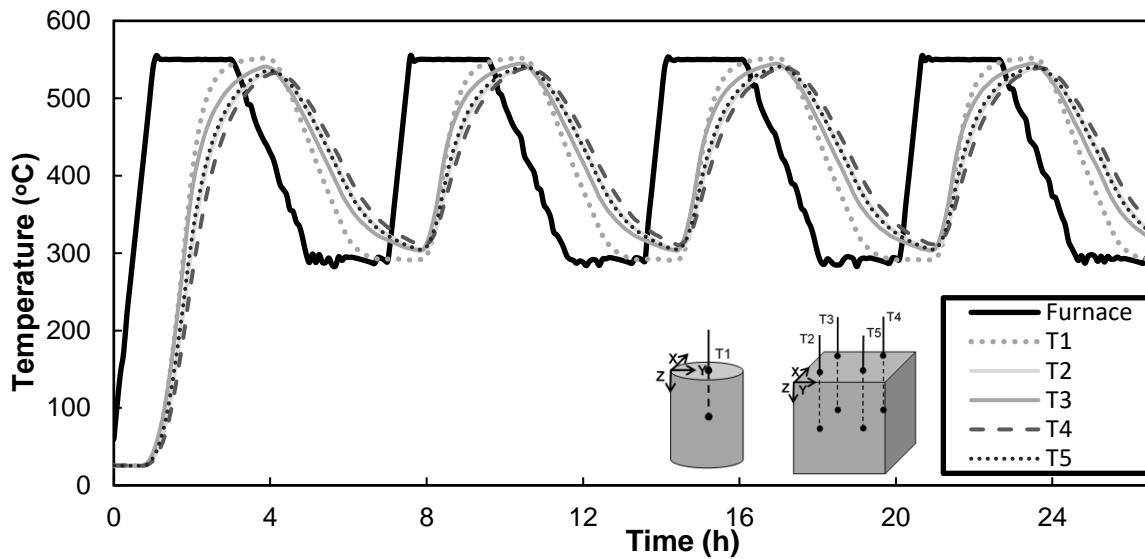
Thermal fatigue of concrete during heat charge/discharge cycles

- **Thermal gradients**

The second stage analysed was the thermal fatigue in the cylindrical and the cubic samples

when temperature ranges between 290-550°C. Figure 7 shows the evolution of the temperature of the furnace and the thermocouples embedded inside the samples. The cylindrical specimen reached the maximum temperature (550°C) and the minimum (290°C) in less than 2 hours. This indicates that the concrete reaches the proposed temperature range and the material remains an approximate period of 1.5 hours at a constant temperature, either at 550°C or at 290°C. On the contrary, the cubic specimen did not reach the set temperatures. It has been verified that the cube would need 2.67 hours to reach 550°C in the thermocouples, but more time would be needed to reach the maximum temperature in the geometric centre. The same happened when cooling down the cubic sample to 290°C. Again, the sample needed 3.5 hours to reach the lowest temperature. This cooling time was even longer than the heating time owing to the thermal inertia related to the mass and hence to the S/V ratio. So, the influence of geometry in thermal gradients has been identified.

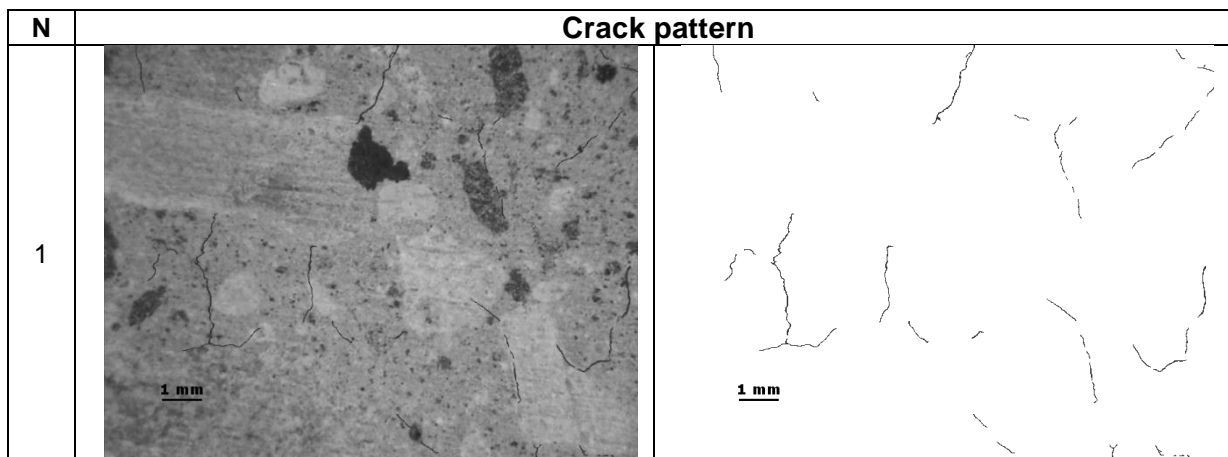
Figure 7 Thermal fatigue response for cubic and cylindrical specimens



- **Crack evolution**

The patterns of cracks were obtained for cylindrical samples and some examples are shown in Figure 8. Before the thermal cycles, the cement paste in the concrete between the aggregates shows a structure with no cracks and good interface between the aggregate and the cement paste. After thermal cycles, the cracks followed mainly the cement paste and the interface aggregate-paste owing to the change in volume of aggregates because of expansion at high temperatures and the cement paste shrinkage.

Figure 8 Crack pattern after 1, 25 and 75 thermal cycles



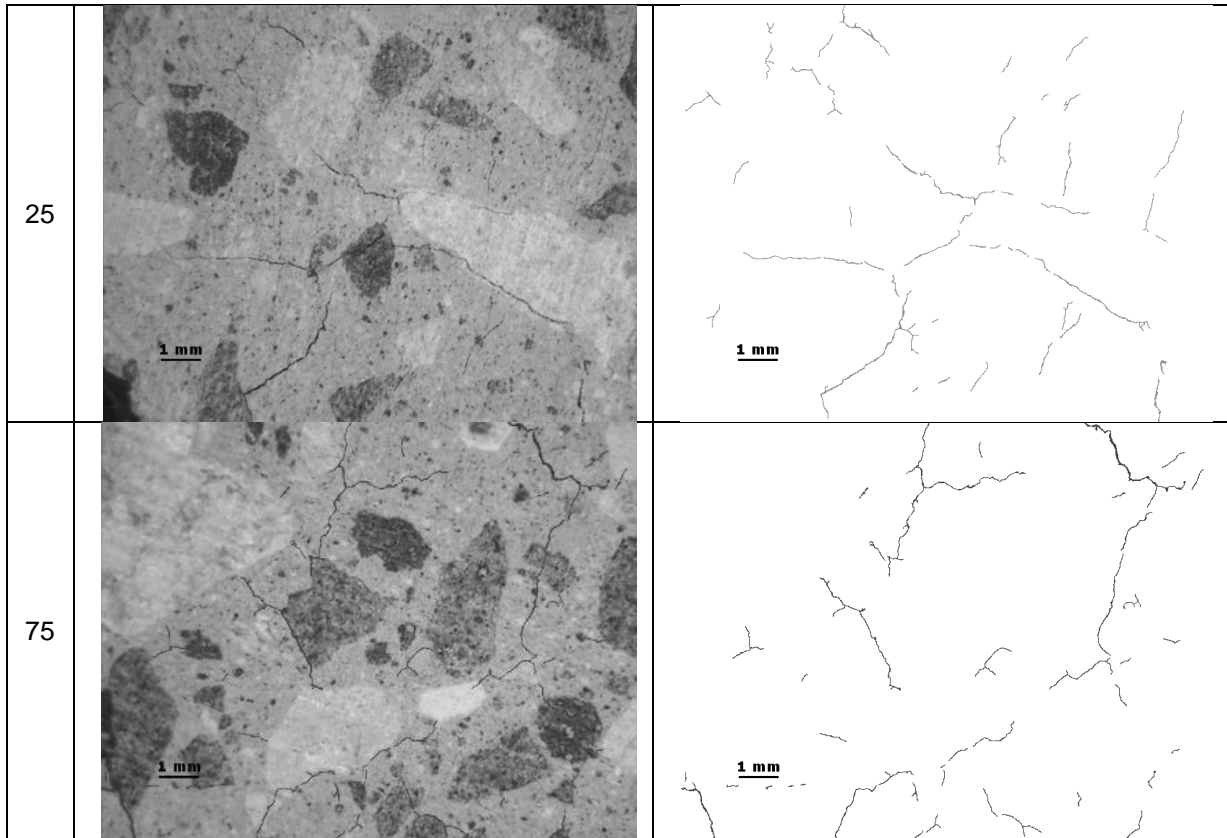
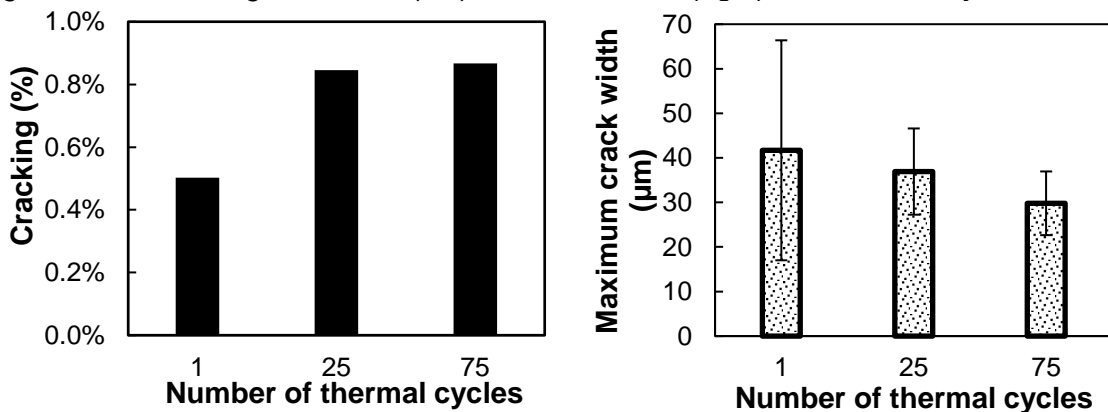


Figure 9-left shows the percentage of cracks and what is remarkable is the maintenance of the parameter after 25 and 75 thermal cycles. This gives information on long-term durability because the concrete subjected to high temperature thermal cycles would operate adequately for the application of thermal energy storage. Figure 9-right shows the maximum width of the cracks and once again, no great variability was found after the cycles.

Figure 9 Percentage of cracks (left) and crack width (right) after thermal cycles



CONCLUSIONS

The present study has led to the following conclusions:

- The sample geometry and size influence on the thermal gradients generated in the concrete. Higher specimen size generated higher thermal gradients that resulted in spalling failure for the same concrete type.

- The thermal cycles have induced a thermal fatigue in concrete after the first cycle, which stabilises at longer heat/cool cycles. Stabilisation of crack sizes and crack percentage are demonstrated up to 75 cycles.
- The concrete components and dosage used in the present work have demonstrated to withstand severe heating/cooling cycles (290-550°C).

ACKNOWLEDGEMENTS

This work was financially supported by the European Union's H2020 grant agreement ID 685445 under the LORCENIS Project. Acknowledge to Dyckerhof, LORCENIS partner, for supplying the cement and clinker aggregate.

REFERENCES

1. Alonso, M.C., Vera-Agullo, J., Guerreiro, L., Flor-Laguna, V., Sanchez, M. and Collares-Pereira, M. "Calcium aluminate based cement for concrete to be used as thermal energy storage in solar thermal electricity plants," *Cement and Concrete Research*, **82**, 74-86, 2016.
2. John, E., Hale, M. and Selvam, P. "Concrete as a thermal energy storage medium for thermocline solar energy storage systems", *Solar Energy*, **96**, 194-204, 2013.
3. Laing, D. Bahl, C., Bauer, T., Fiss, M., Breidenbach, N., and Hempel, M. "High-temperature solid-media thermal energy storage for solar thermal power plants", *Proceedings of the IEEE*, vol. 100, n° 2, pp. 516-524, 2012.
4. Zeiml, M., Leithner, D., Lackner, R. and A. Mang, H. "How do polypropylene fibers improve the spalling behaviour of in-situ concrete?" *Cement and Concrete Research*, **36**, 929-942, 2006.
5. Kanemá, M., Pliya, P., Noumoué, A., Gallias, J.L. "Spalling, thermal and hydrous behavior of ordinary and high-strength concrete subjected to elevated temperature", *Journal of Materials in Civil Engineering*, **23(7)**, 921-930, 2011.
6. Liu, J.C., Tan, K.H., and Yao, Y. "A new perspective on nature of fire-induced spalling in concrete", *Construction and Building Materials*, **184**, 581-590, 2018.
7. Mindeguia, J.C., Carré, H., Pimienta, P., La Borderie, C. "Experimental discussion on the mechanisms behind the fire spalling concrete", *Fire and Materials*, **39 (7)**, 619-635, 2015.
8. Connolly, R., *The spalling of concrete in fires*, Aston University, 1995.
9. Zhang, H., Davie, C. "A numerical investigation of the influence of pore pressures and thermally induced stresses for spalling of concrete exposed to elevated temperatures", *Fire Safety Journal*, **59**, 102-110, 2013.
10. Hertz, K., *Heat-induced explosion of dense concretes*, Technical University of Denmark, Institute of Building Design Report, Lyngby, 1984.

In situ concrete spalling risk assessment in tunnel by means of a mobile oil-fired furnace

Dominique Pardon¹, Pierre Pimienta^{1,*}, Benoît-Louis Marie-Jeanne¹, Stéphane Hameury¹, Nicolas Pinoteau¹, Bérénice Moreau², Laetitia D'aloia Schwartzentruber², Catherine Larive², Pierre Peyrac³, Xavier Thollard⁴

¹Université Paris Est – CSTB (Centre Scientifique et Technique du Bâtiment), Marne-La-Vallée - France

²CETU (Centre d'Etudes des Tunnels), Bron, France

³DRIEA-IF, Département ingénierie Ouvrages d'Art, Le Pré Saint Gervais, France

⁴SETEC Bâtiment, Paris, France

* Corresponding author: pierre.pimienta@cstb.fr, 84, avenue Jean Jaurès, Champs sur Marne, 77447 Marne-la-Vallée Cedex 2, France

ABSTRACT

Concrete structures in tunnel can be severely damaged by spalling phenomena when exposed to fire. Spalling risk is difficult to assess in the case of existing tunnels. Cutting and transporting samples with representative size to the test facilities may be problematic. One solution is to perform on site tests with a mobile furnace. This paper presents a new test campaign which aims to compare results from tests carried out with the CSTB mobile fire furnace and with a standard laboratory furnace. Observed spalling phenomenon was extremely intense and heterogeneous in both furnaces. The power consumed by concrete heating as a function of the concrete spalling rate and its influence on the ability to comply with the standard temperature curve requirements are discussed.

In addition, results from 2 real assessment fire tests carried out in 2016 and 2017 in 2 tunnels located along the Paris ring road are presented.

KEYWORD: Mobile Fire Furnace, Tunnel, Concrete Spalling, Increased Hydro Carbon Temperature Curve

INTRODUCTION

Concrete structures in tunnel can be severely damaged by spalling phenomenon when exposed to fire. Tunnel operators are particularly concerned by this issue. In France, the regulation required the assessment of concrete spalling in specific cases after the dramatic fire in the Mont-Blanc tunnel (between France and Italy) in March 1999 [1]. In accordance with this new mandatory risk assessment, CSTB in collaboration with CETU and DRIEA-IF developed an innovative in situ measurement procedure of spalling sensitivity for large scale structures in tunnels.

Undeniably concrete spalling is a complex phenomenon. Parameters and mechanisms influencing its occurrence are not yet fully understood. There is therefore a general agreement that risk assessment of concrete spalling in tunnels involves carrying out fire tests on specimens. However, the tested samples have to be as representative as possible of the real conditions (composition of concrete, water content, pore pressure, geometry, mechanical stress, restrained thermal expansion, boundary conditions...). Spalling risk is consequently difficult to assess in the case of existing tunnels. Cutting and transporting samples with representative size to the test facilities may be problematic. One approach

is to provide a special mobile test equipment that allows one-sided localized heating of large structures directly in tunnels. This approach offers two important advantages. First, it avoids the difficult cutting operation of concrete specimens. Secondly, it strongly reduces the problem of the representativeness of the tested concrete members. Concrete composition, water content and mechanical stresses are among the most important ones of the assessed structures.

In 2014, 2 sets of tests aiming at comparing experimental results from tests carried out with the mobile fire furnace versus a traditional standard laboratory furnace were presented and published [2]. From the obtained results, it was concluded that the specimen section of concrete to assess spalling with the mobile furnace should be equal or higher than 1.0 m x 1.0 m.

This paper presents a new set of tests aiming again at comparing experimental results from tests carried out with the mobile fire furnace (1 test/1 slab) versus a traditional standard laboratory furnace (1 test/4 slabs). The French Increased Hydrocarbon (HC_{inc}) curve was to be applied in these 2 tests. The paper will discuss: the analysis of the results achieved with the 2 furnaces, the power consumed by concrete heating as a function of the concrete spalling rate and its influence on the ability to comply with the highest target temperature curve.

In addition, 2 actual assessment fire tests performed in 2016 and 2017 in 2 tunnels located along the Paris ring road are presented. These 2 tunnels have been constructed in the years 1970s.

DESIGN OF A MOBILE OIL-FIRED FURNACE

Figure 1 shows a mobile light fuel oil-fired furnace designed and constructed by CSTB to test samples in vertical position. It is designed to carry out 2 hours exposure of standardised ISO 834-1 fire as well as the temperature curves used to assess large scale concrete structures in tunnels as the French Increased Hydrocarbon (HC_{inc}) curve and the RWS curve.

The maximum heating capacity of the furnace is 1300 kW. The combustion air blower, fuel pump, control panel and the heat protective shield which houses two round-flame oil burners are rack mounted on a mobile cart made of a steel frame supplied with caster wheels. The mobile cart can be lifted by a forklift truck. The combustion air blower of rated power 15 kW and maximum flow rate of $1300 \text{ m}^3 \cdot \text{h}^{-1}$ provides preheated air to the burners. To follow a specified time-temperature curve during the test, the thermal load in the fire chamber is regulated from the control panel by continuously and proportionally adjusting the combustion air volume and oil input flow. The furnace is supplied with oil from a mobile vessel of 1000 l capacity. The fuel pump provides circulation between the tank and the burners by means of two flexible hoses with fast couplings. The two round-flame oil burners shown in Figure 2 are of the same type and power (300 to 650 kW each). Their ignition is provided by a propane-fuelled pilot burner that is switched off automatically after a delay and the verification by a photo sensor of the presence of a flame on the burners. The two round-flame oil burners are juxtaposed vertically and oriented towards each other with an angle.

The combustion flames converge at an axial location, concentrating the heating power. The fire chamber has been improved. It has a Z shape and is presented in Figures 3 and 4. Its geometry enables to develop hot gases without direct flame impingement on the surface of the test specimen. The hot gases are released from an opening at the side of the fire chamber (Figure 3 and 4).

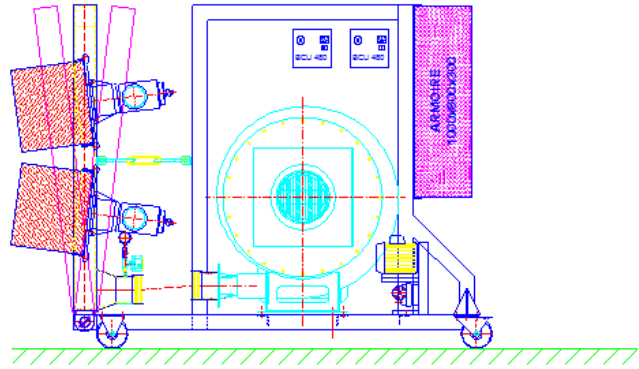


Figure 1 Combustion control cart and heat protective shield of the mobile oil-fired furnace.



Figure 2 Firing hood with two oil burners.



Figure 3 Picture of the fire chamber. The mobile fuel-fired furnace is hidden behind. This picture was taken in one of the tested tunnels located along the Paris ring road.

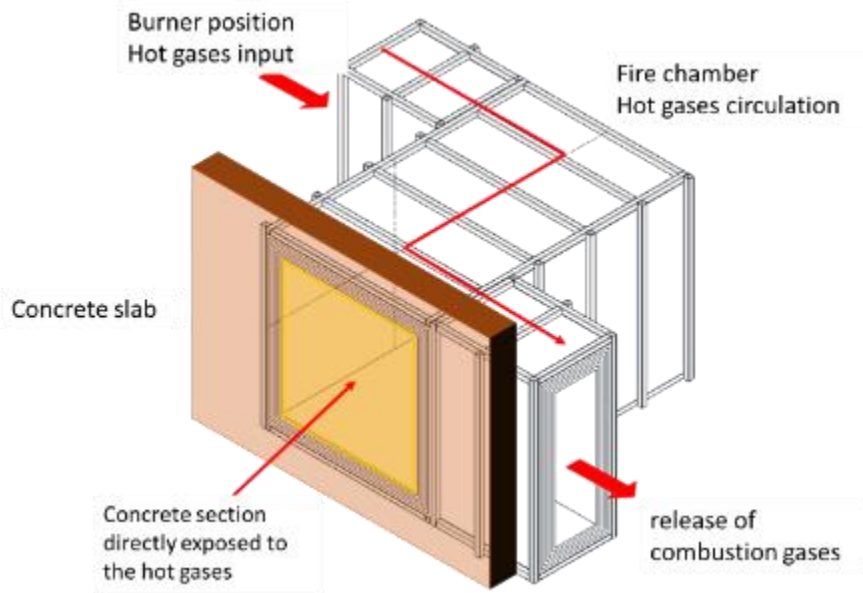


Figure 4 Fire chamber of the mobile fuel-fired furnace

A calibration test was carried out in July 2012 to confirm the ability of the mobile fire furnace to follow the Increased Hydrocarbon curve (Figure 5). Several other tests have confirmed this ability.

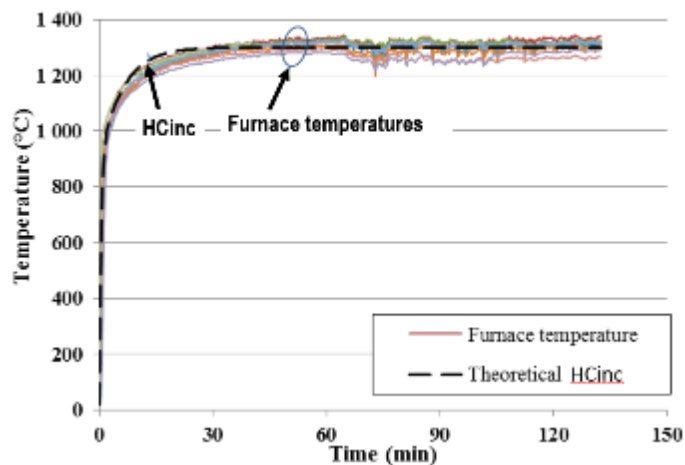


Figure 5 Example of measured furnace air temperature following the increased Hydrocarbon curve.

RESEARCH PROGRAM, CONCRETE MIXES AND TEST METHODS

Research program

The research program is summarized in Figure 6. The main goal of the program is to compare experimental results between tests carried out with the oil-fired mobile furnace and the traditional standard furnaces.

Two slabs were prepared to be exposed vertically to the mobile furnace. Slabs were sprayed with a heat protective coating to leave a 1.2 m x 1.2 m section of bare concrete directly exposed to fire. The choice of this area was determined from the experience gained from the previous experimental results [2]. Only slab 5 was tested. Test on slab 6

was not carried out. Explanation will be given in a section below.

Four slabs were exposed to the large modular Vulcain furnace. The maximum horizontal size of the furnace is 7 m x 3 m. Two slabs (4.1 m x 1.7 m x 40 cm) were unprotected. Two slabs were partially protected (1 m x 1 m and 1.2 m x 1.2 m). Unprotected slabs on the fixed laboratory furnace are considered as the reference specimens.

This program allows to:

- Compare the results between mobile furnace and reference specimens on the fixed laboratory furnace (slab 5 compared to slabs 2 & 4),
- Compare the results between mobile furnace and the same partially protected slab tested in fixed laboratory furnace (slab 5 compared to slab 3),
- Assess the repeatability of the results in the fixed laboratory furnace (slabs 2 and 4),
- Assess the influence of the area of the exposed surface (slabs 1 and 3),
- Assess the influence of the partial protection which induces higher thermal restraint stresses (Slabs 1 & 3 compared to 2 and 4).

All the slabs have been exposed to the conventional French tunnel temperature curve HC_{inc} . The curve is the modified hydrocarbon curve of Eurocode 1 - part 1-2 by increasing the value of the asymptote to 1300 °C, instead of 1100 °C:

$$20 + 1280 (1 - 0.325 e^{-0.167t} - 0.675 e^{-2.5t}) \quad (1)$$

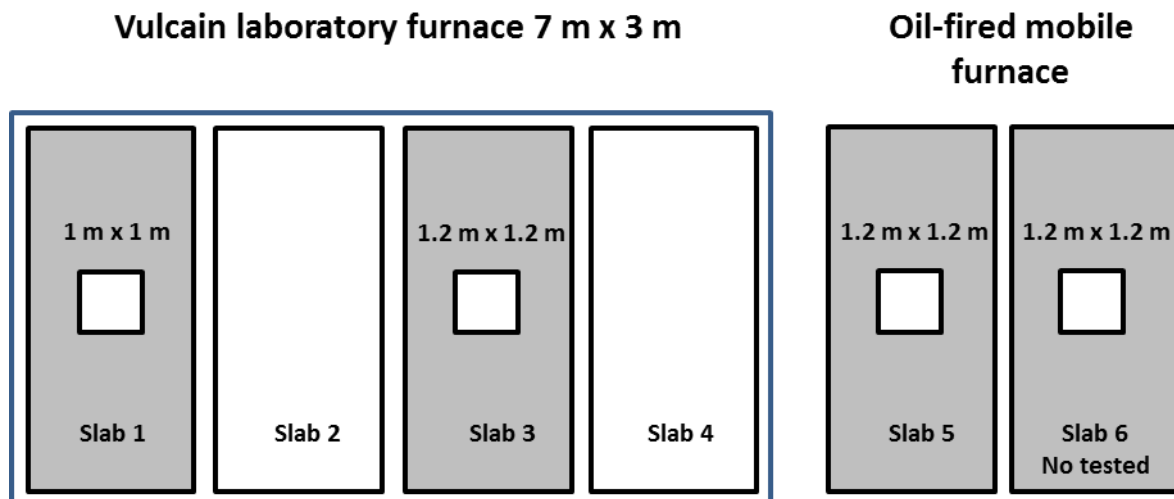


Figure 6 Research program scheme

Concrete mix proportions and properties

The concrete was provided by a ready-mix concrete company with 3 mixer trucks. Slabs were cast in the CSTB laboratory. Concrete composition and properties are given in Table 1. It contains silica fume and limestone fillers. The compressive strength was determined on cubes of 150 mm x 150 mm x 150 mm.

Test method

The slabs geometry was: 4.1 m x 1.7 m x 40 cm. They were reinforced with 3 meshes ST60 positioned in the middle and at 45 mm from each surface. All the slabs have been cured in the same conditions and tested after 6 months (fixed furnace) and 10 months (mobile furnace). All the slabs were instrumented with thermocouples held on the reinforcing bars and at different depths and locations along thin metallic rods in the concrete in order to record the temperature profiles and the progress of spalling.

Table 1 concrete composition and properties

Constituents and properties	
Cement: CEM I 52,5 N CE CP2 NF (kg/m ³)	390
Gravel: 4/20 Crushed Washed (kg/m ³)	485
Gravel: 4/10 Rolled Washed (kg/m ³)	365
sand: 0/4 (kg/m ³)	736
Silica fume	30
Limestones fillers (kg/m ³)	50
Total water including the one from superplasticizer (l/m ³)	223
Effective water including the one from superplasticizer (l/m ³)	163
Superplasticizer (% of cement)	1
Slump, mm	
Mean compressive strength after 147 (MPa) (per truck)	66.8 - 66.5 - 71.4
Mean porosity values (%) (per truck)	16.5 - 17
Mean density(kg/m ³) (per truck)	2145 - 2171
Water content in the first 5 cm (%)	5.4 - 6.2
Mean water content (%)	7.0

After a period of 3 months, the faces to be exposed to fire of 4 slabs (1, 3, 5 and 6) were partially protected with a sprayed heat protective coating. Part of the slabs was not covered (cf. above). The slabs were exposed to the Increased Hydrocarbon temperature curve. A furnace endoscopic camera allowed to display in real time the behaviour of the whole surfaces exposed to the fire and to record it. The concrete spalling depths were measured with a 1 mm depth accuracy with at least 100 measuring points mesh.

RESEARCH PROGRAM RESULTS AND DISCUSSION

The main spalling behaviour test results are presented in Table 2. The first result to mention is that spalling intensity was heterogeneous, extremely severe and continuous along the test on the 5 slabs tested either with the fixed furnace or the mobile furnace. The 40 cm thick slabs 1 and 2, tested with the fixed furnace, were pierced after 52 min. Test was then stopped.

Pictures from slab 5 (mobile furnace) taken during the test with the endoscopic camera and after the tests are presented in Figure 8 and 9. Pictures from slabs 1 to 4 (fixed furnace) are presented in Figure 10. The large quantity of concrete flakes in the fire chamber after the test is shown on the Figure 8 (right). The very high spalling depths observed on all the 5 slabs are visible on these pictures. Owing to the severe damage due to the extremely intense spalling on the furnace chamber, test on slab 6 was not carried out.

Pointed summit shapes can be observed on Figure 8, 9 and 10. This is more noteworthy in the centre of slabs 1, 3 and 5. Part of the thermocouples were positioned along thin metal rods at different depths from 10 mm to 300 mm. Concrete did not spall near these aligned thermocouples. One possible reason is that gas and liquid movements could have been facilitated by the wires and the rods presence, thus inducing lower local pore pressure and thus lower spalling depth. This phenomenon did not occur along the reinforcing bars. Spalling rates could then be assessed by analysing the temperatures measured with the thermocouples mounted on the bars. The almost constant and very high spalling rates were mostly between 5 to 7 mm /min. This result can be partly explained by the silica fume addition and the high water content. However, even these characteristics cannot completely explain this very uncommon result.

To make the spalling depth measurements easier to carry out, reinforcing bars have been removed (Figure 9, right and 10).

The second result to mention is that the Increased hydrocarbon temperature curve could not be followed along all the test in both furnaces. The temperature curves measured on

slab 5 (the mobile furnace test) are presented in Figure 7. Temperatures were limited to about 1000 °C. This can be explained by the large amount of thermal power absorbed by the intense spalling phenomenon.

Power absorbed by the spalling phenomenon could be roughly estimated by the following simplified calculation and assumptions. As concrete flakes geometry is very small, concrete flakes and water (liquid and gas) are assumed to be heated from room temperature to 920 °C (temperature increase: 900 °C). By considering, a concrete section of 1 m², the energies to heat a thickness of 1 cm are approximately of 21 and 6 MJ for the concrete and the water respectively. The absorbed power when spalling rate equal 6 mm/min is then 0.27 MW/m². The exposed area in Vulcain furnace was 13 m². The absorbed power was then 3 MW i.e. 26 % of the 13.4 MW total power of the furnace. In the same way, the exposed area in the mobile furnace was 1.4 m². The absorbed power was then 0.4 MW i.e. 30 % of the 1.3 MW total power of the furnace. Specific heat for concrete, liquid water and vapour were assumed equal to 1000, 4185, and 2000 J/kg.K respectively. Water vaporisation enthalpy was assumed equal to 2.2 MJ/kg.

In both cases, the absorbed power by the intense spalling was high comparatively to the total power of the 2 furnaces (26 % and 30 %). This can certainly explain why the Increased Hydrocarbon curve could not be reached. Figure 5 shows that, in normal conditions, the mobile furnace is able to fulfil the tunnel curves requirements. The spalling observed in this test campaign was extremely intense and, luckily, very uncommon. However, this experience shows that the power of the furnaces used to carry out spalling tests must be high enough to comply with the furnace temperature requirements.

The scattering of our results makes the conclusion difficult. However, we can observe that spalling depth distributions for slabs 1, 2, 3 (fixed furnace) and 5 (mobile furnace) are comparable. This result is in agreement with the ones already given in [2]. It gives confidence in using the mobile furnace to in situ assess concrete spalling behaviour. Moreover, as explained in the introduction, the representativeness of the real conditions (composition of concrete, water content, pore pressure, geometry, mechanical stress, restrained thermal expansion, boundary conditions...) is a very important issue when assessing concrete spalling. The reproduction of these influencing parameters in the laboratory may show deviations. This constitutes an important advantage of the mobile furnace. Then weighing the pros and cons of the mobile furnace shows that this technique is a convenient method to assess tunnel concrete structures in fire conditions.

Spalling depths observed on slab 4 is lower. An explanation to this specific result has been proposed by the authors. However, this cannot be discussed in this paper due to its limited length.

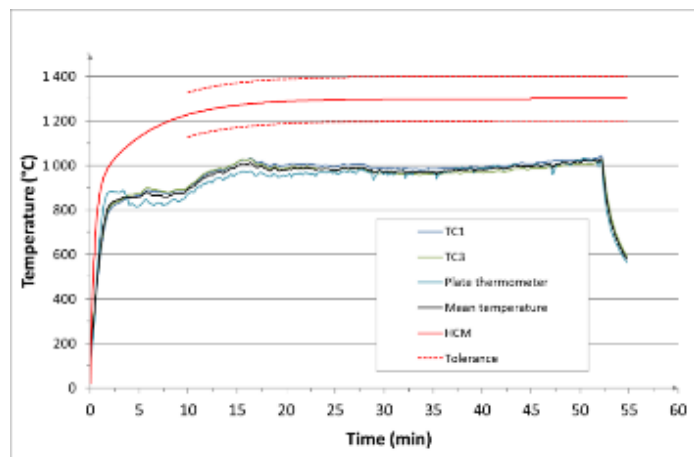


Figure 7 Furnace temperature measured with 2 thermocouples and one plate thermometer. Temperatures could not follow the Increased Hydrocarbon curve.

Table 2 Main spalling behaviour results

	Slab 1	Slab 2	Slab 3	Slab 4	Slab 5
Time of first spall (min)	3 – 4	3 - 4	3 – 4	3 - 4	1 - 2
Identified 1 st mesh visible time (min)	15	8	7	12	8
Mean spalling depth (mm)	295	265	297	160	239
Max spalling depth (mm)	400	400	374	222	315
Spalling depth standard deviation (mm)	117	117	59	45	63



Figure 8 Mobile furnace (slab 5) - Picture from endoscopic camera at the end of the test (52 min) (left). Pile of concrete flakes in the fire chamber after the test (right).



Figure 9 Concrete slab 5 after 52 min exposure in mobile furnace and cooling. Before removing the reinforcing bars (left); after removing the reinforcing bars (right)

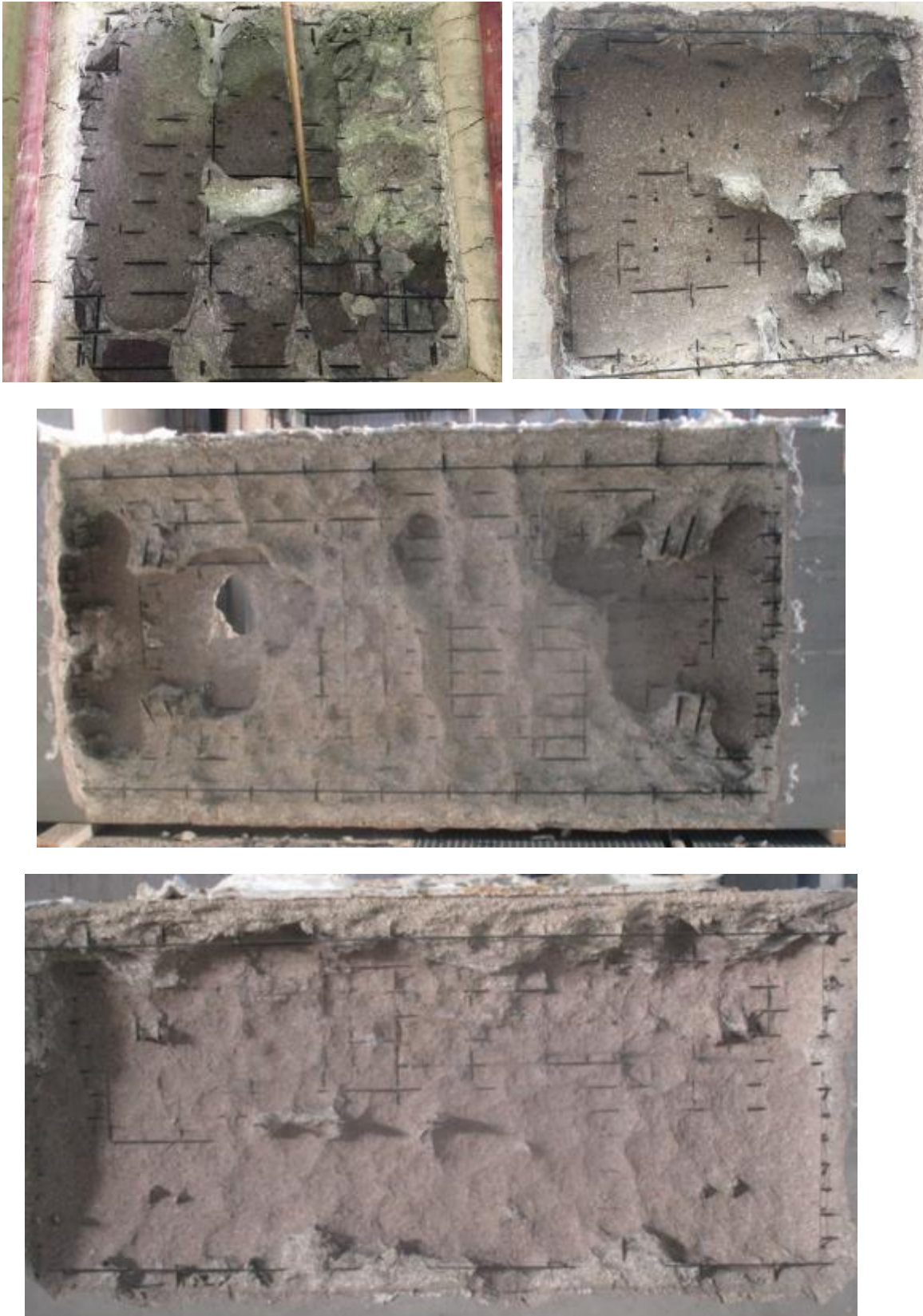


Figure 10 Concrete slabs after 52 min exposure in standard laboratory furnace Vulcain and cooling and after removing the reinforcing bars. Slab 1: partially exposed 1 m x 1 m (top left); Slab 3: partially exposed 1.2 m x 1.2 m (top right); slab 2: unprotected (middle); slab4: unprotected (bottom).

EXAMPLES OF RESULTS FROM 2 REAL CASES

In order to complete the experience gained by the authors, results from 2 real assessment fire tests are presented. Tests were carried out in 2016 and 2017 in 2 tunnels located along the Paris ring road. These 2 tunnels have been constructed in the years 1970s. The exposed sections were 1.2 m x 1.2 m large. The surrounding parts of the walls were protected with a fire-resistant insulation. Exposed concretes after test are shown in Figure 11. No spalling was observed during the fire in the example given on the left. Concrete surface was cracked. After the test, exposed surface was water blasted to determine the non-adhesive damaged concrete thickness. Spalling was observed in the 2nd example. Depth ranged between 40 mm and 60 mm.

The applied temperature exposure complied with HC_{inc} curve requirements in these 2 tests. These results show again that the 1300 kW furnace power of the mobile furnace is sufficient to carry out tests when lower (and less uncommon) spalling is observed.



Figure 11 example of 2 real assessment fire tests carried out in 2016 and 2017 in 2 tunnels located along a Paris ring road. These 2 tunnels have been constructed in the years 1970s.

CONCLUSIONS

Spalling depth was extremely intense, heterogeneous and continuous during the tests. However, the analysis showed that the results from a fixed standard furnace and this mobile furnace are comparable. Hence, in-situ tests (using a mobile furnace) appear as a convenient method to assess tunnels in fire conditions. More results would help to confirm this tendency.

As pointed out, this type of test provides the large advantage of a good, and probably the best, representativeness of the real conditions, which is a very important factor when assessing concrete spalling. The experience shows that the power of the furnaces must be high enough to comply with the furnace temperature requirements. Understanding the reasons of the observed extremely intense spalling could interestingly participate to better understand the spalling phenomenon.

REFERENCES

1. Taillefer, N., Carlotti, P., Larive, C., Lemerle, C., Avenel, R., Pimienta, P., "Ten years of increased hydrocarbon temperature curves in French tunnels", Fire Technology, 49-2, 531-549, 2013
2. Pardon D., Pimienta P., Hameury S., Pinoteau N., Moreau B., Peyrac P., Larive C., Clec'H P., Jacquél A. On site risk assessment of concrete spalling in tunnel by means of a mobile oil-fired furnace. ISTSS 2014, Proceedings from the sixth International symposium on tunnel safety and security, March 12-14, 2014, Marseille, FRA. SP Technical Research Institute of Sweden, SP Report 2014:03, 2014, p. 523-532

Investigation of the preventive effect on fire spalling of natural jute fibre in high performance concrete through ring-restrained specimen tests

Mitsuo Ozawa^{1*}, Makiho Sukekawa¹ & Haruka Akasaka¹

¹ Gunma University, Kiryu, Japan

*Corresponding author (ozawa@gunma-u.ac.jp, 1-5-1, Tenjin-cho, Kiryu, Gunma, 376-8515, Japan)

ABSTRACT

In this research, ring-restraint heat testing was conducted on various types of fibre-reinforced high performance concrete (HPC), i.e., HPC with PP fibre or Jute fibre. The differences in the spalling properties of the reinforced concrete were assessed. The relationship between thermal stress, vapour pressure and temperature was also examined, and the scale of resultant spalling was determined. The concrete used in this study had been cured at two months and fourteen months. The maximum spalling depth of HPC was 12 mm, and the spalling occurred over the whole heated surface. However, no spalling was observed on the HPC reinforced with jute fibre. The results suggested that jute fibre has the potential of preventing spalling.

KEYWORD: High performance concrete, Ring specimen, Jute fibre, PP fibre, Fire spalling

INTRODUCTION

High-performance concrete (HPC) is used in the construction of high-rise buildings, bridges and other major structures worldwide. When it is exposed to high temperatures, it exhibits explosive spalling. In recent literature we identified two spalling mechanisms and related theories. The first mechanism is based on the thermal stress theory proposed by Bazant et al [1] and suggests that spalling is caused by restrained thermal dilation. Restrained thermal dilation is a result of biaxial compressive stress parallel to the heated surface producing tensile stress in the perpendicular direction. The second mechanism is based on the vapour pressure theory proposed by Anderberg et al [2] and suggests that spalling is a result of the build-up of concrete pore pressure due to the vaporization of water in the concrete voids. This results in exertion of tensile stress on the microstructure of the heated concrete. Some research has reported that spalling can be minimised by reinforcing HPC with polypropylene fibre, and we investigated the effects of adding jute to HPC on spalling during a fire [3,4]. Ring-restraint heat testing is commonly used to measure thermal stress and vapour pressure [5,6]. The Japan Concrete Institute Technical Committee (Ref:JCI-TC154A : the potential performance of concrete under high-temperature conditions) discussed spalling test of concrete. The JCI standard method [7] is adopted from the ring restrained heating test. Akasaka et al [8] conducted experiments on the effect of natural jute fibre in HPC in preventing explosive spalling during fires using ring restrained specimen. However, the effect of curing age on the spalling behaviour of HPC reinforced with jute fibre was not assessed.

In this research, ring-restraint heat testing was conducted on various types of fibre-reinforced high performance concrete (HPC) i.e. HPC reinforced with PP fibre or jute fibre to evaluate their effect on spalling. The relationship between tensile strain and the depth from heated surface due to restrained stress, vapour pressure and temperature were also examined, and the scale of resultant spalling was determined. The HPC used was cured at two months and fourteen months.

EXPERIMENTAL OUTLINE

Concrete mixtures and a summary of their fresh properties

The concrete mixtures used are presented in Table 1. The water-cement ratio was 0.3, and high-early-strength Portland cement C (density: 3.14 g/cm³) with two types of fine aggregates referenced as S1 (water absorption: 1.06%; density: 2.63 g/cm³) and S2 (water absorption: 1.93%; density: 2.73 g/cm³); coarse aggregate G (water absorption: 0.94%; density: 2.83 g/cm³); and PP fibre (density: 0.91 g/cm³) and Jute fibre (density: 1.3-1.45 g/cm³) at 0.1% by volume were used.

The fresh-concrete properties, compressive strength and the water content of the concrete of two months and fourteen months old are given in Table 2 and Table 3.

Table 1 Mixture proportion

	W/C	Unit weight(kg/m ³)							
		W	C	S1	S2	G	Admixture	PP fiber	Jute fiber
HPC	0.3	150	500	359	372	1169	4	0	0
HPC+PP								0.9	0
HPC+Jute								0	1.38

Table 2 Properties of fresh concrete

	Air (%)	Slump (cm)	Temperature (°C)
HPC	0.9	21.0	27
HPC+PP	0.8	20.4	27.6
HPC+Jute	2.9	20.0	27.7

Table 3 Mechanical properties and water content

	Ages (Month)	Compressive strength (MPa)	Elastic Modulus (GPa)	Water Content (%)
HPC2	2	102	55.6	3.29
HPC+PP2	2	90.2	55.5	3.11
HPC+Jute2	2	100	52.7	3.54
HPC14	14	96.4	62.1	2.40
HPC+PP14	14	102	57.3	2.39
HPC+Jute14	14	90.3	55.3	2.74

Ring restrained specimen heating test [7]

An outline of ring-restrained specimen heating test is given in Figure 1. The testing ring is made of steel rings (with an outer diameter: 300 mm; height: 100 mm; thickness: 8 mm) and

it is attached to four strain gauges and four thermocouples at 5 mm, 10 mm, 25 mm, 40 mm from the heated surface. A concrete specimen was placed in the ring and stainless steel pipes (outer diameter: 5 mm; inner diameter: 2 mm; length: 170 mm) were placed in the concrete at 5 mm, 10 mm, 25 mm and 40 mm parallel to the heated surface. Four type-K thermocouples were placed in the central zone of the specimens at 5 mm, 10 mm, 25 mm and 40 mm from the heated surface.

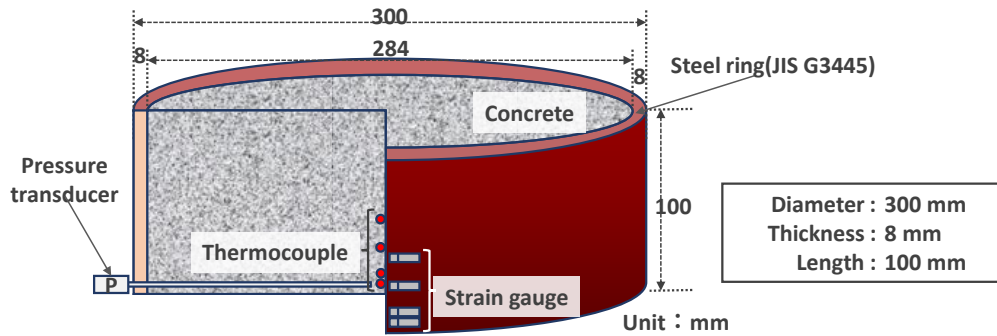


Figure 1 Ring restrained specimen

Properties of fibre [4]

The properties of the PP and jute fibre used in this research study are presented Table 4. The mean density of the jute fibre was 1.38 g/cm³. Jute fibre has a straw-like structure which supports the dispatch of water vapour from the concrete.

Table 4 Properties of fibre

Type of fibre	Length	Diameter	Melting point	Density	Other property
	(mm)	(μm)	($^{\circ}\text{C}$)	(g/cm ³)	
Jute	12	50	-	1.38	Carbonization
PP		110	170	0.91	Melting

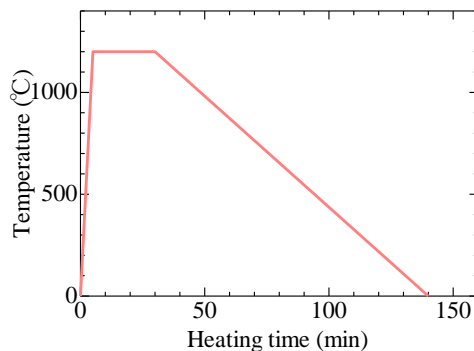


Figure 2 RABT 30 rapid heating curve

Heating test

The heating test was based on the RABT 30 rapid heating curve in Figure 2. The bottom of the ring-restraint specimen was heated, and heat insulation was applied along with steel

ring-contained insulation blankets and temperature increased over time. Spalling observation was based on spalling sound and dispatch of concrete pieces from the scuttle of the gas furnace.

Determination of restrained stress

The restrained stress was determined using the thin-walled cylinder model theory [9]. Restrained stress was determined based on strain measured from the steel ring in the circumferential direction as given in Eq. (1).

$$\sigma_{re} = \varepsilon_{\theta} \cdot E_s \cdot t/R \quad (1)$$

In the above equation, σ_{re} is the restrained stress (N/mm²), ε_{θ} is the steel ring circumferential direction strain, E_s is the steel ring elastic modulus (N/mm²), t is the steel ring thickness (mm), and R is the steel ring radius (mm).

Tensile strain failure model

The index of the tensile strain failure model was determined using Eq.(1), Eq. (2), Eq. (3) and Eq. (4)[5,6]. The apparent Poisson's ratio, the tensile failure strain, and the residual elastic modulus of concrete at high temperature. The apparent Poisson's ratio was assumed to be constant. The apparent Poisson's ratio was taken as 0.20. The elastic modulus residual ratio was calculated using the proposed equation of the elastic modulus residual ratio of concrete [10].

$$\sigma_{re} = \sigma_x = \sigma_y \quad (2)$$

$$\tau_{xy} = 0 \quad (3)$$

$$\varepsilon_{cz} = \nu(\sigma_x + \sigma_y)/(E_c(T)) \quad (4)$$

In above equations, σ_{re} is restrained stress, σ_x is stress in x direction, σ_y is stress in y direction, τ_{xy} is shear stress in xy direction, ν is apparent Poisson's ratio for concrete, $E_c(T)$ is residual elastic modulus for concrete (aij model), and ε_{cz} is Tensile strain at a certain depth from heated surface due to restrained stress.

RESULTS AND DISCUSSION

Heating surface damage

The results of the heating surface on HPC, HPC +PP and HPC+jute specimens are presented in Figure 3. The concrete used was two months and fourteen months old. The maximum spalling depth of the HPC of two months and fourteen months was 29 mm and spalling occurred over the whole heated surface (see Fig.3(a) and Fig.4(d)). Spalling was observed over the whole heated surface and was to a depth of 12 mm for the two months old HPC + PP specimen (Fig.3(b)), however, it occurred on a smaller surface on the fourteen months old HPC + PP specimen (Fig.3 (e)). Spalling was not observed on the two months old and fourteen months old specimens of HPC+Jute, and only cracks were observed (Fig.3(c) and Fig. 3(f)). The results suggest that jute fibre has the ability to prevent the spalling of high performance concrete.

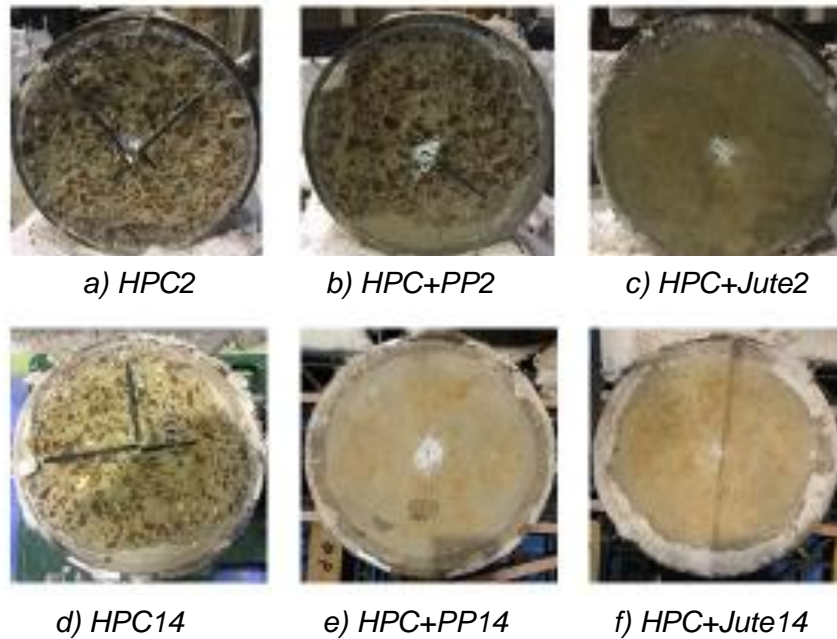


Figure 3 Heating surface damage

Vapour pressure, tensile strain at a depth from the heated surface due to restrained stress and internal temperature at 5mm from heating face

The primary assumption in our research study was that the spalling was as a result of restrained stress due to heating and vapour pressure in the voids due to vaporisation of water. The spalling mechanism is summarized in the steps given below:

Step 1: Horizontal micro-cracks occur in HPC due to high tensile strain (ϵ_{cz}) at a depth from the heated surface resulting from restrained stress.

Step 2: The vapor pressure in the voids increase during heating.

Step 3: The vapor pressure exerts on the interface of the horizontal micro-cracks resulting in spalling.

In this point of view, we consider relationship between vapour pressure, tensile strain at a certain depth from the heated surface due to restrained stress and internal temperature at 5 mm. The relationship linking internal temperature and major factors in spalling (tensile strain at a depth from the heated surface due to restrained stress and vapour pressure) at locations 5 mm from the heated surface in the HPC is given in Figure 4 a). The relationship between ϵ_{cz} and internal temperature is given in Figure 4 b). The maximum ϵ_{cz} for the two months and 14 months old HPC was approximately 30×10^{-6} , when spalling occurred in the specimens. The relationship between vapour pressure and internal temperature in comparison to an SVP curve is given in Figure 4 c). The maximum vapour pressure for the two months old and 14 months old was 1.1 MPa and 4 MPa, respectively, when spalling occurred in the specimens. The relationship between vapour pressure and ϵ_{cz} in the two months old and 14 months old concrete specimens is given in Figure d). Spalling occurred in the two month old and 14 month old specimen at a vapour pressure and ϵ_{cz} of 1.1MPa and 30×10^{-6} , 4MPa and 30×10^{-6} , respectively.

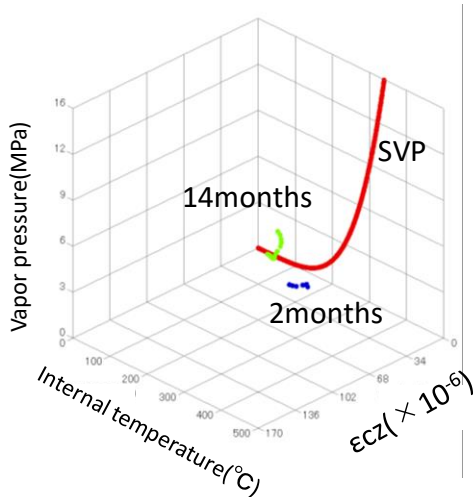


Figure 4 a) Internal temperature, tensile strain, vapour pressure at positions 5 mm from the heated surface(HPC).

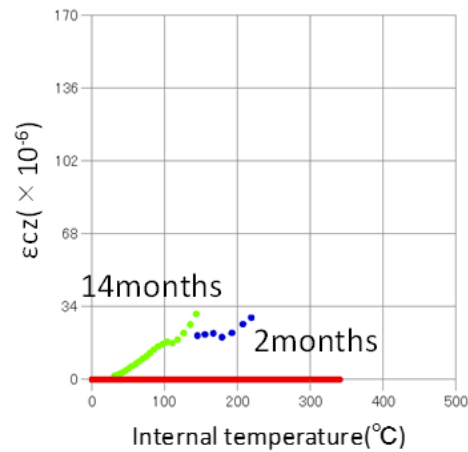


Figure 4b) Relationship between ϵ_{cz} and internal temperature (HPC).

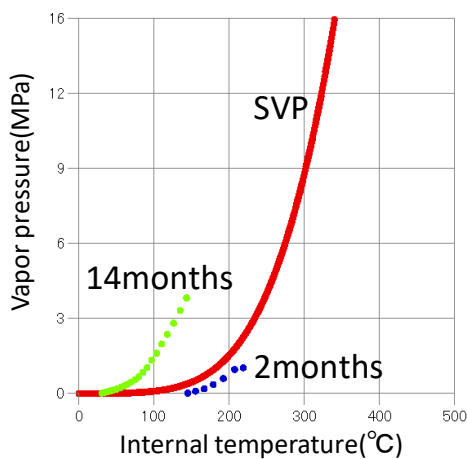


Figure 4 c) Relationship between vapour pressure and internal temperature with SVP curve (HPC).

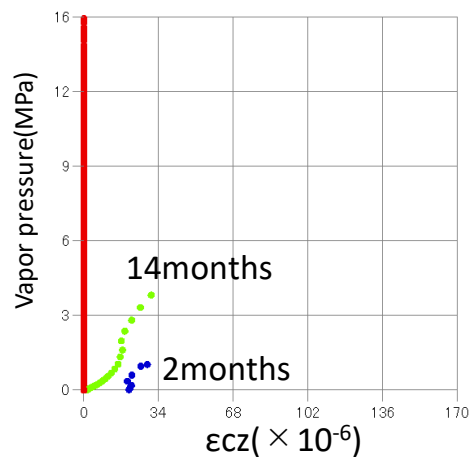


Figure 4 d) Relationship between vapour pressure and ϵ_{cz} in two months and 14 months (HPC).

The relationship linking internal temperature and major factors in spalling (tensile strain at a certain depth from the heated surface due to restrained stress and vapour pressure) at positions 5 mm from the heated surface in the HPC+PP is given in Figure 5 a). The relationship between ϵ_{cz} and internal temperature is given in Figure 5 b). The maximum ϵ_{cz} for the two months old and 14 months old specimen was 54×10^{-6} and 73×10^{-6} , respectively. Spalling only occurred in the 2 months old specimen. The relationship between vapour pressure and internal temperature in comparison to a SVP curve is given in Figure 5 c). The maximum vapour pressure for the two months and 14 months are 9.3 MPa and 3.9 MPa, respectively. The relationship between vapor pressure and ϵ_{cz} in two months old and 14 months old specimen is given in Figure 5 d). The first spalling condition occurred at a vapour pressure and ϵ_{cz} in the two-month specimen of 9.3 MPa and 54×10^{-6} , respectively,

and the damage resulting from spalling was severe.

The maximum vapour pressure and ϵ_{cz} in the 14 months old specimen was 3.9 MPa and 48×10^{-6} , respectively, and spalling damage was minimal. The difference in spalling was because the water content in two months old specimen was greater than that of the 14 months old specimen.

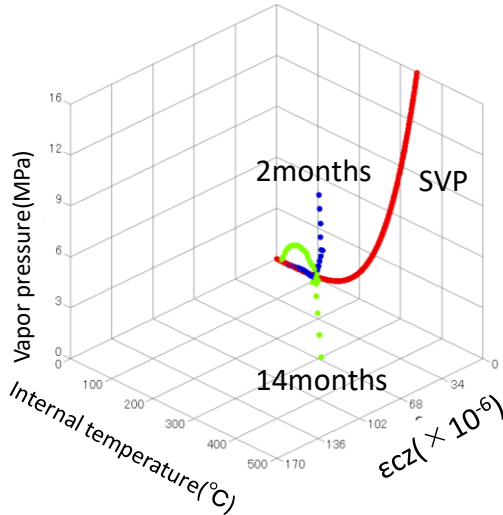


Figure 5 a) Internal temperature, tensile strain, vapour pressure at positions 5 mm from the heated surface (HPC+PP).

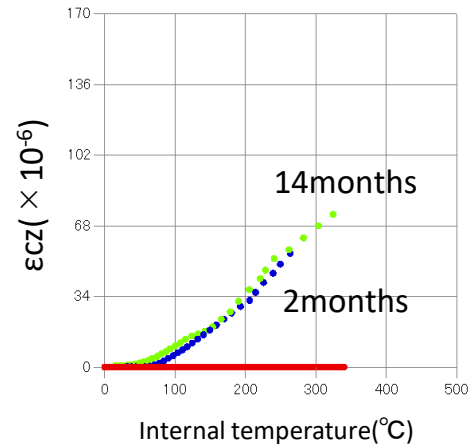


Figure 5 b) Relationship between ϵ_{cz} and internal temperature. (HPC+PP)

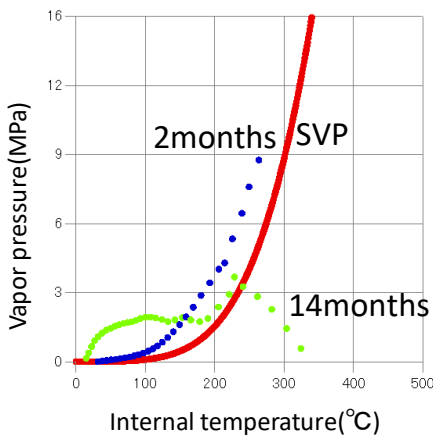


Figure 5 c) Relationship between vapour pressure and internal temperature with a SVP curve (HPC+PP).

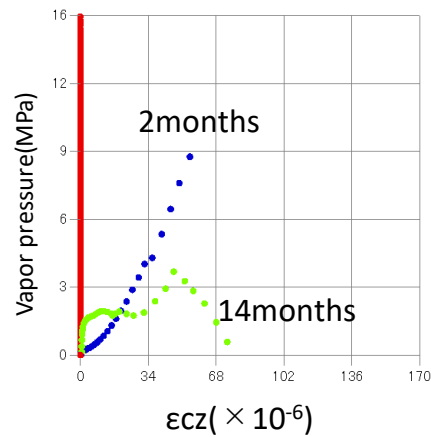


Figure 5 d) Relationship between vapor pressure and ϵ_{cz} (HPC+PP).

The relationship linking internal temperature and major factors in spalling (tensile strain at a certain depth from the heated surface due to restrained stress and vapour pressure) at selected positions 5 mm from the heated surface in the HPC+Jute specimen is shown in Figure 6 a). The relationship between ϵ_{cz} and internal temperature is given in Figure 6 b). The maximum ϵ_{cz} for the two months old and the 14 months old specimens were 109×10^{-6}

and 81×10^{-6} , respectively. Spalling did not occur in the two months old specimen and the 14 months old specimen. The relationship between vapour pressure and internal temperature in comparison to an SVP curve is given in Figure 6 c). The maximum vapour pressure of the two months old and the 14 months old specimens were 12.0 MPa and 7.2 MPa, respectively.

The relationship between vapor pressure and ϵ_{cz} in the two months old and the 14 months old is given in Figure 6 d). The maximum vapour pressure and ϵ_{cz} in the two months old and the 14 month old specimens were 12.0 MPa and 60×10^{-6} ; 7.2 MPa and 56×10^{-6} , respectively. The maximum vapor pressure and ϵ_{cz} were higher in the HPC+Jute specimens in comparison to the HPC and HPC+PP specimen, however, no spalling was observed in the HPC+Jute specimens.

This is because the jute fibre has a straw-like structure [4,8] which creates a network for the

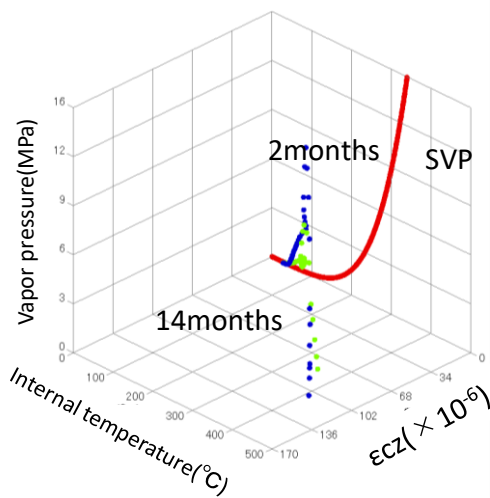


Figure 6 a) Internal temperature and tensile strain, vapour pressure at 5 mm from the heated surface (HPC+Jute).

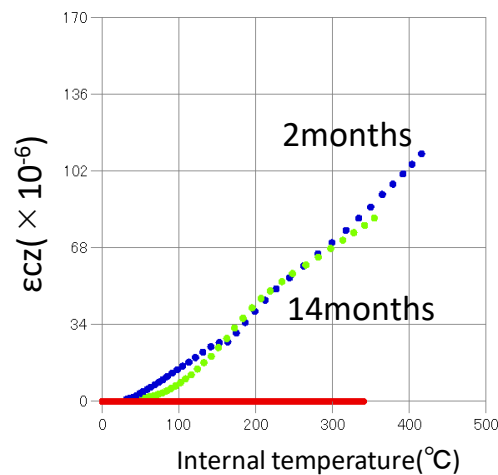


Figure 6 b) Relationship between ϵ_{cz} and internal temperature (HPC+Jute).

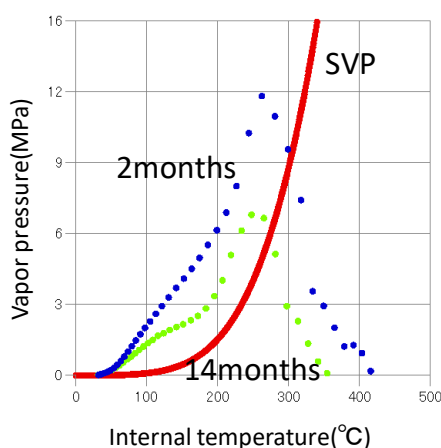


Figure 6 c) Relationship between vapour pressure and internal temperature with SVP curve (HPC+Jute).

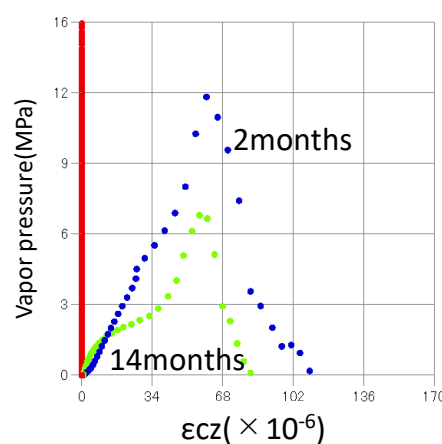


Figure 6 d) Relationship between vapor pressure and ϵ_{cz} (HPC+Jute).

release of vapor pressure in concrete having a preventive effect of spalling for HPC.

Spalling condition with vapour pressure, tensile strain at a depth from the heated surface due to restrained stress and internal temperature at 5 mm

The relationship between spalling occurrence condition with vapor pressure, tensile strain at a certain depth from the heated surface due to restrained stress and internal temperature at 5 mm is given in Figure 7.

Spalling occurred in specimens HPC2, HPC14 and HPC+PP2. Spalling occurrence condition is with vapour pressure and tensile strain at a certain depth from the heated surface due to restrained stress below. Vapor pressure in the specimens ranged between 1.1 and 9.3 MPa, and the tensile strain at depth from the heated surface due to restrained stress ranged between 30×10^{-6} and 54×10^{-6} .

No spalling or related damage were observed on the HPC+PP14 and HPC Jute specimen. Vapor pressure ranged between 3.9 MPa and 12.0 MPa. Tensile strain at a certain depth from the heated surface due to restrained stress was approximately 60×10^{-6} .

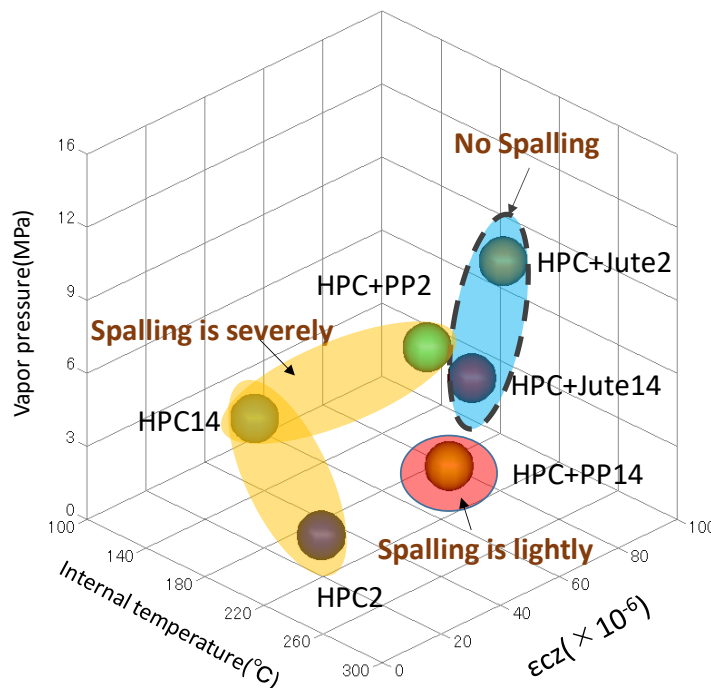


Figure 7 Relationship between vapor pressure, tensile strain at a certain depth from the heated surface due to restrained stress and internal temperature at 5 mm.

CONCLUSION

1. The maximum spalling depth of the HPC specimens of two months old and fourteen months old were 29 mm and spalling occurred over the whole heated surface. The maximum spalling depth of the two months old HPC+PP specimen was 12 mm, and spalling occurred over the whole heated surface. However, minimal spalling was observed on the fourteen months old HPC+PP specimen. No spalling or surface cracks were observed on the two months and the fourteen months old HPC+Jute specimens.
2. Spalling occurrence condition is with vapour pressure and tensile strain at a certain depth from the heated surface due to restrained stress below. Vapor pressure ranged

between 1.1 and 9.3 MPa. Tensile strain at a depth from the heated surface due to restrained stress is ranged between 30×10^{-6} to 54×10^{-6} .

3. No spalling or damage was observed on the HPC+PP14 and the HPC Jute specimens. Vapor pressure ranged between 3.9 MPa and 12.0 MPa. Tensile strain at depth from the heated surface due to restrained stress was approximately 60×10^{-6} .
4. The maximum vapour pressure and tensile strain at depth from the heated surface due to restrained stress were higher for the HPC +Jute specimen in comparison to HPC and HPC+PP and no spalling was observed. This was because jute fibre allows the release of vapor pressure in the concrete. The results suggest it can prevent spalling in HPC.

ACKNOWLEDGEMENTS

This study was financially supported by a Grant-in Aid for Scientific Research C (General) from the Japan Society for the Promotion of Science (No. 25420459; Head: Dr. M. Ozawa) and a Japan Concrete Institute (JCI) researchHPCholarship. The authors would like to express their gratitude to these organizations for their financial support.

REFERENCES

1. Bazant, Z. P., "Analysis of pore pressure, thermal stress and fracture in rapidly heated concrete", in Phan L. T., Carino N. J., Duthinh D., Garboczi E. (eds.), Proceedings of the International Workshop on Fire Performance of High-strength Concrete, NIST, Gaithersburg, Maryland, 155 – 164, 1997
2. Anderberg, Y., "Spalling phenomena in HPC and OC", in Phan L. T, Carino N. J., Duthinh, D., Garboczi, E. (eds.), Proceedings of the International Workshop on Fire Performance of High-strength Concrete, NIST, Gaithersburg, Maryland, pp. 69 – 73, 1997
3. Kalifa, P., Menneteau, F. D., Quenard, D., "Spalling and pore pressure in HPC at high temperatures", *Cement Concrete Research*, 30, pp. 1,915-1,927, 2000.
4. Ozawa, M., Morimoto, H., "Effects of various fibres on high-temperature spalling in high-performance concrete", *Construction and Building Materials*, No. 71, pp. 83-92,2014
5. Tanibe, T. Ozawa, M. Lustoza, D. R. Kikuchi K. Morimoto H. "Explosive Spalling Behavior of Restrained Concrete in the event of Fire, 2nd International RILEM Workshop on Concrete Spalling due to Fire Exposure, pp. 319-326, Delft (Netherlands), 2011, 9.
6. Ozawa, M., Tanibe, T., Kamata, R., Uchida, Y., Rokugo, K., Parajuli, S. S., "Behavior of ring-restrained high-performance concrete under extreme heating and development of screening test", *Construction and Building Materials*, 162, pp. 215 – 228, 2017.
7. Japan concrete Institute, "Test Method for Spalling of Concrete under High Temperature Exposure", JCI-S-014-2018 (In Japanese), 2018
8. Akasaka, H., Ozawa, M., Parajuli, S.S., Sugino, Y., Akutsu, Y., Murakami, M., 2018, Preventive effect on fire spalling of high-strength concrete with Jute fibre in ring-restraint specimen, Proceedings of the 14th International Conference on Concrete Engineering and Technology (CONCET 2018), August 7-10
9. Timoshenko S, Theory of Plates and Shells (Second edition), McGraw-Hill Book Company, 1959.
10. Architectural Institute of Japan: Guidebook for fire-resistive performance of structural materials, 2017 (In Japanese).

Fire-related spalling evaluation of ring-restrained polymer cement mortar and normal cement mortar

Yusuke Sugino¹, Mitsuo Ozawa² & Toru Tanibe¹

¹ Research and Development Laboratory, Taiheiyo Materials, 2-4-2, Sakura, Chiba 285-0802, Japan

² Department of Environmental Engineering Science, Gunma University, 1-5-1, Tenjin-cho, Kiryu, Gunma 376-8515, Japan

ABSTRACT

Repair mortars are often added with polymers to improve bonding with concrete. However, the addition of polymers to mortar has been found to increase spalling during fire. In this study, we performed a heating test using a ring-restrained specimen with polymer cement mortar (PCM) and normal cement mortar (NCM), and examined the spalling behavior during fire. That is, the scale of spalling was evaluated by the maximum depth of spalling after heating. In addition, we examined the occurrence of spalling and the effects of restrained stress and vapor pressure at that time. The dimensions of the specimen were 300 mm in diameter and 100 mm in height. The restrained stress of the mortar was measured by attaching strain gauges to a steel ring. The vapor pressure was measured by stainless steel pipes. Those were installed in parallel with the heating surface. Furthermore, a thermocouple was placed at the same position as the pipe, and the temperature of the mortar was measured. The strain gauges and stainless steel pipes were attached at positions of 5, 10, 25, and 40 mm from the heating surface. Commercially available fire-resistant PCM was used, while NCM consisted of the general composition of mortar. The water-cement ratio of NCM was 0.5, and the sand-cement ratio was 3.0. The heating conditions were RABT 30 and ISO 834 with 60-min standard heating curves. Results indicate the occurrence of spalling in NCM specimens during heating with RABT30 and that the tensile strain failure model can be used to estimate the spalling depth and time in the NCM specimen. On the other hand, spalling did not occur in the PCM specimen during heating. The vapor pressure dropped slowly when the PCM was heated. The nylon fibers in the PCM melted, and the vapor escaped.

KEYWORDS: Fire spalling, Polymer cement mortar, Ring-restrained specimen, Restrained stress, Vapor pressure

INTRODUCTION

Repair mortars are often added with polymers to improve bonding with concrete. However, the addition of polymers to mortar has been found to increase spalling during fire [1]. There are some data on the strength and heat generation of polymer cement mortars at high temperatures [2]. But data on spalling properties are limited. On the other hand, high-strength concrete is known to be damaged by spalling during fire. There are two mechanisms for concrete spalling. One mechanism is the thermal expansion of the restrained concrete to generate compressive stress in a direction parallel to the heating surface [3]. The other is the conversion of water in the pores to steam, as the vapor pressure acts as a tensile stress [4]. In this report, the restrained stress and vapor pressure of concrete under high temperatures, as well as the spalling of polymer cement mortar (PCM) and normal cement mortar (NCM), were evaluated using concrete restrained by steel rings [5]. The test method was based on criteria from the Japan Concrete Institute [6].

Specifically, the scale of spalling was evaluated for the maximum depth of the spalling after heating.

OUTLINE OF HEATING TESTS

Heating test method

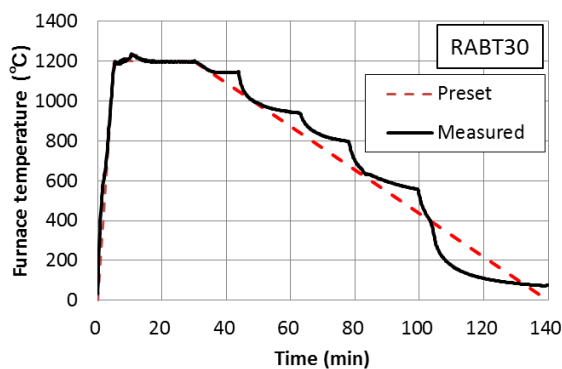
The dimensions of the specimen were 300 mm in diameter and 100 mm in height. The steel ring was filled with a silicon sealing compound, forming a 50-mm high ring in two stages. The restrained stress of the mortar was measured by attaching strain gauges to the steel ring. In addition, thermocouples were attached to the same position to measure the temperature of the ring. The vapor pressure of the mortar was determined in parallel with the heating surface with a stainless steel pipe of inner diameter 5 mm, and the inside of the pipe was filled with silicon oil. The vapor pressure was measured with an external pressure gauge via silicone oil. Furthermore, a thermocouple was placed at the same position as the pipe, and the temperature of the mortar was measured. The strain gauges and stainless steel pipes were attached at positions of 5, 10, 25, and 40 mm from the heating surface. Table 1 shows the test types. Fig. 1 shows the heating condition of the specimen. Fig. 2 shows the heating curve and the temperature in the furnace. The heating conditions were RABT 30 and ISO 834 with 60-min standard heating curves. It was confirmed that the temperature in the furnace substantially matches the heating curve. The heating test was performed after the ring was filled with mortar and cured for 2 months.

Table 1 Test type

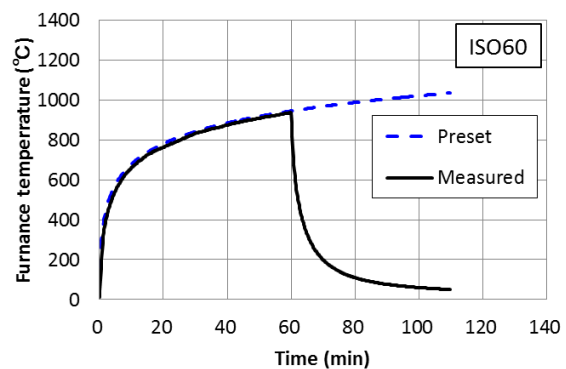
Type	mortar	Heating condition
NR	NCM	RABT30
NI		ISO60
PR	PCM	RABT30
PI		ISO60



Figure 1 Heating condition



a) RABT30



b) ISO834 (heating time: 60 min)

Figure 2 Heating curve and furnace temperature

Mortar

Commercially available fire-resistant PCM was used. In this study, the PCM used satisfied the required performance of the repair material and method selection manual on “Study on securing of cover depth of reinforced concrete buildings” [7]. Table 2 shows the performance for fire resistance based on this manual. PCM contains fiber, and infrared spectroscopy suggests nylon as the main component. Table 3 shows the material details for NCM. The sand-cement mass ratio of NCM was 3.0, and the water-cement mass ratio was 0.5. Table 4 shows the fresh and mechanical properties of the mortars. In the measurement of the moisture content, the sample was dried in a furnace at 105 °C until the sample maintained a constant mass, which was determined from the difference between the sample mass before and after heating. The compressive strengths of PCM and NCM are 46.0 MPa and 56.9 MPa, respectively.

Table 2 The performance for fire resistance

	Test method	Standard value
Cone calorimeter method	ISO 5660-1	$\leq 8 \text{ MJ/m}^2$ and $\leq 200 \text{ kW/m}^2$ Heating time : 20 min
Spalling behavior	Fire resistance test of wall members	There is no spalling of the surface. And there is a heat shield.
Load support	Load heating test	Have fireproof time required as a member

Table 3 Material details for NCM

Name	Density (g/cm ³)	Water absorption rate (%)
Ordinary Portland cement	3.16	-
Silica sand (dry)	2.64	0.25

Table 4 The fresh and mechanical properties of the mortars

Material age	Items	NCM	PCM
After mixing	Flow (mm)	154	172
	Air (%)	10.6	8.0
	Temperature (°C)	30.6	28.1
56 days	Compressive strength (MPa)	46.0	56.9
	Tensile strength (MPa)	2.3	1.9
	Elastic modulus (GPa)	26.0	27.3
	Poisson's ratio	0.18	0.22
	Moisture content ratio (%)	6.3	9.5

RESULTS AND DISCUSSION

Spalling scale

Fig. 3 shows the heating surfaces of the various sample mortars. The specimen of NR is the conditions which heated NCM with RABT30. The specimen of NI is the conditions which heated NCM with ISO 834 with 60-min standard heating curves. The specimen of PR is the conditions which heated PCM with RABT30. The specimen of PI is the conditions which

heated PCM with ISO 834 with 60-min standard heating curves. Spalling occurred in the NR specimen during heating; however, spalling did not occur in the other specimens. The spalling noise was first heard in the NR specimen 5 min after heating started and continued intermittently until 17 min after the commencement of heating. After 17 min, NR broke at the ring joint. Then, heating of the NR specimen was terminated. The cause of fracture is considered to be the generation of the shear stress at the ring joint due to the difference in the thermal expansion between the area 50 mm from the heating surface and the area from 50 mm to 100 mm from the heating surface. The NCM experienced a different scale of spalling depending on the heating rate. In the PCM, no spalling occurred under any heating condition, and any significant cracking was only fine in nature. Fig. 4 shows the spalling depth in the NR specimen after heating. The measurement position segmented the heating surface through a 20-mm mesh and was measured with a precision of 1 mm. The maximum spalling depth of the NR specimen was approximately 82 mm.

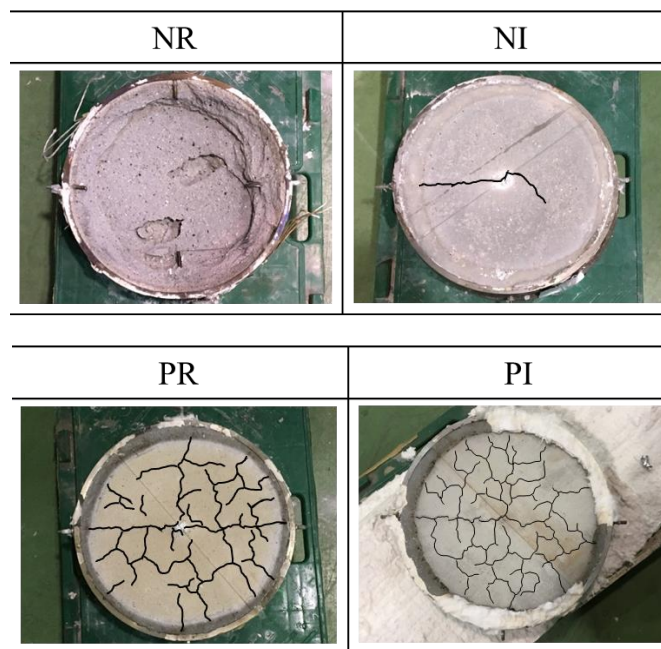


Figure 3 Heating surface after heating test

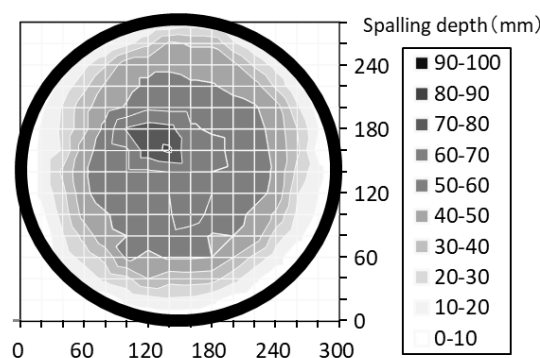


Figure 4 Spalling depth (NR)

Restrained stress and vapor pressure (NCM)

Fig. 5 shows the thermal stress of NR and NI specimens. In the NR specimen, the restrained stress increased from the start of heating, and when the spalling occurred, the restrained stress decreased rapidly as the mortar was broken. Then, spalling continued to occur continuously, and restrained stress repeatedly rose and fell. Spalling did not occur in the NI specimen, while the restrained stress continued to increase. Restrained stress increased more slowly than when NR was heated, as the ISO 834 standard heating curve has a slower rising slope than that of the RABT 30 curve.

Fig. 6 shows how the internal temperature varies with heating time in NR during the heating process. When spalling occurs and the mortar falls off, the thermocouple is exposed to the inside of the furnace, and the temperature rises rapidly. For each spalling depth curve, the point at which this rapid rise in temperature occurs is plotted, indicating how the spalling depth varies with thermocouple temperature inside mortar.

Fig. 7 shows the vapor pressure in the NR and NI specimens during heating. In the NR specimen, the vapor pressure decreased sharply when the spalling occurred. Although the spalling did not occur when the NI specimen was heated, the specimen was dried by heating, and the vapor pressure decreased.

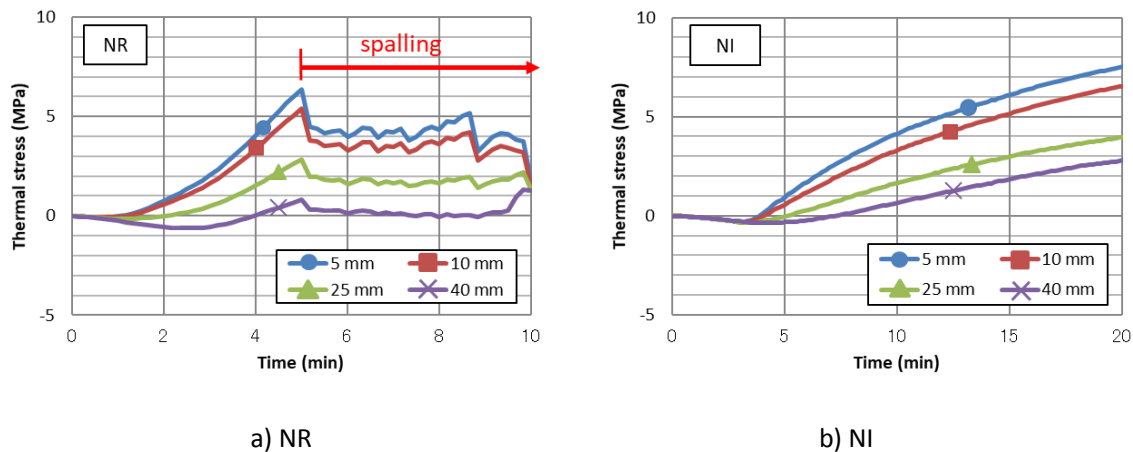


Figure 5 Restrainted stress (NCM)

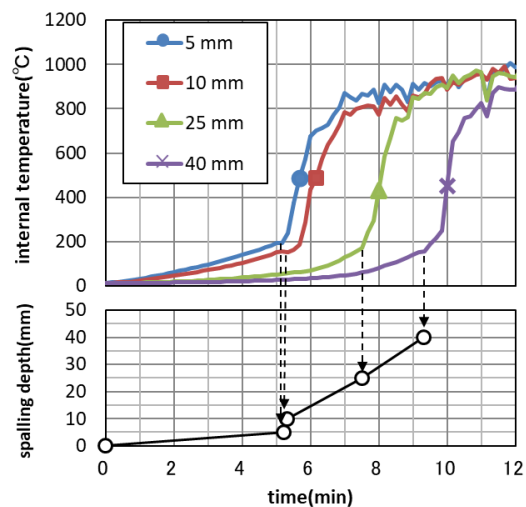


Figure 6 Internal temperature (NR)

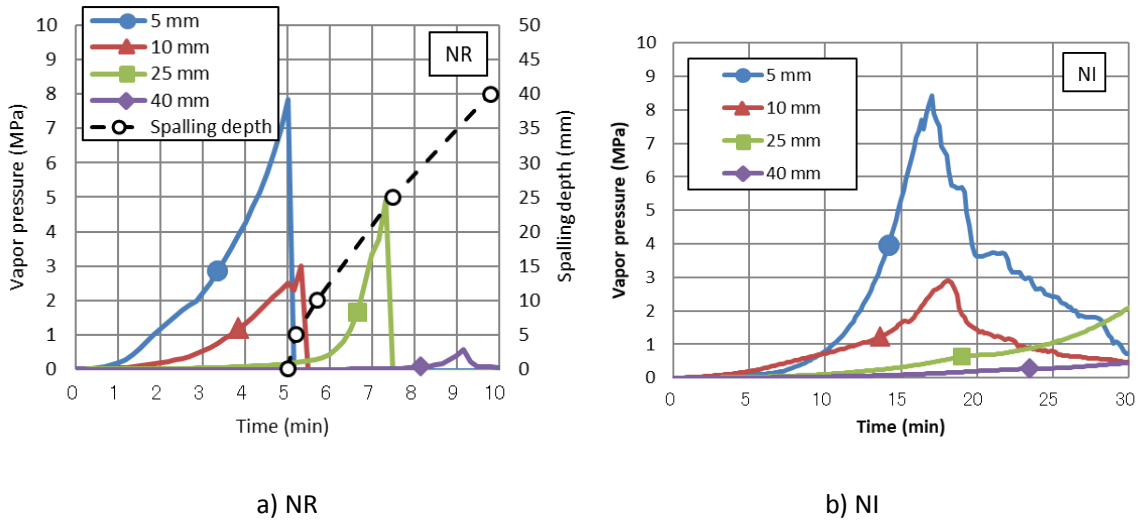


Figure 7 Vapor pressure (NCM)

Restrained stress and vapor pressure (PCM)

Fig. 8 shows the restrained stress at a position of 5 mm, while the restrained stress of NCM exceeds 6 MPa. The restrained stress of PCM is smaller than NCM. Responsible for the small stress of PCM, the elastic modulus, Poisson's ratio, and thermal creep of PCM at high temperatures may be different from those of NCM. In the future, it will be necessary to determine the physical properties of PCM under high temperatures and evaluate the detonation properties.

Fig. 9 shows the vapor pressure at 5 mm. The vapor pressure of PCM slowly decreases compared to that of NCM. This is because nylon fiber is used for PCM. Nylon fibers and polypropylene fibers are used to prevent spalling of high-strength concrete. Those fibers melt when heated, forming a network of escaping vapor [8]. Nylon fibers are melted in PR and PI during heating, creating a vapor escape network.

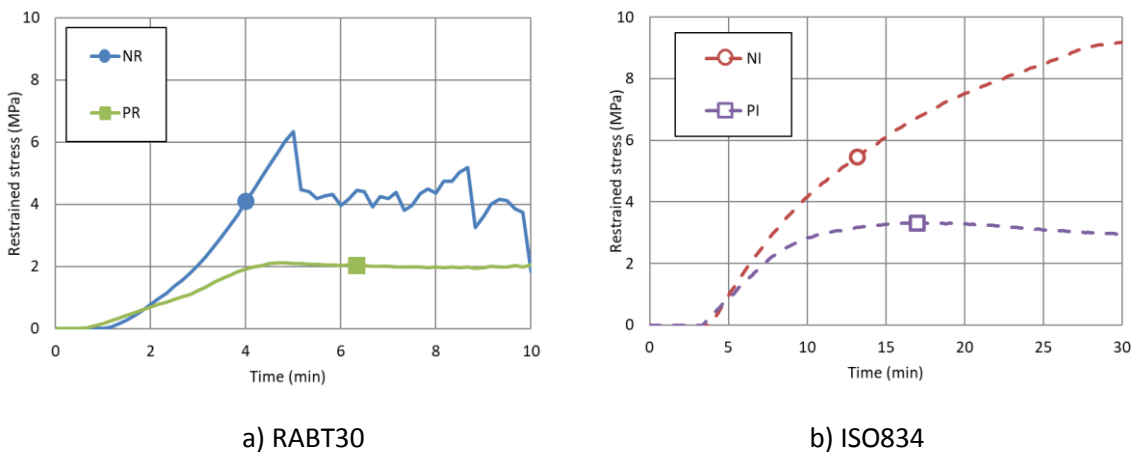


Figure 8 Thermal stress at 5 mm

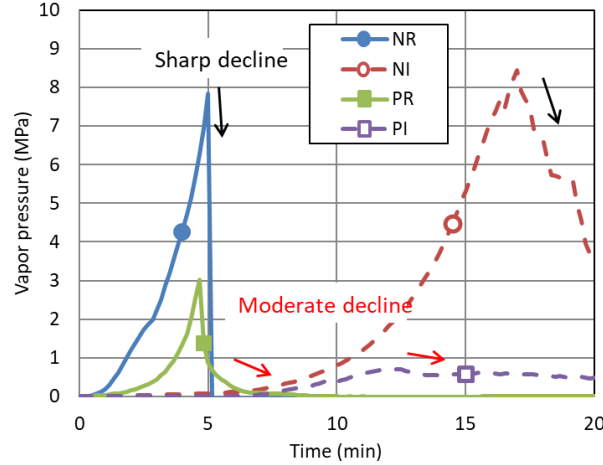


Figure 9 Vapor pressure at 5 mm

Estimation of spalling depth (NCM)

Estimation of the spalling depth based on the tensile strain failure model was performed. The target was the NR specimen as spalling occurred in NR during heating.

Previous studies reported the results of estimating the spalling depth in high-strength concrete during heating, based on the tensile strain failure model [5]. The spalling depth of NR was estimated with reference to that method.

Eq. (1) to (4) show the equations for calculating the index of the tensile strain failure model. The apparent Poisson's ratio, tensile failure strain, and residual elastic modulus for concrete are used to estimate the physical properties of concrete at high temperatures, as previous studies have shown that there is little data on the physical properties of PCM and NCM at these temperatures. The apparent Poisson's ratio and the tensile fracture strain were assumed to be constant, and the temperature dependency was set based on experimental data as an average value in the temperature range at which spalling easily occurs [9]. The apparent Poisson's ratio was 0.15, and the range of apparent tensile strain was 150 μ . The elastic modulus residual ratio was calculated using the proposed equation of the elastic modulus residual ratio of concrete [10].

$$\sigma_{re} = \sigma_x = \sigma_y \quad (1)$$

$$\tau_{xy} = 0 \quad (2)$$

$$\varepsilon_z = \frac{\nu(\sigma_x + \sigma_y)}{E_c(T)} \quad (3)$$

$$I_{\varepsilon-f} = \frac{\varepsilon_z}{\varepsilon_{t-f}} \quad (4)$$

where

σ_{re} : restrained stress

σ_x : stress in x-direction

σ_y : stress in y-direction

τ_{xy} : shear stress in xy-direction

ν : apparent Poisson's ratio for concrete

$E_c(T)$: residual elastic modulus for concrete

ε_z : strain at a certain depth from heated surface
 ε_{t-f} : ultimate strain upon tensile failure
 $I_{\varepsilon-f}$: index of strain failure model ($I_{\varepsilon-f} > 1$ tensile strain upon failure)

Fig. 10 shows the estimation of the spalling depth of NR. The estimation by the index of the tensile strain failure model indicates the time at which the tensile strain failure index of each measured depth reached 1.0. From the figure, the measurement value and the estimated value of the spalling depth by the tensile strain failure index are in good agreement.

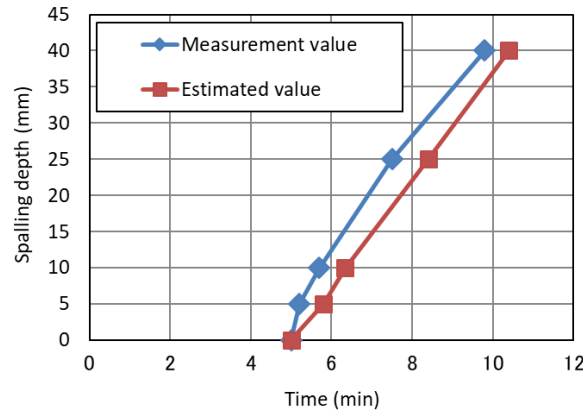


Figure 10 Spalling depth and time

CONCLUSIONS

The results obtained in this paper are shown below.

- The spalling occurred in the NR specimen during heating, while spalling did not occur in the NI, PR, or PI specimens.
- The restrained stress of NCM exceeded 6 MPa, while the restrained stress of PCM was 2 to 3 MPa under the heating conditions of RABT30 or ISO 834. That is, the restrained stress of PCM is smaller than that of NCM.
- The vapor pressure of PCM slowly decreases compared to that of NCM. Nylon fibers are melted in PR and PI during heating, creating a vapor escape network.
- The tensile strain failure model can be used to estimate the spalling depth and time in the NR specimen. It is possible to estimate the spalling depth and time using the data for the apparent Poisson's ratio and tensile fracture strain of concrete under high temperatures. In other words, it was confirmed that the spalling property of NCM can be evaluated under the same conditions as concrete.

In this study, the details for the mixing material of commercially available PCM were unknown, and it was not possible to identify the effects of fiber and polymer separately. The influence of the polymer on the spalling mechanism needs to be examined in detail, using a known composition.

REFERENCES

1. Japan Concrete Institute, "Report of Research Committee on High Temperature Properties of Concrete and Fire Resistance Performance of Concrete Structures", 2012. (in Japanese)
2. Su-jin, L., Se-Ho, K., Jong-Pil, W., "Strength and fire resistance of a high-strength nano-polymer modified cementitious composite", *Composite Structures* **173**, 96-105, 2017
3. Bazant, Z. P., "Analysis of Pore Pressure, Thermal Stress and Fracture in Rapidly Heated Concrete", Proceedings of the International Workshop on Fire Performance of High-Strength Concrete, NIST, Gaithersburg, Maryland, 155-164, 1997
4. Anderberg, Y., "Spalling Phenomena in HPC and OC", Proceedings of the International Workshop on Fire Performance of High-strength Concrete, NIST, Gaithersburg, Maryland, 69-73, 1997.
5. Ozawa, M., Tanibe, T., Kamata, R., Uchida, Y., Rokugo, K., and Parajuli, S. S., "Behavior of Ring-Restrained High-Performance Concrete Under Extreme Heating and Development of Screening Test", *Construction and Building Materials* **162**, 215-228, 2018.
6. Japan Concrete Institute, "JCI Standards and Guidelines", <http://jci-net.or.jp/jci/study/standard.html> (in Japanese)
7. Hamasaki, H., Kage, T., Hagiwara, I., Yoshida, M., Motegi, T., and Nemoto, K., "Study on Securing of Cover Depth of Reinforced Concrete Buildings", Report of the Building Research Institute, No. 147, 2013 (in Japanese).
8. Lee, G., Han, D., Han, M. C., Han, C. G., and Son, H. J., "Combining polypropylene and nylon fibers to optimize fibre addition for spalling protection of high-strength concrete", *Construction and Building Materials*, **34**, 313-320, 2012.
9. Michikoshi, S., Kobayashi, H., and Kuroiwa, S., "Strain Behaviour of Compression Concrete at High Temperature", *Journal of Architectural Institute Japan*, **621**, 169-174, 2007 (in Japanese).
10. Architectural Institute of Japan, "Guidebook on Fire-Resistive Performance of Structural Materials", 2017 (in Japanese).

Spalling behaviour of UHPC with modified microstructure due to fire load

Johannes Kirnbauer¹

¹ Vienna University of Technology, Vienna, Austria

ABSTRACT

Ultra High Performance Concrete (UHPC) is well known for its high compressive strength and its outstanding durability. The main reasons for these properties are a very low water binder ratio and the use of pozzolanic reactive filler (e.g. silica fume) which leads to a dense microstructure with very low permeability. These circumstances makes UHPC very sensitive to fire load and therefore it tends to spall excessively.

In this experimental work, some of the possibilities to modify the microstructure are described and applied to UHPC test specimen: Heat treatment at 105°C and 250°C, artificial air voids, hollow glass microspheres and PP-fibres. All specimens were stored under various conditions for more than half a year to create different moisture contents for the fire tests, which were following the ISO fire curve.

To describe the material properties, air content, slump flow, flexural strength, compressive strength and the pore size distribution (mercury intrusion porosimetry) were determined. The mass changes of the specimens due to treatment and storage are reported, too. During the fire test, the temperature distribution, beginning and duration of spalling were observed. After the fire test the mass of spalled material and its particle size distribution was determined to describe the spalling behaviour additionally.

For some treatment and storage variations, the fire tests showed the expected spalling behaviour of the specimens. However, other variations delivered surprising results.

In the discussion the spalling effects will be related to the treating methods and the changed microstructure and further to the storage conditions and the connected moisture content.

KEYWORD: UHPC, Spalling, Microstructure, Porosity

1 INTRODUCTION

Heat treatment of UHPC is frequently used to increase strength, although the porosity increases and the pore size distribution changes [1], [2]. At a temperature between 230 to 250°C a lot of water is released from amorphous CSH-phases which is a hint of the creation of crystalline Xonotlite that increases strength [3]. Describing the influence of heat treatment of UHPC on the spalling behaviour was one goal of this work.

For some UHPC mixtures PP-fibres were used to prevent spalling. The mode of action of PP-fibres is well described in [4]. These mixtures were also heat treated and the fibres melted during the treatment. Additionally, mixtures with hollow glass microspheres and air-entraining agent were investigated.

2 EXPERIMENTAL PROGRAM

2.1 Mix compositions and components

The mix compositions of all four different mixes are depicted in Table 1. The ratio between cement, silica fume and quartz powder was the same for all compositions. The water cement ratio w/c was 0,28 and the volume ratio water/fines w/f_v was 0,45. As a reference (REF) a common UHPC mix was used. As a first variation PP-fibres were added to this reference mix (F-REF).

Table 1: Mixture composition for 1 m³ concrete, air void content took into account

Components	REF [kg/m ³]	F-REF [kg/m ³]	HGM [kg/m ³]	AEA [kg/m ³]
CEM I 52,5 N C ₃ A free	681,2	681,2	652,3	581,2
Silica fume (SF)	170,3	170,3	163,1	145,3
Quartz powder grade 10000	340,6	340,6	-	290,6
Hollow glass microspheres	-	-	32,6	-
PP-fibres 6/0,15mm	-	3,00	-	-
Quartz sand 0,1-0,5mm	895,7	895,7	901,0	766,7
Superplasticizer 1 (SP1)	30,7	30,7	26,1	26,2
Superplasticizer 2 (SP2)	13,6	13,6	13,0	11,6
Air-entraining agent	-	-	-	2,00
Water incl. liquid part of SP1 and SP2	190,8	190,8	182,6	159,7
Fresh concrete density	2290	2290	1950	1950
Air voids in fresh concrete [vol.%]	4	4	4	18

For the second variation hollow glass microspheres (HGM), sometimes simply called glass bubbles, were used to replace the quartz powder by volume. Such spheres are sometimes used in building materials that reduce density and thermal conductivity. The properties of the used HGM are depicted in Table 2. The fineness is close to cement. As a third variation an air entraining agent was added (AEA). This type of admixture is usually used to improve frost resistance of concrete and creates pores with a diameter of mainly 300 µm. The amount of hollow glass microspheres and air-entraining agents was chosen in such a way that a comparable concrete density of the two mixtures was achieved.

Table 2: Properties of the used hollow glass microspheres

Average density [g/cm ³]	Isostatic compressive strength [MPa]	Volumetric particle size distribution [µm]			
		D10	D50	D90	Max. Ø
0,22	2,8	20	35	60	75

2.2 Mixing

The concrete was prepared with an Eirich R02 intensive mixer by using the pin-type rotor. All the dry components (except HGM) were mixed for 180 s. The water and all additives were added within the following 30 s. The wet mixing time was 120 s. The tool speed of the mixing tool was 7,9 m/s for the whole mixing process. The mixes with HGM were prepared in the same way, however, the HGM's were added after wet mixing and mixed another 3 min with the minimum tool speed (0,4 m/s). This was necessary to avoid breaking the glass bubbles during the intensive mixing process. .

2.3 Test specimen

Prisms measuring 40 x 40 x 160 mm were used to determine the hardened concrete's properties. The filled prism formwork was removed with a trowel and compacted on a vibrating table for approx. 30 s. In order to protect the samples from premature drying, they were covered with a polyethylene film.

The dimensions of the unreinforced test specimens for the fire tests were 250 x 300 x 40 mm. Type K thermal couples were installed in the test specimens at different heights in order to record the temperature curves through the test specimens. The thermocouples were arranged in the middle of the specimens starting directly in the fire surface, then in 1 cm, 2 cm and 3 cm depth.

For each mixture two accompanying specimens of the same size like the fire test specimen were prepared to determine the water content.

After about 24 hours, the specimens were demoulded, wrapped in plastic film and stored at room temperature until further treating or changes in storage conditions were conducted.

2.4 Treating and storage

For the fire tests, 20 test specimens were produced for each mixture variation. Ten for the fire tests and ten to determine the water content. Thus, two fire slabs and two water content slabs were available for each type of treating and storage. In addition, three prisms, which were subjected to the same treating and storage conditions, were produced to determine the compressive and flexural tensile strengths for each fire slab. The hardened concrete properties were determined after the fire test of the respective fire slab.

Figure 1 shows the principle of treating and storage.

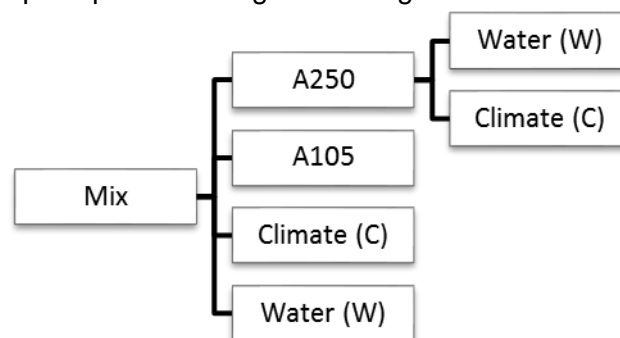


Figure 1: Principle of treating and storage

In the figure above means:

Mix: The four different mix compositions (REF, F-REF, HGM, AEA).

Climate (C): Storage in a climate chamber at 20°C and 65% rel. humidity.

Water (W): Storage under water at room temperature until fire test.

A250: Heat treating at 250°C hot air in a drying oven. The heating and cooling rate was 0,1 K/min to avoid micro cracking due to a thermally induced stress gradient. The maximum temperature of 250°C was kept for 5 hours. This treating took around 80 hours in total.

A105: Heat treating at 105°C hot air in a drying oven. The heating and cooling rate was 0,1 K/min. The maximum temperature of 105°C was kept up to the day prior to fire testing and these specimens were assumed to be dry.

The abbreviations already used give the test specimens their name. As an example, REF_A250_C_1 means: Reference mix heat treated at 250°C hot air and after stored in the climate chamber until the fire test, specimen nr. 1.

The first test series was carried out at an average concrete age of 245 days and the second one at an average age of 273 days.

2.5 Test set up for fire test

The test furnace was simply made of fire-resistant AISi bricks and heated with a propane gas burner following the standard ISO-fire curve (Figure 2). The test specimen was placed on the top of this furnace. The heated area was 23x25 cm. The temperature in the furnace was controlled by the use of mantled thermocouples Typ K. A special feature of the furnace was the 45° inclined bottom. Through a flap the spalled material slipped directly into a metal box. The grading curve was later determined from this material in order to describe the spalling behaviour better.



Figure 2: Test furnace

3 RESULTS

3.1 Mechanical testing

The compressive strength and the flexural strength of all mixes at the age when fire tests were carried out are depicted in Figure 3. Flexural strength was obtained from a 3-point bending test of 6 prisms 40x40x160 mm (3 prisms corresponding to each fire test specimen). Compressive strength was obtained from 6 prisms half the flexural specimen in size of 40x40x40 mm.

The strength values of untreated specimen were in a common range for UHPC. Heat treated specimens always had a higher strength. Heat treated specimens at 105°C had a higher

strength than specimens treated at 250°C, which was unexpected. Probably the very long treating time at 105°C led to these results. No further investigations to clear up this circumstance were carried out for this work. Specimen with HGM and AEA had of course a lower strength related to the lower density.

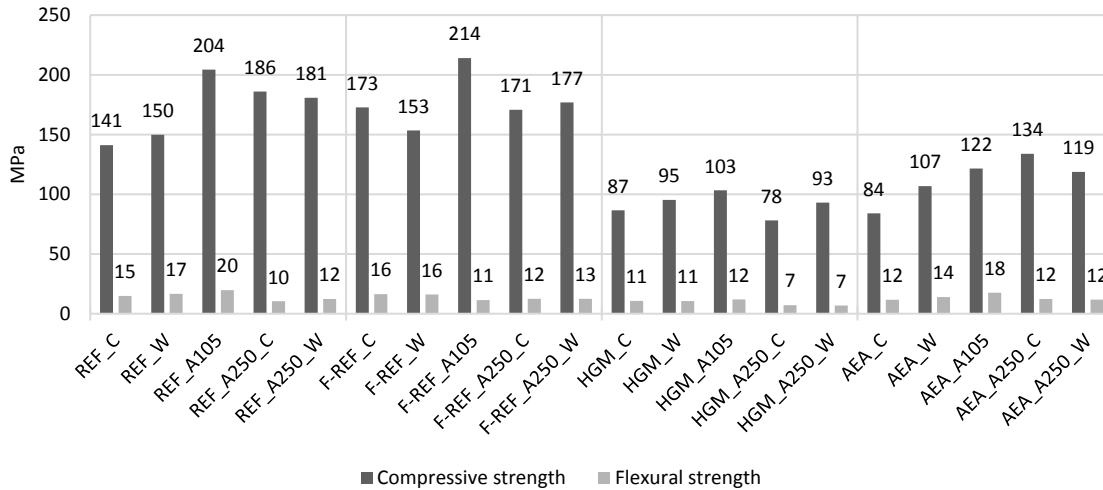


Figure 3: Strength of all mixtures

3.2 Water content

To determine the water content of the fire spalling specimen the two accompanying treated and stored slabs were taken as the references. On the day of the fire test the accompanying specimens were put in the drying chamber at 105°C. It was assumed, that the water content was equal to the fire test slabs. UHPC dries very slowly, however, after approximately 200 days the mass changes were negligibly low and the specimens were assumed to be dry. That means, the result for the water content was available 200 days after the fire test. In Table 3 the temporal course of changes in water content of all mixture-treating-storage variations is listed.

It starts from the added water during mixing to the residual water content after the fire test. Depending on the mix composition the mass of a fire test specimen was approximately between 5,8 kg and 6,7 kg and the added water during mixing therefore weighed 450 g to 550g. This was the mass of water in a test specimen ($w_{init} = 100\%$), with air voids taken into account. The water change due to heat treating Δw_{heat} was around -45% for REF and F-FREF, and around -55% for HGM and AEA. for all specimen treated at 250°C Δw_{heat} was around -70%. The water change due to storage w_{stor} of not heat treated specimen was negligibly low for climate chamber storage and 10 - 17 % for water storage. For the specimens heat treated at 250°C and stored in a climate room the adsorption was around 28 % whereas the water adsorption of the water stored specimens was almost within the same range as the water loss during heat treating before. Next to consider is the water content before fire tests w_{fire} . Depending on treating and storage, fire test specimens had more or less water inside than added during mixing. This amount of water can be divided in two parts: Water bound in CSH-phases w_{csh} and "free" water w_{free} .

The amount of free water was obtained by drying the accompanying test specimen at 105°C and it is named w_{105} in Table 3. This is a rough estimation because it is known that drying at 105°C also removes some bound water, at least partially. Taking the density of the concrete into account, the bound water w_{csh} was quite similar, except for the mixture variations with AEA had less w_{csh} . Next, the water loss during the fire test w_{loss} is reported. It was calculated from the mass of the test specimen before the fire tests compared to the mass after the fire tests, including spalled material (if any) collected in the metal box. The last row of the table

shows the residual water content w_{res} of the specimens after the fire tests. For all the specimens, which did not fail during the fire test and therefore fired for 70 min, this value is very low and they were practically dry. Specimens that failed during the fire test are marked with grey lines in the table.

Table 3: Temporal course of changes in water content

	W_{init} t		ΔW_{heat}		W_{stor}		W_{fire}		W_{105}	W_{free}		W_{csh}		W_{loss}		W_{res}	
	g	%	g	%	g	%	g	%	%	g	%	g	%	g	%	g	%
REF_C	560	100	0	0	5	1	564	101	3,8	253	45	311	55	-469	8	95	17
REF_W	553	100	0	0	63	11	616	111	4,6	308	50	308	50	-509	8	107	19
REF_A105	567	100	-243	-43	0	0	324	57	0,0 (3,7)	0	0	324	100	-69	1	255	45
REF_A250_C	556	100	-371	-67	150	27	335	60	0,3	18	5	316	95	-231	4	104	19
REF_A250_W	558	100	-360	-65	320	57	518	93	3,1	208	40	310	60	-452	7	66	12
F_REF_C	556	100	0	0	7	1	563	101	4,0	267	47	296	53	-512	8	51	9
F_REF_W	567	100	0	0	54	10	621	110	4,7	319	51	302	49	-573	9	48	8
F_REF_A105	553	100	-249	-45	0	0	304	55	0,0 (3,9)	0	0	304	100	-252	4	52	9
F_REF_A250_C	553	100	-380	-69	155	28	328	59	0,4	25	8	302	92	-268	4	60	11
F_REF_A250_W	568	100	-380	-67	367	65	555	98	3,7	253	46	302	54	-486	8	69	12
HGM_C	547	100	0	0	7	1	553	101	5,5	319	58	234	42	-471	9	82	15
HGM_W	559	100	0	0	57	10	616	110	6,3	376	61	240	39	-515	9	101	18
HGM_A105	557	100	-302	-54	0	0	255	46	0,0 (5,4)	0	0	255	100	-223	4	31	6
HGM_A250_C	545	100	-382	-70	147	27	310	57	1,1	67	22	243	78	-270	5	40	7
HGM_A250_W	543	100	-381	-70	376	69	538	99	5,3	305	57	233	43	-500	9	38	7
AEA_C	449	100	0	0	7	2	456	102	4,8	264	58	191	42	-207	4	248	55
AEA_W	469	100	0	0	79	17	548	117	6,1	347	63	201	37	-139	2	409	87
AEA_A105	453	100	-248	-55	0	0	205	45	0,0 (4,7)	0	0	205	100	-171	3	33	7
AEA_A250_C	460	100	-317	-69	127	28	270	59	1,2	67	25	203	75	-232	4	38	8
AEA_A250_W	463	100	-317	-68	320	69	466	101	4,7	269	58	198	42	-394	7	73	16

3.3 Porosity

The porosity was determined by the use of Porotec Pascal 140/440 Mercury Intrusion Porosimeter (MIP). This system can detect pores with a diameter within the range of 3,6 nm up to 116 μm , which is within the range of meso- and macropores. Ultra-macropores and air voids cannot be detected with the used dilatometer. Samples with a volume of 1 cm^3 were dried in an evacuated desiccator at room temperature until mass constancy was reached. The total porosity in this pore size range is shown in Figure 4. The mixtures with HGM and AEA showed much higher total porosity than the other mixtures. Probably both, HGM and AEA, contributed partially to pores in this range.

Heat treating increases the total porosity in all mixtures due to de-watering and changes in the CSH-phases.

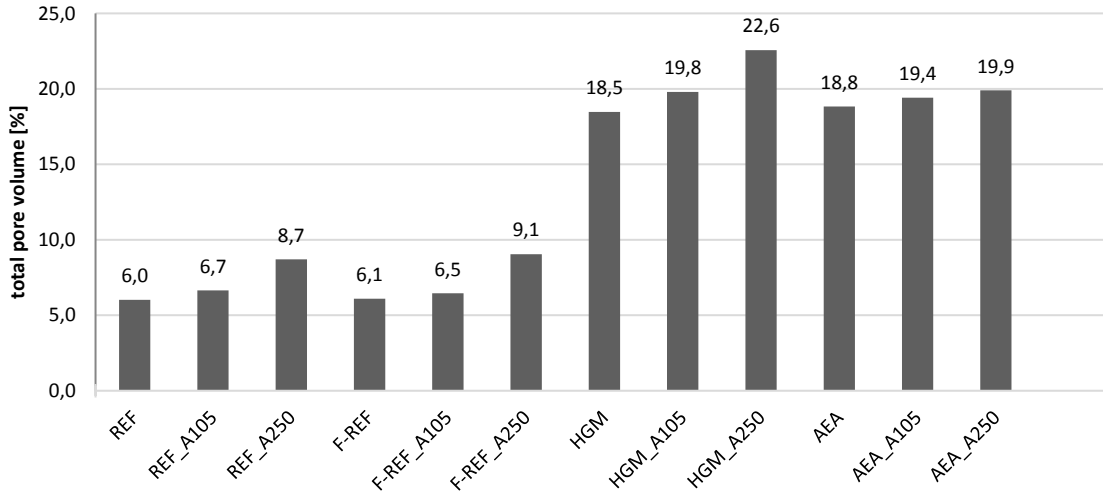


Figure 4: Total pore volume measured by MIP

Furthermore, heat treating at 250°C changes the pore size distribution, too. Figure 5 shows the influence of heat treating at 250°C on pore size distribution and total pore volume of the reference mixture REF.

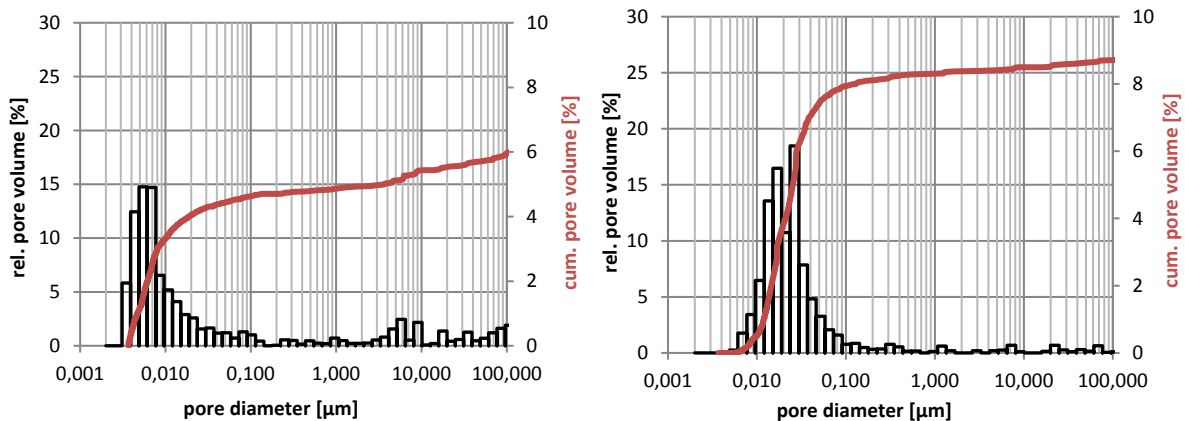


Figure 5: Influence of heat treating at 250°C on pore size distribution and total pore volume of the reference mixture (left: stored at room temperature, right: heat treated at 250°C)

The total pore volume rose from 6% to 8,7%, which is an increase of 45%. The average pore diameter of the untreated concrete was 8,8 nm and the one of the heat treated concrete 20 nm, which is more than double the size. Heat treating at 105°C did not change porosity that much, although specimens for this work were stored at this temperature for more than half a year.

The total pore volume increased slightly to 6,7% and the average pore diameter to 11 nm. This effect was basically evident in the other mixtures as well, because the basic composition of the paste was always the same. Therefore, the other diagrams are not shown.

3.4 Fire tests

The fire tests always lasted until the specimens failed or for 70 min. In Figure 6 the furnace temperatures of all fire test are shown. It can be seen clearly that the furnace temperature of each test was within the limits of the ISO-fire curve. For most of the specimen which failed, a significant temperature decrease occurred during spalling (mainly between minute 10 and 20) due to the release of vapour. To illustrate the temperature measurements in the

specimen the temperature in different depths of REF_A250_C are shown, too. In order not to exceed the length of this article, a further discussion on the temperature course in the test specimens was dispensed with.

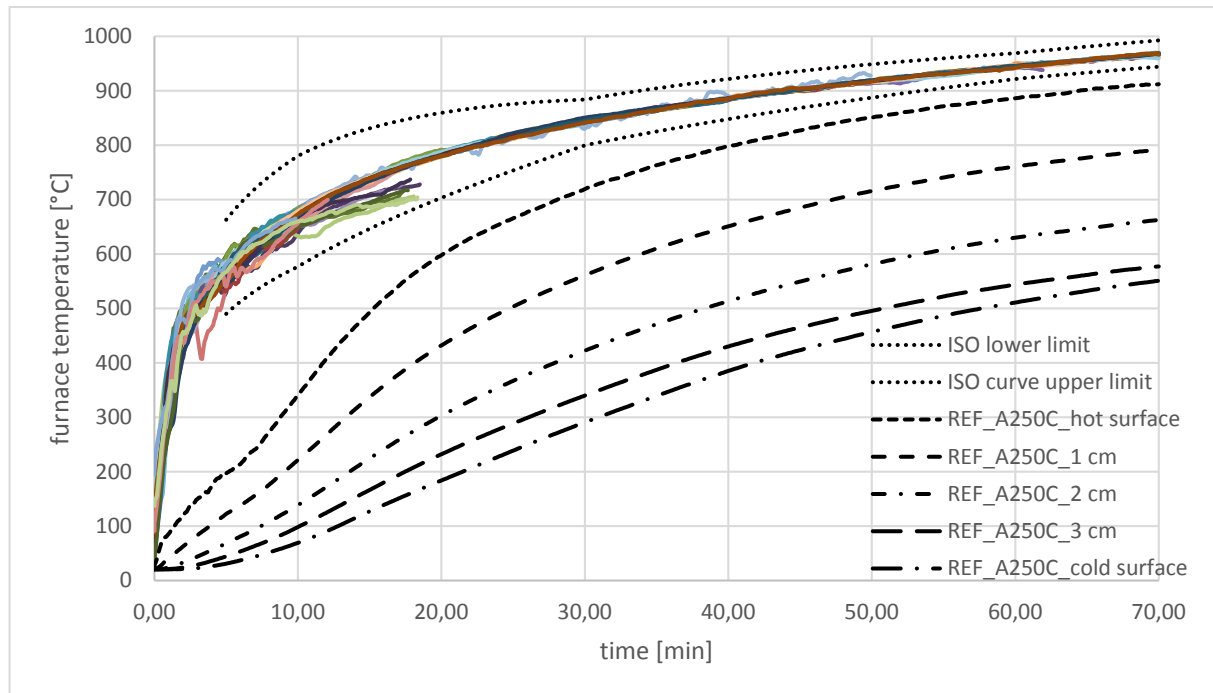


Figure 6: Furnace temperature of all fire tests and temperature in different depths of REF_A250_C (for illustration of temperature measurements in the specimens).

Figure 7 shows the temporal spalling behaviour.

Both of the specimens of all mixtures showed almost the same behaviour. All mixtures that were heat treated at 250°C survived the fire test, even the reference mix. Almost all of them without any spalling. Only the water stored F-REF_A250_W as well as REF_A250_W and HGM_A250_W showed some spalling.

The mixture REF_C had a lower water content than REF_W but the same porosity. REF_W started spalling earlier and spalling lasted longer until failure.

The mixture REF_A105 treated at 105°C until the fire test showed the longest duration from the beginning to the first spall and then failed very quickly with some big explosions.

Although these specimens were dry (no free water) they spalled because of the water released from CSH-phases at higher temperature (late beginning of spalling) and the still tight pore structure which was not changed that much due to heat treating.

The mixture REF_A250_C had a low free water content and did not spall. However, the mixture REF_A250_W with a much higher free water content showed some spalling. Obviously, the higher porosity was not enough to release the vapour quick enough.

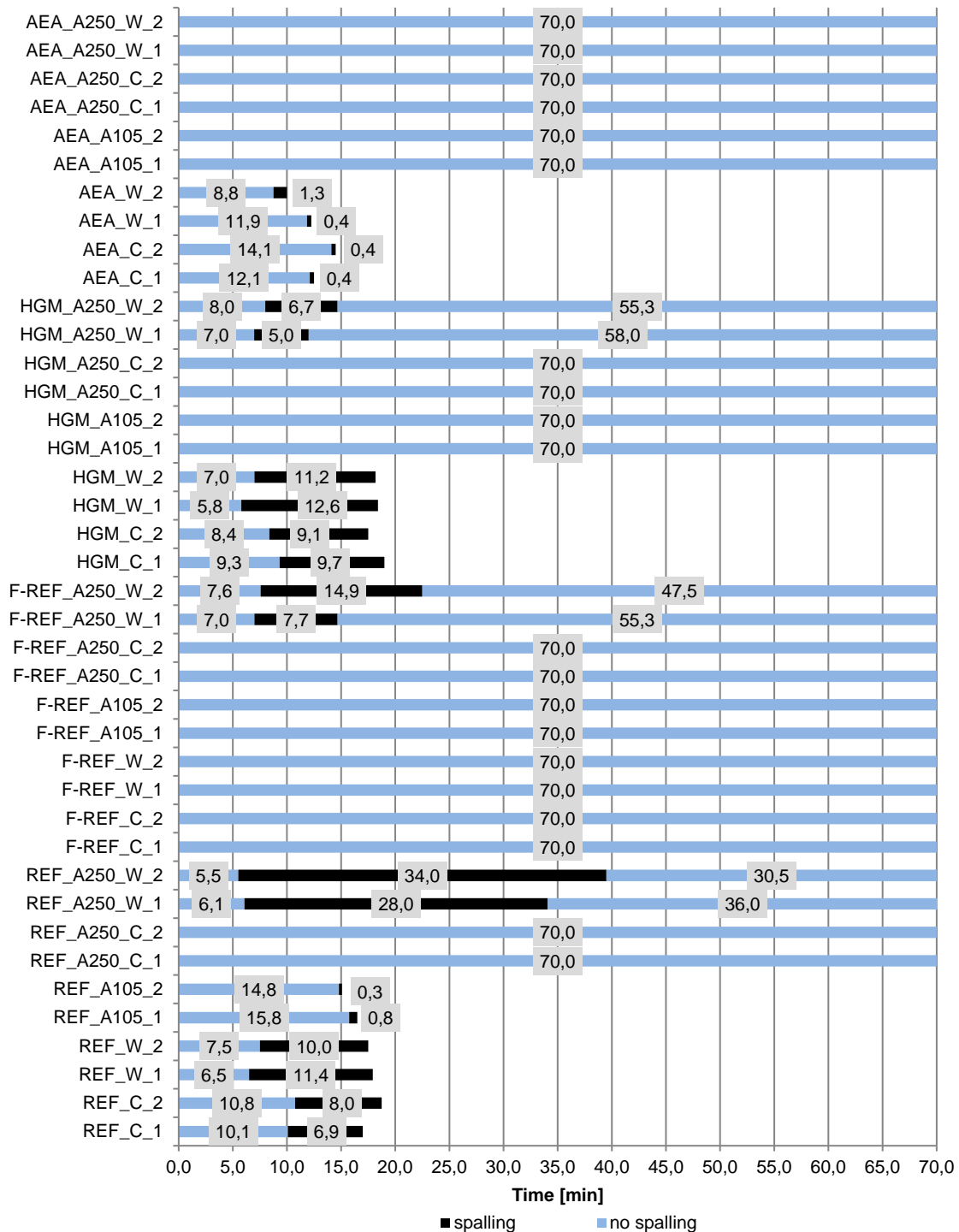


Figure 7: Start of spalling, duration and end of spalling

The mixtures with PP-fibres F-REF_C, F-REF_W and F-REF_A105 did not spall and the PP-fibres worked properly. The mixtures F-REF_A250_C and F-REF_A250_W showed a similar behaviour to the corresponding REF mixes. The properties of the specimens are also comparable. The PP-fibres already melted during heat treating and not during the fire test. The porosity of F-REF-A250 mixtures is slightly higher (0,4%) than of REF_A250. This could be explained with the voids left by the amount of fibres and some micro cracks formed by expanding PP-fibres before melting. This porosity was obviously not enough to prevent spalling for the water stored F-REF_A250_W, however the mass of the spalled material was very low compared to other mixes (Table 4). The conditions in the specimens during a very slow heat treating process are different from the conditions during a fire test. The working

mechanism of PP-fibres under different conditions might differ and influence the formation of pore structure [5]

The mixtures treated at 105°C with AEA as well as the ones with HGM showed no spalling. All the other AEA and HGM mixtures stored under different conditions spalled and failed like the reference mixtures did. However, spalling behaviour is quite different.

The mixtures with HGM and AEA had comparable porosity and water content. However, the mixes with HGM started earlier with spalling and showed a longer spalling duration. The mixtures with AEA started later with spalling and failed very soon after some big explosions. Considering Table 4 and Figure 9 it can be seen, that the spalling behaviour of the HGM mixtures is very similar to the REF mixtures because the hollow space in non broken glass spheres is not accessible as an expansion space for the water vapour produced. For the mixtures AEA the explanation could be similar. The relatively big air voids in relatively long distance to each other entrained by the air-entraining agent were not fully accessible for the vapour through the dense matrix. The start of spalling was only delayed which resulted in stronger explosions.

To describe and illustrate the different spalling behaviour, pictures of some test specimens after the fire test are shown in Figure 8, the masses of spalled material are listed in Table 4 and Figure 9 shows the grading line of the spalled material from the fire tests. This gives, additional to the temporal spalling behaviour, further information.

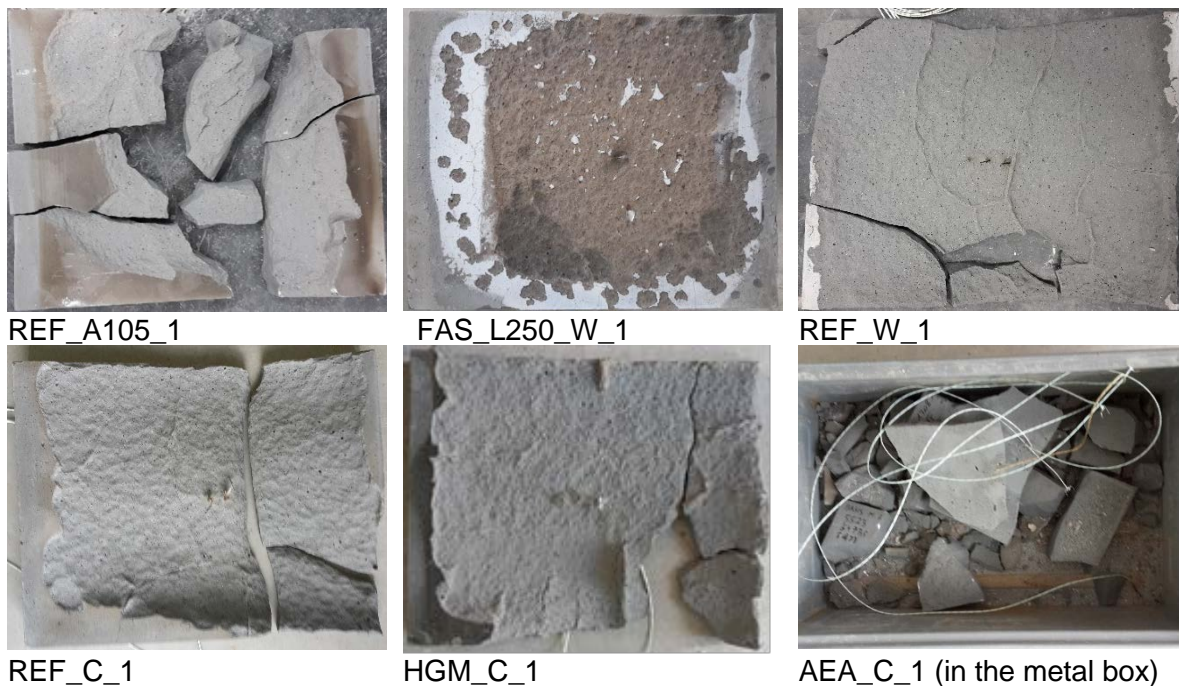


Figure 8: Pictures of some test specimen after fire test

When determining the spalled mass, the best possible attempt was made to separate the spalled parts from the remnants of the test specimen. Most specimen failed by cracking and breaking into big parts.

The REF mixtures lost the most material during the fire tests, followed by the HGM mixtures and the AEA mixtures. Comparing the mixing within each group shows that the specimen with a lower water content always lost more material at a higher spalling rate.

Table 4: Mass of spalled material

	Spalled mass [g]	Spalling rate [g/s]
REF_C	2653	5,9
REF_W	2645	4,1
REF_A105	1026	38,2
REF_A250_W	1726	0,9
HGM_C	2500	4,5

	Spalled mass [g]	Spalling rate [g/s]
HGM_W	2333	3,3
HGM_A250_W	23	0,1
AEA_C	1290	53,8
AEA_W	633	17,5
F-REF_A250_W	69	0,1

A higher spalling rate can have two meanings: More small explosions per time unit, producing fine particles or less big explosions per time unit, producing coarse particles. Figure 9 shows clearly that specimens with higher spalling rate have much coarser grains (D50 between 11,2 and 22 mm) which means lesser, but bigger explosions. The specimens with a lower spalling rate produces much finer spalled material (D50 ~1-2 mm) during a longer time with a high number of small explosion.

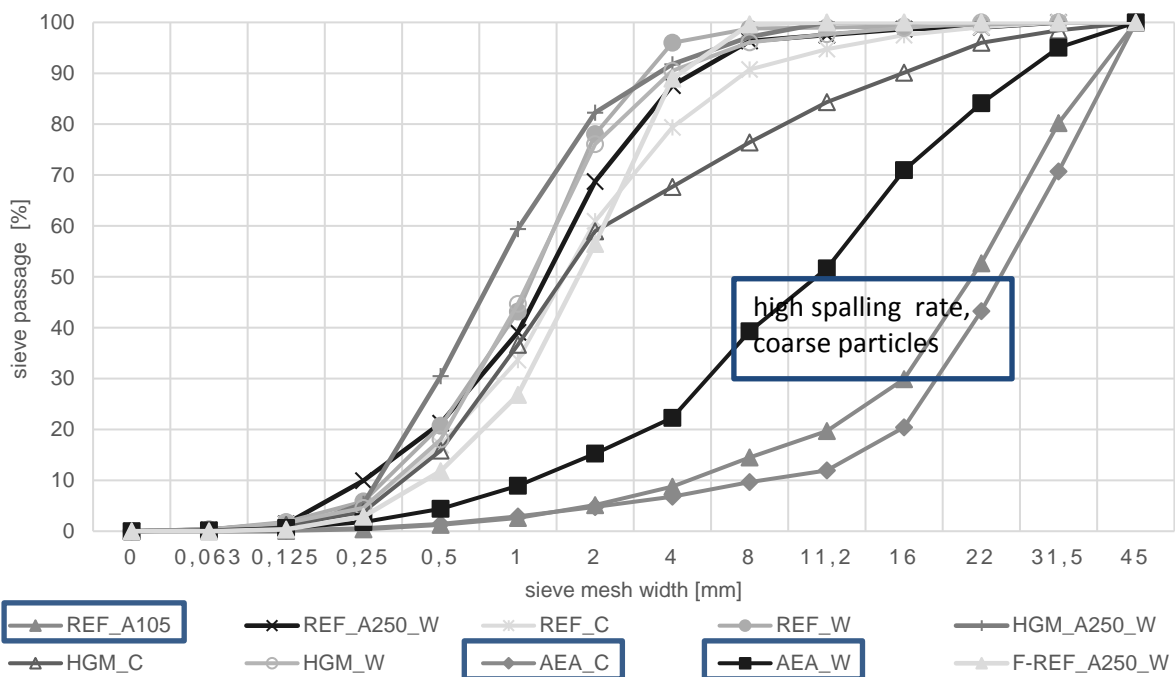


Figure 9: Grading line of spalled material

Together with the temporal course of spalling, there is a tendency. The lower the porosity and the higher the water content, the earlier spalling starts, the longer the spalling lasts with an high number of small explosions producing fine graded spalled material, like sand. Even with some higher porosity and some lower water content UHPC could spall. Later, with less, but stronger explosions and a coarse graded spalled material.

4 CONCLUSIONS

Generally heat treating at 250°C can avoid or reduce spalling due to changes in porosity as well as the appropriate use of PP-fibers. However, when UHPC with PP-fibers is supposed to be heat treated at temperatures above the melting point of the PP-fibers, some loss of

protection against spalling could be expected.

The use of hollow glass microspheres and air-entraining agent could not prevent spalling satisfyingly, not even in high doses like used in this work, which led to a strongly reduced strength.

For most of the mixtures the influence of water content and porosity was obvious and led to different spalling behaviour. To describe these differences, sieving the spalled material and calculating the grading line is a simple, but meaningful method.

5 REFERENCES

- [1] Diederichs, U.; Mertzsch, O.: „Behavior of Ultra High Strength Concrete at High Temperatures“, In: Fehling, E.; Schmidt, M.; Stürwald, S. (Hrsg.): Ultra high performance concrete (UHPC). Proceedings of the Second International Symposium on Ultra High Performance Concrete. Kassel, Germany, March 05-07, 2008. S. 347-354.
- [2] J. Kirnbauer, "The Influence of Vacuum Mixing on the Porosity of Ultra High Performance Concrete", Advanced Materials Research, Vol. 897, pp. 266-269, 2014
- [3] Dehn, F.: „Ultrahochfester Beton“, In: Fraunhofer-Informationszentrum Raum und Bau (Hrsg.): Arconis spezial. Ultrahochfester Beton. Forschungsergebnisse, Entwicklungen, Projekte. Stuttgart: Fraunhofer-IRB-Verlag, 2004, S. 60–64.
- [4] Pistol, Klaus & Weise, Frank & Meng, Birgit & Diederichs, Ulrich. (2014). Polypropylene Fibres and Micro Cracking in Fire Exposed Concrete. Advanced Materials Research. 897. 284-289.
- [5] Pistol, K., *Wirkungsweise von Polypropylen-Fasern in brandbeanspruchtem Hochleistungsbeton*, Doctoral Thesis, TU Braunschweig, 2016.

Australian Large Scale Structural Fire Test Facility for Concrete Tunnel Linings

Maurice Guerrieri^{1,*}, Sam Fragomeni¹, Carlos Sanabria², Wei Ming Lee², & Esteban Pazmino³

¹ Victoria University, Melbourne, Australia

² Cross Yarra Partnership, Lendlease Engineering Pty Ltd

³ Cross Yarra Partnership, John Holland Group

* Corresponding author (maurice.guerrieri@vu.edu.au)
Victoria University, Werribee Campus, PO BOX 14428, Melbourne, Vic 8001)

ABSTRACT

Medium scale flat panel fire testing in unloaded conditions has been used extensively in Australia in order to determine whether a particular concrete mix design would be susceptible to spalling. Recently, the need to test the performance of full scale structural tunnel lining segments under fire exposure has become a requirement driven by the Australian regulators. Victoria University, in conjunction with CYP Design & Construction Joint Venture, the consortium designing and constructing the tunnels and stations for the \$11 billion Metro Tunnel Project in Melbourne on behalf of Rail Projects Victoria, have built a state-of-the-art full-scale structural fire testing furnace. This furnace is the first of its kind in Australia. This paper initially presents the specification details of the furnace and then reports on the experimental fire behaviour of unloaded flat panels and loaded full scale segments to be used in the Metro Tunnel Project. The results indicate that full scale structurally loaded fire tests are essential as unloaded flat panels underestimate the degree of spalling.

KEYWORD: Concrete, Fire Resistance, Spalling, Structurally Loaded

INTRODUCTION

Concrete spalling has received increased attention since the 1960s. Hydrocarbon fires started by hydrocarbon fuel accidents have caused spalling in three major European tunnels: Channel Tunnel in 1996, Mount Blanc Tunnel in 1999, and the St. Gotthard Tunnel in 2002 [1]. During the construction of the Shanghai Metro Line 8 in 2005, a fast burning fire broke out in the tunnel which caused spalling along the 16.8 m long tunnel lining segments (up to 25mm in depth). Whilst the fire was extinguished within 10 minutes, the 430 m long tunnel lining was blackened by hot and poisonous smoke in the upper layer [2].

As noted in [3-5], tunnel fires can have characteristics of rapid temperature rise, extreme maximum temperatures, long fire duration, non uniform temperature distribution and can lead to complex and extensive fire damage of the concrete tunnel lining. Further complexities can also arise from the configuration of the joint connections of the tunnel lining segments [5]. This was critical in relation to the fire in the Shanghai Metro Line 8 tunnel since the tunnel was encased in soft ground with high water pressure. At the time, engineers were concerned that the fire may have jeopardized the joint seal leading to water leakage or tunnel flooding.

In addition, the Daegu Subway fire in 2003 [2] which caused concrete spalling depths of 10-

99 mm within a 22 m range of the fire source, caused the uniaxial compressive strength to decrease from 24 MPa to 11–15 MPa [2, 6]. Aside from significant structural damage and fatalities, fire damage to tunnel linings may lead to a long term tunnel closure with significant financial losses and repair expenses [2, 7].

Only a few full-scale experimental research programs have been documented on the behavior of actual tunnel boring machine (TBM) tunnel linings in a fire, which are available in the literature [8-14]. However, only the works of Richter [14] and Yan et al. [2] have conducted full scale structurally loaded fire testing incorporating real life boundary conditions, external loading and conditioning corresponding to design assumptions. In order to ensure new tunnels in Australia have adequate fire protection, full scale fire tests are warranted. The major design specifications of the Australian first structurally loaded fire testing furnace will be initially presented and then preliminary results of unloaded flat panels and loaded full scale segments from the Metro Tunnel Project Fire Testing Program are given in this paper.

EXPERIMENTAL PROGRAM

Overview of the Structural Fire Testing Furnace

The fire test furnace with the tunnel rig setup is shown in Figures 1 and 2. As well as full scale curved panels the furnace is also capable of testing 4 flat panels at once (unloaded). The 8 burner (3GJ/hr each) gas powered furnace is built in a modular format to allow the testing of beams, columns, floors/ceilings, ducts, walls in both an unloaded and loaded configuration. The internal dimensions of the furnace are approximately 4500 x 3700 x 3000 mm and has inbuilt capability to run any international fire curve including custom designed curves. For example, only the RABT ZTV (Train/Car) fire curves requires the furnace temperatures to reach 1200°C and cool down to ambient within a duration of 110 minutes. This linear cooling phase can be programmed to be executed which differs to the fire curves that do not have any cooling down requirement. The furnace is also equipped with 12 viewing ports and is controlled by 8 type k thermocouples.

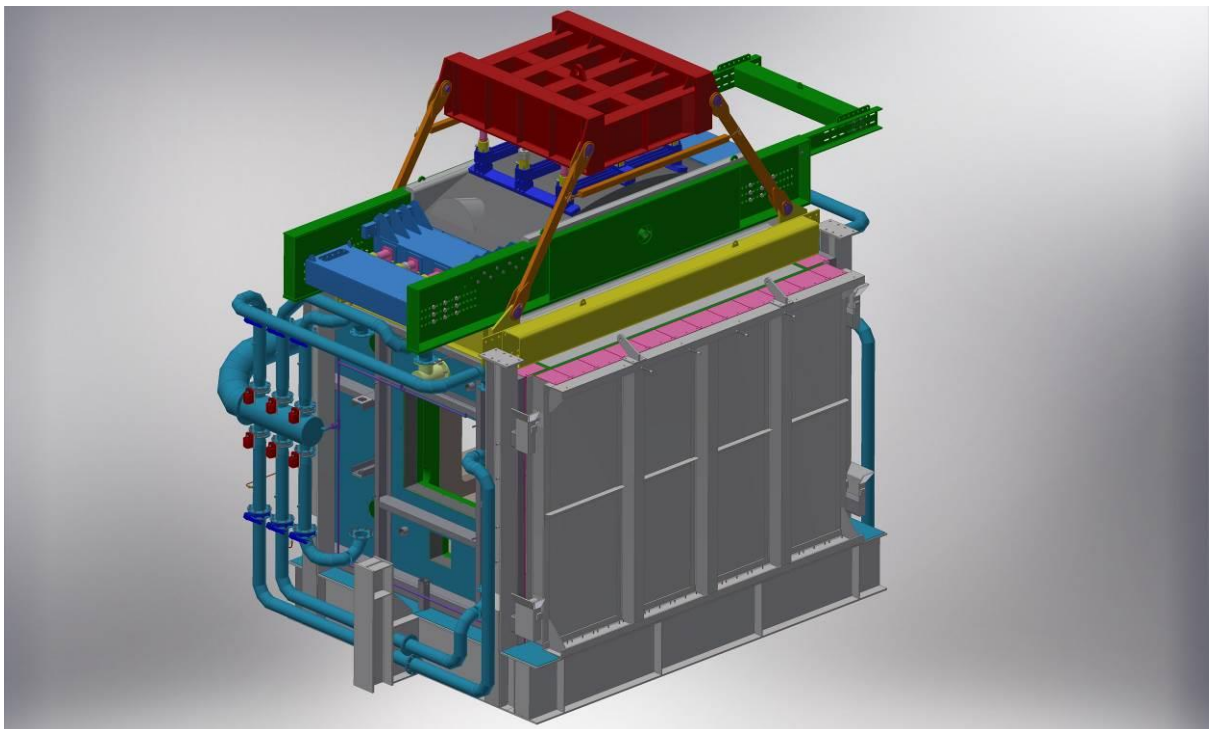


Figure 1 Structural Fire Test Furnace with Tunnel Rig – Isometric View

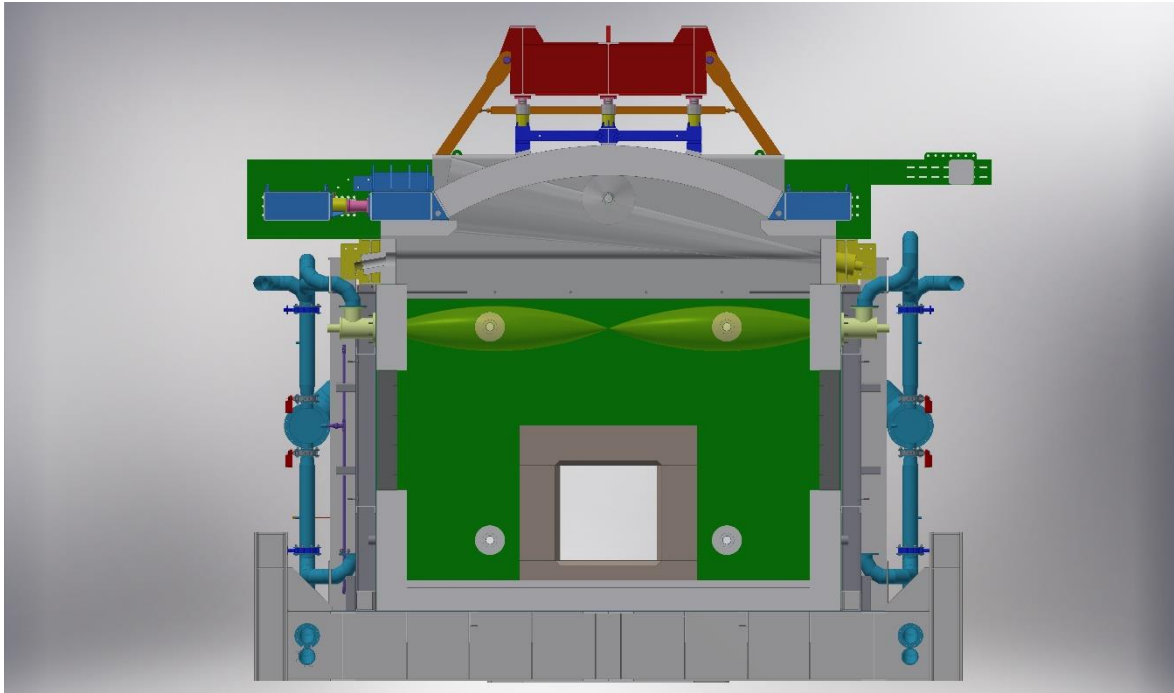


Figure 2 Structural Fire Test Furnace with Tunnel Rig – (Front on View)

Overview of the Metro Tunnel Project's Test Specimens

The proposed route map of the Metro Tunnel Project is shown in Figure 3. The project consists of the construction of twin 9km rail tunnels under the city of Melbourne and five new underground stations. The tunnel will free up space in the existing city loop in order to run more trains to and from the suburbs. The twin tunnels consist of approximately 55,000 precast tunnel lining segments.

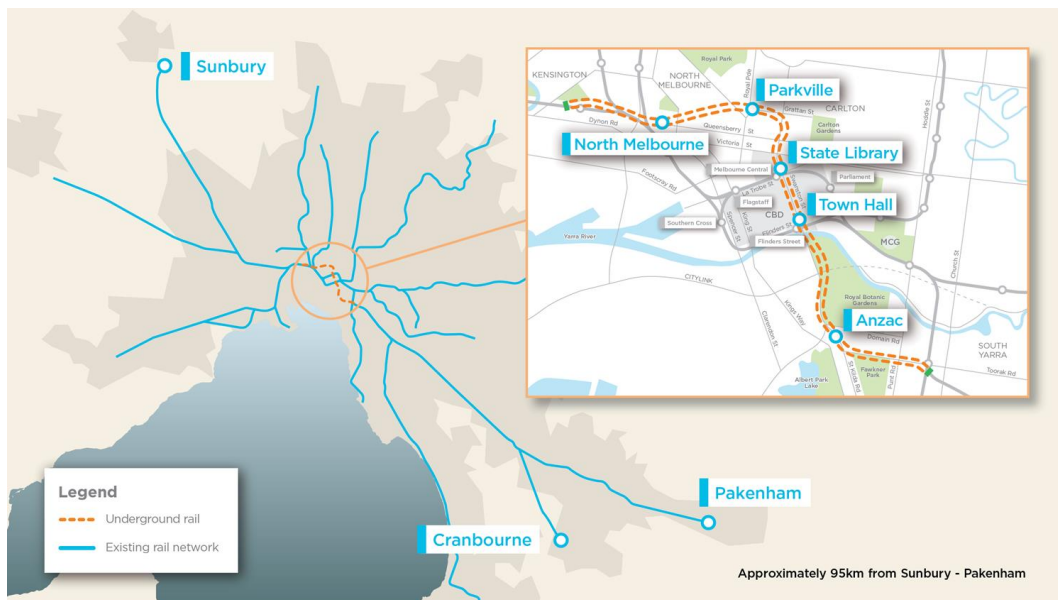


Figure 3 Metro Tunnel Project, Melbourne

The test specimens consisted of 6 full size TBM curved lining segments and 12 flat panel specimens. The tunnel lining segments were 1700 mm in width and 3450 mm in length. The

inner and outer radii was 3150 and 3450 mm respectively whilst the specimen thickness was 300 mm. The flat panels were 1550 x 1550 x 300 mm. The specimens were cast at the Metro Tunnel Project's tunnel lining manufacturing facility in Melbourne's west, Australia as shown in Figure 4.



Figure 4 Tunnel Lining Segments

Three types of concrete material composition were investigated which included two different slag-based blends and one flyash based blend. Two dosages of polypropylene fibers were investigated, 1.5 and 1.75kg/m³ for each concrete blend. For the flat panel tests, only reinforced concrete (RC) was used without fiber addition with two identical panels were tested. Therefore, to accommodate these variations, a total of three fire tests (12 panels) were carried out. For the loaded tunnel lining segments, both RC and steel fiber reinforced concrete (SFRC) was investigated but only at a polypropylene fiber dosage of 1.50kg/m³. Therefore, a total of 6 loaded fire tests were carried out. The mix design and specimen ID is shown in Table 1 below whilst the tunnel lining segment geometry and reinforcement of the RC segment is shown in Figure 5. The compressive and tensile strength results are also shown for comparative reasons.

Table 1: Specimen ID and Mix Design

Mx No			Mix - 1			Mix - 2			Mix - 3		
			Base Concrete - 1	Base Concrete - 2	Steel Fibre Reinforced Concrete	Base Concrete - 1	Base Concrete - 2	Steel Fibre Reinforced Concrete	Base Concrete - 1	Base Concrete - 2	Steel Fibre Reinforced Concrete
Description											
Cement	Cement	kg/m ³	275	275	275	235	235	235	165	165	165
Slag	Slag	kg/m ³	200	200	200	120	120	120	215	215	215
ZEP	ZEP	kg/m ³							95	95	95
FA	FA	kg/m ³				120	120	120			
Aggregate (Basalt)	20mm	kg/m ³	370	370	370	370	370	370	370	370	370
Aggregate (Basalt)	14/10mm	kg/m ³	655	655	655	655	655	655	655	655	655
Sand	C/Sand	kg/m ³	785	785	785	785	785	785	785	785	785
Steel Fibres	Steel Fibres	kg/m ³			35			35			35
Poly Fibres	Poly Fibres	kg/m ³	1.5	1.75	1.5	1.5	1.75	1.5	1.5	1.75	1.5
	Superplasticizer	mL/m ³	1500-2500			1500-2500			1500-2500		
	Accelerator	mL/m ³									
Total water		kg/m ³	165	165	165	165	165	165	165	165	165
W/C		ratio	0.35	0.35	0.35	0.35	0.35	0.35	0.35	0.35	0.35
Compressive Strength (MPa)		28d	92.5	88.5	99.0	86.5	83.5	91.0	89.5	84.0	80.5
		at test	92.5	89.5	101.0	87.0	86.0	88.0	91.0	82.0	81.5
		at test	97.0	93.5		92.5	93.0				
		at test	99.5	90.0		92.0	88.5				
Indirect Tensile Strength 100mm (MPa)		28d			10.5			11.0			8.9
		28d			11.5			11.5			7.4
		28d			10.5			9.7			9.6
		28d			10.5			9.2			9.3
	Flat Panel ID		1.1 & 1.2	2.1 & 2.2		3.1 & 3.2	4.1 & 4.2		M4.1 & M4.2	M4.3 & M3.1	
	Curve Panel ID		1.0		3.0	2.0		4.0	M4		M3

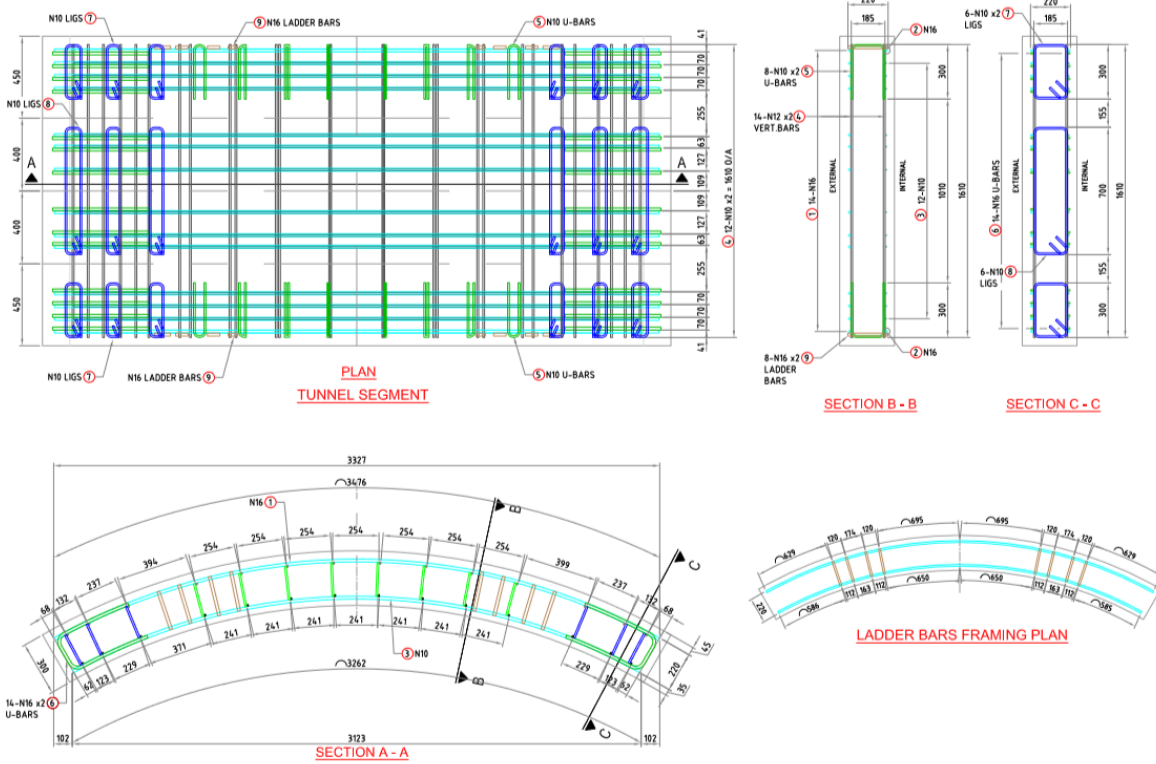


Figure 5 Reinforced Concrete Tunnel Lining Segment Geometry and Reinforcement

The specimens were kept in a professional custom-made curing chamber after 24 hours of being poured as shown in Figure 6 until 90 days where the temperature and humidity were kept constant at 23°C and 50% relative humidity as shown in Figure 7. After the initial curing, the specimens were transported to the Victorian University Fire Test Facility where they were kept inside until the test date.

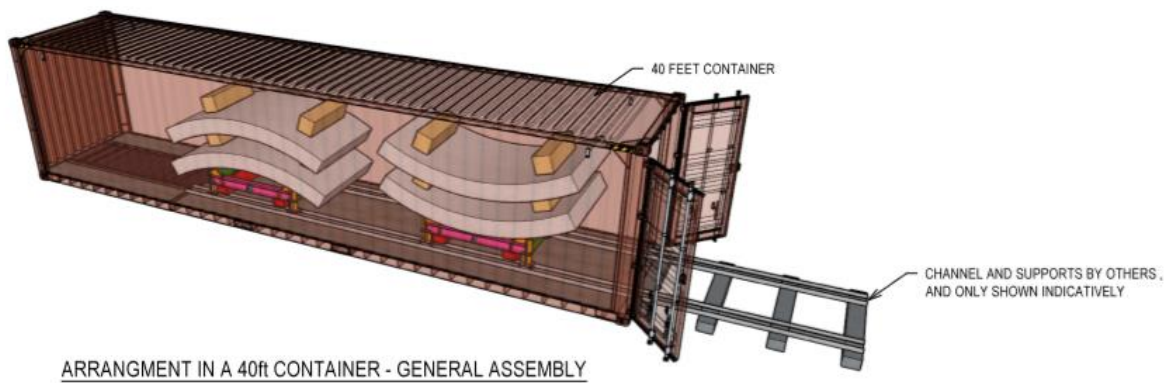


Figure 6 Schematic of Conditioning Chamber

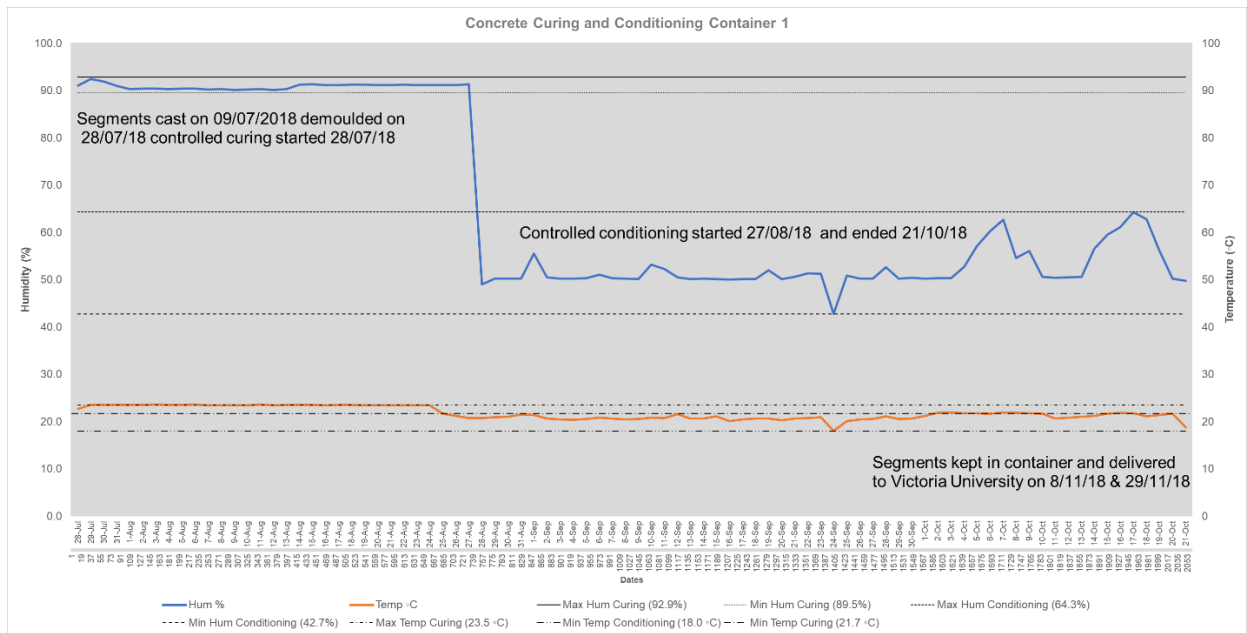


Figure 7 Temperature and Humidity Curing Profile

Test Setup and Procedure

The test system was developed at Victoria University for testing the specimen response to fire in unloaded tests and for testing tunnel lining segments under combined structural and fire loading. The final test setup for the loaded tunnel lining fire test is shown in Figure 8. The schematic of this setup was given in Figures 1 and 2). The test setup was in accordance to the client specification which was based on several test standards: a) Australian Standard 1530.4 [15], b) EFNARC 2006 [16], and c) 2008-Efectis-R0695 [17]. The fire curve used represented the RABT-ZTV (rail) time temperature curve as given in Table 2 below. The furnace was equipped with 8 type K (Nata Certified up to 1300°C) 3-mm diameter, 310 stainless steel mineral insulated metal sheathed) thermocouples to follow the time temperature profile. The thermocouples were positioned 100 mm from the bottom of the specimen for the flat panel tests in accordance to AS1530.4 [15] and 200 mm for the loaded tunnel lining segments in accordance to the Efectis R0695 test procedure [17].

For the flat panel testing, a 2x2 insert was provided that allowed four specimens to be tested simultaneously. The inset had a 65 mm flange perimeter to hold the specimens in place. This provided a fire exposure area of 2.01m² for each panel (1420 x 1420 mm) which meet the minimum fire exposure area of 2.0m² in accordance to the EFNARC Standard [16].

The tunnel segment was loaded so that a uniformly distributed compressive stress equal to the maximum compression level of the fire-exposed surface of the actual tunnel structure was applied to the test panel. The maximum compression level of the fire-exposed surface was determined to be 6MPa. To achieve the desired loading, three loading systems were required, horizontal loading, vertical center loading and vertically offset loading (left and right of center).

The horizontal load required was 1695 kN/m, which equated to 2881 kN (over a width of 1.7m) which was applied as 4-point loads of 720.38 kN (73.43t per ram) acting on a spreader bar.

The center vertical load required was 440kN/m, which equated to 748 kN (over a width of 1.7m) which was applied as 3-point loads of 249.33 kN (25.42t per ram) acting on a

spreader bar.

The left offset vertical load required was 595kN/m which equated to 1011.50 kN (over a width of 1.7m) which was applied as 3 point loads of 337.16kN (34.37t per ram) acting on a spreader bar.

The right offset vertical load required was 595kN/m which equated to 1011.50 kN (over a width of 1.7m) which was applied as 3 point loads of 337.16kN (34.37t per ram) acting on a spreader bar.

The load was applied by means of aligning vertical and hydraulic jacks and controlled by calibrated NATA load cells (four in total positioned in each strip loading section). The loads were applied prior to the commencement of the fire test and monitored during the test procedure. The loads were slowly applied in a step procedure alternating between the vertical and horizontal loads to avoid overstressing the specimen until the required load was reached. The loads were then locked and monitored during the fire test.

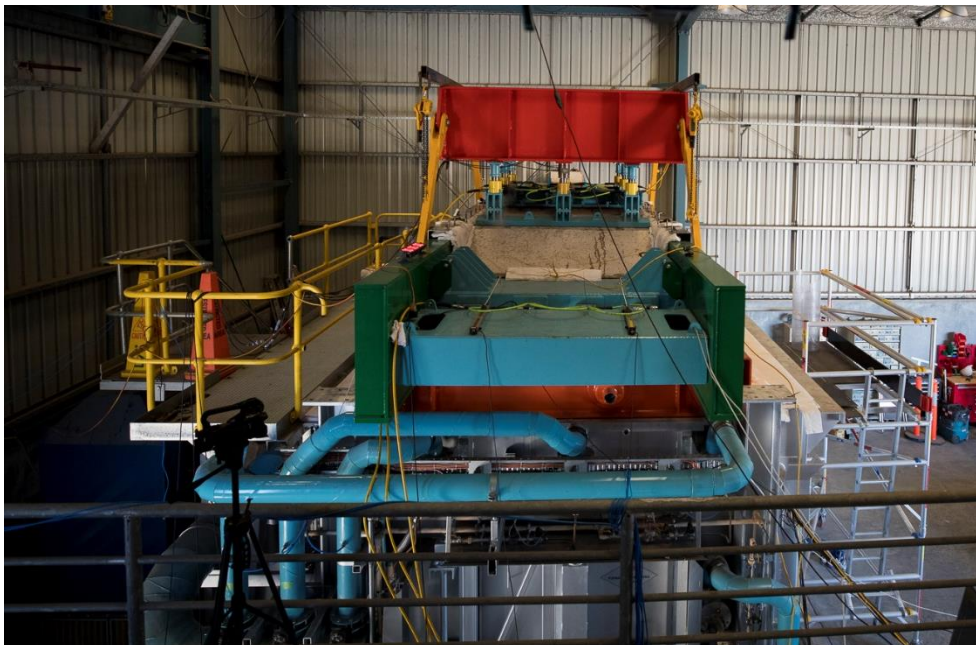


Figure 8 Tunnel Segment Lining Fire Test Setup at Victoria University

Table 2: RABT-ZTV (rail) Time Temperature Curve

Time (mins)	Temperature (°C)
0	20 (Ambient)
5	1200
60	1200
170	20 (Ambient)
360	20 (Ambient)

Instrumentation

Identical type k thermocouples used to control the furnace temperatures were also placed at various locations and depths prior to the concrete being poured. The locations were defined by a 800 x 800 mm area in the middle of the specimen as defined by the EFNARC procedure [16].

EXPERIMENTAL RESULTS

Temperature vs Time Results

Figure 9 shows the furnace performance (Furnace Average) and insitu thermocouple data for the sixth curved panel test (flyash steel fiber mix-Label 4.0). Significantly, the furnace was able to directly simulate the RABT- ZTV curve. Thermocouple denoted T1 050 represents a specimen thermocouple at location T1 at a insitu depth of 50 mm from the surface.

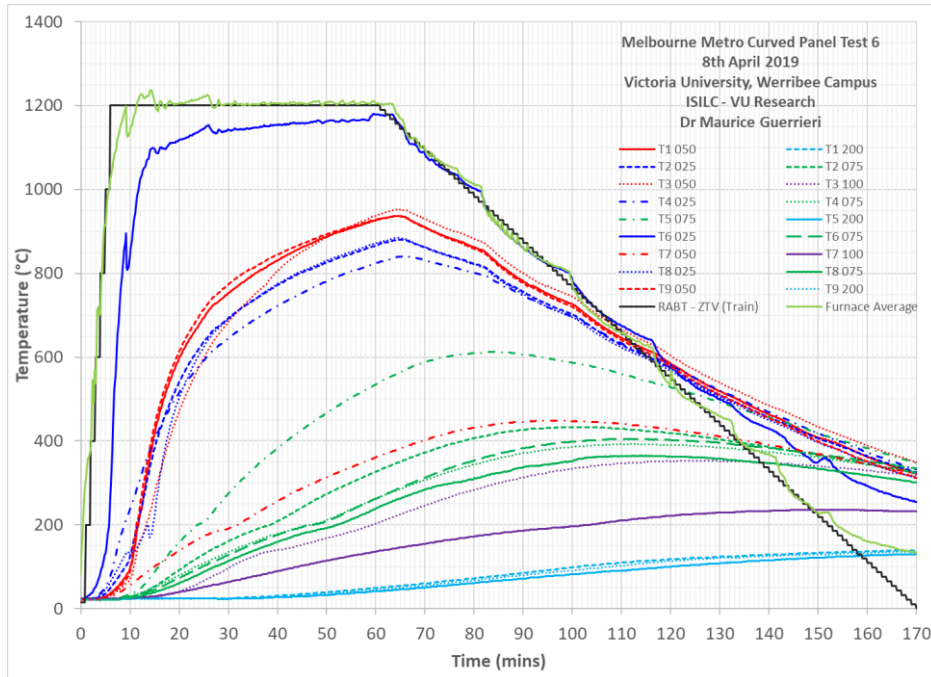


Figure 9 Insitu Specimen Thermocouples Temperature Vs Time

Spalling

Figure 10 represents a photo of the specimen after the fire exposure whilst Figure 11 represents the spalling depth contour plot. Within the central area of 800 x 800 mm in accordance to the EFNARC procedure [16], the average spalling depth was 22.29 mm whilst the average spalling for the entire surface exposed to fire was approximately 11.48 mm. Table 3 represents a summary of the fire tests conducted.

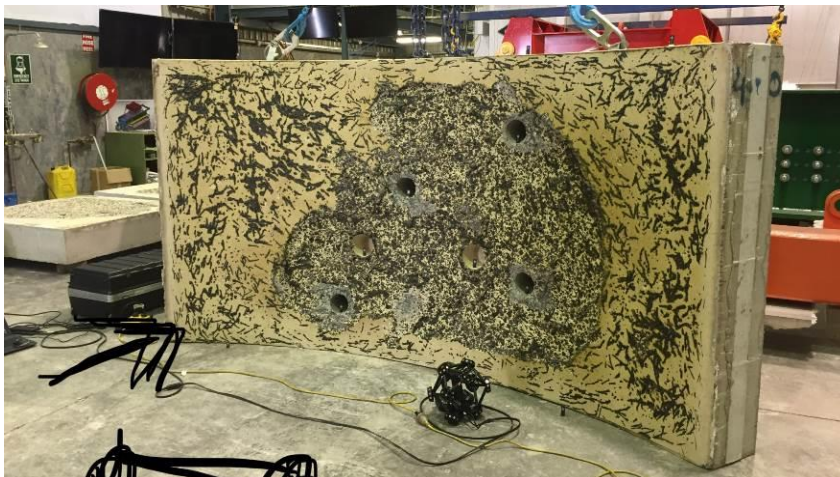


Figure 10 Specimen after Fire Exposure (Specimen ID: Label4.0)

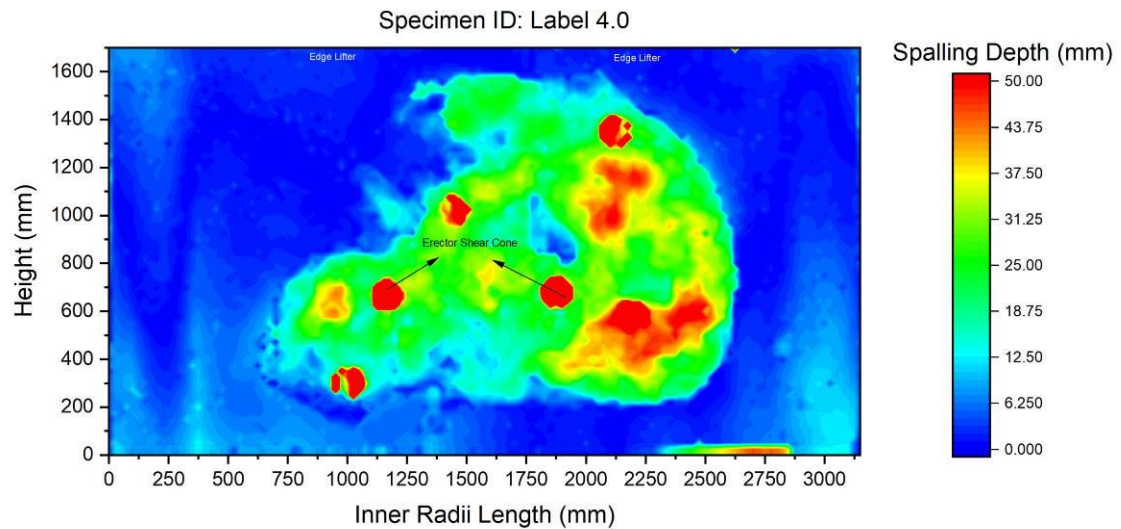


Figure 11 Spalling Depth Contour Plot (Specimen ID: Label4.0).

Table 3: Summary of Spalling Results

FLAT PANELS							
poly con %	Specimen ID	Pre Burn	Post Burn	Mass Loss kg	Mass Loss %	Pass/Fail	Content
1.5	1--1	1734	1700	34	1.93	Pass	Slag
1.5	1--2	1740	1715	25	1.44	Pass	Slag
1.75	2--1	1759	1705	54	3.04	Pass	Slag
1.75	2--2	1740	1690	50	2.87	Pass	Slag
1.5	3--1	1770	1730	40	2.26	Pass	Flyash
1.5	3--2	1764	1705	59	3.32	Pass	Flyash
1.75	4--1	1740	1690	50	2.87	Pass	Flyash
1.75	4--2	1734	1710	24	1.36	Pass	Flyash
1.5	M4.1	1790	1645	145	8.10	Fail	ZEP
1.5	M4.2	1770	1660	110	6.21	Pass	ZEP
1.75	M4.3	1770	1710	60	3.39	Pass	ZEP
1.75	M3.1	1775	1700	75	4.23	Pass	ZEP

CURVED SEGMENTS							
poly con %	Specimen ID	Pre Burn	Post Burn	Mass Loss kg	Mass Loss %	Pass/Fail	Content
1.5	Label 1.0	4550	4400	150	3.30	Pass	Slag
1.5	Label 3.0	4530	4360	170	3.75	Pass	Slag
1.5	Label 2.0	4550	4420	130	2.86	Pass	Flyash
1.5	Label 4.0	4490	4150	340	7.57	Pass	Flyash
1.5	Mix 3 M3	4545	3910	635	13.97	Fail	ZEP
1.5	Mix 3 M4	4580	3855	725	15.83	Fail	ZEP

Note: A specimen which failed indicates that the average spalling within the 800 x 800 mm central area is >30 mm.

CONCLUSIONS

This paper presented an overview of the testing regime/state-of-the art testing facility for full scale tunnel lining specimens'. Preliminary results show that full scale testing give a true and accurate representation, while small panels underestimate results. This is in agreement to the tests conducted by Carre et al [18] on prestress flat panels which showed that concrete is more susceptible to spalling when significant compressive stress is applied.

REFERENCES

1. Khoury, G., et al., *Modelling of heated concrete*. Magazine of Concrete Research, 2002. **54**(2): p. 77-101.
2. Yan, Z.-g., et al., *Full-scale fire tests of RC metro shield TBM tunnel linings*. Construction and Building Materials, 2012. **36**: p. 484-494.
3. Schrefler, B.A., et al., *Concrete at high temperature with application to tunnel fire*. Computational Mechanics, 2002. **29**(1): p. 43-51.
4. Beard, A. and R. Carvel, *The handbook of tunnel fire safety*. 2005: Thomas Telford London.
5. Yan, Z.-g., et al., *Experimental investigation of reinforced concrete and hybrid fibre reinforced concrete shield tunnel segments subjected to elevated temperature*. Vol. 71. 2015. 86-99.
6. Park, S.H., et al., *A case study on the fire damage of the underground box structures and its repair works*. Tunnelling and Underground Space Technology, 2006. **21**(3): p. 328.
7. Kim, J.-H.J., et al., *Fire resistant behavior of newly developed bottom-ash-based cementitious coating applied concrete tunnel lining under RABT fire loading*. Construction and Building Materials, 2010. **24**(10): p. 1984-1994.
8. *International Tunnelling and Underground Space Association (ITA). Guidelines for structural fire resistance for road tunnels*. 2005.
9. A, L., *On the characteristics of fires in tunnels*. 2005, Lund University: Sweden.
10. Caner, A. and A. Böncü, *Structural Fire Safety of Circular Concrete Railroad Tunnel Linings*. Journal of Structural Engineering, 2009. **135**(9): p. 1081-1092.
11. Haack, A., *Fire protection in traffic tunnels— initial findings from large-scale tests*. Tunnelling and Underground Space Technology, 1992. **7**(4): p. 363-375.
12. Haack, A., *Fire protection in traffic tunnels: General aspects and results of the EUREKA project*. Tunnelling and Underground Space Technology, 1998. **13**(4): p. 377-381.
13. Yasuda, F., K. Ono, and T. Otsuka, *Fire protection for TBM shield tunnel lining*. Tunn Undergr Space Technol 2004. **19**(4-5): p. 317.
14. Richter, E. *Fire tests on single-shell tunnel segments made of a new high-performance fireproof concrete*. in *Workshop: Fire Design of Concrete Structures: What now*. 2005.
15. Australia, S., *Methods for fire tests on building materials, components and structures: Fire-resistance test of elements of construction*. 2005, Standards Australia: NSW, Australia.
16. EFNARC, *Specification and Guidelines for Testing of Passive Fire Protection for Concrete Tunnels Linings* 2006.
17. Efectis, *2008-Efectis-R0695: Fire testing procedure for concrete tunnel linings*. 2008: Netherlands.
18. Carré, H., et al., *Effect of compressive loading on the risk of spalling*. Vol. 6. 2013. 01007.

Prevent High Strength Concrete from Spalling Subject to ISO834 Fire

Yong Du^{1,2,*}, Honghui Qi¹

¹ College of Civil Engineering, Nanjing Tech University, Nanjing, China

² Department of Civil and Environmental Engineering, National University of Singapore, Singapore

* Email address: yongdu_mail@njtech.edu.cn

ABSTRACT

High strength concrete encased columns are being developed for erecting high-rise buildings as their higher load bearing capacity and smaller cross section size than normal concrete encased column. At ambient temperature, high strength concrete is always mixed with steel fibers to improve its ductility to match the material properties of high strength steel while constructing concrete encased columns. However, for high strength concrete at elevated temperature, spalling usually can be observed due to different thermal properties of various materials mixed such as siliceous aggregate, cement, silica fume, grit and moisture. Most of previous studies present that pore vapor compression induces high strength concrete spalling and propylene fiber can prevent it from spalling. The aim of the present experimental study is to discover the minimum propylene fiber ratio to prevent spalling of 115~120 MPa concrete with aggregate and steel fiber. The experimental study carried out on 17 specimens with different water-binder ratio, steel fiber ratio and monofilament propylene fiber ratio exposed to ISO834 fire. The test results indicate that 0.15% by volume of propylene fibers can prevent 115/120 MPa high strength concrete with aggregate from spalling. It is worth noting that propylene fiber mixture ratio of 0.15% is lower than that of EN 1992-1-2 proposed up to 0.22%. Lower propylene fiber mixture ratio has been soaked to improve the workability of 115~120 MPa high strength concrete with steel fibers.

KEYWORD: High Strength Concrete, ISO834 Fire, Propylene Fiber, Spalling, Steel Fiber

1. INTRODUCTION

High strength concrete (HSC) with cubic compressive strength of 115~120 MPa can now be manufactured by most concrete plants due to the availability of a variety of additives such as silica fume and water reducing admixture. In terms of economic advantage, cost studies have shown that HSC can carry the same compression load at least cost than normal strength concrete, and thus the higher material costs for HSC are more than compensated for. In terms of architectural advantage, HSC allows smaller size columns to be used in high-rise construction. This results in more usable space in the buildings [1].

A question may be raised as to what behaviors of the HSC in fire [2]. Recent results of fire tests have shown that there is well-defined difference between the properties of HSC and NSC at high temperature [3]. However, what is more important about HSC is the occurrence of explosive spalling when HSC is subjected to rapid heating, as in the case of a fire. This failure mechanism was mentioned but not dealt with sufficiently in the previous studies. Experimental studies have shown that explosive spalling of HSC is affected by the

following factors: rate of temperature rise, mineralogical composition of the aggregates, thermal induced mechanical stress, reinforcement arrangement, moisture content, and density of the concrete matrix.

HSC is achieved mainly by using a low water-cement (W/C) ratio and silica fume. Thus, HSC has lower permeability and water content compared with NSC. It has been theorized, and somewhat qualitatively validated by experiments, that the higher susceptibility of HSC which limits the ability of moisture to escape from the pore. As heating increases the pore compression also increases. This increase in vapor compression continuous until the internal stresses becomes so large as to cause explosive spalling of the heated concrete. This failure mechanism has been observed on an inconsistent basis by researchers [4]. Often, explosive spalling has occurred to online a fewer HSC specimens from a large group of specimens that were subjected to identical testing conditions. This erratic behavior makes it difficult to predict with certainty when HSC will fail by explosive spalling.

HSC is a rather brittle material. Thus, steel fiber has been used to improve the ductility capacity of the HSC. Meanwhile, polypropylene fiber has been proposed to prevent spalling in case of fire. Then, the higher ratio of fiber can led to twist and reduce workability of the HSC. EN1992-1-2 proposed a value of PP ratio 0.22% by volum to prevent spalling dependent on the moisture of the concrete for concrete grades C 55/67 to C 80/95 [5]. The aim of this study is to determine an optimized PP ratio to prevent spalling for cubic strength of 115~120 MPa of the concrete mix designed by this study. The effect of steel fiber on spalling resistance has also been investigate in this study.

2. EXPERIMENTAL STUDY

2.1 Materials and mix design

P·II Type 52.5 Onoda cement, river sand, granite aggregate with size range of 5~15 mm, a high-range water reducing admixture, polypropylene (PP) fiber, steel fiber (SF) were used in the production of concrete. The properties of fibers are listed in Table 1. Two types of mix properties of HSC are listed in Table 2. The cubic strength of HSC increased from 116 MPa to 134 MPa while water-binder ratio decreasing from 0.18 to 0.15. Mixes were casted into 10x10x10 cm prisms (see Figure 1) and the specimens were kept in laboratory environment for 24h. after demoulding, the specimens were labeled and then cured in 98% humidity at 20°C for 28 days. Then, cubic compressive strength under each mixes of HSC have been tested and listed in Table 2 & 3 respectively. Fifteen specimens of HSC with different water-binder ratio and fiber were produced and listed in Table 3 and specimen size shown in Figures 2-3.

Table 1 Properties of fibers

Series	Density (g/cm ³)	Melting point (°C)	Diameter (μm)	Length (mm)	Shape
PP	0.92	170	18	16	Circular
SP	7.85	1535	230	14	Circular

Table 2 Mix proportions

Series	W/B	Cement (Kg/m ³)	Silica fume (kg/m ³)	water (kg/m ³)	Sand (kg/m ³)	Coarse aggregate (kg/m ³)	Superplast-icizer (kg/m ³)	Strength (MPa)
I	0.18	810	90	162	588	882	18	117
II	0.15	821	91	137	593	890	18	134

Table 3 Details of fire test specimens (Note: the ‘—’ in Table 3 represent of ‘none’.)

Specimen	HSC1	HSC2	HSC3	HSC4	HSC5	HSC6	HSC7	HSC8
Mix series			I				II	
Dimension				$\phi 300 \text{ mm} \times 300 \text{ mm}$				
PP (Vol.) %	0.10	0.22	0.15	0.15	—	0.30	0.50	0.22
SF (Vol.) %	—	—	0.15	0.03	—	0.15	0.15	—
Strength (MPa)	116.4	118.0	122.3	127.6	117.8	142.6	136.5	134.2
Specimen	HSC9	HSC10	HSC11	HSC12	HSC13	HSC14	HSC15	
Mix series				II				
Dimension		$\phi 300 \text{ mm} \times 300 \text{ mm}$			$\phi 100 \text{ mm} \times 200 \text{ mm}$			
PP (Vol.) %	—	0.10	0.13	0.15	0.10	0.13	0.15	
SF (Vol.) %	1.00	—	—	—	—	—	—	
Strength (MPa)	134.5	122.5	133.4	130.1	122.5	133.4	130.1	



Figure 1 10x10x10 cm prism



Figure 2 $\phi 30 \times 30$ cm cylinder



Figure 3 $\phi 10 \times 30$ cm cylinder

2.2 Heating procedure

A gas furnace that can operate up to 1250 °C was employed. The heating rate of standard fire curve (i.e. ISO834) has been traced for two hours. A thermal couple was mounted in the core of most specimens to measure the temperature history in the core of HSC specimens as shown in Figure 4. It is worth noting that the temperature in the core of HSC5 specimen suddenly increased after fire ignition about 50mins due to the concrete spalling into debris. The temperature in the core of most specimens is up to 200 °C or so after fire ignition about 2h.

2.3 Mercury intrusion porosimetry test

The characterisation of pore size distribution in the mesoporous and microporous ranges with variety of different concrete. Determination of pore size distribution by mercury intrusion porosimetry. Compression is applied to force mercury into smaller and smaller pores. Measuring the applied compression and the intrusion volume, the pore size distribution can be calculated. As shown in Figure 5, the mercury intrusion porosimetry reduces with the decrease of compression strength of concrete. Comparison of porosity between the previous studies and two types of mix concrete listed in Table 2, the specimens holds the same porosity as the previous study with the same strength shown in Figure 2.

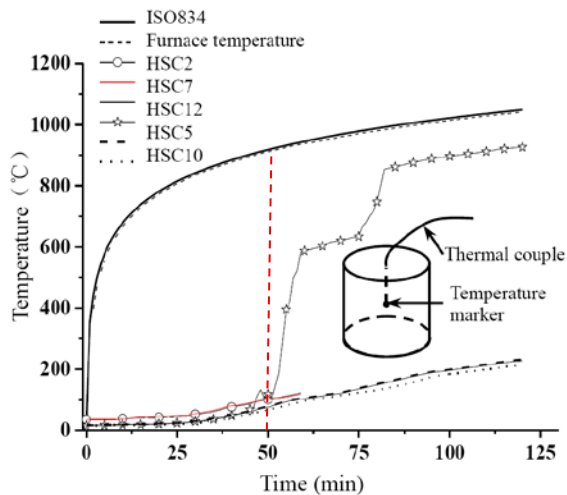


Figure 4 Temperature history in the core of specimens

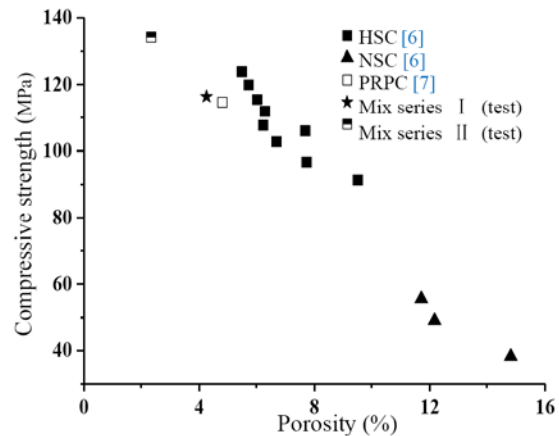


Figure 5 Comparison of porosity between previous studies and present test

3. TEST RESULTS AND DISCUSSION

The experimental test results obtained from fire tests and visual observations are discussed in this section. Outer surface of specimens is destroyed, shown in Table 4.

3.1 Spalling observation

Shown in Table 4, exposed to ISO834 fire, thoroughly explosive spalling was observed after ignition about 50mins about 920°C for HSC5 specimen without PP fiber & steel fiber under 0.18 W/B. As adding 0.10% PP fiber, HSC1 was formed and observed partial spalling, shown in Figure 4. If 0.22% PP fiber has been mixed to form HSC2, no cracking was observed on the outer surface of specimen, shown in Table 4. Regardless of 0.10% PP fiber cannot absolutely prevent HSC from spalling, PP fiber can provide interconnected channel system while melted above 170 °C.

3.2 Effect of SF on spalling

Based on the value of W/B of 0.15, HSC9 specimen was produced by mixing with 1.0% SF, partial spalling was observed as shown in Table 4. This result could be contributed to the effect of steel fiber on spalling. Steel fiber cannot prevent high strength concrete from spalling but can enhance the inter connection of micromaterial.

3.3 Effect of PP fiber on spalling

In the range of PP fiber volume ratio from 0.1% to 0.5%, outer surface crack or partial spalling of specimens has been shown in Table 4. For W/B of 0.18, there was no crack observed on the outer surface of the HSC3 and HSC4 specimen with the same PP fiber ratio of 0.15% and different steel fiber mix ratio. For W/B of 0.15, partial spalling has been observed by heating HSC10 and HSC11 which mixed 0.1 and 0.13% PP fiber respectively. If update the range of PP fiber ratio from 0.15% to 0.30%, there were no cracks on the outer surface of HSC6~HSC9 and HSC12 respectively exposed to ISO834 fire about 2h. Thus, the minimum PP fiber of 0.15% has been proposed to prevent 120MPa concrete from spalling or cracking by this study.

Table 4 Outer surface of specimens



3.4 Effect of size of specimen on spalling

Two sizes of specimen have been produced with the same value of W/B 0.15. One series of cylindrical specimen is with 300 mm diameter and 300 mm height, the others with 100 mm diameter and 200 mm height as shown in Table 3. Two series of specimen are with the same range of PP fiber ratio i.e. 0.10~0.15%. Shown in Table 4, both of mixture series specimen with PP fiber ratio less than 0.15% were observed partial spalling, but no crack on the outer surface of specimen with 0.15% PP fiber exposed to ISO834 fire about 2h. Thus, if the size of a cylindrical specimen is larger than $\phi 100 \times 200$ mm, the factor of size will not influence on spalling or cracking for 120 MPa strength concrete under ISO834 fire.

4. CONCLUSIONS

Behaviours of HSC under high temperature is different from normal concrete due to very dense microstructure. Precaution actions should be taken to prevent the damage when HSC exposed to fire. In this study, effects of PP fiber, steel fiber, water-binder ratio, size of

specimen on spalling of HSC with 120 MPa strength have been investigated. A series of conclusions were drawn as below.

- Spalling of 115~120 MPa HSC is dependent on the ratio of PP fiber mixed in concrete. Explosive spalling was observed especially in non-fibrous specimen after fire ignition 50 minutes.
- For PP fiber ratio below 0.15%, partial spalling and cracks were observed in 115 MPa and 120 MPa HSC with 0.18 and 0.15 water-binder ratio respectively. No spalling and cracks was observed if the PP fiber ratio is not below 0.15%. PP fiber ratio of 0.15% is lower than that of 0.22% by volum proposed by EN 1992-1-2, have a remarkable effect on the risk of spalling of series HSC with cubic compressive strength of 115~120 MPa.
- Partial spalling was observed in HSC with steel fiber ratio of 1.0% and no PP fiber. Steel fiber cannot prevent the risk of spalling for HSC, but can improve the inter connection of material.
- Specimen size cannot influence on the PP fiber ratio of 0.15% to prevent spalling of HSC.
- Based on the results of this study it determined that PP fiber ratio of 0.15% can prevent the risk of spalling for HSC with cubic compressive strength of 115~120 MPa.

ACKNOWLEDGEMENTS

The authors gratefully acknowledge the financial support of the International Structural Fire Research Laboratory (ISFRL) in Nanjing Tech University, China.

REFERENCES

- [1] Priyan, M., "Design of High-Strength Concrete Members: State-of-the-Art", Progress of Structural Engineering Material, 5, 1-15, 2003.
- [2] Abdullah, H., Nilufer O., "High Performance Concrete under Elevated Temperatures", Construction and Building Materials, 44, 317-328, 2013.
- [3] Mehmet S., Turan O., "Mechanical Properties of Normal and High Strength Concrete Subjected to High Temperatures and Using Image Analysis to Detect Bond Deteriorations", Construction and Building Materials, 24, 1486-1493, 2010.
- [4] Kodur V., "Spalling in High Strength Concrete Exposed to Fire-Concerns Cause Critical Parameters and Cures", Proceedings of ASCE Structures Congress, 1-8, 2000
- [5] EN 1992-1-2, Design of concrete structures. Part 1. 2 General rules - Structural fire design, CEN, 2004.
- [6] Poon C.S., Azhar S., Anson M., Wong Y.L., "Comparison of the Strength and Durability Performance of Normal and High-Strength Pozzolanic Concretes at Elevated Temperatures", Cement & Concrete Research, 31(9), 1291-1300, 2001.
- [7] Luo B.F., "Spalling and mechanic properties of high performance silica fume concrete at elevated temperature", PhD. degree thesis, Harbin Technology University, 2014. (in chinese)

Experimental Study on Mechanical Behaviors of Cementitious Grouts after Elevated Temperatures

Lianglin Liu, Jianzhuang Xiao *, Jiangtao Yu & Xian Liu

College of Civil Engineering, Tongji University, Shanghai, China

* Corresponding author (jzx@tongji.edu.cn)

Abstract: The grout sleeve splicing of rebars is one of the mainstream ways to connect the reinforcement bar for precast concrete components in the practical engineering at present. Its performance is mainly affected by the strength of cementitious grout. As fire is a potential disaster of precast concrete structure during its service life, the present investigation experimentally studied the post-fire mechanical behavior of cementitious grouts with different types, namely AP, BP and CP series, after elevated temperature treatments, as well as the influence of cooling regime and specimen shape. Basing on the results of experiment and analysis, there are several findings: 1) there is no spalling occurring by the heating rate of 5 °C/min for the pre-drying specimens; 2) elevated temperature has an obviously effect on the residual strength of cuboid specimen after exposed to 200 °C; 3) the residual compressive strength of the cuboid specimen decreases along with the temperature increasing, but of the cube specimen decreases in advance along with the temperature increasing and then may increase at a certain temperature range; 4) the residual compressive strengths of specimens under furnace cooling are generally larger than under other cooling regimes, and the spraying cooling is the most unfavorable cooling regime; 5) the fire resistance is much better for the thickness specimen after exposed to elevated temperature beyond 200 °C.

KEYWORDS: Grout; Elevated Temperature; Spalling; Residual Strength

1 INTRODUCTION

Spalling was a complex phenomenon that involves the coupling of the thermal, hydraulic, chemical, and mechanical processes [1]. Surface spalling, corner spalling, aggregate spalling and explosive spalling belonged to spalling categories [2]. Especially, explosive spalling was a particularly dangerous spalling and its consequences could be catastrophic [2, 3], and was characterized by the sudden disintegration of the test specimens into fine fragments during heating, which was accompanied by the release of a sufficient amount of energy that projected the small concrete fragments at high velocity in all directions [4]. Since about 1992, the most effective preventing measure for explosive spalling was the thermal barriers covering the surface of the fire-exposed concrete and/or the PP fibers in the concrete mix [5]. In addition, it was reported that the explosive spalling occurred by effects of moisture content,

heating rate, permeability and so on. Through the results of experiments, it was found that there was a critical moisture content of high performance concrete (HPC) for spalling occurrence, which meant that the probability of HPC would increase as the moisture content higher than the critical one [6, 7]. Otherwise, after the study on the effect of heating rate on explosive spalling, it was suggested that the heating rate not be more than 5 °C/min [8].

Nowadays, it was one of crucial problems to bring about the sustainable development of concrete structure [9]. In terms of integrated design, effective use of materials, less construction waste and less site disturbance, prefabricated precast concrete components contributed to sustainable practices [10]. Precast concrete construction usually required connecting precast concrete components, such as wall panels, columns, and pier caps, to form the completed structure whether it was a building or bridge [11]. Grout sleeve splicing of rebars was a typical mechanical connection which had mostly been applied to the joints of precast concrete members [12], and was a designed mechanical coupler that filled with non-shrinkage grout as bonding material to splice reinforcement rebars to ensure continuity during the load transfer [13]. These splices relied primarily on grout strength and confinement to improve bond stress and, thus, resulted in a short development length of the spliced rebars within the grout-filled hardware [14]. In addition, it was suggested that the bond strength between grout and metal material be linear to the square root of compressive strength of grout [14, 15]. There were a lot of findings on requirements of grout compressive strengths for fulfilling the performance of grout sleeve splicing of rebars all over the world, such as 46 MPa at 7th day [16], and no less than 85MPa at 28th day [17]. Therefore, the present paper aimed to study the compressive strength of grout under different conditions.

As wide applications in the practical engineering, the risk of precast concrete structures exposed to fire was increasing. The grouted sleeve splicing of rebars was one of the mainstream rebar splicing method of precast concrete structures. It was found that the tensile capacity of splicing after fire was decreased to 70% of the initial stage at ambient temperature [18]. Otherwise, there might even be such a phenomenon in the fire disaster: the structure experiencing fire did not collapse when the fire was extinguished, but collapse accident occurred to cause serious casualties after a period of time when people entered to rescue materials [19]. Therefore, effects of cooling methods on behaviors of structures should be concerned in the further research. In addition, with the heating rate of 10 °C/min, it was found that explosive spalling occurred in the grout, which was the important part of precast concrete structure with grout sleeve splicing of rebars, but would be inhibited after pre-drying and with the heating rate of 8 °C/min for specimens of grouts and splices [18]. On the basis of explosive spalling inhibited, the present study aims to study factors effects on mechanical behaviors of grouts, including high temperature, cooling regime and grout shape.

2 DESIGN OF EXPERIMENT

2.1 Specimen design

The grout material was provided by a company at Shanghai, China. Three kinds grouts were used to form the specimens with different water contents, i.e., 0.14:1 corresponding to 0.14kg water mixed with 1kg grout, as listed in Table 1. The specimens were blocks with shapes of cuboid (40mm×40mm×160mm) [17] and cube (70.7mm×70.7mm×70.7mm) [20] as listed in Table 2.

Table 1 Compressive strengths of grouts with cuboid shape

Types of grouts	AP series	BP series	CP series
Water content	0.14:1	0.13:1	0.13:1
strengths (MPa)	79.8	78.5	85.0

Notes: all of these data are from average values of six specimens.

Table 2 Details of specimens

No.	Shapes	Types	Temperature (°C)	Quantities
A(B, C)-AT	Cuboid	AP, BP, CP	20	3×3
A(B, C)-200	Cuboid	AP, BP, CP	200	3×3
A(B, C)-400	Cuboid	AP, BP, CP	400	3×3
A(B, C)-600	Cuboid	AP, BP, CP	600	3×3
A(C)S-200	Cube	AP, CP	200	3×2
A(C)S-400	Cube	AP, CP	400	3×2
A(C)S-600	Cube	AP, CP	600	3×2
A(C)A-200	Cube	AP, CP	200	3×2
A(C)A-400	Cube	AP, CP	400	3×2
A(C)A-600	Cube	AP, CP	600	3×2
A(C)F-200	Cube	AP, CP	200	3×2
A(C)F-400	Cube	AP, CP	400	3×2
A(C)F-600	Cube	AP, CP	600	3×2

Notes: a. type represents the strength type of grout, P means prism;

b. A(B, C) represents the type of grout used for cuboid blocks;

c. AS, AA, and AF, the first letter is the strength type of grout, and the second letter is the cooling program, i.e., S, A and F representing spraying cooling, ambient cooling and furnace cooling, respectively.

2.2 Heating and cooling regimes

The heating regime contained four levels including ambient temperature (as 20 °C for calculation), 200 °C, 400 °C and 600 °C as shown in Fig. 1. There were two stages in every temperature level as follows: firstly, specimens were heated at a rate of 5 °C/min until 100 °C and maintained at 100 °C for 120min; secondly, heating was continued to a target temperature and maintained for 60min before turning off the furnace. Afterwards the top cover of furnace was opened, 2/3 amounts of specimens with cube shape were taken out for spraying cooling and ambient cooling, and others were kept cooling in the furnace.

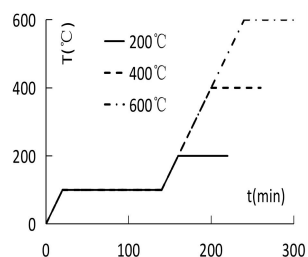


Fig. 1 Heating programs



Fig. 2 Loading setup

2.3 Loading program and setup

There were two kinds loading program: the flexural strength and compressive strength test for the cuboid blocks, and compressive strength test for the cube blocks. According to the

requirements from JGJ/T 70-2009 [20] and GB/T 17671-1999 [21], stress control was used to test the strength of specimen, including 1500 N/s in the compressive strength loading for specimen with cube shape [20], and 50 N/s in the flexural strength loading and 2600 N/s in the compressive strength loading for specimen with cuboid shape [21]. The loading setup, as shown in Fig.2, has the maximum capacity with 1000 kN.

3 EXPERIMENTAL RESULT

3.1 Experimental phenomenon

There is no spalling occurring for the specimens during heating and cooling processes. Surface colors of specimens varied from blue-gray to gray-white as increasing from ambient temperature to 600 °C as shown in Fig. 3. Under different cooling regimes, there are irregular fractures on the surface of specimen, the width of which decreased in the order of the spraying cooling, ambient cooling and furnace cooling as shown in Fig. 4 from left to right. After loading, the middle splitting failure mode occurs in specimens for the flexural strength test as shown in Fig. 5(a), and the inverted cone-shape failure mode belongs to the compressive strength test as shown in Fig. 5(b). Failure modes of the specimens are brittle.



(a) Cuboid blocks

(b) Cube blocks

Fig. 3 Surface changes of different shapes of specimens



(a) Spraying cooling

(b) Ambient cooling

(c) Furnace cooling

Fig. 4 Fractures on the surface of specimens after different cooling regimes



(a) Cuboid specimen

(b) Cube specimen

Fig. 5 failure modes of specimens

3.2 The flexural strength

According to the requirements of JGJ 355-2015 [17] and GB/T 17671-1999 [21], the cuboid shape specimens were carried out on the flexural strength testing after cooling, and the testing results were listed in Table 3.

Table 3 flexural strengths of specimens

Specimens	AP series (MPa)	BP series (MPa)	CP series (MPa)
Ambient temperature	15.1	15.2	13.2
200 °C	15.1	12.9	15.2
400 °C	7.6	8.4	8.2
600 °C	6.3	7.5	6.5

Notes: all of these data are averaged from the values of three specimens.

3.3 Compressive strength

According to the requirements of JGJ 355-2015 [17], JGJ/T 70-2009 [20] and GB/T 17671-1999 [21], others specimens are carried on the compressive strength testing after cooling, and the testing results as shown in Table1, Table 4 and Table 5.

Table 4 Compressive strengths of specimens after flexural strengths testing

Specimens	AP series (MPa)	BP series (MPa)	CP series (MPa)
200 °C	72.2	77.3	74.6
400 °C	45.6	54.7	54.3
600 °C	45.5	54.5	53.1

Notes: all of these data are from average values of six specimens.

Table 5 Compressive strengths of cube specimens

types		Temperatures (°C)	A series (MPa)	C series (MPa)
Cooling levels	A	200	69.2	77.9
		400	61.0	71.3
		600	50.9	69.9
	F	200	66.5	80.8
		400	68.3	68.5
		600	53.7	69.6
	S	200	63.6	66.8
		400	62.1	61.8
		600	53.5	69.8

Notes: a. all of these data are from average values of three specimens.

b. A, F, S represent ambient cooling, furnace cooling, spraying cooling respectively.

4 ANALYSIS OF RESULTS FROM EXPERIMENTS

4.1 Spalling prevention

As shown in Fig. 3, the specimens remain integrity after them exposed to elevated temperature up to 600 °C under spraying cooling, ambient cooling and furnace cooling regimes, which indicates that the grout specimen is prevented from the spalling. Therefore, the measures of pre-drying and low heating rate (5 °C/min) have significant effect on the spalling prevention: the low moisture content by pre-drying descends the volume of vapor and low heating rate reduces the temperature gradient, which leads to pore pressure lower

than the tensile strength of grout under different elevated temperatures.

4.2 High temperature effects on the flexural strength

It is shown in Fig.6 that there are some relationships existing between flexural strength and temperature level, including the residual strength in Fig.6(a) and strength ratio to initial in Fig.6(b). It is found that the relationships between residual flexural strength and elevated temperature contain three parts: moderate descent segment, fast descent segment and slow descent segment corresponding to the specimens after exposed elevated temperatures in the range of 20 °C to 200 °C, 200 °C to 400 °C and 400 °C to 600 °C. Compared with the initial strength at ambient temperature, the flexural strength of grouts after exposed to 200 °C vary in the range of $\pm 15\%$, i.e., 0%, -15.1% and 15.2% for AP series, BP series and CP series respectively, which may show that the CP series are much more suitable to the grout sleeve splicing of rebars.

There are other findings on the flexural strength of specimens after exposed to elevated temperatures: 200 °C is a critical temperature for the grouts, and the strength would decrease abruptly after the specimens exposed to elevated temperature exceeding 200 °C; the strengths of AP, BP and CP series decrease significantly from 200 °C to 400 °C with the extend of 49.7%, 29.6% and 53.1% respectively but decreased slowly with extend of 8.6%, 5.9% and 12.9% corresponding to AP, BP, and CP series respectively from 400 °C to 600 °C; after exposed to 600 °C, the flexural strength reductions of AP, BP, and CP series are 58.3%, 50.66% and 50.76%, which shows that the elevated temperature has a significant effect on the residual flexural strength of grout.

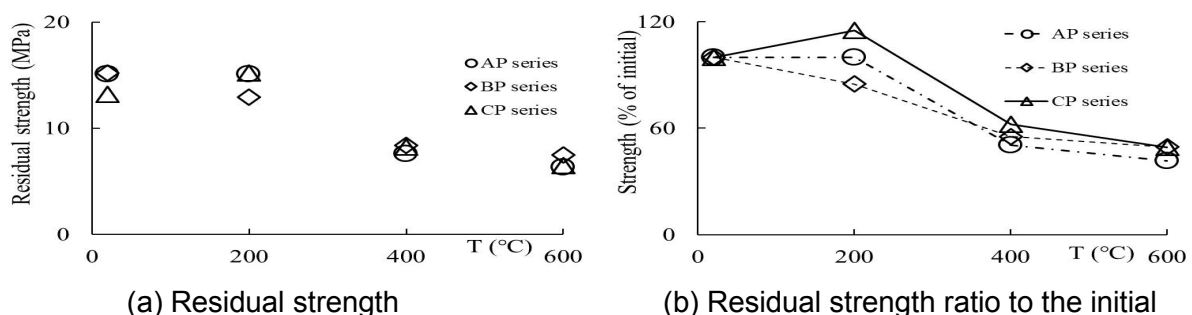


Fig. 6 Relationship between flexural strength of cuboid grout specimen and temperature

4.3 High temperature effects on the compressive strength

The compressive strengths of grouts with different shapes by furnace cooling regimes are illustrated along with temperatures in Fig. 7 and Fig. 8, where includes the change trend between temperature versus residual strength and the divided residual strength by ambient strength respectively.

For the specimens with cuboid shape, it is found that the residual compressive strength decreases along with the temperature increasing as shown in Fig. 7. In addition, the relationships between residual compressive strength and elevated temperature are similar to the development of residual flexural strength as shown in Fig. 6, i.e., containing three parts: moderate descent segment, fast descent segment and slow descent segment, and 200 °C as a critical temperature and the elevated temperature as a significant effect factor on the residual compressive strength of grout. After exposed to 600 °C, the compressive strength reduction of AP, BP, and CP series are 43.0%, 30.6% and 37.5%, which also shows that the elevated temperature has a significant effect on the residual compressive strength of grout.

In order to compare directly, the ambient compressive strength for the specimens with cube shape is from Table 1. It is found that the relationships between residual compressive strength and elevated temperature contain two parts: ascent segment and descent segment as shown in Fig. 8. The ascent segments with increase of 2.3% and 1.3% occur corresponding to the specimens of AF series and CF series after exposed to the elevated temperature with range of 200 °C to 400 °C and 400 °C to 600 °C respectively. After exposed to 600 °C, the maximum compressive strength reduction of AF and CF series are 32.7% and 19.4%, which shows that the elevated temperature has a significant effect on the residual compressive strength of grout again and the CF series present much higher residual compressive strength.

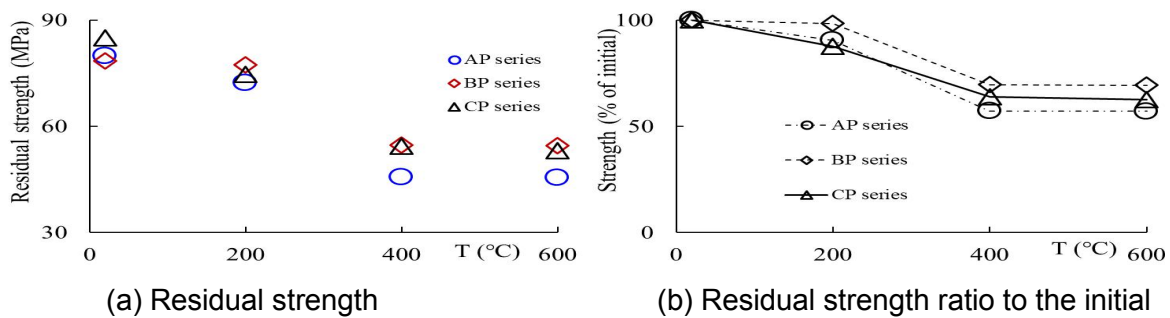


Fig. 7 Relationship between compressive strength of cuboid grout specimen and temperature

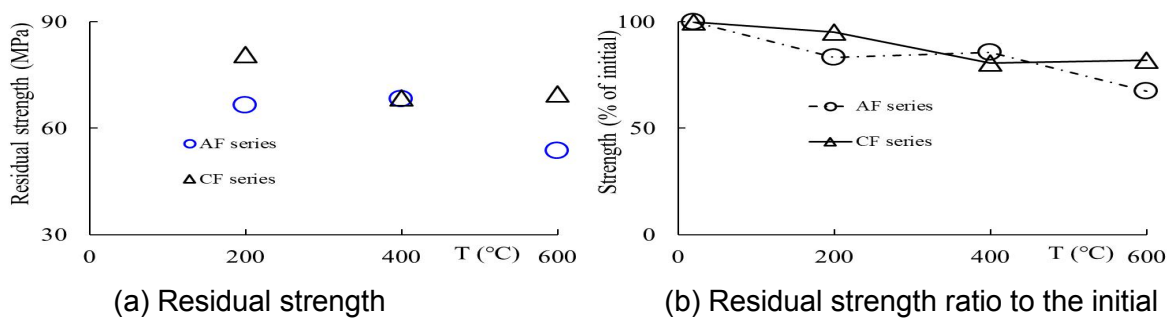


Fig. 8 Relationship between compressive strength of cube grout specimen and temperature

4.4 Cooling regimes effects on the compressive strength

The relationship between compressive strength of specimens after different cooling regimes and temperature is shown in Fig. 9, and the ambient compressive strength for the specimens with cube shape is from Table 1. It is found that the development of compressive strength is regular, i.e., decreasing along with the temperature increasing, when the specimen is under ambient cooling regime, which also occurs in the AS series. The residual compressive strength of other specimens may be a little resilient along with the temperature increasing. Taken CS series for example, the residual compressive strength has an increase of 12.9%, i.e., the largest resilience, when these specimens are under spraying cooling regime after exposed to elevated temperature from 400 °C to 600 °C, which shows that the development of residual strength of grout under spraying cooling regime varies very turbulently as shown in Fig. 9(b).

According to Table 5 and Fig. 9, there are some other findings on compressive strengths of specimens as followings: after exposed to elevated temperature beyond 200 °C, the specimens of AF series compared with AS and AA series have the largest residual compressive strength; after exposed to 200 °C, the specimens of CF series compared with

CS and CA series have the largest residual compressive strength; the residual compressive strength of specimen under spraying cooling regime is generally lower than under other cooling regimes which is corresponding to much wider surface fracture occurred as shown in Fig. 4. Therefore, furnace cooling regime is the best cooling method and the spraying cooling regime is the unfavorable cooling regime for the compressive strength development of grout after exposed to elevated temperature.

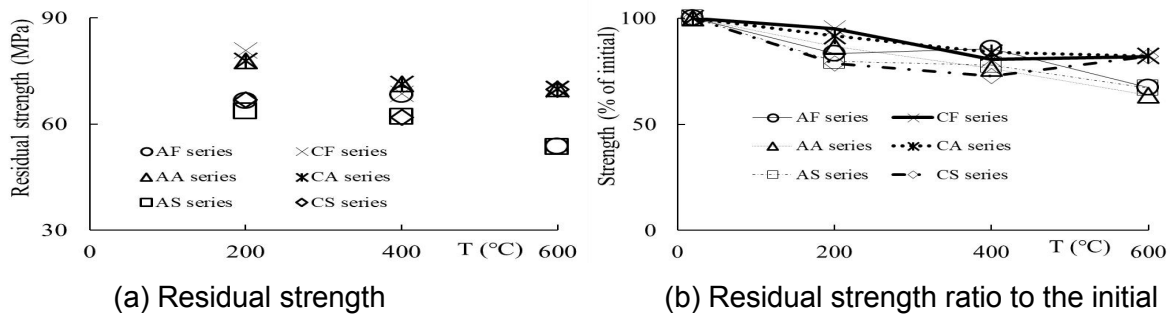


Fig. 9 Relationship between compressive strength of cube grout specimen after different cooling programs and temperature

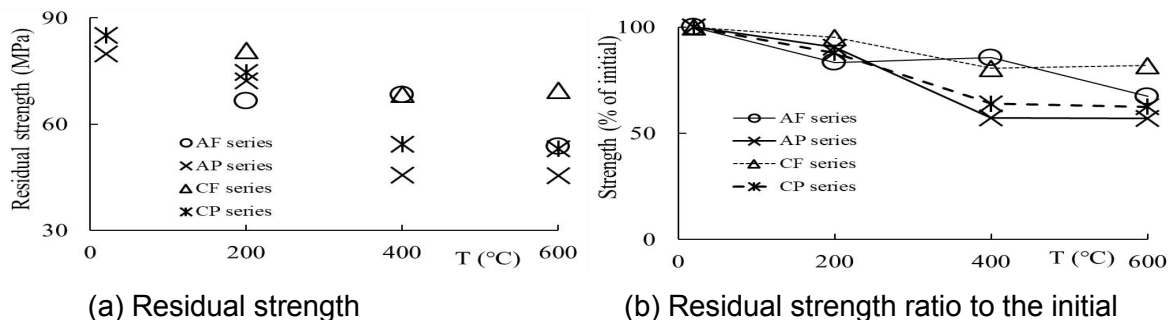


Fig. 10 Relationship between compressive strength of grout with different shapes and temperature

4.5 Effect of the specimen shape on the grout compressive strength

Compressive strengths of the specimens with cube and cuboid shapes are shown with temperatures in Fig.10. It is found that the residual compressive strengths of AP and CP series specimens decrease along with the temperature increasing until the temperature up to 400 °C, and then nearly remain unchanged when the elevated temperature exceeded 400 °C as shown in Fig. 10 (a). However, the compressive strength of AF and CF series are resilient at a certain range of elevated temperature, i.e., 200 °C to 400 °C and 400 °C to 600 °C for AF and CF series respectively.

In addition, according to the results of Table 1, Table 4 and Table 5 and Fig. 10, there are other findings on the development of compressive strength: corresponding to the AF and AP series, the residual compressive strength has a maximum difference of -7.9%, 49.8% and 18.0% when the specimens have been experienced elevated temperature of 200 °C, 400 °C and 600 °C respectively; corresponding to the CF and CP series, the residual compressive strength has a maximum difference of 8.3%, 26.2% and 31.1% when the specimens have been experienced elevated temperature of 200 °C, 400 °C and 600 °C respectively.

Therefore, the shape of specimen has a significant effect on the residual compressive strength of specimen after exposed to elevated temperature up to 600 °C. Moreover, the residual compressive strength is nearly same to the both of cube and cuboid specimen after

exposed to 200 °C for the maximum difference no more than 8.3% but the thick heat-damaged specimen has much larger residual strength especially when the specimen has been exposed to elevated temperature beyond 200 °C.

5 CONCLUSIONS

Based on the results of an experiment with 90 specimens, the residual strength, i.e., flexural strength and compressive strength, of grouts was analyzed and the influencing factors of elevated temperature, cooling regime and specimen shape effects on the residual strength were investigated in the present study. From the analyzed and investigated results, the following conclusions could be drawn as followings:

- 1) There is no explosive spalling occurring during the heating process with the pre-drying and heating rate of 5 °C/min for the specimens with high strength grout.
- 2) High temperature has an significant effect on the residual flexural strength and compressive strength of cuboid specimen when the specimen has been exposed to 200 °C.
- 3) For the cuboid specimen, the residual compressive strength decreases along with the temperature increasing. For the cube specimen, the residual compressive strength decreases in advance along with the temperature increasing and then may increase at a certain temperature range.
- 4) The residual compressive strengths of specimens after exposed to elevated temperature up to 600 °C under furnace cooling regime are generally larger than under other cooling regimes.
- 5) The spraying cooling regime leads to the widest surface fracture on the specimen and lower residual compressive strength of grout, and is the unfavorable cooling regime.
- 6) The maximum difference is not less than 18% between the cube and cuboid specimens after exposed to elevated temperature beyond 200 °C, which indicates that the fire resistance is much better for the thick specimen after exposed to elevated temperature up to 600 °C.

6 ACKNOWLEDGEMENTS

The authors wish to acknowledge the financial support from the Distinguished Young Scholars of China by National Natural Science Foundation of China (NSFC) (NO: 51325802) and NSFC (No: 51661145023).

7 REFERENCES

- [1] Xiao, J.Z., Xie, Q.H., and Xie, W.G., "Study on High-performance Concrete at High Temperatures in China (2004-2016) - An Updated Overview", *Fire Safety Journal*, 95, 11-24, 2018.
- [2] Ali, F., "Is High Strength Concrete More Susceptible to Explosive Spalling than Normal Strength Concrete in Fire?", *Fire and Materials*, 26(3),127-130, 2002.
- [3] Ali, F.A., O'Connor D., and Abu-tair, A., "Explosive Spalling of High-Strength Concrete Columns in Fire", *Magazine of Concrete Research*, 53(3),197-204, 2001.
- [4] Phan, L.T., Lawson, J.R., and Davis, F.L., "Effects of Elevated Temperature Exposure on Heating Characteristics, Spalling, and Residual Properties of High Performance Concrete", *Materials and Structures*, 34(2), 83-91, 2001.
- [5] Khougy, G.A., "Passive Fire Protection of Concrete Structures", *Proceedings of the Institution of Civil Engineers-Structures and Buildings*, 161(SB3), 135-145, 2008.

- [6] Peng, G.F., Jiang, Y.C., Li, B.H., Zhang, J., and Shi, Y.X., "Effect of High Temperature on Normal-strength High-performance Concrete", *Material Research Innovations*, 18(S2), 290-293, 2014.
- [7] Peng, G.F., Chan, Y.N, and Anson, M., "Explosive Spalling Thermally Induced and Fire Property of High Performance Silica Fume Concrete", *Journal of Building Materials*, 2(3), 193-198, 1999. (in Chinese)
- [8] Tao, J., Liu, X., Yuan, Y., and Taerwe, L., "Experimental study of factors affecting the spalling of self-compacting concrete under high temperature", *China Civil Engineering Journal*, 42(10), 22-26, 2009. (in Chinese)
- [9] Xiao J.Z., *An introduction to sustainable concrete structures*, Science Press, 2018.(in Chinese)
- [10] Rahman, A.B.D, Yoon, L.H., Ibrahim, I.S., Mohamed, R.N., Mohammad, S., and Saim, A. A., "Performance of Grouted Splice Sleeves with Tapered Bars under Axial Tension", *Applied Mechanics and Materials*, 789-790, 1176-1180, 2015.
- [11] Henin, E., and Morcou, G., "Non-proprietary Bar Splice Sleeve for Precast Concrete Construction", *Engineering Structures*, 83,154-162, 2015.
- [12] Seo, S.Y., Nam, B.R., and Kim, S.K., "Tensile Strength of the Grout-filled Head-splice-sleeve", *Construction and Building Materials*, 124,155-166, 2016.
- [13] Alias, A., Zubir, M.A., Shahid, K.A., and Rahman, A.B.A., "Structural Performance of Grouted Sleeve Connectors with and without Transverse Reinforcement for Precast Concrete Structure", *Procedia Engineering*, 53, 116-123, 2013.
- [14] Einea, A., Yamane, T., and Tadros, M.K., "Grout-Filled Pipe Splices for Precast Concrete Construction", *PCI Journal*, 40(1), 82-93, 1995.
- [15] Ling, J.H., Rahman, A.B.A., Ibrahim, I.S., and Hamid, Z.A., "Tensile Capacity of Grouted Splice Sleeves", *Engineering Structures*, 111, 285-296, 2016.
- [16] Alias, A., Sapawi, F., Kusbiantoro, A., and Rahman, A.B.A., "Performance of grouted splice sleeve connector under tensile load", *Journal of Mechanical Engineering and Sciences*, 7(1), 1094-1102, 2014.
- [17] *JGJ 355-2015, "Technical Specification for Grout Sleeve Splicing of Rebars"*, China Architecture & Building Press, 2015. (in Chinese)
- [18] Ma, J.J., "The experimental research of semi-grouting sleeves splicing for rebars after exposed to high temperature", Xi'an University of Architecture and Technology, 2017. (in Chinese)
- [19] Wang, Z., Zhang, Z.J., Huang, T., "Experimental Study on Residual Compressive Strength of C40 HPC at High Temperature and after Cooling", *Journal of Zhengzhou University (Engineering Science)*, 31(5), 78-81, 2010. (in Chinese)
- [20] *JGJ/T 70-2009, "Standard for test method of basic properties of construction mortar"*, China Architecture & Building Press, 2009. (in Chinese)
- [21] State administration for market regulation. *Methods of testing cements-Determination of strength (GB/T 17671-1999)*, Standards Press of China, 9-14, Beijing, 1999. (in Chinese)

Influence of the chemical and physical properties of hardened cement paste on the fire-induced spalling of concrete

Jochen Reiners^{1*} & Christoph Müller¹

¹ VDZ, Research Institute of the Cement Industry,
Düsseldorf, Germany

*Corresponding author (jochen.reiners@vdz-online.de,
Tannenstrasse 2, 40476 Duesseldorf, Germany)

ABSTRACT

In an ongoing research project conducted at the Research Institute of the Cement Industry (VDZ) in Düsseldorf, findings of a previous research project which was presented at the “5th International Workshop on Concrete Spalling due to Fire Exposure” in Borås 2017 [1] have been picked up and are transferred to a new test programme.

In the project presented in 2017, a test setup which is described in [2] (“PTM-Test”) was modified by applying a lateral compressive load to the concrete specimens through a steel frame. From the experiments carried out, it was concluded that high pore pressures are not the main mechanism causing the explosive spalling of concrete. Explosive spalling had occurred in high-strength concretes with silica fume as well as in normal-strength concretes with blast furnace cements (CEM III/A) and Portland fly-ash cements (CEM II/B-V). Compared to other concretes in the experimental programme,

- the hardened cement paste of these concretes contained a smaller proportion of capillary pores,
- the hardened cement paste of these concretes contained a smaller proportion of calcium hydroxide than cement paste without blast furnace slag, fly ash or silica fume. When complete hydration is assumed, this corresponds to a larger proportion of CSH phases.

Assumptions were established for why the concretes stated above showed explosive spalling while other concretes in the research programme remained intact. In this paper, the experimental programme to verify these assumptions is introduced. At the time of drafting this paper, the concrete specimens that were produced in 2018 for the project are being stored to reach a target relative humidity for the experimental programme. First results of the experiments will be presented at the “6th International Workshop on Concrete Spalling due to Fire Exposure” in Sheffield.

KEYWORDS: *spalling, pore size distribution, hydration products, hardened cement paste, relative humidity*

1.FINDINGS OF THE PREVIOUS RESEARCH PROJECT

In a previous research project [1] carried out at VDZ in Düsseldorf, a test set-up was used which was first described by Kalifa [2] and has since been applied by many scientists to examine the behaviour of the concrete during heating and the potential occurrence of explosive spalling. In this test, the surface of a concrete specimen with dimensions 30 cm x 30 cm x 12 cm is heated with electric heating elements. The test specimen is placed on a balance to monitor the mass loss during heating. Furthermore, the temperatures and the pore pressures are measured in different distances from the heated surface. As the changes in pore pressure, temperature and mass are recorded, the test is often referred to as the “PTM test”.

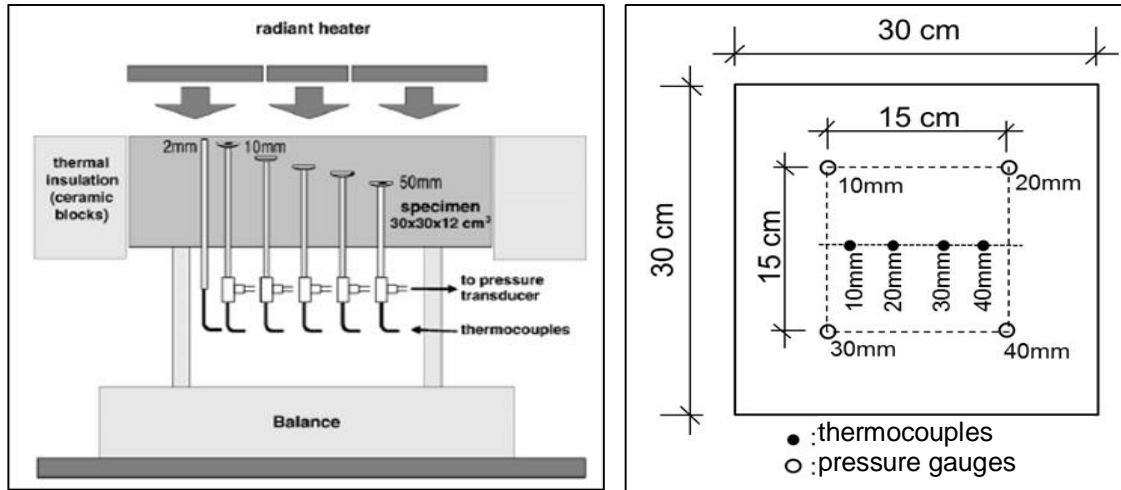


Figure 1: Test set-up according to [1] (left) and positions of temperature/pore pressure measurement chosen in the tests carried out at the VDZ (right)

At the VDZ, the original PTM test was modified by applying a lateral compressive load to the concrete specimens through a steel frame made of U-shaped profiles (Figure 2). Since compressive stresses are known to increase the probability of explosive spalling, it was expected that spalling would occur in some of the tests. Moreover, through the compressive stress it was intended to establish test conditions which are more similar to the conditions of a heated concrete element in practice.

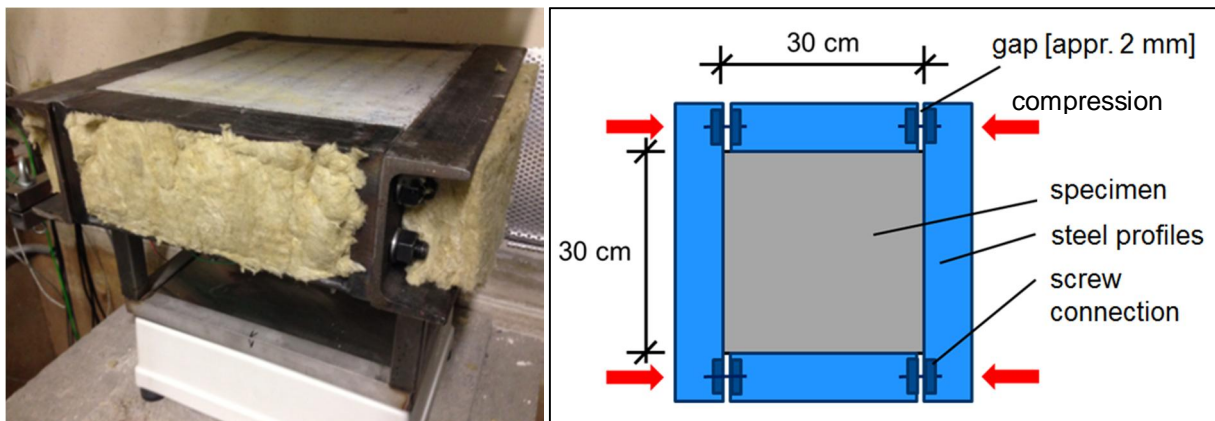


Figure 2: Steel frame employed at the VDZ tests

The test was carried out for normal strength and high strength concrete with five different cement types: Portland cement (CEM I), Portland-slag cement (CEM II/B-S), Portland-limestone cement (CEM II/A-LL), Portland-fly-ash cement (CEM II/B-V) and blast furnace cement (CEM III/A). For more detailed information on the test setup and the tested concretes see [1].

The main results of the tests during the previous project can be summarised as follows:

- While spalling had not been observed in PTM tests without a lateral compressive load described in the literature (even for very dense and high-strength concretes), in the previous project 7 out of 33 concretes showed explosive spalling. It can therefore be concluded that the application of compression is a decisive factor for the occurrence of spalling in the PTM test.
- In cases where explosive spalling occurred, very small pore pressures (less than 0.1 MPa) were measured, whereas
 - in the VDZ's PTM tests under compression, in which no spalling occurred, pore pressures up to approx. 1.4 MPa were recorded
 - in PTM tests carried out by other scientists, in which no spalling occurred, higher

pore pressures up to approx. 4 MPa were measured (e.g. [2]).

It can therefore be concluded that high pore pressures are not the most important factor causing the occurrence of explosive spalling of concrete. This confirms the conclusions of other authors (e.g. [3])

- Explosive spalling occurred for high-strength concretes containing silica fume as well as for a number of normal-strength concretes with blast furnace cements (CEM III/A) and Portland fly-ash cements (CEM II/B-V). It never occurred for normal strength concretes containing Portland cement (CEM I), Portland-limestone cement (CEM II/A-LL) or Portland-slag cement (CEM II/B-S).
- No spalling occurred for high-strength concretes with CEM II/B-V and CEM III/A which had been subjected to more intensive drying prior to the PTM test. This reconfirms the well-known influence of the moisture content on the occurrence of explosive spalling.

2. QUESTIONS AND HYPOTHESES AFTER THE PRECEDING PROJECT

The test results presented above brought up the following questions:

- What do the concretes for which explosive spalling occurred have in common?
- Is one (or are more) of the common characteristics responsible for the occurrence of explosive spalling?
- Why does a higher moisture content increase the susceptibility for explosive spalling in spite of the missing correlation between the magnitude of the pore pressures and the occurrence of spalling?

The following assumptions have been developed by the authors for why the concretes described above showed explosive spalling while other concretes in the research programme remained intact:

- **Influence of the pore size distribution**

Due to their pore size distribution, the moisture content of the affected concretes was generally higher at the time of testing, compared to other concretes tested. A higher moisture content could have a negative effect on the mechanical properties of concrete during heating, as e.g. suspected in [4].

- **Influence of the relative share of hydration products**

Due to the relative share of calcium hydroxide and CSH, the microstructure of the hardened cement paste of the affected concretes underwent more pronounced changes in the temperature range of up to 400 °C. These changes in the microstructure could result in greater differences between the thermal expansion of layers at different distances from the heated surface.

- **Influence of the interfacial transition zone (ITZ)**

Due to a less porous interfacial transition zone (ITZ) in the affected concretes, the thermal expansion of the aggregates generated comparatively higher tensile stresses in the hardened cement paste.

The relative contribution of these three phenomena to the occurrence of explosive spalling is examined in the ongoing project. The assumptions and the corresponding experiments to confirm or reject them will be presented in detail in the following paragraphs.

3. CONCRETE COMPOSITIONS FOR THE RESEARCH PROGRAMME

Table 1 shows the compositions of the concretes that were produced in 2018 for the experiments in the ongoing research project as well as their determined cube compressive strength. Based on a reference mix with 350 kg cement/m³ and a water/cement ratio w/c=0.55, prepared with four different cement types, the following parameters were varied: type of aggregate (gravel/sand; crushed quartzitic stone; crushed basalt), water cement ratio, cement content, addition of fly ash, addition of polypropylene (PP) fibres. Moreover, seven high strength concretes with and without the addition of PP fibres were produced.

Table 1: Compositions of the concretes in the test programme: designation and compressive cube strength (mean value of three tests on 150mm cubes at the age of 28 days after concrete production)

Reference concrete composition: cement content 350 kg/m³; w/c=0,55; Rhine gravel/sand grading curve B16				
Cement type->	CEM I Portland cement 42,5 R	CEM II/A-LL Portland- limestone cement 42,5 N	CEM II/B-V Portland-fly- ash cement 42,5 R	CEM III/A Blast furnace cement 42,5 N
Reference concrete composition	B 1 46.4 MPa	B 2 39.8 MPa	B 3 50.0 MPa	B 4 42.4 MPa
as reference, but crushed quarzitic stone B16 instead of gravel/sand	-	B 5 42.7 MPa	B6 52.2 MPa	-
as reference, but crushed basalt stone B16 instead of gravel/sand	B 7 54.6 MPa	-	-	B 8 (w/c=0,5) 59.5 MPa
as reference, but 318 kg cement/m ³ ; 80 kg fly ash/m ³	B 9 44.3 MPa	-	-	-
as reference, but w/c=0.60	B 10 41.5 MPa	B 11 33.6 MPa	B 12 40.6 MPa	-
as reference, but w/c=0.50	B 13 58.2 MPa	-	B14 56.8 MPa	B 15 56.1 MPa
as reference, but w/c=0.50, addition of pp-fibres (2 kg/m ³), superplasticiser	B 16 58.1 MPa	-	B 17 57.0 MPa	B 18 56.9 MPa
as reference, but cement content 400 kg/m ³	B 19 44.7 MPa	B 20 39.9 MPa	B 21 49.0 MPa	B 22 46.2 MPa
450 kg/m ³ cement; 50 kg/m ³ silica fume, 175 l/m ³ water; Rhine gravel/sand B16, superplasticiser .	B 23 94.7 MPa	B 24 86.8 MPa	B 25 96.8 MPa	B 26 87.5 MPa
450 kg/m ³ cement; 50 kg/m ³ silica fume, 175 l/m ³ water; Rhine gravel/sand B16, addition of pp-fibres (2 kg/m ³),superplasticiser	B 27 92.1 MPa	-	B 28 92.5 MPa	B 29 86.5 MPa

After their fabrication all test specimens are stored at 20 °C/100 % relative humidity (RH) for one year. It can therefore be assumed that at the beginning of the tests, the hydration will be concluded to a large extent.

After one year at 20 °C/100 % relative humidity, the specimens are relocated to three different relative humidities established in desiccators containing saturated salt solutions until they have reached an approximately constant mass. Table 2 shows the target relative humidities for the specimens in the project.

Table 2: Target relative humidities of concrete specimens and salt solutions used

saturated salt solution	relative humidity at 20 °C
potassium nitrate	appr. 95%
sodium chloride	appr. 75%
magnesium nitrate	appr. 55%

After the mass change of the specimens has become negligible and the target relative humidity is virtually reached throughout the whole specimens, they are heated and tested as described in the following chapters. As concrete spalling is known to take place already at relatively low surface temperatures of 300 °C or lower [5], the temperature range between 150 °C and 300 °C will be the focus of the experiments within the project.

4. Hypothesis 1: Negative effect of moisture content on the mechanical properties of concrete

4.1 Background

It is known (e.g. [6]) that with an increasing proportion of blast furnace slag and a decreasing proportion of Portland cement clinker in cement, the pore volume of the gel pores (pore radius 0.001 to 0.01 μm) increases in the hardened cement paste while accordingly the pore volume of the capillary pores (pore radius 0.01 to 100 μm) decreases. Similarly, due to the pozzolanic reaction of fly ash, the use of Portland-fly ash cement (CEM II/B-V) results in a reduced proportion of capillary pores when compared with Portland cement (CEM I) or Portland-limestone cement (CEM II/A-LL). With respect to the sorption isotherms, the Kelvin equation expresses the fact that the water vapour pressure decreases with increasing surface curvature, i.e. with decreasing radius of a capillary. Pores of different sizes will therefore be filled at different values of water pressure/relative humidity. Larger pores lose moisture first when water saturated concretes are exposed to gradually decreasing relative humidities.

The differences in the pore size distribution are directly reflected in the desorption isotherms determined: when comparing concretes with a similar total pore volume, concretes with a higher proportion of capillary pores (and correspondingly a lower proportion of gel pores) show lower equilibrium moisture contents (in particular for typical ambient relative humidities) than concretes with a higher proportion of gel pores (see Figure 3).

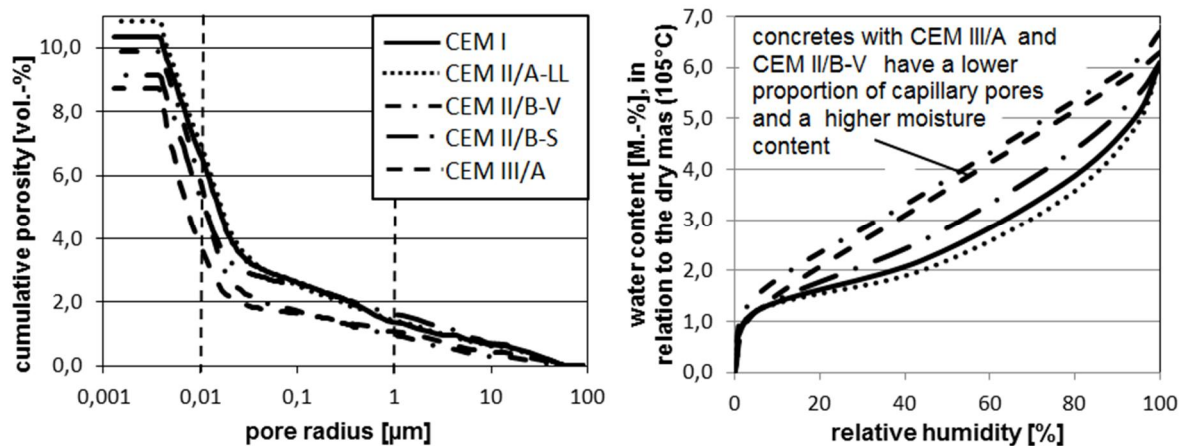


Figure 3 Pore size distribution (left) and desorption isotherms (right) (cement content 350 kg/m^3 ; $w/c=0,55$; Rhine gravel/sand grading curve B16)

As stated above, in the previous project high-strength concretes containing silica fume as well as in normal-strength concretes with blast furnace cements (CEM III/A) and Portland-fly-ash cements (CEM II/B-V) showed explosive spalling. Due to their pore size distribution, compared to other concretes tested,

- these concretes dried significantly more slowly after they were re-located from a climate of $20 \text{ }^\circ\text{C}/100\% \text{ RH}$ to a climate of $20 \text{ }^\circ\text{C}/65\% \text{ RH}$,
- the equilibrium moisture content of these concretes is generally higher at normal ambient conditions. This was demonstrated by determining the sorption isotherms.

Consequently, in spite of similar drying periods, the share of water-filled pores and the moisture content were often higher at the time of testing than for other concretes in the test programme.

4.2 Assumption with respect to the fire-induced spalling of concrete

A higher moisture content could have a negative effect on the mechanical properties of concrete during heating. A reduction in strength could promote the explosive spalling of concrete.

4.3. Experimental verification

4.3.1 Principle

Prisms 16 cm x 4 cm x 4 cm produced from the concretes in Table 1 are stored in three different climates until they have reached an equilibrium moisture content of 95% RH, 75% RH and 55% RH respectively. After heating these prisms in an electric furnace, their flexural and compressive strength is determined.

4.3.2 Residual strength of unsealed specimens

The prisms with three different relative moisture states are heated to temperatures of up to 300 °C. For these tests, to be close to the heating rate of the PTM tests in which spalling occurred, the heating rate of the furnace is selected to be as high as the electric furnace used in the project permits (approximately 7 K/min). After a uniform temperature is reached within the prisms, they are left inside the turned-off furnace to slowly cool down. Subsequently, their dynamic modulus of elasticity and their residual strength are tested.

4.3.3 "Hot strength" of sealed specimens

While for the tests with unsealed specimens, most of the moisture inside the concrete will have evaporated at the time of the strength test, a second series of tests will be performed with sealed specimens. During and after heating, these specimens should ideally maintain a moisture content as close as possible to the moisture content before heating. The strength is then tested in a hot condition. With these test, a potential negative influence of the moisture content on the concrete strength at the time of the elevated temperatures will be verified.

The requirement to "hold" the moisture during the heating time presents a significant challenge as the sealing should ideally

- remain largely intact at elevated temperatures and at the same time
- have a negligible influence on the result of the strength tests.

To identify a suitable sealing method, a number of sealing materials available on the market were tested in comparative tests. In these tests the mass loss of sealed concrete prisms heated to temperatures up to 230 °C was determined. Combinations of high temperature sealants (two-component epoxy or silicone sealants) with a wrapping of metal foils (aluminium or stainless steel) fixed with high temperature adhesive tapes (polyimide-film or aluminium) were examined. The test showed that in comparison the least moisture was lost when a combination of metal foils glued together at the joints with a high temperature epoxy resin and additionally fixed with a high temperature aluminium tape was used. No difference in mass loss was found between aluminium and stainless steel foils, therefore for reasons of price and its better handleability due to its lower stiffness, aluminium foil is used in the project. Furthermore, no relevant difference in mass loss was found between

- applying the epoxy to the whole surface area of the concrete prisms and
- applying it to the areas at the joints of the aluminium foil only.

This demonstrates that the sealing effect of the combined materials is mainly due to the metal foil while the function of the epoxy and the tape is limited to sealing the joints of the foil. Consequently, the epoxy and the tape were applied at the joints only in order to minimize their influence on the strength tests. The joint in the foil which is required in the longitudinal direction of the specimens is positioned at the upper side of the prism which is in compression during the flexural strength test. The foil itself is not applied tightly but with a certain "looseness" so it is not subjected to relevant tensile stresses during the tests.

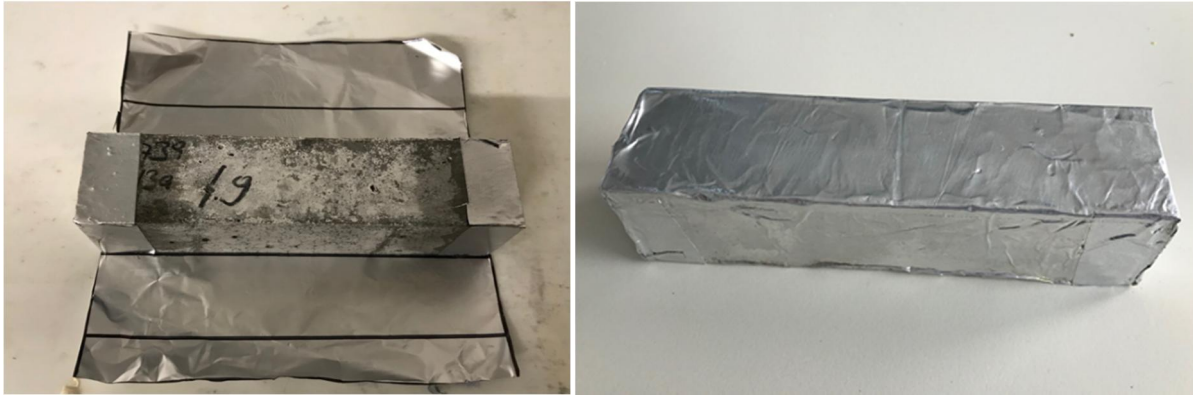


Figure 4 Sealing of concrete specimens 16 cm x 4 cm x 4 cm

A number of producers of high temperature epoxy sealants provided samples of their materials. These were compared in test with sealed prisms heated in a furnace. From the tested materials, one epoxy sealant resulted in the lowest mass loss during heating, which is why this product was chosen for all tests in the project. Following the product's specifications, the epoxy is cured for 2 hours at 65 °C after its application.

A fast heating rate as is chosen for the unsealed prisms (4.3.2) would result in pronounced temperature gradients in the concrete prisms (i.e. a hot surface and a much colder center) at the beginning of the heating time. This in turn would result in a premature failure of the sealing before the core of the specimens has reached the target temperature and the temperature distribution in the prisms is uniform. Comparative tests showed that for this reason, a slow heating rate of 1 K/min or lower should be chosen for the sealed prisms.

An appropriate maximum temperature for heating the prisms was identified by monitoring the mass loss of sealed prisms in a furnace as the temperature was increased gradually (1 K/min). Figure 5 shows the heating curve of the furnace and the corresponding mass loss of a sealed and an unsealed specimen (95% RH) of the same concrete batch. The mass was determined by briefly taking the specimens out of the furnace and quickly putting them back in before the specimens or the furnace could cool down considerably.

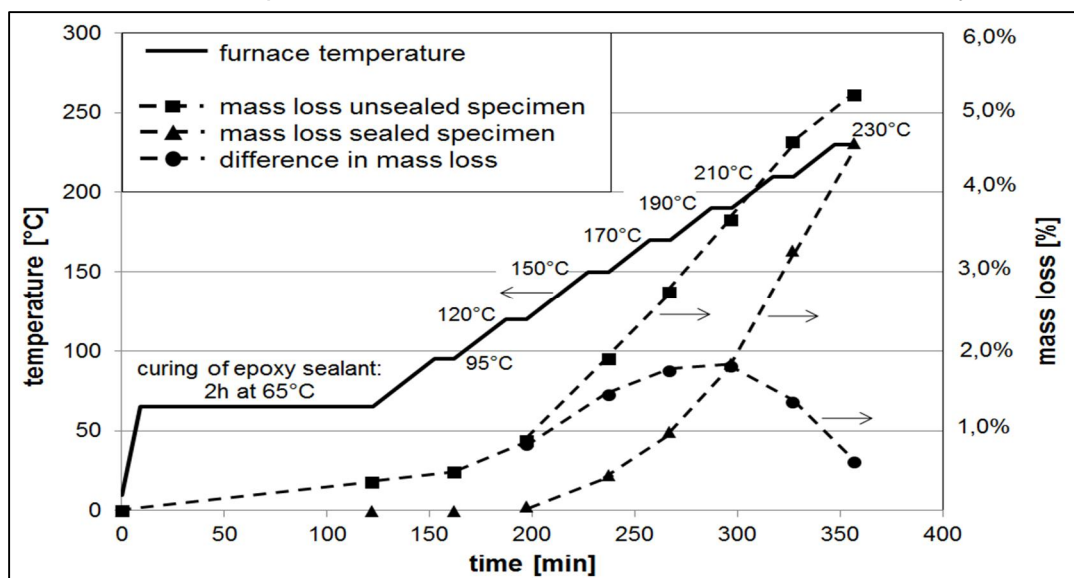


Figure 5 Furnace temperature and corresponding mass loss of sealed and unsealed concrete specimens with a relative humidity of 95% (composition: B13, see Table 1)

Up to 120 °C, the sealing is very effective: only little water can escape. At higher temperatures, the tightness decreases and more water is lost from the sealed specimens. At

a temperature of 190 °C the difference in mass between the sealed and the unsealed specimens is greatest while with a further rise of the temperature the sealing increasingly fails and both curves converge. A maximum temperature of 190 °C is therefore selected for the tests with sealed specimens. This temperature is in the order of magnitude of the temperature in a depth of approximately 1 cm from the heated surface at the time when spalling occurred in the PTM-test in the previous project. Therefore, if hypothesis 1 is true and a higher moisture content has a negative effect on the mechanical properties of concrete during heating, a temperature of 190 °C should be sufficient for a strength loss to show in the experiments.

5. Hypothesis 2: More pronounced heat-induced changes in the cement paste's microstructure due to a higher share of CSH

5.1 Background

After the addition of water to cement, fibrous calcium silicate hydrates (CSH) and calcium hydroxide $\text{Ca}(\text{OH})_2$ (Portlandite) are formed as hydration products as well as, in smaller quantities, ettringite and monosulfate. These hydration products are also referred to as cement gel.

When concrete is heated, the following processes take place in the cement paste:

- The free and physically bound water in the cement paste evaporates at temperatures of up to approx. 105 °C. This is associated with an expansion of the cement paste.
- From a temperature of approx. 150 °C, a dehydration of the calcium silicate hydrates (CSH) takes place in the hardened cement paste. This involves a movement of initially chemically bound water to the porous medium and is associated with a shrinkage of the cement paste. The rate of mass loss reaches a maximum at about 250 °C. Between 250 °C and 400 °C, the dehydration continues at a slower rate (constant temperature increase assumed).
- The chemical conversion of calcium hydroxide $\text{Ca}(\text{OH})_2$ to CaO and H_2O only takes place at temperatures of more than 500 °C, i.e. at temperatures that are outside the typical temperature range of the occurrence of spalling in concrete.

Hardened cement paste containing silica fume, fly ash or blast furnace slag contains a smaller proportion of calcium hydroxide than cement paste without these main constituents/additions. When complete hydration is assumed, this corresponds to a larger proportion of CSH phases.

While unloaded concrete specimens generally show a positive elongation (i.e. a size increase) when heated, specimens that are heated under a constant compressive loading for the first time may shrink depending on the load level (e.g. [7]). The so-called "transient thermal strain" (TTS) can be defined as the difference between the thermal strain under load and the free thermal strain [8].

5.2 Assumption with respect to the fire-induced spalling of concrete

It can be expected that when the above-mentioned main constituents/additions (blast furnace slag/fly ash or silica fume) are used, the microstructure of the hardened cement paste undergoes more pronounced changes in the temperature range of up to 400 °C than without their use, due to the larger proportion of CSH phases. These changes in the microstructure could result in greater differences in the thermal expansion between layers at different distances from the heated surface – particularly under compressive stresses – and in this way contribute to the explosive spalling of concrete.

5.3 Experimental verification

Cylinders with a length of 30 cm and a diameter of 15 cm were produced from the concretes in Table 1. From these cylinders, tubular specimens with an outer diameter of 8.0 cm and an inner diameter of 5.2 cm have been drilled with a diamond core drill device. They are stored in three different climates until they have reached an equilibrium moisture content of 95% RH, 75% RH and 55% RH respectively.

The tubular form was selected because due to the relatively small wall thickness of only 1.4 cm, a uniform hygral state can be reached in a practicable time. At the same time,

relevant compressive loads can be applied in the specimens' longitudinal direction without a premature buckling failure (which would have to be expected for thin solid specimens).

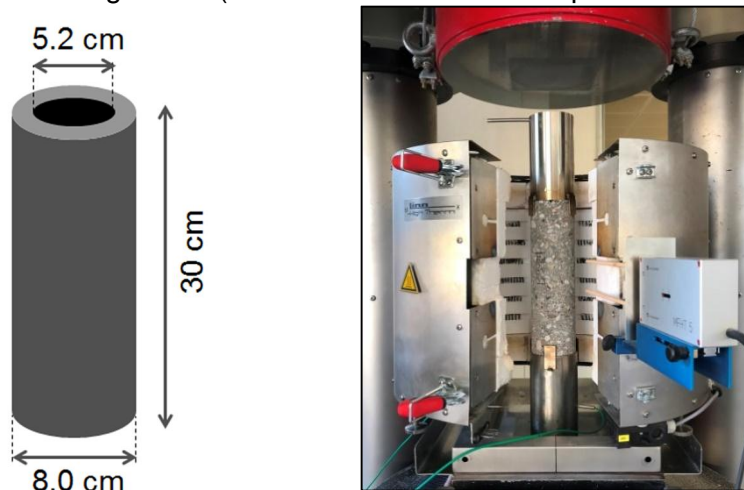


Figure 6 Specimens (left) and test setup (right) to measure the thermal expansion with and without compressive loading

The test setup in Figure 6 is applied to measure the thermal expansion of concrete specimens with different moisture contents. The specimens are placed in a tube furnace which is heated to temperatures of up to 500 °C. In this way, it can be verified if the thermal expansion of cement paste containing silica fume, blast furnace slag or fly ash differs from the expansion of cement paste without these main constituents/additions. Moreover, by comparing the free thermal strain without loads and the thermal strain test under a compressive load, the TTS can be determined for different concrete compositions and different relative moisture contents.

6. Hypothesis 3: Higher thermal stresses due to a denser ITZ

6.1 Background

The Interfacial Transition Zone (ITZ) is the region of the cement paste around the aggregate particles, which is perturbed by the presence of the aggregate. Its origin lies in the packing of the cement grains against the much larger aggregate, which leads to a local increase in porosity [9].

Generally, the ITZ contains excess Portlandite compared to the bulk cement paste, and the porosity in the ITZ is higher than in the bulk. Silica fume in high strength concrete fills the space around the aggregates and triggers a pozzolanic reaction converting Portlandite to CSH. This results in a less porous ITZ [10]. Similarly, in concretes with cements containing fly ash or blast furnace slag, less Portlandite is formed in comparison with CEM I cements due to the lower clinker content. Moreover, blast furnace slag and particularly fly ash consume Portlandite to form CSH.

When concrete is heated, the aggregates expand while from temperatures of approximately 150 °C the cement paste shrinks due to its dehydration (see paragraph 5.1). This can lead to internal stresses inside the heated concrete.

In the previous project the separated parts of the concretes that had spalled in the PTM test were visually inspected. For all affected concretes, it was found that a large part of the aggregates had been thoroughly separated from the bulk concrete and was almost completely free from the remains of hardened cement paste [1].

6.2 Assumption with respect to fire-induced spalling of concrete

Presumably during the PTM test, the bond between aggregate and hardened cement paste is influenced by processes in the area of the interfacial transition zone (ITZ). This may be due to an incompatibility between the aggregates which expand due to the influence of temperature and the cement paste. Explosive spalling could be encouraged by the fact that for the respective concretes in the test programme, the thermal expansion of the aggregates

generated comparatively higher tensile stresses in the hardened cement paste due to a less porous contact zone (ITZ).

6.3 Experimental verification

Cubes with a side length of 10 cm were produced from the concretes in Table 1. From these cubes, slices with an area of 6 cm x 4 cm and a thickness of 1 cm have been cut with a diamond saw. They are stored in three different climates until they have reached an equilibrium moisture content of 95% RH, 75% RH or 55% RH respectively. After heating the slices in an electric furnace, polished thin sections are produced and assessed under a reflected-light microscope to examine their crack pattern.

Similar to the approach described for the prisms (paragraph 4.2) both

- unsealed specimens heated up to 300 °C with a higher heating rate (appr. 7 K/min)
- sealed specimens heated up to 190 °C with a lower heating rate (1K/min or lower)

will be examined after they have cooled down.

7 Summary of the experimental programme

Table 3 summarises the three hypotheses for why spalling occurred in the previous project as well as the experimental programme to verify them. This experimental programme will be complemented by tests on 14 specimens 80 cm x 70 cm x 24 cm which will be subjected to a standard fire according to [11]. The purpose of these tests will be to verify if findings of the previous project using the PTM test can be confirmed on a larger scale.

Table 3: Experimental programme to verify the three hypotheses on why some concretes in the previous research programme showed explosive spalling while others remained intact

Hypotheses for why some concretes in the previous research programme showed explosive spalling while others remained intact	variation of possible influencing parameters ^{a)}		
	influence of the chemical and physical properties of the hardened cement paste	influence of the moisture content	influence of compressive load
1. A higher moisture content of the affected concretes had a negative effect on the mechanical properties during heating and in this way promoted spalling.	verified through determination of the flexural and compressive strength of heated concrete prisms		_____
2. For the affected concretes, a larger proportion of CSH phases resulted in more pronounced temperature-induced changes in the microstructure of the hardened cement paste. These again entailed greater differences between the thermal expansion of layers at different distances from the heated surface which promoted spalling.	verified through measurement of the thermal expansion of tubular concrete test specimens during heating		
3. Due to a denser ITZ, the incompatibility between the thermal expansion of cement paste and aggregates resulted in greater thermal stresses for the affected concretes. This promoted spalling.	verified through image analysis (reflected-light microscopy) of the crack pattern of thin concrete slices after heating		

^{a)} further variation of influencing parameters: heating rate, sealed vs. unsealed specimens

At the time of drafting this report, only preliminary experiments have been carried out. It is expected that first results can be presented at the “6th International Workshop on Concrete Spalling due to Fire Exposure” in Sheffield.

FUNDING NOTE

The present project is funded within the framework of the program for the promotion of industrial joint research (IGF) by the Federal Ministry of Economics and Energy on the basis of a decision of the German Bundestag.

REFERENCES

1. Jochen Reiners, Christoph Müller: The influence of the pore size distribution and the chemical composition of cement paste on the explosive spalling of concrete, Proceedings from the 5th International Workshop on Concrete Spalling, Borås, 2017
2. Kalifa, P. et al. – Spalling and pore pressure in HPC at high temperatures. Cement and Concrete Research 2000, 30, pp 1915-1927
3. Bazant - Analysis of Pore Pressure, Thermal Stress and Fracture in Rapidly Heated Concrete, International Workshop on Fire Performance of High-Strength Concrete, NIST, Gaithersburg, MD, February 13-14, 1997
4. Jansson, R.- Fire Spalling of Concrete, Theoretical and Experimental Studies. Stockholm 2013
5. Fédération internationale du béton (fib) - Fire design of concrete structures – materials, structures and modelling. State-of-the-art report. 2007
6. Romberg, H. - Zementsteinporen und Betoneigenschaften. Beton-Informationen 1978
7. Khoury, G. - Strain of heated concrete during two thermal cycles. Part 1: strain over two cycles, during first heating and at subsequent constant temperature. Magazine of Concrete Research, 2006, 58, No. 6, August, 367–385
8. Mindeguia et al. - Parametrical study of transient thermal strain of ordinary and high performance concrete Cement and Concrete Research 48 (2013) 40–52
9. Scrivener, K. et al.- The Interfacial Transition Zone (ITZ) Between Cement Paste and Aggregate in Concrete; Interface Science, October 2004, Volume 12, Issue 4, pp 411–421
10. Bentur, A. - Microstructure of high strength concrete, Darmstädter Massivbau-Seminar 6, 1991
11. ISO 834-1:1999 Fire-resistance tests - Elements of building construction - Part 1: General requirements

Heat-Induced Concrete Spalling of New and Aged Concrete Encased Steel Columns in Hydrocarbon Pool and Jet Fires

Holly Warren¹, David Wickham^{1,*}

¹ AkzoNobel, Newcastle, United Kingdom

* Corresponding author

(David.Wickham@akzonobel.com, International Paint Ltd., Stoneygate Lane, Felling, Gateshead, Tyne & Wear, NE10 0JY, United Kingdom)

ABSTRACT

Concrete is widely used as a passive fire protection for structural steel in downstream oil and gas assets, such as processing and storage of hydrocarbons. In many cases these assets are ageing, and the concrete has degraded due to process operations and environmental conditions. The concrete degradation varies greatly, including; loss or damage of topcoat, steel substrate corrosion, cracking, retention system corrosion/damage/missing, loss in concrete thickness and in some cases potential for falling hazard from cracked and dis-bonded concrete. Both hydrocarbon pool fires and jet fires are credible fire scenarios for these downstream asset sites. Spalling of concrete passive fire protection at elevated temperatures and potential detachment of installed systems have caused great concern for such asset owners, when planning annual maintenance and repair programs. The work presented in this paper was undertaken to meet the demands in the oil and gas industry for a better understanding of passive fire protection and repair solutions.

This paper reports an experimental series conducted on four, unloaded concrete encased steel columns, with approximate dimensions 350 x 350 mm by 1500 mm height. Two recently cast columns and two aged columns, incorporating repair schemes, are tested in accordance with both hydrocarbon pool fire (UL 1709) and jet fire (ISO 22899-1) test standards.

KEYWORD: Reinforced-concrete column, hydrocarbon pool fire, jet fire, aged concrete, concrete repair.

INTRODUCTION

Current literature on concrete spalling behaviour in fire is principally concerned with two areas of research; firstly, the effects of spalling on structural performance of reinforced concrete elements and secondly, additives such as polymer fibres used to mitigate against spalling. Concrete spalling has been described in three different ways [1]; aggregate spalling, corner spalling and explosive spalling. Explosive spalling is of most concern for structural integrity, though any concrete spalling negatively impacts the heat transfer through a section.

Much of the current knowledge of spalling has been determined from modelling or experimental testing. Design guidance in Eurocode 2 [2] only requires spalling checks to be undertaken where the moisture content is greater than 3 %. These involve calculating

the reduction in load-bearing capacity assuming loss of concrete cover to the steel reinforcing bars (except in cases where concentration of reinforcement is considered high enough). Fire resistance ratings for reinforced concrete structures are often based on tabulated data, that has largely been generated from 'standard' fire tests such as that described in BS 476-Part 20 [3].

Ali et al. [4] reports explosive spalling of loaded, normal strength concrete (NSC), reinforced-concrete slabs, tested in a hydrocarbon fire. All 3 slabs tested recorded explosive spalling after 2 minutes of testing, with a maximum depth of 20 mm. The specimens had 40 mm concrete cover to the tension reinforcement, average concrete strength of 42 MPa at 28-days and average moisture content of 4.3 %.

The factors that influence explosive spalling have been outlined [5], including, "Material parameters ... of initial moisture content, concrete permeability, porosity and the presence of cracks, aggregate type, aggregate size and amount of reinforcement. Geometric factors include section shape and size. Environmental factors include heating rate and profile, temperature level and thermal restraint."

This paper focusses on the behaviour of concrete being used as passive fire protection (PFP) in the oil and gas sector. Concrete is used to protect steel beams, columns, vessel skirts, pipe racking supports, etc. A typical thickness of NSC used to provide 90 or 120 minutes PFP to structural steel is 50 mm [6,7]. Generally, the PFP provides only fire protection and no contribution to structural load-bearing capacity is accounted for in design of the concrete.

EXPERIMENTAL PROGRAMME

Test Configuration

This paper presents an experimental investigation to evaluate what level of spalling would occur in 1500 mm high, unloaded concrete encased steel columns, subject to a furnace hydrocarbon pool fire to UL 1709 test standard [8] and jet fire to ISO 22899-1 test standard [9].

UL 1709 test standard [8] outlines the acceptable tolerances for the temperature curve, controlled by gas furnace thermocouples, whereas ISO 22899-1 standard expresses release conditions which the specimens need to be exposed to, to simulate a 3 kg/s natural gas jet fire, when the test subject is 9 m from the release. ISO 22899-1 standard is based on large and medium scale tests dating back to 1992, with an average heat flux calculated and measured [9] of 240 kW/m² and peak heat flux of 300 kW/m². Among other parameters, the variation of heat flux is influenced by specimen geometry. Therefore the ISO 22899-1 standard outlines requirements for the PFP specimen geometry, size and orientation. The PFP columns reported in this paper were tested generally in line with the configuration for tubular specimens, mounted in the external configuration [9], as shown in Figure 1.

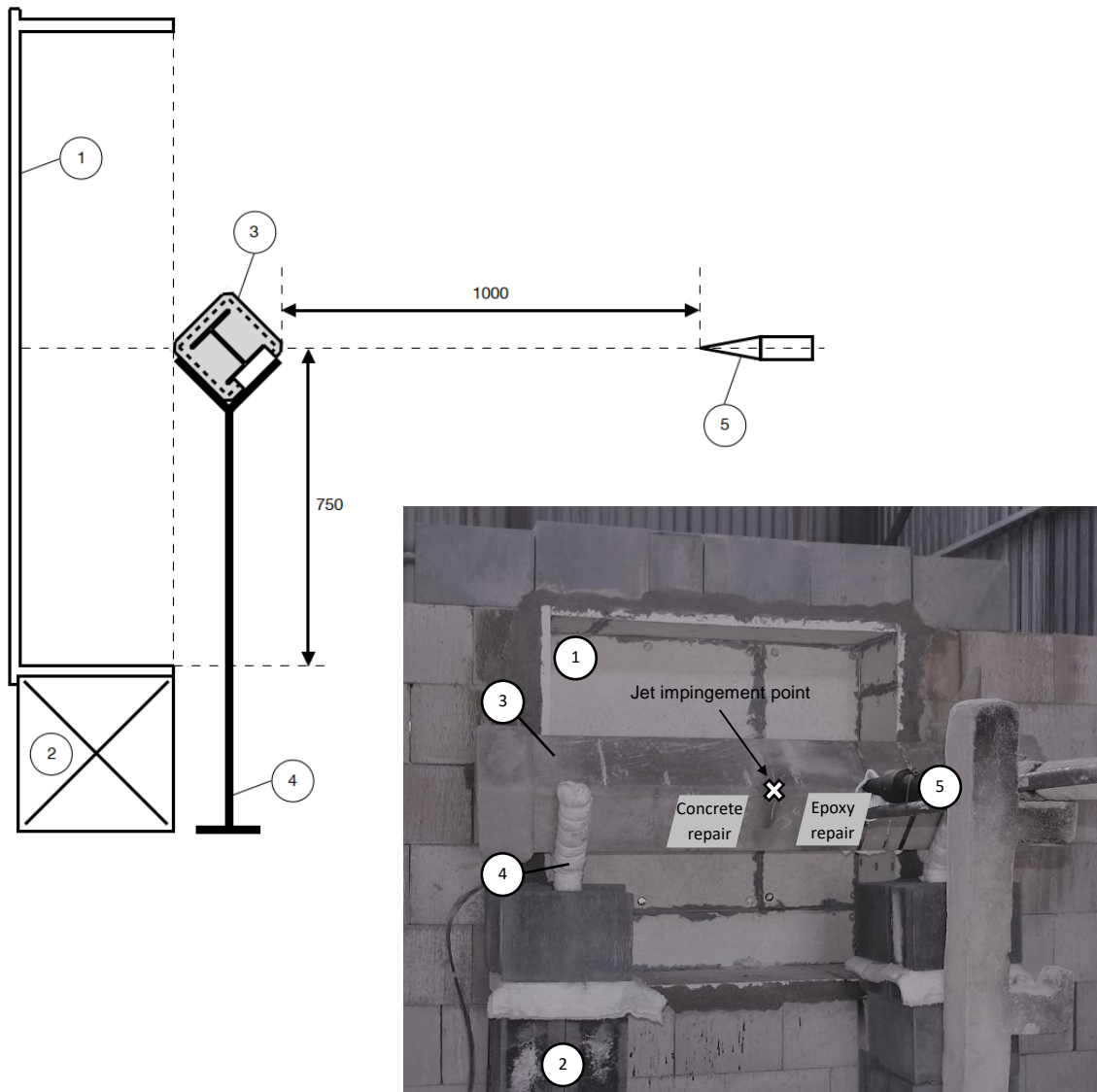


Figure 1 Jet fire external configuration, adapted from [9] (1-flame recirculation chamber, 2-flame recirculation chamber support, 3-test specimen, 4-test specimen support, 5-jet nozzle) (dimensions in millimetres).

When testing a tubular specimen in a jet fire [9], the flow of the jet fire flame over the test piece is predictable, hence the flame luminosity and thickness are similar across all tests. From these flame patterns and post-performance of PFP materials, the areas of greatest heat flux are known. Therefore, it is possible to assume the specimen has been subject to the average and peak heat fluxes mentioned earlier. However, the jet fire flame flow over the square cross-section specimens tested here is different, and therefore it is difficult to say with a high degree of confidence that the heat fluxes are as outlined in [9]. Unfortunately, due to economic limitations, S-type flame thermocouples were not used to measure flame temperatures.

Experience of the visual test observations, for flame luminosity and thickness showed the flame as not as optically thick as in a standard ISO jet fire test [9], therefore we have assumed that whilst a peak heat flux of 300 kW/m^2 may not have been reached, an average value of 240 kW/m^2 was assumed which approximates to a flame temperature of $1200 \text{ }^\circ\text{C}$.

Test Specimens

Four encased columns were tested, two newly cast columns with external dimensions of approximately 350 x 350 mm and two aged columns taken from a structure prior to demolition, approximately 320 x 320 mm, each subject to a hydrocarbon pool fire and jet fire. Standard steel universal column I-sections used were; UC 254x254x73 and UC 203x203x46, for the new and aged specimens, respectively. Standard universal column dimensions are widely documented in the public domain and are also shown in Figure 2. The jet impingement point in the jet fire tests was at the bottom right hand corner.

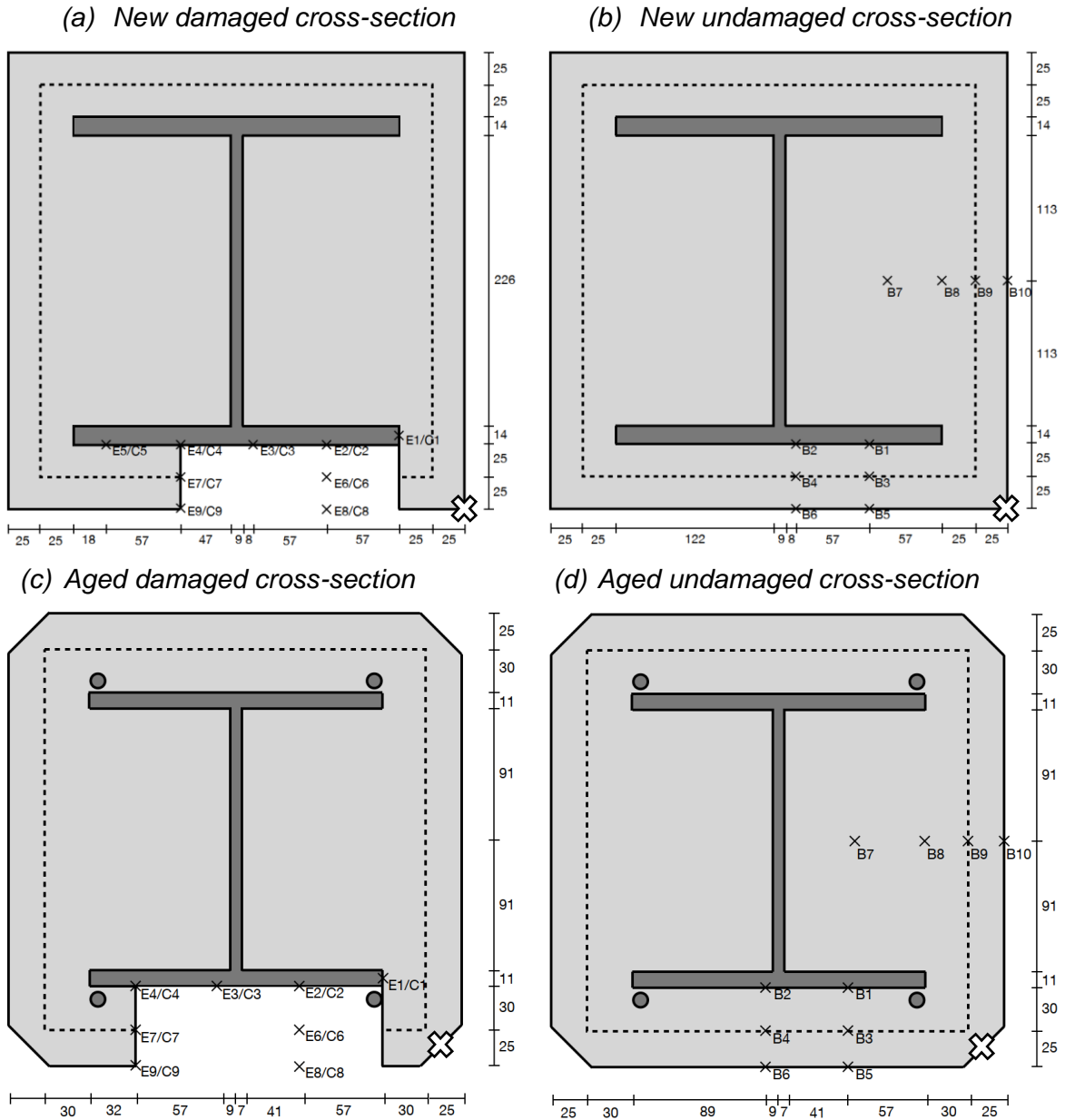


Figure 2 Cross-section schematic of the thermocouple distribution in (a)-(b) new columns and (c)-(d) aged column and the sectional dimensions (dimensions in millimetres), with jet impingement point indicated by the X.

The specimens incorporated two repaired damage areas, to assess the response of an epoxy intumescent material and a common concrete repair material, as concrete PFP repair schemes at high temperature. The undamaged cross-sections in Figure 2 were in

line with the jet impingement point, whereas the damaged cross-sections with the repair materials were off-centre by 150 mm, either side of the impingement point. The damaged areas were taken as a complete loss of PFP concrete, back to the steel member. The areas were approximately 175 mm by 175 mm square, equating to 30,000 mm² area loss, which exceeds the criteria of 3,000 mm² from FABIG Technical Note 13 [11] used in the oil and gas industry as an acceptable area of unprotected steel.

The aged column specimens had additional 10 mm diameter reinforcement bars at each of the four flange tips. All specimens had 2.6 mm diameter wire mesh positioned approximately half-way through the PFP concrete cover, with the new column having a 50 mm mesh spacing and the aged having a 100 mm spacing. Figure 2 shows the PFP concrete cover thickness between the new and aged columns were comparative with approximately 50 mm and 55 mm, respectively.

Normal strength readymix concrete (NSC) was used for the new columns, with a maximum aggregate size of 10 mm, slump of 70 mm, mean ambient compressive cylinder strength of 37 MPa and ambient compressive cube strength of 48 MPa at the time of testing (48 days curing in a 10 °C temperature and approximately 55 % air humidity controlled enclosure). The aged columns were approximately 40 years old with a mean ambient compressive cube strength of 22 MPa at the time of testing. While the heated testing was undertaken unloaded, the difference in strength does show that the concrete mix is not consistent between the aged and new specimens.

An Elcometer 7410 was used to monitor moisture content at the concrete surface, prior to testing. The average new column moisture content reduced from 5.8 % (14-day post cast), 5.5 % (21-day post cast) to 4.8 % at the time of testing. The aged concrete had a similar average moisture content at the time of testing of 4.7 %.

Instrumentation

Temperatures were recorded at three cross-sections with type K thermocouples, in both the undamaged (10 thermocouples) and damaged areas (8-9 thermocouples in each of the epoxy intumescent and common concrete repair material). Figure 2 shows the positions of the thermocouples and the new and aged specimen cross-sectional dimensions. Additionally, there were 20 thermocouples attached to the new column specimen, proportional to the steel length, in line with UL 1709 standard [8]. It was not possible to add these thermocouples nor E5 and C5 thermocouples (see Figure 2(c)) in the aged concrete without destroying the specimen in the process. Furthermore, the thermocouple design allowed for redundancy, Table 1 lists the damaged thermocouples.

EXPERIMENTAL RESULTS AND DISCUSSION

Overview of the Test Results

This paper presents the key results from the testing in terms of specimen temperatures and spalling observations. The jet fire test durations were limited to 120 minutes. Table 1 summarises the key test results.

Table 1 Key test results.

	PFP Column Test			
	Hydrocarbon Pool Fire New	Hydrocarbon Pool Fire Aged	Jet Fire New	Jet Fire Aged
Damaged thermocouples	-	E5	B4, B6, B9	E5, C4, C5
Maximum fire environment temperature (°C)	1138 at 9 min	1143 at 12 min	1200 at 10 min*	1200 at 10 min*
Maximum average steel sectional temperature below concrete PFP (°C)	334 at 120 min (UL1-UL20)	492 at 120 min (B1, B2)	327 at 118 min (UL1-UL20)	477 at 117 min (B1, B2)
Maximum average steel flange temperature below epoxy (°C)	274 at 120 min (E2, E3)	212 at 120 min (E2, E3)	285 at 118 min (E2, E3)	302 at 120 min (E2, E3)
Maximum average steel flange temperature below concrete repair (°C)	358 at 120 min (C2, C3)	310 at 120 min (C2, C3)	353 at 118 min (C2, C3)	358 at 120 min (C2, C3)
Test comments				
Concrete PFP	Aggregate spalling on all exposed surfaces, approximately 1-2 mm depth.	Corner spalling in a few places. Expanded predominantly vertical crack widths of approximately 5 mm, from assumed aged concrete cracks.	Aggregate spalling on lower face exposed to jet fire, approximately 1-2 mm.	Aggregate spalling, 14 mm on back right lower surface.
Epoxy repair material	Epoxy expansion in a mushroom cross-section shape.	Epoxy expansion in square cross-section shape.	Varying epoxy expansion depths, expanded thickness regularly sloughing off due to jet erosion.	Varying epoxy expansion depths, expanded thickness regularly sloughing off due to jet erosion.
Concrete repair material	Explosive spalling of the cover, early during the test. Approximately 10 mm depth in the center.	Explosive spalling of the cover, early during the test. Approximately 10 mm depth in central third vertical strip.	Early explosive spalling of the cover. Approximately 10 mm depth in circular disks.	Early explosive spalling of the cover. Approximately 16 mm depth at right hand half.

* Typical from jet fire conditions

Spalling Observations

Figure 3 shows both the assumed jet fire temperature curve against the average concrete repair surface temperatures and the average steel temperatures for both the aged and new concrete columns; below the concrete PFP, epoxy and concrete repair material. The new column, surface concrete repair material shows an average (C8, C9 thermocouples) of 1068 °C during 120 minutes, which is approximately 140 °C difference to the assumed jet fire curve. Though these thermocouples were positioned approximately 1 mm below the surface, aggregate spalling was visualised during the initial 2 minutes of the new column test, causing the thermocouples to be exposed. Similarly, the cover of the concrete repair material was also seen to have spalled during the aged column test, the post-test spalled depth was measured as 16 mm.

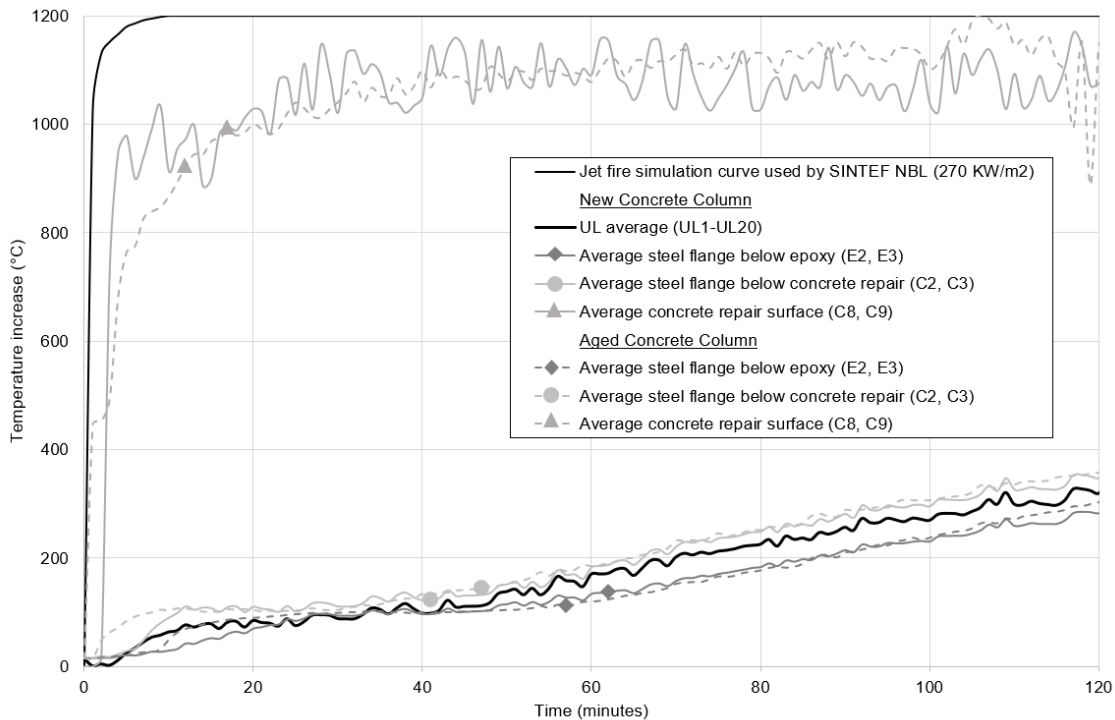


Figure 3 Temperature increase for new (solid lines) and aged (dashed lines) column specimens tested in jet fire conditions.

The surface thermocouples in the concrete repair material were exposed in the hydrocarbon testing, due to explosive spalling of the cover, at an early stage. Therefore Figure 4 shows the average concrete repair surface (C8, C9) to be high, similar to the gas furnace temperature.

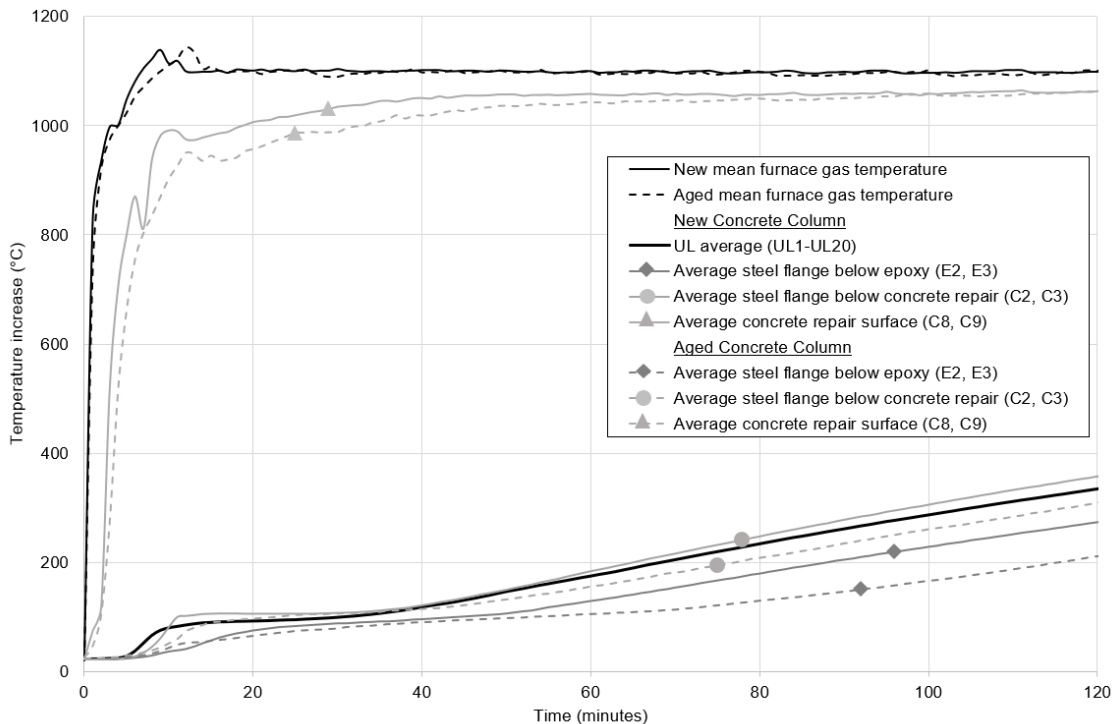


Figure 4 Temperature increase for new (solid lines) and aged (dashed lines) column specimens tested in hydrocarbon pool fire conditions.

For both heating scenarios, the concrete repair material protects the steel in a similar fashion to the concrete PFP, shown by the circle marker in Figures 3 and 4. The average 120 minute, steel flange temperature below the concrete repair (C2, C3) reached 347/358 °C in new/aged column specimens tested in jet fires and 358/310 °C in new/aged column specimens tested in hydrocarbon fires. The steel temperature below the epoxy material (E2, E3) is protected more efficiently, with temperatures at 120 minutes reaching an average of 283/302 °C and 274/212 °C, respectively.

Concrete PFP Temperature Evolution

Figure 5 shows the concrete PFP temperature profile for the new column tested in jet fire conditions. The thermocouples at the steel flange (B1, B2) and mesh (B3) depths (50 mm and 25 mm, respectively) show a steady temperature increase, however those near the concrete surface (B5, B10) show large temperature fluctuations. This uneven temperature distribution in the section is assumed to be caused by the jet flame flow around the section size and shape. The decrease in concrete surface temperature is postulated to be caused by both a lack of recirculation of the flame, coupled with the non-ignited central part of the jet, locally cooling the specimen. The temperature profile of the aged concrete column, shows a similar local cooling behaviour at the surface, seen in Figure 6. The proposed cooling behaviour aligns with the standard ISO/TR 22899-2:2013 (E) [12] statement, which comments that, "The heat fluxes are highest in the upper part of the chamber and lowest in the corners and at the jet impact zone."

Comparatively, Figures 7 and 8 show the new and aged column temperature profiles for the hydrocarbon pool fire condition. These are similar, showing a continual gradual temperature increase through the depth of the section. After 120 minutes the temperature profile is approximately linear, reaching an approximate maximum at the surface of 950 °C and 350 °C/500 °C at the effective steel flange depth for the new/aged specimens, respectively. The lower effective steel flange temperature in the new concrete encased steel column is likely caused by the increased internal moisture content.

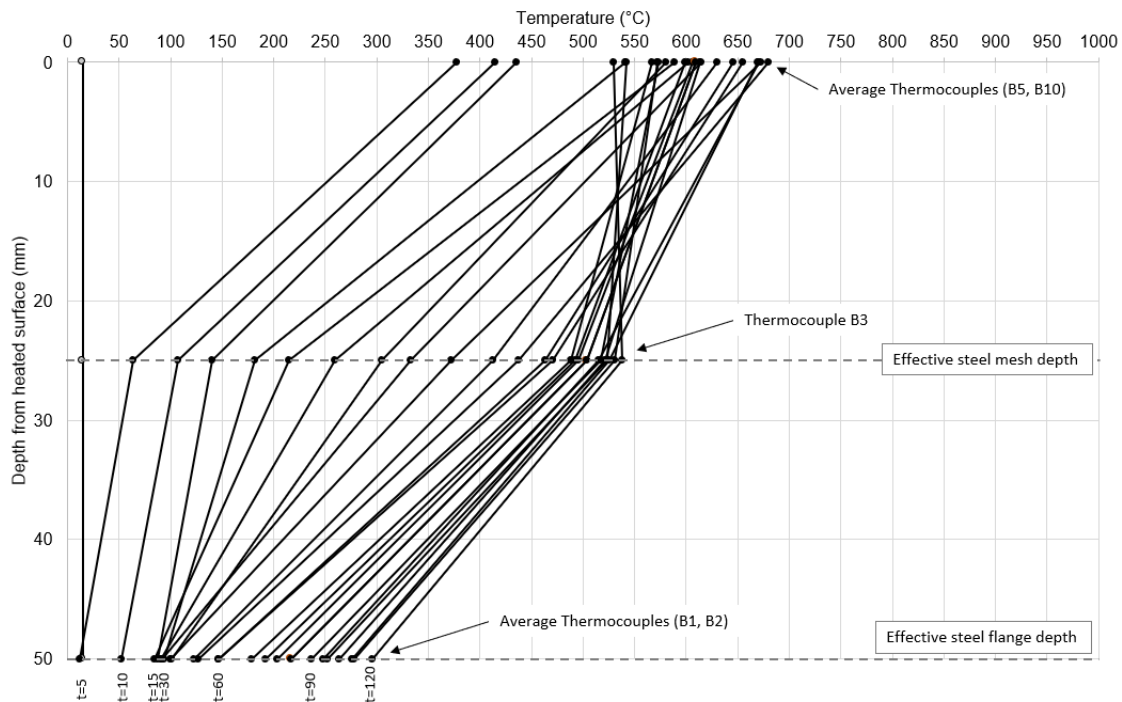


Figure 5 Concrete PFP temperature profile from heated surface to steel flange for new column specimen tested in jet fire conditions.

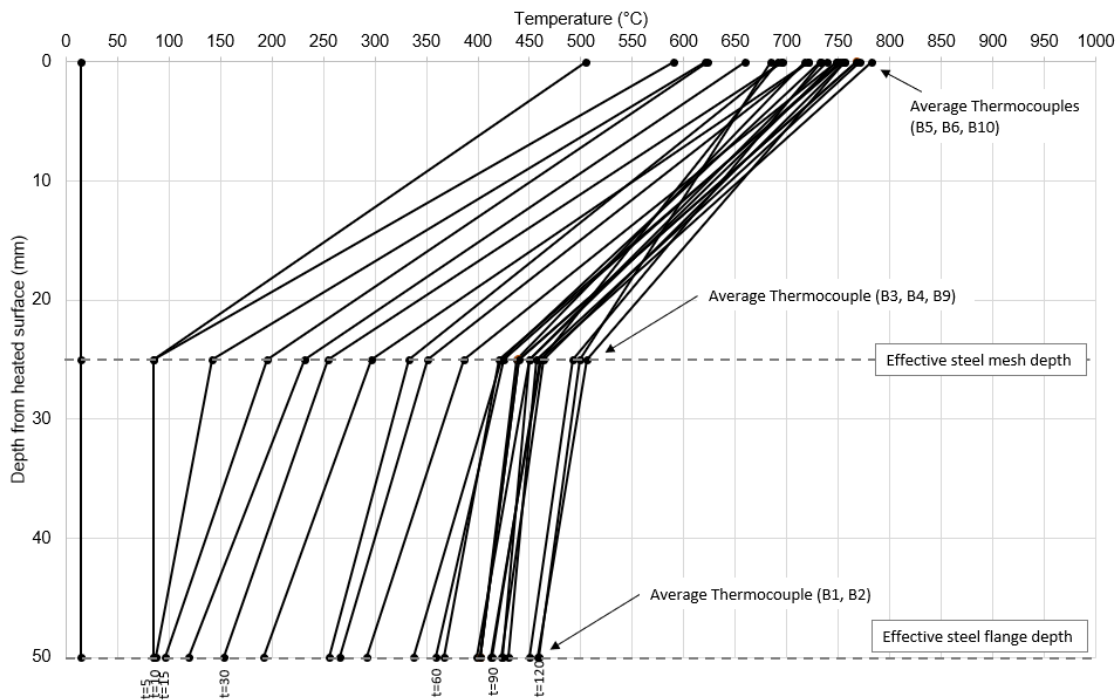


Figure 6 Concrete PFP temperature profile from heated surface to steel flange for aged column specimen tested in jet fire conditions.

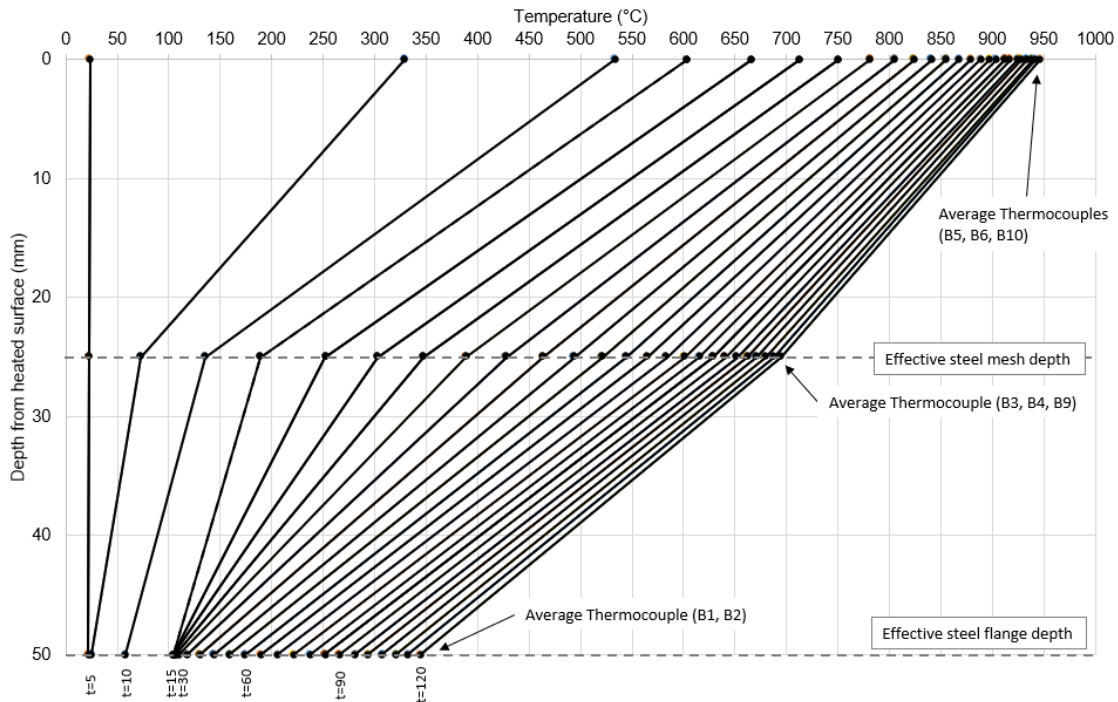


Figure 7 Concrete PFP temperature profile from heated surface to steel flange for new column specimen tested in hydrocarbon pool fire conditions.

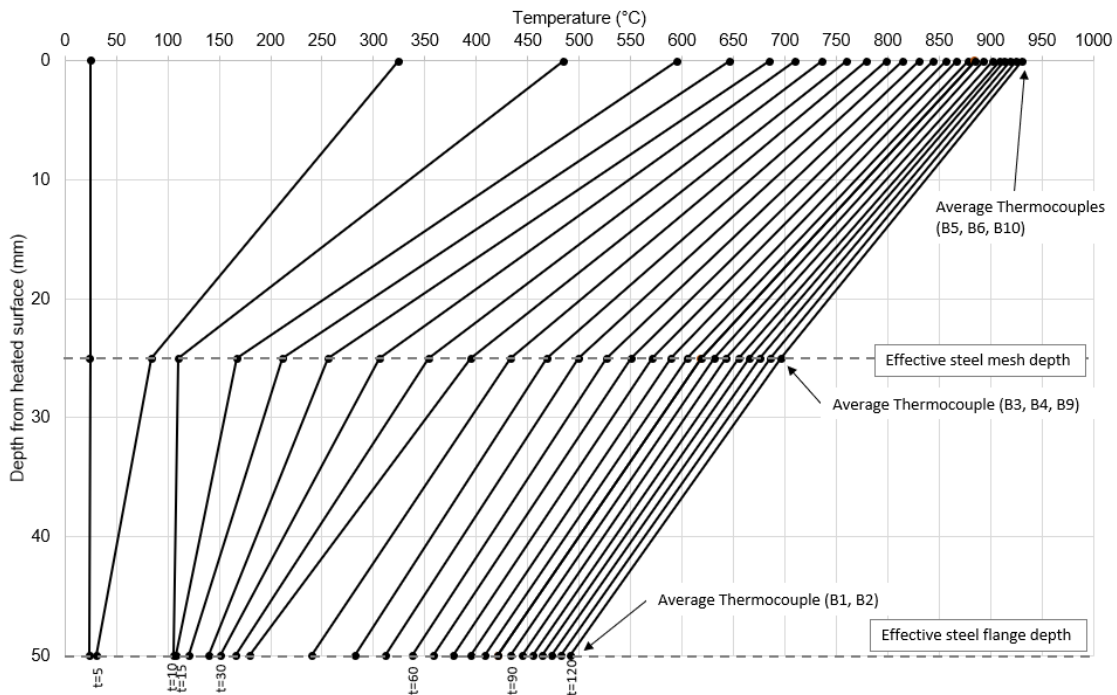


Figure 8 Concrete PFP temperature profile from heated surface to steel flange for aged column specimen tested in hydrocarbon pool fire conditions.

CONCLUSION

This paper has presented a series of tests on unloaded concrete encased steel columns, tested in both a hydrocarbon pool and jet fire condition. A recently cast column and an aged column, which each incorporated an epoxy intumescent and common concrete repair

material, were tested in both fire conditions. The specimen temperatures and spalling observations are discussed.

Overall limited spalling was visualised for the high temperature, erosive conditions of the fires. Aggregate spalling of the passive fire protection concrete was recorded in all tests, in localised areas, up to a maximum of 14 mm depth in the aged jet fire test. The concrete repair material lost approximately 10-16 mm cover by explosive spalling early in the testing. The new and aged concrete PFP behaved in a similar fashion, though existing cracks in the aged concrete were seen to expand on heating. The steel temperature of the aged concrete specimens reached higher average temperatures than the new columns, this is attributed to both the cracking and likely increased internal moisture content of the new columns compared to the aged. It is important to note that these specimens were unloaded, whereas literature shows that loaded members would spall more [5].

The concrete repair material behaved similarly to the PFP concrete, keeping the structural steel temperature low at 347/358 °C and 358/310 °C for new/aged column specimens, after 120 minutes, in jet and hydrocarbon fires, respectively. The epoxy repair material protected the steel more efficiently, with temperatures after 120 minutes reaching an average of 283/302 °C and 274/212 °C, respectively. Temperature profiles through the concrete PFP showed a gradual increase for the hydrocarbon pool fires, whereas the surface temperatures near the jet fire impingement point were seen to cool at later stages in the testing. It is proposed that the decrease in concrete surface temperature is caused by both a lack of recirculation of the flame and the non-ignited central part of the jet, locally cooling the surface.

The work presented in this paper was undertaken to meet the demands in the oil and gas industry for a better understanding of PFP and repair solutions. The observations during testing of the degree of spalling in concrete encased structural steel and two repair materials, provides useful data, however research is needed to further understand the spalling mechanisms that may occur in steel protected with concrete PFP under hydrocarbon pool and jet fire conditions.

REFERENCES

1. Deeny, S, Stratford, T., Dhakal, R.P., Moss, P.J., and Buchanan, A.H., "Spalling of Concrete: Implications for Structural Performance in Fire", *Futures in Mechanics of Structures and Materials – Aravinthan, Karunasena & Wang (eds)*, London, 2009.
2. British Standards Institute, BS EN 1992-1-2:2004 Eurocode 2: Design of concrete structures – Part 1-2: General rules – Structural fire design, London; BSI, 2010.
3. British Standards Institute, BS 476-20:1987 Incorporating Amendment No. 1, Fire tests on building materials and structures – Part 20: Method for determination of the fire resistance of elements of construction (general principles), London; BSI, 1998.
4. Ali, F.A., Nadjai, A., Talamona, D., Rafi, M.M., "Fracture and explosive spalling of concrete slabs subjected to severe fire", *Fracture Mechanics of Concrete Structures - High-Performance Concrete, Brick-Masonry and Environmental Aspects*, Carpinteri, et al. (eds), Taylor & Francis Group, London 2007.
5. Khoury, G.A., "Effect of fire on concrete and concrete structures", *Progress in Structural Engineering and Materials*, John Wiley & Sons, Ltd., 2000.
6. Shell, DEP Specification: Passive Fire Protection for Onshore Facilities (DEP 34.19.20.11-Gen.) – Design and Engineering Practice, Shell, 2011.
7. ExxonMobil, Fireproofing (GP 14-03-01): Version 6.0.0, ExxonMobil, 2013.
8. Underwriters Laboratories, UL 1709: Rapid Rise Fire Tests of Protection Materials for Structural Steel, USA: UL, 2007.
9. International Standards Organisation, ISO 22899-1:2007 (E): Determination of the resistance to jet fires of passive fire protection materials – Part 1: General

- requirements, Geneva: ISO, 2007.
10. FABIG, Technical Note 13: Design Guidance for Hydrocarbon Fires, UK: The Steel Construction Institute, 2014.
 11. British Standards Institute, ISO/TR 22899-2:2013 (E): Determination of the resistance to jet fires of passive fire protection – Part 2: Guidance on classification and implementation methods, London, BSI, 2013.

Evolution of thermal conductivity on CAC concrete at high temperatures and during thermal fatigue tests

T. Lucio-Martin¹, M.C. Alonso^{1,*}, M. Roig-Flores^{1,2} & L. Guerreiro³

¹Eduardo Torroja Institute for Construction Sciences (IETcc-CSIC), Madrid, Spain

²Universitat Politècnica de València, Valencia, Spain

³University of Evora, Évora, Portugal

* Corresponding author (tamara.lucio@ietcc.csic.es, Serrano Galvache 4, CP: 28033, Madrid, Spain)

ABSTRACT

Heat transfer plays an important role when concrete works at high temperatures. For many applications, it is important to evaluate the effect of heat transfer on concrete to predict the thermo-mechanical response. Inside concrete, the dominant mechanism of heat transfer is conduction, and the main parameter involved is thermal conductivity. Heat transfer may play also a relevant role when spalling occurs.

In this paper, the evolution of thermal conductivity of concrete with temperature has been studied for different concrete types up to 600°C. The effect of cooling and thermal gradients are followed.

Results indicate that during the first heating, thermal conductivity decreases in several steps with temperature, first due to pore free water loss and second after dehydration up to 300°C. The mass loss and the temperature gradients are also affected. Thermal gradients play a role in the risk of concrete spalling. When cooling, thermal conductivity recovered almost the same value at 300°C. Repetitive thermal cycles do not modify the thermal performance of concrete.

KEYWORDS: heat transfer, thermal conductivity, thermal gradients, thermal fatigue

INTRODUCTION

There are infrastructures of concrete which operate at high temperatures during its service life. Applications such as nuclear and geothermal power plants condition concrete structures to work at high temperatures. Nowadays, concrete is being considered as a material for thermal energy storage systems for Concentrating Solar Power Plants (CSP). For such application concrete has to operate under high temperature for long periods and heating cycles of charge and discharge. Several authors have already demonstrated at lab scale the potentiality of concrete up to 600°C [1-3].

Nevertheless, when concrete is exposed to high temperatures, the spalling risk increases owing to thermal gradients between the surface and the core and pore pressures. The spalling caused by thermal gradients, which originates stresses, is one mechanism that has been widely accepted to explain the spalling phenomenon in concrete under fire [4-6].

Several authors have studied other factors that affect spalling such as pore pressures, thermal dilation of aggregates and shrinkage due to cement paste dehydration and the thermal incompatibility between the components of concrete [7-8]. Moreover, different thermal expansion coefficients between aggregates and cement paste inducing severe cracking can even produce further spalling risk [9-10].

In order to understand deeper concrete spalling phenomenon, the analysis of heat transfer mechanism when concrete is exposed to heat is of great interest for applications of concrete working at high temperatures. The heat transfer plays an important role in the spalling risk of a concrete. Thus, a better understanding of the thermal performance of concrete will be helpful for the design of concrete as well as for the thermal operation of these type of infrastructures.

When concrete is being heated, thermal conduction within the material is the dominant heat transfer mechanism. Thermal conductivity is the parameter that governs in conduction. By definition, this parameter gives the proportion between the heat flux and the temperature gradient between the external surface and the core. In conventional concrete, around 70% of the volume is occupied by the aggregates having a relevant role in the heat transfer. Since the wide types of aggregates that can be used in concrete have different thermal conductivity, the concrete response to heat will be different. The thermal conductivity of the concrete with siliceous aggregates is around 3 W/mK and the value is reduced to the half using basalt aggregates (1.5 W/mK) [11-12]. Nonetheless, these thermal conductivities are measured at ambient conditions before heating and, when concrete is exposed to high temperature, the thermal response changes significantly. There is limited information in the concrete thermal behaviour, and especially at high temperatures. There are different methods to obtain the thermal conductivity of concrete at high temperature which can be divided into steady or transient methods. Pimienta et al. [12] affirm that under moist conditions the steady state methods give an underestimation of the thermal conductivity due to moisture migration. Transient methods, and specifically, the hot-wire method are the more common methodology for the evaluation of thermal conductivity. The lack of thermal conductivity values and abroad databases of properties results and standardised test methods to measure this parameter at high temperatures make this study necessary to increase the knowledge on the heat transfer phenomenon on concrete and its contribution to the risk of spalling.

This paper deals with the evolution of thermal conductivity of concretes in a wide range of temperatures up to 600°C, during heating and cooling. Different type of aggregates are considered and the relationship with the spalling risk is analysed.

EXPERIMENTAL PROCEDURE

The aim of the experimental work performed is to design first a test protocol for measure the thermal conductivity of concrete at high temperature and to evaluate the evolution at temperatures during heating and cooling between 300-600°C.

Materials and mix design

Two different concrete mixes (Table 1) were used for the experiments with the same cement paste and w/c ratio. The Calcium Aluminate Cement (CAC) was used due to its refractory properties and good response at high temperatures. The effect on concrete thermal conductivity when using aggregates with different thermal response has been considered. One concrete composition with siliceous aggregate was selected representing a high thermal conductivity. Another concrete composition is a ternary mix with low thermal expanded aggregates, containing clinker of CAC (CAT), basalt and a waste slag from São Domingos mine.

Table 1 Concrete CAC compositions

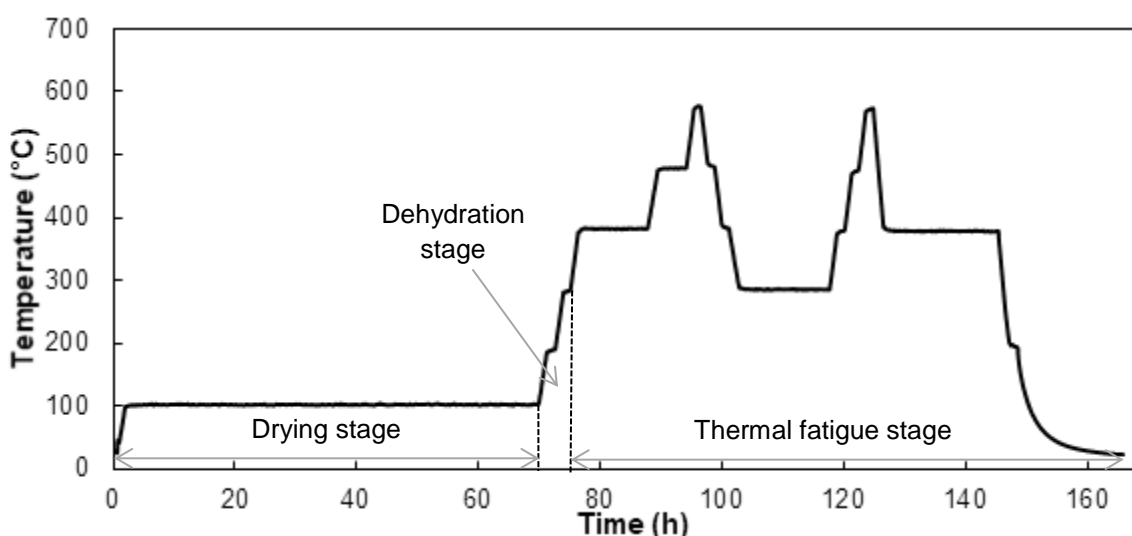
Component	Siliceous mix	Ternary mix
Cement CAC (kg/m ³)	600	600
Water (kg/m ³)	258	258
Sand 1 - Siliceous 0-3 mm (kg/m ³)	1456.4	0
Sand 2 - Basalt 0-3 mm (kg/m ³)	0	691
Sand 3 - CAT 0-3 mm (kg/m ³)	0	745
Sand 4 - São Domingos Slag 0-3 mm (kg/m ³)	0	133
Sand 5 - São Domingos Slag 3-7 mm (kg/m ³)	0	141
Polypropylene fibers (kg/m ³)	0	2
Plasticizer	0.9	0.9
w/c	0.43	0.43

The specimens prepared were prismatic of 40 × 40 × 160 mm³ and were cured in a humidity chamber at 95% relative humidity and 20°C until the age of 7 days. At the time of testing, the ageing of the siliceous mix was 98 days and the ternary mix 45 days.

Thermal regime

To completely determine the thermal conductivity evolution of the concrete during the thermal exposure, three stages are analysed in the thermal regime studied: 1) properties at room temperature and drying up to 105°C during 72 hours, when loss of free pore water takes place, 2) dehydration of cement paste process produced during the first heating between 100-300°C and 3) thermal fatigue stage during heating and cooling cycles from 300 to 600°C. The heating and cooling rates were established at 1°C/min in all stages of the thermal test. During the dehydration and thermal fatigue stages, thermal conductivity was measured at increasing temperatures with a step of 100°C until reaching 600°C, and afterwards, cooled down to 300°C using the same temperature step. Thermal conductivity was measured at each temperature step since the equipment needs constant temperature for evaluating the parameter. Figure 1 shows the thermal regime used during the test.

Figure 1 Thermal cycle with stages

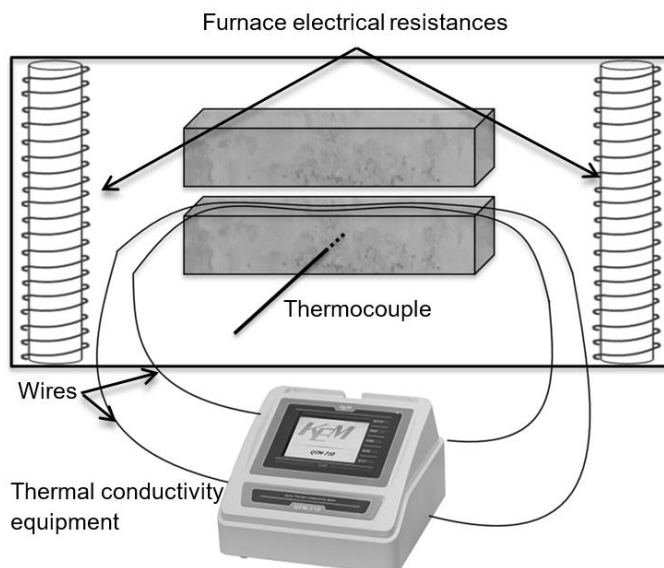


Parameters under measure were: 1) temperatures of the furnace and in the core of the concrete samples, 2) mass loss during drying for both concrete samples and during all heating stages for the ternary mix, and from thermogravimetry test in hydrated CAC powder of the ternary concrete mix and 3) the evolution of thermal conductivity for all the heating and cooling stages in concrete samples.

For measure thermal conductivity, the equipment used was QTM-700 from Kyoto Electronics Manufacturing. This equipment is based on the hot wire method and measures the increase in temperature produced by the pass of electrical current through the wires. Due to the lack of standardised test methods for measuring thermal properties of concrete at high temperatures, a test protocol has been designed.

Samples of $40 \times 40 \times 160 \text{ mm}^3$ were used to performing the tests. Two identical samples were employed in each test. One of them contained a thermocouple embedded to record the evolution of temperature inside the concrete. The sensor wires for measuring thermal conductivity were placed between the two samples, the setup is shown in Figure 2. The whole system was placed inside the furnace. The accurate measurement of the thermal conductivity needs to reach stable temperature of the concrete. The time for each measurement was established in 60 seconds. The preliminary tests performed during the development of the protocol showed minimum dispersion for the same concrete mix. On the other hand, the test carried out displayed significant dispersion on the results when the electrical resistances of the furnace were switched on while the equipment was measuring. This fact motivated a specific analysis to obtain an adequate protocol. The experience showed that the value of thermal conductivity could be right or wrong depending on the situation of the furnace during the exact moment when the equipment measured. The strategy followed consisted of carrying out 10 measurements for each temperature and identify their stability during the measurement.

Figure 2 Setup for the thermal conductivity test



RESULTS AND DISCUSSION

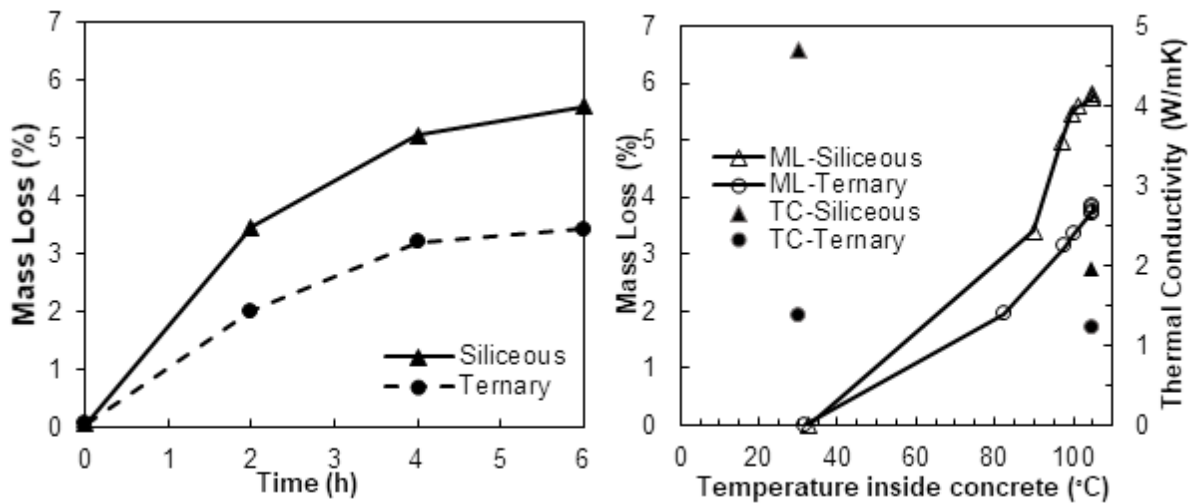
1) Thermal evolution during free water loss (room to 105°C)

In general terms, the measurements obtained of thermal conductivity decreased with the temperature having the highest drop after the first heating at 105°C (see Figure 6). Thus, the

decrease in this parameter can be considered to be produced mainly during the drying phase, where the loss of evaporable water from the pores produced substitution of the volume of water by volume of air in the pores. Air has lower thermal conductivity than water and, for that reason, the thermal parameter decreases.

Since the highest drop in thermal conductivity occurred during heating up to 105°C, the evolution of mass loss and thermal gradients was also analysed. The evolution of mass loss quantifies the loss of evaporable water before starting the heating. Figure 3-left shows the mass loss in time for the two different compositions. The siliceous mix lost more mass than the ternary mix, which is in accordance with the loss on the thermal conductivity during heating up to 100°C, indicating that part of its higher conductivity was produced by its higher humidity. Moreover, the higher thermal conductivity of siliceous aggregates increases the heat conduction favouring the increase in concrete temperature and hence, the escape of free water out of concrete, as can be seen in Figure 3-right.

Figure 3 Evolution of mass loss during drying (left) in time and (right) with temperature in the core of the concrete and thermal conductivity before/after drying.



Regarding thermal gradients, Figure 4-left represents the evolution of temperature in the centre of the samples for the first hours of drying for both concrete compositions. Figure 4-right shows the evolution of thermal gradients between the geometrical centre of the sample and the external surface, which is at the same temperature than the furnace. As the thermal conductivity of the concrete with siliceous aggregates is higher than concrete with the ternary mix (see Figure 6), the increase of internal temperature in the specimen from the first group was transferred at a higher heating rate, while the second group had higher thermal inertia. This difference in the internal evolution of the temperatures is produced because conduction is the governing heat transport mechanism, based on Eq. (1).

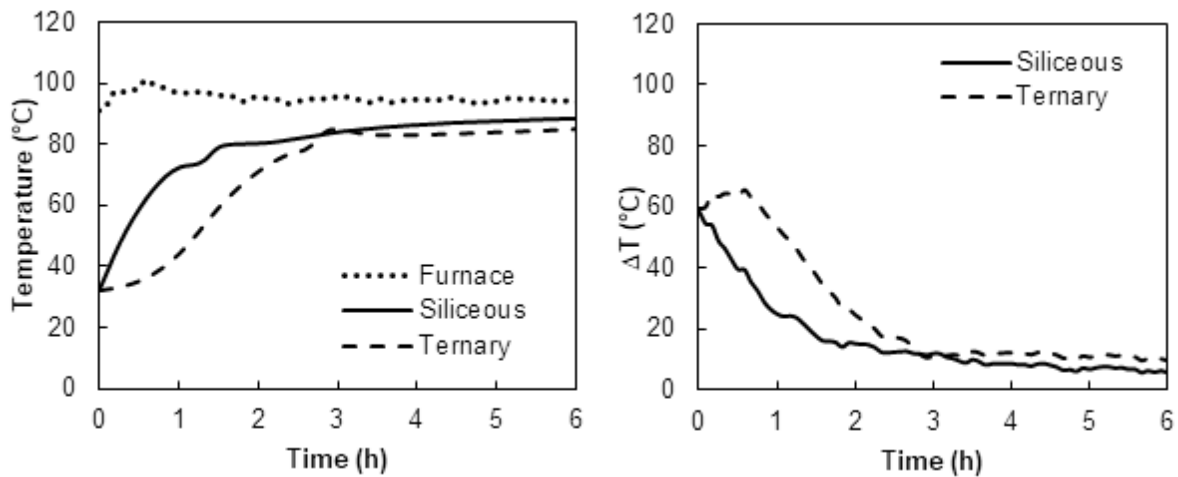
$$\dot{q}'_x = -k \frac{dT}{dx} \quad (1)$$

Where, \dot{q}'_x is the heat flux per length unit [W/m], k is the thermal conductivity [W/mK], dT/dx is the thermal gradient between the distance, x [K].

As thermal conductivity is directly proportional to the heat flux, thermal gradients between the surface and the core were lower in siliceous dosage for the same heat flux. For that reason, higher values of thermal conductivity improve heat transfer to the centre of specimen, reducing the spalling risk due to thermal gradients up to 100°C. This could be

appreciated in Figure 4-right where the siliceous mix had lower thermal gradients for all the time of heat exposure at 105°C. After 1.5 hours of starting the test, thermal gradient (ΔT) in the siliceous mix was 20°C, whereas the ternary mix achieved double ΔT . In spite of having stable aggregates at high temperature, the risk of spalling could be higher with low thermal conductivity aggregates. However, siliceous aggregates make the concrete thermal response more easily to adapt to the temperature for the drying phase, but the amount of vapour generated (mass loss) is higher for the same heat flux, figure 3-left, increasing in this way the risk of spalling.

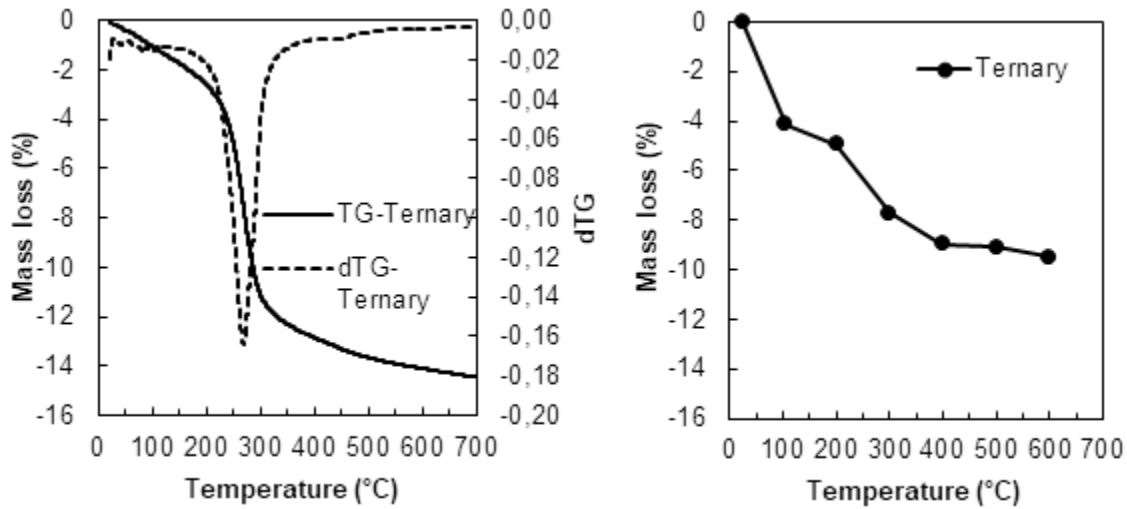
Figure 4 Evolution of left) temperature and right) thermal gradients during drying



2) Dehydration of cement paste stage (100-300°C)

During this stage, two mechanisms work simultaneously: the chemical changes of cement paste with loss of bound water and volume changes in aggregates and expansion followed by shrinkage of cement paste. The microstructural changes in the cement paste are due to dehydration of CAH_{10} at 120°C and AH_3 produced between 210-300°C [13]. Figure 5-left shows the critical temperature of change with mass loss between 200 and 300°C. This is in accordance with the results of concrete mass loss (Figure 5-right), where the highest mass loss was reached when heating up to 300°C, achieving around 4 % between 100-300°C. Z. Xing et al. [14] studied the evolution of thermal conductivity, heat capacity and thermal diffusivity of OPC concrete with siliceous aggregates and also found the highest drop on thermal conductivity at 150°C.

Figure 5 Evolution of mass loss at high temperatures for the ternary mix in, left) concrete powder and right) concrete sample 40x40x160mm



During this stage, the risk of spalling is higher owing to high thermal gradients between the external surface and the core, that affect all these processes in different level inside the concrete. The higher thermal conductivity in siliceous concrete respect to ternary mix make easier the flux heat transport and the dehydration processes in cements paste to occur liberating more vapour increasing the risk of spalling due to pore pressures.

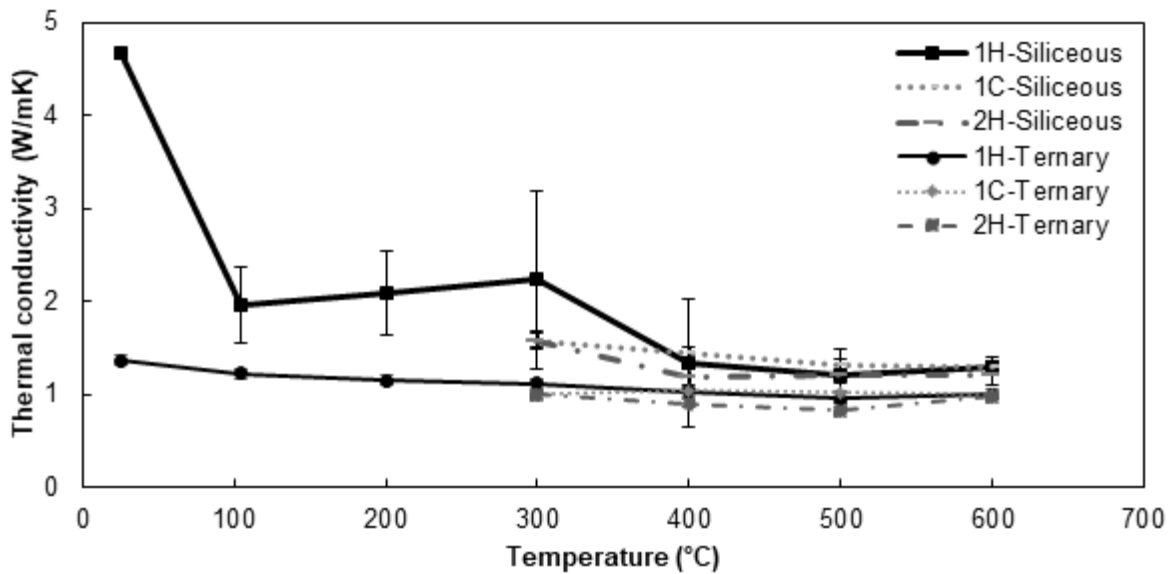
With the purpose to reduce the risk of spalling, the heating rate was established at 1°C/min. Moreover, to reduce the thermal gradients and vapour released and so the spalling risk, every 100°C the temperature was maintained constant. These temperature plateaus were useful for making the temperature homogeneous in the whole sample during heating up to another temperature and to have stable conditions for measuring the thermal conductivity.

Thermal conductivity between 105°C and 300°C remain almost constant but after 300°C thermal conductivity suffered another drop more clearly appreciated in the siliceous mix (see Figure 6).

3) Thermal fatigue during heating 300 to 600°C

Figure 6 shows the evolution of thermal conductivity for both siliceous and ternary mixes during the thermal cycle for the first heating up to 600°C, followed by a cooling to 300°C and a second heating up to 600°C. Having the same volume of cement paste, the differences found between the concretes are related to the type of aggregates and their response when they are exposed to high temperatures after dehydration of cement paste. The higher thermal conductivity the siliceous concrete makes faster the increase of temperature inside the concrete.

Figure 6 Evolution of thermal conductivity for the first heating (1H), first cooling (1C) and second heating (2H) for both concrete.



Ternary mix had a more stable response when it is heated up to 600°C because low thermal conductivity aggregates experienced slower temperature increase and also lower volumetric expansion. Siliceous aggregates are more thermally conductive, but they also originate more volumetric expansion and probably more prone to crack generation. Cracks affect negatively heat transfer because of the creation of air gaps and once they appear, heat transfer is no longer produced by conduction exclusively, and convection mechanisms also participate. Thus, at high temperatures (and after cracking), for the same heat flux, conduction and thermal conductivity decrease significantly in the siliceous mix despite having more thermal conductive aggregates. Moreover, not only is heat transfer affected by thermal cracks, but also by the changes in crystallinity produced in the material components [15]. During the fatigue stage (cooling down to 300°C and second heating up to 600°C) the thermal conductivity remained almost constant.

These results are consistent with the loss of thermal conductivity with temperature also reported by different authors [16-17], as produced by the loss of water (evaporable water and chemically bounded) and thermal cracking.

Analysing the evolution of the thermal parameter, the results led to the conclusion that the most significant and critical stages are the drying and dehydration, especially when using siliceous aggregates.

For the thermal storage application, a balance between more thermal conductive aggregates or stable aggregates at high temperature must be achieved. While the first ones (siliceous in the case studied) improved heat transfer during the drying stage because of having higher thermal conductivity, when are exposed to temperatures up to 600°C its response is negatively affected due to their higher thermal expansion. The dehydration of cement paste and thermal conductivity of the aggregates affects heat flux transport and the rate of vapour generation and also the risk spalling process to occur.

CONCLUSIONS

The work carried out from thermal conductivity measurements at high temperature has led to the following conclusions:

- The thermal conductivity decreased with temperature because of free water loss.
- The dehydration of cement paste produces the critical loss of thermal conductivity and its value remained constant at higher temperatures.
- The siliceous mix achieved higher values of thermal conductivity at room temperature due. However, it also registered the highest drop in thermal.
- The ternary mix with lower thermal conductivity aggregates, with basalt, CAT and São Domingos Slag, is more thermally stable at high temperatures than the siliceous mix as measured by the almost constant result in thermal conductivity. Higher thermal inertia is showed during the heating stage.

ACKNOWLEDGEMENTS

The research was financially supported by the H2020 project NewSol, *New StOrage Latent and sensible concept for high efficient CSP Plants* (Project ID: 720985).

REFERENCES

1. Alonso, M.C., Vera-Agullo, J., Guerreiro, L., Flor-Laguna, V., Sanchez, M. and Collares-Pereira, M. "Calcium aluminate based cement for concrete to be used as thermal energy storage in solar thermal electricity plants," *Cement and Concrete Research*, **82**, 74-86, 2016.
2. John, E., Hale, M. and Selvam, P. "Concrete as a thermal energy storage medium for thermocline solar energy storage systems", *Solar Energy*, **96**, 194-204, 2013.
3. Laing, D. Bahl, C., Bauer, T., Fiss, M., Breidenbach, N., and Hempel, M. "High-temperature solid-media thermal energy storage for solar thermal power plants", Proceedings of the IEEE, vol. 100, n° 2, pp. 516-524, 2012.
4. Bazant, Z.P. "Analysis of pore pressure, thermal stresses and fracture in rapidly heated concrete". International Workshop on Fire Performance of High-Strength Concrete. Gettysburg: NIST Special Publication 919; 1997.
5. Khoury, G.A., Majorana, C.E., Pesavento, F., Schrefler, B.A. "Modelling of heated concrete". *Magazine of Concrete Research*. **54(2)**, 77-101, 2002.
6. Nechnech, W., Meftah, F., Reynouard, J.M., "An elasto-plastic damage model for plain concrete subjected to high temperatures", *Engineering Structures*, **24(5)**, 597-611, 2002.
7. Kalifa, P., Menneteau, F.D., Quenard, D., "Spalling and pore pressure in HPC at high temperatures". *Cement and Concrete Research*, **30(12)**, 1915-1927, 2000.
8. Pan, Z., Sanjayan, J.G., Kong, D.L.Y. "effect of aggregate size on spalling of geopolymer and Portland cement concretes subjected to elevated temperatures". *Construction and Building Materials*, **36**, 365-372, 2012.
9. Bazant, Kazemi, M.T., "Determination of fracture energy, process zone length and brittleness number from size effect, with application to rock and concrete". *International Journal of Fracture*, **44(2)**, 111-131, 1990.
10. Kanemá, M., Pliya, P., Noumoué, A., Gallias, J.L., "Spalling, thermal and hydrous behavior of ordinary and high-strength concrete subjected to elevated temperature", *Journal of Materials in Civil Engineering*, **23(7)**, 921-930, 2011.
11. Bažant, Z. P. and Kaplan, M. F., *Concrete at High Temperatures: Material Properties and Mathematical Models*, London: Addison-Wesley, 1996.
12. Pimienta, P., McNamee, R. and Mindeguia, J.-C. "Physical Properties and Behaviour of High-Performance Concrete at High Temperature". State-of-the-Art Report of the RILEM Technical Committee 227-HPB, Springer International Publishing, 2019.
13. Antonovic, V., Keriene, J., Boris, R. and Aleknevičius, M. "The effect of Temperature on the Formation of the Hydrated Calcium Aluminate Cement Structure", *Procedia Engineering*, **57**, 99-106, 2013.
14. Xing, Z., Beaucour, A.L., Hébert, R., Noumowé, A., and Ledésert, B. "Aggregates's influence on thermophysical concrete properties at elevated temperature", *Construction*

- and Building Material*, **95**, 18-28, 2015.
15. Touloukian, Y.S., Powell, R.W., Ho, C.Y., Nicolaou, M.C. *Thermophysical properties of matter. Volume 2. Thermal conductivity – Non-metallic solids*. Thermophysical and Electronic Properties Information Analysis Center Lafayette In, 1971.
 16. Bazant, Z.P., and Kaplan, M.F. *Concrete at high temperatures*, first ed., Longman, 1996.
 17. Xing, Z., Beaucour, A.L., Hébert, R., Noumowé, A., and Ledésert, B. "Influence of the nature of aggregates on the behaviour of concrete subjected to elevated temperature", *Cement and Concrete Research*, **41**, 392-402, 2011.

Transport and reconfiguration of moisture in HPC due to unilateral heating

Ludwig Stelzner^{1,*}, Frank Weise¹, Tyler Oesch¹, Raphael Dlugosch²
& Bartosz Powierza¹

¹ Bundesanstalt für Materialforschung und -prüfung,
Berlin, Germany

² Leibniz Institute for Applied Geophysics, Hannover,
Germany

* ludwig.stelzner@bam.de, Bundesanstalt für
Materialforschung und -prüfung, Unter den Eichen 87,
12205 Berlin, Germany

ABSTRACT

Explosive spalling is caused by, among others, the thermohydraulic spalling mechanism. During this process, vaporization, dehydration, moisture-transport and condensation processes interact. As a result, a drying and dehydration zone as well as a saturated zone, known as a moisture clog, are observed inside the unilaterally-heated concrete. The presented research is focused on the experimental investigation of the underlying thermohydraulic processes.

To investigate these, a test methodology based on X-ray computed tomography (CT) and nuclear magnetic resonance (NMR) was developed. Thereby, the X-ray CT scans are carried out simultaneously during the application of a defined unilateral-heating regime on a specially-constructed specimen. This miniaturized specimen, equipped with a double-layer casing, reproduces the condition within a planar, unilaterally-heated building component.

A preliminary test methodology and the first experimental results were presented at the 5th International Workshop on Concrete Spalling in Borås, Sweden (2017) [1]. The contribution for the upcoming workshop presents an improved version of this test methodology and new results for a high-performance concrete (HPC) mixture exposed to temperatures up to 500 °C. Regarding the CT measurements, a higher time-resolution of 15 min was achieved and a quantification of the moisture changes was implemented. Due to an increase in signal quality of the NMR measurements, a pore-size specific moisture distribution can now be resolved. This allows to conclude about the moisture reconfiguration between small gel pores and larger interhydrate pores. Additionally, the NMR measurement are no longer limited to first 2.5 cm below the heated surface but a one-dimensional moisture distribution can now be estimated over the whole 10 cm long specimen.

The presented results demonstrate that the combination of X-ray CT and NMR measurements enables to image and quantify the thermally-induced moisture transport and reconfiguration from small gel pores up to macro pores. This provides important insights into the thermohydraulic damage mechanism and leads to a better understanding of spalling avoidance strategies, like the addition of polypropylene fibres.

KEYWORD: Moisture Clog, X-ray CT, NMR, Moisture Transport, HPC

INTRODUCTION

The thermohydraulic spalling mechanism is one of the primary mechanisms responsible for explosive spalling of concrete in the case of thermal exposure. The mechanism is described in detail in [1]. At the present time, the moisture-transport, moisture-release and moisture-reconfiguration processes associated with the thermohydraulic spalling have not been fully analysed. Thus, the experimental analysis of these processes is important to understand the thermohydraulic spalling mechanism in detail. In the past, a variety of measurement methods were applied by different researchers to investigate the moisture distribution and transport in unilaterally-heated concrete. Common among all of these experiments was the goal of recording the moisture-clog effect. The moisture-clog was firstly mentioned by Harmathy in [2] and is described as a water-saturated zone inside heated concrete components, which is built up during the thermal exposure. A compilation of previous experimental approaches of different researchers is given in [3]. These experimental approaches include visual assessment of artificially-fractured specimen surfaces and non-destructive measurement methods such as neutron radio- and tomography [4-6] and nuclear magnetic resonance relaxometry (NMR) [7]. A combination of X-ray computed tomography (X-ray CT) and NMR represents the basis of the research work presented in this paper. An overview about these methods and the test setup is given in [1]. Detailed information about the X-ray CT setup, measurements and evaluation can be found in [8]. The latest results, including a quantification of the moisture changes for both methods (X-ray CT and NMR) are presented in [3].

This paper focusses on the comparison of results gained by X-ray CT and NMR. The presented NMR-measurements were carried out on specimens after different thermal exposure.

MATERIALS

The analysis of the thermally-induced moisture transport was carried out by using a miniaturized specimen with a special double-layer casing. The aim of the specimen design was to simulate a unilaterally-heated, planar building component in a miniaturized manner. The specimen itself is a high-performance concrete (HPC) with and without added polypropylene-fibres (PP-fibres). The concrete mixture is given in Table 1. Due to the low water-to-cement ratio and the added used silica fume, this HPC is prone to fire-induced explosive spalling. Some results of a fire test with a small-scale building component made of this HPC are presented in [1].

Table 1: Concrete mixture without and with the addition of polypropylene fibres (PP-fibres)

Component		Sr-B0	Sr-PPa-2	
		[kg/m ²]		
Cement (CEM I 42.5 R)		580		
Water		173		
Aggregate (quarzitic)	0 to 2	[mm]	764	754
	2 to 4		229	226
	4 to 8		535	528
Silica fume		63.8		
Superplasticizer		14.5	20.3	
PP-fibres		0	2	
w/c-ratio		0.3	0.3	

To ensure a one-dimensional moisture flux inside the specimen, the HPC is surrounded by an impermeable shell made of glass-ceramic (MACOR). Due to the, in comparison with the concrete, lower thermal expansion coefficient of the MACOR shell and the use of this

MACOR shell as formwork during the casting process, significant crack formation between the HPC and the surrounding glass-ceramic is prevented. The one-dimensional thermal flux is ensured by an additional, second shell made of high-temperature aluminium silicate wool. The overall construction of the miniaturized specimen with the double-layer casing is shown in Figure 1. More details describing the construction of the specimen are given in [3].

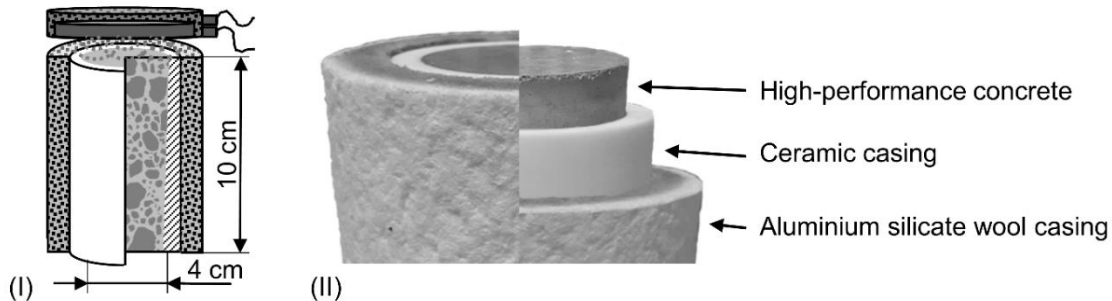


Figure 1: Miniaturized specimen with double-layer casing, schematic drawing with positioned heating device (I) and photo-arrangement of the different layers (II)

Conditioning of the specimen

After the casting process, the specimens are stored for the first 24 hours under plastic foil and subsequently stored under water (21 °C) for a further 27 days. Then the specimens are stored in a climate chamber (20 °C; 65 % humidity) for at least two months prior to the start of the testing procedure.

METHODS

Unilateral heating

The specimens with the double-layer casing are heated unilaterally using an electrical heating element, positioned above the specimen surface. The concrete surface is heated mainly by radiation and the heating process is controlled by means of an electronic controlling unit. Two different heating regimes are used for the investigations presented in this contribution. Both regimes consist of a heating- and a temperature-holding-phase. During the heating-phase, the surface temperature increases with a heating rate of 10 K/min. After the maximum target-temperature of the specimen surface is reached, the temperature is held constant during the holding-phase for further 130 min. Between the two heating regimes, only the maximum target-temperature differs, with values of 300 °C and 500 °C, respectively.

X-ray CT measurements

The X-ray CT measurements presented in this contribution are used to evaluate the moisture changes in the miniaturized specimen during unilateral heating. Details about the X-ray CT setup, the measuring principle and the evaluation process can be found in [3, 8]. The evaluation of sequentially-recorded X-ray CT scans are used to analyse spatial changes in the moisture content and distribution relative to a reference scan conducted prior to the heating. For each measurement, a short scanning time and high spatial resolution are necessary to investigate the temporal course of moisture changes in three dimensions. A photo of the X-ray CT device used for these measurements (General Electric v|tome|x L300 micro-CT) with an assembled specimen and heating device is shown in Figure 2 (I). The key parameters for every X-ray CT scan are given in Table 2. These parameters were optimized to enable one X-ray CT scan every 15 min, including some preparation time for the next scan. During the evaluation process, the calculated differences in grey-values between

two scans are converted to absolute changes in moisture content by comparing them to known moisture content changes, i.e. in macro-pores, which are air filled before heating and water saturated during the heating process. Details about the quantification algorithm that provides useful estimates of moisture changes are given in [3, 9].

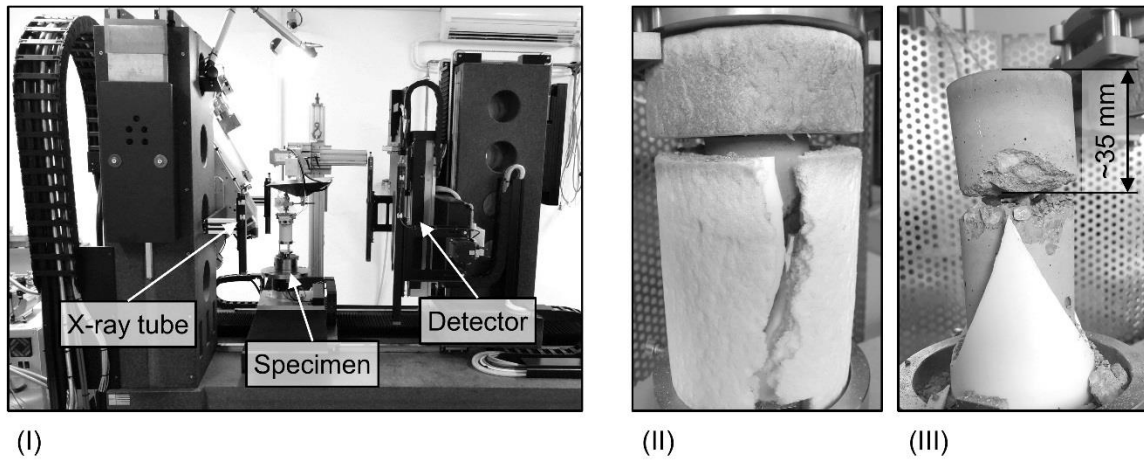


Figure 2: Test setup for simultaneous X-ray CT-measurements during unilateral heating (I), spalled miniaturized specimen without PP-fibres after unilateral heating ($T_{max} = 500 \text{ }^{\circ}\text{C}$) before (II) and after (III) removal of the aluminium silicate wool casing and loose parts of the ceramic casing

Table 2: Key measurement parameters for X-ray CT scans

Acceleration voltage	250 kV
Tube current	150 μA
Pre-filter	0.5 mm Cu
Number of projections	650
Exposure time per projection	1 s
Total measurement time per scan	11 min

The simultaneous X-ray CT measurements are only possible for the heating regime with a maximum surface target-temperature of the specimen of $300 \text{ }^{\circ}\text{C}$. Preliminary tests have shown that a higher surface target-temperature leads to spalling of the miniaturized specimen. The results are depicted in Figure 2 (II+III). The target temperature for this preliminary test was $500 \text{ }^{\circ}\text{C}$ and the specimen spalled in a depth of $\sim 35 \text{ mm}$. This behaviour is in accordance with the description of the thermohydraulic spalling mechanism [10]. To ensure a protection of the X-ray device, especially the panel detector, only measurements with the lower maximum surface temperature are carried out.

NMR-measurements

The NMR-measurements are carried out using a 2 MHz Rock Core Analyzer from Magritek. Compared to the previously presented result [1], the shorter echo times and higher signal quality now enables to detect moisture in the gel pores of the concrete specimens.

Unfortunately, the NMR measurements are only possible at ambient temperatures before and after heating, primarily due to the temperature dependence of the NMR-signal. The detailed measurement and evaluation process, which jointly interprets all NMR scans to an model of the spatial pore size and specific moisture content distribution inside the specimen is given in [3].

The result of two NMR-measurements conducted before and after heating of the specimen is shown in Figure 3 for a two-millimetre-thick slice. Note, that the spatial resolution of the

presented NMR-measurements is limited to one dimension, selected perpendicular to the heated surface of the specimen. However, the moisture detected inside each slice can be assigned to different relaxation times (T_2), indicating different pore sizes or bonding strength of moisture in the cement matrix. The area under the graph represents the total moisture content, which can be detected with NMR inside the layer. The NMR results for the whole specimen are either shown as heat maps (see Figure 5 and Figure 6) to show the relocation of moisture within the cement matrix or summarized to one-dimensional, spatial distribution of the total moisture content (see Figure 7).

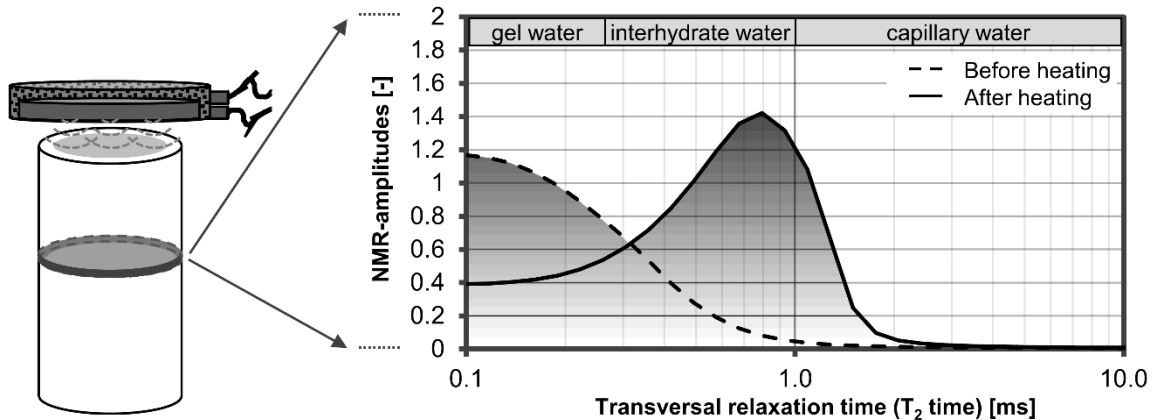


Figure 3: Schematic drawing of the NMR-analysis process, used to display the thermally-induced change of the detectable moisture content relative to transversal relaxation time

RESULTS

In addition to the test specimens used for the NMR and X-ray CT studies, specimens with embedded thermocouples are manufactured and heated using the previous described heating regimes. Six thermocouples (type K) are embedded at depths of 0, 10, 20, 30, 50 and 70 mm below the heated specimen surface.

The resulting depth-dependent temperature distributions are shown in Figure 4 for both temperature regimes.

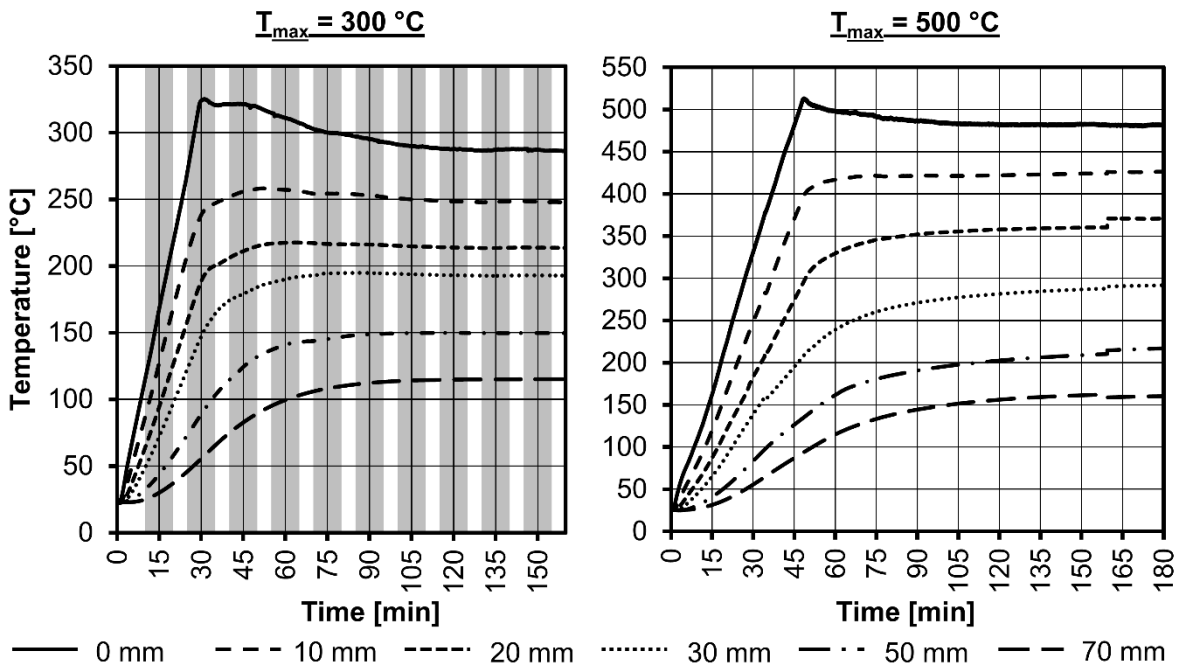


Figure 4: Temperature distribution inside the miniaturized specimens for both heating

regimes $T_{max} = 300\text{ °C}$ (left) and 500 °C (right). Sensors depth ranging from 0 mm (continuous line) to 70 mm (long dashed line).

The temperature evolution during the heating procedure consists of two phases. The heating-phase is characterised by a steep temperature increase at the specimen surface (0 mm) and a more gradual temperature increase in deeper specimen areas. During the subsequent holding-phase, the temperature continues to gradually increase in the deeper specimen until a steady state is reached. For the heating regime with a maximum temperature of 300 °C , the acquisition windows for the CT scans are additionally depicted as grey-marked areas in the temperature plot of Figure 4.

NMR

The results of the NMR-measurements conducted on HPC with and without PP-fibres are shown in Figure 5 for $T_{max} = 300\text{ °C}$ and in Figure 6 for $T_{max} = 500\text{ °C}$, respectively. The one-dimensional moisture distributions for all NMR-measurements are summarized in Figure 7. Before heating, an almost homogenous moisture distribution across the specimen depth is visible for both HPC mixtures. Most of the detectable moisture exhibits transversal relaxation times (T_2 -times) below 0.26 ms indicating moisture in gel pores. After unilateral heating, the moisture content near the heated surface decreases in both the specimen with and without added PP-fibres. This drying area reaches deeper for the specimen with PP-fibres (50 mm) compared to the specimen without PP-fibres (30 mm). This can be attributed to the increased permeability of fibre-reinforced concrete and the resulting improved water vapour transport. Behind the drying zone, a moisture accumulation zone is visible characterized by longer T_2 -times of up to approx. 1 ms (Figure 5) and an increase in total moisture content by up to 5 vol.% compared to the state prior heating (Figure 7).

While the increase in total moisture content is similar for the HPC with and without added PP-fibres, the moisture accumulation in HPC with PP-fibres takes place in deeper areas of the specimen.

The results for the second heating regime with $T_{max} = 500\text{ °C}$ are very similar to the previously described results, except of a deeper extend of the drying area and a deeper location of the moisture accumulation zone. During the heating of the HPC without added PP-fibres, the specimen spalled at a depth of approx. 35 mm (see Figure 2, right). The analysis of the moisture distribution in this specimen (see Figure 6, top left) indicates that the location of explosive spalling is associated with the position of the drying front. The total moisture content behind the drying front measured in the spalled specimen is lower compared to the other specimen after heating (Figure 7), which is most likely due to the release of moisture over the shell surface after the destruction of the specimen.

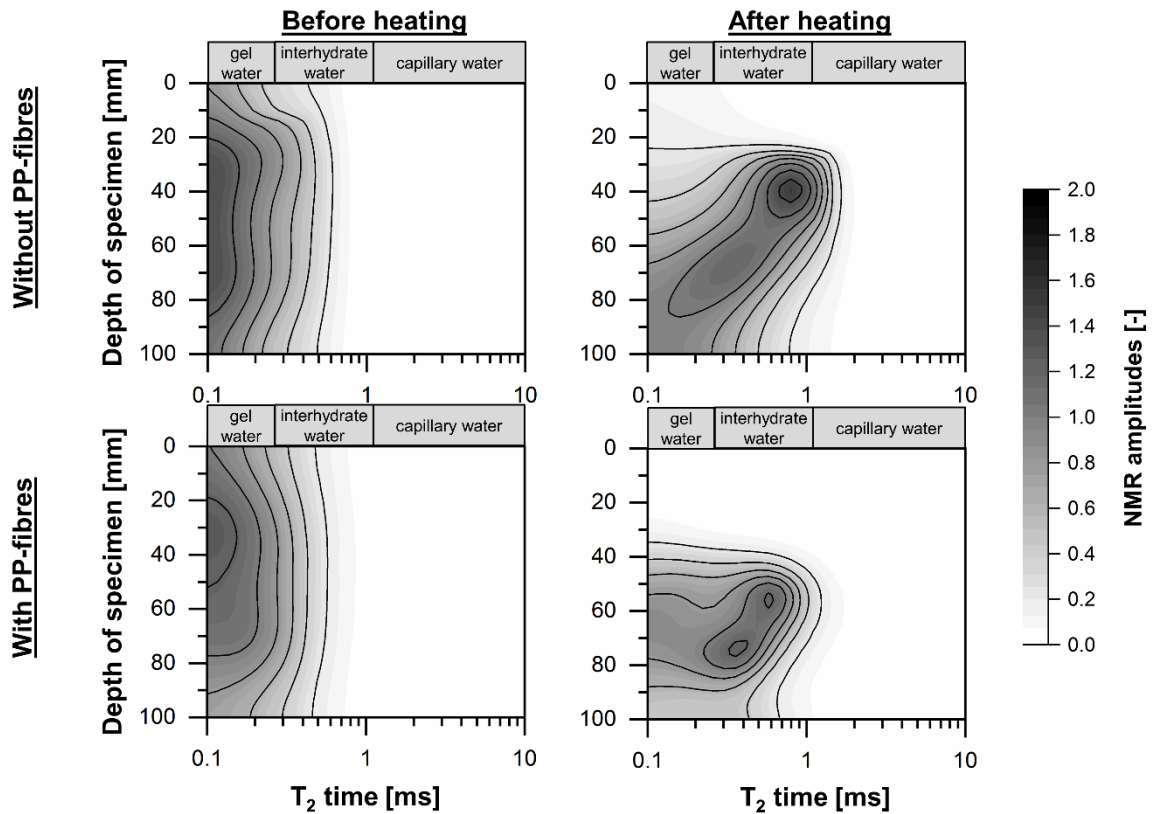


Figure 5: Distribution of the detectable partial moisture content before (left) and after (right) unilateral heating ($T_{max} = 300 \text{ }^\circ\text{C}$) for HPC with and without PP-fibres.

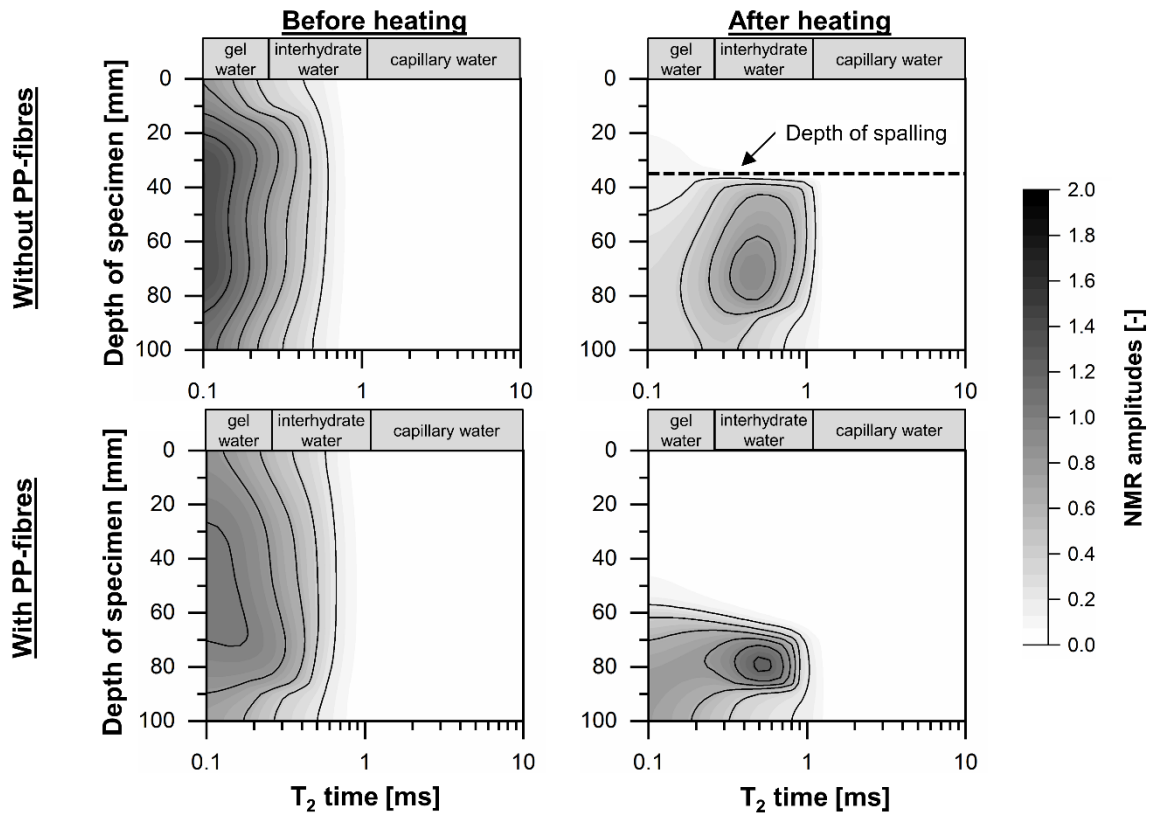


Figure 6: Distribution of the detectable partial moisture content before (left) and after (right) unilateral heating ($T_{max} = 500 \text{ }^\circ\text{C}$) for HPC with and without PP-fibres.

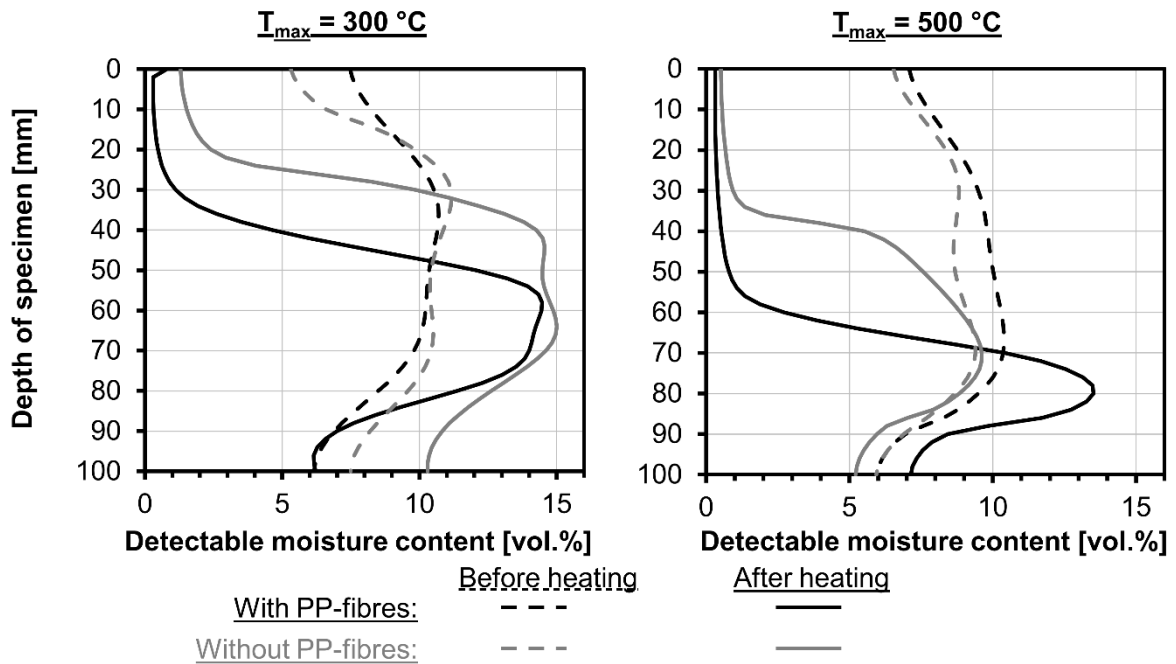


Figure 7: One-dimensional moisture content measured by means of NMR for both heating regimes $T_{max} = 300\text{ °C}$ (left) and 500 °C (right)

X-ray CT

Figure 8 shows the moisture changes estimated by means of X-ray CT for selected time steps. On the left side of the figure (Figure 8 (I)), the moisture changes are presented through the use of virtual cross-sections of the specimens during the heating to $T_{max} = 300\text{ °C}$ for specimens with and without fibre-reinforcement. Moisture loss is visualized in light grey and white and moisture accumulation is visible as dark grey and black colours. The moisture loss comprises free and physical-bound water as well as a partial dehydration of the hydrated cement and mainly occurs in the cement matrix in the top part of the specimens, while the aggregates are not significantly affected. With increasing time during the heating, the drying zone reaches into deeper areas of the specimen. The comparison of the drying zones between fibre-reinforced and unreinforced specimens shows a faster and deeper formation of the drying zone in the fibre-reinforced specimen. A moisture accumulation is visible in the macro-pores in deeper areas of both the specimen with and without added PP-fibres. This increase in moisture appears to be more pronounced in the fibre-reinforced test specimen than in the unreinforced test specimen. However, pores filled with liquid water are visible in both cases. On the right side of Figure 8, the one-dimensional, spatial moisture change is given for selected time steps. These graphs are based on the three-dimensional data, which are averaged for each layer along the specimen depth. The quantification of the moisture loss and moisture accumulation shows that only a moisture accumulation of 2 to 3 percent by volume is measurable for both concretes. In contrast moisture loss in the top part of the specimens achieves -15 to -17 percent by volume.

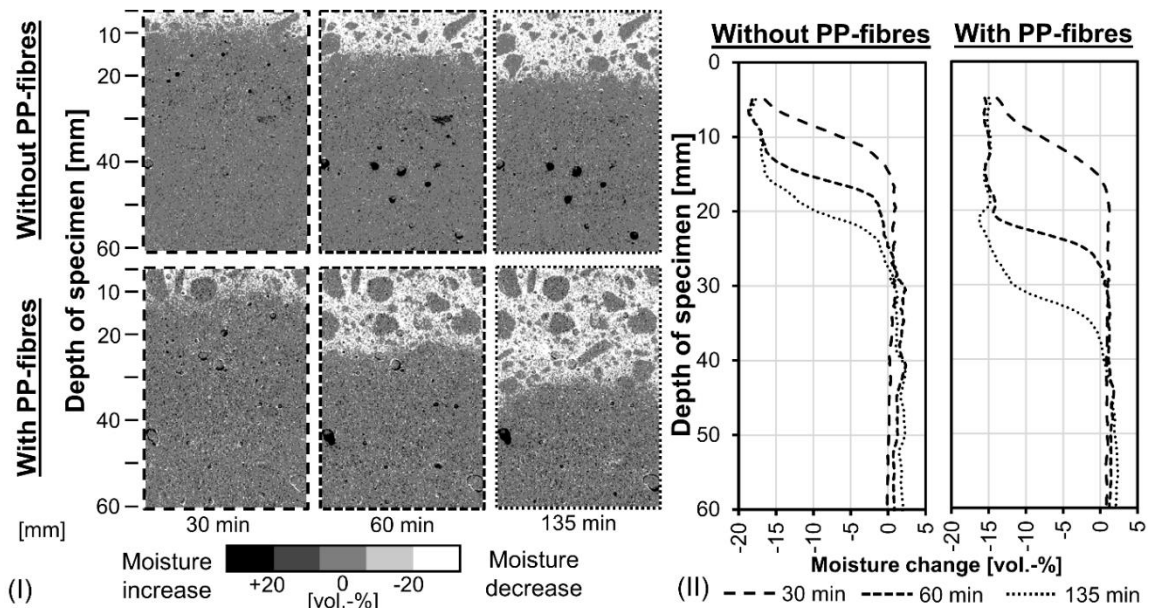


Figure 8: Quantified moisture changes inside heated HPC ($T_{max} = 300\text{ }^{\circ}\text{C}$) with and without PP-fibres for different time steps, (I) two-dimensional moisture change depicted by means of a virtual cross-section, (II) one-dimensional moisture change

CONCLUSION

The following points can be summarized from the experimental results:

- The developed test methodology enables the investigation of the thermally-induced moisture transport in unilaterally-heated HPC.
- The X-ray CT measurements, carried out simultaneously with the heating, show the formation of a drying zone close to the heated surface for all specimens. The moisture loss in this region appears to occur primarily within the cement matrix. Additionally, a moisture accumulation in deeper areas of the specimens is visible. Based on the CT-data, the moisture changes were estimated showing variations between -17 to 3 vol.-%.
- The NMR-measurements, carried out prior and after the heating, also resolved the extend of the drying zone. Additionally, an increase in moisture situated in larger pores was detected in the moisture accumulation zone indicating a change in the bonding state of the water inside the specimen. The variation in total moisture content due to heating ranges between -10 vol.-% and +5 vol.-%.
- The temporal evolution of the moisture distribution exhibits a faster and deeper migration of the drying front into the specimen with added PP-fibres. This may result from the higher permeability of this material and from the formation of a fibre-induced microcrack system.
- Comparing two different heating regimes, reaching surface temperatures of $300\text{ }^{\circ}\text{C}$ and $500\text{ }^{\circ}\text{C}$, show that a severe thermal exposure leads to a deeper migration of the drying zone. During the heating to $500\text{ }^{\circ}\text{C}$, a specimen without fibre-reinforcement was destroyed due to explosive spalling. This provides further evidence that the miniaturized specimen with the double-layer casing is capable of replicating realistic spalling behaviour and, thus, is also well-suited for the investigation of the thermally-induced moisture transport in the context of the thermohydraulic spalling mechanism.

ACKNOWLEDGEMENT

The authors would like to acknowledge all employees of the departments 7.1 "Building materials" and 8.5 "Micro non-destructive testing" from Bundesanstalt für Materialforschung und -prüfung (BAM) for their support during the investigations. They would also like to express further thanks to Mike Müller-Petke from the Leibniz Institute for Applied Geophysics for supporting the NMR-measurements.

This work was internally funded by BAM through the Menschen-Ideen-Strukturen (MIS) Program.

REFERENCES

1. Stelzner, L., Powierza, B., Weise, F., Oesch, T., Dlugosch, R., and Meng, B., "*Analysis of moisture transport in unilateral-heated dense high-strength concrete*", *5th International Workshop on Concrete Spalling*, 2017, Boras.
2. Harmathy, T. Z., "Effect of moisture on the fire endurance of building elements", *ASTM Special Technical Publication*, **No. 385**, 1965
3. Stelzner, L., Powierza, B., Oesch, T., Dlugosch, R., and Weise, F., "Thermally-induced moisture transport in High-Performance Concrete studied by X-ray-CT and ¹H-NMR", *Construction and Building Materials*, **224**, 600-609, 2019
4. Weber, B., Wyrzykowski, M., Griffa, M., Carl, S., Lehmann, E., and Lura, P., "Neutron radiography of heated high-performance mortar", *MATEC Web of Conferences*, **6**, 8, 2013
5. Dauti, D., Weber, B., Dal Pont, S., Tengattini, A., Toropovs, N., and Briffaut, M., "*First results on fast neutron tomography of heated concrete*", *5th International Workshop on Concrete Spalling*, 2017, Boras.
6. Dauti, D., Tengattini, A., Dal Pont, S., Toropovs, N., Briffaut, M., and Weber, B., "Analysis of moisture migration in concrete at high temperature through in-situ neutron tomography", *Cement and Concrete Research*, **111**, 41-55, 2018
7. Van der Heijden, G. H. A., Huinink, H. P., Pel, L., and Kopinga, K., "One-dimensional scanning of moisture in heated porous building materials with NMR", *Journal of Magnetic Resonance*, **208**, 235-242, 2011
8. Powierza, B., Stelzner, L., Oesch, T. S., Gollwitzer, C., Weise, F., and Bruno, G., "Water Migration in One-Side Heated Concrete: 4D In-Situ CT Monitoring of the Moisture-Clog-Effect", *Journal of Nondestructive Evaluation*, **38**, 11, 2019
9. Oesch, T. S., Weise, F., Meinel, D., and Gollwitzer, C., "Quantitative In-situ Analysis of Water Transport in Concrete Completed Using X-Ray Computed Tomography", *Transport of Porous Media*, **127**, 371-389, 2018
10. Harmathy, T. Z., "Experimental study on moisture and fire endurance", *Fire Technology*, **2**, 52-59, 1966

Effect of loss of concrete cover on the fire resistance of Reinforced Concrete (RC) beams: Numerical study using fiber beam-column element

Hitesh Lakhani^{1,*} & Jan Hofmann¹

¹ Institute of Construction Materials,
University of Stuttgart, Stuttgart, Germany

* Corresponding author:

hitesh_lakhani06@rediffmail.com,

Institute of Construction Materials,
University of Stuttgart, Pfaffenwaldring 4, 70569
Stuttgart, Germany

ABSTRACT

The paper presents a fiber based distributed plasticity beam-column element formulated using the flexibility approach. The discussed element has been successfully implemented in a standalone in-house Finite Element (FE) code. The FE code is capable of simulating the response of Reinforced Concrete (RC) framed structures during fire. Basically, the analysis approach is a sequentially coupled thermal stress analysis. The Heat Transfer (HT) module used is also capable to account for moving thermal boundary conditions, to account for changing domain boundaries due to loss of concrete cover. Hence, as the first step of analysis, the temperature distribution at various integration points (sections) along the element length for the given exposure conditions are computed. For the stress analysis the flexibility-based element was implemented within the displacement based global system. The procedure used for determining the element state is based on the algorithm proposed by Taucer et al (1991). The procedure has been updated to consider the thermal effects. The uniaxial constitutive relationships used for concrete and reinforcing steel, as function of temperature were taken from Eurocode2. This implies that the Load Induced Thermal Strains (LITS) for concrete was accounted implicitly.

The paper presents the validation of the FE code against experiment from literature, which shows that the predicted temperatures and the mechanical response were in good agreement with the experimental results. The validated code is then used for performing a parametric study to investigate the influence of time and location of (a chosen) corner spalling configuration, on the thermal and mechanical response of a simply supported beam. Although the example considered appeared to be very simplified, but it helps to give an insight into various complexities involved in such problems. It was observed that the predicted temperatures with different spalling times lies between two limits defined by the no-spalling case and the case where all spalling is assumed to be lumped at time $t=0$ minutes. The results of the parametric study with different spalling location showed that the reinforcement detailed may also play a significant role for quantifying the effect of spalling on the response of simply supported beams during fire.

KEYWORD: Distributed Plasticity, Moving Thermal Boundary Conditions, Flexibility-based Beam Element, Thermal Spalling, Fire Rating

INTRODUCTION

The current prescriptive design approach for Reinforced Concrete (RC) structures against fire, is mainly based on the insulation provided by concrete cover to reinforcement. In real life situation this concrete cover may be lost during fire due to thermal spalling. The loss of concrete cover may affect the fire rating of RC members. Studies dealing with the phenomenon of spalling have gained attention of lot of researches over the years but the effect of spalling on the behaviour of RC members have not been studied. There is a general understanding or presumption that spalling will have a negative effect on the response of RC members during fire. There are also experimental evidences where the RC members made of spalling prone concrete behaves badly as compared to those where no spalling occurs. But there are still lot of questions to be answered/investigated like: what's the influence of spalling time; how conservative can be the simplified approach of lumping all spalling at $t=0$ minutes; how critical the spalling location is; influence of the extent of spalling etc. Hence, there are lot of open question which needs to be answered to quantitatively quantify the effect of spalling on the response of RC members/structures.

To answer the above questions there is also a need of advance tools which can be easily used to investigate the influence of various parameters. The paper presents a flexibility based distributed plasticity fiber beam-column element, which has been successfully implemented in a standalone in-house FE code to simulate the response of 2D RC structures during fire. After presenting the validating of the FE code a parametric study was conducted to study the influence of time and location of corner spalling on the response of RC beam.

NUMERICAL MODEL

Basically, the numerical model presented is a sequentially coupled thermo-mechanical model. As the first step, temperature distribution across the cross-sections are computed for the given exposure condition by conducting 2D transient heat transfer analysis. In the second step thermal stress analysis is performed using distributed plasticity fiber beam-column element. The temperatures computed in the first step is used at various integration points/cross sections along the element length depending on the exposed length of the member. The sectional discretization used for both the steps is kept same.

In the presented modelling approach based on fiber approach, the elements used for modelling the RC member/structure, is subdivided into longitudinal concrete and steel fibers. The fibers are designated as S_i and are geometrically characterised by their centroidal location (x_i, y_i) in the local planer coordinate system and the fiber area A_{S_i} . Hence, the force-deformation characteristics for each section need not be explicitly specified, rather are derived by integrating the response of the fibers. Each fiber follows the temperature dependent uniaxial stress-strain relationship for the correspondingly assigned material.

Transient heat transfer analysis

The heat transfer module with moving thermal boundary conditions, developed by the authors [1, 2] (the validation of the same can also be found in [1, 2]) is used for obtaining the temporal and spatial distribution of temperature. The centroidal location of each fiber S_i , identified as (x_i, y_i) , serve as the computational points at sectional level. Based on the assumption of lumped system, each segment is considered to have uniform temperature and properties are lumped at the centroid of the segment.

The governing differential equation for 2D transient heat conduction problem, given by Eq. (1), is solved using Finite Difference Method (FDM). The Eq. (1) is formulated using implicit central difference scheme, which takes the form of Eq. (2) for a uniform grid mesh. Equation (2) can be further rearranged to yield a simpler forms, given by Eq. (3) in terms of coefficients ($a_P, a_E, a_W, a_N, a_S, b$) and temperatures of the segments/fibers ($T_{SP}^t, T_{SE}^t, T_{SW}^t, T_{SN}^t, T_{SS}^t$). Equation (3) is then solved iteratively to obtain the spatial and temporal distribution of temperature, $T(x, y, t)$. The radiative and convective boundary conditions is given by Eq. (4). The model at every time step checks if some fibers have spalled (based on the user input) and modifies the computational domain and updates the thermal BC's to the new domain boundaries corresponding to the current time step.

$$\frac{k}{\rho c} \left[\frac{\partial^2 T}{\partial x^2} + \frac{\partial^2 T}{\partial y^2} \right] = \frac{\partial T}{\partial t} \quad (1)$$

$$\alpha \left[\frac{T_{SE}^t - 2T_{SP}^t + T_{SW}^t}{(\Delta x)^2} + \frac{T_{SN}^t - 2T_{SP}^t + T_{SS}^t}{(\Delta y)^2} \right] = \frac{T_{SP}^t - T_{SP}^{t-1}}{\Delta t} \quad (2)$$

$$a_P T_{SP}^t = a_E T_{SE}^t + a_W T_{SW}^t + a_N T_{SN}^t + a_S T_{SS}^t + b \quad (3)$$

$$-k \frac{\partial T}{\partial n} = h [T_g - T_s] + \varepsilon \sigma [(T_g + 273)^4 - (T_s + 273)^4] \quad (4)$$

Where, k is the thermal conductivity (W/m °C), ρ is the mass density (kg/m³), c is the specific heat (J/kg. °C), h is convective heat transfer coefficient (W/m² °C), ε is Stephen Boltzmann constant (5.667×10^{-8} W/m² °K⁴), σ is surface emissivity (-), T_g is gas temperature (°C) and T_s is surface temperature (°C).

Since, the reinforcing steel are not considered during the heat transfer analysis, the temperature of the element fibers representing the reinforcing steel are assumed to be same as that of concrete at corresponding reinforcement centroidal location. The lower bound conductivity and specific heat for concrete with 3% moisture, as given by Eurocode2 (2004) [3] are used for the presented study. The selection of these thermal properties is based on the parametric study and validation done by Lakhani et al (2013) [4].

Thermal stress analysis

In order to carry out the thermal stress analysis, the RC member is modelled using flexibility based distributed plasticity fiber beam-column element. The basic assumptions for the element formulation are given below:

1. At sectional level: Plain section remains plain under flexural deformations
2. Perfect bond is assumed between reinforcing steel and concrete
3. The member is straight and prismatic
4. The element is geometrically linear
5. The element does not account for shear and torsion deformations

The matrices/notations used for forces and deformations at various levels of formulations are given in Table 1. At structural level (including rigid body modes) the element has 3 Degree of Freedoms (DOFs) at each node (2D formulation) viz., two translation and one rotational, as shown in Figure 1 (a). In order to formulate the element in flexibility domain the rigid body modes are removed using a compatibility matrix, leaving the element with three natural degrees of freedom i.e., two rotations (θ_1 & θ_2) at the two ends and an axial deformation (e). The forces corresponding to these deformations are the moments at two ends (M_1 & M_2) and the axial force (P). Figure 1 (b) shows the element schematically.

Table 1 Force and deformation matrices at various levels of formulation.

Formulation level	Forces	Deformations
Structural level	P	p
Element level (Flexibility based)	Q	q
Sectional level	$D(x)$	$d(x)$
Fiber level	$E(x)$	$e(x)$

The primary state variables at the sectional level are bending moment and axial force, as shown in Figure 1 (b). The force interpolation matrix $b(x)$ assumes that the bending moment varies linearly, and the axial forces are constant along the element length. The sectional forces are computed from the element forces using Eq. (5).

$$D(x) = b(x)Q \quad (5)$$

For an incremental scheme $D(x)$ & Q will be replaced with $\Delta D(x)$ & ΔQ , respectively. Using the sectional constitutive relationship $\Delta D(x) = k(x)\Delta d(x)$, Eq. (5) yields Eq.(6) stated below, where sectional flexibility matrix $f(x) = k^{-1}(x)$

$$\Delta d(x) = f(x)\Delta D(x) = f(x)b(x)\Delta Q \quad (6)$$

The deformation compatibility, between elemental and sectional deformations (given by Eq. (7)) is obtained by applying the principle of virtual forces. Thus, the residual elemental deformations (r) are given by Eq.(8) where, the elemental flexibility matrix is given by Eq.(9).

$$q = \int_0^L b^T(x) d(x) dx \quad (7)$$

$$F\Delta Q = r \quad (8)$$

$$F = \int_0^L b^T(x)f(x)b(x) dx \quad (9)$$

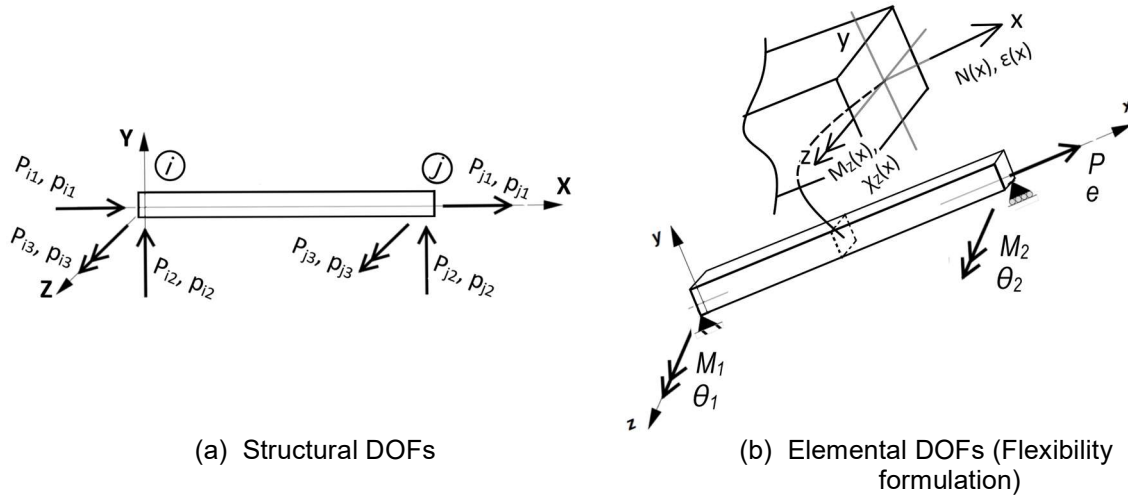


Figure 1 Beam-column element with and without rigid body modes.

The problem of determining the sectional deformations from the sectional forces is an iterative process. An element is said to have converged when convergence have been achieved at every integration point (section) along the length, this process requires an additional iterative loop, referred to as element state determination, within the standard solver procedure. The implementation of the flexibility-based element within the displacement based global system, along with the procedure used for determining the element state is based on the algorithm proposed by Taucer et al (1991) [5]. The

procedure has been updated to consider the thermal effects.

The uniaxial stress-strain constitutive laws & linear thermal strain for concrete and reinforcing steel, as function of temperature were taken for Eurocode2 [3].

VALIDATION

The numerical model discussed in the previous sections was implemented as a standalone finite element program capable of performing non-linear analysis of 2D RC frames subjected to fire. For validating the implementation and the modelling approach, beam B-124 tested by Lin et al (1981) [6] was selected. The beam had a cross-section of 305 mm x 355 mm and a span of 6100 mm between the supports and a cantilever overhang of 1800 mm at both ends. The beam was tested under simply supported condition, with 4 point loads distributed over the span, as shown in Figure 2. Each point load equals 20kN. The load was applied prior to fire exposure and was kept constant during the fire test. The beam was exposed ASTM E119 standard fire.

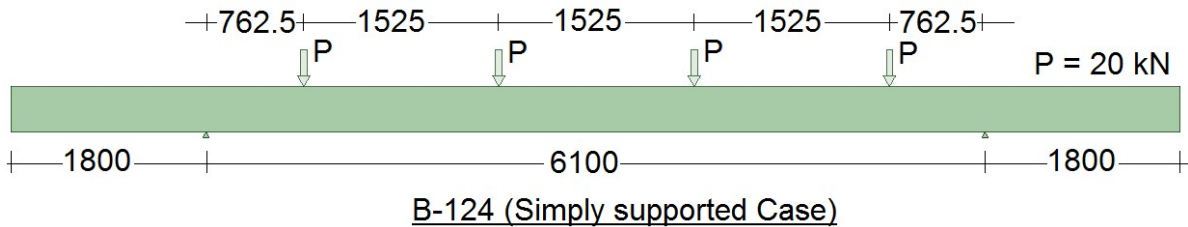


Figure 2 *Beam B-124 loading arrangement* (All dimensions in mm)

The tension reinforcement at mid span consisted of 4-19Φ bars and the compression reinforcement was 2-19Φ bars. For shear reinforcement, 9.5mm diameter bars at a spacing of 152mm near supports and 300 mm in mid span region was provided. The top and bottom clear cover to longitudinal reinforcement was 25mm and the side cover was 38mm. As Lie et al (1981) [6] also tested the beam with different support conditions to simulate the continuity effect, the reinforcement varied along the beam length as shown in Figure 3. The measured average yield strength of longitudinal reinforcement was 435.8 MPa and the average cylinder strength of concrete on the day of testing was 30 MPa. Concrete was made using carbonate aggregate and the reinforcement was assumed to be hot rolled.

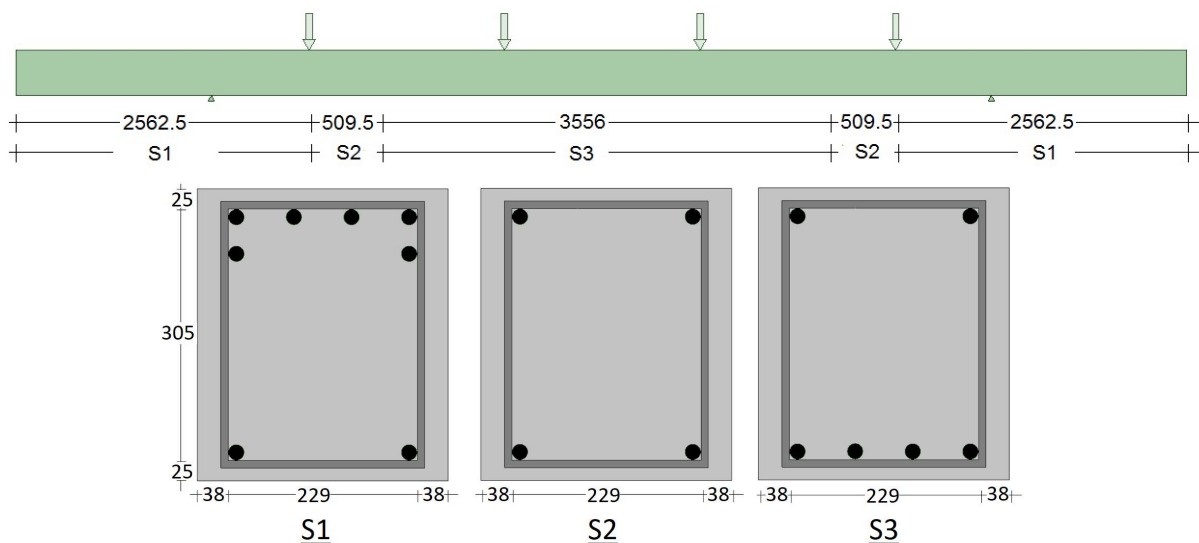


Figure 3 *Reinforcement details for beam B-124* (All dimensions in mm)

The beam cross-section was discretised with an element size of ≈ 14 mm. The beam was exposed to fire from three sides and the top was assumed to be insulated for heat transfer analysis. The comparison between the predicted and the experimental average rebar temperatures of tension reinforcement at mid span (average temperature of 4 tension rebars for section S3) is shown in Figure 4. It can be seen that the numerical results match well with the experimental results.

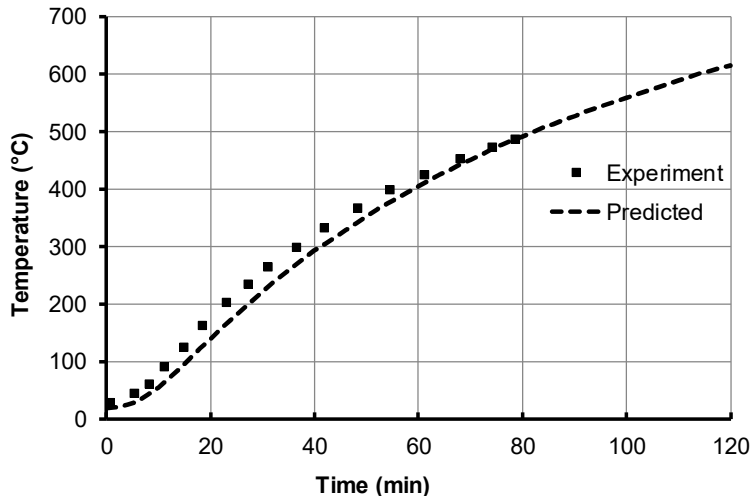


Figure 4 Average temperature of tension reinforcement at mid span for beam B-124

For the stress analysis the beam was discretised used 9 elements with each element having 3 gauss points along the length. The experimental and numerically predicted mid span deflections variation with time is shown in Figure 5. Experimentally the fire test was stopped at 80 minutes due to visibility of large cracks and may be to avoid any damage to the test furnace. The predicted deflections are slightly under predicted but are still in reasonable agreement with the experimental values up to 80 minutes. Numerically the beam failed at 94 minutes. On analysing the plastic hinge formations, it was observed that the beam did not formed a hinge in the mid span (along section S3). But the weakest section was S2 and the beam failed due to a hinge formation along section S2.

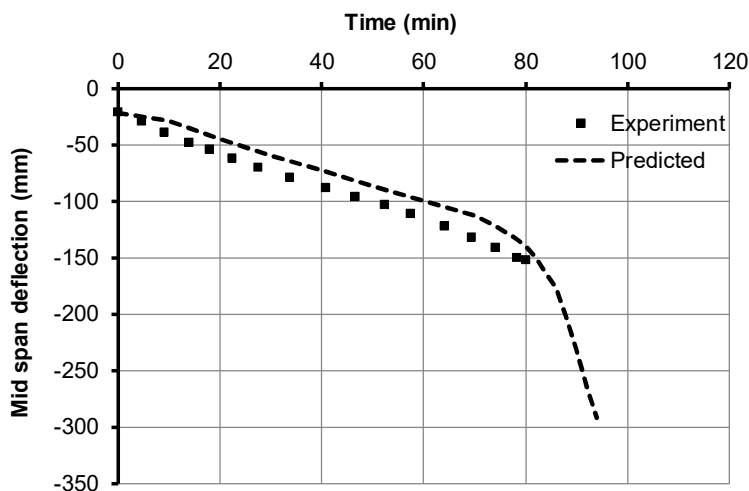


Figure 5 Predicted and numerical variation of mid span deflection with time

PARAMETRIC STUDY: EFFECT OF SPALLING

After having validated the FE code against beam B-124 in previous section, a parametric study was performed to investigate the effect of corner spalling. Corner spalling was chosen under the presumption that it is more common and severe. The spalling profile considered is

shown in Figure 6. For the same spalling profile various parameters investigated includes the following:

1. Effect of spalling time on the predicted reinforcement temperature: Three spalling times were considered viz., 0 minutes, 15 minutes and 30 minutes. The case with 0 minutes represents the simplified conservative case.
2. Effect of spalling location: Two different locations along the member length were analysed. The first location is the intuitive one i.e., at the mid span, being a simply supported case. Hence spalling was assumed to occur along the full length of section S3. For the second case spalling was assumed to occur along the full length of section S2. The second location was chosen because it was found that for the reference case (no spalling - validation case) section S2 is the weakest section.

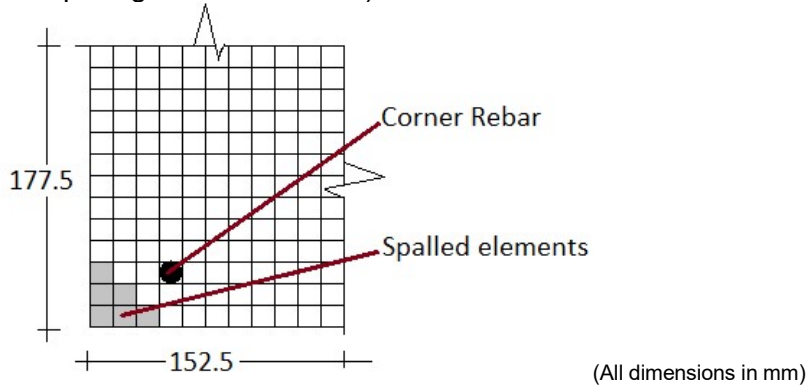


Figure 6 Corner spalling profile for the parametric study

Only two different spalling times 0 and 30 minutes were considered for each spalling location i.e., along section S3 and section S2. Hence, this results in a total for 4 combinations in addition to the no-spalling reference case.

Results: Transient heat transfer analysis

The section discretisation (element size ≈ 14 mm) and the thermal properties (lower bound conductivity and specific heat for concrete with 3% moisture as per Eurocode2) were kept the same as for the validation case. The predicted temperature contours at 60 minutes for the no spalling case and the corner spalling case (@30 minutes) are shown in Figure 7. It may be noted that the heat concentration zone near the corner is lost due to the spalling considered. The predicted temperatures for the corner tension rebar and the middle tension rebar (refer Figure 3 for rebar locations) for different spalling time is shown in Figure 8(a) & (b). The temperatures for the middle rebar were found to be independent of the spalling time. This is due to the chosen spalling configuration which is confined only to the corner.

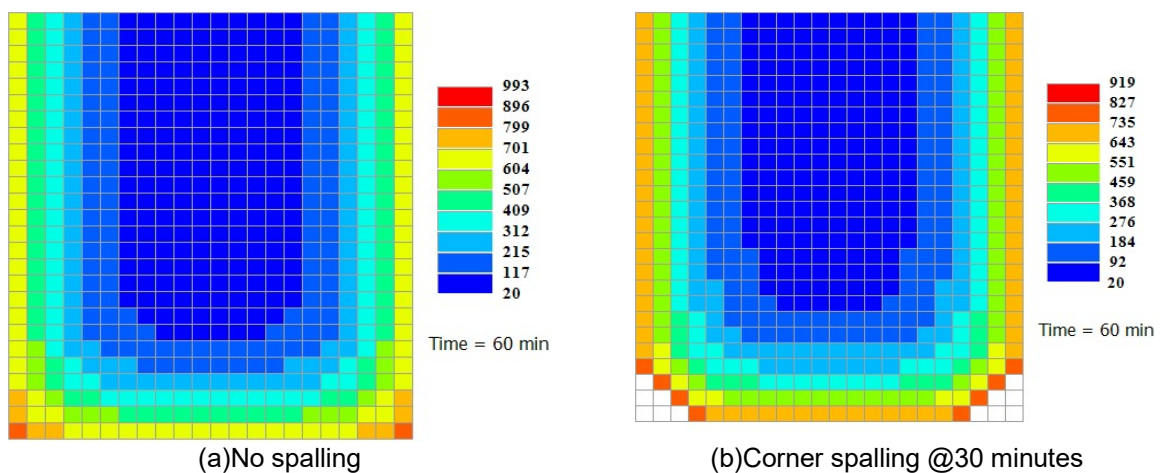


Figure 7 Temperature contours for reference case and spalling (@30minutes) case

As shown in Figure 8 (a), higher temperatures are attained by the bottom corner rebar due to spalling. The predicted temperatures are confined to the band whose upper limit can be defined by the spalling case where $t=0$ minutes and the lower limit is defined by the no-spalling case. The case with spalling time, $t=0$ minutes, gives the highest corner steel temperatures. It is also interesting to observe that the curve for spalling time $t=0$ minutes serves as an envelope to the curves for different spalling time (in this case $t=15$ minutes and $t=30$ minutes).

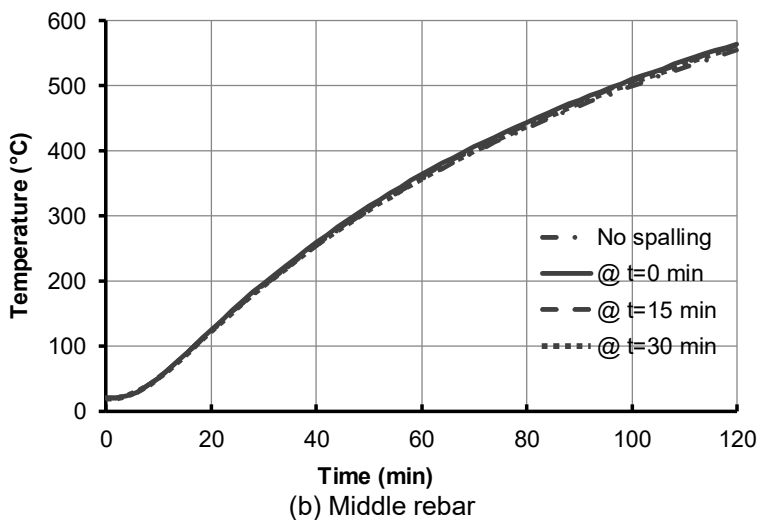
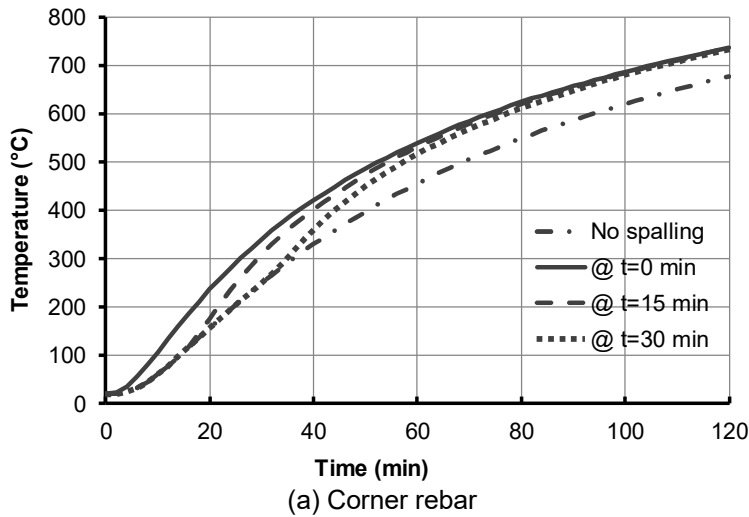


Figure 8 Effect of spalling time on the predicted temperatures for tension reinforcement

Results: Stress analysis

For the stress analysis the beam was again discretised using 9 elements along the length. The central 5.48 m of beam between the supports was exposed to standard fire (ASTM E119). The results of the stress analysis in terms of mid-span deflection with time are shown in Figure 9.

It was observed that the predicted mid span deflections were higher for spalling time $t=0$ minutes as compared to $t=30$ minutes for both the spalling locations. It is also interesting to observe that the spalling location along section S3, although at the location of maximum moment, did not affected the failure time. This observation/behaviour may be attributed to the fact that the section S3 has 4 tension reinforcement and the average temperature of the

tension reinforcement did not alter significantly for the chosen corner spalling profile (ref Figure 6 for spalling profile). Since the temperatures of middle rebars were unaffected due to the chosen corner spalling configuration. But for the spalling along section S2 slight difference (approx. 4 minutes) was observed in terms of failure time for cases $t=0$ and $t=30$ minutes. Spalling along section S2 was decisive as compared to spalling along S3, which is also in line with the observation for the reference no-spalling case.

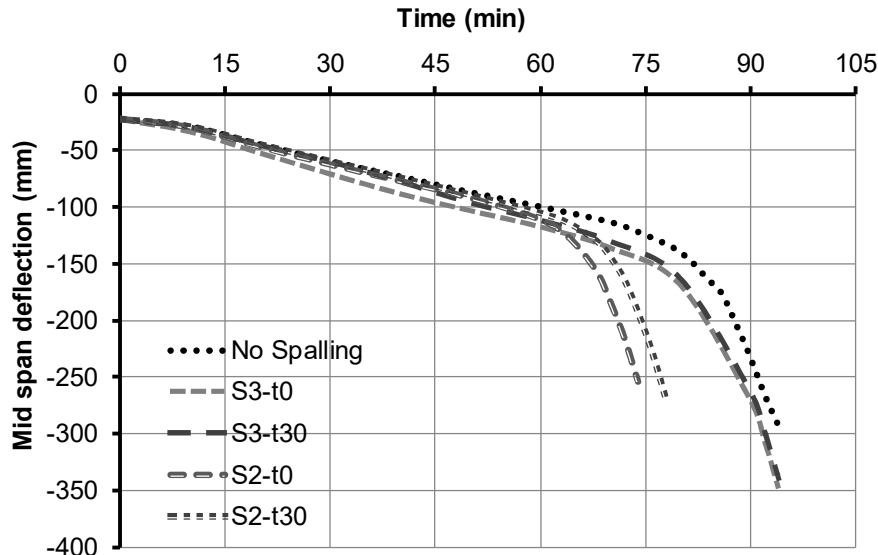


Figure 9 Displacement time graphs for different spalling locations and time

CONCLUDING REMARKS

In this paper, a flexibility based distributed plasticity fiber beam-column element has been discussed for simulating the response of RC beams during fire. The discussed element has been successfully implemented in a standalone FE code. The discussed numerical model uses the previously developed module for 2D transient heat transfer analysis with moving thermal boundary conditions, to simulate the effect caused due to spalling. The validation of the FE code and numerical modelling approach has been presented. Moreover, a parametric study, investigating the effect of time and location of corner spalling along the member length has been presented. The following conclusion were drawn from the parametric study:

1. The predicted temperatures due to different spalling times are confined to the band whose upper limit is defined by the spalling time $t=0$ minutes and the lower limit is defined by the no-spalling case.
2. The effect of spalling is dependent on the chosen spalling configuration and the reinforcement detailing. For example, from the presented cases; if the section has 4 rebars and a corner spalling occurs the average tension reinforcement temperature might not change significantly as compared to individual rebars closer to the spalling zone.
3. It was also observed that even for a case as simple as simply supported beam, reinforcement layout may play a role in deciding the critical section both for the no-spalling cases and also for identifying the critical spalling location.

REFERENCES

1. Lakhani, H., and Hofmann, J., "Effect of spalling on thermal analysis and structural behaviour of reinforced concrete beams under fire", In: Proceedings of the 5th International Workshop on Concrete Spalling, Boras, Sweden, 12-13 October, 2017.
2. Lakhani, H., and Hofmann, J., "Advance heat transfer analysis and capacity curves

- accounting for the effect of spalling”, In: Proceedings of the 10th International Conference on Structures in Fire, Belfast, United Kingdom, 6-8 June, 2018.
3. Eurocode2, “EN 1992-1-2 (2004): Eurocode 2: Design of concrete structures - Part 1-2: General rules - Structural fire design”, Brussels: European Committee for Standardization, 2004
 4. Lakhani, H., Kamath, P., Bhargava, P., Sharma, U., and Reddy, G.R., “Thermal analysis of reinforced concrete structural elements”, *Journal of Structural Fire Engineering*, 4(4), 227–44, 2013.
 5. Taucer, F.F., Spacone, E., and Filippou, F.C., “A fiber beam-column element for seismic response analysis of reinforced concrete structures”, Berkeley: Earthquake Engineering Research Center, College of Engineering, University of California, Report No.: UCB/EERC-91/17, 1991.
 6. Lin, T.D., Gustaferro, A.H., and Abrams, M.S., “Fire Endurance of Continuous Reinforced Concrete Beams”, Report No.: RD072.01B, Portland Cement Association, 1981

Concrete spalling failure: a coupled buckling instability and crack failure analytical model

M. De Poli^{1,*}, C.B.M. Blom^{2,3}, B.B.G. Lottman⁴

¹ Fluor Infrastructure, The Netherlands (matteo.de.poli@fluor.com)

² Stevin II lab, Delft University of Technology, The Netherlands (C.B.M.Blom@tudelft.nl)

³ Municipality of Rotterdam, Stadsontwikkeling, The Netherlands (cbm.blom@Rotterdam.nl)

⁴ Witteveen+Bos, Department. of Underground Infrastructure, The Netherlands
(bas.lottman@witteveenbos.com)

* Corresponding author (Fluor Infrastructure, Taurusavenue 155, 2132 LS, Hoofddorp, The Netherlands, e-mail: matteo.de.poli@fluor.com)

ABSTRACT

This paper presents part of the results of the Delft University of Technology master thesis: “Fire dynamics and spalling mechanism in tunnel infrastructures” [3] and aims at further developing the knowledge on the topic of spalling failure. Elaborating experimental data together with the development of an analytical model, a new description of the spalling failure mechanism has been proposed. The spalling model is based upon the idea of the occurrence of a series of two failures, which are the buckling instability and crack failure of a superficial concrete layer.

The model predicts the failure time for NSC elements and at the same time verifies which is the optimal thickness for the piece to spall. On top of that, some thoughts over the influence of pore pressure, HSC and PPFRC elements on the outcome of the proposed model have been shared.

The paper results suggest that in case the structural design accounting for spalling occurrence is allowed, then the proposed model could allow engineers to estimate the cross-section reductions and consequently design the structure in accordance with these conditions. Additional spalling full-scale test are recommended, in particular with the objective of recording the progress in time and crack development during the spalling failure with the use, for example, of high-speed image recording [13] and acoustic emission tomography [18].

KEYWORDS: Spalling failure, spalling analytical model, Instability spalling model

1. INTRODUCTION

In the last few years, within the field of civil engineering, there has been a growing interest in underground infrastructures, and in particular in tunnels. One of the main issues of concern is fire safety. Scientific research and regulations are currently tackling the numerous topics related to this field driven by the need to reach safer and more economical ways to design and

use underground infrastructures. One of the topics of interest is understanding the spalling mechanism, endangering the capacity of concrete structures during a severe fire. Despite the great interest on this topic and the relatively high number of research studies, a general theoretical framework seems to be still missing. In this paper, the focus is on proposing an original analytical model to explain the spalling mechanism, aiming for a more practical approach.

Following the definition of Khoury et al. [1], spalling is defined as: "The violent or non-violent breaking off of layers or pieces of concrete from the surface of a structural element when it is exposed to high and rapidly rising temperatures as experienced in fires". The consequences for the concrete structure could be multiple, leading in extreme cases to redistribution of forces with associated deformations and ultimately possible collapse of part of the structure, as reported by Khoury et al. [1]. In order to limit the damage and ensure that the structural resistance is maintained protective measures are applied. In the fib technical report [2], for instance, polypropylene fibres in the concrete mix or thermal barriers applied to the fire exposed surface are indicated.

In this paper we present in section 2 the common spalling mechanisms currently mentioned in literature. Section 3 is dedicated to the explanation of the new proposed spalling model and in section 4, the way in which the proposed model might account for the influence of pore pressure or different concrete types is being articulated together with the future possibilities and outlooks offered by this model. The paper concludes by presenting the main results, possible use of the model and needs for its further extension and practical use.

2. COMMON SPALLING MECHANISM MODELS

Many studies in order to explain the mechanism causing the spalling phenomenon have been conducted and various possible models have been proposed. In 1963, Kordina [4] developed a theory describing spalling as the consequence of imposed deformations with corresponding thermal stresses caused by the temperature development in the element. A different approach was followed by Harmathy [5], who in 1965 developed a theory pointing the attention to moisture evaporation in the element causing pressure development in the pore system leading to spalling. Following his work, Waubke [6] did one of the first calculations based on pore pressure development. Meyer-Ottens [7] and Zhukov [8] associated the possible causes of the spalling mechanism to be a combination of pressure development and thermal stresses. More recently, according to Lottman [9], an alternative possible explanation for the spalling mechanism has been proposed, extending on the principle of thermal stresses. The occurrence of spalling is linked to restrained thermal deformations with the instability of heated layers at the fire exposed surface being governed by a form of buckling. This conclusion is based upon the results obtained with a FEM model coupling fracture mechanics and temperature/pore pressure developments.

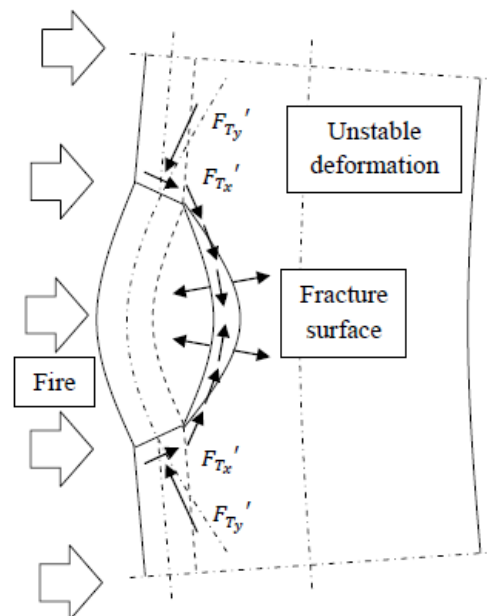


Figure 1 Schematic overview of fire induced spalling according to [9]

3. COUPLED BUCKLING INSTABILITY AND CRACK FAILURE SPALLING MODEL

(*the author would refer to as "*Instability spalling model*" from this point and onwards)

Based on the conclusions made by Lottman [9] and highlighted in the previous section, the *instability spalling model* is hereafter proposed. The main idea behind the model is the description of the phenomenon as the buckling instability of concrete layers exposed to the fire. The model is based upon the occurrence of a series of two inter-related failures:

- Buckling instability;
- Crack failure.

Modelling the problem in this way allowed us to include the effect of the imposed thermal deformations. On the other hand, it does not yet take into account the effect of the pore pressure. This choice follows the considerations formulated in the work of Lottman [9] over the minor influence on the spalling mechanism of the pore pressure in a cracked element. In the following subsections the explanation of the *instability spalling model* will be presented. The different assumptions, ideas and concepts used in the model will be explained and the obtained results presented and analyzed.

3.1 Overall instability spalling model overview

The overview of the *instability spalling model* is shown in Figure 2. The model is divided in two parts, following the 2 failure mechanisms involved. The first part (preliminary) aims at giving a first estimate of the spalling time while the detailed part aims at confirming or providing, after an iterative process, the occurring spalling time caused by the simultaneous buckling and crack failure.

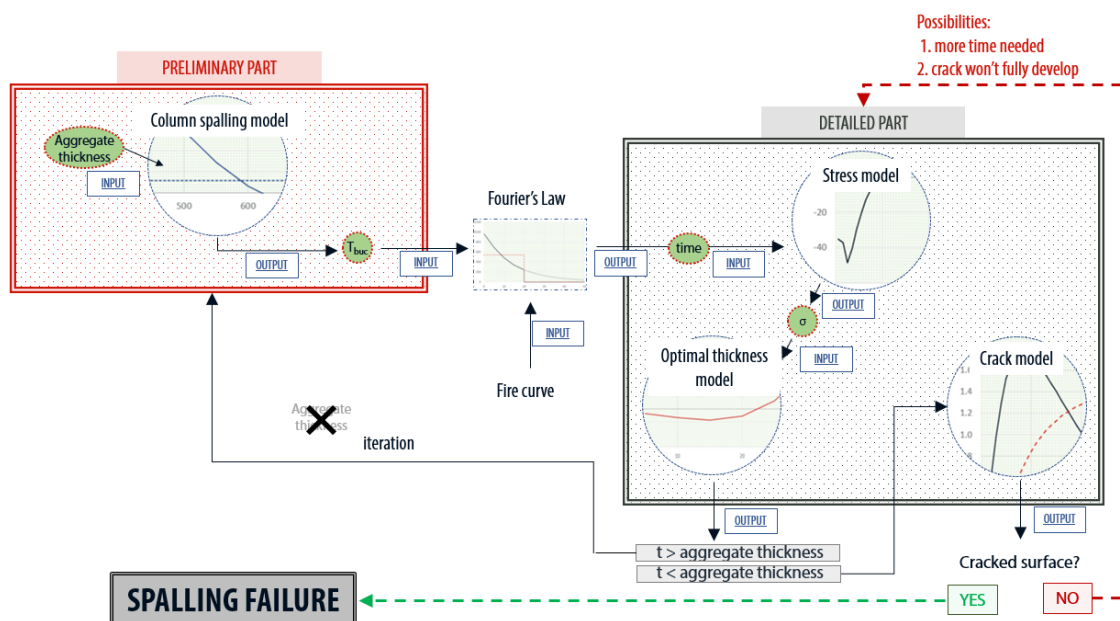


Figure 2 Overview "*Instability spalling model*"

In the preliminary part, given an initial assumption over the spalling thickness (equal to the aggregate size), an estimate for the occurrence or not of spalling is obtained using the *column spalling model*. In the former case, the time of occurrence can be derived. Based on the time outcome, a more accurate calculation can be carried out in the detailed part of the model. Given the fire curve and the time of spalling, knowledge of the stress in the cross section is possible through the *stress model*. Afterwards the optimal thickness for the piece to spall can be calculated and the presence of the crack checked, both determined

by separate models. In case the optimum required thickness is smaller than the aggregate size, the initial estimate for the thickness is found to be valid. If the opposite holds true then the optimal thickness is chosen and an iteration is carried out.

Basically the proposed method assumes that spalling failure is caused by the combined buckling instability (preliminary part) and crack failure (detailed part). Both separate processes do not allow spalling to occur.

3.2 Experimental results and temperature gradients

In order to have data regarding the detailed spalling mechanism development in time, test results were searched in literature. One of such test series available and containing this information was carried out by FSV [10]. The detail level of the results reported in this study are considered of interest and used to calibrate and verify the proposed spalling model.

These tests are carried out on concrete elements (1400x1800x500mm) with a load applied in the longitudinal direction through prestressing. In the transverse direction, prestressing is also applied. The transversal prestress load is applied with a magnitude such to simulate a fully clamped condition in that direction. In this way a plane strain situation simulating an infinitely long cross section can be achieved. In Figure 3 an example of the test setup is shown. The tests were carried out on multiple elements with different characteristics. In particular: different loads applied, different concrete types, different aggregate types, different fire curves used.

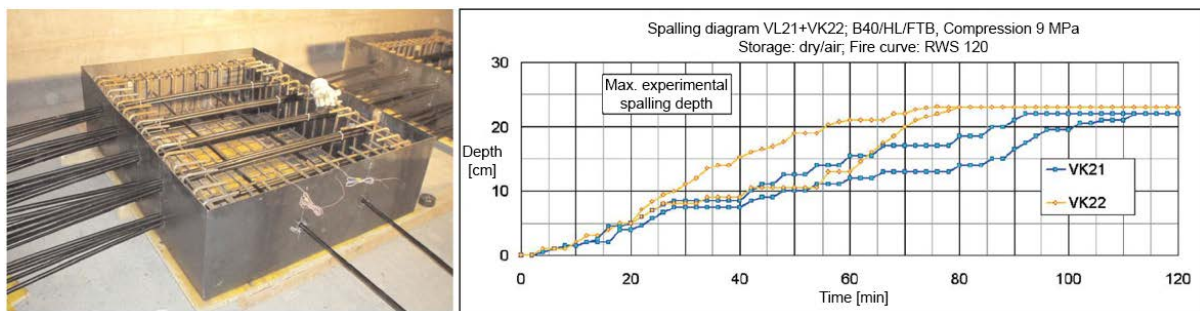


Figure 3 FSV544 spalling tests [10]

For calibration and verification purposes our focus was on the extensive set of data coming from NSC tested elements. A list of the considered test results used with the different characteristics of each test is shown in Table 1. In particular, of importance are the results showing the behaviour of the spalling mechanism in time. The basis for the creation of time-spalling diagrams in [10] were the observations of ejected debris on the smoke pipe during the experiments. These observations were compared with probe temperatures and acoustic recordings, which could show sudden increase in temperature together with single splitting noises at the moment of spalling.

In Figure 3 an example of such results is shown with the spalling depth in time recorded. In order to understand if the proposed spalling mechanism model can become a viable option to describe spalling, we will only focus on the first piece that spall. In Table 1 the first spalling depth (t) and time of occurrence (t_s) extrapolated from the graphs, such as the one of Figure 3, are listed.

The temperature gradients of concrete elements exposed to a given fire curve can be obtained through the use of Fourier's Law which describes the heat flux through a material. Various numerical models based on Fourier's Law exist. This paper is based on the numerical model described in [3] which includes radiative and conductive B.C. and a temperature dependent thermal conductivity.

Table 1 List of spalling test results

Test	Fire Curve	Calc/Silic	f_{cm} [Mpa]	σ_{ext} [Mpa]	t [mm]	t_1 [min]
VK01	RWS 120 (reduced)	C	33	1.16	21	12
VK02	RWS 120	C	33	1.16	20	6
VK05	RWS 120	C	33	1.16	18	4
VK06	RWS 120	C	33	1.16	22	3
VK11	RWS 120	C	33	9	26	2
VK12	RWS 120	C	33	9	31	1.5
VK19	ETK 240	C	33	1.16	21	7
VK20	ETK 240	C	33	1.16	16	4
VK21	RWS 120	C	38	6.5	15	4
VK22	RWS 120	C	38	6.5	10	2
VK33	Lainz 180	S	33	1.16	15	3
VK34	Lainz 180	S	33	1.16	32	2.5
VK43	RWS 120	S	33	1.16	17	3
VK44	RWS 120	S	33	1.16	17	3
VK58	Lainz 180	S	33	1.16	16	4
VK59	Lainz 180	S	33	1.16	33	4

3.3 Buckling instability failure

Buckling instability is one of the two failure mechanisms regarded in the model proposed in order for spalling to occur. This phenomenon has been idealized and modelled in the *column spalling model*. The reader is referred to Figure 4 for a graphical visualization of the model.

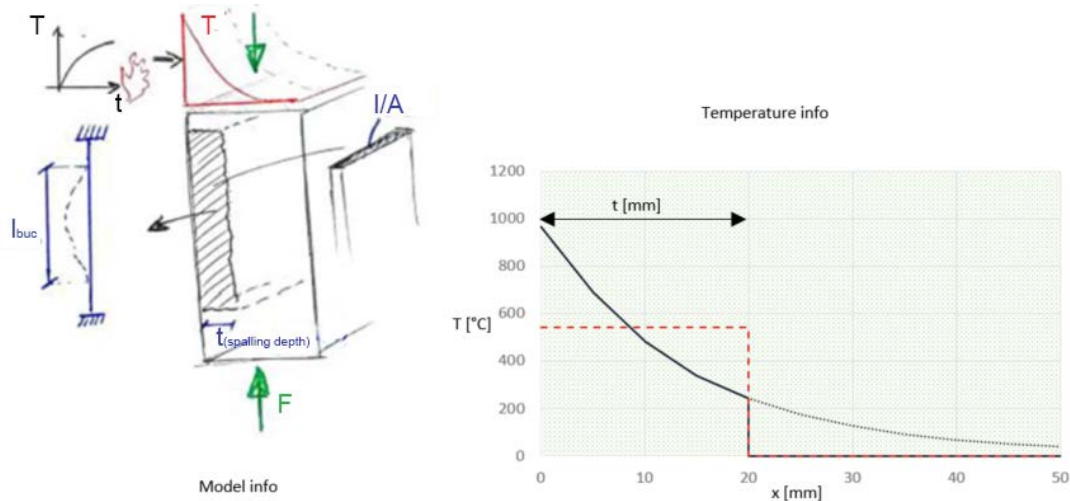


Figure 4 Column spalling model

At the moment in time when spalling could occur, it is assumed that the concrete is already cracked at a certain known depth (t). Considering the results of the tests and what is seen in practice, it was chosen to assume the aggregate size of the concrete mix as the initial depth. The spalled piece is regarded as a column of rectangular cross section, with dimensions equal to the thickness of the spalled piece (t), the width of the element (b) and the buckling length (l_{buc}). In general, the acting load (F_{Ed}) is composed by the external load (F_{ext}) and the thermal load ($F_{\Delta T}$) caused by the imposed deformation. As such the spalled piece is regarded as fully clamped at the supports. The resistance (F_{Rd}) is given by the Euler buckling resistance (F_{buc}), assuming linear elasticity. In the equations below the acting load and the resistance are related to each other.

$$F_{Ed} \geq F_{Rd} \leftrightarrow F_{ext} + F_{\Delta T} \geq F_{buc} \quad (1)$$

$$\sigma A + E_c(T)\epsilon_c(T)A \geq \frac{\pi^2 E_c(T)I}{l_{buc}^2} \leftrightarrow \sigma bt + E_c(T)\epsilon_c(T)bt \geq \frac{\pi^2 E_c(T)bt^3}{l_{buc}^2 12} \quad (2)$$

The temperature profile in the cross-section has a gradient, but for simplicity a constant temperature is assumed over the thickness of the spalled piece. This is the average temperature as it is shown in Figure 4. The Young's Modulus ($E_c(T)$) and the thermal elongation ($\epsilon_c(T)$) are temperature dependent and have been modelled according to [11]. As can be seen in Eq. (2), the model is independent of the width of the spalled piece (b). In order to use the model knowledge of the buckling length (l_{buc}) is needed. Using the tests data of Table 1 the model is calibrated in order to derive the buckling lengths for the various tests. In order to do so, the following info retrieved from the test data were used:

- the spalled depth (t);
- the time at which spalling occurs (t_I).

Knowing the fire curve that was applied, the average temperature (T_{avg}) at time tI , the Young's Modulus ($E_c(T)$) and the thermal elongation ($\epsilon_c(T)$) can be derived. These can be inserted into Eq. (2) after which the unknown buckling length (l_{buc}) can be obtained. A repetitive relation between the length and depth of the spalled piece has been found. As shown in Figure 5, at a macroscopic level the spalled piece forms an averaged angle of 85° between the spalling depth and the buckling length. Surprisingly the result just mentioned is obtained from tests including elements with different characteristics or exposed to distinct fire curves. This relation has thus been used in the *instability spalling model*.

In order to improve understanding and facilitate the use of the model, Eq. (1) is expressed using the external force and reads:

$$F_{ext} = F_{buc} - F_{\Delta T} \quad (3)$$

With use of Eq. (3), the average temperature causing spalling can be determined. In Figure 5, an example of the results obtained with the *column spalling model* is shown. Buckling failure occurs in this case at an average temperature across the thickness of the spalled piece greater than 580°C .

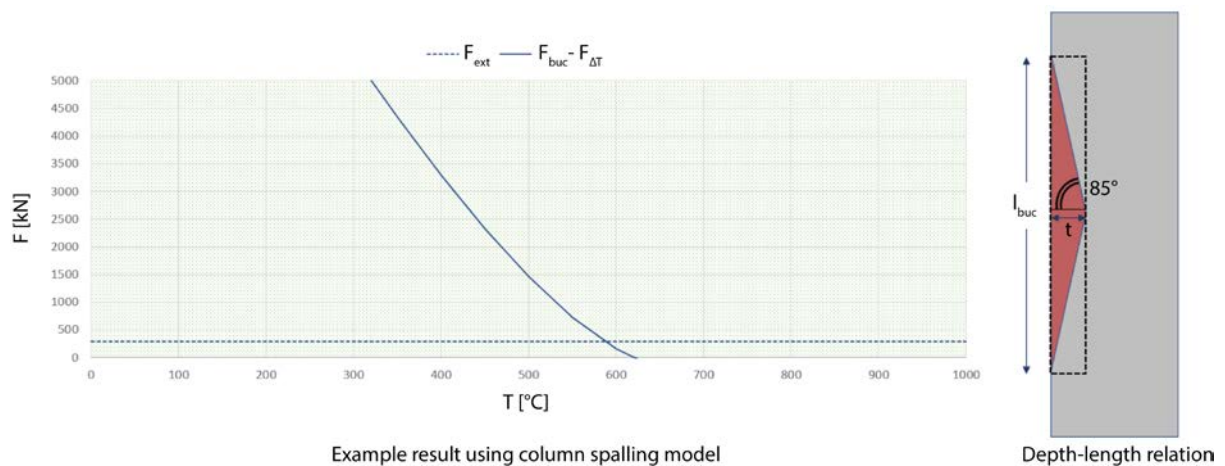


Figure 5 Column spalling model output and assumptions

3.4 Crack failure

Crack failure is the second mechanisms considered in order for spalling due to buckling to occur. The formation of a cracked surface at the rear of the spalled piece is necessary for its detachment from the element and in particular for the buckling instability to take place. The cracking mechanism has been modelled through a strut&tie approach [17]. The forces applied to it are derived from the acting stresses. The *stress model* is used to obtain the stress state and verify whether the depth at which the crack is forecasted is the optimal one. The optimal thickness is the thickness that will most likely characterize the first spalled piece.

Stress model

The stress model is based on the work of Lottman in [9] which gives formulas to calculate the linear elastic stresses in the cross section exposed to a single sided fire while subjected to external load and support conditions.

Optimal thickness model

Knowing the stress in the cross section from the *stress model*, it is possible to investigate the spalled piece thickness which is more prone to buckle and cause spalling using Eq. (2). If we compare, for every possible thickness, the buckling force resistance (F_{Rd}) and the acting load ($F_{Ed}=\sigma A$), which includes both external load and thermal expansion, we can find for which thickness the load overcomes the resistance. The optimal thickness is the one that has the higher probability to cause buckling and it is, in this case, the thickness with a higher difference between the load and the resistance.

Crack model

The strut & tie model idealization used to assess crack failure can be seen in Figure 6 and it is composed of a double triangular truss.

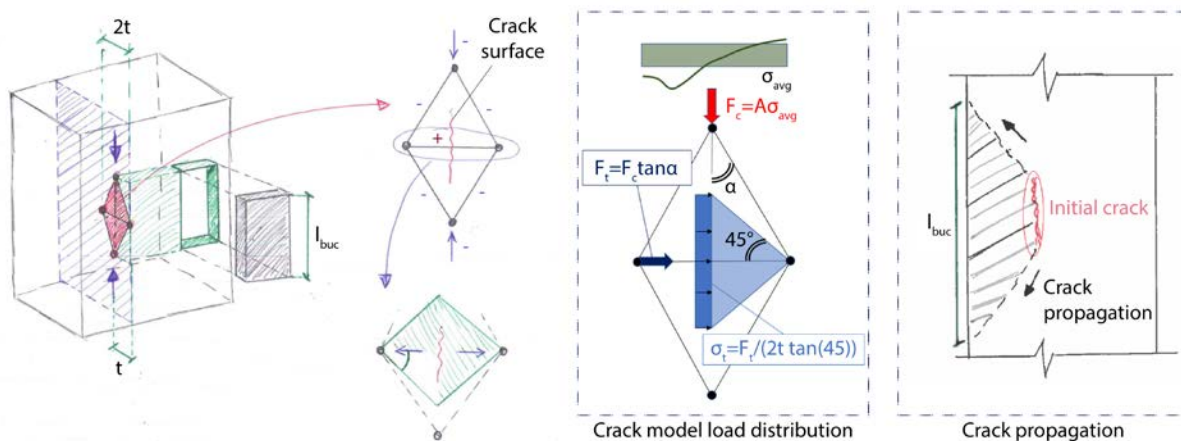


Figure 6 Crack model idealization

The width of the truss is equal to two times the optimal spalled piece thickness. This is due to the fact that the crack is assumed at the middle of the horizontal truss since this direction is in tension. The length of the truss is taken equal to the buckling length and the force acting at the nodes is proportional to the average stress over the thickness. In the case the average stress results in tension, the force acting is assumed to be null. This is related to the fact that in that case the horizontal truss is subject to compression which do not give rise to cracks in the concrete. The concrete crushing verification is neglected.

An additional feature of the model is the load spreading from the 2 side nodes of the truss subjected to tension. It is assumed that the tension force spreads in the direction of the middle cracked surface forming an angle of 45° as visualized in Figure 6. In the same figure the expressions to calculate the loads acting on the strut & tie model are highlighted. The angle α is assumed constant and equal to 85° .

As shown the tension force is determined based on the spalling piece angle ($\alpha = 85^\circ$) while the tensile stress governing the crack formation is based on the 45° spreading angle. The reasoning for this difference in assumed angles is found in that the initial crack formed tends to have a smaller length compared to the buckling length of the piece eventually spalled. This is an assumption based on the fact that a simultaneous crack over the entire buckling length would not be possible due to the stresses being spread over a considerable length. Moreover, it is considered valid given the shape of the remaining concrete voids caused by spalling which are often recorded on spalling depth plans as done in [10]. The crack development could also be further investigated in future spalling tests using acoustic emission topography techniques [18].

After the initial crack has originated, during continued compression, it propagates till the piece is separated as can be seen in Figure 6. In this idealized crack model, this two-steps crack phenomenon is assumed to occur simultaneously.

3.5 Results

This subsection shows the results obtained with the proposed spalling model. The following standard elements have been chosen as a reference and analyzed in detail:

A: concrete element C20/25 with 16mm calcareous aggregate subjected to an external axial stress of 5 MPa;

B: concrete element C20/25 with 32mm calcareous aggregate subjected to an external axial stress of 5 MPa.

The effects of some of the most common fire curves have been investigated, namely:

- **ISO:** the cellulosic curve based upon building materials burning rates;
- **Hydrocarbon:** the hydrocarbon design fire curve proposed, used in the ROK [12] to model the worst scenario temperature curve in the open parts of tunnels;
- **RWS:** the RWS design fire curve proposed, used in the ROK [12] to model the worst scenario temperature curve in the closed parts of tunnels.

In Table 2 the average temperature over the spalled thickness for which the *column spalling model* forecasts buckling instability is listed for different elements. It can clearly be noted that for different thicknesses the same buckling temperature is predicted. This outcome doesn't mean that for different thicknesses the spalling mechanism occurs at the same time. In fact, a wider thickness requires more time to be heated till the critical average temperature is reached. Another feature is the independence of these results of the fire curve and that an increasing load has as a consequence of buckling failure occurring earlier in time. This result is confirmed by the test results of FSV [10].

Table 2 Average spalling temperature over the spalled thickness - Model results

t [mm]	σ_{ext} [MPa]	Aggregate type	Concrete	l_{buc} [mm]	T_{avg} [°C]
16	5	Calcareous	C20/25	366	221
32	5	Calcareous	C20/25	732	221
32	0	Calcareous	C20/25	732	247
32	5	Calcareous	C20/25	732	221
32	10	Calcareous	C20/25	732	195

In Table 3 the spalling times, as a result of buckling instability, for concrete elements exposed to various fire curves are shown. It can be noted that more severe fire curves (RWS and Hydrocarbon), both in terms of maximum temperature and gradients, cause buckling to occur earlier in time. The results obtained for the RWS curve are in line with results of full-scale tests [10]. In particular, the tests conducted in similar conditions compared to the ones here assumed, such as VK21/VK22 of Table 1, fit particularly well the model outcome having spalling times in the range of 2-4 min. Conversely, it must be noted that exposure to the ISO fire curve causes as well buckling instability, even though delayed compared to RWS. This result contrasts with recorded evidences of concrete elements exposed to the ISO curve not experiencing spalling. However, it must be kept in mind that spalling, according to the proposed model, can arise only if both failure mechanisms occur. The latter implies that the element could be prone to buckling while the crack has not fully developed. This could apply for elements exposed to moderate fire curves such as the ISO curve where the crack propagation might be a governing factor while the current version of the model assumes an instantaneous crack growth.

Table 3 Spalling times - Model results

	ISO	Hydrocarbon	RWS
<i>A (16mm)</i>	7.4 min	2.2 min	3.2 min
<i>B (32mm)</i>	11 min	4 min	4.4 min

Table 4 summarizes the results obtained with the detailed part of the model. The optimal thickness is often found to be lower than the aggregate size. Taking the aggregate size as the minimum thickness along which the crack can form is however considered a good choice for NSC elements. For this concrete typology, the matrix is the weakest part of the mixture where the crack can freely form and propagate. For HSC the aggregate substitutes the matrix on being the weakest part allowing the crack to develop at a smaller depth than the aggregate size. This statement agrees with observations in practice of HSC spalled pieces being thinner (smaller thickness) compared to NSC ones.

Furthermore, it can be noted that for elements with wider aggregate size, the crack failure is suggested to be governing over the buckling instability. This causes a delay or prevention of the spalling occurrence. It has also been found that taking an aggregate of double the thickness can considerably delay or prevent the buckling instability. At the same time, this delay does not match with the better spalling performances shown in practice by concrete mix containing aggregates of reduced size. The micro structural behavior and its influences on the crack failure could explain this mismatch. For NSC with calcareous/siliceous aggregate, the thermal deformation of the aggregate is considerably greater compared to the mortar [14]. At the same time NSC shows a greater stiffness reduction with temperature of the mortar compared to the aggregate [15],[16]. This causes the aggregate to take a higher share of the applied external load while pushing against the mortar causing internal crack

patterns. This behavior suggests that larger sized aggregates have a bigger impact on the crack formation and propagation causing spalling to occur.

Table 4 Detailed part outcome - Model results

Case	t [mm]	Fire curve	t_{opt} [mm]	Crack	Iteration
A	16	ISO	5	Yes	No
	16	Hydrocarbon	5	Yes	No
	16	RWS	5	No	No
B	32	ISO	10	No	No
	32	Hydrocarbon	10	No	No
	32	RWS	10	No	No

4. FUTURE POSSIBILITIES AND OUTLOOK

A pilot analytical model able to describe the spalling mechanism coupling buckling instability and crack failure has been developed. The model estimates the initial spalling time of NSC elements subjected to fire, gives an indication over the optimal thickness of the first concrete piece prone to spalling and it also checks whether the cracked surface necessary for the occurrence of the mechanism forms. The *instability spalling model* describes the spalling mechanism as a series of 2 failure mechanisms:

1. crack failure is the necessary first step for spalling to occur. The spalled piece needs to be detached from the element before having the possibility of being suddenly pushed off from the concrete element;
2. buckling instability is the second step of the spalling mechanism resulting in the expulsion of the fragment from the concrete element.

In this paper a modelling approach is elaborated which first checks the possibility of a piece to fail under buckling instability and subsequently checks if the necessary crack failure has formed. This reversed procedure has been carried out due to the complexity of the problem, involving a relation between time, temperature, material properties and stress. As such it was found that estimating the buckling instability time is needed in order to check for crack failure.

The *instability spalling model* aims at proposing a new idealization of the spalling mechanism. The interesting results obtained require additional tests with a more detailed approach to assess and quantify the spalling behavior on the basis of which the mechanisms could be investigated further. The model and more in general the fundamental ideas and assumptions could be used, integrated and developed in order to obtain a practical and intuitive analytical model that can be directly used in practice.

As stated earlier, the use of the model is currently limited to NSC, but additional considerations regarding the effect of HSC and PPFRC and pore pressure have been treated in the work of De Poli [3]. In this section a brief summary of the main findings will be highlighted.

In general terms, according to [2], HSC elements and elements containing an elevated moisture content shows worst performances and PPFRC elements improved ones in terms of spalling failure prevention. Referring to these known behaviors, the following considerations partially explaining the above-mentioned performances are highlighted:

- the relation between depth and length of the spalled piece seems to play a fundamental role. It is suggested that HSC elements show spalled pieces of considerable length and reduced thickness which reduce the resistance to buckling instability;
- the moisture content is directly related to the raise and dissipation of pore pressure within the concrete element. The numerical results presented in the work of Lottman [9] indicated that the effective stresses due to pore pressure were of a minor importance when compared to the thermal stresses. The model showed that the connectivity of the crack pattern in the heated surface layer allows moisture to escape and mitigate the pore pressure development. The resultant influence on the local stress state was found to be limited in comparison to the stresses arising from the steep temperature gradient.

On the other hand, the crack failure might be greatly affected by elements with distinct moisture contents. The *instability spalling model* checks the formation of the initial crack. When this happens, it is assumed that the crack propagation towards the element surface takes place instantaneously (Figure 6). It is therefore possible that the pore pressure dissipation has a great effect on the crack propagation causing elements with a higher moisture content to experience an earlier spalling occurrence;

- With respect to PP-fiber influence on spalling performances and water movement behavior, the question over their relation remains. New evidences are necessary in order to have an insight into the driving mechanisms. According to the presented mechanical model, factors influencing PPFRC elements spalling behaviour could be the different thermal elongation and stress build-up which would affect the spalling mechanism. Additionally, the melting of PP-fibers could influence the thermal degradation of Young's modulus, crack initiation and propagation behaviour and temperature development due to increased moisture movement and evaporation processes. These hypotheses would need to be confirmed by additional test results.

The *instability spalling model* could be used in a way that given a known temperature development in time for the concrete surfaces of a structure and dividing these surfaces into a series of homogeneous regions, the cross-section reduction in time of these regions could be estimated. Re-modelling the structure with a reduced cross section could allow the verification over the possibility to redistribute forces and understand the time for which the structural collapse is forecasted. The *instability spalling model* provides an estimation of the depth, length and moment in time when the first piece of NSC detaches from the concrete element due to the spalling failure mechanism. In order to take into account repetitive spalling, the model could be iterated, allowing for a cross-sectional reduction in time. Recalculation is then based on modification of the various parameters according to the progressive spalling process.

5. CONCLUSION

Understanding the spalling mechanism is still of importance in the field of civil engineering and a clear and definitive explanation for its description has not been formulated yet. In order to address the current gap both in research and practice, we propose an analytical model which incorporates a combination of two failure mechanisms (buckling instability and crack failure). Following these premises, the paper elaborates the theories, explaining the *instability spalling model*, highlighting and reviewing the results obtained with this model and assessing the limits and possibilities for further extensions of the proposed model. Besides of practical relevance the *instability spalling model* also aims at providing a better theoretical understanding of the spalling occurrence. It could form the base and inspiration

for further development of a straightforward engineering tool, which allows for an analytical estimation of the concrete spalling mechanism caused by fire scenarios. This could allow the model to be used following the philosophy of performance-based design as done in standards such as Eurocode 2, part 1-2 [11].

However, as mentioned earlier, the proposed model presents limitations and requires further elaboration. One of the reasons for the current limitations of the model is the reduced amount of experimental results available over the spalling failure progress in time. A series of experimental tests for NSC, PPFRC, HSC recording the development in time of depth, length, width and shape of the detached piece during spalling is necessary to expand, calibrate and verify the model. Zeiml in [13] recorded the spalling failure of concrete elements using high speed camera images. Yang et al. in [18] tried to relate the crack development to the elastic wave velocity using acoustic emission tomography. These experimental methods could be used to collect a series of spalling results. Additional improvements could also come from the introduction of the effects of acting moments into the model, the use of different support conditions in the *column spalling model* and a better idealization and modelling of the crack initial pattern and development.

This model shows good general agreement with observed spalling behaviour and the rare available experimental data. Therefore, more data sets from tests are required to establish verification to this promising theory.

NOMENCLATURE

α		[°]	F_{ext}	External load	[kN]
σ_{ext}	External stress	[MPa]	F_{buc}	Buckling load	[kN]
ε_c	Concrete thermal elongation	[-]	$F_{\Delta T}$	Thermal load	[kN]
b	Spalled piece width	[mm]	F_{Ed}	Acting load	[kN]
f_{cm}	Mean cylinder compr. strength	[MPa]	F_{Rd}	Buckling force resistance	[kN]
l_{buc}	Spalled piece length	[mm]	<i>HSC</i>	High Strength Concrete	
t	Spalled piece thickness	[mm]	I	2 nd Moment of Area	[mm ⁴]
t_1	First spalling occurrence	[min]	<i>PPFRC</i>	Polypropylene Fibre Reinforcement Concrete	
A	Spalled piece cross section	[mm ²]	T	Concrete temperature	[°C]
E_c	Concrete Young's Modulus	[MPa]	T_{avg}	Concr. Average Temp.	[°C]

REFERENCES

1. Khoury, A., and Anderberg, Y., "Fire safety design—Concrete spalling review", Report submitted to the Swedish National Road Administration, 2000.
2. The International Federation for Structural Concrete, "Fire design of concrete structures-materials, structures and modeling", Report-bulletin 38. fib, 2007.
3. De Poli, M., "Fire dynamics and spalling mechanism in tunnel infrastructures", MSc Thesis at Delft University of Technology, 2018.
4. Kordina, K., *Das Verhalten von Stahlbeton- und Spannbetonbauteilen unter Feuerangriff*, Heft 2. Institut für Baustoffkunde und Stahlbetonbau der Technischen Hochschule Braunschweig, 1963.
5. Hermathy, T.Z., "Effect of moisture on the fire endurance of building materials. Moisture in Relation to Fire Tests", ASTM Special Technical Publication, 385, 74–95.
6. Waubke, N.V., "Transportphänomene in Betonporen", Doctoral dissertation at Technische Hochschule Braunschweig, 1966.

7. Meyer-Ottens, C., *Zur frage der abplatzungen an bauteilen aus beton bei brandbeanspruchungen*, Deutscher Ausschuss für Stahlbeton, 1975.
8. Zhukov, V.V., *Explosive failure of concrete during a fire*, Translation No. DT 2124. Borehamwood, Joint Fire Research Organization, 1975.
9. Lottman, B.B.G., "The spalling mechanism of fire exposed concrete", Doctoral dissertation at Delft University of Technology, 2017.
10. Kusterle, W., et al., "Brandbeständigkeit von Faser-, Stahl- und Spannbeton [Fire resistance of fiber-reinforced, reinforced, and prestressed concrete]", Bundesministerium für Verkehr, Innovation und Technologie, Heft 544, 2004.
11. European Committee for Standardization, EN 1992-1-2:2004, Design of concrete structures: General rules - Structural fire design, 2004.
12. Rijkswaterstaat, ROK 1.4:2017, Richtlijn ontwerp kunstwerken, 2017.
13. Zeiml, M., "Concrete subjected to fire loading - From experimental investigation of spalling and mass-transport properties to structural safety assessment of tunnel linings under fire", Doctoral dissertation at Technischen Universität Wien, 2008.
14. Flynn, R.D., et al., "Response of high performance concrete to fire conditions : review of thermal property data and measurement techniques", MD: National Institute of Standards, Technology, Building, and Fire Research Laboratory, NIST GCR 99-767, Gaithersburg, 1999.
15. RILEM TC-HTC, "Behaviour of concrete at high temperatures - part 1 - ordinary concrete. State of the Art Report", RILEM publications S.A.R.L., 2004.
16. Dmitriev, A.P., *Physical properties of rocks at high temperatures*, Springfield: National Aeronautics and Space Administration, 1972.
17. European Committee for Standardization, EN 1992-1-1:2005, Design of concrete structures: General rules - and rules for buildings, 2005.
18. Yang, Y., Zhang, F., Hordijk, D. A., Hashimoto, K., Shiotani, T., "A comparative study of acoustic emission tomography and digital image correlation measurement on a reinforced concrete beam", Proceedings of the 6th International Symposium on Life-Cycle Civil Engineering, 2419-2426, Ghent, Belgium, 28 October, 2018.

Open issues in modelling concrete at high temperature

Benedikt Weber^{1,*}

¹ Empa, Dübendorf, Switzerland

* Benedikt.Weber@empa.ch, Empa, Swiss Federal Laboratories for Materials Science and Technology, Überlandstrasse 129, 8600 Dübendorf, Switzerland

ABSTRACT

Sophisticated numerical models have been available for some time to simulate the behaviour of concrete exposed to high temperature. These models are based on the theory of porous media, and include heat transfer, transport of vapour and liquid water, evaporation and dehydration. For model validation, experiments from the literature are usually employed that provide data for pressure, temperature, and mass loss (PTM tests). However, to reasonably reproduce the experimental data, some input parameters need to be tuned to values that are quite far from the actual measured parameters. This deficiency has been observed in several models used by members of the RILEM Technical Committee 256-SPF and seems to be inherent to current state-of-the-art models. It is not clear, whether this is a problem of interpretation of the material tests or if some essential physics are missing in the models.

This paper intends to make researchers aware of these open issues by showing a typical simulation with experimentally determined and with tuned input parameters. Then some physics that might be important are critically reviewed and their impact on the overall results is discussed. Although some theoretical insight has been gained, no substantial improvement with respect to the experimental results could be obtained. In this sense, the discussed issues are still open.

KEYWORD: Modelling, Permeability, Klinkenberg, Dehydration, Retention curves

INTRODUCTION

The past RILEM Technical Committee 227-HPB recently published a state-of-the-art report on "Modelling of Concrete Behaviour at High Temperature" [1]. The models described in this report have been used by several researchers to simulate experiments with temperature, pressure, and mass loss tests (PTM tests) (see e.g. [2]). Although many of the current models are able to reproduce the measured temperatures and pressures, this is only possible by tuning some key input parameters. This fact has already been pointed out in a previous spalling workshop [3,4]. However, many researchers seem not to be aware that the tuned parameters are quite far away from the measured material parameters, since the latter are often not readily accessible. These issues have been discussed extensively in the current RILEM Technical Committee 256-SPF. This grouping of experts in experimental methods and in numerical modelling formulated some internal benchmark tests and collected the necessary material properties. These tests were used to compare various numerical models implemented by members of the committee. Although some differences between the models have been revealed, the main discrepancies with the experimental results could not be resolved yet. This suggests that the standard models might not capture all the physics correctly. It appears that, despite the high level of knowledge, there are still a number of open issues.

The present paper intends to make researchers aware of the inconsistencies observed in the classical models and discusses some open points from a physical point of view. The two major tuning factors often applied for matching the simulations with the experimental results of the benchmark problems are the heating temperature and the permeability. While the adjustment needed for the heating temperature is partially due to oversimplified thermal boundary conditions, the issue of the permeability is more complex. The permeability is the most influential parameter for adjusting the pore pressure, but other factors, in particular the vapour production due to evaporation and dehydration, also affect the pressure. Also important are the retention curves, for which no experimental data are available for high temperatures.

EXPERIMENTAL DATA USED IN ANALYSIS

PTM tests

In the so-called PTM tests, a concrete slab is heated and temperatures and pressures are measured at several depths. Also monitored is the global weight loss due to evaporation and dehydration of water. A typical setup is shown in Figure 1a). A concrete slab with a surface of $30 \times 30 \text{ cm}^2$ and a thickness of 12 cm is heated from above by a ceramic radiator whereas the sides are insulated against heat loss. Temperature and pore pressure are monitored by combined sensors, which are cast in at different depths from the heated surface. The complete setup rests on a balance, which monitors the total weight loss. In this paper, we use the tests by Kalifa [5] on a concrete M100. This concrete has been characterized extensively in the French national research project BHP2000. The material characteristics of this concrete reported in different places have been collected in an internal document [6] for the purpose of the benchmark simulations in the Technical Committee 256-SPF.

Neutron experiments

In neutron experiments, a concrete plate is placed into a neutron beam, which produces a radiography on a detector. Since neutrons are highly absorbed by hydrogen, free and chemically bound water appears dark in the radiography. Neutron test have been reported in [7]. A typical setup is shown in shown in Figure 1b). A plate with $100 \times 100 \text{ mm}^2$ surface and 25 mm thickness is placed vertically on an electrical heating plate and heated on the lower face up to 600°C . The other faces are thermally insulated to produce a nearly one-dimensional heat flow. The setup is placed into a neutron beam and radiographs are taken at certain time steps. To eliminate the neutron absorption by the anhydrous components, the initial image is subtracted from subsequent images. The resulting grey values can be related to the water change due evaporation and dehydration. Thermocouples cast into the concrete measure the temperature at different depth from the heated face. The information from the thermocouples and the neutron images can be combined to monitor the water loss due to evaporation and dehydration versus temperature.

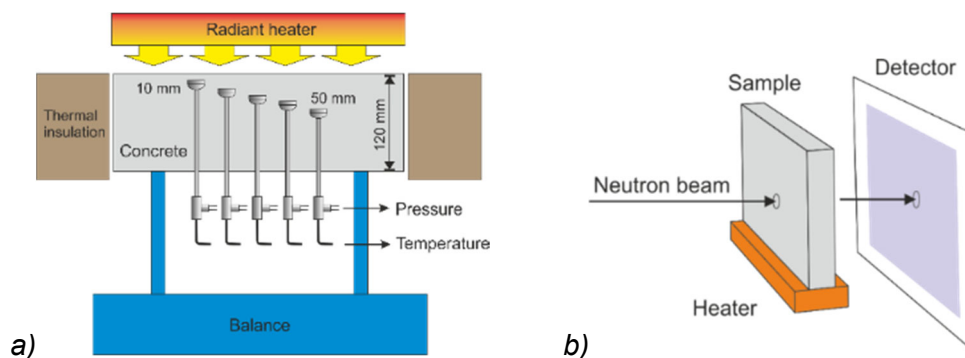


Figure 1: Setup for a) PTM test, b) for Neutron experiment.

HYGRO-THERMAL SIMULATIONS

Thermal boundary condition

The benchmark test used here is the PTM test with a concrete M100 as described in [5]. A first open issue when simulating this test is the heating boundary condition. In standard models, the simple boundary condition

$$q = \varepsilon\sigma(T_{ext}^4 - T^4) + h_T(T_{ext} - T) \quad (1)$$

is used which includes a radiative and a convective term. The two parameters that can be specified are the emissivity ε of the concrete surface and the heat transfer coefficient h_T . The emissivity determines how much of the incoming radiation energy is absorbed by the concrete. The heat transfer coefficient describes the heat transfer through the air moving around the concrete. Both parameters are usually selected based on empirical values.

Already Gawin et al. [2] have observed that using the Eq. (1) with a radiator temperature of 600°C as reported in [5] results in too high temperatures. For their simulations, they specified a radiator temperature starting at 400°C and rising up to 460°C as shown in Figure 2a). The temperature on the concrete surface resulting from the original and from the modified heating temperature can be analysed using a simplified model with only heat conduction in the concrete and a radiation boundary condition with $\varepsilon = 0.9$. As shown in Figure 2a), the modified specification reduces the surface temperature on the concrete to the desired values close to the measured surface temperature.

Changing the radiator temperature does not really explain the physical aspects of the problem but can be considered a means to start the hygro-thermal simulations with correct temperatures. As an alternative, one could use a more sophisticated radiation model taking into account also the surface properties of the radiator and the geometric configuration with two finite surfaces at a certain distance. The physics of radiation will not be detailed here but can be found in any textbook on heat transfer [8]. However, for two parallel plates, a simplified expression is available [8]:

$$q = \frac{\sigma(T_{rad}^4 - T_{samp}^4)}{(1 - \varepsilon_{rad})/\varepsilon_{rad} + (1 - \varepsilon_{samp})/\varepsilon_{samp} + 1/F} \quad (2)$$

where F denotes the view factor. The view factor depends on the geometry of the plates and their distance and considers the fact that not all the radiative energy from the radiator reaches the concrete plate. The emissivity of the radiator considers the effect that the heater emits less radiative energy than an ideal black body. Eq. (1) is recovered by setting $F = 1$ and $\varepsilon_{rad} = 1$.

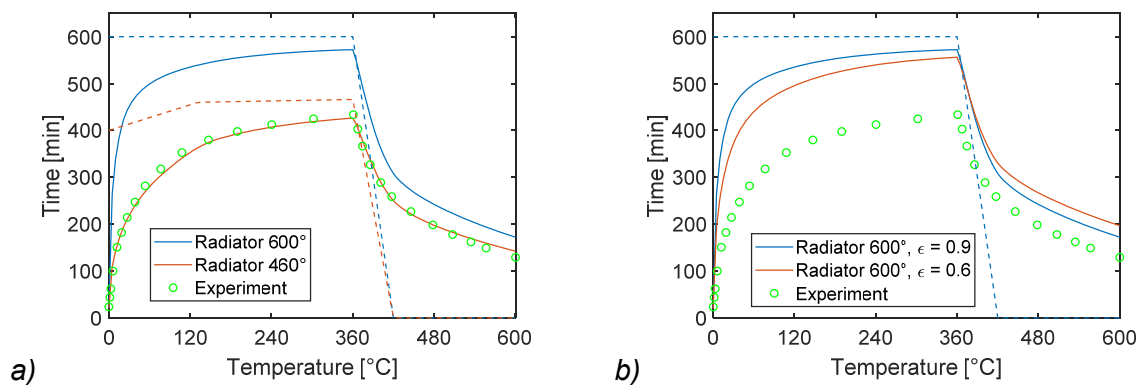


Figure 2: Surface temperature due to radiation, a) Original and modified radiator temperature, b) Effect of reduced emissivity.

View factors for different situations can be found in many books or online calculators [9]. For the PTM test described above (squares 30 cm, distance 3 cm), the view factor is $F = 0.827$. The emissivity of the radiator is similar to the one of the concrete. However, the emissivity generally depends on the wavelength of the radiation spectrum, which itself depends on the temperature. Based on the specification of a similar radiator, the emissivity of the radiator at 600°C can be estimated to be $\varepsilon_{rad} = 0.75$. In this case, the equivalent emissivity calculated from Eq. (2) would drop down to 0.6. This low value can thus be justified on physical reasons. However, even this low emissivity does not resolve the discrepancy between the simulation and the experiment as shown in Figure 2b).

Not considered in the above considerations is the convective heat transfer between the concrete plate and the radiator. Heat transfer coefficients can be found in the literature for typical situations like horizontal hot plates but not for an air gap between two plates. However, it is difficult to imagine that the moving air in the gap should have a cooling effect. Another reason for the discrepancy between theory and experiment could be a non-uniform temperature due to fact that the radiator was composed of different segments with possibly lower temperature on their edges. In addition, the reported temperature probably refers to the thermocouple inside of the ceramic body, which might be higher than the surface temperature.

Since even a more sophisticated radiation model cannot reproduce the measured temperatures and since the thermal input problem is not the focus of concrete modelling, we follow the same route as other researchers and use the boundary condition (1) with a reduced radiator temperature.

Pore pressure

For the hygro-thermal simulation, we use an implementation in COMSOL Multiphysics that follows mainly the State-of-the-Art Report [1]. For the material properties, we used values specifically determined for the concrete M100 [6].

For the intrinsic permeability, we used the value measured at ambient temperature, $K_g = 2 \cdot 10^{-17} \text{ m}^2$. Figure 3a) compares the resulting pore pressure (solid lines) with measured values (dashed lines). Clearly, the simulated pressures are much too low. Reducing the permeability to $K_g = 10^{-19} \text{ m}^2$, leads to an acceptable match with the measured pressures (Figure 3b). Incidentally, the same permeability has also been used in [2]. The heights are comparable to the measured values. However, the peak positions are shifted and the shapes are different.

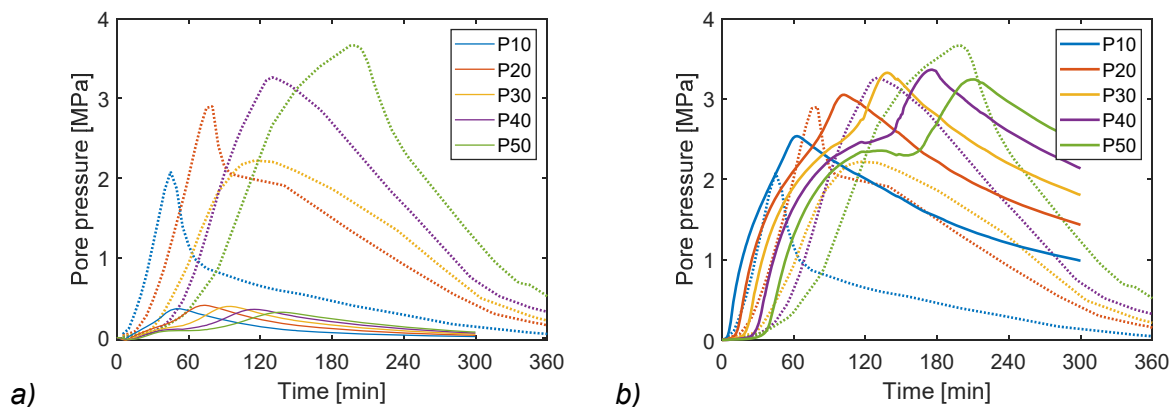


Figure 3: Pore pressure for simulation with a) $K_g = 2 \cdot 10^{-17} \text{ m}^2$, b) $K_g = 10^{-19} \text{ m}^2$.

Before going into a discussion on permeability, we look at some typical values in the literature. Yanko [10] found for a similar concrete (lime aggregates, water to binder ratio 0.3, compressive strength 104 MPa) an intrinsic permeability of $K_g = 2.68 \cdot 10^{-17} \text{ m}^2$, which confirms the measurements for M100. On the other hand, Baroghéi-Bouny [11] derived a permeability of $K_g = 5 \cdot 10^{-22} \text{ m}^2$ for high-performance concrete from calibration with a drying experiment, which is even much lower than the tuned value from our simulation.

In the following, we look at different physical mechanism that control the pressure and possibly explain the difference between simulated and measured pressures. We are not going into the accuracy of the pressure measurements, which would be a subject of its own. Rather we look at the gas transport and the vapour sources due to dehydration and evaporation.

GAS TRANSPORT

Gas transport is typically modelled by Darcy's law, where the mass flux is driven by the pressure gradient ∇p_g :

$$\mathbf{q}_g = -\rho_g \frac{\kappa_{rg} K_g}{\mu_g} \nabla p_g \quad (3)$$

The main reference parameter is the intrinsic gas permeability K_g . For partially saturated media, the permeability is modified by the relative gas permeability κ_{rg} , which depends on the liquid saturation. The other variables are the density ρ_g and the dynamic viscosity μ_g .

For the mixture of air and vapour, molecular diffusion as described by Fick's law is also important. It describes the mixing of the two gases but has little influence on the pressure. Another gas transport that can be important in low-permeability materials is the Knudsen diffusion, which is usually taken into account in the form of the Klinkenberg correction discussed further below.

Intrinsic permeability

The main tuning parameter for the pressure is the intrinsic permeability. In the simulations described above, a reduction of the intrinsic permeability by a factor of 200 was necessary to match the pressure peaks with the experimental data. It is thus natural to look first at the various modifications of the permeability. The material models used in the classical models follow mostly the pioneering work by Gawin and coworkers [12] and presented in more detail in the thesis by Pesavento [13]. These models consider an evolution of the intrinsic permeability with temperature and pressure, which can be expressed by the following function

$$K = K_0 \cdot 10^{A_T(T-T_0)} \left(p_g / p_0 \right)^{A_p} \quad (4)$$

with $A_T = 0.005$ and $A_p = 0.368$ [13]. The temperature evolution captures reasonably well the measured residual permeabilities for M100 at five different temperatures as shown in Figure 4a). The increase with temperature is probably due the increase of pore size due to dehydration. The increase of permeability with pressure is less obvious. According to [13], this modification considers the crack opening due to pore pressure. However, the model is based on experiments by Schneider and Herbst [14] with a maximal pressure of 4 bar, which is way below the typical pressures measured in heating tests. The pressure peaks in our example are around 4 MPa (40 bar), which leads to an increase of permeability in the simulation by a factor of 3.9 when Eq. (4) is used. Although this seems like a high value, it cannot not explain the large tuning factor needed in the simulation.

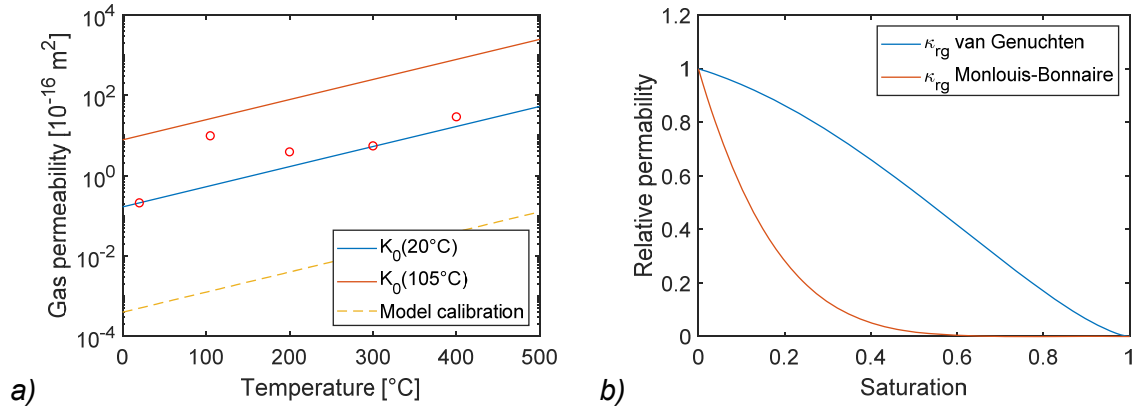


Figure 4: a) Intrinsic permeability as a function of temperature, b) Relative permeabilities.

Relative permeabilities

Another important factor modifying the permeability is the relative gas permeability. A popular law used in the classical models is the one by van Genuchten:

$$\kappa_{rg} = \sqrt{1-S} (1-S^b)^{2/b} \quad (5)$$

where S denotes the liquid saturation and b is material parameter. A typical value for high-performance concrete is $b = 2.06$ [11]. The relative permeability according to Eq. (5) is shown in Figure 4b).

Experiments by Monlouis-Bonnaire [15] show that the relative gas permeability according to van Genuchten, which has been obtained from granular materials, is not appropriate for concrete. The relative permeability in Eq. (5) can be written in a more general form as

$$\kappa_{rg} = (1-S)^d (1-S^b)^{2/b} \quad (6)$$

The original law according to van Genuchten corresponds to $d = 1/2$. However, as shown in Monlouis-Bonnaire [15], a value of $d = 5.5$ is more appropriate for cementitious materials. This curve is also presented in Figure 4b). Since pressure peaks arise at low saturation ($S = 0.1 \div 0.2$), the permeability by Monlouis-Bonnaire is lower by a factor of two, compared to the classical law by van Genuchten.

Knudsen diffusion and Klinkenberg correction

For narrow pores, there is another transport mechanism, called Knudsen diffusion. Knudsen diffusion takes place when the pore size is so small that the gas molecules collide mainly with the walls and interaction with other molecules is negligible. A simple way to model Knudsen diffusion is to apply the well-known Klinkenberg correction to the Darcy permeability. However, before discussing the Klinkenberg correction, the character of Knudsen diffusion is elaborated first.

The flux due to Knudsen diffusion is driven by the gradient of the number density of a gas (number of molecules per volume) [16]. Molecules thus migrate from regions with a larger number of molecules to regions with less molecules. This diffusion can occur in a gas with a single component as opposed to Fick's diffusion, which is a diffusion between at least two components. For an ideal gas, the number of molecules depends on the pressure and the Knudsen diffusion can be written as

$$\mathbf{j}_{Kn} = -D_{Kn} \frac{\rho_g}{p_g} \nabla p_g \quad (7)$$

where \mathbf{j}_{Kn} is the mass flux and D_{Kn} is the Knudsen diffusion coefficient. In this form,

Knudsen diffusion is driven by the pressure gradient as is the Darcy flow, but it is inverse proportional to the pressure. The similar form of the Darcy and the Knudsen flow makes it possible to write the total mass flux from both mechanism as a modification of the Darcy coefficient.

$$\mathbf{q}_{tot} = \mathbf{q}_{Darcy} + \mathbf{j}_{Kn} = -\frac{\kappa_{rg} K_g (1 + b_{Klink} / p_g)}{\mu_g} \nabla p_g \quad (8)$$

where b_{Klink} is the Klinkenberg coefficient defined as

$$b_{Klink} = \frac{\mu_g D_{Kn}}{\kappa_{rg} K_g} \quad (9)$$

The Klinkenberg correction is usually used for determining the intrinsic gas permeability from experiments. To this end, the apparent permeability is measured at different mean pressures and plotted against the inverse of the mean pressure. According to the theory, this should give a linear plot, where the intercept gives the intrinsic gas permeability K_g and the slope is $K_g b_{Klink}$. An example for concrete with lime aggregates and a water-to-binder ratio of 0.3 is given in Figure 5a).

As seen from Eq. (9), the Klinkenberg coefficient is not a constant. Besides the influence of the dynamic viscosity and the relative permeability, the Knudsen diffusion coefficient itself depends on the temperature and the molar mass of the gas. In a simulation, the Klinkenberg coefficient should thus be adjusted as [16]

$$b_{Klink} = b_{Klink}^{ref} \frac{\kappa_{rg}^{ref}}{\kappa_{rg}} \frac{\mu_g}{\mu_g^{ref}} \sqrt{\frac{M_g^{ref}}{M_g}} \sqrt{\frac{T}{T_{ref}}} \quad (10)$$

Since the Klinkenberg coefficient is not directly used for the analysis of permeability measurements, most researchers are not aware that it is generally not a constant. However, when applying the experimental data to a different gas or a different temperature, the adjustment given in Eq. (10) needs to be considered. This is especially true when the Knudsen diffusion is included in a numerical simulation. An adjustment for the molar mass M_g is only necessary if different gases are used in the simulations and in the experiment.

As the Klinkenberg coefficient is not usually reported from permeability measurements, it has to be obtained from the literature for numerical modelling. Klinkenberg himself validated his theory with many different samples and he used different gases [17]. He also proved experimentally that the intrinsic gas permeability equals the liquid water permeability.

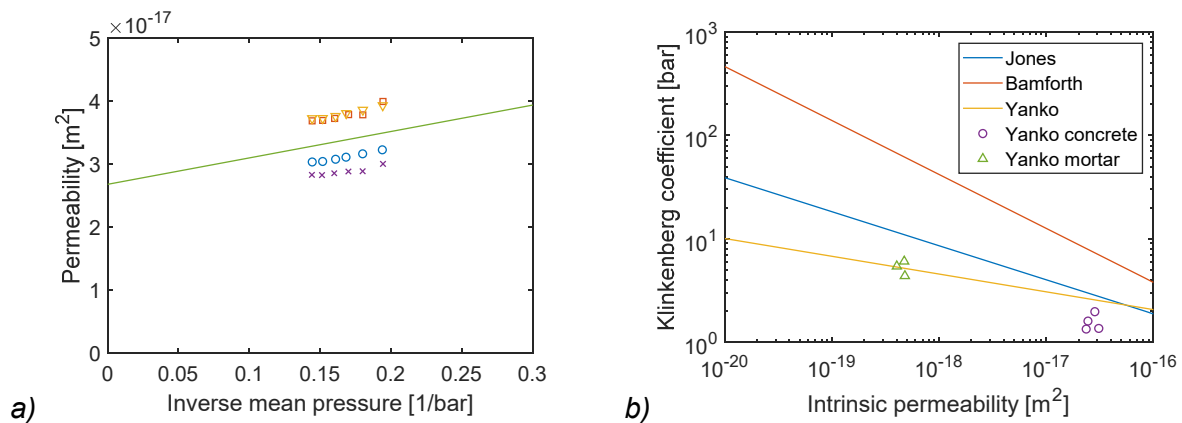


Figure 5: a) Klinkenberg plot for concrete, b) Klinkenberg coefficient vs. intrinsic permeability (data from [10]).

However, his results extend only down to 2 millidarcy ($2 \times 10^{-15} \text{ m}^2$), which is still too high for high-performance concrete. Jones and Owens [18] observed that the Klinkenberg plot still yields a straight line for sands with low permeabilities down to 10^{-19} m^2 . This is in the range of high-performance concrete. From their measurements, Jones and Owens found the following relationship for the Klinkenberg coefficient in terms of the intrinsic permeability:

$$b_{Klink} = 0.98 \cdot 10^{-5} \cdot K_g^{-0.33} \quad (b_{Klink} \text{ in bar, } K_g \text{ in m}^2) \quad (11)$$

Note that in these kind of data fitting, physical units are important. For a permeability of 10^{-19} m^2 , Eq. (11) gives a Klinkenberg coefficient of 18 bar. Considering a pressure peak of 4 MPa (40 bar), the Klinkenberg effect could increase the apparent permeability by 45%, which is still small compared to other factors such as the temperature effect (see Figure 4).

While the above-discussed experiments refer to granular materials (soil), experiments on cementitious materials are also available. Bamforth [19] compared gas permeabilities to water permeabilities in high-strength concrete with a water to cement ratio of 0.33 and proposed the following relationship for the Klinkenberg coefficient:

$$b_{Klink} = 1.635 \cdot 10^{-8} \cdot K_g^{-0.5227} \quad (b_{Klink} \text{ in bar, } K_g \text{ in m}^2) \quad (12)$$

For a permeability of 10^{-19} m^2 , this gives a Klinkenberg coefficient of 140 bar, which is almost eight times larger than the value according to Jones and Owens. However, these values have to be taken with caution since they were not determined from Klinkenberg plots but rely on the equivalence of intrinsic gas permeability and water permeability.

An exhaustive experimental campaign on high-performance mortar and concrete is presented in Yanko [10]. He showed that for cementitious low-permeability materials, the water permeability could be three order of magnitudes lower than the intrinsic gas permeability found from Klinkenberg plots. His Klinkenberg coefficients are thus much lower than the ones by Bamforth. He gives the following relationship:

$$b_{Klink} = 3.564 \cdot 10^{-3} \cdot K_g^{-0.1725} \quad (b_{Klink} \text{ in bar, } K_g \text{ in m}^2) \quad (13)$$

The Klinkenberg coefficients from different authors are compared in Figure 5b). Also included are some experimental values from Yanko for mortar and concrete with a $w/b = 0.3$, which is comparable to the concrete M100. The law by Yanko seems to be the most appropriate for concrete since it has been determined from experiments with different pressures on a comparable material and not from water permeability. For this law, the Klinkenberg coefficient is typically below 1 bar and the correction at a pressure of 40 bar (at typical pressure peaks) is only 2.5%.

DEHYDRATION

The mass loss due to dehydration has been determined by several researchers. The experiments published in the literature typically measure the mass loss of a sample during slow heating. This can be done by suspending a sample in a furnace while it is attached to a scale or by a thermo-gravimetric analysis (TGA) [20,21].

Figure 6a) shows the mass loss with respect to the dehydratable mass. Dehydration is a continuous process in the temperature range of interest (up to 500°C) because the main contribution comes from the amorphous C-S-H phase. The two solid curves show the mortar that has been used in the neutron experiments (see above). One curve shows the water loss in a TGA and the other curve shows the water loss observed from the neutron images at a distance of 10 mm from the heated surface [21]. The latter curve includes some water condensation near 100°C . The temperature shift of the main evaporation process from 100°C in the TGA to 300°C in the neutron test is clearly visible. For comparison, the TGA for cement paste determined by Harmathy [20] is also shown. This curve has been employed for modelling purposes by Pesavento [13].

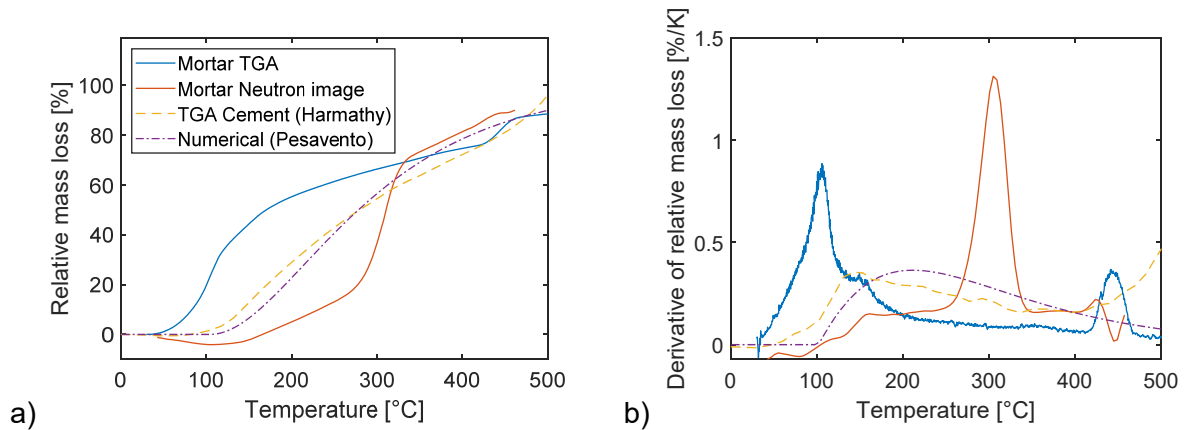


Figure 6: Dehydration: a) relative mass loss, b) Derivative of relative mass loss.

For the vapour release, the derivative of the dehydrated mass is more important. This quantity is shown in Figure 6b). Here the temperature shift between a TGA and a larger test such as the neutron experiment is even more obvious. Compared to the classical model by Pesavento, the mass release in the neutron test shows a sharper peak, indicating a more sudden release, which could increase the pressure compared to a more continuous release.

The comparison between the TGA and the neutron experiment shows that dehydration depends not solely on temperature. Other important influences are the heating rate and the pressure. Experiments that show the pressure dependence of dehydration have been reported by Manns and Neubert [22]. A model that considers kinetic effects has been proposed by Sabeur and co-workers [23]. No models capturing the pressure dependence are known to date.

EVAPORATION

Phase change

In the classical formulation by Gawin et al. [2], the vapour pressure is always assumed to be the vapour saturation pressure modified by capillary effects. This poses a problem when the critical temperature (374 °C) of water is reached. However, it is very likely that all liquid has been evaporated before this temperature is reached. When only vapour exists, its pressure need not be the vapour saturation pressure. This is shown in Figure 7 for a constant volume that is partially filled with liquid and subjected to increasing temperature (isochoric conditions [24]).

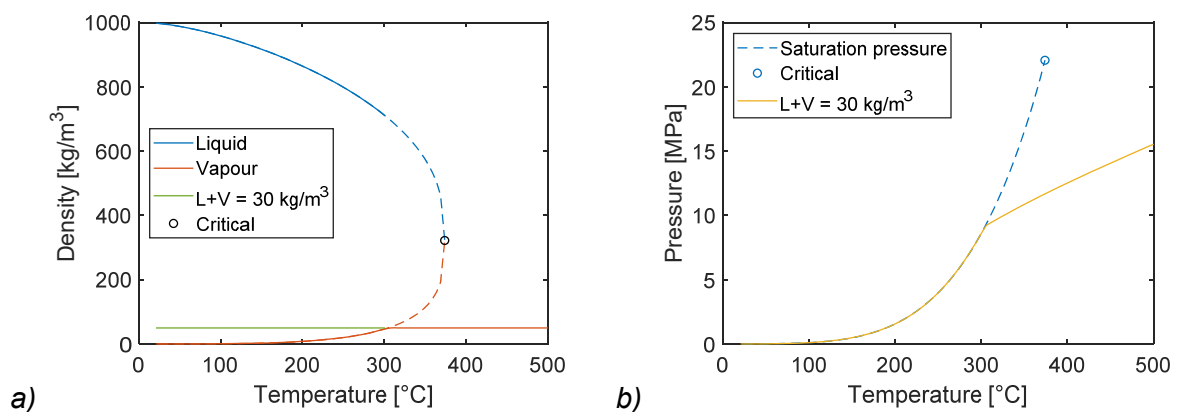


Figure 7: a) Liquid and vapour density for water, b) Vapour pressure in a constant volume (isochoric condition).

Capillary effects are not included in this consideration. Figure 7a) shows the densities of liquid and vapour up to the critical point. The line labelled "L+V = 50 kg/m³" refers to the constant water mass, which is partially liquid and partially vapour. Slightly above 300°C, all liquid is evaporated. At this point, the pressure deviates from the vapour saturation pressure, as shown in Figure 7b). This idea has been used in an alternative implementation presented in [25], which models evaporation as a mass source that depends on the difference between the actual pressure and the vapour saturation pressure. If the saturation is zero, the mass source is stopped and the gas pressure follows the ideal gas law.

Retention curves

Besides the phase change, the evaporation is also controlled by the water retention curves or sorption isotherms. These curves describe the link between capillary pressure and liquid saturation and are an essential property of a porous medium. The capillary pressure has been described by van Genuchten as a function of saturation:

$$p_c = a(S^{-b} - 1)^{1-1/b} \quad (14)$$

Parameters for high-performance concrete have been determined experimentally at ambient temperature in [11]. Experimental data for other temperatures are only available up to 80°C [26]. For higher temperatures, the capillary pressure has to be extrapolated using the temperature-dependence of the surface tension $\gamma(T)$:

$$p_c(T) = p_c^{ref} \gamma(T) / \gamma(T_{ref}) \quad (15)$$

In the classical models, the capillary pressure is a primary variable and the saturation is determined from p_c . Eqs. (14) and (15) have thus to be inverted. The saturation is plotted in Figure 8a) as a function of capillary pressure for different temperatures.

In classical models, the pressure is assumed to be equal to the vapour saturation pressure modified by the Kelvin equation. Assuming the ideal gas law, the vapor density can be expressed as a function of temperature and capillary pressure:

$$\rho_v = \frac{p_{sat}(T)M_w}{RT} \exp\left(-\frac{p_c M_w}{\rho_l RT}\right) \quad (16)$$

The total water mass per volume is given by

$$m_w = S\rho_l + (1-S)\rho_v \quad (17)$$

It is instructive to analyse the simple case when the total mass is kept constant while increasing the temperature. The saturation has to fulfil both equations (16) and (17) which are interconnected by the retention law $p_c(S, T)$. Results from an iterative solution are shown in Figure 8b). Generally, the saturation is increasing due to the thermal expansion of water. This behaviour is particularly pronounced when approaching the critical temperature. Nevertheless, the vapour pressure is increasing with temperature (not shown). More importantly, it has been found that for low initial saturations and high temperatures, the iteration did not converge, but the saturation alternated between two values. Thus, some curves end below the critical temperature (374°C) in the plot. This means that no consistent saturation value could be found in these cases. Note that the exact behaviour depends on the retention curves and especially their dependence on temperature.

Although this analysis considers a simple case, it shows that the saturation and thus the evaporation depends on several material laws (vapour saturation, ideal gas, thermal expansion of liquid, retention curves), which are strongly interconnected and cannot be considered independently. The fact that no solution was found for some cases could also explain why the finite element models sometimes had convergence problems for certain input parameters.

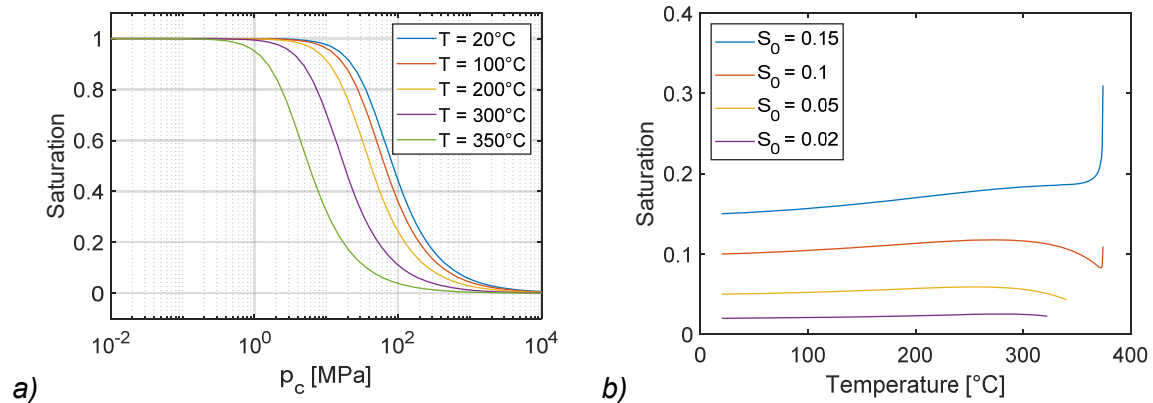


Figure 8: a) Retention curves, b) Saturation in function of temperature for constant volume (isochoric condition).

SUMMARY AND CONCLUSIONS

This paper starts with the observation that current state-of-the-art models are still not able to reproduce some benchmark tests without severe tuning of input parameters. In the model employed here, the permeability had to be reduced by a factor of 200 to match the measured pore pressure. Starting from this fact, several mechanisms controlling the gas pressure have been discussed in more detail. The evolution of permeability with temperature and pressure as well as the influence of water saturation have been analysed. These factors influence the permeability to certain extent but cannot explain the large tuning factor. The Knudsen diffusion and the Klinkenberg correction have been treated in more detail, since they are less known. However, based on some newer literature they are believed to have even less influence than the temperature. As far as the vapour source is concerned, dehydration is possibly a key factor. Results from neutron experiments show that in a larger sample the water release takes place at a higher temperature and occurs more suddenly than in a TGA analysis. Finally, the evaporation of free water is largely controlled by the retention curves, for which no experimental results are available for elevated temperatures. Commonly used laws might lead to convergence problems in some cases.

ACKNOWLEDGEMENTS

Many ideas discussed in this paper were inspired by discussions with my colleagues from the RILEM Technical Committee 256-SPF. I would like to mention in particular Jean-Christophe Mindeguia, who summarized all the results from material tests, and the modelers Alain Millard, Colin Davie, Jiayi Wang, Stefano Dal Pont, Dorjan Dauti, and Matthias Zeiml, who contributed with their simulations.

REFERENCES

1. Millard, A. and Pimienta, P., "Modelling of Concrete Behaviour at High Temperature: State-of-the-Art Report, RILEM Technical Committee 227-HPB", Springer, 2019.
2. Gawin, D., Pesavento, F., and Schrefler, B.A., "Modelling of hygro-thermal behaviour and damage of concrete at temperature above the critical point of water", *Int. J. Numer. Anal. Meth. Geomech.* **26**(2002):537–562.
3. Wang, J., Davie, C.T., and Masoero, E., "RILEM TC 256 – Numerical benchmark of experiments on heated concrete", 5th International Workshop on Concrete spalling due to Fire Exposure, 185–196, Borås, Sweden, 12-13 October, 2017.

4. Dauti, D., Dal Pont, S., Sciumé, G., and Briffaut, M., "Numerical benchmark of experiments on heated concrete", 5th International Workshop on Concrete spalling due to Fire Exposure, 197–203, Borås, Sweden, 12-13 October, 2017.
5. Kalifa, P., Menneteau, F.D., and Quenard, D., "Spalling and pore pressure in HPC at high temperatures", *Cement and Concrete Research* **30**(2000):1915–1927.
6. Mindeguia, J.-C., "Experimental results on the High-Performance-Concrete M100C", Internal report, RILEM TC 256-SPF, Aug. 29, 2018.
7. Toropovs, N., Monte, F.L., Wyrzykowski, M., Weber, B., Sahmenko, G., Vontobel, P., Felicetti, R., and Lura, P., "Real-time measurements of temperature, pressure and moisture profiles in High-Performance Concrete exposed to high temperatures during neutron radiography imaging", *Cement and Concrete Research* **68**(2015):166–173.
8. Holman, J.P., *Heat transfer*, 9th ed., McGraw-Hill, 2002.
9. Maya HTT, Thermal Wizard: <https://thermal.mayahtt.com/tmwiz/default.htm>
10. Yanko, W.A., "Experimental and numerical evaluation of concrete spalling during extreme thermal loading", Doctoral dissertation, University of Florida, 2004.
11. Baroghel-Bouny, V., Mainguy, M., Lassabatere, T., and Coussy, O., "Characterization and identification of equilibrium and transfer moisture properties for ordinary and high-performance cementitious materials", *Cement and Concrete Res.* **29**(1999):1225–1238.
12. Gawin, D., Pesavento, F., and Schrefler, B.A., "What physical phenomena can be neglected when modelling concrete at high temperature? A comparative study. Part 1: Physical phenomena and mathematical model", *International Journal of Solids and Structures* **48**(2011):1927–44.
13. Pesavento, F., "Nonlinear modelling of concrete as multiphase porous material in high temperature condition", doctoral thesis, University of Padua, 2000.
14. Schneider, U. and Herbst, H.J., "Permeabilität und Porosität von Beton bei hohen Temperaturen", Deutscher Ausschuss für Stahlbeton, Heft 403, 1989 (in German).
15. Monlouis-Bonnaire, J.P., Verdier, J., and Perrin, B., "Prediction of the relative permeability to gas flow of cement-based materials", *Cement and Concrete Research* **34**(2004):737–744.
16. Webb, S.W., "Gas transport mechanisms", Chapter 2 in Gas transport in porous media, Ho, C.K. and Webb, S.W. (Eds.), Springer 2006.
17. Klinkenberg, L. J. "The permeability of porous media to liquids and gases", *Drilling and Production Practice*, American Petroleum Institute, 1941.
18. Jones, F.O. and Owens, W.W., "A laboratory study of low-permeability gas sands", *Journal of petroleum Technology* **32**(1980):1–631.
19. Bamforth, P.B., "The relationship between permeability coefficients for concrete obtained using liquid and gas", *Magazine of Concrete Research*, **39**(1987):3–11.
20. Harmathy, T. Z. "Thermal properties of concrete at elevated temperatures", *Journal of Materials* **5**(1970):47–74.
21. Dauti, D., Dal Pont, S., Weber, B., Briffaut, M., Toropovs, N., Wyrzykowski, M., and Sciumé, G., "Modeling concrete exposed to high temperature: Impact of dehydration and retention curves on moisture migration", *Int. J. Numer. Anal. Meth. Geomech.* **42** (2018):1516-1530.
22. Manns, W. and Neubert, B., "Wassergehalt von Beton bei Temperaturen von 100 °C bis 500 °C im Bereich des Wasserdampfpartialdruckes von 0 bis 5.0 MPa", Deutscher Ausschuss für Stahlbeton, Heft 403, 1989 (in German).
23. Sabeur, H., Meftah, F., Colina, H., and Platret, G., "Correlation between transient creep of concrete and its dehydration", *Magazine of Concrete Research* **60**(2008):157–163.
24. Thermophysical Properties of Fluid Systems, NIST Chemistry WebBook, SRD 69, <https://webbook.nist.gov/chemistry/fluid/>
25. Weber, B., "Alternative Implementation of a Porous Media Model for Simulating Drying of Heated Concrete", COMSOL conference, Lausanne, 2018.
26. Drouet, E., Poyet, S., and Torrenti, J.M., "Temperature influence on water transport in hardened cement pastes", *Cement and Concrete Research* **76**(2015):37–50.

The Effect of Micro-structural Mechanisms on the Macro-level Behaviour of Cementitious Materials at Elevated Temperatures

Jiayi Wang¹, Colin T Davie^{1,*}, Enrico Masoero¹

¹School of Engineering, Newcastle University

Newcastle upon Tyne, United Kingdom

* Colin T Davie (colin.davie@ncl.ac.uk, Drummond Building, Newcastle University, Newcastle upon Tyne, NE1 7RU)

ABSTRACT

The benchmark problem [1] presented by Wang et al. [2] has been further explored to consider the effect of micro-structural mechanisms on the macro-level behaviour of concrete at elevated temperatures, again using an existing fully coupled, hygro-thermo-mechanical model [3] cast in a finite element framework and implemented in the research code FEAP [4]. Results relating to the evolution of temperature and gas pressure are presented. Early investigations and previous works have confirmed that intrinsic permeability and its evolution with temperature is key to the development of gas pressures [2, 5]. Additionally, the amount of water introduced into the system as a result of dehydration of the cement paste, the influence of micro-scale gas flow behaviour and the evolution of capillary pressures are investigated and all found to have considerable effect on the development of macro-scale behaviours. Further work will consider more specifically the evolution of the pore size distribution, its relationship to dehydration and its effect on macro-scale material properties such as porosity, permeability and sorption isotherms.

KEYWORD: concrete, micro-structural, high temperature, numerical model, dehydration, gas slip, capillary pressure

INTRODUCTION

Spalling is one of the most severe failure modes for concrete under high temperature yet there remains no consensus on the underlying causes of spalling with two main theories tying it to thermally induced stresses [6, 7] or the developed of internal pore pressures [8, 9]. Whatever the cause, it is hypothesised here that many of the behaviours observed at the macro-scale in concrete exposed to elevated temperatures are in fact a function of behaviour occurring at the micro-scale within the porous micro-structure of the material. However, due to the complexity of the coupled hygro-thermo-chemo-mechanical behaviours that occur in cementitious materials when heated, the effect on macro-scale behaviour of processes occurring at the micro-scale and the evolution of the micro-structure itself with temperature is not holistically understood. Concrete is a multi-phase material and the mechanical characteristics of concrete at high temperatures are not only determined by those components within it but also associated with its intrinsic properties, such as

permeability, porosity, thermal conductivity and strength [3] all of which can be related to the micro-structure. Most of these intrinsic characteristic properties are seen to be temperature dependent when measured empirically at the macro-scale. However, fundamentally, all of these properties and their temperature dependence should be relatable to the micro-structure of the material and its evolution with temperature. For example, porosity is a direct measure of the micro-structural space within the cementitious structure and controls the limits of fluid content in the material. Permeability and diffusivity are functions of the connectivity of that space and control the transport of fluids through the material. Dehydration of the cement paste during heating releases water into the pore space, affecting overall transport behaviour and energy balance, and in doing so leads to changes in the pore structure and the pore sizes and hence changes the porosity, permeability and diffusivity. In turn, those micro-structural changes will affect the development of capillary menisci, thus affecting the water/vapour equilibrium (sorption isotherms) for the material [5].

To investigate some of these micro-structural influences a fully coupled hygro-thermo-mechanical model for concrete originally developed by Davie *et al.* [3] has been employed. The model is cast in a finite element framework and implemented in the research code FEAP [4]. The complex behaviours of concrete are captured through the adoption of multi-phase material descriptions which represent strong coupled behaviours of solid, liquid and gas phases which are considered separately [3]. The model has been employed here to reproduce the results of the benchmark tests [1] (specifically temperatures and gas pressures) and explore the effects of several micro-structural behaviours. These are namely, variation in the quantities of water derived through dehydration, the influence of Klinkenberg gas-slip effects [8] and the evolution of capillary pressure with water contents, which is related to pore size distribution. (It should be made clear that, at this stage, spalling is not explicitly considered). By tuning of macro-scale properties and modifying modelling assumptions, insight can be gained into the influence of key factors in controlling the observed experimental results which in turn help to identify avenues for further research.

MATHEMATICAL MODEL

The fully coupled hygro-thermo-mechanical model considers concrete as a multi-phase material consisting of solid (cementitious skeleton), liquid (free water) and gas (water vapour and dry air) phases and solves for the primary variables of temperature, gas pressure and vapour content. The concrete is considered to behave elastically with the degradation of the material due to both mechanical and thermal loading accounted for via an isotropic thermo-mechanical damage formulation. The liquid phase is subject to Darcian pressure driven flow while the gas phase (considered as a mixture of ideal gases) is subject to both Fickian diffusion and pressure driven flow. Evaporation and condensation of the liquid water and vapour are possible and dehydration of water from the solid skeleton is also considered. Coupling between the fluid and solid phases is achieved via a Bishop-type effective stress approach. The governing conservative, fluid transport and mechanical strain equations of the model are briefly described below while the full details of the formulations and implementations with auxiliary functions are presented in Davie *et al.* [3].

Governing Conservative Equations

The model consists of four governing equations: mass conservation of dry air (1), mass conservation of moisture (inc. water vapour and liquid water) (2), energy conservative equation (3) and linear momentum balance (4):

$$\frac{(\varepsilon_G \tilde{\rho}_A)}{\partial t} = -\nabla \cdot \mathbf{J}_A \quad (1)$$

$$\frac{(\varepsilon_G \tilde{\rho}_V)}{\partial t} + \frac{(\varepsilon_L \rho_L)}{\partial t} - \frac{(\varepsilon_D \rho_L)}{\partial t} = -\nabla \cdot (\mathbf{J}_V + \mathbf{J}_L) \quad (2)$$

$$\left(\rho C\right) \frac{\partial T}{\partial t} - \lambda_E \frac{\partial(\varepsilon_L \rho_L)}{\partial t} + (\lambda_D + \lambda_E) \frac{(\varepsilon_D \rho_L)}{\partial t} = -\nabla \cdot (k \nabla T) + \lambda_E \nabla \cdot \mathbf{J}_L \quad (3)$$

$$\nabla \cdot (\boldsymbol{\sigma}' - \eta P_{Pore} \mathbf{I}) + \mathbf{b} = 0 \quad (4)$$

where, ε_θ is the volume fraction of a phase θ ($\theta = L, V, A, G, D$ refer to liquid water, water vapour, dry air, gas mixture and dehydrated water phases, respectively), ρ_θ is the density of a phase θ , $\tilde{\rho}_\theta$ the mass of a phase θ per unit volume of gaseous material, \mathbf{J}_θ the mass flux of a phase θ , ρC the heat capacity of concrete, k the effective thermal conductivity of concrete, λ_D is the specific heat of dehydration, λ_E is the specific heat of evaporation (or of desorption), T is the temperature, $\boldsymbol{\sigma}'$ is the Bishop's stress, \mathbf{I} is the identity matrix, η is the Biot coefficient, P_{Pore} is the pore pressure, \mathbf{b} is the body force and t is time [3].

Fluid Transport Equations

Transport of the liquid water phase is described by Darcy's law where the water is assumed to flow through the pore structure of concrete under pressure, while the concentration driven diffusion of the gas phase is assumed to obey the Fick's law. The mass fluxes of water vapour, dry air and liquid water per unit area of concrete are then given respectively by:

$$\mathbf{J}_A = \varepsilon_G \tilde{\rho}_A (\mathbf{v}_G) - \varepsilon_G \tilde{\rho}_G D_{AV} \nabla \left(\frac{\tilde{\rho}_A}{\tilde{\rho}_G} \right) \quad (5)$$

$$\mathbf{J}_V = \varepsilon_G \tilde{\rho}_V (\mathbf{v}_G) - \varepsilon_G \tilde{\rho}_G D_{AV} \nabla \left(\frac{\tilde{\rho}_V}{\tilde{\rho}_G} \right) \quad (6)$$

$$\mathbf{J}_L = \varepsilon_L \rho_L (\mathbf{v}_L) \quad (7)$$

where, D_{AV} is the coefficient of diffusion for the dry air/water vapour mixture within the porous concrete and \mathbf{v}_G & \mathbf{v}_L are the Darcian velocities of the gas and liquid water phases, given by:

$$\mathbf{v}_G = -\frac{k_g K \cdot K_G}{\mu_G} \nabla P_G \quad \mathbf{v}_L = -\frac{K \cdot K_G}{\mu_G} \nabla P_L \quad (8)$$

where K is the intrinsic permeability of the concrete, K_θ , μ_θ and P_θ are the relative permeability, dynamic viscosity and pressure of the phase θ and k_g is the gas-slip factor, given by:

$$k_g = \left(1 + \frac{b \cdot P_{Atm}}{P_G} \right), \text{ with } b = e^{(-0.5818 \ln(K) - 19.1213)} \quad (9)$$

where, $P_{Atm} = 101325$ Pa is standard atmospheric pressure and b is the Klinkenberg gas-slip flow constant [8].

The relative permeabilities that describe the variations in flow induced by the partial content of gas and liquid phases in the concrete pore spaces and are defined by [3]:

$$K_G = 10^{5\lambda} - 10^\lambda S \quad K_L = 10^{(1-S)\lambda} - 10^\lambda (1 - S) \quad (10)$$

Where, S is the degree of liquid water saturation and λ is a function of porosity, ϕ .

$$S = \frac{\varepsilon_L}{\phi} \quad \lambda = 0.05 - 22.5\phi \quad (11)$$

Capillary suction is considered by way of the Kelvin equation:

$$P_L = P_G - P_C, \text{ with } P_C = \begin{cases} -R_V T \rho_L \ln \left(\frac{P_V}{P_{Sat}} \right) & \text{for } S > S_{SSP} \\ 0 & \text{for } S \leq S_{SSP} \end{cases} \quad (12)$$

where, R_V is the ideal gas constant of water vapour [12], P_V is the vapour pressure and P_{Sat} is the water vapour saturation pressure. S_{SSP} is the solid saturation point, below which all water is assumed to exist as adsorbed water, physically bound to the concrete skeleton [8] and so capillary menisci cannot form.

Ideal gas behaviour is assumed for the dry air and water vapour:

$$P_A = R_A \tilde{\rho}_A T \quad P_V = R_V \tilde{\rho}_V T \quad (13)$$

and their partial pressures and densities are assumed to obey Dalton's law of additivity [12]:

$$P_G = P_A + P_V \quad \tilde{\rho}_G = \tilde{\rho}_A + \tilde{\rho}_V \quad (14)$$

The saturation with liquid water (and hence the volume fraction of liquid water (11)) in the concrete is calculated by the sorption isotherms:

$$S = f(A, B(T), h) \quad (15)$$

where, A is a set of material constants, $B(T)$ is a set of temperature dependent material properties and h is the relative humidity. The volume fraction of gas, ε_G , is calculated by:

$$\phi = \varepsilon_L + \varepsilon_G \quad (16)$$

Detailed functions for the material parameters employed in the formulation above are presented in [2, 9].

Mechanical Formulation

As mentioned above, the model has a fully coupled hygro-thermal-mechanical formulation, however the mechanical behaviour is not explicitly considered here and so for brevity the mechanical component is omitted. The detailed formulation is presented in [2, 9].

Boundary Conditions

Heat transfer across the boundary is described by:

$$\frac{\partial T}{\partial n} = \frac{h_{qr}}{K_{TT}} (T_\infty - T) \quad (17)$$

where T_∞ is the atmospheric temperature and h_{qr} is the sum of radiation and convection heat transfer coefficients on the boundary. It is assumed that the boundary is dry and no liquid water flux occurs [12] so only water vapour transfer is considered:

$$\frac{\partial \tilde{\rho}_V}{\partial n} = -\frac{K_{VT} h_{qr}}{K_{VV} k} (T_\infty - T) + \frac{\beta}{K_{VV}} (\tilde{\rho}_{V,\infty} - \tilde{\rho}_V) \quad (18)$$

where, β is the coefficient of water vapour mass transfer on the boundary and $\tilde{\rho}_{V,\infty}$ is the vapour content in the atmosphere. (Full formulations for the terms K_{TT} , K_{VT} & K_{VV} can be found in [3]). The gas pressure on the boundary is given by:

$$P_G = P_{G,\infty} \quad (19)$$

NUMERICAL ANALYSES

The model set up for this high-temperature problem, representative of concrete slabs 120mm thick and 300 × 300mm in plan area subjected to different heating scenarios on one face, is shown in Figure 1. For simplicity, a 1D approach is adopted in the first instance.

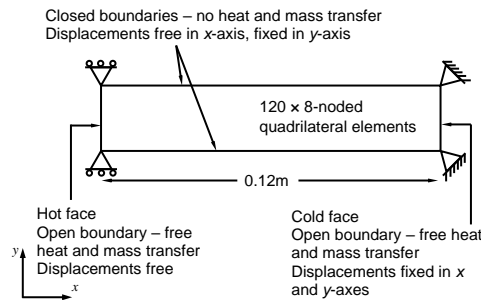


Figure 1 One-dimensional model set up.

The model was employed to reproduce as closely as possible the experimental heating scenario where the temperature in the atmosphere was raised instantly to 600°C and held

constant throughout the test. The key material parameters and the initial internal conditions of the three types of concrete were provided from the [1] and [13] and are shown in Table 1. In [3], the model was set up using these parameter values in order to directly compare the model prediction to the experimental results. These results are here used as a benchmark to study the influence of the various micro-scale mechanisms described above.

Table 1 Initial conditions and material properties for two concrete types.

Parameter	Initial conditions and material properties	
	B40	B60
Initial internal temperature	20°C	20°C
Initial internal gas pressure	101325Pa	101325Pa
Initial internal vapour content	0.0074336 kg/m ³ \equiv ~43% RH	0.0134842 kg/m ³ \equiv ~78% RH
Initial porosity	13.85%	10.55%
Initial permeability, K_0	1.0×10 ⁻¹⁹ m ² (@20°C)	6.0×10 ⁻²⁰ m ² (@20°C)
Bulk density	2285 kg/m ³	2364 kg/m ³
Solid density	2583 kg/m ³	2551 kg/m ³
Young's modulus	24 GPa	39 GPa
Poisson's ratio	0.2	0.2
Compressive strength	30 MPa	67 MPa
Tensile strength	2.4 MPa	3.8 MPa

The boundary heat transfer properties for these analyses were taken from previous work [3], which in turn followed the work of [14], looking at the experiments of [13].

RESULTS

Analysis 1 – Permeability: As presented in Wang et al.[2], the initial permeability was adjusted by trial and error until a good match was reached between the numerical and experimental gas pressure peaks. Results of gas pressure and temperature are given in Figure 2a-d with the numerical permeability indicated on the right.

(Experimental K_0 : B40 - 5.53×10⁻¹⁶ m²; B60 - 1.67×10⁻¹⁶ m²).

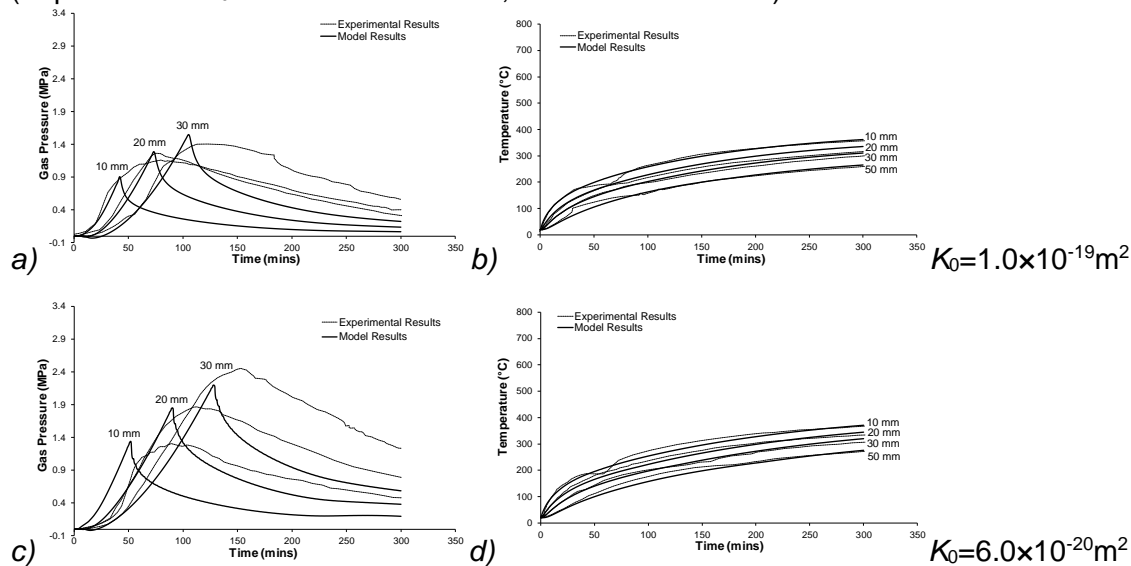


Figure 2 Numerical and experimental results showing gas pressures (left) (tuned via permeability) and temperatures (right) with time for a) & b) B40, c) & d) B60

As discussed in [2], firstly, it can be seen that the temperature profiles are matched reasonably well in all cases with only slight differences in the early stages. Secondly, the gas pressure peak heights and their evolution with depth and time can be matched reasonably well in all cases however the shape of the experimental peaks are quite rounded and

elongate under moderate heating whereas the model predicts sharp peaks. It should also be noted that the permeabilities applied in the model are several orders of magnitude smaller than those measured experimentally (~ 2 for B40; ~ 4 for B60). It is well known that the intrinsic permeability plays a great role in controlling gas pressure development [12, 15,16] but other factors including the amount of moisture introduced into the system, differences in gas and liquid transport behaviour and capillary suction may also be significant. *Analysis 2 - 5* explore these issues further.

Analysis 2 – Volume of water released by dehydration

Independent of the permeability, the moisture content within the concrete has a significant effect on the development of gas pressures. The moisture content is not only determined by the initial saturation (the volume of free water within the microstructure before heating starts) but is also related to the amount water released by dehydration of the cement paste upon exposure to high-temperatures. Figure 3a shows the dehydration function described by:

$$\varepsilon_D \rho_L = \begin{cases} 0 & \text{for } (T_c \leq 200^\circ\text{C}) \\ a(f_{rec})T_c^3 + b(f_{rec})T_c^2 + c(f_{rec})T_c + d & \text{for } (200^\circ\text{C} < T_c \leq 300^\circ\text{C}) \\ 0.4 \times 10^{-4} \rho_c (T_c - 300) + (f_{rec} - 0.02) \rho_c & \text{for } (300^\circ\text{C} < T_c \leq 800^\circ\text{C}) \\ f_{rec} \rho_c & \text{for } (T_c > 800^\circ\text{C}) \end{cases} \quad (20)$$

where ρ_c is the volume fraction of cement paste in the concrete mix, $f_{rec} = 0.09$ is the fraction of cement paste that is recoverable as water and $a, b, c,$ and d are coefficients of a cubic function (and functions of f_{rec}) such that $\varepsilon_D \rho_L(T)$ and its derivative, $\partial \varepsilon_D \rho_L / \partial T$ are continuous. This function, employed in the model used here [3], was adapted from [12] who cites [17, 18] as its source. Upon inspection of (12) it may be noted that for the concretes employed in the benchmark problem, where $\rho_c = 300 \text{ kg/m}^3$, the $f_{rec} = 0.09$ fraction given by [12] produces a maximum volume of water from dehydration of 27 kg/m^3 , making it a secondary source of water compared to the initial free water content. It may also be noted that this volume is significantly less than the volumes of water resulting from dehydration suggested by [15, 16].

To investigate the significance of this source of water into the coupled system, equation (21) was modified using two larger fractions of cement content ($f_{rec} = 0.4$ & $f_{rec} = 0.6$). These are shown in Figure 3b and result in maximum volumes of 120 kg/m^3 and 180 kg/m^3 of water from dehydration respectively.

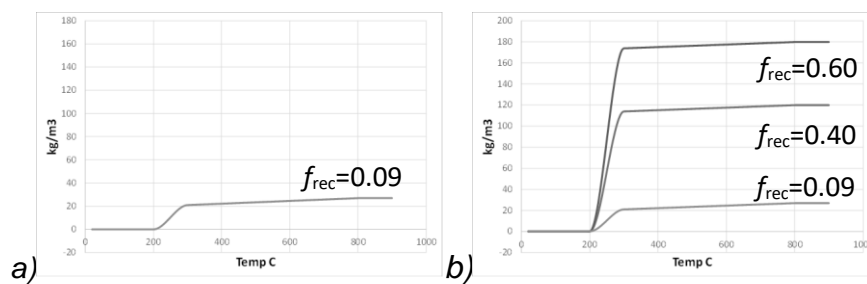


Figure 3 Mass of water released by dehydration with temperature for a) original dehydration function, b) increased dehydration functions

The benchmark analyses conducted in *Analysis 1* were repeated using the same permeabilities and applying these two new curves. Results of gas pressure and temperature are shown in Figure 4a-h.

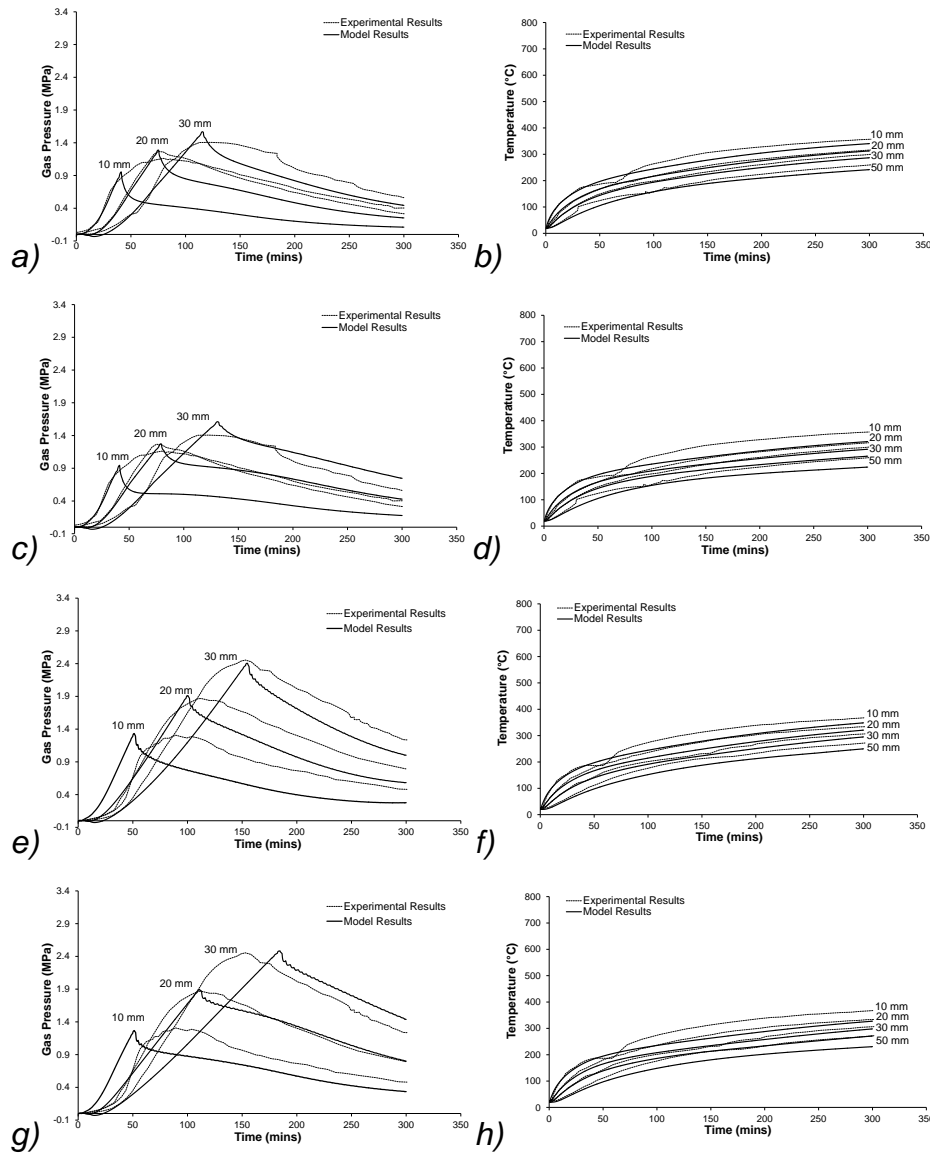


Figure 4 Numerical and experimental results showing gas pressures (left) and temperatures (right) in time for a) & b) B40 with $f_{rec}=0.4$, c) & d) B40 with $f_{rec}=0.6$, e) & f) B60 with $f_{rec}=0.4$, g) & h) B60 with $f_{rec}=0.6$

From examination of these results and comparison with results in Figure 2 several things should be noted. Firstly, although the height of the gas pressure peaks has not changed significantly the shape of them, particularly in the post peak section has changed considerably. The tails of the peaks are now much higher and match much better with the experimental results. This change is directly due to the increased volume of water being released into the system by dehydration. The reason that this effect does not significantly change the height of the peaks is that, according to equation (21) and supported by [15], dehydration does not begin until the temperature reaches 200°C. As can be seen from the temperature profiles (Figures 4b, d, f & h) this temperature is not reached until after the peak gas pressures have been passed. Although the gas pressure profiles seem to suggest that the updated dehydration curves offer a better representation of the true volumes of water being introduced into the system, it can also be seen that the temperature profiles are adversely affected. As the volume of water from dehydration increases the temperatures fall and no longer match the experimental temperatures in the latter part of the analyses. This is simply because there is more water in the system to absorb energy through heat capacity

and phase change (evaporation). The solution to this problem may lie with the material properties or, may be a function of the heat and mass transfer through the boundary [3].

Analysis 3 – Gas-slip

Gas-slip is a phenomenon whereby, in contrast to laminar flow of a liquid passed a solid, gases exhibit non-zero flow at the fluid-solid interface. In porous materials like concrete this has been shown to affect the flow rate of gases through the material such that it significantly deviates from macro-scale predictions of Darcian flow behaviour [8]. To account for this behaviour this model uses a formula developed in [8] that introduces a factor, k_g , a function of the Klinkenberg gas-slip flow constant, that increases the permeability for gas flow above that of liquid flow (9). As can be seen this factor is dependent on the intrinsic permeability of the material and the gas pressure. It is therefore variable in a transient problem such as the one studied here and can produce gas permeabilities several orders of magnitude larger than the liquid permeability.

To study the influence of this factor the benchmark analyses conducted in *Analysis 2* were repeated with the gas-slip factor set to 1. Figure 5a shows the result when gas-slip is neglected (cf. Figure 4c). As can be seen the gas pressures are overestimated by a large amount and the numerical analysis failed after approximately 70 mins as 100% saturation with liquid water was reached. Re-tuning these results via permeability (Figure 5b) shows that an order of magnitude reduction can be achieved in the model permeability, bringing it closer to the experimentally measured values (See Figure 2). Figures 5c & d show similar results for B60 concrete, with a 2 order magnitude reduction achieved (cf. Figure 4g). These results suggest that the model for the Klinkenberg constant overestimates the difference between the gas permeability and liquid permeability in these concretes. More work is required to understand why when an additional micro structural mechanism is added to the formulation a poorer correlation is seen with macro-scale results but it may be that gas-slip is not as significant under high temperature conditions.

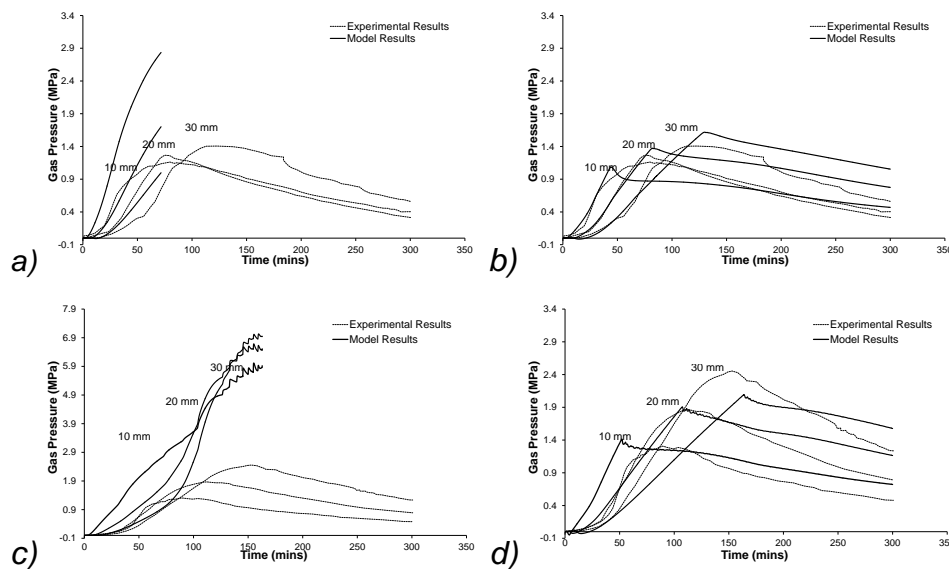


Figure 5 Numerical and experimental results showing gas pressures in time for a) B40 without gas-slip effect $K_0=1.0 \times 10^{-19} \text{m}^2$; b) B40 without gas-slip effect $K_0=6.0 \times 10^{-18} \text{m}^2$; c) B60 without gas-slip effect $K_0=6.0 \times 10^{-20} \text{m}^2$; d) B60 without gas-slip effect $K_0=4.0 \times 10^{-18} \text{m}^2$

Analysis 4 – Evolution of capillary pressure

Another important phenomenon rooted in the micro-structure is capillary pressure, i.e. the difference between the gas and liquid pressures found across capillary menisci that form in the partially saturated porous structure. This micro-scale pressure difference has an effect on the macro-scale pressure gradients that drive fluid flow behaviour. To account for

capillary pressure, the model used here employs Kelvin's equation (12). However, following the work of Gawin et al. [9], the development of capillary pressure is limited to the range above the solid saturation point ($S \geq S_{SSP} = 0.55$) where liquid water exists.

The authors can find no argument to support the assumed value of $S = 0.55$ apparently used by Gawin et al. as a cut-off for capillary menisci and so, to explore the influence of the evolution of capillary pressure in the lower saturation range *Analysis 2* was again re-run, but this time with the solid saturation point set to zero, i.e. with no limit to the development of capillary pressures. Figures 6a & b show the results when the capillary pressures are not limited. As can be seen there is little overall change in the position or height of the pressure peaks when compared to Figures 4c & g. However, a critical difference, most noticeable in Figure 6a, is that the shape of the peaks changes from being a sharp point to a more rounded peak, much more like those seen in the experimental results. This seems contrary to the findings of [11] where capillary pressures were found to have almost no influence on the development of gas pressures in heated concrete. However, in that case very rapid heating took place that led to the development of a steep drying front and almost no areas of lower saturation. By contrast, the relatively slower heating rates applied in this benchmark problem result in a much less steep drying front and a large zone of lower saturation. Thus, the development of capillary pressure and its influence on fluid flow at low saturations has a significant effect on the hygro-thermal behaviour of these concretes and as will be shown, this becomes even more significant when combined with other factors.

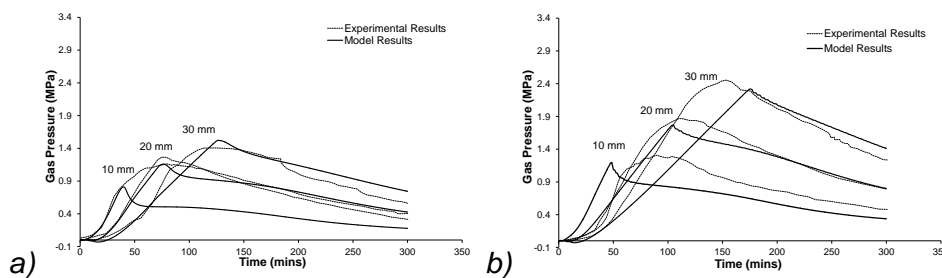


Figure 6 Numerical and experimental results showing gas pressures in time for a) B40 with $S_{SSP}=0.0$ and b) B60 with $S_{SSP}=0.0$

Analysis 5 – Combined microstructural considerations

As a final comparison the effects of permeability, dehydration, gas-slip and capillary pressure have been tuned together to give the best fit to the experimental results. As can be seen when Figure 7 is compared to Figure 2, a significant improvement is seen over the original analysis.

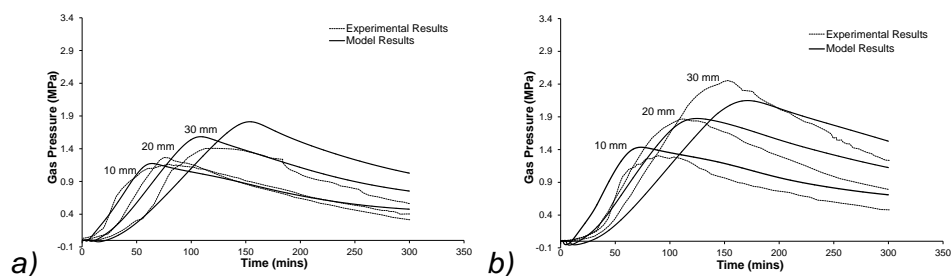


Figure 7 Numerical and experimental results showing gas pressures in time for a) B40 & b) B60 both with $K=3.0 \times 10^{-18} \text{ m}^2$, $f_{rec}=0.4$, no gas-slip effect and $S_{SSP}=0.0$

Conclusions

The experimental tests developed and reported in [1] have been employed as a benchmark problem with which to explore numerically the influence of various micro-structural mechanisms on the observed macro-scale behaviour of concrete exposed to elevated

temperatures. Specifically, consideration has been given to intrinsic permeability, the quantity of water recoverable through dehydration of the solid, cement paste skeleton, the difference between the flow of a gas and the flow of a liquid passed a solid surface (gas-slip) and the evolution of capillary pressures, particularly at lower saturation levels.

In considering dehydration of the cement paste, it was found that the amount of water released by dehydration has a significant effect on the shape of the gas pressure peaks. While, due to the temperature regime in this problem, the heights of the peaks (and hence the apparent permeability) were generally unaffected, the post peak pressures were much better matched when larger amounts of water were available through dehydration. However, the addition of this water had a negative effect on matching of the temperature profiles as heat energy was absorbed by heat capacity and phase change. It may be further noted that the release of water from the solid skeleton is directly related to an increase in the micro-structural pore size and therefore, the macro-scale properties of porosity and permeability should be related to dehydration. To address this, the evolution of the pore size distribution with temperature will be further explored.

In considering gas-slip, it was found that it can have a very significant effect on the development of gas pressures in this problem. More work is required to understand if the gas-slip model employed here is specifically unsuitable or if the phenomenon itself is not significant under high temperature conditions. It is clear that for this problem, neglecting gas-slip produces quite different results and moves the predicted permeability one or two orders of magnitude closer to experimentally measured values.

In considering capillary pressures it can be seen that their development and influence on fluid flow at low saturations has a significant effect in this problem and particularly affects the shape of the gas pressure peaks. It can be further seen that this effect is even more significant when taken in combination with other micro-structural factors. Contrasting with previous work [11], it is clear that they must be taken into account when relatively low heating rates lead to shallow drying fronts and zones of low saturation.

In addition to this, as has been shown before, e.g. [2], intrinsic permeability remains a very significant factor in the development of gas pressures in heated concrete. While improved consideration of the other factors explored here leads to closer alignment with experimentally measured permeabilities there remains a significant difference with numerical values required to match gas pressure results. More work is still required here.

Reference

1. Mindeguia, J.-C., "Numerical Benchmark of experiments on heated concrete", Proceedings of 5th International Workshop on Concrete Spalling due to Fire Exposure. Borås, Sweden, 12-13, September, 2017.
2. Wang, J., Davie, C.T., Masoero, E., "RILEM TC 256 - Numerical Benchmark of experiments on heated concrete", Proceedings of the 6th International Workshop on Concrete Spalling due to Fire Exposure, 185-196, Borås, Sweden, 12-13, September, 2017.
3. Davie, C.T., Pearce, C.J., and Bićanić, N., "A fully generalised, coupled, multi-phase, hygro-thermo-mechanical model for concrete", *Materials and Structures*, **43**, 13-33, 2010.
4. Taylor, R.L., *FEAP - A Finite Element Analysis Program. Version 8.2 User Manual*, University of California at Berkeley. 2008.
5. Davie, C. T. et al., "Modelling of transport processes in concrete exposed to elevated temperatures – An alternative formulation for sorption isotherms." *Cement and Concrete Research*, **106**, 144-154, 2018.
6. Witek, A. et al., "Finite element analysis of various method for prediction of concrete structures against spalling during fire." *Comput. Mech.* **39**, 271-292, 2005.

7. Tenchev, R. T. and Purnell, P., "An application of a damage constitutive model to concrete at high temperature and prediction of spalling." *International Journal of Solid and Structures*, **42**, 6550-6565, 2005.
8. Chung, J.H., Consolazio, G.R., "Numerical modelling of transport phenomena in reinforced concrete exposed to elevated temperatures". *Cement and Concrete Research*, **35**,597–608, 2005.
9. Gawin, D., Majorana, C.E., and Schrefler, B.A., "Numerical analysis of hygro-thermal behaviour and damage of concrete at high temperature", *Mechanics of Cohesive-frictional Materials*, **4**, 37-74, 1999.
10. Cengel, Y.A., *Heat Transfer: A Practical Approach*, Mcgraw-Hill. 2002.
11. Davie, C.T., Pearce, C.J., and Bićanić, N., "Coupled Heat and Moisture Transport in Concrete at Elevated Temperatures—Effects of Capillary Pressure and Adsorbed Water", *Numerical Heat Transfer, Part A: Applications*, **49**, 733-763, 2006.
12. Tenchev, R.T., et al., "Finite Element Analysis of Coupled Heat and Moisture Transfer in Concrete Subjected to Fire", *Numerical Heat Transfer: Part A: Applications*, **39**, 685-710, 2001a.
13. Kalifa, P., Menneteau, F.D., Quenard, D., "Spalling and pore pressure in HPC at high temperatures", *Cement and Concrete Research*, **30**, 1915-1927, 2000.
14. Mounajed, G., Obeid, W., "A New Coupling F.E. Model for the Simulation of Thermal-Hydro-Mechanical Behaviour of Concretes at High Temperatures", *Materials and Structures* **37**, 422-432, 2004.
15. Dauti, D., et al., "Modeling concrete exposed to high temperature: Impact of dehydration and retention curves on moisture migration." *International Journal for Numerical and Analytical Methods in Geomechanics* 42(13), 1516-1530, 2018.
16. Davie, C. T., et al., "Aspects of Permeability in Modelling of Concrete Exposed to High Temperatures." *Transport in Porous Media*, **95(3)**, 627-646, 2012.
17. Bažant, Z. P. and M. F. Kaplan., *Concrete at High Temperatures: Material Properties and Mathematical Models*. Harlow, Longman, 1996.
18. Harmathy, T. Z., "Thermal Properties of Concrete at Elevated Temperatures." *ASTM Journal of Materials* **5(1)**, 47-74, 1970.

Flash vaporization next to an opening crack: a possible explanation of the explosive nature of concrete spalling

Roberto Felicetti^{1,*}, Ramin Yarmohammadian¹, Stefano Dal Pont² &
Alessandro Tengattini³

¹ Politecnico di Milano, Milan, Italy

² Université Grenoble Alpes, Grenoble, France

³ Institut Laue-Langevin, Grenoble, France

* Corresponding author (roberto.felicetti@polimi.it)

ABSTRACT

In this paper the very quick vaporization of water in the pores of hot concrete next to an opening crack is regarded as way to convert the considerable amount of thermal energy stored in the material into kinetic energy of the fractured splinters. To this purpose, a special setup has been developed in order to suddenly release the vapor pressure accumulated at a sealed edge of a heated sample. The quick local cooling observed confirmed that a sizeable loss of thermal energy occurs in a rather thin layer of concrete facing the depressurized surface. Fast sequences of Neutron Radiographic images allowed to recognize that the influenced zone doesn't exceed 1mm thickness. This has a direct impact on the time scale of thermal and hygral transients and corroborates the idea that a significant contribution to the explosive nature of spalling may be provided by water vaporization.

KEYWORD: neutron radiography, thermal energy, water vaporization

INTRODUCTION

In spite of the number of studies conducted in the field, explosive spalling of concrete in fire keeps being a complex phenomenon that can hardly be governed by the structural designer, since the influence of fire scenario, applied loads, moisture content and inherent permeability of the material has not yet formalized in the shape of a practical spalling criterion. Nonetheless, it is generally agreed that the combined effect of pore pressure and high compressive stress ensuing from restrained thermal dilation is required to produce this critical instability within the exposed concrete cover [1]. Some recent studies allowed to corroborate this perspective.

The potential of pore pressure in promoting the fracturing process was ascertained by testing the splitting tensile strength of small concrete cubes (100mm side) under transient thermo-hygral conditions [2]. The linear decrease of apparent tensile strength with pore pressure confirmed the significant role of this variable. However, the systematic analysis of a series of concrete mixes [3] showed that in High-Performance concrete just a minor share of pore pressure (about 25%) translates into an effective tensile stress borne by the solid skeleton, due to the poorly interconnected porosity. Since pore pressure not exceeding 5MPa is generally measured in the temperature range at which the phenomenon takes place (250-300°C), it turns out that pore pressure can just promote the onset of cracks rather than

overcome alone the tensile strength of concrete. In fact, under the minor thermal stress experienced by slowly heated small cubic samples, none of the tested specimens broke before the implementation of the splitting test, though a remarkably violent failure was observed at testing. Similar conclusions were drawn from compressive tests on 150mm cubes heated at 230°C for 2-3 hours [4].

The twofold contribution of compressive stress due to thermal gradients and external loads consists in triggering cracks parallel to the heated face and reducing moisture leakage by preventing orthogonal cracks. This was investigated by testing square slabs under strictly controlled biaxial compressive loading [5]. While ordinary concrete was able to switch from no effects to substantial spalling upon application of just 5MPa compression, Ultra High-Performance steel fibre reinforced concrete exhibited sizeable spalling regardless of the external load, possibly because of the inherently lower permeability and higher thermal stress. The benefits brought in by monofilament polypropylene fibre (lower pore pressure and faster drying of the cover) confirmed the synergistic role of the hygral transient.

Many numerical models have been developed over the past four decades aimed at assessing the mutual interaction between mechanical and hygral effects of concrete heating [6]. A general result in lightly loaded elements (e.g. concrete tunnel linings) is that the thermally induced compressive stress doesn't exceed 50-60% of the material strength [7], which seems not sufficient to trigger microcracks in High-Performance concrete. This drew more attention to the meso-scale heterogeneity [4, 8], since the higher local stress peaks occur at the interface between coarse aggregate and mortar are likely to originate scattered cracks. Coarse aggregate and microcracks have a sizeable impact also on the penetration of the drying front from the heated surface, as highlighted by Neutron Tomography [9] and confirmed by 3D modelling [10].

The cited developments allowed an important progress in the recognition of the causes for the onset of spalling, which is generally denoted by a combination of mechanical stress, pore pressure and damage which cannot be anymore be borne by the material. However, it is not yet fully understood why in many cases the fractured cover remains in place [11], with little detriment to fire safety, while in other situations concrete splinters are thrown many meters away, with possible direct exposure of rebars to the flames.

Some Authors [12] proved to be sceptical about the role of pore pressure in accelerating the fractured shards, because crack opening implies a huge increase of the initial pore volume and, in their opinion, no significant amount of water could flow into this gap from the surrounding concrete in the very short duration of the explosive spall. Then a sudden pressure drop is expected and just the elastic strain energy due to thermal stress would be converted into fracture and kinetic energy. This point of view was partly corroborated by the energy balances proposed in [13], though the contribution from pore pressure was recognized necessary when the splinter velocity exceeds 5m/s, which is often the case [14]. Involving in the energy balance the adiabatic expansion of an initial volume of pressurized vapor required considering an already widely open crack (0.5mm) filled with gas at significant pressure (4MPa), a steady condition which looks not realistic to reach, since concrete loses most of tensile strength already with a tenfold thinner crack [15].

An alternative to account for the mechanical work developed by pressurized fluids was the definition of the "influencing region" [14], namely the domain around the crack contributing to the inflow of water vapor into the opening gap (Figure 1). Unfortunately, no indication was provided in this study about the thickness d_{max} of this band of moist concrete facing the opening crack, though this is a crucial parameter to determine the rate of moisture migration and then to rebut the original arguments against this perspective [12].

The focus of this paper is to gain a deeper insight into the intriguing concept of the influencing region. Direct observation by means of Neutron Radiography (NR) during fast thermo-hygral transients is the key objective of the research project. The background idea, the test setup and some first results are illustrated in the following sections.

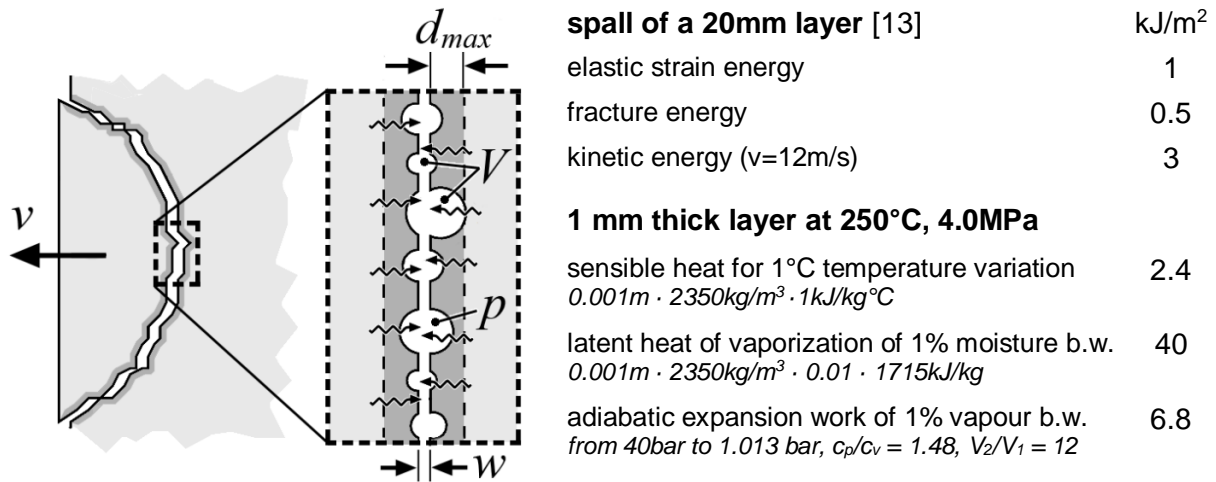


Figure 1 The influencing region next to an opening crack [14] and magnitudes of energy contributions involved in the spalling phenomenon.

TEST PRINCIPLE AND FIRST VALIDATION

As discussed, the magnitude of the different energy shares governing the sudden separation of concrete fragments from the exposed cover was the object of former studies available in the literature [13, 14]. Some indicative figures per unit spalled area are reported in Figure 1, together with the terms entailed by unit temperature and moisture content variations within a unit thickness layer under typical conditions for incipient spalling. These latter values should be doubled, since both faces of the opening crack are influenced by the surrounding concrete.

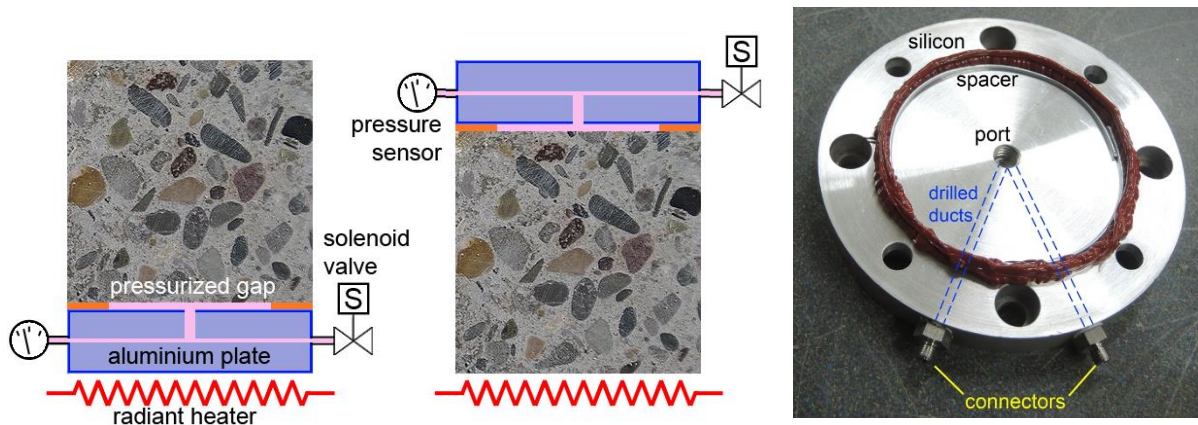
What stands out is the dominant role of thermal energy and latent heat of vaporization compared to what is demanded for fracturing and accelerating the surface splinters. Cooling a thin layer of hot concrete by a few tens of degrees provides far more energy than required for vaporizing water and pressurizing the opening crack. If one considers that the heat flux entering the exposed face of a concrete member during the first ten minutes of severe fire scenarios (from standard to RWS fires) can be as high as 25-50kW/m², the energy mobilized by explosive spalling corresponds to the thermal flux accumulated by the concrete cover in less than one second.

Another important outcome of the cited figures is that the amount of water which should be quickly vaporized to accelerate the fractured shards to their maximum observed velocity can be taken from a layer much thinner than 1mm. Reducing the size of the involved region has a significant impact on the time scale of thermal and hygral transients. Heat conduction transients are ruled by Fourier's dimensionless time, which goes with $1/d^2$ (where d is the distance through which conduction occurs). While heating rebars across a 30mm cover may take one hour, moving heat within the influencing region would take a fraction of a second. Water movement is also expected to be considerably faster, because of both the reduced path distance and the steeper pressure gradients (i.e. higher fluid velocity according to Darcy's law).

In order to confirm the ability of the influencing region to exhibit a fast thermal response under a sudden drop of pore pressure, a simple test setup was devised (Figure 2). One face of a concrete cylinder was sealed by gluing the rim of an aluminium plate with heat resistant silicon (OTTOSEAL S17 by Otto Chemical). A small gap was left between the concrete face and the plate by inserting a spacer (1mm). A blind central hole and two radial ducts drilled in the plate allowed connecting the gap to a pressure sensor and a solenoid valve. The plate was packed with threaded ties to balance the thrust produced by vapour pressure. The temperature of the concrete face was monitored with a thin shielded thermocouple (1mm diameter) inserted in a sub-surface hole.

After insulating the sample with ceramic fibre, one end of the concrete cylinder was heated by means of a ceramic radiator. Both configurations in Figure 2 were checked. In principle, heating the sealing plate has the pros of a faster response and no risk of vapour condensation in the ducts within the aluminium plate. On the other hand, a significant temperature difference develops between the plate and the sample (due to high thermal flux), the concrete face has a higher tendency to dry and the silicon undergoes more demanding operational conditions. In summary, the reversed layout with the sealed gap opposite to the heater proved more effective and reliable and was preferred thereafter.

The samples were some spare cylinders of ordinary concrete kept for several years in the laboratory environment. Despite of the relatively low saturation and the lack of any lateral sealing, a significant pressure was produced in the gap ($\approx 1\text{MPa}$). Upon opening the solenoid valve the gauge pressure dropped to zero and a sudden vaporization of moisture at the sealed surface was made possible (Figure 3). At the same time, a remarkable drop of temperature was observed (-90°C), confirming that vaporization occurs at the price of a loss of thermal energy stored in the material. It has to be remarked that the response time of isolated shielded thermocouples to step temperature variations is not very fast (in the magnitude of some seconds). Then, the recorded rate of temperature change may have been partly reduced by the thermal inertia of the sensor. Nonetheless, the observed initial cooling rate was as high as 120°C/s .



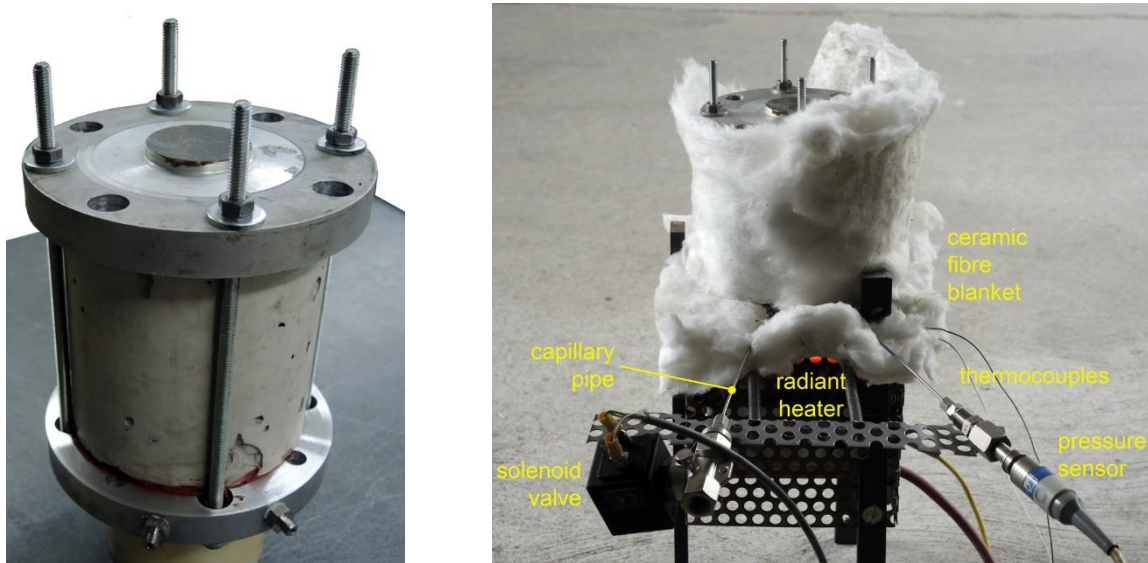


Figure 2 Test schemes for the first trial tests and details of the setup for sealing one face of the concrete sample and then releasing the pressure developed in the gap.

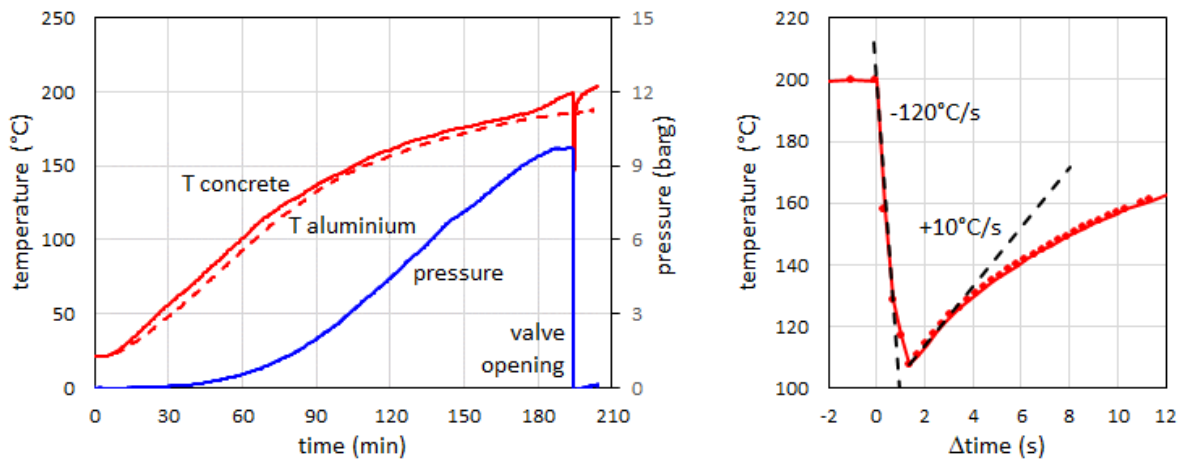


Figure 3 Temperature and pressure trends in a preliminary trial test (sealed face opposite to the heater) and temperature drop at valve opening.

After 1.38s from valve opening, the temperature suddenly stopped decreasing and a sharp inversion of rate was exhibited (from -30°C/s to $+10^{\circ}\text{C/s}$). This indicates the end of water vaporization and settling of the local thermal disturbance by plain heat conduction. The relatively short time to settle ($\approx 30\text{s}$) denoted a relatively thin disturbed layer and confirmed the above considerations about the expected size of the influencing region. This encouraged the development of a similar setup allowing direct observation of moisture migration by means of Neutron Radiography.

TEST SETUP FOR NEUTRON RADIOGRAPHY

As documented by several references in the literature (see [9]), an effective monitoring of moisture migration in concrete samples can be obtained by exploiting the high penetration capabilities of neutrons into dry cement and aggregates in contrast with the high attenuation produced by the nuclei of hydrogen atoms in water molecules. In case of quick hygral transients, a high neutron flux and a not too thick specimen would allow to perform fast radiographic scans, as required by the thorough monitoring of the process. The first requirement was fulfilled by taking advantage testing facilities available at the

Institute Laue Langevin (ILL) in Grenoble, France [16], which currently has the highest neutron flux in the world (about 10^8 neutrons per second per cm^2 at the instrument). Concerning the specimen thickness, based on past experience 30mm was found to be a good compromise between reducing the beam attenuation and averaging the inherent material heterogeneity (Figure 4). A relatively small aggregate size (6mm) was also chosen to this latter purpose.

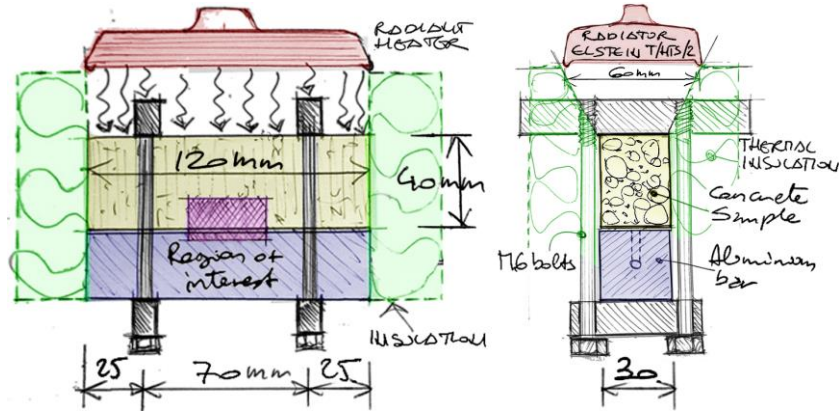
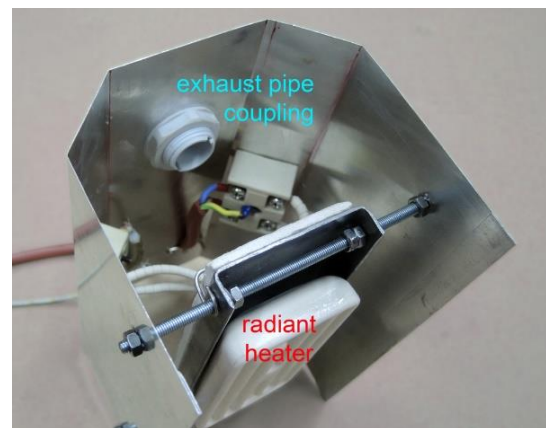
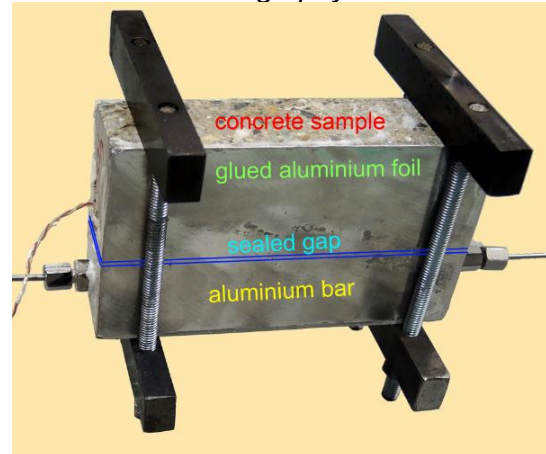
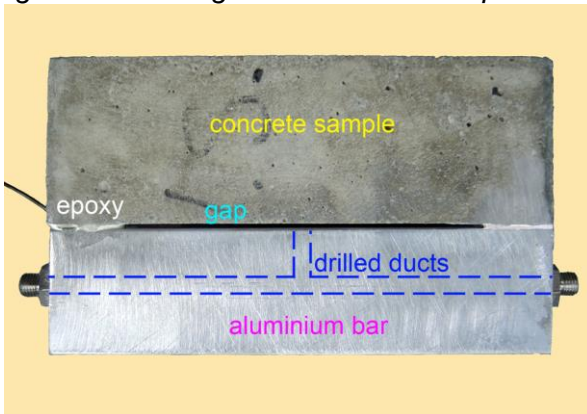


Figure 4 Design sketch of the setup for tests in the Neutron Radiography beam line.



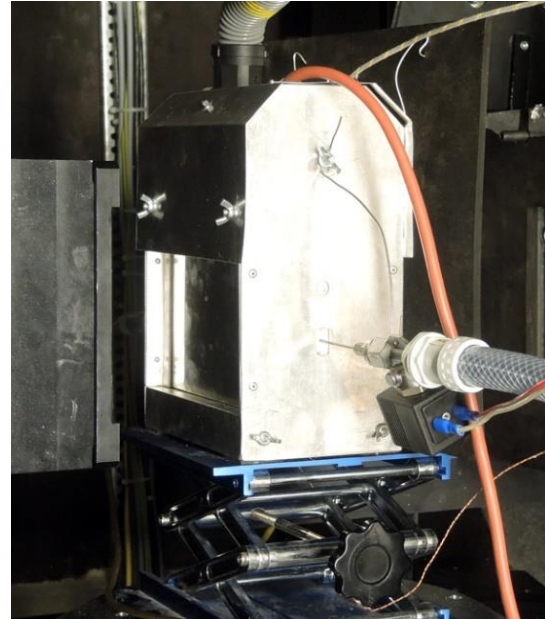
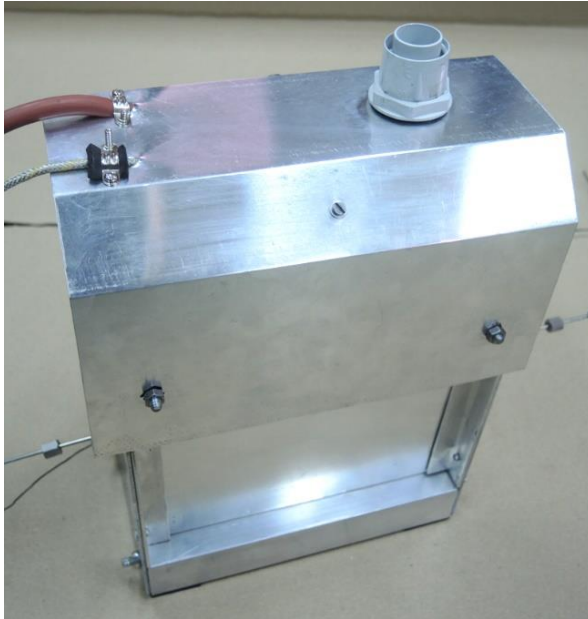


Figure 5 Details of the setup for tests in the Neutron Radiography beam line: thin gap created between the concrete sample and the aluminium bar; sealed and tied sample before and after installation in the insulated aluminium holder; hood fitted with the radiant heater and installation of the complete setup in the beamline.

Contrary to tomographic 3D reconstructions [9], a single radiographic image reports the integral of the attenuation along the beam direction and then moisture variations across the specimen thickness should be minimized. For this reason, the opposite faces crossed by the beam were sealed with aluminium foils (0.3mm thickness) glued with heat-resistant epoxy resin (DP760 by 3M). As regards the face to be submitted to pressure transients, a thin thermocouple with exposed junction (0.3mm wires) was glued directly onto the surface with an epoxy droplet. Then, an aluminium bar (30x30mm) provided with drilled ducts and pipe connectors was glued with the same epoxy glue while interposing some spacers so to leave a 1mm gap (Figure 5). The initial idea to leave the gap open (as reported in the picture) and then to seal the sides just with the aluminium foils proved to be prone to blistering effect, due to the remarkable brittleness of the glue and stress concentration at the edges of the concrete prism. Hence, a thin rim of glue (about 3mm) was applied along the major sides of the rod as well.

After mounting of the restraint frames for balancing the pressure developing in the gap, the sealed specimen was insulated with ceramic fibre and installed in the aluminium holder. The upper hood fitted with the radiant heater and the exhaust pipe connector was then mounted on top of the holder. Finally, the whole box containing the sample was positioned in the Neutron and X-Ray imaging beamline D50 at ILL.

The tests were run by switching on the heater at full power until the target temperature 500°C was reached by the built-in control thermocouple of the radiator. Pressure and temperature in the sealed gap opposite to the heated face were continuously monitored and neutron images were taken at regular time steps (about 90s). When a change in the increasing rate of pressure was recognized, denoting the impending attainment of a pressure peak (normally after 30-60min heating), the maximum image acquisition rate was set (33 frames/s) and the solenoid valve was opened, while recording temperature and pressure at the maximum available rate (4 samples/s). At this frame rate the image

resolution was 0.09mm/pixel, which is still adequate to monitor the shallow drying process occurring next to the sealed gap.

FIRST RESULTS AND DISCUSSION

A first series of tests was performed on concrete samples of normal strength batched according to the mix design of Table 1. Rectangular slabs were cast parallel to their plane, demoulded after one day and cured in water for one week. Curing continued in the laboratory environment till the time of testing. The samples were 40mm deep prisms obtained by cutting the slabs with the diamond disc. Based on this scheme, the moulded faces were sealed with the aluminium foils whereas the saw-cut faces were the object of the hygral transients, so to better replicate the material texture facing a natural crack. Right before testing, the capillary pipe connecting the pressure sensor was filled with silicon oil and the drilled ducts in the aluminium bar were partly filled with water, so to limit moisture loss from the region of interest during the preliminary heating stage.

Table 1 Mix design and orientation of saw cut samples relative to the casting direction.

cement	500 kg/m ³
water	200 kg/m ³
w/c	0.4
siliceous aggregate (d=6mm) Bolomey's grading curve, workability A=12	1693 kg/m ³
plasticizer (% of cement weight)	1%
age at testing	35 days
compressive strength (100mm cubes)	49 MPa

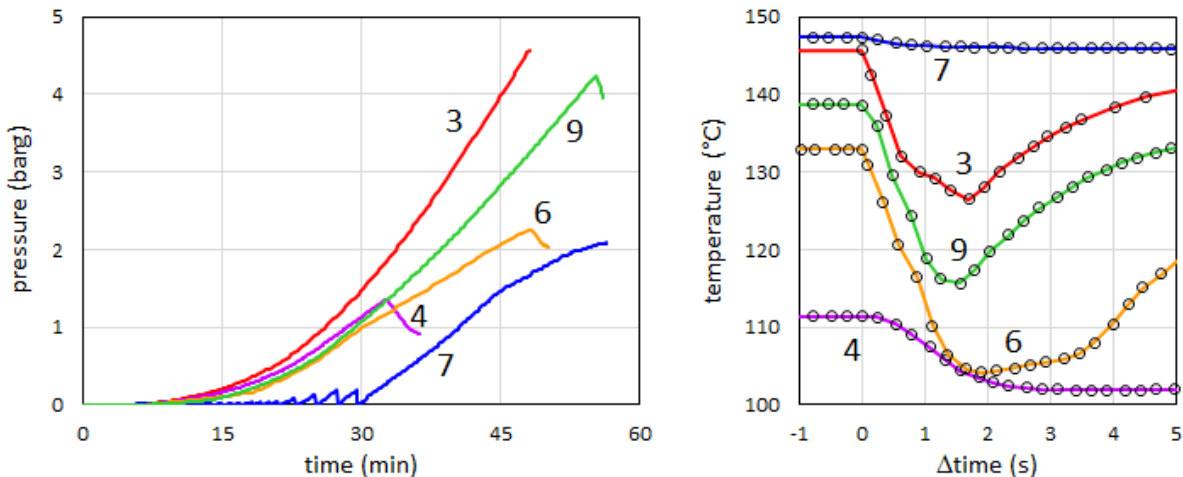
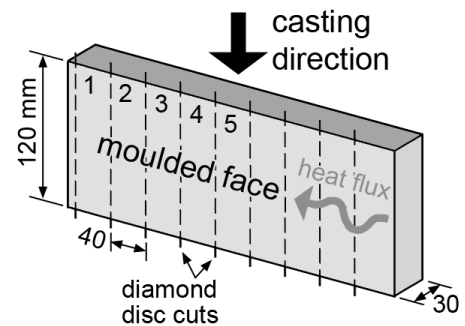


Figure 6 Pressure trends until the opening of the valve and following temperature drops in the first tests performed in the Neutron Radiography beamline.

The pressure and temperature plots obtained (Figure 6) were similar to the above discussed preliminary trial test (see Figure 3). However, lower pressure peaks (1-5 barg) occurring at lower temperature were observed, probably because of the more critical sealing conditions and possible vapour leakage in the preliminary stage of the test (see sample #4). The temperature drops at the valve opening were of lower magnitude as well (up to -30°C) according to the milder transient induced in these tests. In most cases an almost linear trend could be recognized (-20°C/s) and the minimum temperature was reached in about 2s. In these tests the results should not have been affected by the

response time of the exposed junction thermocouples, thanks to their faster response. In one case (sample #7) the valve was opened several times during the heating stage, so to allow some drying of the sample. Despite of the sizeable pressure reached afterward, a very weak thermal transient was produced by the valve opening. Also in tests on samples #4 and #9 it was possible to re-pressurize the gap (1.0-1.5 barg pressure) in the same test run, but no thermal perturbation was induced by the second valve aperture.

As concerns NR images, the drying front penetration from the upper side of the samples during preliminary heating (10-15mm) was denoted by a lighter grey tone (Figure 7).

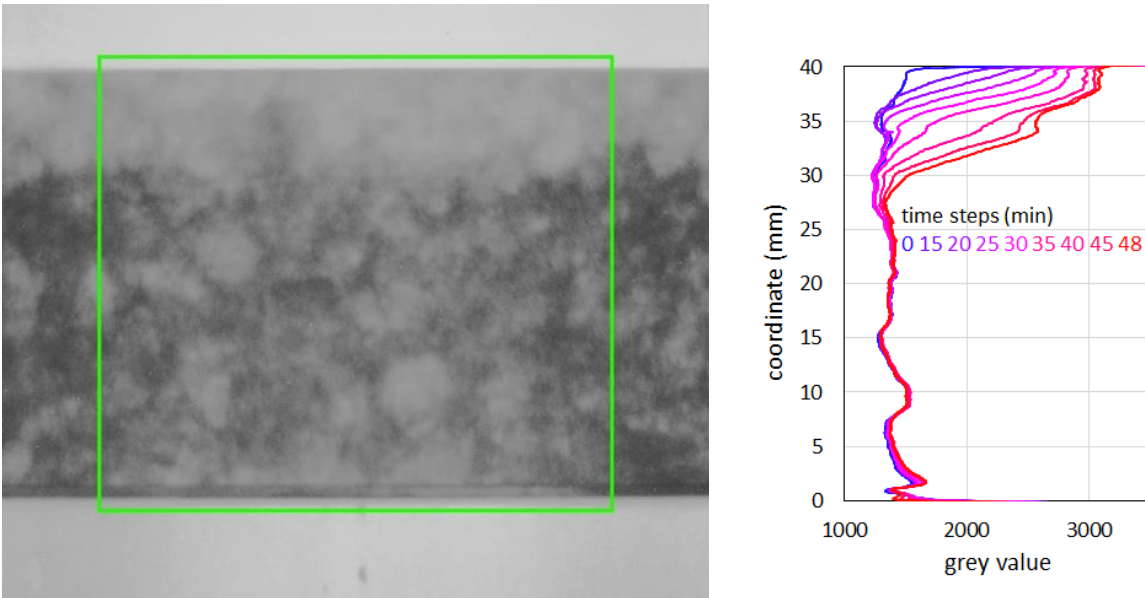


Figure 7 NR image of sample #6 right before valve opening and profiles of the grey value averaged along horizontal lines in the highlighted region of interest.

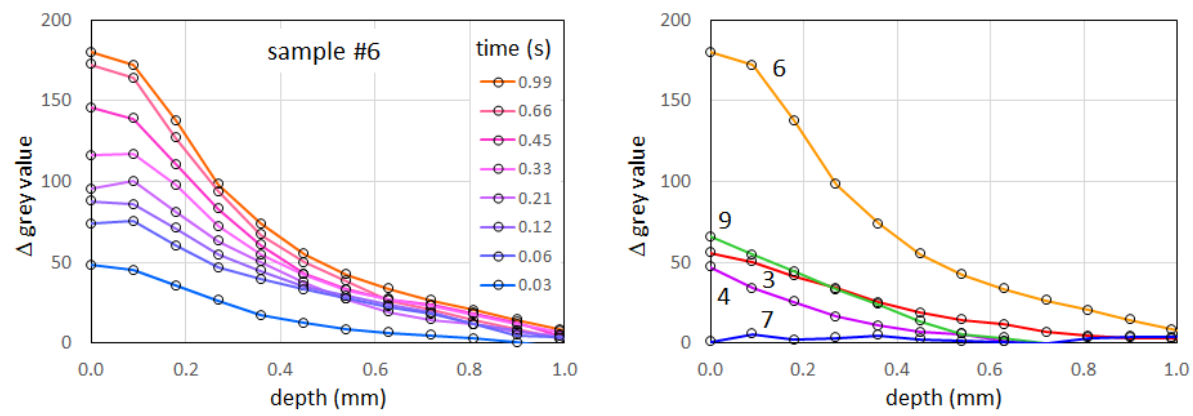


Figure 8 Evolution of grey value profiles during the fast transient following the valve opening and final profiles observed in the first 5 tests performed in this project.

In order to highlight the local perturbation caused by pressure transients, the last 10 images acquired prior to valve opening were averaged and subtracted from the following frames. The results show that within one second a local increase of grey value occurred in the first millimetre from the drying face (Figure 8). Nonetheless, some disturbance can be recognized already in the first frames, namely after a few hundredths of second from the valve opening. The final magnitude of grey value variations was within 10% of the total change induced by substantial drying at the heated face of the samples.

This preliminary analysis of raw data seems to corroborate the idea that the quick temperature drop following the sudden depressurization of an interface in hot moist concrete is caused by quick vaporization of a share of the water available in the pores.

CONCLUDING REMARKS

In this paper the quick thermal and hygral transients occurring upon depressurization of an internal interface in hot moist concrete have been addressed as a possible explanation of the explosive nature of spalling in fire. A special test setup was developed for taking fast Neutron Radiography images during this kind of transients. The first results allow drawing the following conclusions.

A sudden temperature drop is caused by depressurization of pores. A decrease by 30-90°C and a cooling rate of 20-120°C/s were observed in laboratory tests starting from relatively low initial pressure and temperature (up to 10barg at 200°C). Higher figures are expected in realistic fire conditions.

Fast NR images confirm that during these transients a relatively small share of the available moisture content was quickly vaporized within a thin layer facing the depressurized interface (about 1mm thickness). In this region a first decrease of neutron absorption could be recognized already after 0.03s.

It is worth mentioning that the sensible heat mobilized by cooling a unit volume of concrete by 100°C is three orders of magnitude higher than the expected elastic energy due to thermal strain [13]. This thermal energy would be sufficient to vaporize 6% of liquid water by weight within the same unit volume (see Figure 1). If such free moisture content were available, the work of adiabatic expansion of vaporized water coming from just a 0.05mm thick layer of concrete on both sides of an opening crack would be able to accelerate the fractured splinter to the maximum velocity documented in real fire tests. This tiny thickness would imply a very fast development of transients, as required by the highly dynamic instability involved by explosive spalling.

These early results and the connected considerations ask for a renewed attention to the role of the thermo-hygral transient on the possible ejection of the fractured concrete cover exposed to fire. The development of more realistic experiments and of numerical models adapted to the unusually short time scale at issue are the current tasks in this project.

REFERENCES

1. Khoury, G.A. and Anderberg, Y., "Concrete spalling review", Fire Safety Design, report submitted to the Swedish National Road Administration, Sweden, 60p., 2000.
2. Felicetti R., Lo Monte F. and Pimienta P., "A new test method to study the influence of pore pressure on fracture behaviour of concrete during heating", *Cement and Concrete Research*, **94**, 13-23, 2017.
3. Lo Monte F., Felicetti R. and Miah M.J., "The influence of pore pressure on fracture behaviour of Normal-Strength and High-Performance Concretes at high temperature", *Cement and Concrete Composites*, 11 p, 2019.
4. Bosnjak J., "Explosive spalling and permeability of high-performance concrete under fire - numerical and experimental investigations", PhD thesis, University of Stuttgart, 180p, 2014
5. Lo Monte F. and Felicetti R., "Heated slabs under biaxial compressive loading: a test set-up for the assessment of concrete sensitivity to spalling", *Materials and Structures*, **50** (192), 2017.

6. Millard A. and Pimienta P. (eds.), "Modelling of Concrete Behaviour at High Temperature", State-of-the-Art-Report of the RILEM TC 227-HPB, Springer, 127p., 2019.
7. Lo Monte F. Felicetti R., Meda A and Bortolussi A., "Assessment of concrete sensitivity to fire spalling: A multi-scale experimental approach", *Construction and Building Materials*, **212**, 476-485, 2019.
8. Lottman B.B.G., "The spalling mechanism of fire exposed concrete", PhD thesis, TU Delft, 404p., 2017.
9. Dorjan Dauti D., Tengattini A., Dal Pont S., Toropovs N., Briffaut M. and Weber B., "Analysis of moisture migration in concrete at high temperature through insitu neutron tomography", *Cement and Concrete Research*, **111**, 41-55, 2018.
10. Dauti D., Dal Pont S., Briffaut M. and Weber B., "Modeling of 3D moisture distribution in heated concrete from continuum towards mesoscopic approach", *Int. Journal of Heat and Mass Transfer*, 2019.
11. Felicetti R., "Assessment Methods of Fire Damages in Concrete Tunnel Linings", *Fire Technology*, **49** (2), 509-529, 2013.
12. Bazant Z.P. and Cusatis G., "Concrete creep at high temperature and its interaction with fracture: recent progress", Proc. CONCREEP 7, Nantes, France, Sept 12-14, 2005.
13. Gawin D., Pesavento F. and Schrefler B.A., "Towards prediction of the thermal spalling risk through a multi-phase porous media model of concrete", *Computer Methods in Applied Mechanics and Engineering*, **195** (41), 5707-5729, 2006.
14. Zeiml M., Lackner R. and Mang H.A., "Experimental insight into spalling behavior of concrete tunnel linings under fire loading", *Acta Geotechnica*, **3**, 295-308, 2008.
15. Bamonte P. and Felicetti R., "High temperature behaviour of concrete in tension", *Structural Engineering International*, **4**, 493-499, 2012.
16. Dal Pont S., Briffaut M.; Felicetti R.; Helfen L.; Lenoir N.; Tengattini A. and Yarmohammadian R., "Monitoring of fast moisture migration in heated concrete", Institut Laue-Langevin (ILL), doi:10.5291/ILL-DATA.UGA-70, 2019.

Correlation between concrete tensile strength and intrinsic permeability towards the evaluation of spalling susceptibility

Johann van der Merwe^{1,*}, Fangxia Lu² & Mario Fontana¹

¹ ETH Zürich, Switzerland

² Baertschi Partner AG, Switzerland

* Corresponding author

(vanderMerwe@ibk.baug.ethz.ch, Institute of Structural Engineering, HIL D37.2, Stefano-Franscini-Platz 5, 8093 Zürich)

ABSTRACT

Some proposed mechanisms for explosive spalling of concrete suggest that it is initiated when the concrete stress state at elevated temperature exceeds the tensile strength of concrete. In addition to the degree of saturation, the intrinsic permeability of concrete is known to govern the contribution of pore pressure to the development of this high-temperature stress state. A practical, adequate and appropriate estimation of intrinsic permeability and high-temperature tensile strength is therefore essential when evaluating the spalling susceptibility of concrete. Methods exist to test the permeability of concrete on site and it is hypothesised here that results from such tests can also be used to estimate concrete tensile strength at elevated temperature.

This paper presents results from an experimental investigation of concrete intrinsic permeability and residual splitting tensile strength. In addition to observations compiled from literature, results are used to develop ordinary least squares linear regression models for the estimation of residual splitting tensile strength. It is shown that an adequate and appropriate correlation exists between the initial intrinsic permeability of concrete and its residual splitting tensile strength. Moreover, this correlation is compared with boundary values for intrinsic permeability to the susceptibility of spalling in fire. A case study is presented to show how this correlation enables a more practical estimate of the concrete tensile strength associated with spalling susceptibility.

KEYWORDS: Explosive spalling, tensile strength, intrinsic permeability, linear regression, residual analysis.

INTRODUCTION

Based on the spalling mechanism proposed by Zhukov [1], a numerical spalling criterion model has previously been developed at ETH Zürich [2]. The model suggests that spalling of concrete is initiated when the combined effect of pore pressure, thermal stress and applied compressive stress exceeds the temperature dependent tensile strength of concrete, as shown in Eq. (1)

$$\sqrt{(1-2\cdot\nu)\cdot b^2\cdot\sigma_p^2 + \nu\cdot(b\cdot\sigma_p)\cdot(\sigma_l + 2\cdot\sigma_t)} \geq f_{t,\theta} \quad (1)$$

According to this coupled model, the degree of saturation and high-temperature development of intrinsic permeability governs the extent of pore pressure build-up. Although such a numerical model allows for a precise solution of the governing coupled differential equations, its accuracy depends on the adequate and appropriate estimation of these material properties. Although a non-destructive test method is available to measure the permeability of existing concrete [3], similar methods do not exist to determine its tensile strength.

Since many factors contribute to the intrinsic permeability of concrete, it is known that a causal relationship to compressive strength does not exist [4]. Nevertheless, various experimental observations have shown a correlation between these two parameters, with a denser concrete matrix resulting in an increased compressive strength and reduced intrinsic permeability (e.g. [5]). Concrete compressive and tensile strength are known to be closely related, with a log-transformed linear relationship typically proposed [6]. A viable correlation might therefore also exist between the intrinsic permeability of concrete and its tensile strength. This study investigates such a correlation to develop a means of estimating residual tensile strength development. This correlation is compared to a more classical residual tensile strength ratio development model and one based on a correlation with compressive strength. Finally, a strategy is proposed for the estimation of both initial intrinsic permeability and high-temperature tensile strength as input parameters for the spalling criterion model.

EXPERIMENTAL METHOD

Table 1 summarises six reference concrete mixes that were considered in this study, covering a range of normal strength concrete (NSC) and high-strength concrete (HSC).

Table 1 Reference concrete mixes.

Reference mix	M1	M2	M3	M4	M5	M6
Cement type (CEM I)	42.5 N	42.5 N	52.5 R	52.5 R	52.5 R	52.5 R
Cement [kg/m ³]	310	310	330	400	539	560
Silica fume ^(a) [kg/m ³]	0	0	0	32	44	59
Fine aggregate ^(b) [kg/m ³]	700	676	1260	596	464	933
Coarse aggregate ^(b) [kg/m ³]	1156	1202	678	1105	1105	638
Water [kg/m ³]	186	170	173	190	190	192
Superplasticizer ^(c) [kg/m ³]	0	0	4.40	2.20	3.95	6.82

a Microsilica by BASF

b Siliceous aggregate

c BASF MasterGlenium ACE 30

Concrete specimens were cured in a humidity controlled environment (20 °C and 95% relative humidity (RH)) for 28 days after casting, after which they were stored in a laboratory environment (20 °C ± 2 °C and 50% RH). Tests were performed between 90 and 110 days.

Ambient temperature results

Standard cylinders (150 mm diameter × 300 mm long) were used to determine the 90-day compressive strength, whilst splitting tensile strength tests were performed on smaller cylinders (75 mm diameter × 150 mm long). At the age of 90 days, standard concrete cubes (150 × 150 × 150 mm³) were predried at 105 °C to constant mass, after which they were allowed to cool down in the predrying oven to ambient room temperature. Intrinsic permeability was subsequently measured using a Torrent Permeability Tester. Inspection of experimental results (Figure 1) and associated histograms supports a log-transformed linear correlation between all three concrete material properties considered.

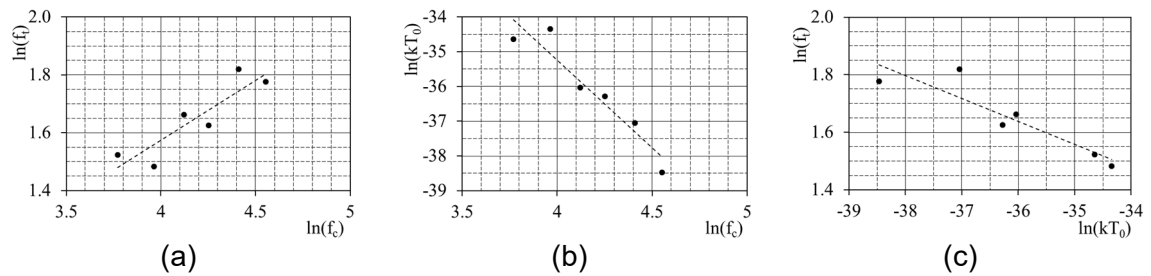


Figure 1 A log-transformed linear correlation seems to exist between mean log-transformed experimental observations of all three material properties considered.

Residual tensile strength results

The residual splitting tensile strength of each reference concrete mix was subsequently determined by testing three cylinders before and after heating to target temperatures of 100 °C, 200 °C, 300 °C, 400 °C and 700 °C. At the age of 90 days, cylinders were heated to target temperatures in an electrical oven at a maximum heating rate of 1.3 °C/min to avoid thermal stress damage [7]. Once the concrete surface material reached the target temperature, the oven temperature was maintained for one hour. Cooling was manually controlled to achieve a cooling rate of no greater than 1.3 °C/min. Splitting tensile strength tests were performed after the cylinders reached ambient room temperature.

Figure 2 compares mean results. With the exception of mix M6, a slight reduction in tensile strength is generally observed at 100 °C, followed by a slightly reduced rate of strength loss to 200 °C. The rate of strength loss after 200 °C generally seems more severe than before this temperature. Not all tensile strength was lost at 700 °C.

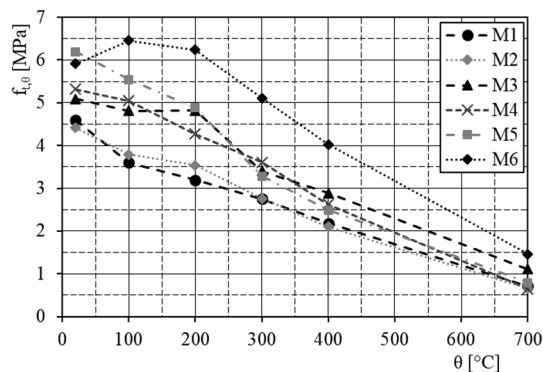


Figure 2 Average residual tensile strength of the six reference concrete mixes.

ESTIMATION OF CONCRETE INTRINSIC PERMEABILITY

Fib Model Code 2010 [8] proposes the log-transformed linear correlation shown in Eq. (2) between the gas permeability of oven-dried concrete and mean compressive strength. Figure 3 compares this model with own experimental results and observations reported in literature [9]. The model generally seems to underestimate own intrinsic permeability observations, resulting in a coefficient of determination of $R^2 = 0.608$. Results reported in literature show a much less adequate fit for concretes of lower strength ($R^2 < 1$). When, however, considering literature results for concretes of compressive strength greater than 35 MPa, a substantial improvement in adequacy of fit is obtained ($R^2 = 0.502$). Residual analysis showed that, although continuously underestimating own experimental observations, it does so at a constant rate. In contrast, the model fit is shown to violate the underlying assumptions of linear regression for literature results from lower concrete strengths.

$$k_0 = \frac{2 \times 10^{-9}}{f_c^4} \quad (2)$$

Although a more adequate and more appropriate fit was obtained from an alternative OLS linear regression model based on own results ($R^2 = 0.841$), the model increased response values by less than 5%. Moreover, its 95% confidence interval included the model proposed by Fib Model Code 2010 [8]. No improvement of appropriateness of fit to lower concrete strengths was obtained. As such, the alternative model cannot be seen as a substantial improvement.

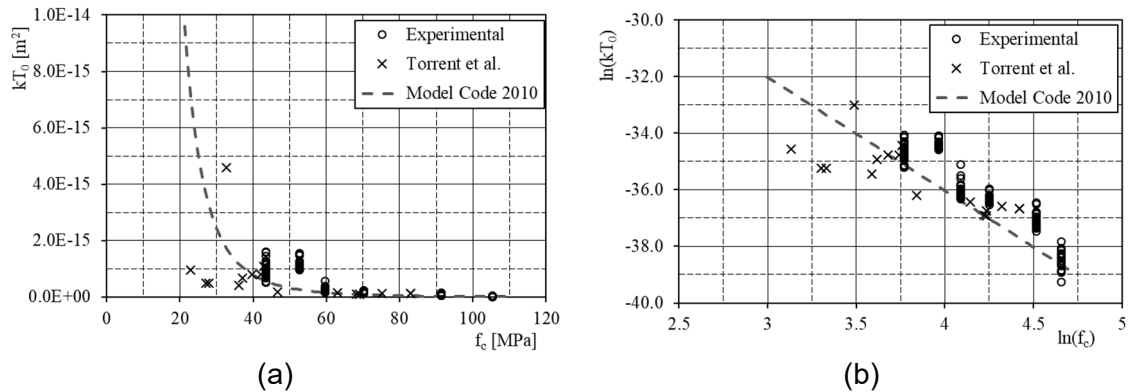


Figure 3 Own experimental results and observations by Torrent et al. [9] compared with the model proposed by Fib Model Code 2010 [8]. The comparison is shown both (a) without and (b) with log-transformation.

With no substantial difference between the two models, the Fib Model Code 2010 [8] correlation is deemed to provide a conservative estimate of intrinsic permeability on an element level, with the lower bound of the 95% confidence interval of the alternative model, shown in Eq. (3), providing a conservative localised estimate.

$$k_0 = \frac{2.877 \times 10^{-10}}{f_c^{4.013}} \quad (3)$$

INTRINSIC PERMEABILITY AS PREDICTOR VARIABLE OF TENSILE STRENGTH

The significance and relevance of concrete compressive strength and intrinsic permeability as predictor variables for tensile strength estimation was investigated by fitting the model shown in Eq. (4) to own experimental results in R [10].

$$\ln f_t \sim \beta_0 + \beta_1 \cdot \ln kT_0 + \beta_2 \cdot \ln f_c + \varepsilon \quad (4)$$

Output showed substantial collinearity between the two predictor variables. P-values of regression coefficients showed that compressive strength is approximately 30% less significant than intrinsic permeability. Calculating the relative relevance as the maximum effect that each predictor variable has on the response variable, compressive strength was found to be approximately 3% less relevant than intrinsic permeability.

An AIC stepwise backward variable selection technique [11] was subsequently performed from this full model in R [10]. This technique systematically evaluates each predictor variable and discards the one that is least significant (based on its p-value) until a model is obtained with only significant predictor variables. The model subsequently obtained was one with only intrinsic permeability as predictor variable, as shown in Eq. (5). Residual analysis suggests that the resulting model is appropriate.

$$f_t = \frac{0.293}{kT_0^{0.08}} \quad (5)$$

To compare the predictive capability of estimating concrete tensile strength with either compressive strength or intrinsic permeability as predictor variable, such models were considered when fitted to own experimental results. Five-fold cross-validation [12] was subsequently performed to calculate the mean squared prediction error (MSPE) of each model, with a lower MSPE suggesting greater predictive capability. Whilst the coefficient of determination of the two models differ by only 1.8%, the expected predictive capability of a model relying on concrete compressive strength (MSPE = 0.0144) is approximately 20% greater than that of a model relying on intrinsic permeability (MSPE = 0.0172). The two MSPE results are, however, considered small when compared to the range of log-transformed tensile strength results, and are therefore considered sufficiently similar. It follows that the correlation shown in Eq. (5) can be considered equally appropriate, and even more relevant, than a correlation between compressive and tensile strength.

ESTIMATION OF HIGH-TEMPERATURE CONCRETE TENSILE STRENGTH

Different mechanical and chemical processes influence concrete to a different extent as its temperature increases [13]. A piecewise linear regression model for the estimation of residual tensile strength was developed by considering knots at temperatures typically associated with the evaporation of free moisture, the release of water from the cement gel, differential thermal expansion between aggregates and the cement matrix, as well as decomposition of CSH.

Residual tensile strength ratio development

As reference model, the most adequate fit to residual tensile strength ratio development was determined from own results by minimising the sum of squared residuals up to a temperature of 800 °C. This resulted in a model with knots at 20 °C, 100 °C, 200 °C and 800 °C, with an associated coefficient of determination of $R^2 = 0.869$. The model is shown in Eq. (6) and is compared with own experimental results in Figure 4a. Residual analysis (Figure 5a) indicates that the model can be considered appropriate. The model also shows an adequate and appropriate fit to observations compiled from literature (Figure 4b and Figure 5b), with $R^2 = 0.893$.

$$\frac{f_{t,\theta}}{f_{t,20}} = \begin{cases} 1.04 - 1.87 \times 10^{-3} \cdot \theta & 20^\circ\text{C} \leq \theta < 100^\circ\text{C} \\ 0.85 & 100^\circ\text{C} \leq \theta < 200^\circ\text{C} \\ 1.13 - 1.42 \times 10^{-3} \cdot \theta & 200^\circ\text{C} \leq \theta \leq 800^\circ\text{C} \end{cases} \quad (6)$$

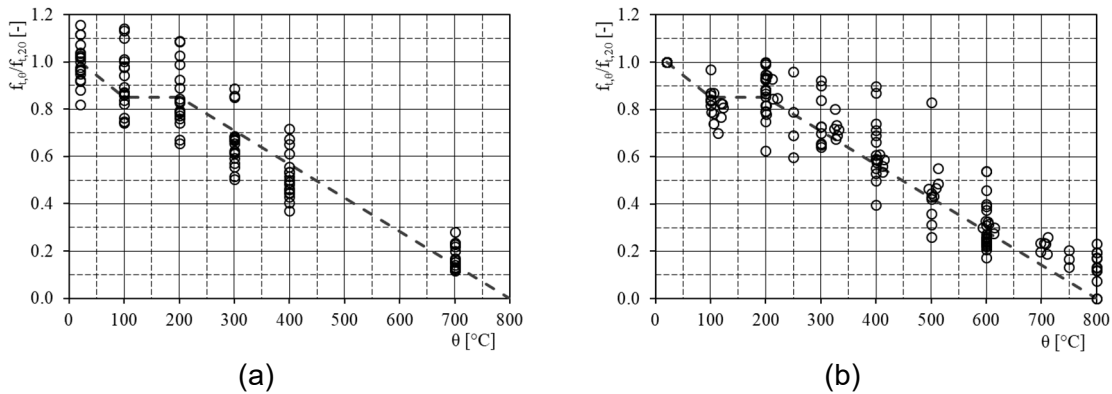


Figure 4 (a) Piecewise linear regression model fitted to own results of residual tensile strength ratio. (b) Model compared to observations compiled from literature.

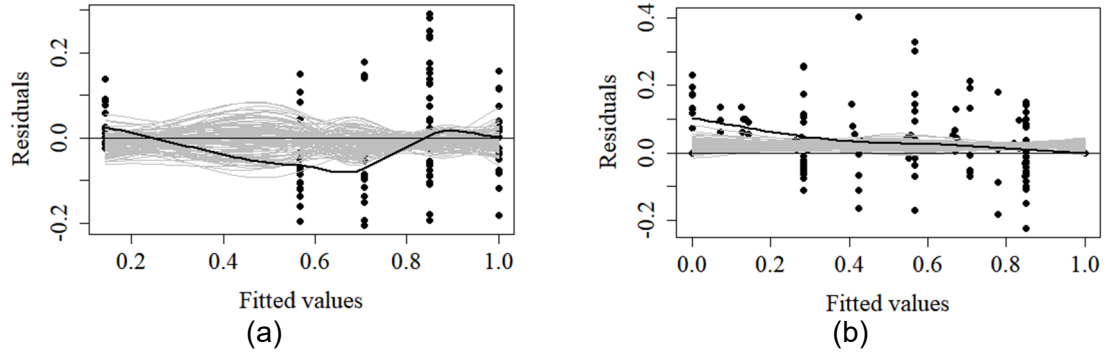


Figure 5 Tukey-Anscombe plot of residuals (with resampling plots) between the piecewise linear regression model and (a) own experimental results, as well as (b) observations compiled from literature. Local deviations of the data smoother fitted to residuals are within acceptable limits.

Alternative estimation of residual tensile strength

The relevance of considering ambient temperature compressive strength or intrinsic permeability as denominator for a residual tensile strength ratio was subsequently investigated. By considering the typical linear log-transformed relationship between ambient temperature compressive strength and tensile strength, the residual tensile strength ratio was rewritten to the form $f_{t,\theta}/(f_{c,20})^b$. An earlier investigation indicated an adequate and appropriate ambient temperature correlation between concrete tensile strength and compressive strength of the form $f_{t,20} \sim (f_{c,20})^{2/3}$. As such, a power of $b = 2/3$ was adopted. The same method of model optimisation was followed as for the reference model.

Although a highly adequate fit was obtained in this manner to both own experimental results ($R^2 = 0.828$) and results compiled from literature ($R^2 = 0.996$), residual analysis showed severe heteroscedasticity, suggesting that variable transformation should be considered. The most adequate and appropriate model was obtained by considering log-transformation of both the alternative residual tensile strength ratio and temperature, and by adding a knot at 600 °C. The model (Eq. (7) and shown in Figure 6) shows an adequate fit to own experimental results ($R^2 = 0.979$) as well as observations compiled from literature ($R^2 = 0.865$).

$$\ln\left(\frac{f_{t,\theta}}{f_{c,20}^{2/3}}\right) = \begin{cases} -0.896 - 0.084 \cdot \ln \theta & 20^\circ\text{C} \leq \theta < 100^\circ\text{C} \\ -1.286 & 100^\circ\text{C} \leq \theta < 200^\circ\text{C} \\ 3.322 - 0.870 \cdot \ln \theta & 200^\circ\text{C} \leq \theta < 600^\circ\text{C} \\ 15.828 - 2.825 \cdot \ln \theta & 600^\circ\text{C} \leq \theta \leq 800^\circ\text{C} \end{cases} \quad (7)$$

Residual analysis (Figure 7) suggests that the appropriateness of fit is improved. The range of residual variation compared to own results is sufficiently constant over the range of fitted values. However, at the smallest fitted value (which corresponds to a temperature of 700 °C) mainly negative residuals are obtained. This correspond to an overestimation of residual tensile strength at this temperature. Nevertheless, over the temperature range typically associated with explosive spalling, the smoother is deemed sufficiently close to a straight and zero line. The variation of residuals from literature observations is sufficiently constant over the range of fitted values. Although the data smoother fitted through residuals shows some local deviation, it shows no systematic structure. Moreover, compared to resampling plots, the local deviations do not seem substantial.

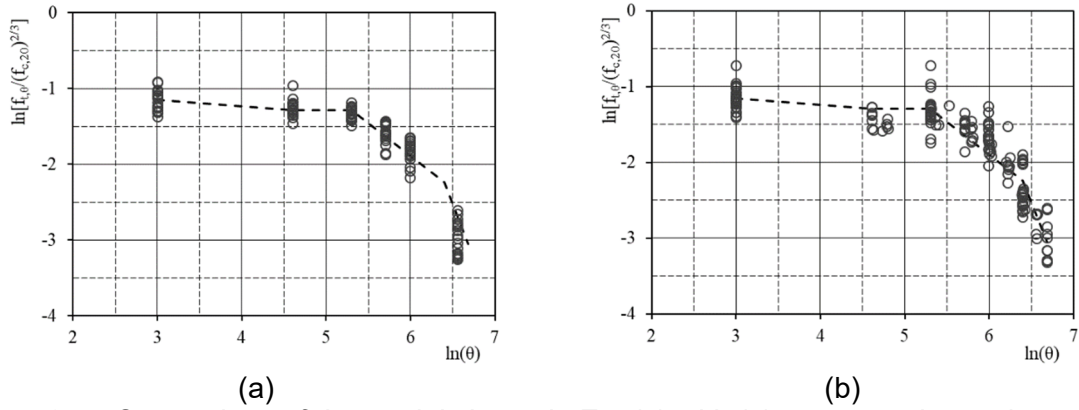


Figure 6 Comparison of the model shown in Eq. (7) with (a) own experimental results and (b) results compiled from literature.

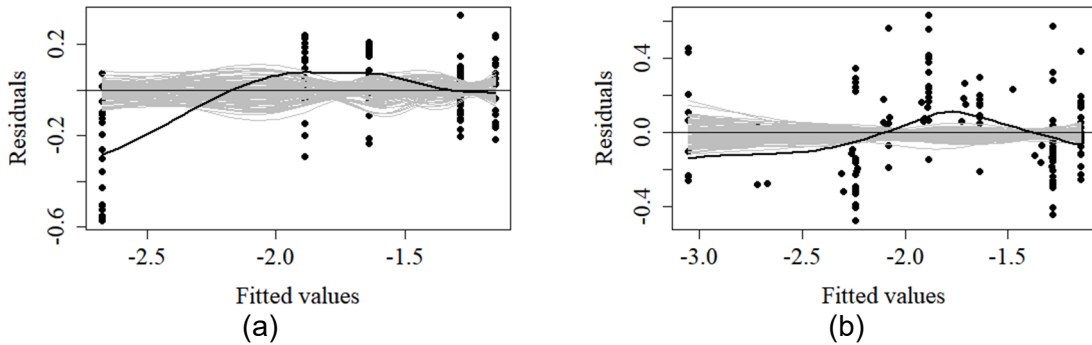


Figure 7 Tukey-Anscombe plot of residuals (with resampling plots) between the model shown in Eq. (7) and (a) own experimental results, and (b) results compiled from literature.

From Eq. (5) it follows that $f_{t,20} \sim kT_0^{-0.08}$. A subsequent alternative residual tensile strength product term of $f_{t,\theta} \cdot kT_0^{0.08}$ was considered. With no literature data available for a comparison of intrinsic permeability and residual tensile strength, a model was fitted and evaluated only considering own experimental results. Similar to the residual tensile strength ratio based on ambient temperature compressive strength, residual analysis suggested that a log-transformed piecewise linear regression model is more appropriate. In this case, the most adequate and appropriate model was obtained by considering a piecewise linear regression model with no knot at 600 °C and with log-transformation of the response variable. In this manner, the model shown in Eq. (8) was obtained, resulting in a coefficient of determination of $R^2 = 0.940$. Figure 8 shows the model against own experimental results and the resulting Tukey-Anscombe plot of residuals, which suggests that the model is appropriate.

$$\ln(f_{t,\theta} \cdot kT_0^{0.08}) = \begin{cases} -1.226 \times 10^{-3} \cdot \theta - 1.216 & 20^\circ\text{C} \leq \theta < 100^\circ\text{C} \\ -1.338 & 100^\circ\text{C} \leq \theta < 200^\circ\text{C} \\ -3.340 \times 10^{-3} \cdot \theta - 0.671 & 200^\circ\text{C} \leq \theta \leq 800^\circ\text{C} \end{cases} \quad (8)$$

Table 2 compares the piecewise linear regression models for the estimation of residual tensile strength development. Although the model relying on compressive strength as denominator shows a more adequate fit, the coefficient of determination is reduced by only 4% when considering intrinsic permeability instead. Moreover, residual plots suggest that a slightly more appropriate fit to data is obtained when considering intrinsic permeability as reference temperature parameter. Both are shown to agree well with a more classical residual tensile strength ratio model.

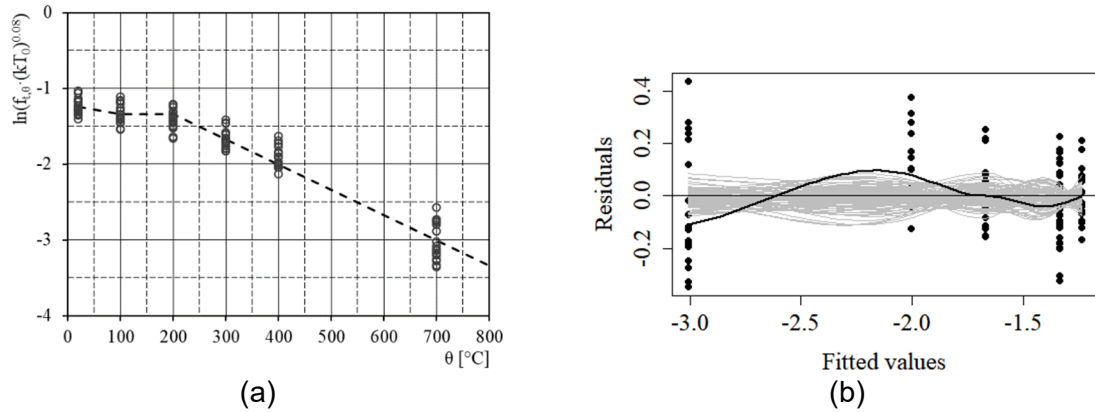


Figure 8 (a) Model shown in Eq. (8) compared with own experimental results. (b) Although the data smoother fitted to residuals on the Tukey-Anscombe plot shows some local deviations, these are deemed small in comparison with resampling plots. Moreover, no systematic structure is observed and the variation of residuals is considered sufficiently constant over the range of fitted values.

Table 2 Comparison of piecewise linear regression models for an estimation of residual tensile strength. A quantitative comparison is provided between the adequacy of fit (R^2) to own results and observations compiled from literature. In addition, a qualitative comparison of model appropriateness to own experimental results is provided.

Model	R^2 (own)	R^2 (literature)	Residual plot
$\frac{f_{t,\theta}}{f_{t,20}} \sim \theta$	0.869	0.893	Accept (Figure 5)
$\ln\left(\frac{f_{t,\theta}}{f_{c,20}^{2/3}}\right) \sim \ln \theta$	0.979	0.865	Accept (Figure 7)
$\ln(f_{t,\theta} \cdot kT_0^{0.08}) \sim \theta$	0.940	N/A	Good (Figure 8)

COMPARISON WITH BOUNDARY PERMEABILITY

A series of analyses were previously performed according to the spalling criterion model developed at ETH Zürich [2] to determine a boundary value of intrinsic permeability associated with spalling susceptibility. An unloaded, 150 mm thick, concrete slab with an initial tensile strength of 2.5 MPa was considered as case study. The correlation between concrete tensile strength and intrinsic permeability presented in this study allows for a more accurate estimation of concrete tensile strength. Moreover, it enables the estimation of an initial concrete tensile strength associated with the risk of spalling for a given slab geometry. The same case study slab geometry as before was considered here to illustrate the assessment.

A comparison of a material correlation between intrinsic permeability and concrete tensile strength, with that for boundary intrinsic permeability values determined according to the spalling criterion model, is shown in Figure 9. The development of pore pressure and thermal stress during fire exposure results in a triaxial stress state of compression-compression-tension. Following experimental observations by Wong and Song [14], a reduction factor of two was applied to the effective tensile strength resisting the stress state when spalling is triggered. The material correlation shows a rate of intrinsic permeability reduction with increased tensile strength that is approximately five times greater than the rate of boundary permeability reduction. The intersection between these two lines, i.e. where intrinsic permeability equals the boundary value, identifies the intrinsic permeability below which

there exists a spalling risk for the slab geometry considered. The lower sensitivity of boundary values of intrinsic permeability to concrete tensile strength highlights the substantial influence of intrinsic permeability to the susceptibility of concrete to spall during fire exposure.

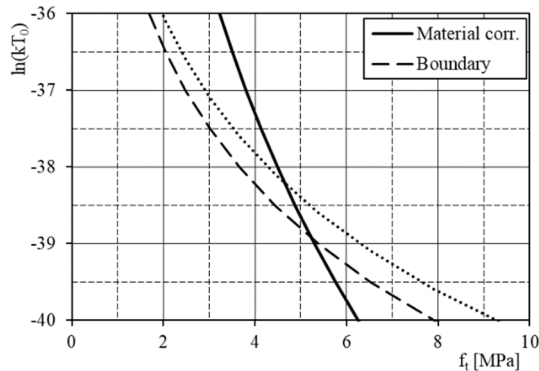


Figure 9 An estimation of intrinsic permeability from concrete tensile strength compared to the development of boundary values determined from a spalling criterion model [2]. The intersection indicates conditions corresponding to a risk of explosive spalling. Increased applied compressive stress can be expected to shift the boundary line in the direction of the dotted line, thereby increasing the intrinsic permeability and reducing the associated concrete tensile strength at which spalling can be expected.

CONCLUSIONS

Whilst the correlation between the compressive and tensile strength of concrete is widely accepted, this study has shown that a similarly suited correlation exists between the intrinsic permeability and tensile strength of concrete. This supports the hypothesis that the initial intrinsic permeability of concrete can be considered as predictor variable also for the tensile strength of concrete exposed to elevated temperature. Indeed, a highly adequate and appropriate residual tensile strength estimation is obtained when considering a development model of the product term $\ln(f_{t,\theta} \cdot kT_0^{0.08})$.

A practical means of estimating the intrinsic permeability and high-temperature tensile strength of concrete can improve the practical relevance of a spalling criterion model previously developed at ETH Zürich [2]. Where an initial approximation of spalling susceptibility of a proposed concrete element is required, Eq. (2) and Eq. (7) can be used to estimate the intrinsic permeability and tensile strength development from the expected mean compressive strength. For the evaluation of existing structural elements, permeability tests, together with an assessment of the concrete degree of saturation and Eq. (8) could provide these input parameters.

NOMENCLATURE

B	Biot's coefficient
f_c	Concrete compressive strength at ambient temperature [MPa]
f_t	Concrete tensile strength at ambient temperature [MPa]
$f_{t,\theta}$	Concrete tensile strength at temperature θ [MPa]
k_0 and kT_0	Intrinsic permeability [m^2]
R^2	Coefficient of determination
β_i	Regression coefficient of predictor variable i
ε	Random error term
θ	Temperature [$^{\circ}C$]
ν	Poisson ratio

σ_c	Compressive stress [MPa]
σ_p	Pore pressure [MPa]
σ_t	Thermal stress [MPa]

REFERENCES

1. Zhukov, V., "Reasons of explosive spalling of concrete by fire", *Beton I zhelezobeton (Concrete and Reinforcement Concrete)*, vol. 3, 1976.
2. Lu, F., "On the prediction of concrete spalling under fire", PhD thesis, ETH Zürich, Switzerland, 2015.
3. Torrent, R.J., "A two-chamber vacuum cell for measuring the coefficient of permeability to air of the concrete on site", *Materials and Structures*, vol. 25, pp. 358-365, 1992.
4. Abbas, A., Carcasses, M. and Ollivier, J.P., "The importance of gas permeability in addition to the compressive strength of concrete", *Magazine of Concrete Research*, vol. 52, no. 1, pp. 1-6, 2000.
5. Dhir, R.K., Hewlett, P.C. and Chan, Y.N., "Near surface characteristics of concrete: intrinsic permeability", *Magazine of Concrete Research*, vol. 41, no. 147, pp. 87-97, 1989.
6. Neville, A., *Properties of Concrete*, 5th edn, Pearson Education Limited, 2011.
7. RILEM Technical Committee, "Recommendations of RILEM TC 129-MHT: Test methods for mechanical properties of concrete at high temperatures. Part 4; Tensile strength for service and accident conditions", *Materials and Structures*, vol. 33, pp. 219-223, 2000.
8. International Federation for Structural Concrete, "Model Code 2010 – Final draft, Volume 1", *Bulletin 65, Fédération Internationale du Béton*, Lausanne, 2012.
9. Torrent, R., Moro, F. and Jornet, A., "Coping with the effect of moisture on air-permeability measurements", *Proceedings of the RILEM International Workshop on Performance-based Specification and Control of Concrete Durability*, pp. 489-498, Zagreb, Croatia, 2014.
10. R Core Team, "R: A Language and Environment for Statistical Computing", Foundation for Statistical Computing, Vienna, Austria. Available at: <http://www.R-project.org/>.
11. Faraway, J.J., "Practical regression and ANOVA using R", 2002.
12. James, G., Witten, D., Hastie, T. and Tibshirani, R., "An Introduction to Statistical Learning with Application in R", Springer, 2013.
13. Bažant, Z.P. and Kaplan, M.F., "Concrete at high temperatures: material properties and mathematical models", Longman, 1996.
14. Wang, H.L., Song, Y.P., "Behavior of mass concrete under biaxial compression-tension and triaxial compression-compression-tension.", *Materials and Structures*, vol. 42, pp. 241-249, 2009.

Assessing spalling risk in buildings: Considering spalling in probabilistic fire safety design

Ieuan Rickard^{1,*}, Ian Fu¹, Danny Hopkin¹ & Luke Bisby²

¹OFR Consultants, Edinburgh/Oxford, UK

²The University of Edinburgh, UK

* Corresponding author

(Ieuan.Rickard@OFRConsultants.com)

ABSTRACT

This paper describes research aimed at allowing consideration of fire compartment specific spalling risk within an open source analysis package, 'SfePrapy', developed by the authors. This software has been developed primarily to allow the efficient consideration of a range of credible design fires within a probabilistic structural fire safety engineering risk framework.

The rate of change of gas temperature in the design fires has been considered as a potentially appropriate driving parameter, since spalling has been experimentally observed to be exacerbated by high heating rates, rather than heating duration or even peak exposure temperature. Initial concepts for categorisation of compartment specific spalling risks are presented on this basis.

This paper is not – at this stage – intended to provide definitive design solutions, but rather to showcase spalling design methods currently being used in practice and to promote discussion regarding the integration of empirical spalling knowledge into fire safety design. It is not suggested that this method is suitable for design without further development, along with a more complete phenomenological understanding of spalling. However, the proposal demonstrates how consideration of spalling might be captured within a risk based framework, leading to risk categorisations and the ability to quantitatively establish circumstances in which further mitigation measures might be warranted.

KEYWORD: Design, Spalling Risk, PRA, Buildings.

INTRODUCTION

Heat induced explosive concrete spalling continues to pose a hazard to concrete structures when exposed to fire. As the research community continues to progress spalling knowledge, it is important to consider ways in which developments in understanding can be considered in design practice, and to ensure that the state-of-the-art spalling knowledge can be incorporated as early as possible. This paper touches on some of the more advanced design methods being used in practice and proposes novel ways in which spalling could be explicitly considered in future fire engineering design.

The open source Python program SfePrapy [1], developed by OFR consultants, has been used to model a range of 10,000 credible design fires, both 'parametric' [2] and 'travelling' [3]–[5], which could occur within a given fire compartment. The resulting (gas) temperature time curves can be compared against the traditional ISO 834 [6] cellulosic standard fire

curve. Whilst crude, comparison of the predicted rate of temperature increase relative to the ISO 834 standard fire curve may allow the potential spalling risk to be predicted from a thermal exposure perspective, rather than being based on the properties of the specific concrete mix and assumed to be exposed to the ISO 834 fire. This paper is not intended to propose a solution (yet) to be applied in design for spalling, but rather to initiate conversation about modern structural fire design of concrete structures, and means by which probabilistic spalling risk indicators might be considered.

CURRENT DESIGN FOR SPALLING

Despite the efforts of many researchers over the past century, heat induced explosive spalling of concrete remains poorly understood. Spalling is not typically considered directly in the design of modern concrete structures. Indirect consideration is widely assumed to be realized through concrete elements having been tested in standard fire testing furnaces when developing the largely prescriptive guidance now used to specify concrete cover depths to reinforcement and overall member dimensions required to achieve a given 'fire resistance' rating.

With the development of modern high strength and high performance concretes, the available guidance on concrete cover depths to achieve fire resistance ratings may not be sufficient; this guidance was not developed based on testing of modern concretes which are known to respond significantly differently to severe heating in a fire [7]. The tunnelling industry is an exception to this, as the spalling performance of candidate concrete mixes in tunnelling applications will often be tested for each specific tunnelling project [8]. This is due to a perception of increased spalling risk (and consequence) in tunnelling applications.

Current structural engineering design guidance is limited with respect to concrete spalling. Eurocode 2 [9] provides limited guidance as to when spalling should be explicitly considered by designers, and suggests possible measures to mitigate against heat-induced spalling. Notably, such guidance is only applicable to concrete tested according to the ISO 834 standard. The Eurocodes are currently being updated. However, spalling mitigation measures are likely to remain based on the performance of isolated concrete structural elements when tested to the ISO 834 standard fire curve within a fire testing furnace.

Developments in concrete mix design technology and the optimisation of concrete structural elements and building systems, while enhancing the performance and sustainability of concrete structures in many important respects, are likely to have detrimental effects on the propensity for heat-induced spalling. It is the authors' view that it is strictly necessary to consider the likelihood and consequences of heat-induced concrete spalling more explicitly and comprehensively in design.

PARAMETERS INFLUENCING SPALLING

While there are many parameters believed to influence spalling, the majority of these are material specific. For example, the addition of polypropylene (PP) fibres to the mix is widely accepted to reduce the spalling risk, and different aggregates are thought to result in different spalling propensities. These material specific parameters are covered in more detail in other publications [10], [11].

Key external parameters which influence heat induced spalling are the severity of the thermal exposure (and the resulting in-depth thermal gradients) and the externally applied load (i.e. compressive stress in the concrete). An increase in compressive stress in the sample has been observed by researchers, including the authors, to both increase the likelihood of spalling occurring and the severity of spalling should it occur [12].

The thermal exposure, particularly in terms of the heating rate and resulting thermal gradients within the concrete has been observed to influence spalling propensity, with increased spalling under increasing heating rates. Within the research community, researchers typically focus on achieving the same temperature-time history in experiments as imposed by standard fire curves (cellulosic, hydrocarbon, or tunnel fire exposure standard heating curves). Researchers have observed that the more severe thermal exposure of the various tunnel fire curves (such as the HCM curve used in France) lead to a greater likelihood and severity of spalling when compared to identical tests carried out – for example – to the less severe ISO 834 temperature time curve [13], [14]. It is also noteworthy that spalling typically (but not always) occurs in the early stages of heating and that the initial rate of heating (i.e. steep in-depth thermal gradients) is of concern.

STRUCTURAL FIRE ENGINEERING DESIGN

In fire engineering design, more representative design fires specific to the building in question are sometimes assessed. This may be in the form of Eurocode parametric fires, travelling fires, or other design fires based on local, zone or field models. The design fires may be considered deterministically or stochastically, and the accuracy of the predictions depends on both the appropriateness of the input values used and the fundamental physics accounted for (or otherwise) within the fire models themselves.

When design fires are considered, an appropriate level of fire resistance for the structure may be defined – for some structural forms – by calculating a ‘time equivalence’ value. Whilst providing a method for benchmarking the severity of the design fire to that of the ISO 834 standard fire curve, defining a time equivalence does not directly reflect the time history of temperature development which has been predicted, a parameter which is assumed, on the basis of the available literature, to be amongst the primary risk factors for spalling.

This paper is based on the premise that the predicted temperature developments in a compartment, and hence the in-depth thermal gradients within the concrete, whilst potentially crude and based on a range of assumptions, could be used to compare the relative spalling risk for different compartments (based on at least this criterion of known importance).

THE SFEPRAPY PYTHON PACKAGE

‘Sfeprapy’ is an open source probabilistic analysis package, written in python, which has been developed to allow probabilistic risk assessments (PRA) to be carried out efficiently and to suggest risk-appropriate fire resistance levels for buildings (notably, in terms of time equivalence [15] or direct computations of element fragility [16]). The framework for carrying out a probabilistic risk assessment of this nature is set out in PD 7974-7:2019[17], and SfePrapy has been created to enable a wide spectrum of credible design fires to be considered on a stochastic basis, using stochastic input variables (such as fire load density, opening factor, etc). Many of the limitations of prescriptive fire safety engineering design methods can be addressed (at least in part) by considering the building-specific fires which may occur, along with the desired reliability of the building in question.

Sfeprapy uses Monte Carlo simulation (with Latin Hypercube optimisation) of the credible fires for a compartment based on stochastic input parameters. Currently Sfeprapy uses so-called parametric and travelling fires, although development is ongoing, and functionality is continuously being added. SfePrapy has been used to propose risk-appropriate fire resistance ratings for the structure on a range of buildings both within the UK and internationally. Further information on the Sfeprapy process can be found in recent literature [18].

MODELLING SAMPLE COMPARTMENTS

Simple fire compartments have been modelled to allow demonstration of the capabilities of the SfePrapy analysis package as a tool to assess the fires which could occur within a given fire compartment. A normal design process would consider the different compartments within the building in question.

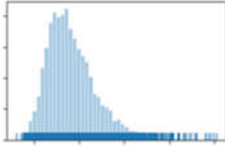
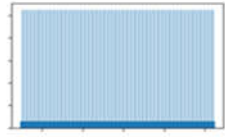
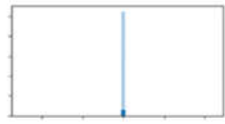
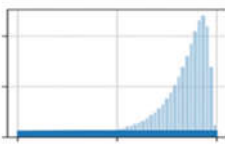
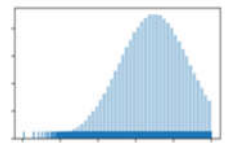
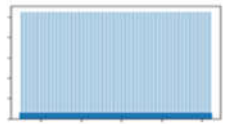
The compartments used for this paper have been chosen so that the predicted fire types will vary. Otherwise the geometries of these compartments are semi-arbitrary and used simply for the purposes of illustration within the current paper; these are given in Table 1.

Table 1: Compartment geometries used for each case

Model Case	A	B	C	D
Length (m)	15	15	10	15
Breadth (m)	15	15	10	100
Room Height (m)	3	3	3	3
Window Height (m)	2	2	2	2
Window Width (m)	10	10	10	10

In addition to the basic compartment geometries, a number parameters relating to the design fires must be assumed. These are summarised in Table 2. While the values selected represent those typical of either an office or a store room, they have primarily been selected to demonstrate the different fires which could occur in different occupancies. The SfePrapy analysis package currently selects which fire type will occur based on opening factors and fire spread rates. A parametric fire will be simulated if the fire spreads to cover the full compartment before burnout of fuel at source and if the opening factor is within the limits defined in BS EN 1991-1-2 for application of the parametric fire method (0.02 to 0.2 m^{0.5}). In all other cases a travelling fire is simulated.

Table 2: Input parameters used for the four cases considered

Input Metric	Distribution Type	Boundaries/ Ranges	Comments
Fire load density	 Gumbel	Cases A B D Mean: 420 MJ/m ² SD: 126 MJ/m ² Case C Mean: 1780 MJ/m ² SD: 1260 MJ/m ²	Data for offices from BS EN 1991-1-2 Data for storage of combustibles [19]
Combustion efficiency	 Linear	Linearly distributed between 0.8 and 1.0, inclusive.	Between values specified by BS EN 1991-1-2 and PD 6688-1-2 [20]
Heat release rate per unit area	 Constant	Cases A C D 250 kW/m ² Case B 500 kW/m ²	The inputs proposed are from BS EN 1991-1-2 [2]
Glazing failure ratio	 Inverse truncated lognormal	Mean: 0.2 SD: 0.2 Truncated between 0 and 1	Based on JCSS model code [21]
Near field temperature	 Normal	1 st percentile: 854°C 50 th percentile: 1050°C 100 th percentile: 1,200°C	Informed by Stern-Gottfried [3]
Travelling fire spread rate	 Linear	Minimum – 5 mm/s Median – 12 mm/s Maximum – 19 mm/s	Based on literature [4], [5]

RESULTS

For each of the geometrical cases modelled, 10,000 fires were simulated using Sfeprapy with the input parameters as previously defined in Table 2. For each model case and simulation a predicted temperature time history in the compartment was produced. Figure 1 shows a selection of 17 of these predictions for Case A in Table 1, along with the ISO 834 temperature time curve for comparison.

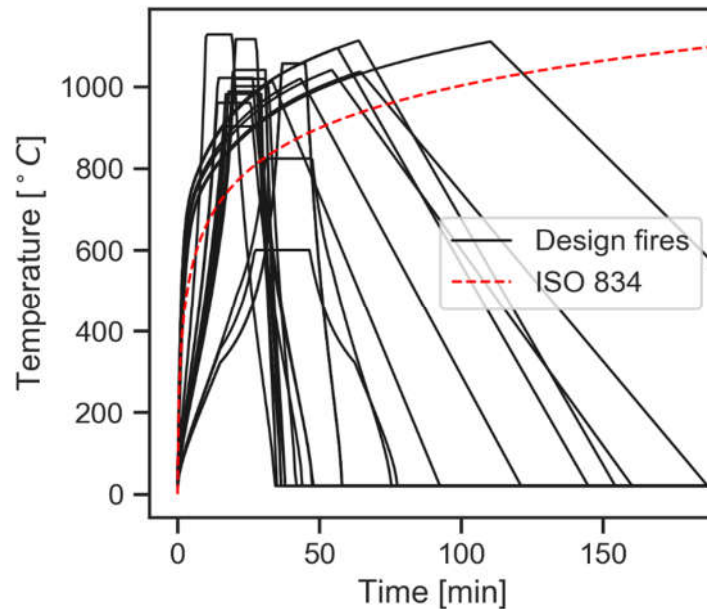


Figure 1: Sample of design fires generated for Case A compared with ISO 834 curve

The rate of gas temperature increase, \dot{T} , has been chosen as the parameter with which to attempt to assess compartment specific spalling risk. The rate of temperature increase is assessed over 60 second intervals during the heating phase of the respective design fires. The maximum \dot{T} value for each of the 10,000 design fire curves can then be compared.

As previously mentioned, spalling research is typically carried out by attempting to follow one of the prescribed standard temperature versus time fire curves, and the majority of design guidance which is currently available has been created based on testing to the ISO 834 curve.

In order to be able to link the design fires from SfePrapy with the ISO 834 curve, the maximum gradient of the ISO 834 curve has been computed in the same manner.

Comparison of the peak heating rates allows benchmarking of the heating rate against the ISO 834 curve. The histograms in Figure 2 show the distribution of maximum \dot{T} values for the 10,000 design fires simulated for each case. The maximum \dot{T} value for the ISO 834 curve is shown as a vertical line to allow comparison of the 'severity' (by this metric) of design fire heating rates as compared with that of the ISO 834 curve.

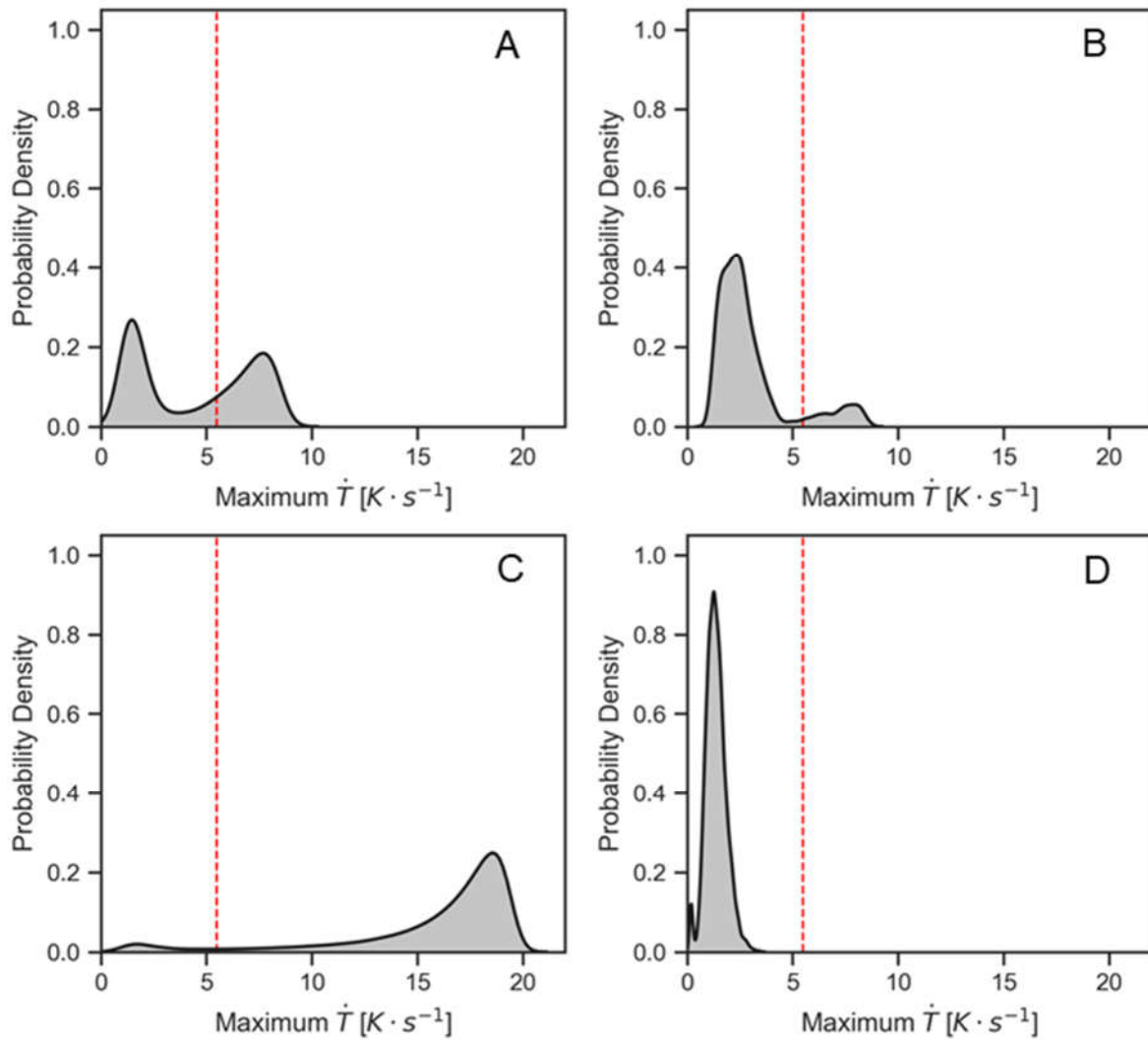


Figure 2: Probability density curves for the cases considered

As shown in Figure 2, different compartments can produce very different design fires. The distributions of maximum \dot{T} show that in the cases considered, Case C is likely to produce much more significant fires as regards spalling probability (in terms of \dot{T}) than the other cases. Cases A and B also pose higher probabilities for spalling than case D. The authors propose that this type of assessment of \dot{T} (or a similar parameter) is a reasonable first step in order to attempt to rationally assess the compartment specific spalling risk for different compartments within a probabilistic, performance-based framework.

It is noteworthy that the multi-modal ‘peaks’ that can be seen in the distributions are a result of Sfeprapy switching between Parametric and Travelling Fires. Case C predominantly results in parametric fires, while Case D is predominantly travelling fires. While these are the two types of design fires currently considered within the assessment framework, it is of course possible to introduce additional design fires into SfePrapy in the future.

ASSESSMENT CRITERIA

To illustrate the potential ways in which the data could be analysed, in the absence of a more definitive spalling criterion, it is proposed that a simple comparison of heating rates to that of the ISO 834 curve be used to categorise the relative spalling risk in each case based on the distribution of fires predicted

Table 3 shows an example of criteria which could be defined for design. It is important to note that this is a crude and qualitative comparison at this stage, intended as a demonstration of concept, and that further development and experimental work could be used to improve this categorisation. The authors are enthusiastic to discuss criteria to use for future development and work with the research community to arrive at a science-based consensus on these issues.

Table 3: Possible example categories for design criteria

Fire Compartment Specific Risk Classification	Criteria* (arbitrary at this stage)	Comments	Example design approach
Low [†]	99 % of design fires have a lower rate of temperature increase than the ISO 834 temperature time curve	With respect to the thermal exposure to a concrete element it would be assumed to be less severe than in furnace testing (with respect to heating rate with duration not considered)	Design as per Eurocode guidance.
Medium [†]	80% of design fires have a rate of temperature increase equal to, or lower than, that of the ISO 834 curve	This likelihood of the heating rate in a fire being more severe than in a furnace test is acceptable.	Design as per Eurocode guidance.
High [†]	Greater than 20% of the credible design fires have a predicted rate of temperature increase higher than that of the ISO 834 curve.	The percentage of fires with a more severe heating rate than the ISO 834 standard curve is sufficient that further measures should be considered.	Heating conditions more likely to cause spalling than in other compartments. Potential for spalling should be considered more seriously. The loading conditions and concrete mix design should be considered and appropriate measures taken to mitigate against spalling.

* The criteria for spalling should eventually be a function of the impact of failure, including reliability differentiation, i.e. the thresholds for a low rise building would be different to those for a high rise building. This should consider to what extent spalling undermines the reliability of an element and to what extent can we tolerate spalling depending upon the target failure probability.

† This example risk classification is concerned only with the fire compartment specific spalling risk and material specific risk factors are not dealt with here. It is the view of the authors that further assessment of material specific factors should also be carried out.

INCORPORATING RESULTS INTO DESIGN

The kind of assessment presented herein is not likely to be viable for every concrete structure but could form part of a PRA analysis or similar detailed assessment in some cases. When a thorough assessment of credible design fires for a building is carried out (possibly for other reasons), considering the design fires and highlighting areas of increased spalling risk in the manner proposed becomes viable. Less computationally demanding approaches to considering spalling in design will always be required by practitioners.

If the results of an assessment highlight increased spalling risk areas, there are a number of precautions which could be taken. Aside from taking steps to mitigate spalling by altering the concrete mix design, there is the potential to provide additional insulation to the structure in high risk areas, as is sometimes the approach taken in concrete tunnels [22].

PRA analysis can inform the fire resistance in a building on an area by area basis as a function of ignition frequency and resulting fire hazards. In some key areas of a building the fire resistance may be increased to address the fire hazard appropriately. It is proposed that a suitable approach, in the absence of a more comprehensive understanding of spalling, would be to consider increasing the fire resistance of key concrete elements using insulation boarding rather than by increasing the cover to reinforcement. This approach would be viable in isolated high-risk compartments. For example, in a refuse store with the potential for a high fuel load which might have a maximum \dot{T} value distribution similar to that of Case C above.

LIMITATIONS OF METHODOLOGY

It is important to note that this paper has been drafted to demonstrate a potential method of considering the changes in spalling risk between buildings/compartments. There are many assumptions involved in the determination of the design fires and the example criteria which have been used herein are merely suggestions to demonstrate what these criteria *could* be. Further work will be required to determine and demonstrate suitable criteria.

Much work has previously been carried out by the authors and others [23], [24] to develop an experimental method which controls the thermal boundary condition in spalling experiments in terms of incident heat flux to samples rather than gas temperatures. Gas temperatures in a furnace or compartment do not directly relate to the thermal exposure experienced by a sample/structural element; this has been documented in the literature [25]. The use of gas temperatures in this paper is a result of the current capabilities of the SfePrapy software package being developed and reflective of the status quo in structural fire safety design. While not ideal, the use of gas temperatures may be appropriate as an indicator of spalling risk. It may be possible in future to consider incident heat flux, in depth thermal gradient or similar. This is the authors' preferred approach to defining the thermal boundary conditions for testing and experimental work.

CONCLUSIONS

The capabilities of the SfePrapy analysis package for evaluating the full spectrum of credible fires has been demonstrated. An initial approach to defining a key parameter for compartment specific spalling risk has been proposed along with initial categories of spalling risk.

The authors would welcome collaboration from the research community and are happy to make all the data used in this paper available to anyone interested.

REFERENCES

- [1] Y. Fu and D. Hopkin, "sfepropy (Structural Fire Engineering - Probabilistic Reliability Analysis)," 2019. [Online]. Available: <https://github.com/fsepy/sfepropy>. [Accessed: 04-Feb-2019].
- [2] British Standards Institution, "BS EN 1991-1-2:2002 - Eurocode 1: Actions on structures - Part 1-2: General actions- Actions on structures exposed to fire." BSI Standards Institution, London, p. 62, 2002.
- [3] J. Stern-Gottfried and G. Rein, "Travelling fires for structural design-Part II: Design methodology," *Fire Saf. J.*, vol. 54, no. C, pp. 96–112, 2012.
- [4] D. J. Hopkin, "Testing the single zone structural fire design hypothesis," in *Interflam 2013 - 13th International Conference and Exhibition on Fire Science and Engineering*, 2013, p. 139.
- [5] E. Rackauskaite, C. Hamel, A. Law, and G. Rein, "Improved Formulation of Travelling Fires and Application to Concrete and Steel Structures," *Structures*, vol. 3, no. C, pp. 250–260, 2015.
- [6] International Organisation for standardization, "ISO 834-1 Fire-resistance tests - Elements of building construction - -Part 1: General Requirements," vol. 1999. International Organisation for standardization, 1999.
- [7] T. Hulin, C. Maluk, L. Bisby, K. Hodicky, J. W. Schmidt, and H. Stang, "Experimental Studies on the Fire Behaviour of High Performance Concrete Thin Plates," *Fire Technol.*, vol. 52, no. 3, pp. 683–705, 2016.
- [8] N. Taillefer, P. Carlotti, C. Larive, C. Lemerle, R. Avenel, and P. Pimienta, "Ten Years of Increased Hydrocarbon Temperature Curves in French Tunnels," *Fire Technol.*, vol. 49, no. 2, pp. 531–549, 2013.
- [9] British Standards Institution, "BS EN 1992-1-2 : 2004 Eurocode 2 : Design of concrete structures," BSI, London, 2005.
- [10] H. L. Malhotra, "CIRIA Technical Note 118 - Spalling of concrete in fires," Construction Industry Research and Information Association, London, 1984.
- [11] R. Jansson, "Fire Spalling of Concrete : Theoretical and Experimental Studies," KTH Royal Institute of Technology, 2013.
- [12] I. Rickard, L. Bisby, S. Deeny, and C. Maluk, "Predictive Testing for Heat Induced Spalling of Concrete Tunnels - The Influence of Mechanical Loading," in *Structures in Fire - Proceedings of the Ninth International Conference*, 2016, pp. 217–224.
- [13] I. Rickard, C. Maluk, L. Bisby, and S. Deeny, "Predictive testing for heat-induced spalling of concrete," in *IABSE Conference, Geneva 2015: Structural Engineering: Providing Solutions to Global Challenges - Report*, 2015.
- [14] R. Jansson and L. Boström, "Spalling of concrete exposed to fire (SP Report 2008:52)," Boras, Sweden, 2008.
- [15] C. Mayfield and D. Hopkin, *Design fires for use in fire safety engineering*. Bracknell: BRE Press, 2011.
- [16] D. Hopkin, R. Van Coile, and I. Fu, "Developing Fragility Curves & Estimating Failure Probabilities for Protected Steel Structural Elements Subject to Fully Developed Fires," in *SIF 2018- The 10th International Conference on Structures in Fire*, 2018, p. 8.
- [17] BSI, "PD 7974-7:2019 Application of fire safety engineering principles to the design of buildings. Part 7: Probabilistic risk assessment." BSI Standards Institution, London, p. 52, 2019.
- [18] I. Fu, I. Rickard, D. Hopkin, and M. Spearpoint, "Application of Python Programming Language in Structural Fire Engineering - Monte Carlo Simulation," in *Interflam 2019 - 15th International Fire Science and Engineering Conference*, 2019, pp. 1713–1723.
- [19] P. Thomas, "Design guide: Structure fire safety CIB W14 Workshop report," *Fire Saf. J.*, vol. 10, no. 2, pp. 77–137, 1986.
- [20] British Standards Institution, *PD 6688-1-2:2007 - Background paper to BS EN 1991-1-2*, no. 1. London: BSI, 2007.
- [21] Joint Committee on Structural Safety, *Probabilistic Model Code - Part 1 - Basis of Design*, 12th ed. JCSS, 2001.
- [22] T. G. van der W. van Gulik, A. J. Breunese, L. DeGraff, and P. Bourdon, "Design, assessment and application of passive fire protection in the Port of Miami tunnel according to NFPA 502," in *Seventh International Symposium on Tunnel Safety and Security*, 2016, pp. 147–157.
- [23] I. Rickard, C. Maluk, F. Robert, L. Bisby, S. Deeny, and C. Tessier, "Development of a Novel Small-Scale Test method to Investigate Heat-Induced Spalling of Concrete Tunnel Linings," in *4th International Workshop on Concrete Spalling Due to Fire Exposure*, 2015, pp. 195–205.
- [24] C. Maluk, L. Bisby, M. Krajcovic, and J. L. Torero, "A Heat-Transfer Rate Inducing System (H-TRIS) Test Method," *Fire Saf. J.*, pp. 1–13, 2016.
- [25] C. Maluk, G. Pietro Terrasi, L. Bisby, A. Stutz, and E. Hugi, "Fire resistance tests on thin CFRP prestressed concrete slabs," *Constr. Build. Mater.*, vol. 101, pp. 558–571, Dec. 2015.

Thermal and mechanical response of reinforced concrete slabs under natural and standard fires

Siyimane Mohaine^{1,*}, Nataša Kalaba¹, Jean-Marc Franssen², Luke Bisby³, Alastair Bartlett³, Jean-Christophe Mindeguia⁴, Robert McNamee⁵, Jochen Zehfuss⁶ & Fabienne Robert¹

¹CERIB, Epernon, France

²Liège University, Belgium

³School of Engineering, the University of Edinburgh, UK

⁴I2M, University of Bordeaux, France

⁵Brandskyddslaget, Sweden

⁶IBMB, Germany

* Corresponding author (s.mohaine@cerib.com)

ABSTRACT

This paper aims to investigate the structural behaviour of reinforced concrete slabs exposed to standard and natural fires, both experimentally and numerically. The emphasis herein is mainly on the evolution of deflections during and after fire exposure. As a part of the 'Épernon Fire Tests Programme', four large scale simply supported reinforced concrete slabs have been tested: one under standard fire exposure and three in compartments with different ventilation factors. The slabs were subjected to a superimposed mechanical load of 1.3 kN/m² representative of dwellings according to Eurocode 1. A fire load of 891 MJ/m² was used in the compartment fire tests. Temperatures inside the fire compartment and within the concrete slabs, as well as vertical deflections of the simply supported slabs were measured. The slabs can be classified as REI120 based on the standard furnace test (load bearing capacity was exceeded at 125 minutes). None of the failure criteria typically applied during standard furnace testing were reached during the natural fire tests. The maximum deflection value as well as the residual displacement of the slab after exposure varied with the severity of the fire. The finite element software SAFIR[®] was used to predict temperature gradients and displacements of the slabs during heating and decay phases. Thermal and mechanical properties of concrete and steel given in EN 1992-1-2 and the recommendations of the horizontal group fire project team used for the numerical simulations yielded predictions that compared well with experiments.

KEYWORD: Reinforced concrete, Thermomechanical behaviour, Standard fire, Natural fire, Numerical modelling

INTRODUCTION

Properly understanding and evaluating structures' and elements' behaviour under realistic fire scenarios is important when performance-based structural fire engineering approaches are deployed, where the structural behaviour and the loss of the load-bearing capacity have to be assessed during the heating as well as the decay phases of real fires. In those cases, the structure is often - if not always - requested to survive the total duration of the fire until complete burnout. During the cooling phase of a fire, the loadbearing capacity continues to drop off due to the delayed thermal wave inside the element, and, in the case of concrete structures, to the additional loss of material strength even when temperatures are decreasing. As such, this may eventually lead to failure during the cooling phase, depending on the severity of the fire as well as on the geometry of the tested concrete element [1]. To the knowledge of the authors, few studies have focused on the investigation of the behaviour of concrete structures subjected to standard fire followed by a decay phase, and even fewer in the case of a natural fire (i.e. a compartment fire with a real fire load, with the main objective being the study of the residual properties of the element, or, less frequently, to study the failure during or after the cooling

phase of the tested element. These studies were mainly conducted on loaded or non-loaded reinforced concrete beams experimentally [2] [3] [4] [5] and numerically [6] [7] [8] [9]; on column elements experimentally [10] [11] [12] and numerically [1] [13] [14]; a more recent work was reported on continuous reinforced concrete floor slabs under compartment fires [15]. The key parameters affecting the behaviour of isolated concrete members are generally found to be maximum temperature in the rebars, the extent to which spalling occurs, concrete properties, the superimposed load level, and the fire duration. The displacement during the decay phase of the tested element, as well as its residual deformations, also depend on the decay rate. This paper presents a comparison of the thermal and mechanical response of concrete slabs under both standard (furnace) and natural (compartment) fire exposures, as well as attempts to predict the displacements of the slabs during heating and decay phases using analysis software (SAFIR®) [16]. This study is part of a multi-partner project called the 'Épernon Fire Tests Programme' which aims to investigate the response of structures made of both combustible (i.e. timber) and non-combustible (i.e. reinforced concrete) materials under standard furnace and natural fire conditions [17] [18] [19].

EXPERIMENTAL SETUP

Test facility

Three natural (compartment) fire tests as well as a standard fire resistance (i.e. furnace) test were performed on one-way spanning, simply supported loadbearing reinforced concrete slabs. The compartments for the natural fire tests had internal dimensions (6 000 x 4 000 mm² in plan, and 2 520 mm in height) similar to the internal dimensions of the fire testing furnace used. Each natural fire test had a different configuration of openings in one of the long faces of the compartment. The opening geometries are given in Table 1, along with the corresponding opening factors calculated according to EN 1991-1-2 Annex A, using the formula $\frac{A_o\sqrt{H_o}}{A_t}$ where A_o and H_o are the area and high of the openings and A_t is the total area of the boundary surfaces (including floor and ceiling) [20]. These specific opening factors were chosen so as to induce a fuel-controlled fire (Scenario 1) as well as ventilation-controlled fires (scenarios 2 and 3). The opening geometries are illustrated in Figure 1 along with the corresponding opening factor.

Six wood cribs with 12 layers of five spruce wood sticks (dimensions of the sticks: 0.09 x 0.09 x 1 m³) each were used for the fire load inside the compartment. The total mass of the cribs was 1 191 kg, based on a mean timber density of 408.4 kg/m³ (including an average moisture content of 11.4 %). Three litres of heptane per crib were used for ignition. Assuming a heat of combustion of 17.5 MJ/kg [20] for wood and 45 MJ/kg for heptane [21] (and a heptane density of 680 kg/m³), the total achieved fire load density related to the total floor surface area was thus 891 MJ/m². Boundaries of the compartments were made from solid aerated concrete blocks of thickness 300 mm.

Table 1. Summary of opening geometries in the compartment fire tests

Scenario #	Number of openings	Height of opening [m]	Width of opening [m]	Opening factor [m ^{1/2}]
1	2	2	2.5	0.144
2	3	1.2	1.25	0.050
3	1	2	1.1	0.032

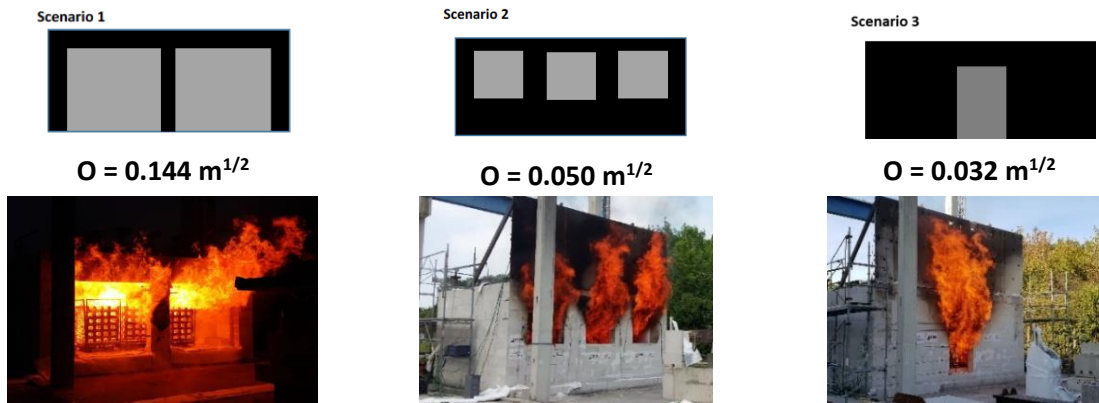


Figure 1. Illustration of compartment configurations and corresponding opening factor

Tested elements

The tested elements were 5 900 x 3 900 mm² in plan and 180 mm thick. They were cast in situ with a welded reinforcing mesh (ST50C, 5.03 cm²/m, Ø8 mm every 10 cm in both directions), a clear concrete cover of 20 mm (axis distance of 24 mm), and C35/45 concrete with calcareous aggregates. Details of the concrete mix are given in Table 2. Concrete mix used for the study. Table 3 shows measured moisture content at the day of the test and compressive strengths (measured at each maturity date on three 150 x 150 x 150 mm³ cubic specimens) of concretes for each experiment.

Table 2. Concrete mix used for the study

Components		Quantity (kg/m ³)
Aggregates	4/10 (calcareous)	695
	0/4 (silico-calcareous)	965
Cement (CEM I 52.5 N)		350
Water		185
Admixture		1 % of cement mass

Table 3. Compressive strength and water content of concrete used for the experiments

	Age at testing	Compressive strength ± standard deviation		Moisture content by mass (at the day of the test)
		28 days	Test day	
Standard test	90 days	44 ± 3 MPa	46 ± 5 MPa	5.4 % (± 0.2 %)
Natural fire test: Scenario 1	98 days	50 ± 1 MPa	49 ± 2 MPa	5.8 % (± 0.4 %)
Natural fire test: Scenario 2	194 days	42 ± 1 MPa	42 ± 1 MPa	5.0 % at the surface 5.3 % in the core (± 0.1 %)
Natural fire test: Scenario 3	391 days	47 ± 2 MPa	42 ± 2 MPa	3.6 % at the surface 4.2 % in the core (± 0.1 %)

The slabs were installed over the horizontal opening of the fire compartment or the furnace so that a span of 5600 mm was obtained between simple supports. The total surface exposed to fire was 5 300 x 3 900 mm². The slabs were subjected to an imposed load composed of five dead weights, as illustrated in Figure 2, with a total load of 29.5 kN, i.e. an average load of 1.3

kN/m², representing a design load for dwellings in the fire situation with an accidental load combination of (G + 0.5 Q) [10]. The total applied load consisted of:

- The slab covering of 0.10 kN/m²;
- Partitions of 0.5 kN/m²; and
- An occupation load (for dwellings) of 1.5 kN/m².



Figure 2. Mechanical load used for standard fire tests (left) and compartment fire tests (right)

Further illustrations and schemes of the test setups and the specimens can be found in the corresponding test reports in [22].

Instrumentation

Temperatures inside the compartment or the furnace were recorded using 15 plate thermometers located within the gas phase below the tested elements. Temperatures within the concrete were monitored using embedded Type K thermocouples at five different locations (in plan, referenced G1 to G5 as illustrated in Figure 4 and at various depths (0, 10, 20, 30, 40 and 60 mm from the fire-exposed face of the slabs as illustrated in Figure 3), as well as on the internal steel reinforcement as illustrated in Figure 3. Vertical deflections were measured using sensors at mid-span and mid-width of the slabs, as well as at mid-width at each end of the slabs. Figure 4 shows the positions of the deflection sensors (D1 to D4).

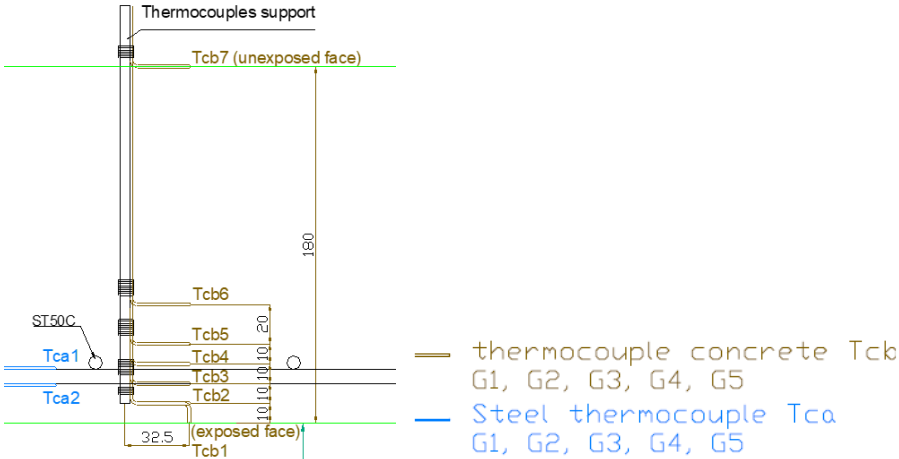


Figure 3. Cross-section of the concrete slab and thermocouples' position over the slab's thickness

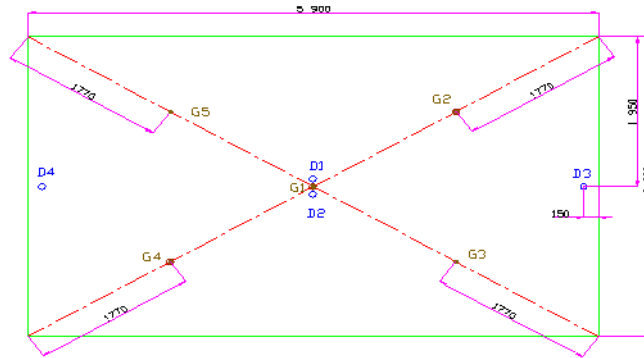


Figure 4. Top view of the slab with positions of deflection sensors (D1 to D4) and positions of thermocouples (G1 to G5)

EXPERIMENTAL RESULTS

Compartment temperatures

Figure 5 shows the mean (continuous lines) and maximum and minimum (dotted lines) temperatures measured by plate during all four experiments. Compared to the standard curve, scenarios 1 and 2 had higher heating rates, while the mean temperature registered for Scenario 3 showed a similar heating rate during the first 20 minutes. For the natural fires, the total duration of heating and the maximum temperature (around 1200 °C for scenarios 2 and 3) correlate with the ventilation factors as should be expected; i.e. the lower the opening factor, the less available oxygen and the longer the burning duration within the compartment.

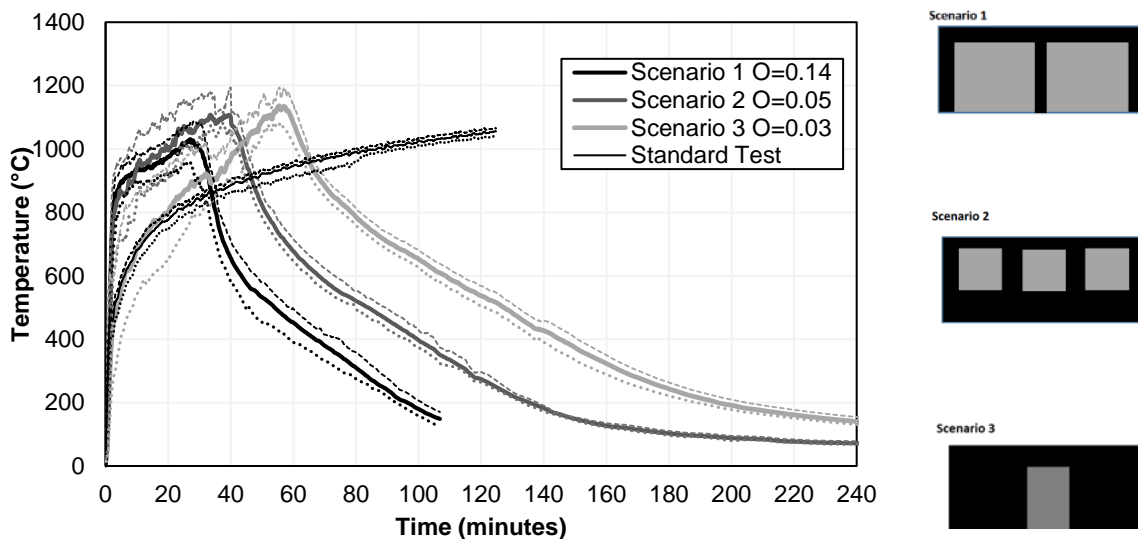


Figure 5. Average plate thermometers measurements inside the compartment for three scenarios (with dotted lines representing minimum and maximum values)

Mid-span deflection

Mid-span deflections of the four slabs are shown in Figure 6¹. The presented measurements are the averages of the two sensors installed at mid-span (except for Scenario 1 for which one sensor gave unreliable values).

All three slabs subjected to compartment fires deflected following a similar overall pattern. In the first stage, the deflections increased due primarily to the establishment of thermal gradients

¹ For Scenario 1, data acquisition has been disrupted at 120 minutes. For Scenario 3, data acquisition has been disrupted from 170 minutes to 398 minutes. What is shown beyond 170 minutes in the graph is an interpolation between deflection measurements at 170 and 398 minutes, respectively.

(as well as minor losses of stiffness and strength). Shortly after the start of the decay phase within the compartment (with a delay due to the continued progression of a ‘thermal wave’ through the concrete), and as soon as the rebars began to cool and thermally contract (and partially recover their strength and stiffness), the deflection trend reversed, and deflection recovery was observed. The more rapid the heating rate inside the compartment, the more rapid the initial deflection; the highest deflection rate was observed for Scenario 1, followed closely by scenarios 2 and 3 in that order. However, the highest maximum mid-span displacement was observed for Scenario 3 (approximately 260 mm in this case) for which the pseudo-steady burning phase was the longest and the temperature in rebars resultingly the highest (approximately $500\text{ }^{\circ}\text{C} \leq T \leq 600\text{ }^{\circ}\text{C}$). During the decay phase, the evolution of the displacements was similar for all three compartment tests. When comparing the stabilized deflection value for Scenarios 2 and 3 after a long period of decay (approximately 8 hours after ignition), the deflection of the slab under Scenario 2 was approximately 78 mm against 102 mm under Scenario 3. This is directly linked to the peak temperature reached in the reinforcement, and the resulting irrecoverable (creep) strains that are imposed due to reinforcement plasticity. It is noteworthy that the peak deflection occurs, in all cases, about 10-20 minutes *after* peak compartment temperatures are experienced.

Compared to the standard furnace test, the rate of initial deflection for the three natural fire tests during the heating was higher in all cases except for scenario 3, for which the deflection rate was similar to the one under standard fire during the first 20 minutes (given the similar heating rates for those two cases during the first 20 minutes). Continuous heating in the furnace led to structural collapse of the slab at 125 min, corresponding to the time when the limiting deflection (503 mm) and deflection rate (22 mm/min) according to EN 1363-1 were reached.

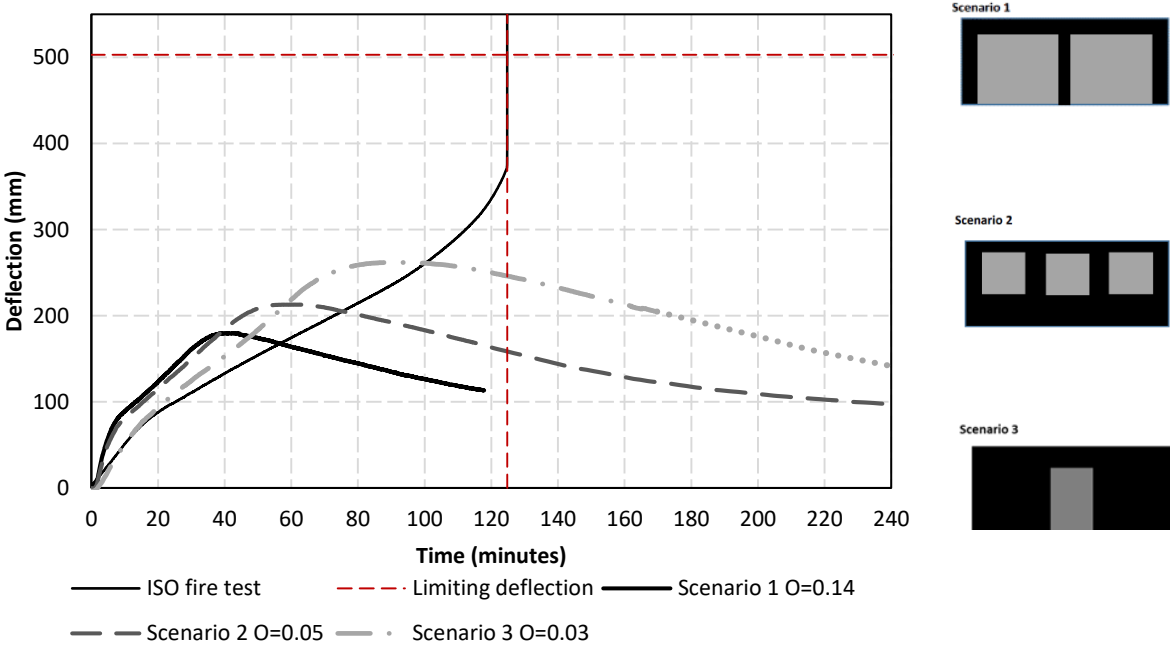


Figure 6. Mid-span deflection for the three concrete slabs under natural fires

Occurrence of spalling

Figure 7 shows the exposed face of the slabs during the test for the standard test (a) and for the natural fire test Scenario 1 (b).



(a) – Standard Fire Test



(b) – Natural Fire Test Scenario 1

Figure 7. Exposed face of concrete slabs during (a) - standard test and (b)- natural fire test, Scenario 1

During the standard furnace test minor spalling was observed at two different locations during the 12th and 14th minute. More intense spalling was observed during natural fire Scenario 1 (from the 3rd minute to the 8th minute). However, this spalling remained essentially superficial (around 1 cm depth except at one location where reinforcement was locally exposed) and more localised close to the supports. It is noteworthy that no spalling was observed in scenarios 2 and 3, particularly given that the heating rate was quite similar (and more severe) for Scenarios 1 and 2. Due to the longer storage duration for scenarios 2 (6 months) and 3 (12 months), the moisture contents at the surfaces of these slab were also lower; this may also have played a role in reducing the propensity for concrete cover spalling.

MODELLING

Description of the models

The slabs were modelled as simply supported beams.

Sequentially coupled thermo-mechanical analysis was performed using the finite element software SAFIR[®] developed at The University of Liege [16]. Two sub-models were used: (1) a model for thermal analysis and (2) a model for mechanical response. The temperatures in the slabs obtained from the thermal analysis acted as thermal loads in the structural models for subsequent mechanical analysis. The primary objective of the mechanical analysis was to compare the predicted displacements of the slabs with experimentally measured values.

Thermal analysis

Linear conductive triangular elements, with nodal temperature as the only active degree of freedom, were used to discretize the concrete and reinforcing steel (

Figure 8). At the boundaries of the heat exposed surfaces, linear convection with convective coefficient of 35 W/m²K was assumed, while for the unexposed surfaces the convective

coefficient was set to $4 \text{ W/m}^2\text{K}$, accounting for the radiation. Radiation with $\varepsilon = 0.7$ was assumed for all the heat-exposed concrete surfaces (in this case, the slab was heated from the bottom) [20].

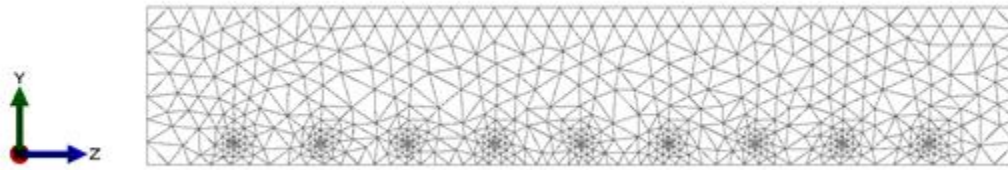


Figure 8. Discretized section used for the thermomechanical analysis (SAFIR®)

Evolution of thermal properties of concrete and steel with temperature were assumed following Eurocode 2 [23] except for the evolution of thermal conductivity of concrete prescriptions of the horizontal fire group project team [24] were used. The density of concrete was taken as 2400 kg/m^3 . Thermal properties of steel were taken as reversible during decay/cooling, whereas the thermal properties of concrete during decay/cooling were set to those at maximum experienced temperature [25].

The temperature field in the section represented the input data for the mechanical analyses in which the temperature-dependent material strength and stiffness were continuously evaluated.

In the subsequent mechanical analyses, the structure was discretized into 2D beam finite elements. A uniformly distributed load was applied, equivalent to the load present on the slabs during the tests. The materials' uniaxial constitutive models were based on EN 1992-1-2 [23]. For the concrete constitutive law, the definition of the aggregate type, the compressive strength and the tensile strength at room temperature are required. Given that the slab was exposed to a natural fire, with a cooling phase, the choice was to use the model that treats the transient creep explicitly – the 'ETC Model'. This explicit formulation is a refinement of the EN 1992-1-2 model that also accounts for the non-reversibility of transient creep strain when the stress and/or the temperature are decreasing [26]. During cooling, concrete does not completely recover its strength and an additional reduction of 10 % of the concrete compressive strength has been assumed with respect to the value at maximum temperature, in accordance with the Eurocode horizontal fire group project team prescriptions [24].

The steel models were based on Eurocode 2. Required parameters for the constitutive law definition were the Young's modulus and the yield strength. The steel mechanical properties were considered fully recoverable upon cooling.

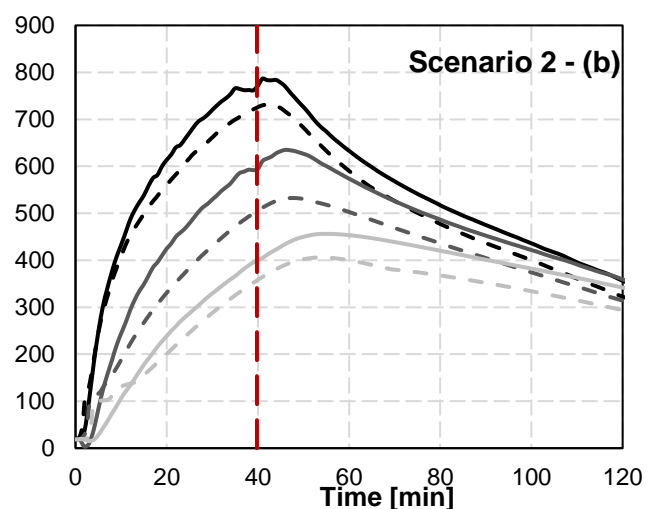
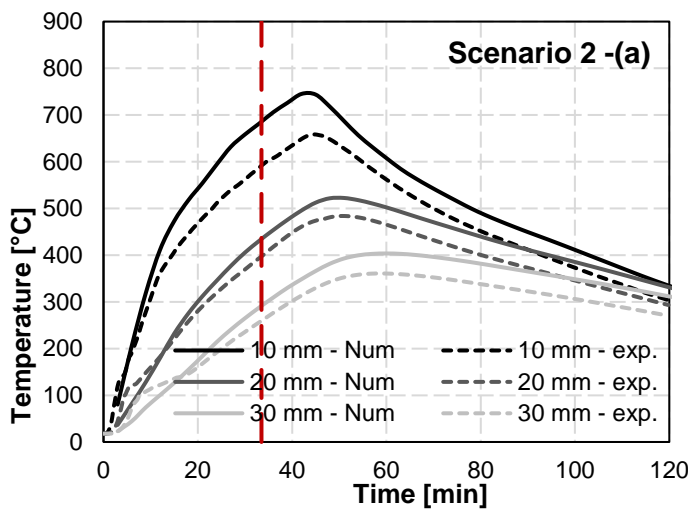
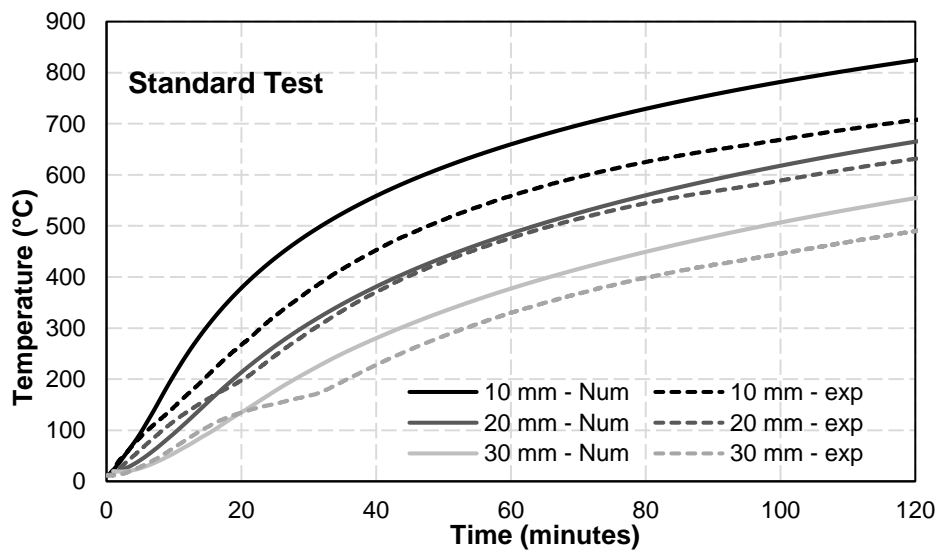
Thermal transfer: Experimental and predicted

Two candidate compartment temperature inputs were used in predictive modelling; for each compartment scenario computation was performed using the *mean* compartment temperature as well as the *maximum* compartment temperature (Figure 5). The maximum temperature was used for comparison as it was believed to be more representative of the local temperature at mid span of the slab where the plastic deformations were likely to have been concentrated. For the maximum compartment temperature curve, readings at position G1 (see Figure 4) were taken.

Temperatures obtained numerically at 10 mm, 20 mm and 30 mm from the exposed surface of the concrete were compared with the thermocouple readings at the same locations. Since two candidate compartment temperatures were used as inputs, the two predicted temperatures within the slab were compared with the *mean* and *maximum* experimental measurements at

10 mm, 20 mm and 30 mm from the exposed surface. This comparison was not performed for Scenario 1 due to lack of data for some of the heating phase.

Experimental and predicted temperatures within the slabs are shown in Figure 9. The measured and predicted temperature evolutions show similar patterns with the predicted temperature during both heating and decay phases for both mean and maximum compartment temperatures as inputs. The evolution of the temperatures within the slabs in time again shows that there was a delay in the temperature rise compared to compartment temperatures, and that the maximum temperature within the slab is reached in the decay phase of exposure. For each of the natural fire tests, the time when the highest temperature was reached in the compartment during heating for each of the heating curves used as inputs (i.e. the *mean* and *maximum* compartment temperatures respectively) is illustrated by a vertical bar in Figure 6.



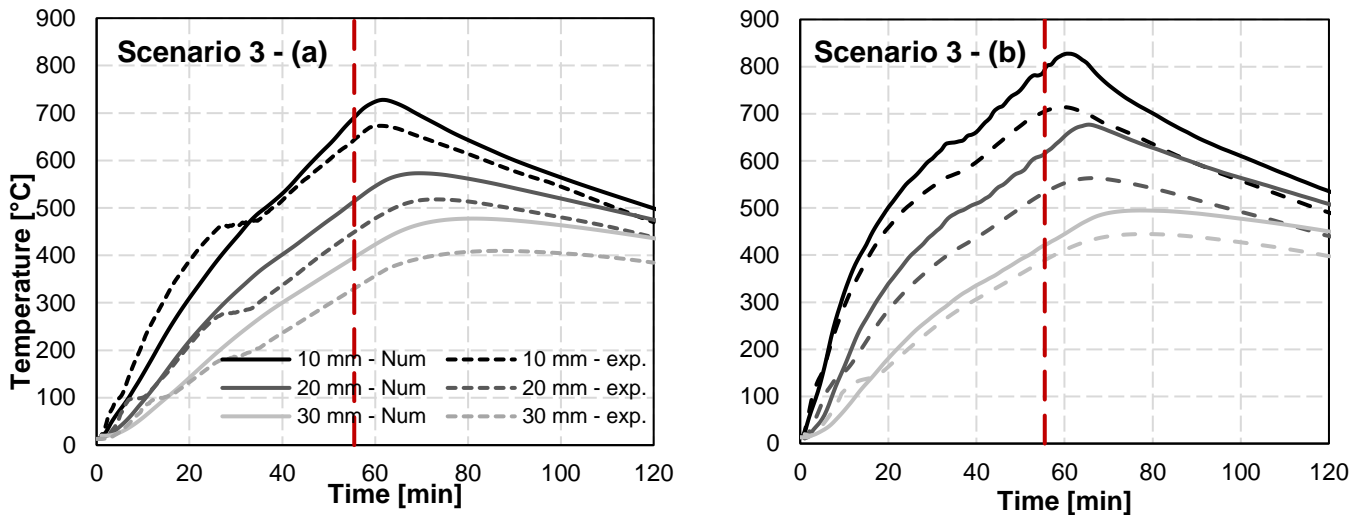


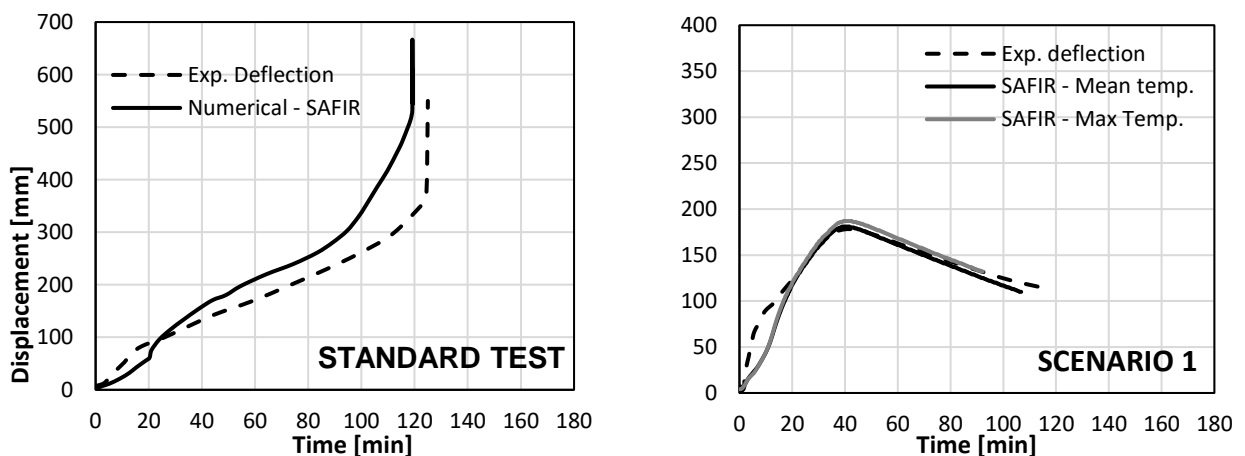
Figure 9 – Experimental and numerical temperatures evolution within the concrete slabs (at 10, 20 and 30 mm from the exposed face) using (a) – *mean* temperatures and (b) – *maximum* temperatures for compartment fire tests. *Continuous lines*: numerical results; *dotted lines*: experimental results

Predicted deflections

Evolution of the deflection in time for the four slabs is shown in Figure 10. For the standard furnace test, the predicted deflection is conservative and leads to failure 5 minutes prior to that observed in the test. In the case of natural fires, the predicted deflections are also in a good accordance with experimental data. The best fit was observed for scenario 1. For scenarios 2 and 3, a slight overestimation of the maximum deflection value is observed when the *maximum* compartment temperature was used as input for modelling.

A range in the deflection prediction by again using *mean* compartment temperature and *maximum* compartment temperature curves as thermal inputs is given for all the three slabs subjected to compartment fires. For Scenario 1, only a slight difference is observed between predictions using *mean* and *maximum* compartment temperatures. This leads to similar deflection values. For scenarios 2 and 3, the *maximum* compartment temperatures during heating are consistently higher than the *mean* values, thus leading to significantly larger predicted deflections when the *maximum* compartment temperature curve is used.

Residual deflections are around 70 % and 50 % lower than the peak values for scenario 2 and scenario 3, respectively. Less deflection recovery for scenario 3 can be explained by a more severe fire scenario and consequently with higher rebar (and to less extent concrete) temperatures.



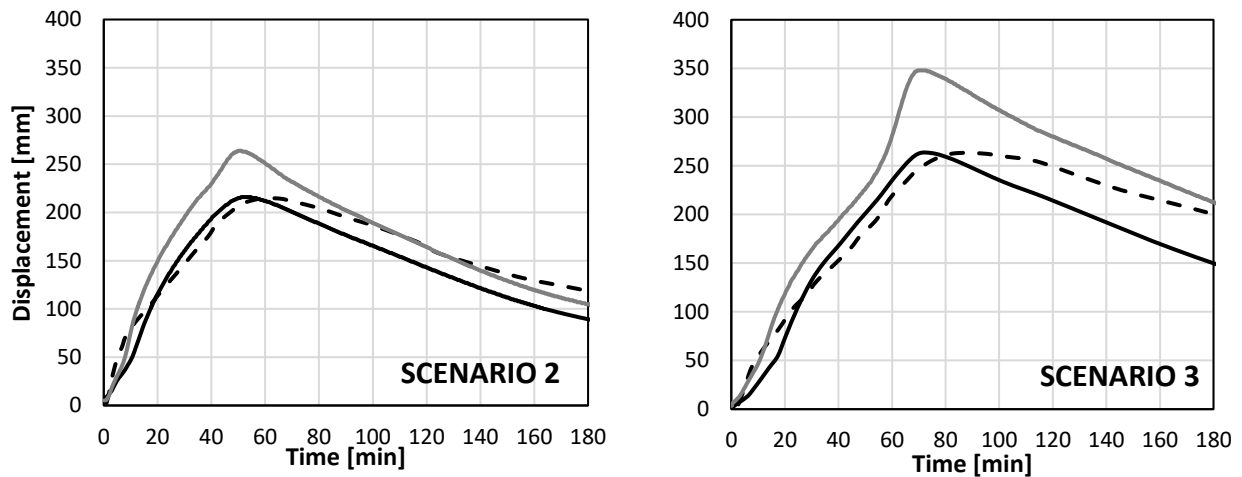


Figure 10. Experimental and numerical mid-span deflection for concrete slabs under Standard fire and compartment fire tests, resulting from using both *mean* (black dotted line) and *maximum* (grey dotted line) compartment temperature as input for modelling natural fire

CONCLUSIONS

The experimental and numerical studies conducted on a furnace test as well as three compartment fire experiments have shown that:

- The slab is classified REI120 in the standard test (failure at 125 minutes). No failure was observed for the natural fire tests;
- In this study, the use of physical and thermomechanical properties of concrete (except the thermal conductivity which was taken from the recommendations of the horizontal group fire project team) and reinforcing steel given in EN 1992-1-2 leads to conservative predictions of in-depth temperature profiles within the concrete slabs for both standard furnace and natural fire tests. It also leads to a realistic estimation of the failure time in the case of a standard fire. For the compartment fire tests, the predicted deflections are in reasonable accordance with experimental results.

AKNOWLEDGMENTS

The authors would like to acknowledge ongoing support from the project partners: CERIB, Fire Testing Centre; the School of Engineering, The University of Edinburgh; Bordeaux University; Brandskyddslaget AB; the Institute of Building Materials, Concrete Construction and Fire Safety of Technische Universität Braunschweig, Division of Fire Safety; and Liège University.

REFERENCES

- [1] M. S. Dimia, M. Guenfoud, T. Gernay et J.-M. Franssen, «Collapse of concrete columns during and after the cooling phase of a fire,» *Journal of fire protection engineering*, vol. 21, n° 14, pp. 245-263, 2011.
- [2] B. Elingwood et T. Lint, «Flexure and shear behaviour of concrete beams during fires,» *Journal of structural fire engineering*, vol. 117, n° 12, pp. 440 - 458, 1991.
- [3] A. Kumar et V. Kumar, «Behavior of RCC Beams after exposure to elevated temperatures,» *IE Journal*, vol. 84, pp. 165-170, 2003.
- [4] V. Kodur et A. Agrawal, «Critical factors governing the residual response of reinforced concrete beams exposed to fire,» *Fire Technology*, vol. 52, n° 14, pp. 967-993, 2016.

- [5] M. B. Dwaikat et V. Kodur, «response of restrained concrete beams under design fire exposure,» *Journal of structural fire engineering*, vol. 135, n° 111, pp. 1408 - 1417, 2009.
- [6] V. Kodur, M. Dwaikat and R. Fikre, "An approach for evaluating the residual strength of fire-exposed RC beams," *Structural Engineering and Mechanics*, vol. 16, no. 6, pp. 695-712, 2003.
- [7] V. Kodur, N. Raut, X. Mao et W. Khaliq, «Simplified approach for evaluating residual strength of fire-exposed reinforced concrete columns,» *Materials and Structures*, vol. 46, pp. 2059-2075, 2013.
- [8] S. Bratina, I. Planinc, M. Saje and G. Turk, "Non-Linear Fire-Resistance Analysis of Reinforced Concrete Beams," *Structural Engineering and Mechanics*, vol. 16, no. 6, pp. 695-712, 2003.
- [9] P. Bamonte, N. Kalaba et R. Felicetti, «Computational study on prestressed concrete members exposed to natural fires,» *Fire Safety Journal*, vol. 97, pp. 54-65, 2018.
- [10] B. Wu, Y.-H. Li and S.-L. Chen, "Effect of heating and cooling on axially restrained RC columns with special-shaped cross section," *Fire Technology*, vol. 46, pp. 231-249, 2010.
- [11] N. Raut and V. Kodur, "Response of high-strength concrete columns under design fire exposure," *Journal of structural fire engineering*, vol. 137, no. 1, pp. 69-79, 2011.
- [12] V. Kodur, D. Hibner and A. Agrawal, "Residual response of reinforced concrete columns exposed to design fires," in *Proceedings of the 6th International workshop on performance, protection and strengthening of structures under extreme loading*, Guangzhou (Canton), China, 2017.
- [13] T. Gernay et M. S. Dimia, «Structural behaviour of concrete columns under natural fires,» *Engineering Computations*, vol. 30, n° 16, pp. 854-872, 2013.
- [14] T. Gernay, "Fire resistance and burnout resistance of reinforced concrete columns," *Fire Safety Journal*, vol. 104, pp. 67-78, 2019.
- [15] Y. Wang, Y. Duan, S. Ma, Z. Huang, Y. Zhang, W. Jiachao, G. Yuan, M. Zhou et G. Zhang, «Behaviour of continuous reinforced concrete floor slabs subjected to different compartment fires,» *Engineering Structures*, vol. 197, pp. 1-20, 2019.
- [16] J.-M. Franssen et T. Gernay, «Modelling structures in fire with SAFIR®: theoretical background and capabilities,» *Journal of Structural Fire Engineering*, vol. 8, n° 13, pp. 300-323, 2017.
- [17] A. Bartlett, R. McNamee, J. Zehfuss, S. Mohaine, C. Tessier et L. Bisby, «Heat fluxes to a façade resulting from compartment fires with combustible and non-combustible ceilings,» chez *3rd International Symposium of Fire Safety of Façades*, Paris, 2019.
- [18] J. C. Mindeguia, S. Mohaine, L. Bisby, F. Robert, R. McNamee et A. Bartlett, «Thermo-mechanical behavior of cross-laminated timber slabs under standard and natural fires,» chez *Inteflam Conference*, Royal Holloway College, London, 2019.

- [19] R. McNamee, J. Zehfuss, A. I. Bartlett, M. Heidari, F. Robert et L. A. Bisby, «Enclosure fire dynamics with a combustible ceiling,» chez *Interflam Conference*, Royal Holloway College, London, 2019.
- [20] *EN 1991-1-2; Eurocode 1 : Action on structures - Part 1-2 : General actions - Actions on structures exposed to fire*, 2003.
- [21] M. J. Hurley, *SFPE Handbook of Fire Protection Engineering*, Fifth Edition, Springer, 2016.
- [22] «Epernon Fire Tests Programme,» 2019. [En ligne]. Available: <http://www.epernon-fire-tests.eu/>.
- [23] *EN 1992-1-2; Eurocode 2 : Design of concrete structures - Part 1-2: General rules - Structural fire design*, 2005.
- [24] CEN/TC250, «Report of Project Team HGF.T1; Fire-Harmonization of fire parts of Structural Eurocodes,» 2017.
- [25] R. Jansson, "Measurement of concrete thermal properties at high temperatures," in *Proceedings from the fib Task Group 4.3 workshop, Fire Design of Concrete Structures: What now? What next?*, Milan, Italy, 2004.
- [26] T. Gernay et J.-M. Franssen, «A formulation of the Eurocode 2 concrete model at elevated temperature that includes an explicit term for transient creep,» *Fire Safety Journal*, vol. 51, pp. 1-9, 2012.
- [27] M. J. Hurley, *SFPE Handbook of Fire Protection Engineering*, Fifth Edition, Springer, 2016.

Atomic structural evolution of calcium-containing alkali-activated metakaolin exposed to fire conditions

Karina Alventosa¹ & Claire E. White^{1*}

¹Civil and Environmental Engineering, and the Andlinger Center for Energy and the Environment, Princeton University, Princeton, USA

*Corresponding author: whitece@princeton.edu

Postal address: Department of Civil and Environmental Engineering, Princeton University, Princeton NJ 08544, USA

ABSTRACT:

Alkali-activated materials (AAMs) are one type of sustainable alternative for ordinary Portland cement (OPC), providing significant reductions in CO₂ emissions. AAMs based on fly ash or metakaolin are found to possess good fire performance, where the binder gels crystallize and form ceramic phases on heating. However, the ambient temperature setting properties and short-term strength development of select low-calcium AAMs are unfavorable, requiring the optimization of the mix design and a re-evaluation of the chemical, mechanical and physical properties at elevated temperatures (i.e., fire conditions). In this investigation, the influence of calcium hydroxide on the thermal evolution of alkali-activated metakaolin has been assessed, where gel crystallization and restructuring have been evaluated using X-ray diffraction and Fourier transform infrared spectroscopy. It is found that the 10 wt. % replacement of metakaolin with calcium hydroxide, together with a reduction in silicate activator concentration from 10 to 5M, does not adversely impact the phase evolution on heating since similar crystalline phases are seen to emerge. However, the exact location of calcium in the high temperature phases of silicate-activated metakaolin remains unknown.

KEYWORD: Alkali-activated cement, metakaolin, fire resistance, calcium hydroxide, FTIR, XRD

INTRODUCTION:

Concrete is the most readily available construction material worldwide [1] due to both structural and economic advantages. Thus, it has become an integral component of infrastructure projects (i.e., roads, bridges, buildings, drainage, water and transport). As a result, the production of ordinary Portland cement (OPC), a principle component of concrete, currently accounts for 5-8% of anthropogenic CO₂ released into the atmosphere [2]. The global impact of these CO₂ emissions necessitates the development of alternative materials to simultaneously mitigate CO₂ emissions as well as support the demands of an increasingly industrialized and consumption-oriented society.

Sustainable concrete alternatives have emerged over the decades, including alkali-activated materials (AAMs) [3]. Alkali activation describes a precursor, typically of the aluminosilicate form, that when combined with an alkaline solution (an 'activator'), forms a mechanically-hard binder product [3]. The majority of research on AAMs has focused on the use blast furnace slag and coal derived fly ash as precursors [4]. However, metakaolin, a calcined dehydroxylated form of kaolinite clay [5], is an additional precursor option for alkali activation that has largely been confined to laboratory studies due to its high water demand [6]. However, with the recent emergence of flash calcined kaolin, which produces a metakaolin with a

reduced water demand, the use of metakaolin in AAMs in commercial applications warrants further investigation.

Alkali activation of metakaolin is a multi-step process. The precursor dissolves into ionic species when exposed to the alkaline activating solution, where small silicate and aluminosilicate oligomers form via condensation reactions between the dissolved ions (forming Si-O-T linkages, where T denotes tetrahedral Si or Al), and then a final gel product precipitates through further condensation reactions [7], [8]. The precipitated sodium-aluminosilicate-hydrate (N-A-S-H) gel structure is comprised of alternating SiO_4 and AlO_4 tetrahedra linked via the oxygen atoms. The presence of positive cations is required to balance the $\text{Al}(\text{OH})_4^-$ tetrahedral sites [9]. Comparatively, calcium-silicate-hydrate (C-S-H) gel, typical of OPC cements, can be broadly described as consisting of finite length chains of silicate tetrahedra on either side of a two-dimensional calcium oxide layer, where the silicate chains form a “dreierketten” structure that involves silicate pairs linked together by bridging silicate sites [10]. Additional calciums and water molecules are located in the interlayer spacing between adjacent chain-CaO-chain motifs. AAM precursors with high calcium contents, or AAM systems with calcium additions, can form a similar C-S-H structure known as C-(N)-A-S-H gel, which is created by the insertion of aluminum as a substitute for the silicate bridging tetrahedra in C-S-H along with the existence of Na ions in the interlayer region of the structure [11].

Prior literature has proposed that alkali-activated concretes have a higher thermal stability than OPC concrete. This stability is an essential safety consideration when designing structures with thermal insulation and protection. OPC starts to lose strength at approximately 300°C and this can be attributed to the loss of bound structural water as the C-S-H gel dehydrates during the vapor pressure build-up mechanism [12]–[14]. However, the expanding water molecules are seen to separate the C-S-H layers and the calcium hydroxide dehydroxylates at approximately 450°C into lime (CaO) [15]. At higher temperatures C-S-H has been seen to transform into a disordered calcium silicate with a structure similar to larnite [16]. The reduced amount of structural water in N-A-S-H gel compared with C-S-H gel implies that the vaporization of such water may not have the same damaging effects on the macroscopic structure [17]. Additionally, when exposed to temperatures greater than 800°C the final gel product of alkali-activated metakaolin, N-A-S-H gel, crystallizes into the stable ceramic phase of nepheline (NaAlSiO_4) [13], [18]–[23].

In this investigation, we have analyzed the influence of calcium hydroxide on the thermal evolution of the N-A-S-H gel formed in sodium hydroxide-activated and sodium silicate-activated metakaolin, with the aim to understand the impact of calcium on the performance of alkali-activated metakaolin used in fire-resistance applications. To understand the interaction of calcium hydroxide in the N-A-S-H gel, as well as the atomic structural changes associated with exposure to high temperatures up to 900°C we have employed fourier transform infrared spectroscopy (FTIR) and X-ray diffraction (XRD).

MATERIALS AND METHODS:

Synthesis of Materials

Several types of alkali-activated metakaolin have been studied through the use of two activating solutions, specifically a Na_2SiO_3 solution (silicate-activated), and a NaOH solution (hydroxide-activated). The Na_2SiO_3 solutions were prepared using PQ Corporation product “D” sodium silicate solution with a $\text{SiO}_2/\text{Na}_2\text{O}$ wt. ratio of 2 [24]. The PQ D silicate solutions were mixed with solid NaOH and deionized water for at least 24 hrs prior to activation, where a 28 wt. % (13.9 wt. % for the lower alkali solution) of Na_2O was used relative to solid precursor, with a $\text{Na}_2\text{O}/\text{SiO}_2$ ratio of 1.0 and a $\text{H}_2\text{O}/\text{precursor}$ wt. ratio of 0.9 to obtain the Na_2SiO_3 solution with the equivalent Na content of 10M NaOH solution (5M for the lower alkali solution). To prepare the NaOH solutions, solid NaOH pellets (CAS#1310-73-2, Sigma-Aldrich, St. Louis, MO) were dissolved in deionized water to obtain 5 and 10M activators.

Two types of precursor powders were studied, specifically metakaolin (denoted as 100MK in figures and text) and metakaolin mixed with 10 wt. % replacement using calcium hydroxide (denoted as 90MK). BASF MetaMax was used as the metakaolin source, which is a highly reactive form of metakaolin with 1.7 wt. % of anatase impurity [25] (denoted as 100MK). The second precursor powder consisted of 90 wt. % MetaMax and 10 wt. % calcium hydroxide (reagent grade, >95%, Sigma Aldrich, St. Louis, MO). Prior to activating the 90MK precursor, the two powders were thoroughly mixed by vibration. To study the impact of calcium hydroxide on the alkali activation reaction of metakaolin, the powders (100MK and 90MK) were mixed with each activating solution type in the appropriate proportions at each molarity to maintain a H₂O/precursor ratio of 0.9 by weight (where the calcium hydroxide is counted as a precursor). Synthesis of the alkali-activated binders was carried out by mixing the precursor powder and activating solution manually for 1 min after initial combination, followed by 2 minutes of vibration mixing at 2500 rpm. The binders were then sealed in airtight containers and left to solidify at ambient conditions for 7 days prior to exposure to high temperature soaks, XRD and *ex situ* FTIR testing.

Ex situ heating of the cured samples was carried out using a Barnstead Thermolyne 6000 furnace with a ramp rate of 10°C/minute. The solid samples were placed in alumina crucibles in the furnace at ambient temperature and once 300°C was reached, the samples underwent a 2 hour soak duration. Once the 300°C samples were removed, the same steps were repeated for the 600°C and 900°C samples. After removal from the furnace, each sample was cooled for 20 minutes, converted into a powder via mortar and pestle, and then sealed in an air tight container.

Data Collection

For each sample, FTIR data were collected using a Perkin Elmer Frontier FT-IR Spectrometer with an UATR attachment. The instrument was purged with N₂ gas to eliminate atmospheric H₂O and CO₂ contributions.

A Bruker D8 Advance X-ray diffractometer was used to collect X-ray diffraction patterns on each sample. After a 7-day set time, the samples were loaded into 1mm polyimide capillary tubes and subsequently sealed with 5-minute epoxy. An Ag-tube was used as the X-ray source together with a LYNXEYE-XE detector.

RESULTS AND DISCUSSION:

Figures 1-3 display the FTIR data of alkali-activated metakaolin with and without calcium hydroxide. These plots indicate that the vibration spectra are similar for the ambient temperature samples, regardless of the type and concentration of activator, and presence of calcium hydroxide. The main features in Figure 3 are the OH stretching band at ~3400 cm⁻¹, the H₂O bending band at ~1600 cm⁻¹, and the Si-O-T asymmetric stretching band at ~950 cm⁻¹. Unreacted metakaolin and precipitated (C-)N-A-S-H gel contribute to the Si-O-T stretching band, and a shift from higher to lower wavenumbers correlates to the progression of the alkali activation reaction (from 950 cm⁻¹ to 943 cm⁻¹). It is clear from the evident shoulder at ~1100 cm⁻¹ in Figure 1 that the 5M hydroxide-activated samples (100MK and 90MK) at ambient temperatures have not formed a significant amount of gel, in contrast to the 10M hydroxide-activated samples.

A number of evident changes occur in the FTIR data when alkali-activated metakaolin is exposed to high temperatures. The data demonstrate a lack of hydroxyl stretching bands after heating to 300°C (see Figure 3 containing the silicate-activated samples; hydroxide-activated sample have similar spectra in this region), which is consistent with the loss of free and bound water as water begins to evaporate at 100°C. The Si-O-T band at ~950-1000 cm⁻¹ shifts to higher wavenumbers between ambient temperature and 300°C, which may be due to an increase in the degree of polymerization (i.e., reorganization) of the aluminosilicate network.

However, other structural changes cannot be discounted, such as a loss of aluminate (and calcium, if present) from the gel, generating a highly-polymerized silicate network.

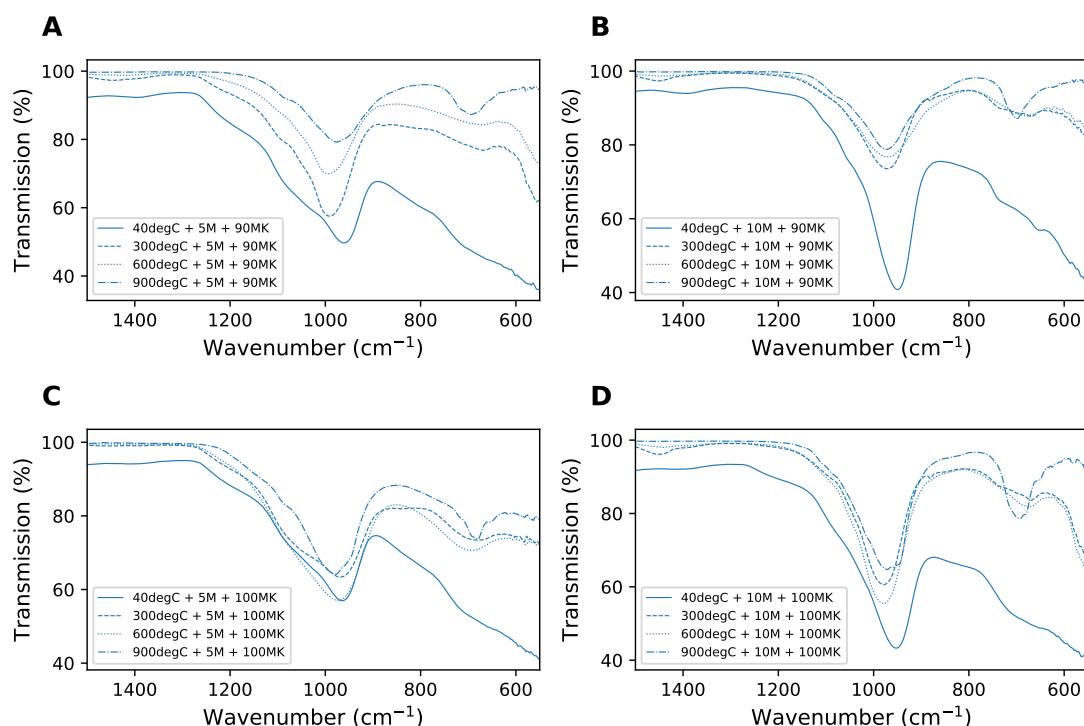


Figure 1: FTIR data (from 550 to 1500 cm^{-1}) for hydroxide-activated metakaolin with varied molarities and calcium addition at ambient temperature and after exposure to 300, 600 and 900 $^{\circ}\text{C}$. (a) 90MK activated with 5M, (b) 90MK activated with 10M, (c) 100MK activated with 5M, and (d) 100MK activated with 10M.

Between 300 and 900 $^{\circ}\text{C}$ there are minimal changes occurring to the wavenumber of the Si-O-T band, aside from (i) a slight shift to lower wavenumbers (from ~ 971 to ~ 976 cm^{-1}) for hydroxide-activated metakaolin (5M+90MK and 10M+100MK), and (ii) a similar shift but to higher wavenumbers for silicate-activated metakaolin (5M+100MK, 5M+90MK, 10M+100MK and 10M+90MK) (from ~ 968 cm^{-1} at 300 $^{\circ}\text{C}$ to ~ 995 cm^{-1} at 900 $^{\circ}\text{C}$). This is the first indication that exposure to 900 $^{\circ}\text{C}$ results in different behaviors for the hydroxide- and silicate-activated metakaolin.

At 900 $^{\circ}\text{C}$ both the hydroxide- and silicate-activated samples possess a well-defined vibration band at ~ 675 cm^{-1} , as will be discussed further with the XRD data, indicating the emergence of the crystalline sodium aluminosilicate phase, nepheline, in certain samples. This phase forms at a temperature between 600 and 900 $^{\circ}\text{C}$ [13], [19], [22]. It is important to note that (i) the well-defined 675 cm^{-1} band exists in all 900 $^{\circ}\text{C}$ samples, irrespective of whether calcium hydroxide is present, and (ii) there are no significant differences in the thermal behavior of alkali-activated metakaolin with and without calcium hydroxide.

The presence of calcium results in subtle differences in the FTIR data, specifically, a lower Si-O-T wavenumber for the 300 $^{\circ}\text{C}$ samples, likely due to its incorporation in the N-A-S-H gel at ambient temperature. For hydroxide-activated 10M+100MK the peak is at 952 cm^{-1} and shifts to 949 cm^{-1} when calcium is added (10M+90MK). For silicate-activated (10M+100MK to 10M+90MK) the peak shifts from 950 to 943 cm^{-1} for the same calcium addition. Exposure to 900 $^{\circ}\text{C}$ shifts the calcium-containing samples to 990 cm^{-1} for silicate-activated metakaolin (compared to 1000 cm^{-1} without calcium) and 973 cm^{-1} for hydroxide-activated metakaolin

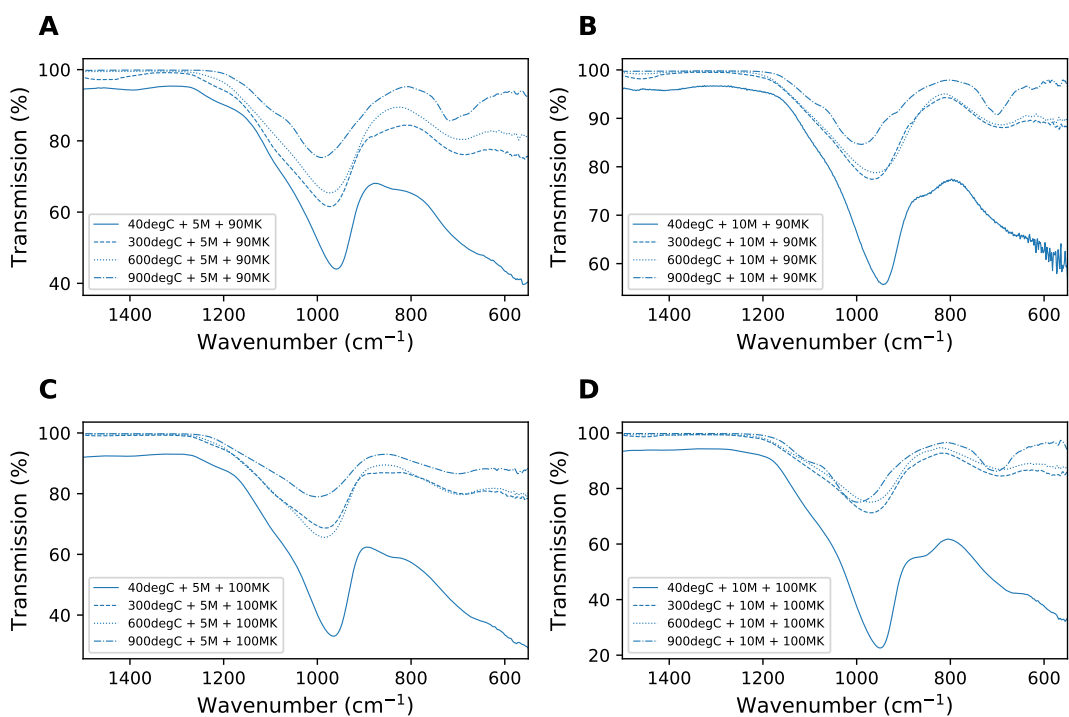


Figure 2: FTIR data (from 550 to 1500 cm^{-1}) for silicate-activated metakaolin with varied molarities and calcium addition at ambient temperature and after exposure to 300, 600 and 900 $^{\circ}\text{C}$. (a) 90MK activated with 5M, (b) 90MK activated with 10M, (c) 100MK activated with 5M, and (d) 100MK activated with 10M.

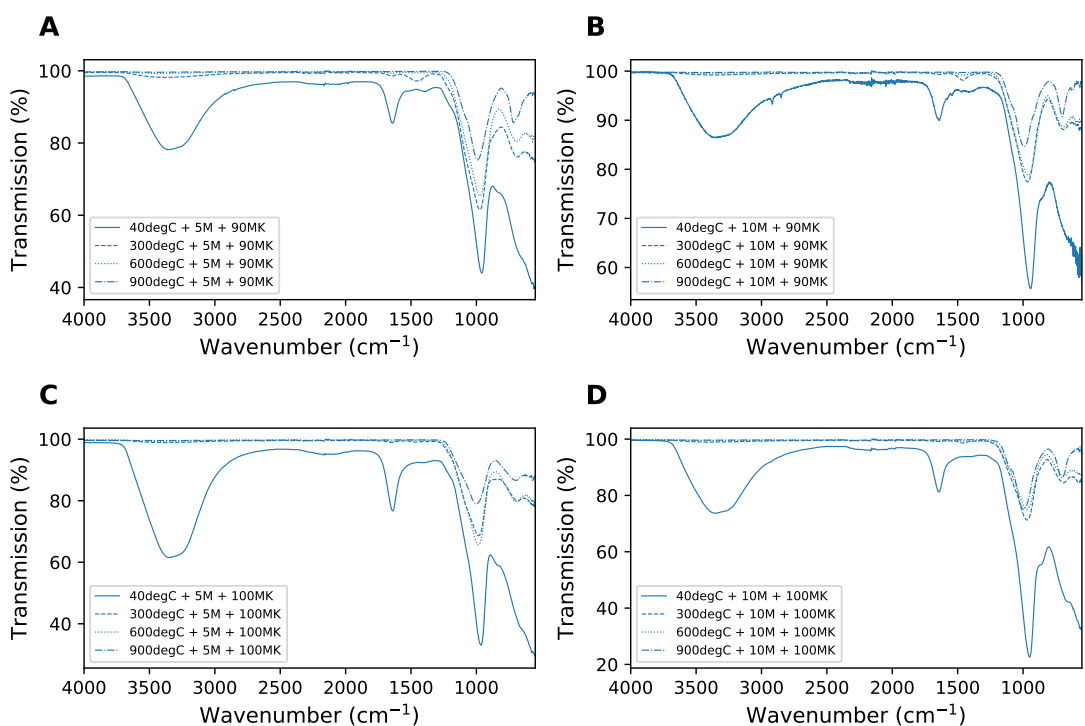


Figure 3: FTIR data (from 550 to 4000 cm^{-1}) for silicate-activated metakaolin with varied molarities and calcium addition at ambient temperature and after exposure to 300, 600 and 900 $^{\circ}\text{C}$. (a) 90MK activated with 5M, (b) 90MK activated with 10M, (c) 100MK activated with 5M, and (d) 100MK activated with 10M.

(compared to 978 cm^{-1} without calcium). An increase in activator concentration leads to a more defined peak at 675 cm^{-1} for samples without calcium, especially for silicate-activated 10M+100MK when compared to 5M+100MK; therefore, this increase in activator concentration corresponding to a greater amount of nepheline on heating. Furthermore, Figure 1a-b and Figure 2a-b indicate that nepheline was more readily formed in the presence of calcium, demonstrated by the well-defined vibration band between 450 cm^{-1} and 675 cm^{-1} .

XRD analysis was performed to further understand the crystallization process of alkali-activated metakaolin with and without calcium (Figures 4 and 5). The ambient temperature samples contain a titanium dioxide impurity, specifically anatase, from the original metakaolin precursor. The broad peak positioned at $10\text{-}11^\circ$ is indicative of N-A-S-H gel, which disappears after exposure to 300°C . The broad peak positioned at $7\text{-}8^\circ$ demonstrates a presence of unreacted metakaolin (clearly visible in Figures 4c and 5c). At 300 and 600°C all hydroxide-activated samples, except 5M+100MK, contain crystalline zeolites, specifically zeolite A. The formation of zeolites in hydroxide-activated metakaolin has been extensively documented in the literature, where zeolites are often identified in ambient temperature cured samples and further form on heating [26]–[29].

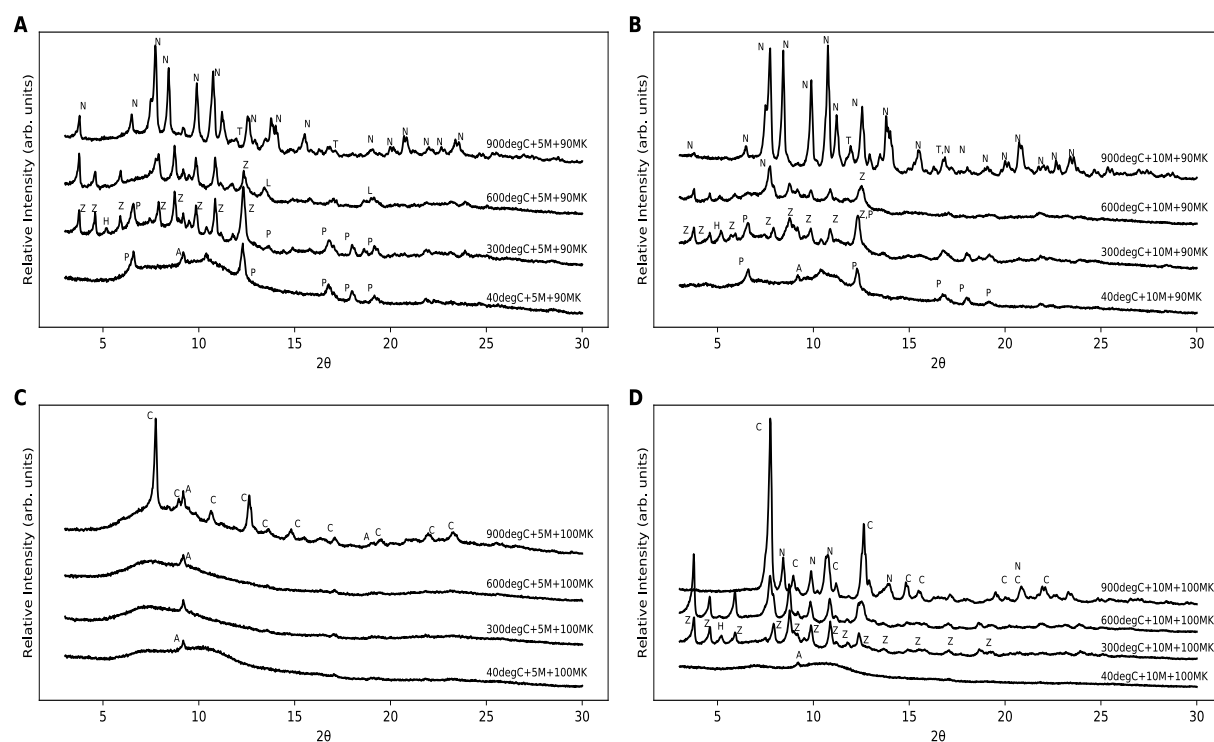


Figure 4: XRD data for hydroxide-activated metakaolin with varied molarities and calcium addition at ambient temperature and after exposure to 300 , 600 and 900°C (N = Nepheline, A = Anatase, Z = Zeolite A, C = Carnegieite, P = Portlandite, H = Hydroxysodalite, T = Calcium titanate, L = Lime). (a) 90MK activated with 5M, (b) 90MK activated with 10M, (c) 100MK activated with 5M, and (d) 100MK activated with 10M.

The hydroxide-activated metakaolin samples with calcium form nepheline by 900°C (5M+90MK and 10M+90MK), while those without calcium predominantly form carnegieite. Therefore, calcium promotes the formation of nepheline in hydroxide-activated metakaolin. The well-defined FTIR band at $\sim 675\text{ cm}^{-1}$ for the 100MK samples is likely associated with carnegieite and not nepheline. For the 90MK hydroxide-activated samples, portlandite dehydroxylates at $\sim 450^\circ\text{C}$ and, as seen in the 5M+90MK sample at 600°C , lime (CaO) is

present. However, by 900°C, this phase has disappeared and instead, peaks tentatively assigned to calcium titanate (a perovskite) are visible. Therefore, it is likely that lime and anatase have reacted to form the titanate phase.

Heating of silicate-activated metakaolin samples results in similar behavior to hydroxide-activated samples, as demonstrated by crystalline phases in the XRD patterns (Figure 5). For the 5M hydroxide- and silicate-activated metakaolin systems without calcium (100MK), there is a large amount of an amorphous phase(s) prevalent in all samples (up to 900°C), due to unreacted metakaolin (Figures 4c and 5c). As was the case for 5M+90MK and 10M+90MK hydroxide-activated metakaolin, the silicate-activated equivalent systems form nepheline between 600 and 900°C. However, in contrast to the formation of carnegieite by 900°C in the 10M+100MK hydroxide-activated system, the silicate-activated 10M+100MK sample shows the formation of nepheline by 900°C. There are no zeolite phases detected in any of the silicate-activated samples, contrary to the hydroxide-activated samples. Furthermore, no lime is seen to form in the 600°C 90MK samples, nor calcium titanate at 900°C, in contrast with the 90MK hydroxide-activated systems.

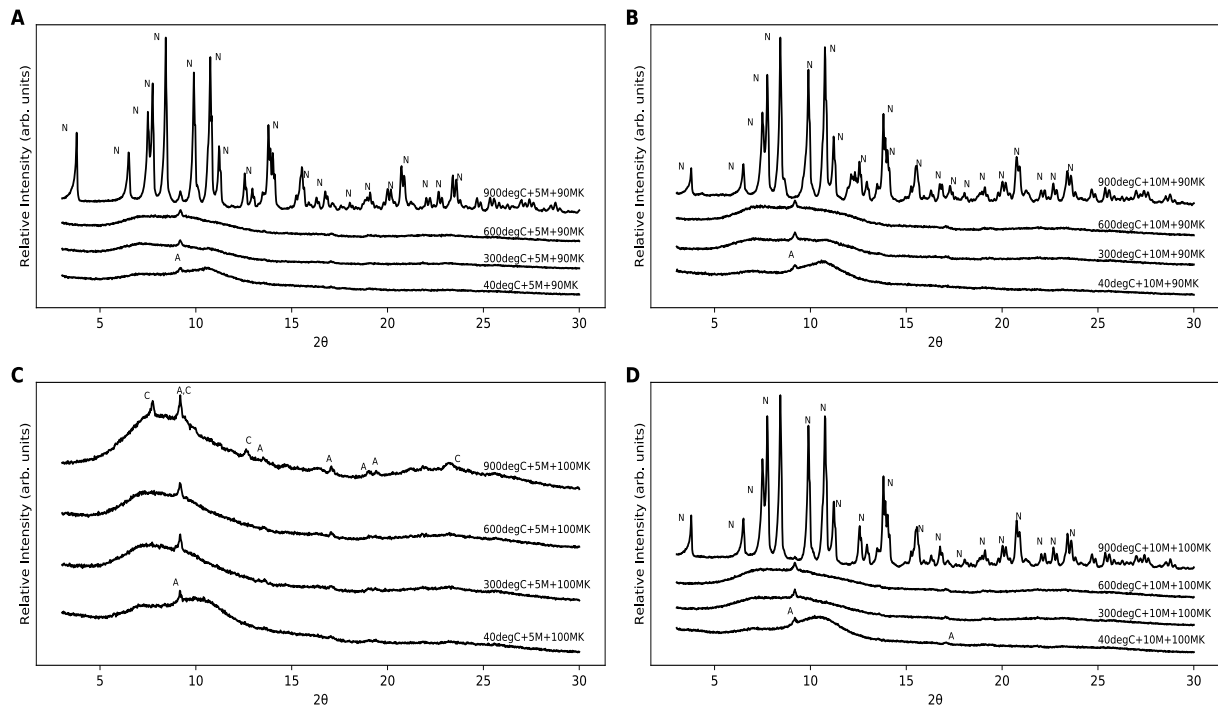


Figure 5: High temperature XRD data for varied molarities and calcium addition of Na_2SiO_3 (N = Nepheline, A = Anatase, Z = Zeolite A, C = Carnegieite). (a) 90MK activated with 5M, (b) 90MK activated with 10M, (c) 100MK activated with 5M, and (d) 100MK activated with 10M.

Although not directly detectable from the XRD data, the addition of calcium enhances (C-)N-A-S-H gel formation, particularly for lower molarity activating solutions. Both the hydroxide- and silicate-activated 5M samples without calcium addition remain predominantly amorphous throughout all stages of heating (Figures 4c and 5c), due to a lack of N-A-S-H gel and its associated crystallization. Comparatively, the 5M samples containing calcium form nepheline after exposure to 900°C and undergo extensive crystallization.

In contrast to the findings outlined above for calcium-containing silicate-activated metakaolin (no distinct behavior associated with calcium-containing phase), calcium in C-S-H gel in OPC exhibits a distinct phase transition on heating to form free lime (CaO) and/or a disordered calcium silicate with atomic structures similar to larnite [16]. This degradation mechanism

reduces the mechanical properties of the microstructure, and thus a loss of compressive strength at the macroscopic level. Although hydroxide-activated metakaolin with calcium is seen to form free lime, silicate-activated metakaolin samples with calcium do not contain crystalline peaks associated with lime or another calcium-containing phase. The addition of calcium hydroxide used to improve the ambient temperature properties of silicate-activated metakaolin is therefore not seen to negatively affect the high temperature behavior of this material, as assessed using FTIR and XRD. Key outstanding questions regarding material performance include whether calcium-containing silicate-activated metakaolin experiences detrimental volumetric changes on heating (preliminary results indicate minimal structural rearrangements at the atomic length scale) and spalling. Further experiments will determine the location of calcium within the high temperature phase(s) of silicate-activated metakaolin.

CONCLUSION:

Here we have determined the atomic structural changes that occur in alkali-activated metakaolin when exposed to temperatures up to 900°C and the influence of calcium hydroxide (as an alkali activation precursor) on these changes. Two activating solutions were studied, specifically sodium hydroxide and sodium silicate, at two concentration levels, 5M and 10M (NaOH equivalent). Samples with and without a 10 wt. % replacement of metakaolin with calcium hydroxide were studied. Atomic structural changes were evaluated using Fourier transform infrared spectroscopy and X-ray diffraction, where the results revealed that calcium enhances the formation of nepheline, particular in lower molarity samples. The formation of nepheline indicates that calcium hydroxide can be used to enhance (C-)N-A-S-H gel formation during the alkali activation process. Moreover, although calcium was present in the silicate-activated samples, none of the typical calcium-containing phases that form during heating of OPC, such as CaO, were apparent in the silicate-activated metakaolin data. Ultimately, the results indicate that silicate-activated metakaolin with minor calcium hydroxide replacement is a viable ambient temperature construction material with promising high temperature performance properties.

ACKNOWLEDGMENTS:

This material is based on work supported by the National Science Foundation under Grant No. 1727346

REFERENCES:

- [1] E. Gartner, "Industrially interesting approaches to 'low-CO₂' cements," *Cem. Concr. Res.*, vol. 34, no. 9, pp. 1489–1498, 2004.
- [2] J. G. J. Olivier, G. Janssens-Maenhout, M. Muntean, and J. A. H. W. Peters, "Trends in Global CO₂ Emissions Report," The Hague, Netherlands, 2016.
- [3] J. L. Provis, "Alkali-activated materials," *Cem. Concr. Res.*, vol. 114, pp. 40–48, Mar. 2018.
- [4] J. L. Provis and J. S. J. van Deventer, *Geopolymers - Structure, Processing, Properties and Industrial Applications*. Woodhead Publishing Limited, 2009.
- [5] S. Salvador, "Pozzolanic properties of flash-calcined kaolinite: A comparative study with soak-calcined products," *Cem. Concr. Res.*, vol. 25, no. 1, pp. 102–112, 1995.
- [6] A. Palomo and F. P. Glasser, "Chemically-bonded cementitious materials based on metakaolin," *Br. Ceram. Trans. J.*, vol. 91, no. 4, pp. 107–112, 1992.
- [7] S. Alonso and A. Palomo, "Calorimetric study of alkaline activation of calcium hydroxide-metakaolin solid mixtures," *Cem. Concr. Res.*, vol. 31, no. 1, pp. 25–30, 2001.
- [8] J. L. Provis and S. A. Bernal, "Geopolymers and related alkali-activated materials," *Annu. Rev. Mater. Res.*, vol. 44, no. 1, pp. 299–327, 2014.
- [9] J. Davidovits, "Properties of geopolymer cements," in *First International Conference on Alkaline Cements and Concretes*, 1994, pp. 131–149.
- [10] L. Gomez-Zamorano, M. Balonis, B. Erdemli, N. Neithalath, and G. Sant, "C-(N)-S-H and N-A-S-H gels: Compositions and solubility data at 25°C and 50°C," *J. Am.*

- Ceram. Soc.*, vol. 100, no. 6, pp. 2700–2711, 2017.
- [11] R. Si, S. Guo, and Q. Dai, "Influence of calcium content on the atomic structure and phase formation of alkali-activated cement binder," *J. Am. Ceram. Soc.*, vol. 102, no. 3, pp. 1479–1494, 2019.
- [12] O. G. Rivera *et al.*, "Effect of elevated temperature on alkali-activated geopolymeric binders compared to portland cement-based binders," *Cem. Concr. Res.*, vol. 90, pp. 43–51, 2016.
- [13] M. Lahoti, K. K. Wong, E. H. Yang, and K. H. Tan, "Effects of Si/Al molar ratio on strength endurance and volume stability of metakaolin geopolymers subject to elevated temperature," *Ceram. Int.*, vol. 44, no. 5, pp. 5726–5734, 2018.
- [14] M. S. Morsy, S. S. Shebl, and A. M. Rashad, "Effect of fire on microstructure and mechanical properties of blended cement pastes containing metakaolin and silica fume," *Asian J. Civ. Eng.*, vol. 9, pp. 93–105, 2008.
- [15] G. A. Houry, "Effect of fire on concrete and concrete structures," *Prog. Struct. Eng. Mater.*, vol. 2, no. 4, pp. 429–447, 2002.
- [16] C. E. White, "Effects of temperature on the atomic structure of synthetic calcium-silicate-deuterate gels: A neutron pair distribution function investigation," *Cem. Concr. Res.*, vol. 79, pp. 93–100, 2016.
- [17] O. Burciaga-Díaz and J. I. Escalante-García, "Comparative performance of alkali activated slag/metakaolin cement pastes exposed to high temperatures," *Cem. Concr. Compos.*, vol. 84, pp. 157–166, 2017.
- [18] P. Duxson, G. C. Lukey, and J. S. J. van Deventer, "Thermal evolution of metakaolin geopolymers: Part 1 - Physical evolution," *J. Non. Cryst. Solids*, vol. 352, no. 52–54, pp. 5541–5555, 2006.
- [19] P. Duxson, G. C. Lukey, and J. S. J. van Deventer, "The thermal evolution of metakaolin geopolymers: Part 2 - Phase stability and structural development," *J. Non. Cryst. Solids*, vol. 353, no. 22–23, pp. 2186–2200, 2007.
- [20] S. A. Bernal, E. D. Rodríguez, R. Mejía De Gutiérrez, M. Gordillo, and J. L. Provis, "Mechanical and thermal characterisation of geopolymers based on silicate-activated metakaolin/slag blends," *J. Mater. Sci.*, vol. 46, no. 16, pp. 5477–5486, 2011.
- [21] K. Dombrowski, A. Buchwald, and M. Weil, "The influence of calcium content on the structure and thermal performance of fly ash based geopolymers," *J. Mater. Sci.*, vol. 42, no. 9, pp. 3033–3043, 2007.
- [22] V. F. F. Barbosa and K. J. D. MacKenzie, "Thermal behaviour of inorganic geopolymers and composites derived from sodium polysialate," *Mater. Res. Bull.*, vol. 38, no. 2, pp. 319–331, 2003.
- [23] K. K. Mandal, S. Thokchom, and M. Roy, "Effect of Na₂O content on performance of fly ash geopolymers at elevated temperature," *Int. J. Civ. Environ. Eng.*, vol. 91, no. 033, pp. 34–40, 2011.
- [24] N. Garg and C. E. White, "Mechanism of zinc oxide retardation in alkali-activated materials: An in situ X-ray pair distribution function investigation," *J. Mater. Chem. A*, vol. 5, no. 23, pp. 11794–11804, 2017.
- [25] A. Autef, E. Joussein, G. Gasgnier, and S. Rossignol, "Importance of metakaolin impurities for geopolymer synthesis," in *Developments in strategic materials: a collection of papers*, 2008.
- [26] M. Król, J. Minkiewicz, and W. Mozgawa, "IR spectroscopy studies of zeolites in geopolymeric materials derived from kaolinite," *J. Mol. Struct.*, vol. 1126, pp. 200–206, 2016.
- [27] Z. Sun and A. Vollpracht, "One year geopolymerisation of sodium silicate activated fly ash and metakaolin geopolymers," *Cem. Concr. Compos.*, vol. 95, pp. 98–110, 2019.
- [28] J. Temuujin, A. Minjigmaa, W. Rickard, M. Lee, I. Williams, and A. van Riessen, "Preparation of metakaolin based geopolymer coatings on metal substrates as thermal barriers," *Appl. Clay Sci.*, vol. 46, no. 3, pp. 265–270, 2009.
- [29] S. A. Bernal, J. L. Provis, V. Rose, and R. Mejía De Gutierrez, "Evolution of binder structure in sodium silicate-activated slag-metakaolin blends," *Cem. Concr. Compos.*,

vol. 33, no. 1, pp. 46–54, 2011.

Application of Laminated Ferrocement, High Tensile Laminated Ferrocement and Cellular Concrete to fire prevention and fire restoration of concrete structures.

Michael Pemberton¹, Alasdair Beal², Anthony Tucker³, Paul Nedwell⁴, Martin Pullan⁵.

¹Trafalgar Marine Technology Ltd, Leeds, UK

²Thomasons Ltd, Leeds, UK

³Tucker-Designs, Edlesborough, UK

⁴University of Manchester (retired), Manchester, UK

⁵Trafalgar Marine Technology Ltd, Leeds, UK

ABSTRACT

This paper explains the history, development and importance of ferrocement to the concrete industry. It is the authors' opinion that the subject of ferrocement and concrete/cement history is insufficiently represented in today's engineering curriculums.

The paper includes references to illustrate and demonstrate the superior fire resistance of ferrocement compared with normal concretes.

Reference will be made to proposals for the complete restoration and redevelopment of GRENFELL TOWER and to proposals for the complete roof restoration of NOTRE DAME CATHEDRAL in ferrocement materials to replicate the original roof.

The authors' proposals for SUSTAINABUILDABILITY.org and three "Dunkirk" projects will be discussed.

KEYWORD: Ferrocement, Cellular Concrete, Replication.

A BRIEF HISTORY OF THE AUTHOR'S FERROCEMENT ACTIVITIES.

After attending in 1981, in Bergamo, Italy, the NERVI SYMPOSIUM, the very first International Ferrocement Symposium, named after the great Italian Engineer and inventor of 'ferrocemento' Pier Luigi Nervi. Michael Pemberton obtained a license, for the UK and Europe, to use the spray and laminating technology of the late Mr Martin Iorns. The author has 38 years experience and interest in ferrocement, its use and its development. He has produced concrete pontoons to support houses, sewer liners, construction panels and small utility products.

He has previously produced the most accurate and technically advanced ferrocement in the world for the deMenil Museum, Houston, Texas.

WHY IS THIS PAPER PRESENTED?

Our construction industry has generally forgotten its roots. We, as engineers and contractors have to solve the problems of Grenfell Tower and provide a new roof to Notre Dame Cathedral.

Ferrocement offers solutions not generally understood by our construction industry.

The first reinforced concrete was in fact ferrocement and the boats produced by Lambot in 1855.

The author's enthusiasm for ferrocement, cement and concrete product and the realisation that this material really is the basis of our worldwide construction industry - is not reflected in commercial success.

An understanding of its far superior properties when compared to ordinary concretes remains relatively unknown. Its fire resistance and fire restoration potential is not recognised and so this paper seeks to illustrate and demonstrate the potential of this material.

No concrete history is complete without a mention of Aspdin, Smeaton and Leeds. Oil, Wheat and Cement are our most important materials to support our lifestyles. They are 'natural products'. Cement is a manufactured product. It is the author's opinion therefore, that Aspdin's Patent for the manufacture of Portland Cement is probably mankind's most important Patent. The subject of ferrocement and cement and concrete history is inadequately represented in today's engineering curriculum.



Figure 1 The team who built the deMenil Museum roof (1985): the author (with white hard hat) is next to architect Renzo Piano. The rest of the team are from American contractors, demenil museum and Ove Arup. In the middle is the late Martin Iorns inventor of the laminating process.

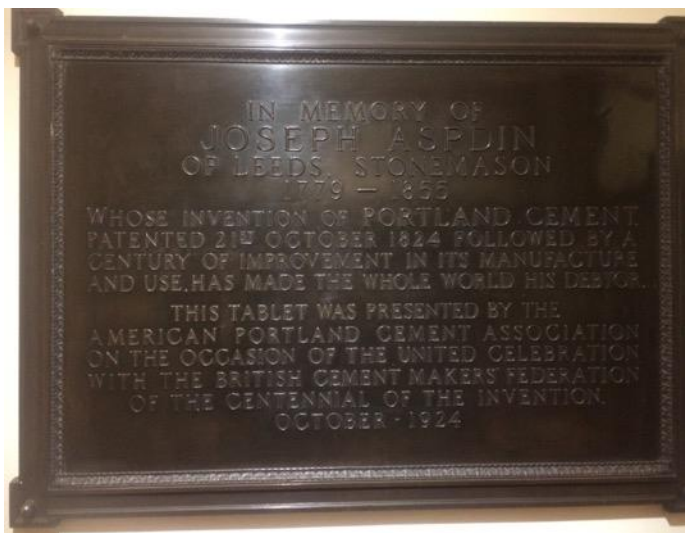


Figure 2 This is the plaque presented by the American Concrete Institute when visiting Leeds in 1924. It is in Leeds Town Hall. There is an amusing story to be told of the Americans visit to Leeds in 1924 when Sir William Airey inventor of Airey houses and homes for heroes was the Lord Mayor of Leeds.



Figure 3 Section of deMenil roof leaf displayed in Leeds University Civil Engineering Department



Figure 4 Author with a visitor by the plaques dedicated to Aspdin and Smeaton at the entrance to department building.



Figure 5 garden display of a section of deMenil leaf.



Figure 6 section of the leaf which has been in a fire temperature over 1,000 degrees, sufficient to make steel 'white hot'. The ferrocement maintains its integrity after cooling.

The deMenil roof section has been a garden sculpture since manufacture in 1985. It shows no deterioration whatsoever.

In previous research, the author has read several reports of fires on ferrocement yachts where the whole interior of a yacht has burnt out completely and the occupants of the yacht have managed to survive on the foredeck (upwind) until the fire has burnt out, and when the hull has cooled off the yacht and its occupants have survived.

This would not happen if the yacht had been built of any other material, steel, wood or glass fibre.

In other research, many years ago, the author learned of a warehouse fire in Nottingham and the fire damaged structure was repaired by Gunite – sprayed concrete. In this particular warehouse a subsequent fire occurred in the same warehouse and was also repaired by Gunite methods.[1]

This report details the accepted best methods to repair fire damaged structures.

In the case of this second warehouse fire, it was noted that following the second fire, the gunite repairs carried out after the first fire, had survived far better than the original concrete of the structure. This indicates the superior nature of Gunite sprayed concrete when applied to repair of fire damaged structures.

What is not generally understood is that ferrocement, because of its multiple distribution of fine mesh reinforcements with a strong mortar matrix is an even better fire resistant material.

The lack of heavy reinforcement and large aggregate produces a far more fire resistant material than Gunite, which is presently considered the best material to repair fire damaged structures.

The objective of this paper is to introduce ferrocement to our engineers and architects.

WHY DO WE LAMINATE FERROCEMENT?

There are several ways of constructing ferrocement and over the years methods have been found to increase productivity. The original and traditional method of making an armature of wire and hand plastering has been used since Lambot's invention in 1848 and Patent of 1855 but it is too laborious to be commercial. The application of positive displacement mixers and 'mono' type pumps to convey the mortar permits spraying of mortar onto a mold. The embedding of reinforcements into a plastic mortar is the essential methodology of the laminating techniques invented in California in the 1960s. This was proved to be the best method to manufacture the roof leaves for the deMenil museum project in 1985 and subsequently for the manufacture of sewer lining systems and pontoons.

So why does the spray and laminating technology produce the best in quality ferrocement?

- 1) Firstly, the mixing of mortar in a positive displacement mixing machine and then passing that mortar through a mono type pump is almost self-controlling.
- 2) A ferrocement mortar mix of 2 to 1 sand/cement ratio of plastering sand and cement with the appropriate plasticizers, produces a mortar with <.40 water cement ratio which can be pumped through a pipe and sprayed.
- 3) Using flat sheet reinforcements of expanded metal and flat sheets of reinforcing meshes is the most efficient way of handling the reinforcing materials and placing them into a plastic (wet) mortar.
- 4) There is no need to roll out and flatten rolls of small mesh materials and there is no need to wire together the small meshes to an armature.
- 5) There is no need to work by hand plastering to force mortar into an armature and worry about the correct penetration and total encapsulation of the wires.
- 6) The spray and laminating technology can be used for both vertical walls and horizontal casting.
- 7) The spraying of mortar produces excellent compaction against the mold surface. Thus replicating the features of that mold surface when demolded.
- 8) The spraying process drives out any excess moisture and therefore delivers an excellent low water-cement ratio with good compaction at the mold surface. This also provides the impermeable 'gel coat'.
- 9) Surface cracking is controlled by two layers of expanded metal which is set next to the gel coating. These three layers - of gel coat plus expanded metals (1) and expanded metals (2) provides an impermeable barrier with crack control and yet might also be regarded as a 'sacrificial layer' protecting the subsequent layers of reinforcements.
- 10) IMPORTANT – Expanded Metal meshes dissipate surface cracking whereas round wire meshes of a square welded mesh concentrate cracks along the wires.
- 11) IMPORTANT - These three layers of super quality ferrocement - forming the first 8 - 10mm of the section are the essential barrier to chloride penetration and crack control.

If the surface of 'gel coat' is damaged and corrosion starts to form on the bare metal where expanded metal is sheared in manufacturing, the oxidation is minimal and is restricted to the cut ends of the sheared metal. The sheet metal used to manufacture the expanded metal is galvanized.

"The process of oxidation (rusting) of the fine wire ends of expanded metal sheeting is never stronger than the surrounding matrix of quality mortar so 'spalling' as known in normal poor concrete work, does not occur in this type of quality ferrocement. In fact, the slight expansion

of fine wire oxidation actually 'tightens' the matrix in the area and further oxidation is prevented. Thus the 'gellcoat' and expanded metal crack control form a perfect protective layer.

12) The placing of 'steel reinforcement' closer to the outside of any element cross section and away from the 'neutral' axis provides a more efficient use of steel.[2]

GRENFELL TOWER.

We are all familiar with the tragedy of the Grenfell Tower and it stands today scaffolded and sheeted up with a Public Enquiry at a standstill, police conducting surveys, engineers writing structural reports and so on Government makes commitments it cant keep and the Friends of Grenfell Organisation despair. What will happen? Do they want demolition or development? Do they want a blank space as a memorial or a more fitting and lasting memorial?

It is the author's opinion that the tower can stand, as it is, for any many years. It is a fire damaged concrete structure which can be repaired and it is the Friends of Grenfell and the Government 50/50 who will soon have to decide a course of action.

In the meantime let us consider the application of new technologies and a new business plan for Grenfell and the community. Let us look at the cost/benefits of a redevelopment to restore the tower as an example of modern architectural practise. Sustainable, Green, Eco and user friendly, all the things it was not before that terrible fire.

The author suggests the application of laminated ferrocement and High Tensile Laminated Ferrocement could alter opinions and costs to help determine the future of the tower. Innovative ferrocement construction systems could strengthen and improve the tower's structure together with changing the plan areas of the tower and the façade. The tower could be adopted by a charitable foundation for the overall benefit of the community and the demonstration of much better design and engineering for the construction industry so that it might lift its head from this disaster. Imagine a Green Tower, Three Lift shafts, roof lawns and green vegetation growing from the balconies. It can be done.

CELLULAR CONCRETE

Sometimes called lightweight concrete because it can be made in various densities. It can be mixed and pumped by small machines.

In Grenfell Tower one of the main causes of the spread of flame up and across the tower was the 'Trench Effect', Coanda Effect and ' Flashover, because the void left between the insulating panels and the main structure created a chimney effect. There were inadequate fire breaks and the void acted like a chimney to draw fire up and across the building. This would not have happened if there was no void to cause the chimney effect. With a small flame, chimney effect (150 mm and 50 mm air gaps) and polyisocyanurate insulation, no wonder the flames spread.

There are many tower blocks which require the removal of cladding similar to that of Grenfell Tower but this may not be necessary if the ' void ' between the cladding, the insulation materials and the concrete structure were filled with cellular concrete. The cellular concrete of appropriate density can be pumped and injected into the voids so as to prevent the 'chimney effect'. Cellular concrete is fire proof and also forms an insulation.

At the moment many structures are still being clad with various materials - leaving a void. At the same time some structures are being stripped of materials which no longer comply but this work might not be necessary if the voids were injected with cellular concrete. Some R and D work is required together with demonstration.

NOTRE DAME CATHEDRAL.

It is possible to replicate the timbers of the Notre Dame roof in ferrocement - a non-combustible material. It is possible to replicate the lead work of the original roof timbers in ferrocement - a non-combustible material.

The author is competent to demonstrate the methods of manufacturing to replicate the large timber beams as shown in the picture of the roof underdrawing. These can be manufactured to the same strength and density of the original Oak timbers.

Subject to some prototype and R and D work, the roof of Notre Dame Cathedral can be replicated in ferrocement.

The black and white drawings illustrate how ferrocement cement reinforcements can be formed into box sections for the beams and into sheet panels simulating a lead roof. The picture of an imprinted concrete drive shows the 'lead effect' that it is possible to create. By moulding and texturing and colouring techniques, all accepted concrete practice, it is possible to replicate the appearance of Oak Timbers and Lead Roofs. By these means it will be possible to replicate the roof of Notre Dame in non-combustible materials which look like the original.

An article appeared in the July 30TH *Times* arts section with recent reports that the French Authorities are seeking to replicate the roof of the cathedral as near as possible to the original. Legislation has been introduced by the French Parliament to favour this approach. To find sufficient large sections of Oak Timbers today is almost impossible.

Where in Europe are we to find 13,000 large Oak Trees and who would permit the felling of these trees?

Using ferrocement and well established concrete manufacturing techniques a replication of the Notre Dame Cathedral roof is possible.



Figure 7 This picture shows an imprinted concrete drive with a 'lead look' finish. This colour can be replicated in a ferrocement long tile to simulate a lead roof of a Church or Cathedral.



Figure 8 This is the under-drawing of the Notre Dame Roof before the fire. It can be replicated in ferrocement to give the same appearance, density and strength as the original oak roof timbers.

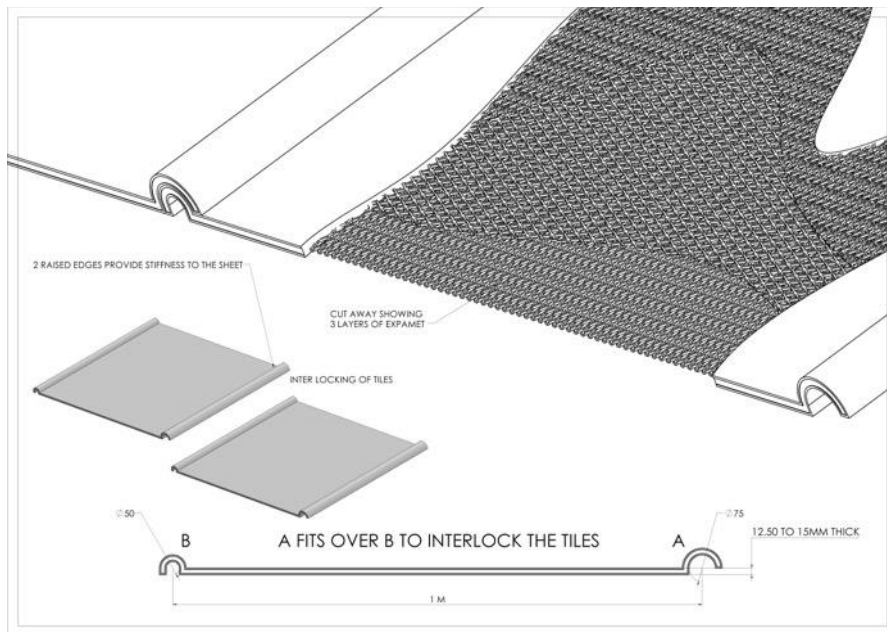


Figure 9 This drawing illustrates a panel of simulated lead roofing made of ferrocement in three layers of expanded metal about 20mm thick. It will have a lead effect in appearance.

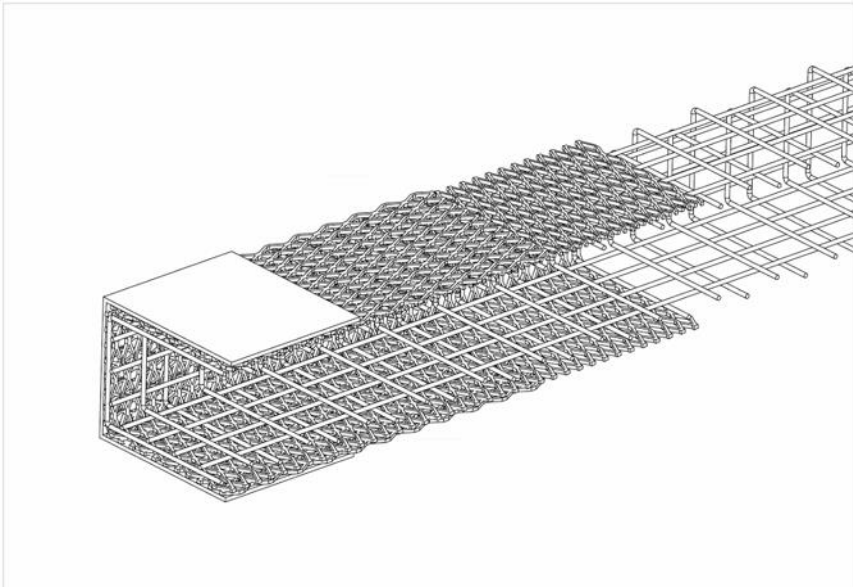


Figure 10 This drawing shows the ferrocement reinforcements in a box to replicate an oak beam. Colours and Texture by known techniques will produce replica beams. The box section may be filled with a lightweight and none combustible cellular concrete.

SUSTAINABILITY.ORG

This is the name of a charitable organisation proposed by the author and suggested that initial support from Leeds Civic Trust and Leeds University who will eventually be endowed by the Charity from licence and publication rights.

Various construction industry organisations and institutions will be asked to support the Charity.

The Objective is for the charity to hold the Intellectual Property and knowledge of the author and his colleagues for the future benefit (i.e. endowment) to the Leeds Civic Trust and Leeds University and the further promotion of education about ferrocement and its potentials for the construction industry. The charity will encourage sustainable construction methods and licence technology to those businesses who choose to adopt the spraying and laminating technologies together with the development of High Tensile Laminated Ferrocement and the use of 'super quality sprayed mortars'.

The application of Silica Fume and Graphene to produce nano-concrete will be adopted.

These 'super concrete' technologies are under constant development to produce exceptional material strengths. This is the future for ferrocement.

The application of alternative binders and "Green" cements will be promoted together with aspirations to transfer technology under licence to the developing world.

The charity objectives are to promote Ferrocement and the author's three audacious "Dunkirk" projects.

Why are they called Dunkirk Projects?

Because each project presently represents a 'dead loss' to UK tax payers and an embarrassment to our UK construction industry. The application of 'innovative and disruptive' construction technologies and new business models can reverse disasters into a new and sustainable business.

You cannot have sustainability without profitability.

Pallion Shipyard, London Garden Bridge (SUSTAINABILITY BRIDGE) and Grenfell Tower project.

Detailed explanations of SUSTAINABILITY business plans are omitted.
This paper relates to the engineers fire spalling workshop 2019 and the application of ferrocement to three major UK construction industry opportunities.
Grenfell Tower and Notre Dame Roof and Void filling of existing cladding systems.
The author suggests the answers lie in the application of ferrocement and cellular concrete.
There is still much 'kicking of the can down the road' until the can stops and decisions are made.
Re the Garden Bridge. The Charity Commission finally winds up the London Garden Bridge Trust by giving its 'residuals' to another charity.
Re the Grenfell Tower. Decisions are made to either demolish or redevelop the site.
The author's proposals have been expressed in this paper.

FURTHER READING ON FERROCEMENT

Pemberton. J.M.

Ferro-Past and Ferro- Future. Proceedings of the 11th International Symposium on Ferrocement, Aachen, Germany. 7th- 10th June. 2015.
deMenil Museum Project and Potential Applications of Ferrocement/Concrete Laminates.
Ferro 5. International Symposium on Ferrocement, Manchester 6 - 9th of September 1994.
"Ferrocement – an insight and a review – So what is new" 6th International Symposium on Ferrocement. University of Michigan, Ann Arbor, June 1998.

Naaman, Antoine. E.

'Ferrocement and Laminated Cementitious Composites'. 1st Ed ISBN: 0-9674939-0-0(2000)

Ions. M.E.

"Shotcrete Laminating-an improved ferrocement construction technique". Ferro 1 Nervi International Symposium on ferrocement July 22 24th. 1981.

REFERENCES

1. Concrete Society Technical Report 15 (1978)
2. A C I Committee 549 State of the art a report on ferrocement 549-R97

Experimental and numerical study of the influence of the PP fiber diameter on spalling behaviour of concrete

Fariza Sultangaliyeva^{1*}, Chhainan Leang², H  l  ne Carr  ¹, Christian La Borderie¹, Nicolas Roussel³

¹ SIAME, Universit   de Pau et des Pays de l'Adour, Anglet, France

² INSA Rennes, Rennes, France

³ IFSTTAR, Champs-sur-Marne, France

* Corresponding author (fariza.sultangaliyeva@univ-pau.fr,
1 All  e du Parc Montaury, 64600 Anglet, France)

ABSTRACT

In this work, the influence of diameter of polypropylene (PP) fiber on the spalling of concrete was studied. Concrete prisms of 20 x 20 x 10 cm³ containing 2 different diameters of fibers (32 and 20   m) were tested under ISO 834-1 fire curve. In addition to this, tests of residual radial permeability to nitrogen were performed for the same mixes after heating to 80, 150 and 200   C. Following this, numerical simulations using thermo-mechanical model were performed in order to investigate the influence of the PP fiber diameter on the damage behaviour of cementitious materials. The expansion of fibers during heating can be sufficient for a formation of cracks around the fibers which can increase the permeability and then reduce the risk of concrete instability. The simulations are performed using finite-element code developed in Cast3M. The work carried out made it possible to investigate the influence of PP fiber diameter on the concrete exposed to a high temperature.

KEYWORD: Polypropylene Fiber, Damage, Fiber Diameter, Fire Tests, Simulation.

INTRODUCTION

Polypropylene fibers are used to counteract the thermo-hydric mechanism of spalling through the increase of the permeability of heated concrete by creation of additional vapor channels when polypropylene is melted. Current literature presents the influence of the PP fiber diameter for the same volume of fibers. Consequently, for the same fiber volume slender fibers have a higher number of fibers compared to thicker ones. For example, in [1] 28   m fibers had the highest increase in permeability compared to 32   m fibers (L= 6mm). For the same fiber volume the number of fibers was 3.2 times higher for slender fibers. In [2], addition of 0.68 kg/m³ of 18   m fibers was as effective as 1.2 kg/m³ of 32   m fiber in terms of spalling prevention. Knack [3] has concluded on the efficiency of a finer cross section of fibers over a larger one based on the total number of fibers. In [4], samples containing two fiber diameters of 20 and 40   m at the same number of fibers were tested for spalling extent. It was noted that regardless a diameter, when 133/cm³ was reached, spalling was prevented.

In this study, the influence of PP fiber is evaluated using fire tests on concrete prisms and residual radial permeability tests to nitrogen on hollow cylinders. Two fiber diameters were studied at two fiber dosages that were fixed to same total number (and total length)

of fibers. To complete the study, numerical simulations of PP fiber were conducted as well.

EXPERIMENTAL STUDY

Concrete mixes

Concrete samples with $w/c=0.4$ were prepared using cement CEM III/A 52.5 L CE from Eqiom, Heming. The contents of clinker and of ground granulated furnace slag were 35 and 61 % respectively. The information about the concrete mixes is presented in Table 1. The aggregate skeleton constitutes of 60% of siliceous sand 0/1 and 40% of calcareous gravel 6.3/10. A size of the gravel 6.3/10 was obtained through screening and sieving of gravel 4/10. The aggregates were dried in oven at 80 °C for 24 hours and cooled to a room temperature prior to casting. PP fibers used in this study were monofilament polypropylene fibers from Baumhüter. Two fiber geometries $L = 12 \text{ mm}$, $D = 32 \mu\text{m}$ and $L = 12\text{mm}$, $D = 20 \mu\text{m}$ were used. Fiber dosages were fixed to obtain the same total length (and total number), i.e. 683 and 1366 km/m^3 . Therefore, for fibers of 12/32 (L/D) this has resulted in two fiber dosages of 0.50 and 1.00 kg/m^3 , while for 12/20 fibers- in 0.20 and 0.39 kg/m^3 .

The example of the mix reading (see Table 1): C1-12/20-0.2 stands for concrete with PP fibers of length of 12 mm and diameter of 20 μm with a dosage of 0.20 kg/m^3 .

Table 1 Information about concrete mixes studied*.

	Unity	C1-0	C1-12/32-0.5	C1-12/32-1	C1-12/20-0.2	C1-12/20-0.4
Cement CEM III/A 52.5 - Eqiom	kg/m^3			500		
Water	kg/m^3			200		
Siliceous filler - Sibelco	kg/m^3			120		
Siliceous sand 0/1 - Messanges	kg/m^3			623		
Gravel 6.3/10 - Sare	kg/m^3			945		
PP fibers 12/32 - Baumhüter	kg/m^3		0.50	1.00		
PP fibers 12/20 - Baumhüter	kg/m^3				0.20	0.39
SP - SIKA Krono 26	kg/m^3			3.75		
w/c ratio	-			0.4		
Slump flow	mm	809	830	792	843	764
$f_{c,cyl}$ at 28 days	MPa			90.1 ± 5.3		
Water content	%	4.24	5.14	5.40	5.23	4.40

* The expressed values are theoretical, the real density of fresh concrete was not taken into account.

The samples were cast and demolded after 24 hours and placed in the water for 59 days. The compressive strength was measured on three cylinders 11 x 22 cm^2 of C1-0 only.

Fire test

The fire tests were conducted using gas furnace (see Figure 1) on loaded prismatic samples of 20 x 20 x 10 cm^3 . All the samples were tested in water saturation condition. The fire curve was the standard fire curve ISO 834-1 with a duration of 30 minutes. Temperature was tracked by three K-type thermocouples installed 1 cm from heated face and 4, 10 and 16 cm from the bottom of the furnace opening (see Figure 1). A uniaxial loading of 5 MPa was applied before test and maintained throughout the test. One face of the sample was heated, area exposed to fire was 20 x 20 cm^2 . The lateral sides of the sample were insulated with aluminium foil glued with a high temperature resistant glue.

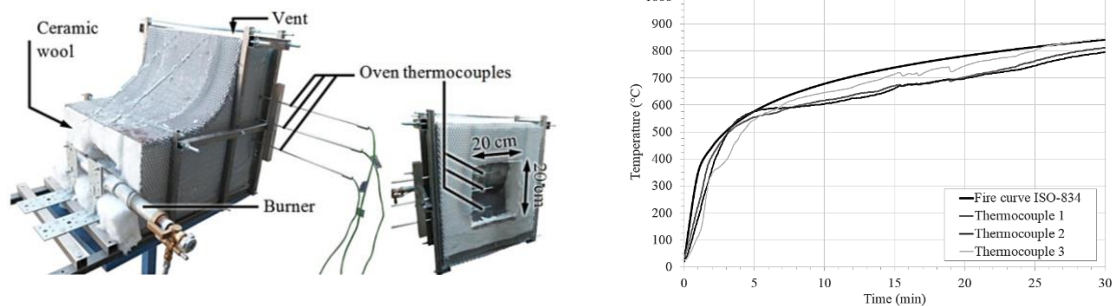


Figure 1 Gas furnace [5] and ISO 834-1 followed by thermocouples.

The sample was placed between two fiber-reinforced concrete samples for mechanical load distribution. The sides of the setup were insulated by 12 cm of rock wool. The opening of the gas furnace was located in front the sample and gas was burned. When the test was finished, the spalling depth of the sample was measured by means of photogrammetry. The error from photogrammetry is calculated to be 4.2 %.

Residual radial permeability to nitrogen

Residual radial permeability to nitrogen was performed after heating-cooling cycle on hollow cylinders. The samples were double cored from cubes of $15 \times 15 \times 15 \text{ cm}^3$. Top and bottom surfaces were grinded to ensure flatness and parallelism. Dimensions of the final sample are: outer and inner radius R_1 and R_2 of 5.50 and 2.85 cm accordingly with a height of 14 cm. Before start of the test, the samples were dried at 80°C until mass stabilization. The sample is considered dry when the difference between the two consecutive daily mass loss measurements is less than or equal to 0.02% of the mass of the dry sample. Drying of samples was accomplished in order to evaporate free water without provoking a change in the microstructure.

The measurements are performed on the cooled samples that were heated to 80, 150 and 200°C . The heating rate of the samples was fixed to $1^\circ\text{C}/\text{min}$ in order to avoid creation of significant thermal stresses. After reaching a required temperature, the stabilization time of 3 hours was set to ensure uniformity of temperature across the sample. Cooling of samples was performed in the furnace with an estimated rate of $1^\circ\text{C}/\text{min}$.

The setup for the measurement of the radial permeability is shown in Figure 2. Before each permeability test, steel inox plates were glued on the top and on the bottom surfaces of the sample to prevent gas leakage. The bottom plate has a borehole to which a connector for the gas flow with a tube are fixed. The sample with metal plates is placed on the top of the support sample. A support sample is a hollow cylinder $11 \times 22 \text{ cm}^2$ that is used to pass the tube that supplies gas. The test sample and the support sample are placed between two plates of press. A constant uniaxial compressive load is applied in order to counteract the injection pressure.

Nitrogen is injected with injection pressure P_i through the borehole. The flow rate of gas is measured using the mass flow meters that is then converted into volume flow rate. Depending on the flow rate, the flow meter for the measurement is selected. Pressure and temperature are recorded. The flow rate is recorded when the gas flow stabilization is achieved. Then, another injection pressure is applied and the same procedure is repeated. In this study a steady-state flow of the gas is considered.

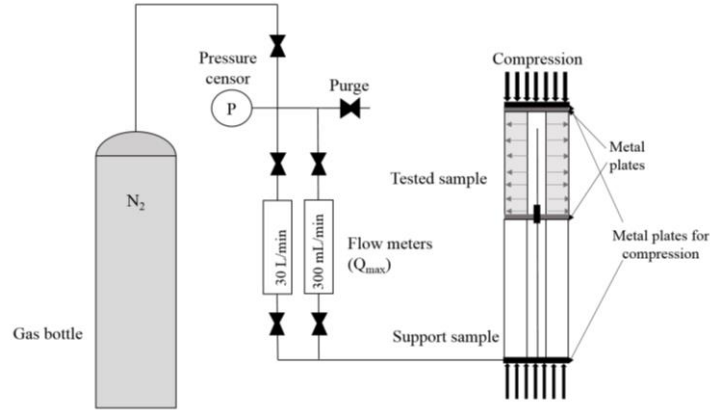


Figure 2 Schematic representation of radial permeability setup.

We can then compute the apparent permeability K_a (m^2) derived from Darcy's law for the laminar flow of compressible gas [6] using Eq.(1).

$$K_a = \frac{Q_i P_i \mu \ln \left(\frac{R_1}{R_2} \right)}{\pi H (P_i^2 - P_{atm}^2)} \quad (1)$$

where Q_i is the flow rate (m^3/s), P_i is the injection pressure (Pa), μ is the dynamic viscosity of gas (Pa.s), R_1 is the outer radius of the sample (m), R_2 is the inner radius of the sample (m), H is the sample height (m), P_{atm} is the atmospheric pressure (Pa).

We compute intrinsic permeability of the material K_i (m^2) by using Klinkenberg's method (see Eq.(2)) that would allow considering viscous flow only [7].

$$K_a = K_i \left(1 + \frac{\beta}{P_m} \right) \quad (2)$$

where β is Klinkenberg's coefficient, P_m is mean pressure. The mean pressure is computed as $P_m = (P_i + P_{atm})/2$.

We measure radial permeability at five different injection pressures: 1, 1.5, 2, 2.5 and 3 bars. The values of apparent permeability are plotted as a function of mean inverse pressure $1/P_m$. The intrinsic permeability is then found at the intersection of the line traced from apparent permeability measurements done at various injection pressures with apparent permeability axis.

EXPERIMENTAL RESULTS

Fire tests results

The results for the spalling tests such as mean, maximum spalling depth as well as spalled volume were obtained by the means of photogrammetry. A linear relationship between mean spalling depth, maximum spalling depth and spalled volume was observed; therefore, in Figure 3 we present mean spalling depth results only. It should be noted that for the same total length of fibers we have the same total number of fibers as the fiber length is 12 mm. For each of the mix three samples were tested. The average values are shown with a cross sign.

For non-fibred samples C1-0, mean spalling depth varied between 0.23 and 1.61 cm with an average value of 1.04 cm. As fiber dosage was increased from 0 to 0.5 kg/m^3 for samples C1-12/32-0.5 and from 0 to 0.2 kg/m^3 for samples C1-12/20-0.2 resulting in total

fiber length of 686 km/ m³, mean spalling depth has decreased for both materials to 0.26 and 0.58 cm respectively.

An increase of the dosage from 0.5 kg/m³ and 1 kg/m³ had almost no effect for concrete with 32 μm PP fibers. However, for 20 μm fibers mean spalling depth has decreased passing from 0.2 to 0.4 kg/m³. It is interesting to note that at the total length of fibers of 1366 km/m³ the values for mean spalling depth for both 32 μm and 12 μm PP fibers almost coincide. The results show that at lower dosage larger fibers are more efficient than thinner ones. However, as we increase the dosage, almost no difference in terms of the influence of fiber diameter on spalling is observed.

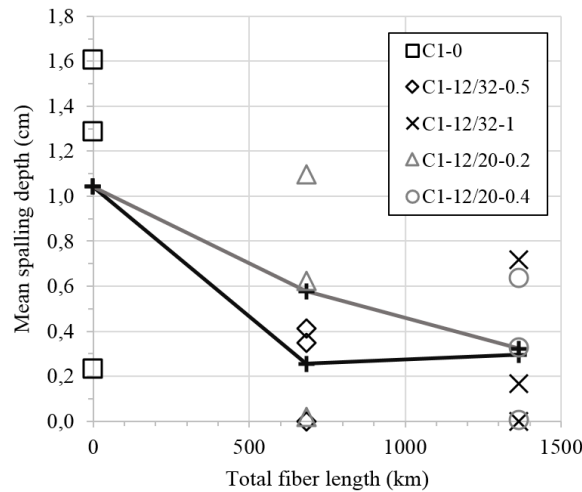


Figure 3 Mean spalling depth for tested concrete mixes.

Residual permeability results

The evolution of the intrinsic permeability with a temperature was obtained for all concrete mixes (see Figure 4). Two samples were tested for each mix. The values presented are the average ones, the error bar gives the range of the data. The maximum total error including the measurement error and eccentricity error due to coring is 4%. All the values of the intrinsic permeability for non-fibred and fibrous materials are low, the order of values is 10⁻¹⁷-10⁻¹⁸ m².

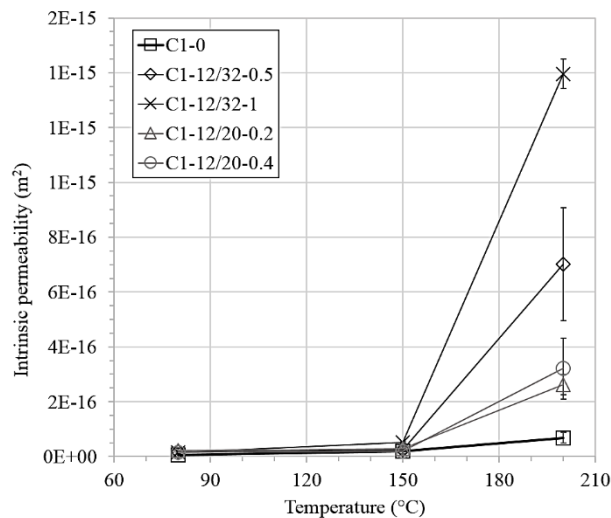


Figure 4 Intrinsic permeability evolution with temperature for tested concrete mixes.

Figure 4 shows an increase of the intrinsic permeability of concrete with the temperature. The increase of the permeability between 80 and 150 °C is 4.4 times for non-fibred C1-0 and 1.3 to 3.5 times for fibrous mixes. At 150 °C, PP fibers have not melted yet, thus, no substantial increase in the permeability should be observed. In [8], a significant increase of the permeability is observed starting 130 °C even before the melting of PP fibers. The authors have explained this phenomena by the loss of the thermal stability of polypropylene that creates the cavities between matrix and fiber before its melting. In [9], the increase of the permeability was linked to cracking caused by a high difference of linear coefficients of thermal expansion of concrete and polypropylene.

From Figure 4 at 200 °C, significant increase in the intrinsic permeability for all the materials is observed. A part of the increase of the permeability is attributed to the thermal mismatch between aggregates and cement paste. Starting from 150 °C, a dehydration of cement paste causes its shrinkage whereas aggregates constantly expand [10]. For fiber reinforced materials, drastic increase of the intrinsic permeability is noted. For concrete with 32 µm fibers there is a remarkable increase of the permeability with the increase of the dosage of PP fiber: 40 and 952 times the initial permeability for 0.5 and 1 kg/m³ of fibers. For the concrete with 20 µm fibers, the increase of the permeability is less significant: 12 and 18 times the initial permeability for dosages of 0.2 and 0.4 kg/m³.

The dosage of 0.5 kg/m³ of 32 µm fibers was efficient for a significant reduction of spalling extent compared to 0.2 kg/m³ of 20 µm fibers. This is linked to the fact that 32 µm fibers provoke a higher increase in the permeability compared to 20 µm fibers. The results show that for fully saturated concrete samples, the beneficial influence of PP fibers in terms of permeability increase is not sufficient for total elimination of spalling phenomenon.

NUMERICAL STUDY

Material properties

- Polypropylene

PP fibers are used for a prevention of concrete spalling due to fire based on their ability to melt at relatively low temperature, to flow into cracks and pores and to leave the empty channels that serve for vapor escape. In general, melting of PP starts at 150 °C, peaks at 165 °C and ends around 176 °C [11]. During that stage, PP, a semi-crystalline material, undergoes a phase change: its crystalline phase is destroyed and turned into amorphous one. Mechanical properties of polymers are linked to the crystallinity, the destruction of latter will lead to the decrease in former. PP has an elastic modulus of 1100 MPa at 20 °C as seen in Figure 5A [12]. As material is heated, it's elastic modulus decreases and eventually drops to zero at the melted state.

PP as a bulk material is isotropic. Manufacturing process of PP fibers (extrusion and injection molding) imposes anisotropy on fibers. When fibres are heated, the energy introduced into the system releases the imposed stresses and allows for the rearrangement of molecules in the preferential orientation leading to anisotropic volume change. This change is characterized by the contraction in length and expansion in thickness. At 20 °C the density of PP is 910 kg/m³ and in melted state - 850 kg/m³ [11, 12] resulting in 7 % volume expansion [11]. It is important to precise that in our calculations we consider isotropic behaviour of fibers. The evolution of the coefficient of thermal expansion (CTE) of PP is presented in Figure 5B [14]. Similar values are observed in [13], where the linear CTE for PP is given as $1 \times 10^{-5} / ^\circ\text{C}$ for $T = 20 - 60$ °C, $15 \times 10^{-5} / ^\circ\text{C}$ for $T = 60 - 100$ °C and $21 \times 10^{-5} / ^\circ\text{C}$ for $T = 100 - 140$ °C. In Figure 5B [14],

the CTE of PP skyrockets around 160 °C due to expansion linked to phase transition. When polypropylene has melted, the shrinkage due to thermal contraction as well as the compressibility of the melted material occurs.

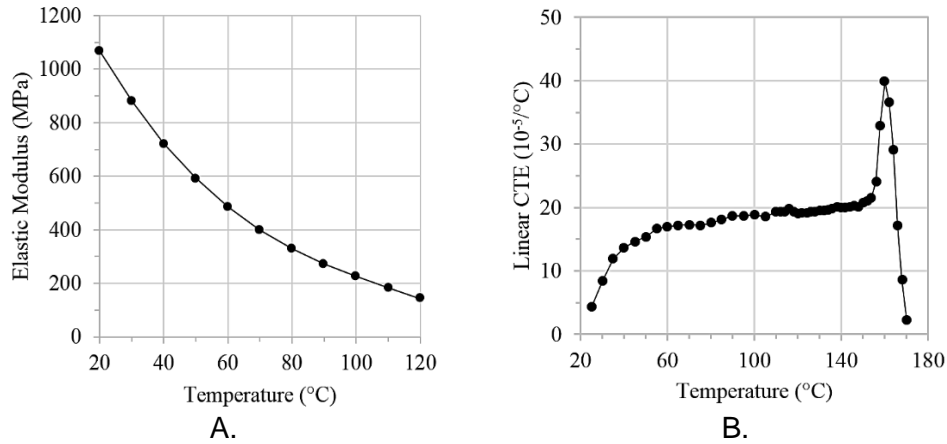


Figure 5 Evolution of the properties of polypropylene with temperature (A): elastic modulus (adapted from [12]), (B): linear coefficient of thermal expansion with temperature for polypropylene (adapted from [14])

Poisson ratio of polypropylene at 20 °C is 0.42 [12]. As polypropylene passes from the semi-crystalline material to completely amorphous rubbery material, our hypothesis is that its Poisson's ratio is close to the rubber (=0.49) in melted state.

- Mortar

Experimentally determined evolution of mortar properties with a temperature is presented in Table 2. Poisson's ratio is considered constant (= 0.2).

Table 2 Evolution of density, CTE, elastic modulus, tensile strength, fracture energy with temperature for mortar.

Temperature (°C)	Density (kg/m ³)	CTE (10 ⁻⁵ /°C)	Elastic modulus (MPa)	Tensile strength (MPa)	Fracture energy (J/m ²)
20	2300	1	15	4	40
120	2297	1.3	10	3.2	47
250	2254	1.5	10	3.48	69
400	2185	1.5	6	3.36	71
600	2145	1.5	2	2.4	122

Numerical model

Thermo-mechanical (TM) computations are accomplished in Cast3M. In terms of thermal conditions, the evolution of the temperature is imposed, no heat transfer is performed. For mechanical model, an improved elasto-plastic damage model named 'microiso' is used. This computational model is based on the continuum damage mechanics of [15] and takes into account fracture energy [16].

From continuum mechanics, the relationship between total stress and effective stress is:

$$\tilde{\sigma}_{ij} = C_{ijkl}^0 \varepsilon_{kl} = C_{ijkl}^0 (C^{endom})_{klmn}^{-1} \sigma_{mn} \quad (3)$$

where $\tilde{\sigma}_{ij}$ is effective stress, σ is total stress, C_{ijkl}^0 is rigidity of undamaged material,

C_{ijkl}^{endom} is rigidity of damaged material.

An evolution law for damage variable is determined [16]:

$$d = 1 - \frac{\varepsilon_{d0}}{\varepsilon} \exp [B(\varepsilon_{d0} - \varepsilon)] \quad (4)$$

where ε_{d0} is threshold for damage, ε is deformation and B is slope of softening curve defined by exponential expression.

Damage threshold is computed as:

$$\varepsilon_{d0} = \frac{f_t}{E} \quad (5)$$

where f_t is tensile strength, E is elastic modulus.

Evolution parameter B is given as:

$$B = \frac{f_t}{G_f} \quad (6)$$

where G_f is fracture energy.

3D TM calculations on the quarter of the cylinder were accomplished. Fiber was placed in the center, radius of concrete modelled around the fiber was 1 mm. The displacement of the upper face of the quarter of the cylinder is equal for both fiber and mortar. This does not correspond neither to plain stresses nor to plain strains. For this reason, 3D calculations were completed.

NUMERICAL RESULTS

Two fiber diameters were modelled: 20 and 32 μm . Temperature was increased from 20 to 220 $^{\circ}\text{C}$. The results of the damage of mortar (damage is greater than 0.94) at 220 $^{\circ}\text{C}$ for two fiber diameters are presented in Figure 6. The results show that damage radius increases with the diameter of the fiber. To compare, at 220 $^{\circ}\text{C}$, damage radius for mortar with 32 μm fiber is 40 μm compared to 24 μm for 20 μm fiber.

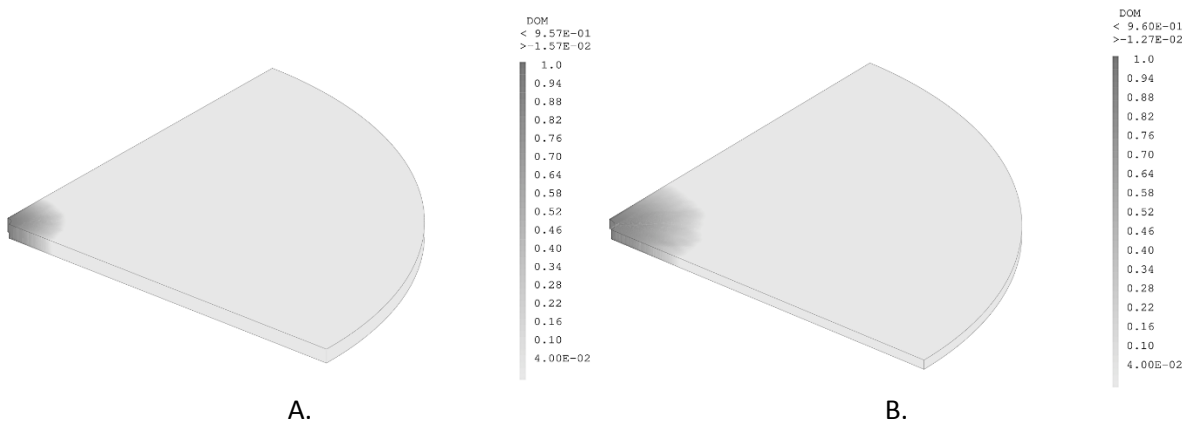


Figure 6 Damage of mortar at 220 $^{\circ}\text{C}$ for fiber diameter (A): $D = 20 \mu\text{m}$, (B) $D = 32 \mu\text{m}$.

In Figure 7, the evolution of the damage radius with temperature for 20 μm and 32 μm fibers is shown. First, it is notable that the damage increases with temperature. A slight damage appears at 45 $^{\circ}\text{C}$ and its value increases till 115 $^{\circ}\text{C}$. Thermal deformations occur due to the increase of the CTE of polypropylene with temperature. Then, no evolution of damage is

observed between 110 and 155 °C. A sudden increase of the damage radius at 155 °C is linked to the expansion of the fibre provoked by its phase change. After this temperature, the value of the CTE of polypropylene decreases and no evolution of damage is observed. The results contradict the findings in [9], which observe the cracking appear at 105 °C.

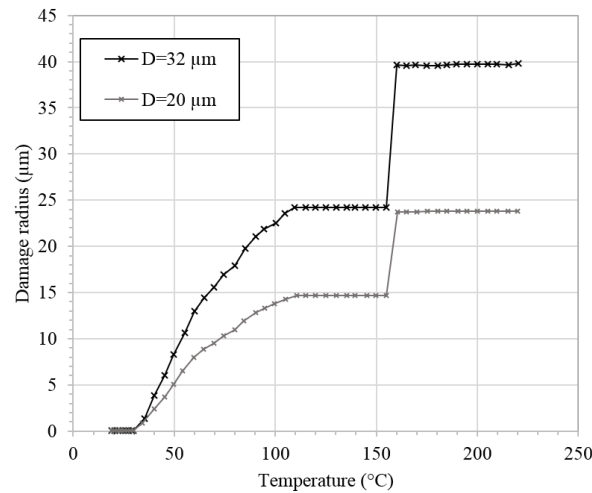


Figure 7 Evolution of the mortar damage radius with temperature for two fiber diameters.

DISCUSSION

Experimental and numerical studies show the existence of the effect of the PP fiber diameter on the behaviour of the fiber-reinforced concrete at high-temperature. From spalling tests on water saturated samples, at dosage of 0.5 kg/m³ efficiency of 32 μm fibers over fibers of 0.2 kg/m³ of 20 μm is observed. At 0.4 kg/m³, spalling depth for 20 μm decreases but for 32 μm fibers at 1 kg/m³ remains the same as at 0.5 kg/m³. Permeability tests show that concrete with 32 μm fibers has a higher permeability compared to concrete with 20 μm fibers. From numerical simulations, it is clear that fibers can induce damage due to a high CTE at temperatures close to their melting point. The damage zone increases with temperature and reaches its maximum value during phase transition. Calculations show that damage radius increases with fiber diameter.

Permeability increases significantly with damage of the material [6]. Therefore, at high temperature expansion of larger fibers introduces damage that affects a larger zone around the fiber which improves percolation of cracks and pores leading to a higher increase of permeability. Consequently, increase of permeability may lead to pore pressure drop and reduction of spalling.

CONCLUSIONS

In this paper, we have examined the influence of PP fiber on the behaviour of concrete at high temperature. Two fiber diameters were examined (20 and 32 μm), the dosage of fibers was fixed to obtain the same total number and total length (fiber lengths are the same: 12 mm). Fire tests performed on water saturated samples show that at dosage of 0.5 kg/m³, fibers of 32 μm are more efficient than 20 μm. Residual radial permeability tests show a significant increase for 32 μm fiber compared to 20 μm for two fiber dosages. The results are explained by numerical simulations that show that the damage radius around the fiber increases with fiber diameter. The damage zone increase induces improved percolation, higher permeability and reduced spalling risk.

ACKNOWLEDGEMENTS

The authors would like to acknowledge that this work is carried out using the financial assistance from the program of the Investments for the Future of the French government managed by ANDRA.

REFERENCES

1. Lu, F. and Fontana, M, "Effects of Polypropylene Fibers on Preventing Concrete Spalling in Fire", Proceedings of the 9th International Conference on Structure in Fire SiF' 16, Princeton, USA, 8-10 June, 2016.
2. Maluk, C., Bisby, L. and Terrasi, G. P., "Effects of polypropylene fibre type and dose on the propensity for heat-induced concrete spalling", *Engineering Structures*, **41**, 584-595, 2017.
3. Knack, I., "New pp-fibre with exceptional melting characteristics for improved fire protection in concrete building", Proceedings of the 1st International Workshop on Concrete Spalling due to Fire Exposure, 238-247, Leipzig, Germany, 3-5 September, 2009.
4. Heo, Y.-S., Sanjayan, J.G., Han, C-G., Han, M.-C., " Limited effect of diameter of fibres on spalling protection of concrete in fire", *Materials and Structures*, **45**, 325-335, 2012.
5. Miah, Md. J., Carré, H., Pimienta, P., Pinoteau, N. and La Borderie, C., "Effect of uniaxial mechanical loading on fire spalling of concrete", Proceedings of the 4th International Workshop on Concrete Spalling due to Fire Exposure, 124-131, Leipzig, Germany, 8-9 October, 2015.
6. Choinska, M., "Effets de la température, du chargement mécanique et de leurs interactions sur la perméabilité du béton de structure" (in French), PhD Thesis, Ecole Centrale de Nantes et l'Université de Nantes, Nantes, France, 2014.
7. Klinkenberg, L.J., "The permeability of porous media to liquid and gases", *Drilling and Production Practice*, 200-213, 1941.
8. Bošnjak, J., Ožbolt, J., Hahn, R., " Permeability measurement on high strength concrete without and with polypropylene fibers at elevated temperatures using a new test setup", *Cement and Concrete Research*, **53**, 104-111, 2013.
9. Zhang, D., Dasari, A., Tan, K.H., "On the mechanism of prevention of explosive spalling in ultra-high performance concrete with polymer fibers", *Cement and Concrete Research*, **113**, 169-177, 2018.
10. Bazant, Z.P. and Kaplan, M.F., "Concrete at High Temperatures: Material Properties and Mathematical Models", Pearson Education, 1996.
11. Khoury, G.A., and Willoughby, B., "Polypropylene fibres in heated concrete. Part I: Molecular structure and materials behaviour", *Magazine of Concrete Research*, **60**, 125-136, 2008.
12. Maier, C., and Calafut, T., "Polypropylene: The Definitive User's Guide and Databook", William Andrew, 1998.
13. Tripathi, D, "Practical Guide to Polypropylene", Smithers Rapra, Shrewsbury, United Kingdom Publishing, 2002.
14. Kanapitsas, A., Tsonos, C., Pandis, C., Pissis, P., Kontou, E., Mamunya, Y.P., Lebedev, E.V. and Delides, C.G., " PTC Effect and Structure of Polymer Composites Based on Polypropylene/Co-Polyamide Blend Filled with Dispersed Iron", Proceedings of the 25th International Conference on microelectronics, Belgrade, Serbia and Montenegro, 14-17 May, 2006.
15. Fichant, S., La Borderie, C. and Pjaudier-Cabot, G., "Isotropic and anisotropic description of damage in concrete structures", *Mechanics of Cohesive-frictional Materials*, **4**, 339-359, 1999.
16. Matallah, M., La Borderie, C. and Maurel, O., "A practical method to estimate crack openings in concrete structures", *International Journal for Numerical and Analytical Methods in Geomechanics*, **34**, 1615- 1633, 2010.

Experimental contribution to the optimization of the choice of polypropylene fibers in concrete for its thermal stability

Fariza Sultangaliyeva^{1*}, Bruno Fernandes¹, H  l  ne Carr  ¹, Pierre Pimienta², Christian La Borderie¹, Nicolas Roussel³

¹ SIAME, Universit   de Pau et des Pays de l'Adour, Anglet, France

² CSTB, Champs-sur-Marne, France

³ IFSTTAR, Champs-sur-Marne, France

* Corresponding author (fariza.sultangaliyeva@univ-pau.fr,
1 All  e du Parc Montaury, 64600 Anglet, France)

ABSTRACT

Numerous studies conducted by researchers have indicated a positive effect of polypropylene fibers (PP fibers) in terms of the reduction of concrete spalling due to fire. Variation of test parameters such as concrete composition, curing conditions, heating curve, aggregate nature and size, etc. creates a challenge for identification of optimal fiber dosage and geometry. The purpose of this work is to study the influence of the fiber length with respect to aggregate size in order to identify optimal fiber length necessary to prevent spalling of concrete. Prisms of cementitious materials of three aggregate sizes ($D_{max} = 1, 10$ and 20 mm) and two fiber lengths (6 and 12 mm) at three fiber dosages (0, 0.5 and 1 kg/m³) resulting in total of 15 different mixes are prepared. These prisms are uniaxially loaded at 5 MPa and tested in water saturated condition under ISO 834-1 heating curve. The results show that the maximum aggregate size has an influence on the cracking patterns of the cementitious materials exposed to high temperature. The addition of PP fibers at low dosage produces a positive influence on the reduction of concrete spalling due to fire exposure.

KEYWORD: Polypropylene Fibers, Concrete Spalling, Fiber Length, Fire Tests.

INTRODUCTION

Polypropylene fibers have become a cost-effective and efficient solution for the reduction of the risk concrete spalling due to fire exposure. Eurocode 2 EN 1992-1-2:2004 on "Design of concrete structures - Part 1-2: General rules - Structural fire design" states that for high performance concretes of class strength ranging from 80/95 to 90/105 the addition of more than 2 kg/m³ of monofilament polypropylene fibers is necessary. In French annex of the code it is specified that fiber diameter should be less than or equal to 50 μ m and fiber length should vary between D_{max} and $4D_{max}$ where D_{max} is the size of the largest aggregate.

Numerous studies attempting to optimize the polypropylene fiber geometry and dosage choice have been presented in literature. The first work on this subject by Bentz [1] provided a percolation model of ITZ (interfacial transition zones) of high performance concretes by use of PP fibers. He suggested the use of 0.2 % to 0.5 % vol. of PP fibers to achieve percolation. Debicki et al. [2] has stated that 1 kg/m³ was sufficient for prevention of spalling of high performance concrete. It was found that higher dosage of fibers results in the higher pressure drop during heating [3], [4]. Kalifa et al. [3] has

completed fire tests on samples containing fibrillated fibers of a rectangular section of $150 \times 50 \mu\text{m}^2$. He suggested a dosage of 1 kg/m^3 of 20 mm PP fibers for high performance concretes under ISO 834-1 fire curve. Bilodeau et al. [5] proposed to use 1.5 kg/m^3 for ultra-high performance concretes. Persson [6] concluded that a minimum dosage for conventional use should be around 0.7 kg/m^3 and 1.4 kg/m^3 for tunnels. Arai and Furuichi [7] found necessary to use 1.82 kg/m^3 for tunnels and railroads.

As fibers are used to ensure percolation between pores, air bubbles and cracks in the cementitious matrix, their length should be sufficient for this purpose. Therefore, it appears logical that longer fibers are preferred to shorter ones. In [5] it was shown that longer fibers of 20 mm vs. fibers of 12.5 mm have improved spalling resistance for the samples after hydrocarbon fire (dosage of 1.5 kg/m^3). For the same fiber diameter, Mugume et al. [8] has found that for 12 mm fibers gas pore pressures are lower than for 6 mm fibers. For the same dosage, Heo et al. [9] has found fibers shorter than 12 mm to be less efficient. Sideris and Manita [10] having compared fibers of 6 mm and 12 mm found the longer fibers to decrease the intrinsic permeability while Hager and Tracz [11] have compared fibers of 6, 12 and 19 mm and found that the longest fibers lead to the highest permeability increase. A relation between the size of the largest aggregate and minimal fiber length was described in Heo et al. [12]. In his work it was found that the optimum fiber length increases with the size of the aggregate.

The purpose of this work is to study the effect of fiber length and dosage on the behaviour at high temperature of different cementitious materials. A mortar and two concretes with different aggregate skeleton are studied to evaluate the efficiency of two fiber geometries with regard to spalling.

PRESENTATION OF THE STUDY

Cementitious mixes

The cement used is CEM III/A 52.5 L CE from Heming (Eqiom). Silica filler from Sibelco (99.1 % SiO_2) was used as filler. The aggregates are siliceous sand 0/1 from Messanges and two types of calcareous gravel 4/10 and 10/20 from Sare. Their particle size distribution curve are given in Figure 1A. Two types of PP fibers were used in this work; the corresponding information is given in Table 1. For flowability, superplasticizer Krono 26 from SIKA was used.

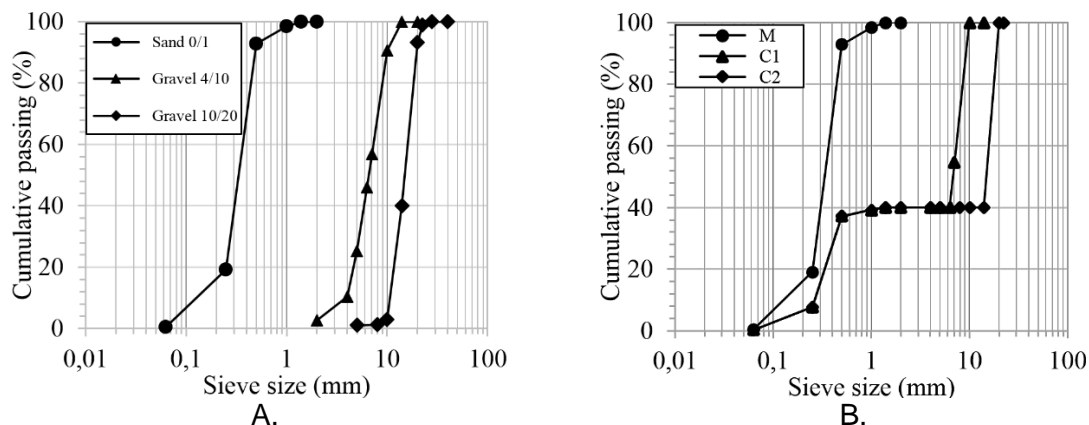


Figure 1 Particle size distribution for (A): aggregates, (B): granular mixes.

Three types of the cementitious materials are produced, their mix proportions are given in Table 2. The first is mortar (M) prepared using a sand 0/1. The second one is concrete (Concrete 1 or C1) made with a granular mix of 40 % of the sand 0/1 and 60% of the gravel 6.3/10. The third one (Concrete 2 or C2) contains a mix of 40 % of the

sand 0/1 and 60% of the gravel 14/20. The particle size distribution for granular mixes of each of the cementitious materials is given in Figure 1B. Discontinuous aggregate skeletons were chosen in order to obtain different cracking patterns. A requested size of the aggregate for concretes C1 and C2 namely sizes 6.3/10 and 14/20 were obtained by screening, passing through the sieves the aggregates 4/10 and 10/20 respectively. Before mixing, all of the aggregates were dried in the oven at 80 °C for 24 hours and then cooled down.

Table 1 Tested polypropylene fibers.

Fiber		Length (mm)	Diameter (µm)	Total number (10 ⁶)		Total length (km)	
				0.5 kg/m ³	1 kg/m ³	0.5 kg/m ³	1 kg/m ³
1	EUROFIBER PRO-MIX 6/32	6	31.7	114	228	683	1366
2	EUROFIBER PRO-MIX 12/32	12	31.7	57	114	683	1366

Two types of PP fibers from Baumhüeter were used (see Table 1). In addition to fiber-free case, two fiber dosages of 0.5 and 1 kg/m³ were used. Table 2 presents all the tested mixes. Example of explanation of mix name: C2-12/32-1 stands for concrete 2 containing PP fibers with a length of 12 mm and a diameter of 32 µm with a dosage of 1 kg/m³.

Table 2 Mix proportions of the materials in kg/m³.

Mix	Cement CEM III/A	Water	Filler	Sand 0/1	Gravel 6.3/10	Gravel 14/20	PP fibers 6/32	PP fibers 12/32	SP
M-0	500	200	120	1557	-	-	-	-	10
M-6/32-0.5							0.5	-	
M-6/32-1							1	-	
M-12/32-0.5							-	0.5	
M-12/32-1							-	1	
C1-0				623	-	-	-	-	3.75
C1-6/32-0.5							0.5	-	
C1-6/32-1							1	-	
C1-12/32-0.5							-	0.5	
C1-12/32-1							-	1	
C2-0	-	952	-	-	-	2.5			
C2-6/32-0.5				0.5	-	2			
C2-6/32-1				1	-				
C2-12/32-0.5				-	-				
C2-12/32-1				-	-				

Cylindrical samples of 11 x 22 cm² for compressive strength test at 28 days and prismatic samples of 20 x 20 x 10 cm³ for fire tests were cast and demolded after 24 hours and placed in water for 60 days. The properties of fresh and hardened materials such as compressive strength at 28 days and water content of mixes are given in Table 3.

Table 3 Fresh and hardened properties of cementitious materials.

Mix	Fresh properties		Hardened properties	
	Slump (mm)	Slump flow (mm)	Average $f_{c28, cyl}$ (MPa)	Water content (%)
M	354 ± 15	-	41.3 ± 2.5	6.10 ± 0.62
C1	-	790 ± 21	90.1 ± 5.3	4.90 ± 0.47
C2		626 ± 41	79.7 ± 0.3	4.54 ± 0.39

Compressive strength was measured on three samples and water content - on two samples. In order to determine water content, samples were dried at 80 °C until mass stabilization. The sample is considered dry when the difference between the two consecutive daily mass loss measurements is less than or equal to 0.02% of the mass of the dry sample.

Experimental procedure

The fire tests were conducted using a furnace with a gas burner as seen on Figure 2A. The opening of the furnace is 20 x 20 cm². Butane is supplied to the burner and temperature is followed by three K-type thermocouples placed at 4, 10 and 16 cm from the bottom of the furnace opening and 1 cm from the heated face of the concrete specimen. Gas pressure is adjusted during the test so that the temperature measured close to the heated surface follows the ISO 834-1 fire curve (see Figure 2B).

Before conducting the test, an aluminum foil was glued on the lateral sides of the sample with a high temperature resistant glue in order to block moisture escape as seen from Figure 3A. The fire tests are performed on uniaxially loaded prismatic samples of 20 x 20 x 10 cm³ during 30 minutes. The loading is fixed to 5 MPa before beginning of the test. All of the tests were conducted on water saturated samples. The tested specimen was placed between two concrete blocks to distribute uniformly mechanical loading. The lateral sides of the tested specimen and support blocks were insulated by 12 cm of rock wool. The insulated and loaded setup before the start of the fire test is presented in Figure 3B. The furnace is placed in front of the setup and the gas in the burner is ignited (see Figure 3C). One face of the concrete sample was heated (20 x 20 cm²). During the test, each of the spalling events has been recorded. At the end of the test (see Figure 3D), after 30 minutes, the gas supply from the bottles is shut down, the burner is closed and sample is discharged.

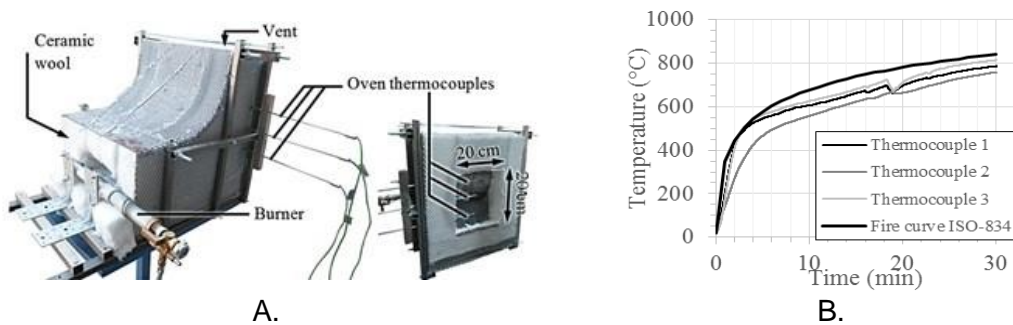


Figure 2 Experimental setup (A): Furnace [13] (B): ISO 834-1 fire curve and thermocouples' readings.

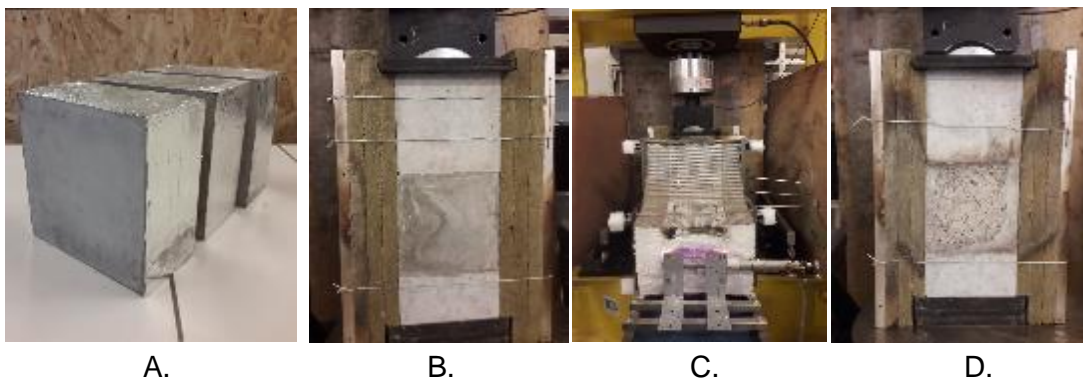


Figure 3 Testing procedure (A): insulation of lateral sides with aluminium foil, (B): before fire test, (C): during fire test and (D): after fire test.

EXPERIMENTAL RESULTS AND DISCUSSION

The average values of the results for the fire tests including time of the 1st spalling event, number of spalling events, mean and maximum spalling depth are presented in Table 4. Mean and maximum spalling depth were determined by means of photogrammetry. An image of spalled surface and spalling depth cartography for sample C2-6/32-0.5 are provided in Figure 4. The error from photogrammetry is 4.2%.

Table 4 Average values of test results.

Mix	1 st spalling event (min)	Number of spalling events	Mean spalling depth (cm)	Maximum spalling depth (cm)
M-0	15	1.5	0.95	3.75
M-6/32-0.5	12	1.67	0.62	2.18
M-6/32-1	-	0.33	0.27	1.3
M-12/32-0.5	14.5	0.67	0.49	1.9
M-12/32-1	-	0	0	0
C1-0	9.3	3.33	1.04	2.78
C1-6/32-0.5	8	3.5	0.35	1.17
C1-6/32-1	9	2.5	0.39	1.68
C1-12/32-0.5	13	1	0.25	0.84
C1-12/32-1	9	1.67	0.3	0.84
C2-0	5.7	6.5	0.54	1.36
C2-6/32-0.5	6	4	0.04	0.58
C2-6/32-1	5	3	0.03	0.53
C2-12/32-0.5	6	4.67	0.1	0.79
C2-12/32-1	6.3	3.33	0.18	1.22

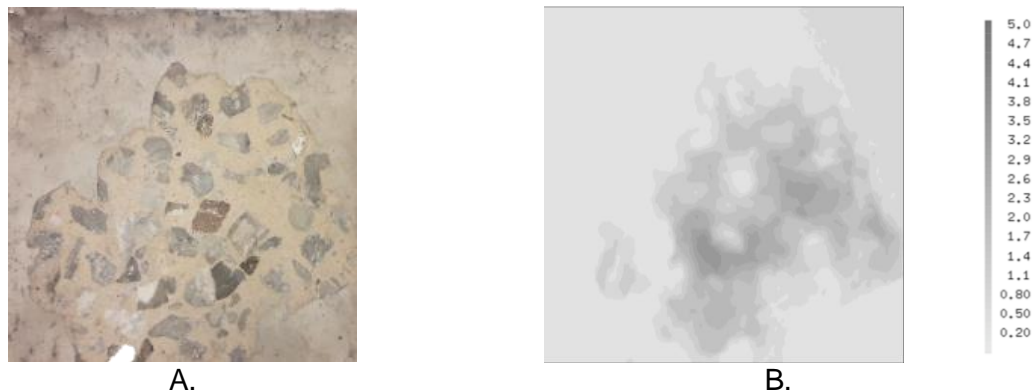


Figure 4 An image of the spalled surface for C2-6/32-0.5 (A) and cartography of the spalling depth (B). All the measurements are in cm.

Relationship between mean and maximum spalling depth and spalled volume

Mean spalling depth is calculated as a spalled volume over the exposed surface of the sample; therefore, a linear relationship between these variables is expected. We then plot an average value of maximum spalling depth as a function of an average value of mean spalling depth in Figure 5. It is observed that the relationship between these two quantities is linear. Therefore, in this study we will present spalling results in terms of mean spalling depth.

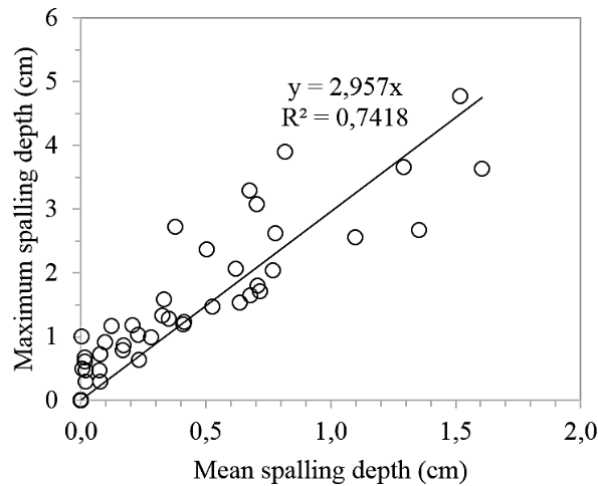
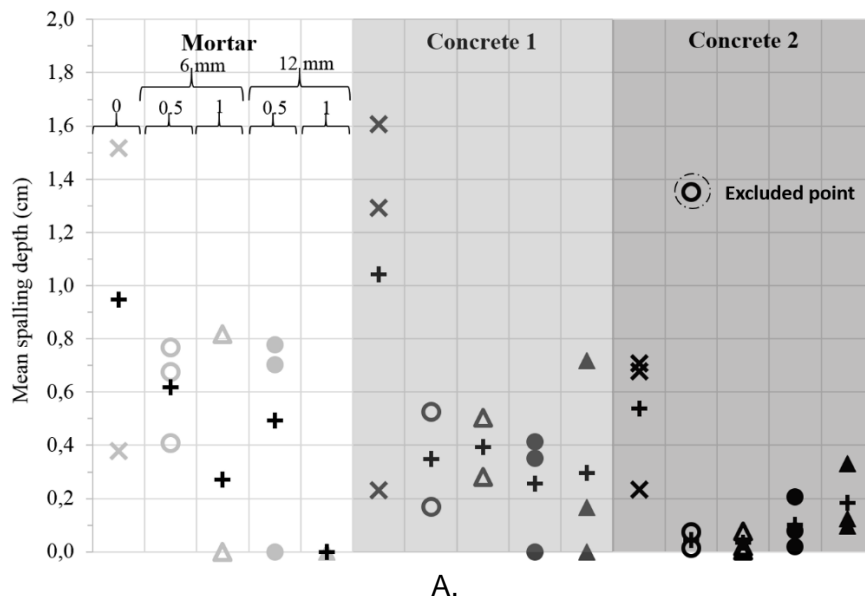
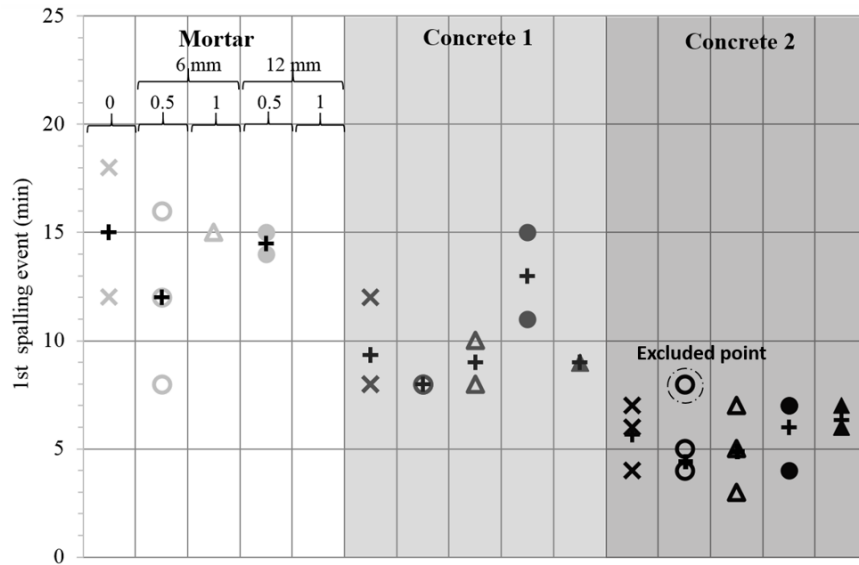


Figure 5 Linearity between average values of maximum and mean spalling depth.

Influence of aggregate size on spalling

Next we study the influence of the aggregate size on spalling of cementitious materials. As observed from Figure 6A, mortar samples (M) have the highest values of mean spalling depth for spalled samples compared to concrete 1 (C1) and concrete 2 (C2). The increase of the aggregate size decreased the spalling as well as in [14, 15]. It is noted that spalling of C2 samples was less severe than of C1 in terms of spalling depth even if the compressive strength is just 12 % lower for C2 than for C1. It is interesting to notice that in [16], on contrary, the increase of the aggregate size from 18 mm to 25 mm has increased the extent of spalling. Concerning spalling pattern, spalling for mortar samples is more profound on the sides than in the center which is the opposite of what is observed on concrete samples C1 and C2.





B.

Figure 6 Spalling tests results: (A): Mean spalling depth, (B): 1st spalling event time.

The results of the literature show an increased risk of spalling with an increase of mechanical strength [17, 18]. The mortar (M) without fibers, despite its relatively low strength, exhibits spalling as important as C1 and more important than C2, whose compressive strengths are almost 2.5 times and twice higher than that of M. Two phenomena occur during heating that have contradictory effects. The increased strength of a cementitious material leads to a decrease in its permeability, an increase in pore pressures and an increase in the risk of spalling. At the same time, heating induces strains that are different for cement paste and aggregates: from about 150 °C, the cement paste shrinks while the aggregates have a positive coefficient of thermal expansion at any temperature [19-21]. This difference in behaviour, named as a thermal mismatch, induces cracks developing at the interface between the paste and the aggregates. The larger are the aggregates, the more developed the cracking network is.

In our study, at the end of the fire tests, mortar samples present less cracks, highly spaced between each other. For most of the mortar samples one big crack with a possible orthogonal crack was observed. A network of microcracks is very limited and dispersed with a distance between the cracks of about 50 mm. For the concrete samples, the cracking is more pronounced and visible. The distance between cracks increases with the size of the aggregate (approximately 15 mm and 30 mm for concrete 1 and concrete 2 respectively).

Evolution of spalling with a time

During the fire test the information about the 1st spalling event, number and time of each spalling event has been recorded. The 1st spalling event time for each mix is presented in Figure 6A. The graph of the cumulative number of spalling events as a function of the fire test duration for all the tests performed on each material can be observed in Figure 7. It can be seen that as the size of the aggregate increases, the 1st spalling event occurs earlier and number of spalling events increases. As we increase the size of the aggregates, we observe the increase in the frequency of the spalling events.

Concretes have significant cracking and high pore pressures due to their high compacity and water saturation [17]. Spalling can thus occur early after the start of heating, affecting a thinner layer which has been weakened by the formed crack network. The low-cracked mortar also has a relatively low pore pressure development. Due to its high permeability, delay in development of pore pressures and maximum of pore pressures appears leading to

delay of spalling.

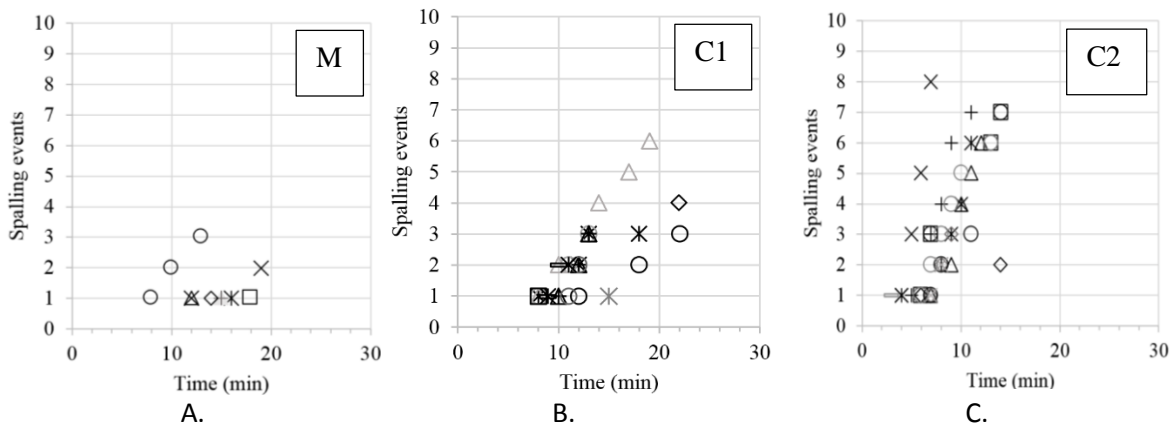


Figure 7 Cumulative number of spalling events as a function of test duration for (A): mortar, (B): concrete 1 and (C): concrete 2.

Influence of PP fibers on spalling

In order to evaluate the influence PP fibers on the spalling behaviour of cementitious materials, we plot Figure 8. Three different tracing lines were produced in order to observe the influence of the dosage for the same length of fibers, the influence of length for the same total length and for the same total number.

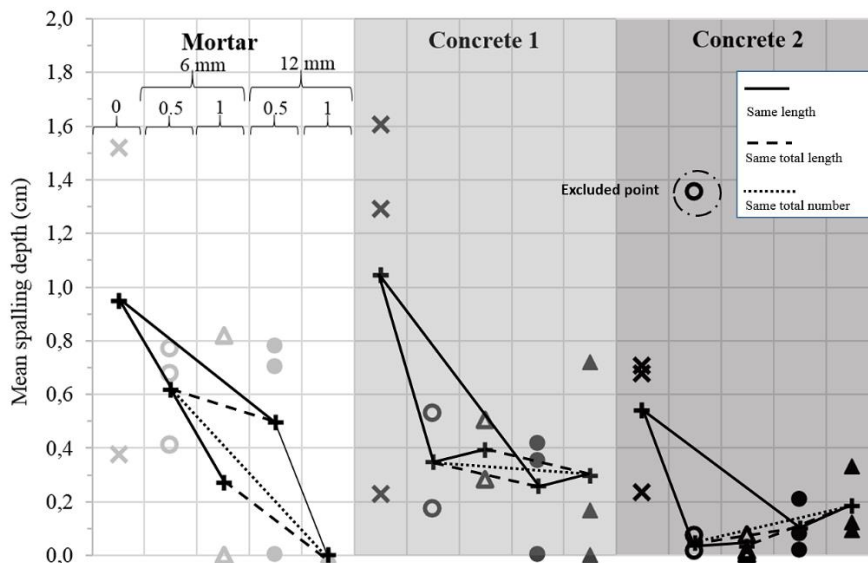


Figure 8 Mean spalling depth for all tested cementitious mixes. Full line shows PP fibers of the same length with a different dosage, dotted line- different length for the same total length and dot line – different length for the same total number.

Figure 8 shows the efficiency of fibers in reducing the risk of spalling even at relatively low dosages: 0.5 and 1 kg/m³. The addition of 0.5 kg/m³ of 6 mm fiber reduces the average spalling depth by 1.5, 3 and 13 times respectively for M, C1 and C2. The addition of 0.5 kg/m³ of 12 mm fiber is slightly more effective than 6 mm fibre in mortar and C1 but slightly less effective for C2.

The fibre network coupled with the crack network induces an increase in permeability if the fibre dosage and the fibre dimensions are sufficient to ensure percolation and decrease pore

pressures. In the case of mortar, 1 kg/m³ of 12 mm fibre is required to avoid spalling. In the case of C2, only 0.5 kg/m³ of 6 mm fibre is required to nearly prevent spalling (less than 0.1 mm average spalling depth). For C1 and C2, the addition of fibers above 0.5 kg/m³ has no efficiency in reducing spalling. It seems to be explained by the appearance of spalling very soon after the start of heating, which the fibers do not seem to help to avoid. This is due to the water saturation of samples as explained above. Indeed, the fiber-free C1 specimens showed instabilities between the 8th and the 22nd minutes. But 70% of the C1 fiber containing specimens showed instabilities between the 8th and 13th minutes. This highlights the ability of fibers to avoid the instabilities that occur later in the test and not the ones that occur early.

CONCLUSIONS

This paper presents an experimental study aimed at contributing towards the optimization of fiber geometry and dosage choice according to the granular skeleton of cementitious materials. First, a linear relationship between mean spalling depth, maximum spalling depth and spalled volume was established. Then, the influence of the aggregate size on the spalling depth and 1st spalling event occurrence was examined. We explain the high spalling depth of the mortar by its low cracking that leads to low increase of permeability during heating and high pore pressure development which results in delayed spalling. As concrete is cracked very early due to thermal mismatch of aggregate and cement paste, the pore pressures are released and less instabilities occur. As aggregate size increases, the number of events increases as well; whereas, mean spalling depth decreases. Lastly, we have investigated the influence of the PP fiber addition. The positive influence of fibers was observed for all the samples as the dosage of fibers increased to 0.5 kg/m³. It was noted that 1 kg/ m³ of 12 mm fibers was efficient for spalling prevention of mortar and 0.5 kg/m³ is sufficient to decrease significantly spalling in particular for C2. The increase of fiber dosage between 0.5 and 1 kg/m³ has no significant effect on spalling for C1 as well as for C2. A saturated state of samples presents a difficulty for PP fiber to prevent instabilities occurring early during the fire tests.

ACKNOWLEDGEMENTS

The authors would like to acknowledge that this work is carried out using the financial assistance from the program of the Investments for the Future of the French government managed by ANDRA.

REFERENCES

1. Bentz, D.P., "Fibers, Percolation, and Spalling of High-Performance Concrete", *ACI Materials Journal*, **97**, 351-359, 2000.
2. Debicki, G., Haniche, R., and Delhomme, F., "An experimental method to investigate concrete spalling in temperature", Proceedings of the 2nd International Workshop on Concrete Spalling due to Fire Exposure, 189-195, Delft, Netherlands, 5-7 October, 2011.
3. Kalifa, P., Chéné, G., Gallé, C., "High- temperature behaviour of HPC with polypropylene fibres: From spalling to microstructure", *Cement and Concrete Research*, **31**, 1487-1499, 2001.
4. Bei, S., Zhixiang, L., "Investigation on spalling resistance of ultra-high strength concrete under rapid heating and rapid cooling", *Case Studies in Construction Materials*, **4**, 146-153, 2016.
5. Bilodeau, A., Kodur, V.K.R., and Hoff, G.C., "Optimization of the type and amount of polypropylene fibres for preventing the spalling of lightweight concrete subjected to hydrocarbon fire", *Cement and Concrete Composites*, **26**, 163-174, 2004.
6. Persson, B., "Fire resistance of self-compacting concrete-SCC", *Materials and Structures*, **37**, 575-584, 2005.

7. Arai, T. and Furuichi, K., Persson, B., "Experimental study on reinforced concrete segment using fireproof concrete for shield tunnel in highway or railway", Proceedings of the 2nd International Workshop on Concrete Spalling due to Fire Exposure, 255-262, Delft, Netherlands, 5-7 October, 2011.
8. Mugume, R.B. and Horiguchi, T., "Effect of fiber type and geometry on maximum pore pressures in fibre-reinforced high strength concrete at elevated temperatures", Cement and Concrete Research, 42, 459-466, 2012.
9. Heo, Y.-S., Sanjayan, J.G., Han C.-G. and Han M.-C., "Effect of fiber type, length and numbers of fibers per unit volume on spalling protection of high-strength concrete", Proceedings of the 4th International Workshop on Concrete Spalling due to Fire Exposure, 211-220, Leipzig, Germany, 8-9 October, 2015.
10. Sideris, K. K. and Manita, P., "Influence of length and dosage of polypropylene fibres on the spalling tendency and the residual properties of self-compacting concrete after heated at elevated temperatures", Proceedings of the 3rd International Workshop on Concrete Spalling due to Fire Exposure, 02004, Paris, France, 25-27 September, 2013.
11. Hager, I. and Tracz, T., "The impact of the amount and length of fibrillated polypropylene fibres on the properties of HPC exposed to high temperature", *Archives of Civil Engineering*, **56**, 57-68, 2010.
12. Heo, Y.-S., Sanjayan, J.G. and Han M.-C., "Relationship between interaggregate spacing and the optimum fiber length for spalling protection of concrete in fire", *Cement and Concrete Research*, **42**, 549-557, 2012.
13. Miah, Md. J., Carré, H., Pimienta, P., Pinoteau, N. and La Borderie, C., "Effect of uniaxial mechanical loading on fire spalling of concrete", Proceedings of the 4th International Workshop on Concrete Spalling due to Fire Exposure, 124-131, Leipzig, Germany, 8-9 October, 2015.
14. Pan, Z., Sanjayan, J.G., and Kong, D.L.Y., "Effect of aggregate size on spalling of geopolymer and Portland cement concretes subjected to elevated temperatures", *Construction and Building Materials*, **36**, 365-372, 2012.
15. Nince, A. and Figueiredo A.D., "The influence of aggregate size in the risk of spalling in normal and high-strength concrete subjected to hydrocarbon fire", Proceedings of the 5th International Conference on Concrete for Structures, 9-20, Coimbra, Portugal, 7-8 July, 2005.
16. Robert, J., "Material properties related to fire spalling of concrete", Division of Building Materials, LTH, Lund University, Report TVBM-3143, Lund, Sweden, 2008.
17. Mindeguia, J.-C., "Contribution expérimentale à la compréhension des risques d'instabilité thermique des bétons" (in French), PhD Thesis, Université de Pau et des Pays de l'Adour, Anglet, France, 2009.
18. Mindeguia, J.-C., Carré, H., Pimienta, P. and La Borderie, C., "Experimental discussion on the mechanisms behind the fire spalling of concrete", *Fire and Materials*, **39**, 619-635, 2014.
19. Hager, I.G., "Comportement à haute température des bétons à haute performabce-évolution des principales propriétés mécaniques" (in French), PhD Thesis, l'Ecole Nationale des Ponts et Chaussées et l'Ecole Polytechnique de Cracovie, Krakow, Poland, 2004.
20. Lankard, D.R., Birkimer, D.L., Fondriest, F.F. and Snyder, M.J. "Effects of moisture content on the structural properties of Portland cement concrete exposed to temperatures up to 500 F", Proceedings of the 21st ACI Fall Meeting, 59-102, Memphis, Tennessee, USA, 1 January, 1971.
21. Schneider, U., "Verhalten von Beton bei hohen Temperaturen Deutscher Ausschuss für Stahlbeton", Ernst & Sohn, Berlin, 1982.